The Role of Aggregation of Melamine and Uric Acid in Kidney Stone Formation and its Inhibition by Small-Molecule Inhibitors in Solution and at the Solid-Liquid Interface: A Computational Approach

A Thesis Submitted

in Partial Fulfillment of the Requirements

for the Degree of

DOCTOR OF PHILOSOPHY

by

Krishna Gopal Chattaraj

to the

Department of Chemistry

Indian Institute of Technology Guwahati, India

2021

DEDICATED TO
MY PARENTS

Declaration

I hereby declare that the matter manifested in this thesis entitled "The Role of Aggregation of Melamine and Uric Acid in Kidney Stone Formation and its Inhibition by Small-Molecule Inhibitors in Solution and at the Solid-Liquid Interface: A Computational Approach" is the result of research carried out by me in the Department of Chemistry, Indian Institute of Technology Guwahati, India under the supervision of Prof. Sandip Paul.

In keeping with the general practice of reporting scientific observations, due acknowledgement has been made wherever the work described is based on the findings of other investigators.

Krishna Gopal Chattaraj

IIT Guwahati

Certificate

It is certified that the work contained in this thesis entitled, "The Role of Aggregation of Melamine and Uric Acid in Kidney Stone Formation and its Inhibition by Small-Molecule Inhibitors in Solution and at the Solid-Liquid Interface: A Computational Approach" has been carried out by Mr. Krishna Gopal Chattaraj for the Degree of Doctor of Philosophy under my supervision and the same has not been submitted elsewhere for adegree.

Prof. Sandip Paul
Thesis Supervisor
Department of Chemistry
Indian Institute of Technology Guwahati
Guwahati-781039, India

Preface

With the completion of my doctoral studies, it is a true pleasure to express my gratitude to the people who made this trip a fact and an incredible experience for me. First and foremost, I would like to express my heartfelt appreciation to my superior, Prof. Sandip Paul, for his excellent advice, relentless motivation, tremendous support, and assistance over the years. His door was always open for countless discussion sessions with him that taught me how science and its challenges could be made fascinating to ease out a solution, even during the tough times of the Ph.D. pursuit. I am also grateful to him for allowing me to pursue my ideas, and I could not have dreamed of having a better advisor and mentor for my Ph.D. career.

Besides my supervisor, I am sincerely obliged to the doctoral committee members, Prof. Gopal Das, Dr. Lal Mohan Kundu, Dr. Kalyan Raidongia, for regularly appraising my work and contributing valuable suggestions for its improvement. My sincere thanks go to all other faculty members in the department for their kind help at various stages of my doctoral work. I gratefully acknowledge the Ministry of Human Resource and Development (MHRD), India, for financial support and IIT Guwahati for providing the research facilities to carry out my research work. I would like to appreciate the IIT Guwahati super-computing facility PARAM-ISHAN, without which the completion of my thesis was not achievable within this period.

No words can express how grateful I am to my labmates Srijita, Saikat, Rabindranath, Rituparna, Aritra, Madhusmita, and Rimjhim for their consistent support, insightful discussions, and creating a harmonious working environment in the lab. Sincere gratitude to my seniors Dr. Rahul Sarma, Dr. Subrata Paul, Dr. Bhanita Sharma, Dr. Gargi Borgohain, and Dr. Shubhadip Das for sharing their helpful thoughts and insights during my Ph.D. days. I want to thank Tausif, a friend from my department, for his valuable scientific suggestions during my Ph. D. I would also like to thank Vikram, a project student whose contributions cannot be overlooked. I owe a lot to my IITG friends for making my Ph.D. journey joyful and memorable.

I take this opportunity to express my sincere gratitude and respect to all my teachers in school, college, and university days for preparing me academically and non-academically in various aspects of life. All the learning from them will be an asset in every walk of my life.

Finally, this dream could not have come true without my family's eternal love, encouragement, and blessings. I want to express my heartfelt appreciation to my mother for always being my best friend, philosopher, and guide. I sincerely thank my parents for their great sacrifices and patience, encouraging me to be a better person and inspiring me to fly high. Last but not least, I am fortunate to have my elder sister as one of the strongest pillars in my life.

Krishna Gopal Chattaraj

2021

"All great achievements in science start from intuitive knowledge, namely, in axioms, from which deductions are then made. ⋯ Intuition is the necessary condition for the discovery of such axioms."

— Albert Einstein

Outline of the Thesis

Chapter 1

Introduction

"All things are poisons, for there is nothing without poisonous qualities. It is only the dose which makes a thing poison."

— Paracelsus

■ MELAMINE IN THE URINARY STONE FORMATION

Contagions and pollutants in the atmosphere produce a viable number of health perils as synthetic compounds get more prevalent in all facets of life. Melamine (MM, Figure 1-1(a)) has appeared as a nephrotoxin in both pets and humans over the last several years. It contains 66 percent nitrogen by weight, and it was applied in adulterating pet food since 2003, apparently to misinterpret the protein content. The prevalent protein assays, such as the Kjeldahl method, were used to quantify total nitrogen content in non-protein and protein.[1, 2] MM (2,4,6-triamino-1,3,5-triazine) is a commercially synthesized organic base derived from urea. It was patented in the United States in 1958 as a low-cost non-protein nitrogen source for ruminants. On the other hand, ruminants fed MM were found to have advanced kidney disease as early as 1968. MM was later thought to be an unacceptable non-protein nitrogen source for ruminants.[1, 3, 4, 5, 6, 7, 8] MM industrial production and industrial uses were primarily raised in China during the 1990s.[1] The first case of MM-related nephropathy was recognized in March 2004, when at least 6,000 dogs and cats in several Southeast Asian countries accommodated renal malfunction. After three years, a significant outbreak of renal dysfunction in animals due to MM occurred in Northern America. The first records of disease and death among the cats consuming their items were sent to pet foods manufacturers (Menu Foods, Mississauga, ON, Canada) in February 2007. Around the same time, one company carrying out routine palatability tests for animal feed suppliers had confirmed that 7 out of 20 cats who had eaten the foods in question had died or been euthanized. On March 16, 2007, on account of fears about kidney disease in animals consuming the meal, Menu Foods recalled their canned pet food. Despite this, over 39,000 cats and dogs had been reported to have developed renal failures in the outbreak, and 8,500 unconfirmed animal deaths had been befallen. Reports on urinary stones in children started to appear in the summer of 2008 in China. Following the diagnosis of kidney stones in 16 infants in Gansu Province, it had been found that all had been used formula milk produced by a dairy firm (Sanlu Group, Shijiazhuang, China).[1, 9, 10, 11, 12, 13, 14]

Several experiments had shown that in rats and mice, bladder stones were formed from diets including MM.[15, 16, 17, 18] Ogasawara *et al.* used high-performance liquid chromatography to investigate the structure of these MM-related bladder stones and found the equimolar concentrations of MM and uric acid (UA, Figure 1-1(b)).[17] Moreover, [illegible] on MM toxicity were not available at that time. On the other hand, the

effects of MM contamination in human babies were similar to animal tests of pure MM toxicity and resembled those of young children with reflux nephropathy (formerly known as chronic atrophic pyelonephritis). In general, the death rate of humans is minimal, but the stone forming rate is high. Examination of kidney stones from Chinese babies who consumed formula milk contaminated with MM constantly revealed that the stones were composed of a MM-UA mixture. Such mixture has been supposed to form a crystalline lattice structure with an equimolar ratio of MM and UA (Figure 1-2). On the other hand, in infant stones, the ratio of UA to MM was between 1:2 to 2.1:1.[19, 20, 21, 22, 23, 24, 25, 26] These findings indicated that MM-UA stones could differ in structure or consist of heterogenous mixtures of UA crystals and MM-UA complexes. Research into MM-related toxic effects, including obstructive nephropathy from MM precipitation in the lower urinary region, with stones believed to consist of MM-UA complexes, was suggested by human renal histopathology. Several trials had used ultrasonographic imaging in the renal collecting system, including the renal calyces, pelvis, ureters bilaterally, bladder, and urethra, to locate MM-related kidney stones in infants. The difference between various types of stone found on humans and animals showed that MM-UA stones is developed when MM is present, but cyanuric acid is not. When MM and cyanuric acid both are present, MM-cyanuric acid stones can easily be formed. Studies of MM-UA and MM-cyanuric acid crystals by X-ray diffraction study showed that such propensity could exist, as crystals of MM-cyanuric acid use less energy to build than crystals of MM-UA. Although the vast proportion of human renal disease due to MM was confirmed in babies and young children due to milk powder malnutrition devoured in this section of the population, one study found that adult patients with UA urolithiasis had higher levels of urinary MM than age-matched controls.[1, 2, 17, 23, 24, 27, 28, 29, 30, 31]

However, the amount of urinary MM found in adults with UA urolithiasis was much lower than in children measured by Lam *et al.* (median: 21.0g/mmol versus 0.50g/mmol creatinine).[29, 31] This result indicated that there might be a persistent risk of renal injury for adults with chronic exposure to low levels of MM, likely from non-food sources, including plasticware. MM-UA stones are radiolucent and lack calcium. B-mode ultrasonography is recommended for their detection. MM-related stones possess less echogenicity than calcium oxalate stones, with minimal or no posterior acoustic shadowing and frequent comet-tail artifacts. The stones with MM are usually smaller, and most stones have a diameter of less than 1.5 cm. Large stones are associated with a higher concentration of MM in foods

eaten. All foods suspected of being tainted with MM should immediately be avoided when calculi linked to MM are found.[25, 32, 33, 34, 35, 36]

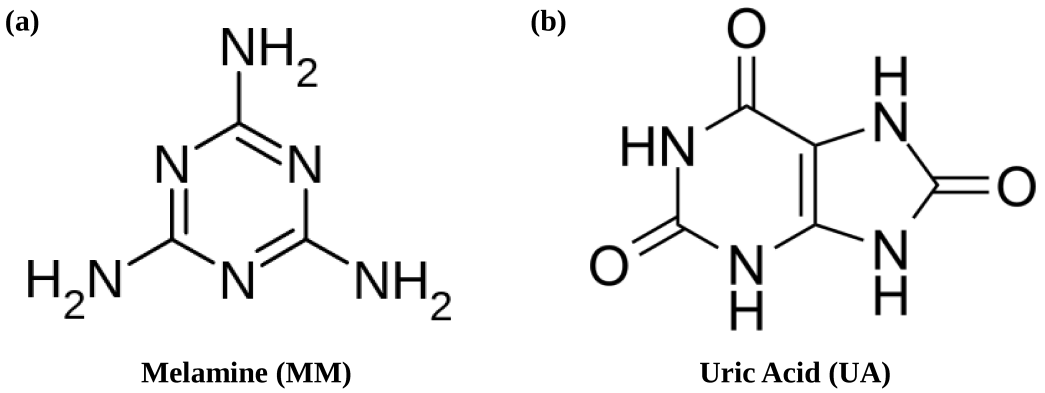

Figure 1-1. Chemical structures of (a) Melamine (MM) and (b) Uric Acid (UA).

■ MELAMINE TOXICITY COUPLED WITH URIC ACID

MM being a nitrogen-rich compound, can make multiple hydrogen bonds with UA and others (Figure 1-2 (a)). MM is safe when precisely utilized, but it can be perilous when consumed in large quantities, which can take place when ingredients are adulterated. Few experimental studies had investigated the development of MM aggregates in the aqueous medium.[37, 38, 39, 40, 41, 42, 43] While the critical aggregation of MM was not achieved due to its poor water solubility, the aggregation trends of MM and its variance with concentration were determined. Furthermore, MM aggregates were suggested to form clusters, including dimers, trimers, or polymers, by hydrogen bonding in water. In addition, with the increasing concentration of MM, this aggregation trend was increased. There have been allegations of illegally adulterating foods with MM, particularly in baby feed, to increase its nitrogen content in the constituent proteins. As a result, several food safety accidents

worldwide, including the development of kidney stones, have occurred in newborns. The evaluation of these kidney stones showed the existence of MM and UA. In addition to human effects, animal toxicity, including nephrolithiasis, chronic kidney infection, and bladder cancer, has also been found.[1, 2] The risk of developing kidney stones is steadily increased with the use of MM. In baby kidney stones, the [UA]:[MM] molar ratio ranged from 1:2 to 2.1:1, meaning the MM-UA stone ratio changes.[1, 2] Anderson *et al.*[26] had first estimated the crystal structure of MM-UA composite, revealing the shape of hydrogen-bonded sheet-like lattices in MM and UA mixture. These lattices are supposed to form sheet-like structures joined by hydrogen bonding to form a 3D structure kept together by stacking interaction between the two layers. The hydrogel was shown to consist of two separate hydrogen-bonding adjustments of complementary donor-acceptor pairs in equimolar amounts in the body.[26, 44] The analysis results show that the stone development is caused by the 1:1 hydrogen-bonded interactions between all components. The 1:1 complex of UA and MM was later found to form a nonplanar structure that was marginally folded in regards to the MM plane and maintained stability with several hydrogen bonds.[45] In 2015, it was

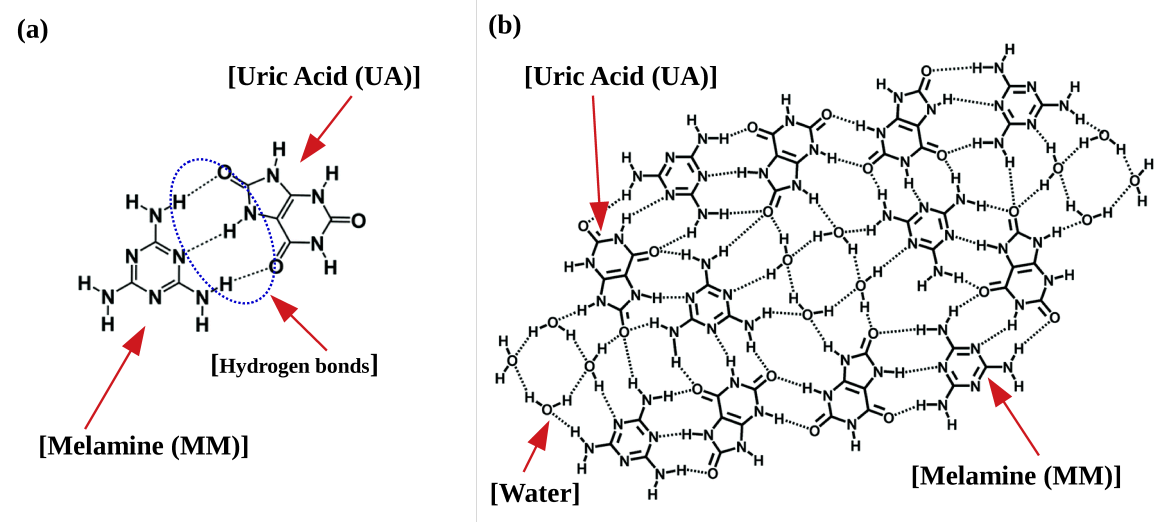

Figure 1-2. (a) Hydrogen bonding between MM and UA, and (b) planar supramolecular structure for MM-UA interaction. .

proposed that hydrogen bonds and π-π stacking interactions are responsible for the snug

complex association.[46] MM and UA associations in the formation of kidney stones imply that reducing UA levels in the kidney may reduce the appearance of renal stones. Since the production of renal calculi has been shown in the supersaturated (as a result of excessive MM dosage) urine, but not in the under-saturated urine. Therefore, the low-dose consumption of MM can be beneficial in the prevention of renal calculi. Thus in the debate about MM-UA-related renal calculi, MM and UA are of essential importance.[1, 2]

■ POSSIBLE TREATMENT FOR KIDNEY STONE

Calculi concerning MM were classified as either "sand-gravel-like" or "lump-like." After a few days of conservative therapy, including urinary alkalinization, most sand-grave-like stones (80% of all stones) can be instantaneously dislocated. Nevertheless, lump-like stones are difficult to remove and often require invasive urological treatments, such as percutaneous nephrolithotomy, cystoscopy, cystostomy, or retrograde ureteral catheterization, despite the conservative management. Renal dysfunction is commonly caused by a urinary obstruction in a small number of patients with urolithiasis associated with MM. The complications encountered in these cases include nausea, vomiting, abdominal distention, fever, hematuria, oliguria, and anuria.[25, 35, 47]

Most patients suffering from renal failure with MM should be treated with conservative fluid injection and urinary alkalinization. Consequently, the restoration of renal function usually occurs shortly upon extinction of the calculi. The reduction in the propensity for increased probabilities of MM-related calculi and the deportation rate can be made evident from potassium sodium hydrogen citrate use. Infants who are given early peritoneal dialysis or hemodialysis have restored renal function.[27, 47, 48, 49, 50] However, there is evidence of renal replacement therapy, such as hyperkalemia and acidosis. Because MM combines with UA to form stones, a reduction in the UA level in the urine may be a technique for treating MM-UA stones. Medicines to reduce uricosuria, including allopurinol,[51, 52, 53] theobromine,[256, 257, 56] vitamin C,[57, 58, 59, 60, 61, 62, 63, 64, 65, 66] potassium citrate,[44] and febuxostat inhibitors of xanthine oxidase,[1] may be helpful as adjunct therapeutics minimizing and preventing the production of calculi associated with MM. Moreover, they can expedite the removal of kidney stones.

Intakes of MM in children have tended to induce retrograde nephropathy attributable to lower urinary tract MM precipitation, and to MM-UA stones. Most MM-UA stones (sand-gravel (80%) are removed in weeks, but in infants 'lump stones' (20%),

intrusive therapy may require transplant.[27, 47, 48, 49, 50] Due to the MM-UA composite structure's unique structural and functional features and its relation with the MM-induced renal stone formation, we have studied the structural aspects of MM and UA in ambient conditions to proffer their underlying mechanisms of interactions. Therefore, in the present thesis, an attempt has been performed to explain the molecular mechanism of aggregation of MM and UA in kidney stone formation and its inhibition by small-molecule inhibitors in solution and at the solid-liquid interface. Crystal precipitates are kidney stones identified free or attached to renal papillae in the renal calyx and pelvis. Organic and crystalline segments produced by supersaturation of urine are included. On renal papillary facades, the most common type of kidney stone is formed. The stone's growth is achieved by aggregating preformed crystals or secondary crystal nucleation on the matrix-coated surface. Substances are inhibitors that reduce the initiation of supersaturation, nucleation, crystal expansion, rate of aggregation, or processes of stone-forming. Inhibitors may have an undeviating effect on urinary conditions or behave obliquely by feuding with crystals. There is, hence, an imperative mechanism for the development and preservation of the deposition of kidney stones and the adsorption to the crystal surface of antibodies.[67, 68, 69, 70] Thus, a detailed study of the adsorption nature of UA and MM-UA composite on a solid surface would be beneficial to undestand the molecular nature of kidney stones developed in humans. The simulation works and concluding statements are manifested in the succeeding seven chapters. The following section of the present chapter deals with the fundamental techniques of molecular dynamics (MD) simulations used in our works. The comprehensive summaries of the applications of these techniques for explicit systems are presented in succeeding chapters. This is followed by a concise summary of the work impersonated in the current dissertation.

■ METHODOLOGY

In the present thesis, classical MD simulation technique has been used. It is a widely used method to investigate the structure and dynamics of biomolecular systems, such as proteins, nucleic acids, and small molecules like amino acids, sugars and drugs. In MD simulation, the potential energy function (U) is described by all interactions between the atoms that are covalently bonded as well as non-bonded interactions between atoms and molecules in the condensed phase. The interactions between particles are governed by The [illegible] force field parameterization [71].

The potential energy function is written as a sum of bonded and non-bonded interaction terms

$$U = U_{bond} + U_{angle} + U_{dihedral} + U_{vdw} + U_{Coulomb} \tag{1.1}$$

The first three terms (U_{bond}, U_{angle}, $U_{dihedral}$) are the bonded terms, which describe the bond stretching, angle bending, and torsion rotation, and the last two terms are for the non-bonded potential. In bonded terms, the bond and angle contributions are described by harmonic potentials and all of the interactions between directly bonded atoms (1-2 interactions), angles (1-3 interactions, where two atoms bonded to a common atom), and torsion (interactions between pairs of 1-4 atoms) are defined as:

$$U_{bond} = \sum_{bonds} K_b(b_{ac} - b_{eq})^2 \tag{1.2}$$

$$U_{angle} = \sum_{angles} K_\theta(\theta_{ac} - \theta_{eq})^2 \tag{1.3}$$

$$U_{dihedral} = \sum_{dihedrals} \frac{V_n}{2}(1 + cos(n\phi - \delta)) \tag{1.4}$$

The letters b, θ, ϕ, and δ represent the bond length, bond angle, dihedral angle, and phase angle, respectively. The subscripts ac stands for actual and eq stands for equilibrium. The parameters K_b, K_θ, and V_n are the force constants for bond length, bond angle, and dihedral angle, respectively.

The non-bonded potentials are calculated using two terms, the first one is the Lennard-Jones term (U_{vdw}) [72] describing the van der Waals interaction [73], and the second one is the Coulomb term ($U_{coulomb}$) [74] that deals with the electrostatic interactions between particles having partial charges on them. The non-bonding interaction terms are defined as:

$$U_{vdw} = \sum_i \sum_{i<j} 4\epsilon_{ij}\left[\left(\frac{\sigma_{ij}}{r_{ij}}\right)^{12} - \left(\frac{\sigma_{ij}}{r_{ij}}\right)^{6}\right] \tag{1.5}$$

$$U_{coulomb} = \sum_i \sum_{i<j} [\frac{q_i q_j}{4\pi\epsilon_o r_{ij}}] \tag{1.6}$$

where the overall sum is over all the atom pairs i and j. Lennard-Jones parameters σ and ϵ are the diameter of atomic sites and well depth energy, respectively. r_{ij} is the inter-atomic distance. q_i and q_j are the partial charges on interaction sites i and j and ϵ_o is the electrical

The aim of the MD simulation is to observe the evolution of atomic coordinates in time. We consider an N-particle system characterized by the following Hamiltonian

$$H = \sum_{i=1}^{N} \frac{p_i^2}{2m} + U(\mathbf{r}^N) \tag{1.7}$$

where m is the mass of each particle, p_i is the momentum of the i-th particle and $U(\mathbf{r}^N)$ is the total potential energy of the system which includes all particle-particle interactions. The coordinates of the particles are denoted by $\mathbf{r}^N = \{\mathbf{r}_1, \cdots, \mathbf{r}_N\}$. The position and velocity of i-th particle is represented by $\mathbf{r}_i$ and $\mathbf{v}_i$, respectively. The method of molecular dynamics consists of solving the equation

$$a_i = \frac{\mathbf{F_i}}{m_i} \tag{1.8}$$

where $i = 1, 2, ...N$, m_i is the mass of i-th particle and $\mathbf{F}_i$ is the force acting on particle i. This equation is obtained easily from the Lagrangian

$$L = \frac{1}{2}\sum_{i=1}^{N} m_i \mathbf{v_i}.\mathbf{v_i} - \frac{1}{2}\sum_{i=1}^{N}\sum_{j\neq i}^{N} u(r_{ij}) \tag{1.9}$$

where the potential U has been assumed to be the sum of pair potentials u_{ij}. The Lagrangian equation of motion is

$$\frac{d}{dt}(\frac{\partial L}{\partial \dot{q}_i}) - \frac{\partial L}{\partial \dot{q}_i} = 0 \tag{1.10}$$

It is clear from eq. 1.10 that the dynamics of particles is described by 3N number of second order differential equations.

It is also possible to write down the Hamiltonian (H) for the system and solve the the Hamiltonian equations of motion

$$\dot{\mathbf{q}}_k = \frac{\partial H}{\partial p_k} \tag{1.11}$$

$$\dot{\mathbf{p}}_k = -\frac{\partial H}{\partial q_k} \tag{1.12}$$

where $\mathbf{q}_k$ and $\mathbf{p}_k$ represent generalized coordinates and momenta. For a system with pairwise interaction potential, the Hamiltonian is

$$H = \frac{1}{2}\sum_{i=1}^{N} m_i \mathbf{v_i}.\mathbf{v_i} + \frac{1}{2}\sum_{i=1}^{N}\sum_{j\neq i}^{N} u(r_{ij}) \tag{1.13}$$

and Eqs. 1.11 and 1.12 yield

$$\frac{dr_i}{dt} = \frac{\mathbf{p_i}}{m_i} \tag{1.14}$$

$$-\dot{\mathbf{p}}_i = -\nabla \mathbf{u} = \mathbf{F_i} \tag{1.15}$$

where i=1,2,....N. There are now $6N$ first order differential equations to be solved.

The equation of motion is solved numerically to yield particle velocities and positions as a function of time. It is usually integrated by using finite difference approach. The Verlet algorithm is one of the most commonly used algorithm for this purpose [75]. The advantage of using the Verlet algorithm is that its implementation is straightforward and storage requirements are modest. Although, it has the disadvantage of moderate precision during the calculation and velocity does not appear explicitly in the Verlet integration. As an improvement to the Verlet algorithm, the leap-frog algorithm [76] has been developed. But, it has a disadvantage that the positions and velocities are not synchronized. As an alternative of Verlet or the leapfrog algorithm, Velocity Verlet algorithm has been developed and the following relations are used to calculate new position and velocity at the same time:

$$r(t+dt) = r(t) + v(t)dt + \frac{1}{2}a(t)dt^2 \tag{1.16}$$

$$v(t+dt) = v(t) + \frac{1}{2}[a(t) + a(t+dt)]dt \tag{1.17}$$

To calculate the velocities at time t+dt, this method requires acceleration at time t and t+dt. In the present work, we have employed Velocity Verlet algorithm.

■ PRESENT WORK

Hydrogen bonding has been extensively used for the noncovalent synthesis of various supramolecular assemblies, including polymers, arrays, and networks. In particular, MM, a nitrogen-rich organic compound, is known to form remarkably stable lattices joined by the network of hydrogen bonds with UA. Analysis of the Kidney stones showed that they are composed of MM and UA in nearly equimolar amounts and suggested that 1:1 hydrogen-bonded interaction of the two components may be responsible for the kidney stone formation. In this thesis, we have examined the detailed mechanisms of the interaction of MM and UA in ambient conditions. Along with this, we have focused on the self-aggregation properties of MM and UA also. Moreover, the effect of small molecule inhibitors on the MM-UA aggregates is also studied in the solution phase and at the solid-liquid interface.

 Chapter 1 introduces the MM-UA conjugate cluster's formation and stability along

with their individual aggregated structure through a literature survey. Moreover, the probable inhibition mechanisms of MM-UA interaction by proffering inhibitory methods are also discussed. **Chapter 2** manifests the structure and thermodynamics of MM association in aqueous solution (**Chapter 2a**) and the modulation of its structural properties in aqueous solution by the alteration of temperature (**Chapter 2b**). **Chapter 3** deals with the underlying mechanistic insights into MM and UA complexes' structural properties with compositional variation under ambient conditions. **Chapter 4** presents the inclusion of small π-stacking inhibitors like theobromine (TB, **Chapter 4a**) and allopurinol (AP, **Chapter 4b**) to modify the UA aggregation with possible changes in MM-UA clusters responsible for kidney stone formation. **Chapter 5** introduces an inhibitor, potassium citrate (K_3Cit), with a prominent hydrogen bonding ability to alter the MM-UA aggregation. **Chapter 6** illustrates MM-UA inhibition, including UA accumulation's repression, by proposing several small inhibitors like vitamin C (Vit-C, **Chapter 6a**), TB, and AP (**Chapter 6b**) in the solution phase and solid-liquid interface. In the last chapter, i.e., **Chapter 7**, we have summarized the overall conclusions to ponder the interpretation of MM-UA interaction inhibition and their self-aggregation under different chemical and thermal conditions and their structural alternation introducing various drugs (or inhibitors).

Chapter 2

2a: The Structure and Thermodynamics of Melamine Association in Aqueous Solution

"Wherever the art of medicine is loved, there is also a love of humanity."

— Hippocrates

Overview: The aggregation propensity of melamine (MM) molecules in aqueous solutions in a range of MM concentrations is investigated by means of a combination of theoretical and experimental approach. It is observed that the hydrogen bonding interactions of sp^3 nitrogen atoms of one MM with sp^2 nitrogen atoms of another MM play a major role in the MM association. This finding is complemented by the observed favorable electrostatic energies between MM molecules. The estimation of the orientational probability of MM aromatic ring rules out any role of $\pi - \pi$ interaction in MM association. Further, the quantum chemical calculations suggest that a MM molecule prefers to bind with another like molecule with a dihedral angle ranging from 36^o to 46^o. We have also determined the dimer existence autocorrelation functions to investigate the MM-dimer stability with time in aqueous solution. Our results are well validated by the experimental findings. Moreover, the thermodynamics of MM association reveals that the association process is essentially driven by enthalpy and this enthalpy driven phenomenon is also confirmed by the experimental isothermal titration calorimetry (ITC) measurements.

■ INTRODUCTION

Melamine (MM), also called 1,3,5-triazine-2,4,6-triamine (Figure 2a-1), is a trimer of cyanamide. It can form MM resin through condensation polymerization with formaldehyde making it an important chemical for plastics and coating industries. It has also wide applications in laminates, glues, adhesives, and flame retardants industries due to the presence of 66% nitrogen (by molecular weight) in it.[77, 78, 79] In general, MM is considered to be safe for normal use but can be unsafe for consumption. The study of MM rose to attention with shocking "poisonous milk" scandal in China.[2] Since MM has high nitrogen content, a key indicator in protein content detection in dairy products, it was added into mainstream milk powder brands in 2008, which on consumption led to urinary bladder or kidney stones in infants and young children, with even few deaths.[2] Thus MM is prohibited for use in food, feed or fertilizer production.[2] Therefore, the studies on the structure of MM and its detection are of significant value.

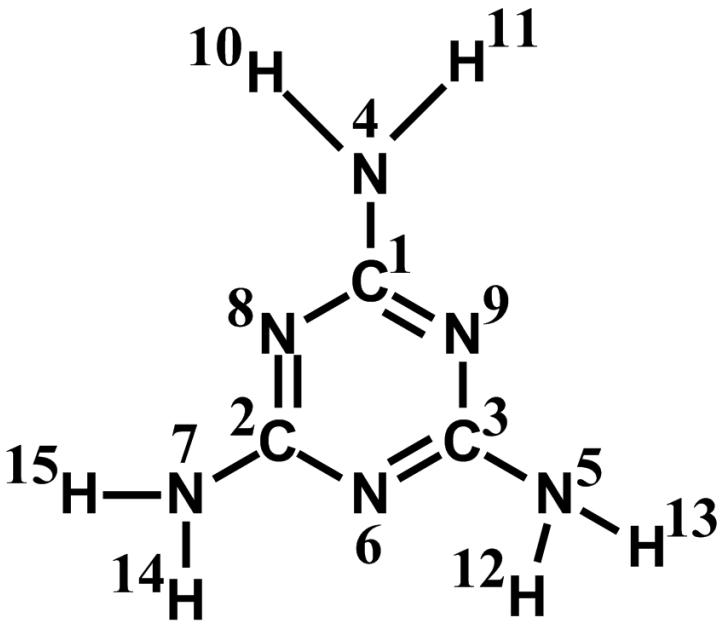

Figure 2a-1. *Structure and atom numbering of melamine (MM) molecule.*

The studies of the structural and spectral characteristics of MM molecules can be tracked back ages ago. Hughes[80] first studied the crystal structure of MM in 1941, which was subsequently validated[81] in 1974. In 1997, Yu-Lin Wang *et al.*[82] reported IR spectroscopy and theoretical vibrational calculations of the MM molecule, from which, the

structure of MM can be easily resolved. Structurally, MM contains 3- endocyclic nitrogen-atoms in the triazine ring with 3- exocyclic $-NH_2$ groups by which it can hydrogen-bond to itself and also with other molecules.

Currently, one of the most significant areas of research in supramolecular chemistry is the study of self-assembly process to create complex structures. In recent years, an increasing interest in nanoscale devices has stimulated the research of intra- and intermolecular forces that control and lead to the creation of ordered one-, two- and three-dimensional nanostructures from the self-assembly of small molecular building blocks by using hydrogen bonds and $\pi - \pi$ interactions. MM has an immense contribution in this field due to its structural functionalism.[83] C. T. Seto *et al.*[84] developed a methodology to construct large, soluble, self-assembling structures, based on the hydrogen-bonded complex by introducing MM with the determination of enthalpy of formation and entropy of solvation of the complex. Liana Vella-Zerb *et al.*[85] and Zhaocun Shen *et al.*[86] separately showed that the hydrogen bond interactions between MM and other molecules forces MM to crystallize in layers using MM as one of the main building blocks. The determinants of cyanuric acid and MM assembly in water were also observed.[87] The supramolecular frameworks of MM by extensive hydrogen bonds between different sites have been proposed[88, 89, 90, 91, 92, 93, 94, 95, 96, 97, 98] in solvents as well as upon solid surfaces [99, 100, 101]due to having its hydrogen donor-acceptor property. Single component assembled MM structures on various surfaces like Cu/Au(111) were shown both experimentally and theoretically.[102, 103, 104, 105, 106, 107]

In 2007, an elastic hydrogel was prepared from the sonication of rigid small complementary molecules such as MM and uric acid (UA).[26] Later on Hiroya Asami *et al.*[45] in 2014, and Hiroyuki Saigusa *et al.*[108] in 2015, reported separately about the exact mechanism of formation of urinary stone by the hydrogen bonded 1:1 complex between MM and UA by using different spectroscopic methods. The kidney stone is a serious threat, caused mainly by the aggregation and deposition of MM in kidneys in human beings and animals. Roy L. M. Dobson *et al.*[109] identified the toxicity of MM-contaminated pet food leading to an outbreak of renal toxicity in cats and dogs. For these reasons, the researchers developed various methods for facile detection of MM.[110, 111, 112, 113, 114, 115, 116, 117, 118, 119, 120, 121, 122, 123] From the work of Jiao Peng *et al.*[110] it is clear that the chemistry of MM in water is of great interest. R. P. Chapman *et al.*[124] determined the solubility of MM in water over a temperature range experimentally. Furthermore, the

supramolecular assembly of MM in water by crystallization, which clearly shows the formation of MM association through hydrogen bonding interactions (solely through its $sp^2 - sp^3$ bonding sites) has also been reported in several studies.[125, 126, 127] Moreover, it has been reported that MM, with its ability to form nine hydrogen bonds in total, directs the self- assembly to form a hexagonal porous network in two dimensions. It is further observed that each MM molecule interacts with like molecules at an angle of 120 ± 12^o at the apex between two interacting units.[128]

Although various studies investigated the aggregation tendency of MM in water experimentally, very little attention has been paid towards the atomistic details of MM association in water. Nicolate E. Mircescu *et al.*[129] carried out FTIR, FT-Raman, SERS and DFT measurements on MM clusters taking 10 MM molecules. The structural and spectral characteristics of isolated MM cluster in the ground state were reported by few other studies too.[130, 131, 132, 133]

A few recent experimental studies[129, 130, 125, 134, 126, 135, 136] have explored the tendency of formation of MM aggregates in aqueous medium. Though they did not achieve the critical aggregation concentration of MM due to its low solubility in water, but the aggregation tendency of MM and its variation with concentration has been shown. Moreover, it has been proposed that the MM aggregates through hydrogen-bonding in water with the formation of various clusters like dimers, trimers or polymers. Furthermore, this aggregation tendency of MM increases with the increase of MM concentration. From the above discussions, it is clear that though a great many research studies have been devoted to exploring both the importance as well as the toxicity, arising mainly due to its tendency to form aggregates of MM, a very little attention has been paid to understand the molecular mechanism of MM association in water. As a result, a definitive answer towards the molecular level understanding of MM association in aqueous solution is yet to be achieved. Therefore, in this work, we have carried out classical MD simulations to investigate the aggregation of MM in aqueous solutions with a range of melamine concentrations. Complimentary to this, we have also performed high level quantum calculations as well as isothermal titration calorimetry (ITC) experiments to validate the main outcome of our results obtained from classical molecular dynamics simulation. Moreover MM does not alter the water structure with the change of concentration and temperature as is reported in a recent study.[137] So, our focus will only be on the exact effects that cause the aggregation of MM.

The remaining of this chapter consists of three sections. Section II includes the models and simulation details, section III discusses the results in detail, displaying the related data and in the last section (section IV) summary and conclusions are drawn.

■ MODELS AND SIMULATION METHOD

In order to examine the mechanism of MM association in water, classical molecular dynamics (MD) simulations of 8 MM molecules were carried out by immersing 8 MM molecules in water in a range of MM concentrations. For each of the systems, the MM concentration was adjusted by changing the number of water molecules keeping the number of melamine molecules fixed. Moreover, to understand the thermodynamics of MM association for the system with highest MM concentration three different temperatures (with a constant temperature difference of 20 K), 280 K, 300 K and 320 K, and ambient pressure condition was considered. This was performed to determine the enthalpy-entropy contribution in MM association at ambient temperature and pressure conditions. The different systems considered here are summarized in Table 2a-1.

For MM, at first, the structure data file was downloaded (PDB ID: AX2). Then, a single-point quantum calculation with a HF/6-31G** level theory and basis set using Gaussian09 [138] was carried out. The partial charges of each of the atomic sites were assigned based on molecular electrostatic potential with the aid of the RESP module of AMBER 12 program package.[139, 140] The atomic partial charges of MM developed for the present MD simulation are given in Table 2a-2. The force field parameters of different atomic sites of MM were generated using the General Amber Force Field (GAFF) with the ANTECHAMBER module of AMBER12.[142, 141] The TIP3P model for water was used for all systems.[143]

The initial configurations of all systems were prepared using PACKMOL program.[144] The MD simulations were carried out using a cubic box in isothermal-isobaric (NPT) ensemble using a time step of 2 fs. For all the systems, the initial configurations were first energy minimized for 10000 steps of which the first 4000 steps in steepest descent minimization, which was then followed by 6000 steps of conjugate gradient method minimization. This ensures the removal of bad local contacts. The systems were then heated with a gradual increment of temperature from 0 K to 480 K for 20 ps at an interval of 50 K. This helps to better relaxing of the systems and to overcome the global minimum barrier energy. This is followed by quenching the systems to the desired temperature with a decre-

ment interval of 25 K in canonical ensemble (NVT). Then, for each of the systems, an equilibration for 5 ns and followed by the production run for 180 ns in NPT ensemble was performed. The trajectories generated were used to calculate different structural properties of the systems. Periodic boundary conditions were applied in all three dimensions for all the simulations and the temperature was controlled by means of Langevin thermostat[145] method with a collision frequency of 1 ps^{-1}. To maintain the physical pressure of each system, Berendsen barostat was used with a pressure relaxation time of 2 ps.[146] The long-range electrostatic interactions were treated using the particle mesh Ewald (PME) method.[147] The lengths of the covalent bonds involving hydrogen atoms were kept fixed using the SHAKE algorithm.[148] A cut-off radius of 10.0 Å was used for all non-bonding short-ranged interactions. The Ptraj and Cpptraj programs of AMBER12 toolkit along with visual molecular dynamics (VMD)[149] were used to analyze the trajectories obtained from the production run whenever required. Thus, a total of 6 systems were considered to describe the mechanism of aggregation of MM in details. Moreover, to calculate the potential of mean force (PMF) between two MM residues, umbrella sampling[150] was performed. For this, a pair of systems with different MM solutions were prepared (systems P0, P1, Table 2a-1). Following the same procedure as for our other systems, these systems were simulated for 410 ns each. The starting 41 configurations for PMF calculations were then selected from the trajectory for each system, with windows separated from each other by 0.25 Å . The value of reaction coordinate as a function of a distance between N4 and N9 of two reference MM molecules was varied from 2 to 12 Å to obtain the PMFs. The results were then post-processed using Weighted Histogram Analysis Method (WHAM).[151]

The thermodynamic behavior of the MM-MM interaction is investigated by isothermal titration calorimetry (ITC), experiment carried out on a MicroCal iTC-200 (MicroCal, Northampton, MA, USA). In general, ITC is an efficient and widely applied technique to analyze the thermodynamic parameters of host-guest interactions occurring in vitro systems and it also provides binding constant (K_a), binding stoichiometry (n), total enthalpy change (ΔH) as well as total entropy change (ΔS) during the binding reaction. In the present study, a number of consecutive injections of small volume of MM solution (20 mM) was injected to the very dilute solution of MM (0.0001 mM) at 300 K temperature. A constant stirring speed of 200 rpm was maintained to ensure proper mixing during the experiment. MM solutions were properly centrifuged and degassed prior to measurements in order to eliminate the possibility of bubble formation during titration. The raw heat change

data is analyzed on MicroAnalyze software provided with the instrument and is fitted with best-fit with a set of binding sites. According to the convention of the instrument (that is, MicroCal iTC-200), an exothermic or endothermic process is plotted through downward or upward heat change diagram respectively. It is also mentioned that the upward/downward trend of the raw ITC data is different for various ITC instruments. The sign of ΔH as obtained from the fitting of the experimental data must be regarded as the genuine thermodynamic signature and we have interpreted our data accordingly.As mentioned above, we have chosen a aqueous solution of MM with very low concentration (20 mM) due to the fact that MM has a very low solubility in water (3.1 g/L in water at 293K).[2] This 20 mM solution mimics with our system P1 (concentration of MM is 0.0272 mol/L).

Table 2a-1. Overview of systems[a]

			Box Length (Å)			Conc.(M)		
System	N_{MM}	N_{wat}	280 K	300 K	320 K	280 K	300 K	320 K
S0	8	1500	35.740	35.880	36.176	0.2909	0.2876	0.2805
S1	8	2500	—	42.465	—	—	0.1735	—
S2	8	4000	—	49.654	—	—	0.1085	—
S3	8	6000	—	56.805	—	—	0.0725	—
P0	2	2000	—	39.312	—	—	0.0547	—
P1	2	4000	—	49.609	—	—	0.0272	—

[a] N_{MM} and N_{wat}, respectively, are the number of melamine (MM) and water molecules. M is the molar concentration of MM.

Table 2a-2. Partial charges for different atomic sites of melamine (MM)[a]

Atom	Charge (e)
C1/C2/C3	1.3069
N6/N8/N9	-1.0794
N4/N5/N7	-1.2006
H10-15	0.4866

[a] e is the elementary charge.

In this section first we discuss MM association in different aqueous solutions which are prepared by varying MM concentrations. The snapshots of different systems studied here are considered first and they are shown in Figure 2a-2. These snapshots are taken by the use of VMD package. In order to obtain the proper visual clarity of the snapshots, the water molecules are left off. Focusing on the effect of MM concentration at a fixed temperature (Figure 2a-2(a)-(d)) of 300 K first, we find that the association propensity of MM molecules decreases as the concentration is decreased and this finding is as per with the expectation. Next, the effect of temperature change on the association tendency of MM molecules is probed and the same is shown in Figure 2a-2(a), (e) and (f). It is observed that the association propensity of MM molecule decreases with the increase of temperature. Here it is worth to mention that these snapshots provide qualitative pictures only and they depict the instantaneous states of the systems without revealing much about the driving force and thermodynamics of MM association. We further proceed

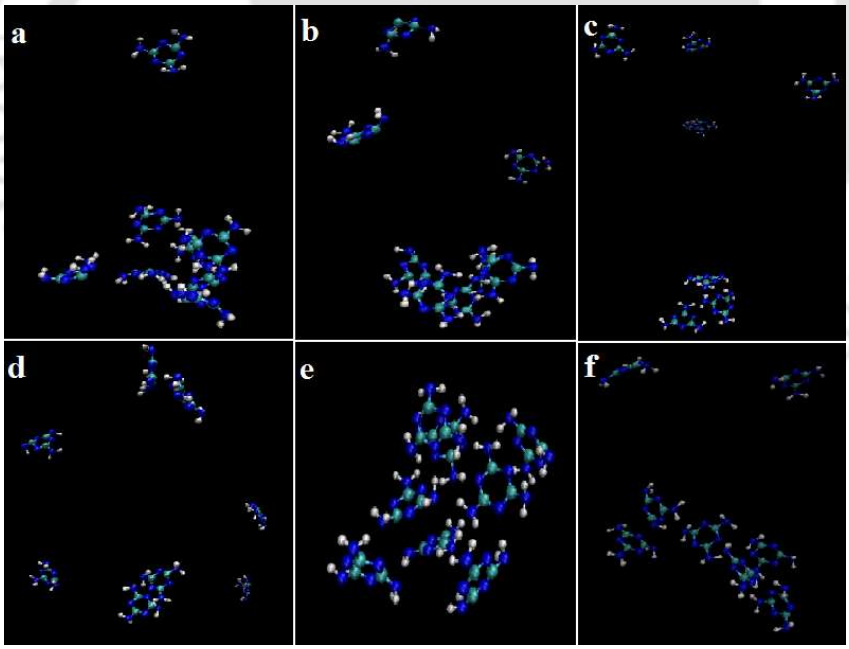

Figure 2a-2. *Snapshots of MD simulations of different systems. (a)-(d) are the snapshots of different systems at 300 K temperature and (e) and (f) represent the snapshots for system S0 at 280 K and 320 K respectively. In order to obtain the proper visual clarity of the snapshots, the water molecules are left off.*

to calculate the average number of hydrogen bonds, coordination number, dimer existence probability function etc to strengthen this qualitative measurement in more convincing

way. Moreover, we would like to mention that, since we are interested in the understanding of molecular mechanism of MM association in aqueous solution in ambient temperature-pressure condition, the succeeding discussion focuses on the structure and thermodynamics of aqueous MM solutions at 300 K temperature only.

In order to compare different systems having different densities, we first examine the MM-MM and MM-water radial distribution functions (rdfs) multiplied by the number density ρ of the observed atom. This is done because of the fact that the comparison of the $g(r)$'s can be misleading as the peak intensity is not related to the number of selected atoms at a given distance, but it depends mainly on the density. Therefore, in order to appreciate the variation of the first shell coordination number, the $g(r)\rho$ function is better suited as in this case the integral of the first peak is directly related to the number of atoms present in the first shell.[152, 153] At first $g(r)\rho$ for, N4 and N9 nitrogen atoms of MM molecules and oxygen atom of water (Ow) are considered. The choice of N4 and N9 nitrogen atoms over other atomic sites of MM is made because of the fact that it is the MM-MM hydrogen bonding interaction, which is believed to be mainly responsible for MM association in aqueous solution (discussed below). Here it is to be noted that in MM the chemical environments of sp^3 hybridized N4, N5 and N7 nitrogen atoms are identical. In the same note, the sp^2 hybridized N6, N8 and N9 nitrogen atoms of MM are also identical. Thus, in MM-MM hydrogen bonding interactions one would expect N6, N8 and N9 nitrogen atoms to act as hydrogen bond acceptors only and N4, N5 and N7 nitrogen atoms to act as both hydrogen bond acceptors and hydrogen bond donors. Thus, it is logical to consider N4-N4 and N4-N9 $g(r)\rho$ for estimating MM-MM distribution functions and the same for different systems are displayed in Figure 2a-3. Similarly, to probe the hydration of MM molecules qualitatively, as the concentration changes, it is important to calculate $g(r)\rho$ involving N4-Ow and N9-Ow. These two distribution functions are shown in Figure 2a-4. Concentrating on the N4-N4 $g(r)\rho$ distribution function first (Figure 2a-3(a)) we observe the appearance of sharp first and second peaks at around 2.95 Å and 3.85 Å respectively and the heights of these two peaks decrease as the MM concentration is decreased. The concentration dependent change in the N4-N9 pair correlation functions multiplied by number density (Figure 2a-3(b)) is very similar to that for N4-N4 $g(r)\rho$ except for the fact that the positions of appearances for both first and second minima of the former are shifted towards high-r value.

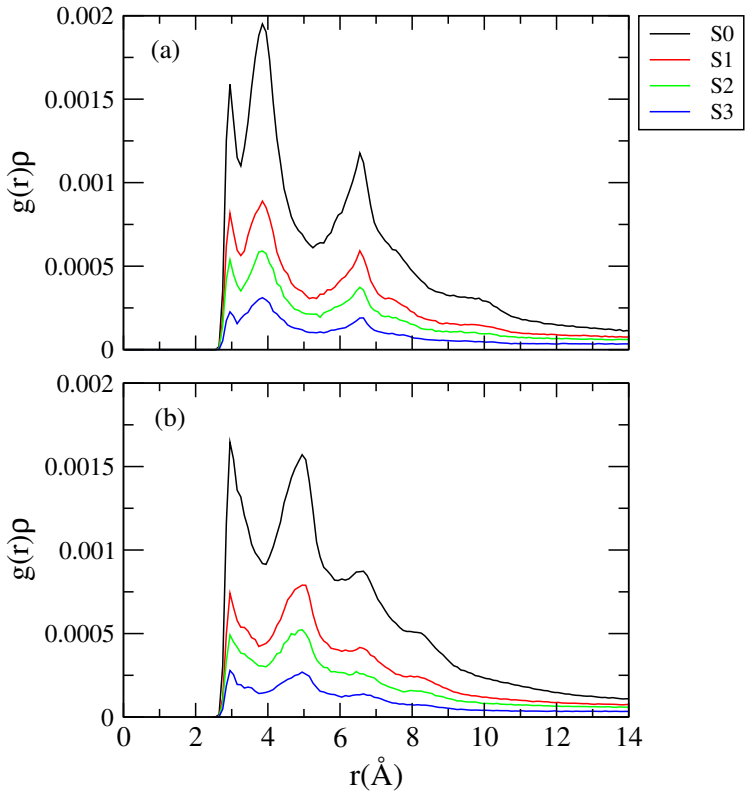

Figure 2a-3. *Radial distribution functions multiplied by the numerical densities, $g(r)\rho$, involving N4 and N9 nitrogen atoms of MM for different systems. (a) and (b) are for N4-N4 and N4-N9 $g(r)\rho$ distribution functions respectively.*

Since, the hydration pattern of solute molecules in aqueous solution provides, albeit indirectly, the information about the association propensity of them, it is important to calculate solute-water distribution functions. These $g(r)\rho$ functions give a qualitative picture of the structure of the solvent molecules around the reference solute. These facts prompted us to calculate N4-Ow and N9-Ow $g(r)\rho$ with varying MM concentrations (see Figure 2a-4). A sharp first peak, which appears at around 2.85 Å followed by a much smaller second peak (appears around 4.05 Å) is observed for N4-Ow $g(r)\rho$ for system S0 (Figure 2a-4(a)). As MM concentration is decreased, the heights of both first and second peak decrease. Figure 2a-4(b) represents the site-site pair correlation function multiplied

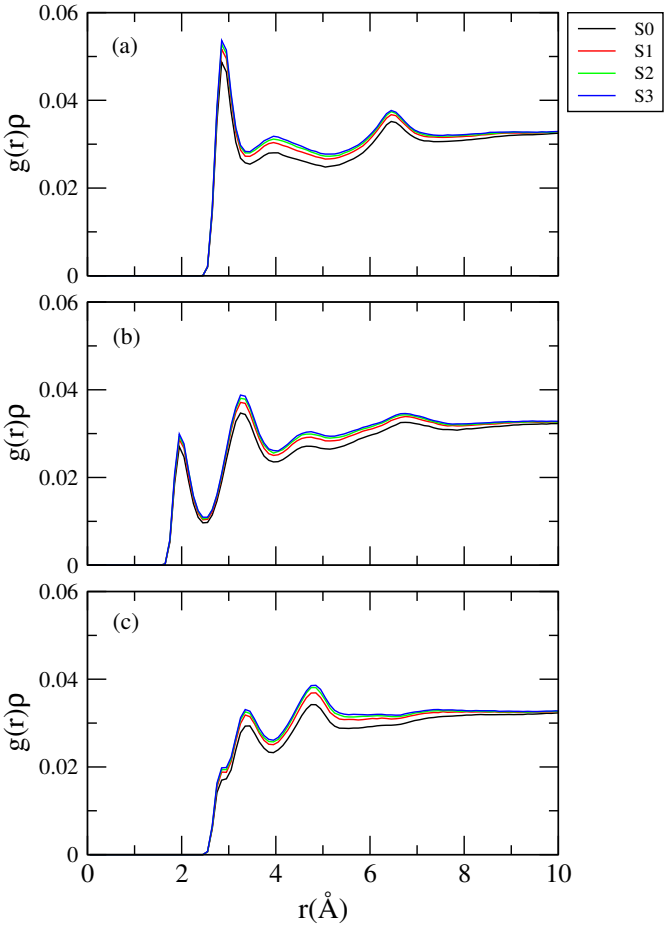

Figure 2a-4. *Radial distribution functions multiplied by the numerical densities, $g(r)\rho$, involving N4, N9, H11 atomic sites of MM and water oxygen (Ow) for different systems. (a), (b) and (c) refer to N4-Ow, H11-Ow and N9-Ow $g(r)\rho$ distribution functions respectively.*

by ρ involving H11 atom of MM (hydrogen atom attached to N4 nitrogen atom of MM) and water oxygen. From this distribution function, we make following observations: (i) The appearances of a strong first peak at 1.95 Å (attributed to hydrogen bonding peak), which is followed by an even stronger second peak at around 3.25 Å and (ii) the heights of these peak are increased with decreasing MM concentration suggesting more and more solvation of MM molecules. For MM N9-Ow $g(r)\rho$ (Figure 2a-4(c)), we observe a shoulder at 2.7 Å and this is followed by the appearance of a sharp first peak at 3.35 Å . A pronounced second peak (larger than that of the first peak) is also observed at 4.75 Å . The heights of both these

peaks increase with the decrease of MM concentration. These observations suggest more and more hydration of MM molecules (and less association) as MM concentration decreases and act as corroborative evidences to that observed for N4-N4 and N4-N9 $g(r)\rho$ functions discussed above. Now, for a given MM concentration, a comparison of the first peak heights of N4-Ow and N9-Ow $g(r)\rho$ distribution functions implies that in the hydrogen bonding interactions with water molecules it is the N4 nitrogen atom of MM, which interacts more favorably than that of N9 nitrogen atom. This is further confirmed by the calculations of the average number of MM-water hydrogen bonds for different systems (discussed below).

In order to quantify, how does the average number of MM and water molecules around a reference MM molecule change with distance from it, the running coordination number (RCN) is calculated. Following earlier works[154] RCN can be calculated as:

$$RCN = 4\pi\rho_\beta \int_0^r r^2 g_{\alpha\beta}(r) dr \tag{2.1}$$

RCN is defined as the number of atoms of type β surrounding atom α in a shell extending from 0 to a distance, r, and ρ_β is the number density of β in the system. In Figure 2a-5 and Table 2a-3 the average numbers of MM and water molecules around a reference MM molecule are shown as a function of distance. The distribution functions N4-N9 and N4-Ow are used to calculate these RCNs. As the concentration of MM is decreased, for a given distance, a sharp drop in the RCN value in the number of MM molecules and a prominent rise in the RCN value in the number of water molecules are quite apparent. These findings are in line with that of MM-MM, MM-water rdfs and snapshots of different systems discussed above.

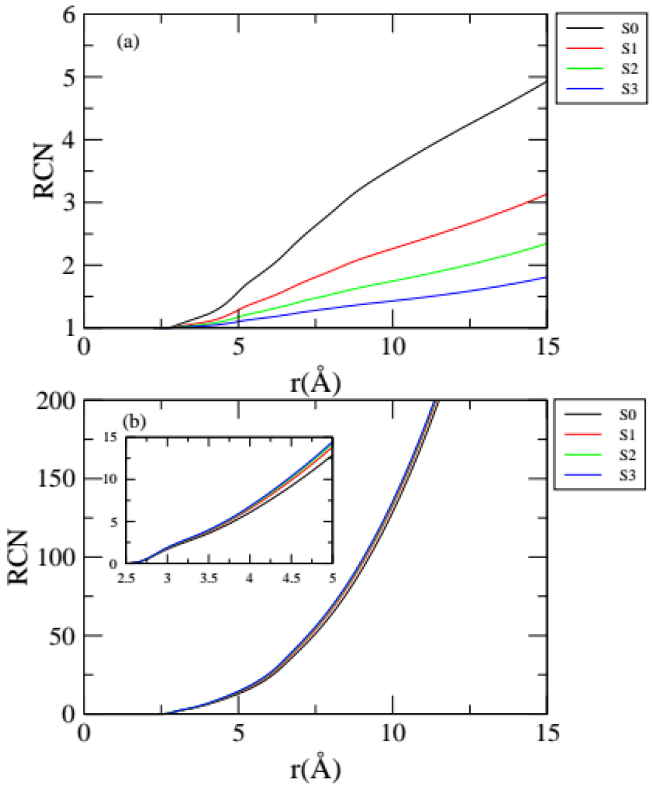

Figure 2a-5. *(a) MM-MM and (b) MM-water running coordination numbers for different systems. Inset represents magnified running coordination numbers for MM-water.*

Table 2a-3. Running coordination numbers[a]

System	MM-MM	MM-water
S0	1.21	3.38
S1	1.09	3.61
S2	1.04	3.71
S3	1.01	3.76

[a] Average number of MM-MM first shell coordination numbers within 3.95 Å around a MM and first shell MM-water coornation numbers within 3.45 Å around a MM.

It is important to examine the water-water distribution functions with the variation of MM concentration, as it provides, although indirectly, the details of solvation of MM molecules. In Figure 2a-6, the distribution functions involving Ow-Ow and Ow-Hw (water hydrogen) are shown. From the Ow-Ow distribution function for system S0 (Figure 2a-6(a)) the appearances of the first and second peaks at 2.75 and 4.55 Å respectively are observed. The first peak corresponds to the hydrogen bonded first neighbor and the second peak is attributed to the tetrahedrally located second neighbor. Here we note that the appearances of these peaks in the Ow-Ow rdf resembles that already reported elsewhere. Interestingly, the change of MM concentration does not influence much to this distribution function. As per as the Ow-Hw distribution function is concerned (Figure 2a-6(b)), we also find the appearance of the hydrogen bonding peak at around 1.8 Å and similar to that for Ow-Ow rdf, the effect of MM concentration on the change in Ow-Hw correlation function is also very negligible.

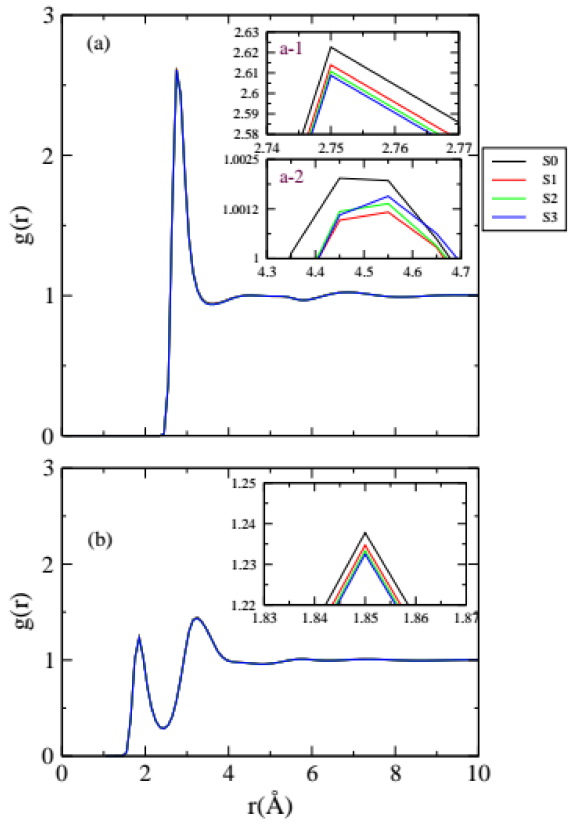

Figure 2a-6. *Water-water radial distribution functions for different systems. (a) and (b) are for water oxygen-water oxygen and water oxygen-water hydrogen respectively. Insets represent the magnified water-water rdfs. For water oxygen-water oxygen rdfs, a-1 and a-2 represent the magnified portions of first peak and second peak positions respectively.*

Hydrogen bond properties

In aqueous solution, MM molecule can form hydrogen bonds with like molecules as well as with water molecules. As mentioned above that a MM molecule has six hydrogen bonding sites and these are three sp^3 hybridized nitrogen atoms, namely, N5, N4 and N7, which act as both hydrogen bond donors and acceptors and ring nitrogen atoms N6, N8 and N9, which are sp^2 hybridized and can act as hydrogen bond acceptors only. Therefore, in MM-MM (per MM) hydrogen bonds, we consider hydrogen bonds involving sp^3 N-H$\cdots$ sp^3 N, sp^3 N-H$\cdots$ sp^2 N, sp^2 N-H$\cdots$ sp^3 N-H$\cdots$ sp^2 N. Similarly, for the estimations of average number of MM-water

(per MM) hydrogen bonds sp^3 N-H$\cdots$ Ow, sp^3 N$\cdots$ Hw (water hydrogen) and sp^2 N$\cdots$ Hw are considered. Needless to say that, water-water (per water) hydrogen bonds are also possible in which the oxygen atom of the water molecule can act as a hydrogen bond donor as well as an acceptor. Thus, in aqueous MM solution, five different types of hydrogen bonds are possible i.e., water-water (H_{w-w}), MM sp^3 N-water (H_{sp3N-w}), MM sp^2 N-water (H_{sp2N-w}), MM sp^3 N-MM sp^3 N ($H_{sp3N-sp3N}$) and MM sp^3 N-MM sp^2 N ($H_{sp3N-sp2N}$). Following previous studies,[154, 155, 156, 157, 158] a set of geometric criteria is used to define a hydrogen bond.

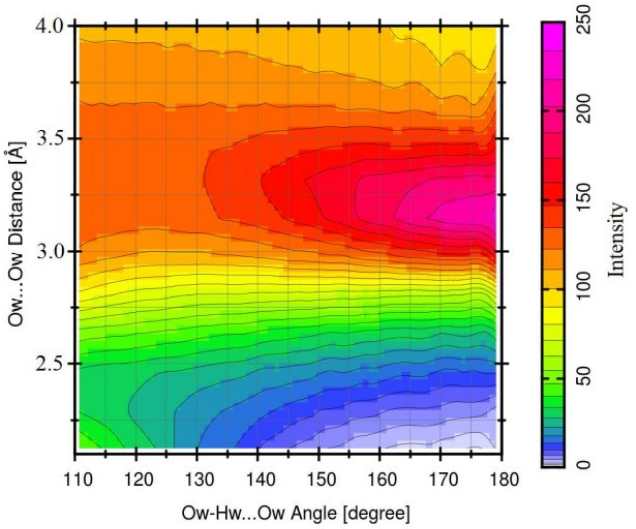

Figure 2a-7. *Combined angular-radial distribution function showing the variation of Ow-Hw$\cdots$Ow angle with respect to Ow$\cdots$w distance for system S0.*

Two molecules are considered to be hydrogen bonded if the distance between the donor atom (D) of one molecule falls within the cut-off distance (r_{cut}) of the acceptor atom (A) of another molecule and, simultaneously, the angle D-H$\cdots$ A is greater than and equal to some cut-off angle (r_{angle}). In this study, the value of r_{cut} is determined from the position of the first minimum in the corresponding rdf and r_{angle} is taken as 120^o. The criteria for defining the hydrogen bonds considered in this study are further justified by the calculation of combined radial-angular distribution function of water-water hydrogen bonds for system S0 shown in Figure 2a-7. In this figure, the donor-acceptor distance (in Å) is taken as the distance between Ow of one water molecule and Ow atom of another water

molecule) is plotted against donor-hydrogen-acceptor angle. It can be noticed that the distance and angular cut-off used in this study to define a hydrogen bond falls within the high-intensity region. Now, for different systems, the average number of different MM-MM, MM-water, and water-water hydrogen bonds are presented in Table 2a-4. It is quite apparent that in MM-MM hydrogen bonding interaction, it is the $H_{sp3N-sp2N}$ hydrogen bonds, which contributes predominantly and in total number of MM-water hydrogen bonds the contribution of H_{sp3N-w} hydrogen bonds is much higher than that of H_{sp2N-w} hydrogen bonds. These findings are in good agreement with that observed in MM-MM and MM-water pair correlation functions. Now considering the effect of change of MM concentration on these hydrogen bonds we find that a reduction in the MM concentration causes an increase in MM-water average hydrogen bond number as well as a depletion in the number of MM-MM hydrogen bonds and these changes in the hydrogen bond numbers, which are as per our expectation, are not very dramatic rather a gradual change is observed. Moreover, as expected, with a decrease in MM concentration there is an increment in the water-water hydrogen bond number.

Table 2a-4. Average number of hydrogen bonds of water-water per water (H_{w-w}), MM-water per MM (H_{sp3N-w}, where sp3N represents sp^3 N atoms of MM), MM-water per MM (H_{sp2N-w}, where sp2N represents sp^2 N atoms of MM), MM-MM per MM ($H_{sp3N-sp3N}$), and MM-MM per MM ($H_{sp3N-sp2N}$) for different systems.[a]

System	H_{w-w}	H_{sp3N-w}	H_{sp2N-w}	total$_{m-w}$	$H_{sp3N-sp3N}$	$H_{sp3N-sp2N}$	total$_{m-m}$
S0	3.87	6.60	2.82	9.42	0.75	1.57	2.32
S1	3.96	7.35	3.15	10.50	0.45	0.81	1.26
S2	4.03	7.71	3.33	11.04	0.24	0.47	0.71
S3	4.09	7.92	3.45	11.37	0.14	0.30	0.44

[a] Total$_{m-w}$ and total$_{m-m}$ refer to total MM-water and MM-MM hydrogen bonds per MM.

Spatial Density Plots

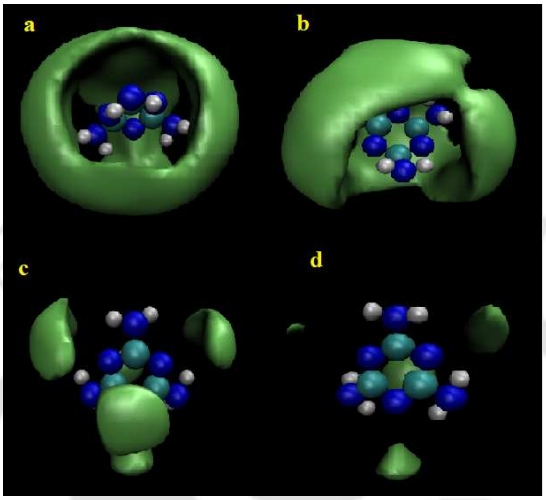

Figure 2a-8. *Spatial density maps of MM around a reference MM molecule for different systems (averaged over last 80 ns of simulated trajectory). (a)-(d) Systems S0, S1, S2, and S3, respectively.*

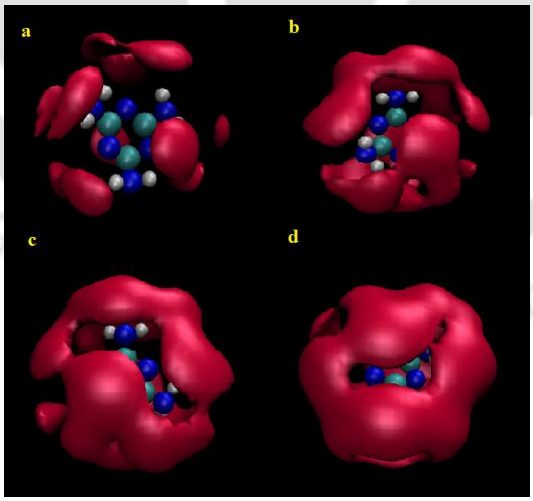

Figure 2a-9. *Spatial density maps of water around a reference MM molecule for different systems (averaged over last 80 ns of simulated trajectory). (a)-(d) Systems S0, S1, S2, and S3, respectively.*

In Figure 2a-8, for all systems, the spatial distribution of solute MM density within 3.95 Å of MM with the isovalue of 0.5 $\mathring{A}^{-3}$ are presented. As one gradually moves from system S0 to S3 (Figure 2a-8 (a)-(d)) the density of MM molecules around a reference MM

molecule is decreased. These MM-MM spatial density maps are further complemented with the determination of water density (within 4.0 Å distance) around a reference MM molecule for different systems (Figure 2a-9). An increment in the water density as the concentration of MM is decreased from system S0 to system S3, which acts as a corroborative evidence to that for MM-MM spatial density maps, is observed.

Preferential Interaction Parameters

The above discussions reveal that the association tendency of MM with the like molecules is getting enhanced with increasing MM concentration. Thus, it is instructive to calculate the preferential interaction parameter, τ, to further evaluate the effect of MM concentration on the interactions between different solution species. Using Kirkwood-Buff theory, which provides a statistical thermodynamic framework for estimating τ, the preferential interaction parameters of MM with like molecules (over water) for different systems, τ_{mw}^{m}, can be calculated as:

$$\tau_{mw}^{m} = \rho_m(G_{mm} - G_{mw}) \tag{2.2}$$

where m and w refer to the solute MM and water molecules, respectively. ρ_m is the number density of MM in a given system. G_{mm} and G_{mw} represent the Kirkwood-Buff integrals and they are calculated from the MM center of mass-MM center of mass and MM center of mass-water oxygen pair correlation functions respectively as follows: [159, 160]

In grand canonical ensemble, G_{ij} (for species i and j) can be defined as

$$G_{ij} = 4\pi \int_0^\infty [g_{ij}(r) - 1] r^2 dr \tag{2.3}$$

In case of a closed system, the above equation can be expressed as:

$$G_{ij} \approx 4\pi \int_0^R [g_{ij}(r) - 1] r^2 dr \tag{2.4}$$

where R refers to the distance at which the above integral approaches zero. From the above equation 2.2, it is quite obvious that the value of τ_{mw}^{m} becomes positive when a MM molecule interacts preferentially with other MM molecules over water. On the other hand, its negative value implies the preferential hydration of MM molecules. For different systems the values of τ_{mw}^{m} are shown in Figure 2a-10. As is evident from the figure that the value of τ_{mw}^{m} for system S0 is well above 1 implying a MM molecule prefers to interact with other MM molecules over water molecules. As one moves from system S0 to system S1 the value

of τ_{mw}^{m} decreases suggesting the interactions between MM-MM is becoming less favorable. Further decrease in MM concentrations (systems S2 and S3) makes MM-water interactions more favorable than that for systems S0 and S1 indicating enhanced hydration of MM molecules.

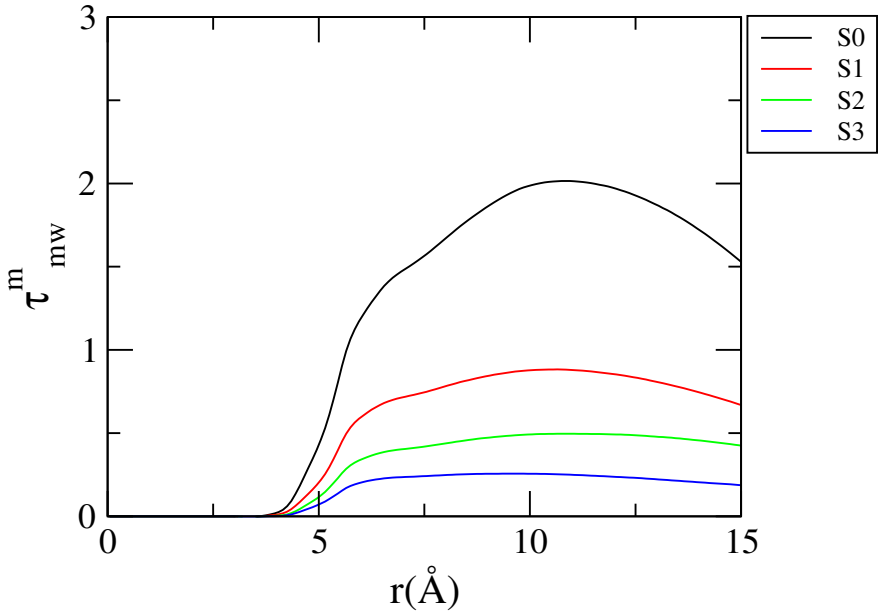

Figure 2a-10. *Preferential interaction parameters of MM for a MM over water for different systems.*

Thus, the observations made from the above discussions lead us to conclude, rather qualitatively, that as the concentration of MM decreases more and more solvation of MM molecules takes place. But, neither the quantitative estimations of an average number of MM clusters of different sizes in different systems nor the thermodynamics of MM association in aqueous solution is explored. Moreover, the role of stacking interactions between the hetero-cyclic rings of MM molecules on the MM association, if any, is not explored so far. Thus, in the following sections, we focus on these aspects and try to explain the underlying mechanisms that drive the MM molecules to associate in aqueous

Orientational Preference of Melamine (MM) Aromatic Plane

In order to investigate the role of π-π interactions between the aromatic planes of two MM molecules, the inter-plane angle is considered. The inter-plane angle is defined as the angle between the vectors normal to the aromatic planes of two reference MM molecules. Thus, the angles 0^o, 90^o and 180^o refer to the parallel, perpendicular and anti-parallel orientations respectively of the two aromatic planes.

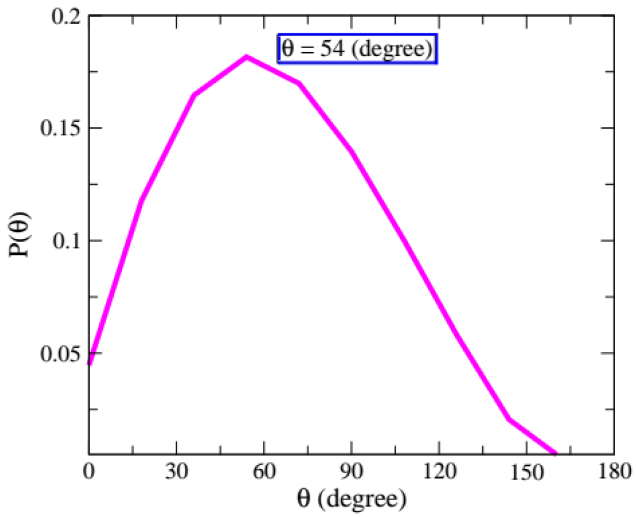

Figure 2a-11. *Probability distributions of orientational angles between the aromatic rings of two MM molecules for system S0 where P(θ) is maximum at θ=54^o.*

In Figure 2a-11, the normalized probability distribution of angle θ, P(θ) as a function of inter-plane angle (θ) is plotted for system S0. We have chosen system S0 over other systems considered in this study because of the fact that in system S0, the concentration of MM is the highest and the maximum MM association is observed. Since, we consider 8 MM molecules in our study, a total 28 combinations between the aromatic planes of any two MM molecules are possible. Thus, 28 combinations of P(θ) vs θ plots can be obtained. Interestingly, all 28 combinations produce very similar P(θ) vs θ plots. Thus we chose only one P(θ) vs θ out of these 28 combinations. Clearly, a random distribution of P(θ)

vs θ represents no orientational preferences and the maximum value of P(θ) reaches when θ=54^o. The probability lies at minimal when θ=0^o that substantially rules out the presence of $\pi - \pi$ between the aromatic planes of the MM molecules. Strictly speaking, when two aromatic planes interact through $\pi - \pi$ interactions, the angle between the vector normals of those two planes should be close to 0^o or 180^o. Thus, it is safe to conclude that in the association of MM molecules in water, the $\pi - \pi$ interaction between the aromatic planes of the MM molecules plays an insignificant role. Here, we note that a recent molecular dynamics simulation study of guanidium chloride reported the presence of π-π interactions when the angle between two aromatic planes is less than 20^o.[161]

Umbrella Sampling

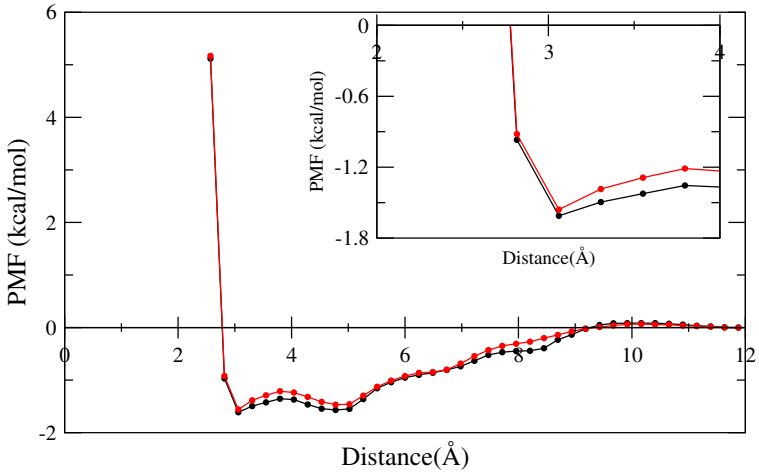

Figure 2a-12. *MM-MM potential of mean forces (PMFs) for systems P0 (black) and P1 (red). Inset represents the magnified potential of mean forces (PMFs) for both systems, where the X-axis represents the N4(mol.1)-N9(mol.2) distance in the unit of Å .*

To explore the energy cost of growing clusters from monomers, we have performed umbrella

sampling method to calculate the potential of mean forces (PMFs) of MM-MM interactions as a function of a distance between N4 and N9 atomic sites of two different MM molecules. The PMFs for the systems P0 and P1 are presented in the Figure 2a-12. The system P0 resembles with the system S3. It is apparent that the first minimum, which appears at 3.06 Å is attributed to contact minimum (CM) and a second shallow well that appears at 4.77 Å corresponds to the solvent separated minimum (SSM) for both systems. In order to reach to CM state from the SSM state one small barrier (appears at 3.79 Å) of energy -1.35 kcal/mol and -1.21 kcal/mol for P0 and P1 systems respectively has to overcome. It is also evident for both the systems that the CM is slightly more stable than the SSM state. Moreover, since the system S3 contains of ≈15% dimers and mostly monomers (see the cluster structure analysis in the next section below), the nearly equal stability of CM and SSM state of system P0 is certainly expected. Nevertheless, this result suggests that the formation of a dimer of MM molecules is energetically favorable indicating the self-aggregation of MM molecules and the cluster formation through hydrogen bond between N4-N9 atomic sites are highly preferabble. Furthermore, it can be assumed that the growth of higher order clusters from the association of other monomers with the newly formed dimers may also be due to the favorable interactions between them. Here, it is to be noted that the potential of mean forces for binding of two MM monomers to form a dimer are nearly about same for two systems and this value is in well accordance with the isothermal titration calorimetry (ITC) measurement where ΔG of 1:1 binding of MM monomers is -2.16 kcal/mol at 300K temperature (discussed below).

Cluster Structure Analysis

In this section, for different systems, the quantitative description of MM clusters of different sizes are introduced. In order to examine the number of MM clusters of different sizes, we use the following criteria. Two MM molecules, say M1 and M2, are considered to form a dimer if they are engaged through a hydrogen bond. Similarly, a third MM, M3, will be the part of a trimer consisting of M1 and M2 if M3 forms hydrogen bond either with M1 or M2. The same definition for MM cluster goes on for other higher order clusters. Since MM molecules are associated mainly through hydrogen bonds (as prevailed above), consideration of this definition is quite logical. In Figure 2a-13, for different systems, we present the probability of formation of MM clusters of different sizes. Here we note that we have used last 80 ns of our simulation run for cluster structure analysis purpose. It is

found that for system S0, the probability of finding heptamer is close to 23%.

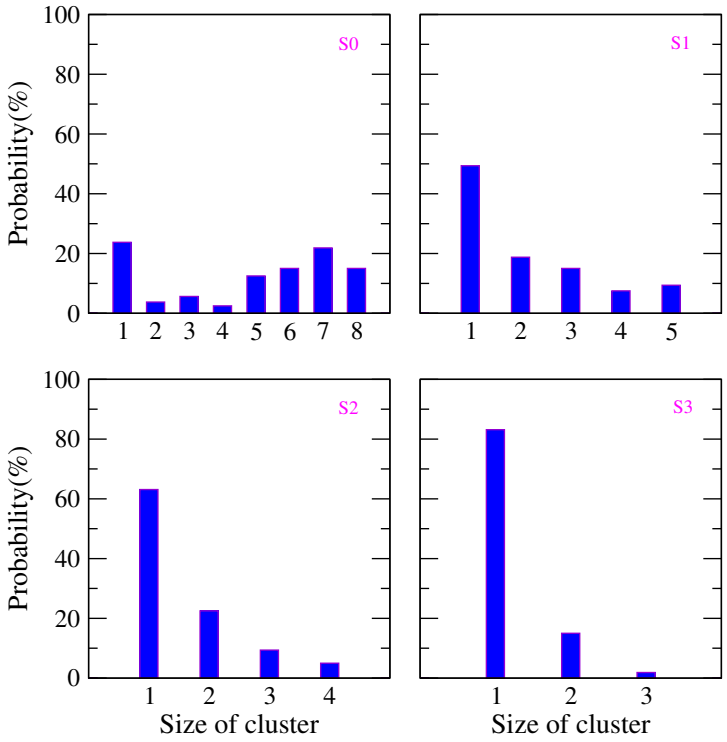

Figure 2a-13. *Probability distributions (in percentage) of MM clusters of different sizes for different systems.*

Besides this, a considerable amount of formation of pentamer, hexamer, and octamer can also be observed whereas, a very low percentage of MM monomer (25%) is observed. Now practically 25% is not very low indeed, but in comparison with the other systems say S1, S2 and S3 where monomer percentages are 50%, 65% and 84% respectively, one can draw a conclusion that a very low probability of MM monomer can be found in system S0 over the other systems. As the concentration of MM is decreased, the probability of formation of lower order MM clusters (at the expense of breaking of higher order clusters) increases. For system S3, on average, more than 82% MM monomers with 15% dimers and the rest are trimers are present.

Melamine (MM)-Melamine (MM) Interaction Energies

The estimation of total MM-MM interaction energy followed by its decomposition into electrostatic and van der Waals (vdW) components are considered. In Table 2a-5, the average electrostatic and vdW components of MM-MM interactions for different systems considered in this study are shown. This decomposition of total energy into electrostatic and vdW components is carried out by using NAMD energy plug-in of VMD.[149]

Table 2a-5. Average electrostatic and van der Waals energies of MM-MM interactions for different systems[a]

System	Electrostatic	van der Waals (vdW)
S0	-4.81	-1.51
S1	-2.48	-0.83
S2	-1.47	-0.50
S3	-0.64	-0.24

[a] All energy values are expressed in kcal/mol unit.

It can be observed that in the interactions of MM with the like molecules, it is the electrostatic component of energy which dominates over its vdW component and this is true for all the systems. For example, the MM-MM average electrostatic energy is -4.81 kcal /mol for system S0 and the vdW energy for the same system is -1.51 kcal /mol. The effect of decreased MM concentration on these two energy components is very pronounced. In specific, as the MM concentration is decreased, both electrostatic and vdW energy components become less favorable and for system S3 the average values of these two energy components are -0.64 and -0.24 kcal/mol. This can be attributed to the more and more hydration of MM molecules by water molecules as the concentration decreases.

Dimer existence Autocorrelation Functions

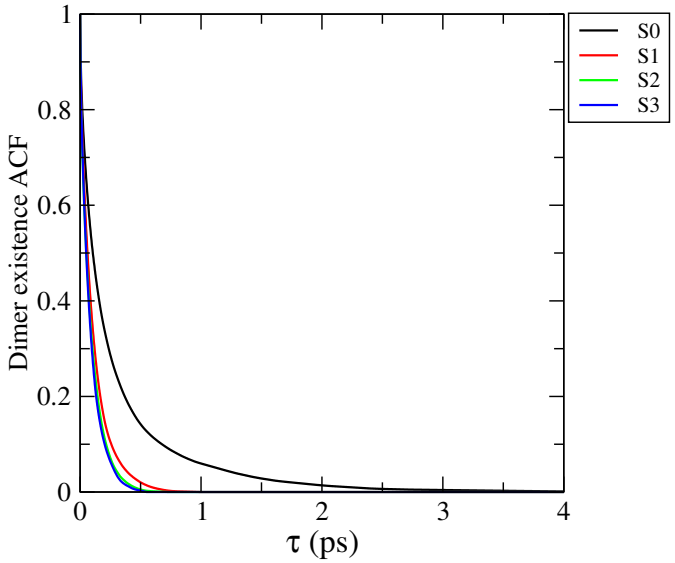

Figure 2a-14. *Dimer existence autocorrelation functions (DACFs) for the all systems.*

As the formation of higher-order clusters by the association of MM molecules is now well understood by the above discussions, it will be interesting to estimate the lifetime of aggregated species to get the dynamic nature of them. In order to evaluate the lifetime of a dimer as an aggregated species defined by distance criteria, a dimer existence autocorrelation function is computed here. The DACF for a given pair of particles i,j is defined as the autocorrelation of a simple function β_{ij} , which has the value 1 as long as the criteria are fulfilled, and switches to 0 as soon as the criteria fail for the first time according to this equation:[158]

$$DACF(\tau) = N. < \sum_{t=0}^{T-\tau} \beta_{ij}(t+\tau).\beta_{ij}(t) >_{ij} \qquad (2.5)$$

The value of DACF stays at 0, even if the criteria are again fulfilled later on. The final DACF is the average over all different pairs i,j. According to this definition, DACFs

start with the value 1 and then fall to 0 with increasing τ. The statement contained in the resulting function DACF(τ) is as follows: "How large is the probability of the criteria being still fulfilled (without interruption) at a given time τ, when they were fulfilled at time 0?".[158] Here we have defined distance criteria to define a distance between molecules and taken into account the nearest neighbors according to this distance definition. This makes it possible for one molecule to form a dimer with its next neighbor (or with its next 'n' neighbors) at each time. Dimers, defined in this way, break if the neighborhood relations change, i.e. if the formerly next neighbor is no longer the next neighbor. In Figure 2a-14, DACFs between MM molecules corresponding to four different systems are shown. DACFs are very sensitive in regard to the chosen dimer definition. Here we have chosen the maximum distance of 3.95 Å between two MM monomers (sp^3 N-sp^2 N distance). From the Figure 2a-14 it is apparent that DACF falls to zero at 3.84 ps, 0.90 ps, 0.68 ps and 0.55 ps for S0, S1, S2 and S3 systems respectively. Thus, the analysis of the dynamical nature of dimers as aggregates of MM molecules shows the sharp distinctions over lifetimes between S0 and S1 systems where dimer lifetime for S0 is higher than the system S1 and thereafter it gradually decreases from S1 to S3. These findings are in accordance with our earlier analyses discussed above.

Thermodynamics of MM Association

To probe the thermodynamics of MM association, from our temperature-dependent simulations, it will be useful to determine the enthalpy-entropy contribution to the free energy of MM association. Towards this, considering system S0, for all three temperatures (i.e., 280 K, 300 K and 320 K), at first the potentials of mean forces (PMFs), W(r), as a function of MM-MM N4-N9 distance, r, are calculated first by using equation 2.6.

$$W(r) = -k_B T ln g_{nn}(r) \tag{2.6}$$

where, k_B and T are the Boltzmann constant and absolute temperature respectively and $g_{nn}(r)$ is the pair correlation function involving N4 and N9 nitrogen atoms of MM. As is discussed above that in the association of MM molecules the $\pi - \pi$ interaction of MM molecules has essentially no role and it is the hydrogen bonding interactions involving N4 and N9 nitrogen atoms (and the corresponding hydrogen atoms attached to the former)

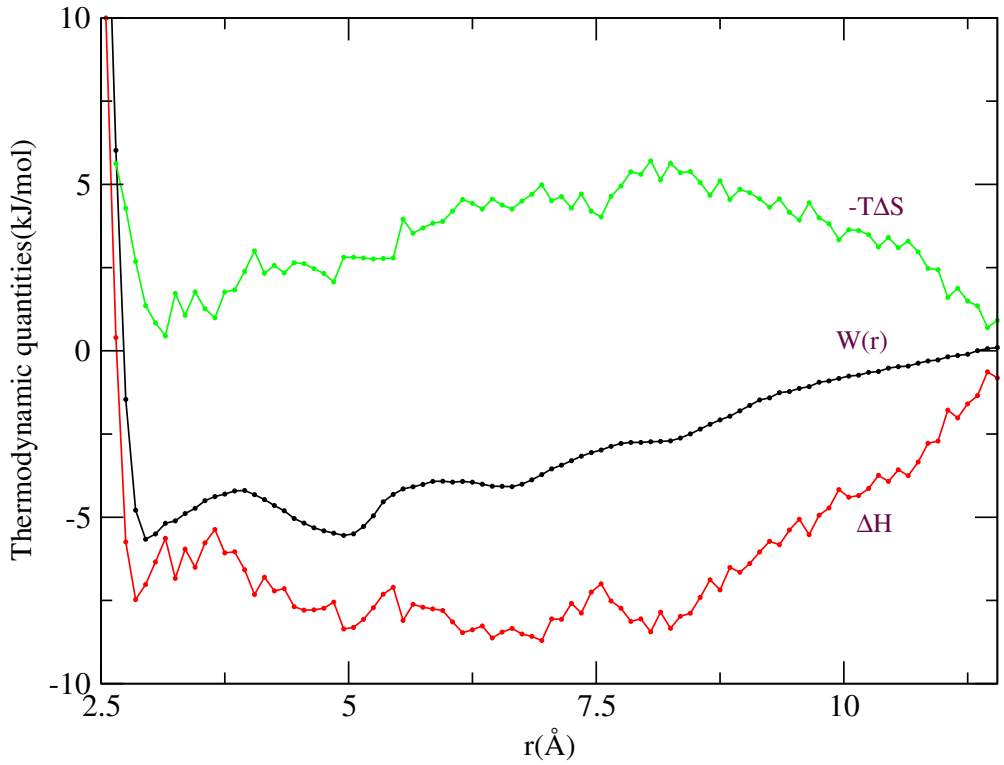

Figure 2a-15. *Entropy and enthalpy contributions to MM-MM PMF for system S0 at 300 K temperature.*

of MM, which plays a dominant role. This directs us to consider the distribution function involving N4 and N9 nitrogen atoms of MM over the center of mass of it in the PMF calculation. The entropy can be calculated from the PMFs of three temperatures by using the finite difference temperature derivative.[162]

$$-\Delta S(r) = 1/2[\frac{\delta W(r, T+\delta T)}{\delta T} - \frac{\delta W(r, T-\delta T)}{\delta T}] \tag{2.7}$$

In the above equation (eq. 2.7) the value of δT is 20 K. From the above value of $\Delta S(r)$ the corresponding enthalpy contribution ($\Delta H(r)$) can be calculated by

$$\Delta H(r) = W(r) + T\Delta S(r) \tag{2.8}$$

The entropic (-TΔS(r)) and enthalpic (ΔH) contributions to the PMF at 300 K temperature is shown in Figure 2a-15.

Table 2a-6. Magnitudes of W(r), ΔH, and -TΔS of MM-MM interactions for system S0[a]

	r	W(r)	ΔH	-TΔS
CM	3.0	-5.66	-7.02	1.36
SSM	4.97	-5.54	-8.35	2.81

[a] Here, CM, SSM, and r represent the contact minimum, solvent separated minimum, and distance (N4-N9) at which CM and SSM appear. All energy values are expressed in kcal/mol units, and the distance is in Å.

The PMF plot shows two distinct minima. The first one, which corresponds to contact minimum (CM), is at a distance of 3.0 Å and the second one, which is attributed to solvent separated minimum (SSM), appears at 4.97 Å. These two minima are separated by a small potential barrier positioned at 3.8 Å distance. Focusing on the contributions of enthalpy and entropy on the PMF values, it can be observed that the $\Delta H(r)$ and -TΔS(r) act in the opposite direction and the value of these two quantities depend on the separation of N4 and N9 atoms of two MM molecules. Moreover, for CM, the value of -TΔS(r) and $\Delta H(r)$ are positive and negative respectively suggesting that the contact minimum is stabilized solely by enthalpy (Table 2a-6) Thus, it is quite apparent that in aqueous solution, the association of MM molecules is enthalpy driven. On the other hand, for SSM the values of both -TΔS(r) and $\Delta H(r)$ become positive and negative respectively (Table 2a-6). These findings are in accordance with the experimental findings(discussed below) where MM association is found to be solely enthalpy driven by isothermal titration calorimetry (ITC) measurement.

Quantum Chemical Calculations

In order to get more details about the MM ring orientations, we have optimized all the ground state monomer and dimer structures of MM with the high level quantum calculations by using B3LYP-D3 functional with triple zeta basis set 6-311++G(d,p). From the equilibrated structure, we get a nearly co-planar structure and a perpendicular structure, which are denoted as Type-1 and Type-2 respectively (Figure 2a-16).

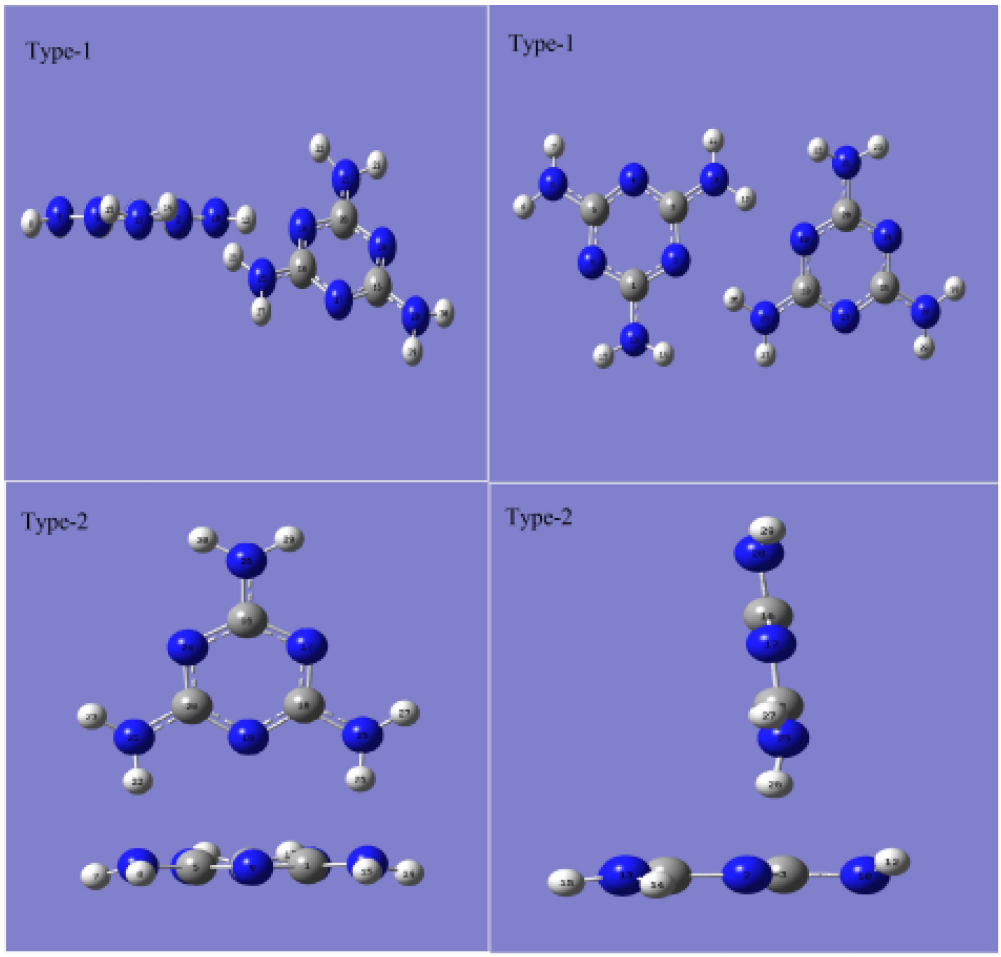

Figure 2a-16. *Structural representations optimized by B3LYP-D3/6-311++G(d,p) where Type-1 and Type-2 represent a nearly coplanar and a perpendicular structures respectively. In this figure the second column represents the differnt portrayals of same configurations of Type-1 and Type-2 respectively.*

In search of an energetically more stable conformation, we have performed relaxed

potential energy surface (PES) scan using same level (B3LYP-D3/6-311++G(d,p)) with respect to the dihedral angle (C3-N2-N25-C18) of the structure Type-1. In the relaxed scan process, we have fixed the dihedral angle value only at each point and all the remaining parameters are optimized. We find that the Type-1 structure is the most stable conformation over all the other structures (see Figure 2a-17).

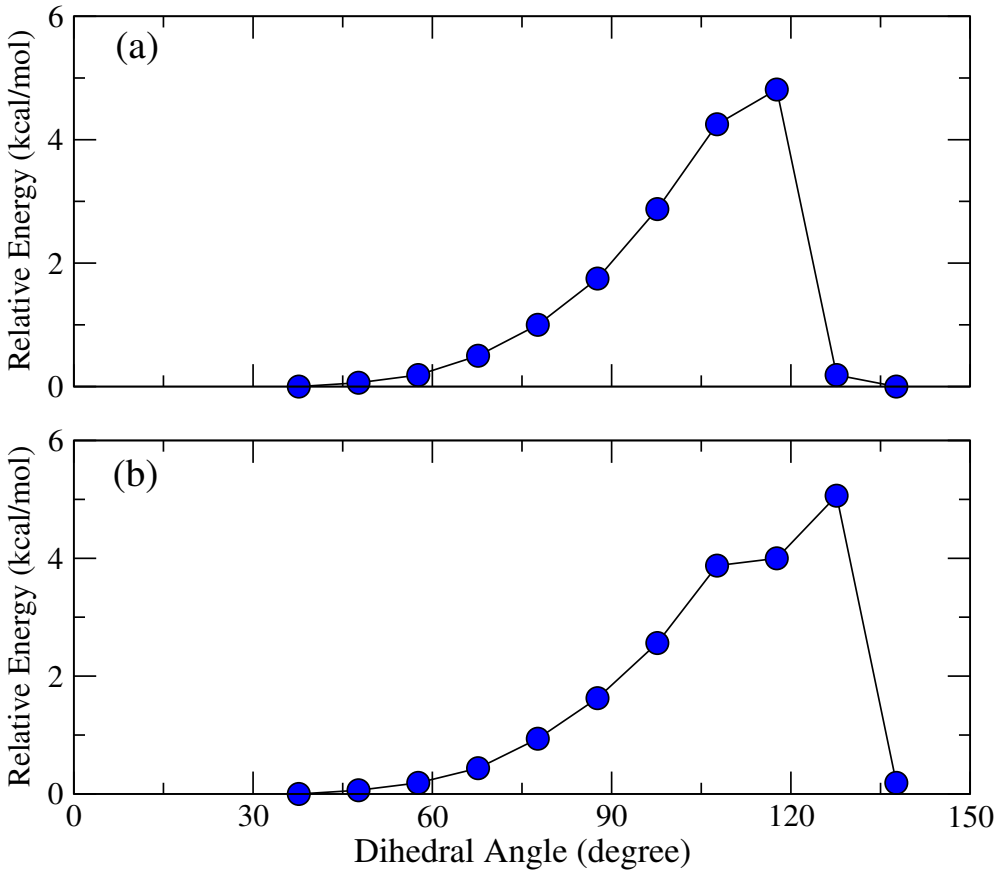

Figure 2a-17. *Potential energy surface of Type-1 complex calculated by using B3LYP-D3/6-311++G(d,p) level of theory. (a) Gas phase and (b) polarizable continuum model using water as the media. The relative energies of different conformations are calculated by rescaling the most stable structure to zero energy.*

In addition to this, another structure, where one monomer is almost perpendicular to other (Figure 2a-18(a)), is found to be the energetically least favorable conformer over all the structures. This PES scan is done in the gas phase (Figure 2a-17(a)) as well as by using polarizable continuum model using water as a media (Figure 2a-17(b)). Both Figure 2a-17

(a) and (b) provide similar results where one can find that Type-1 (nearly co-planar) is the most stable conformer among the others. To crosscheck this result, we

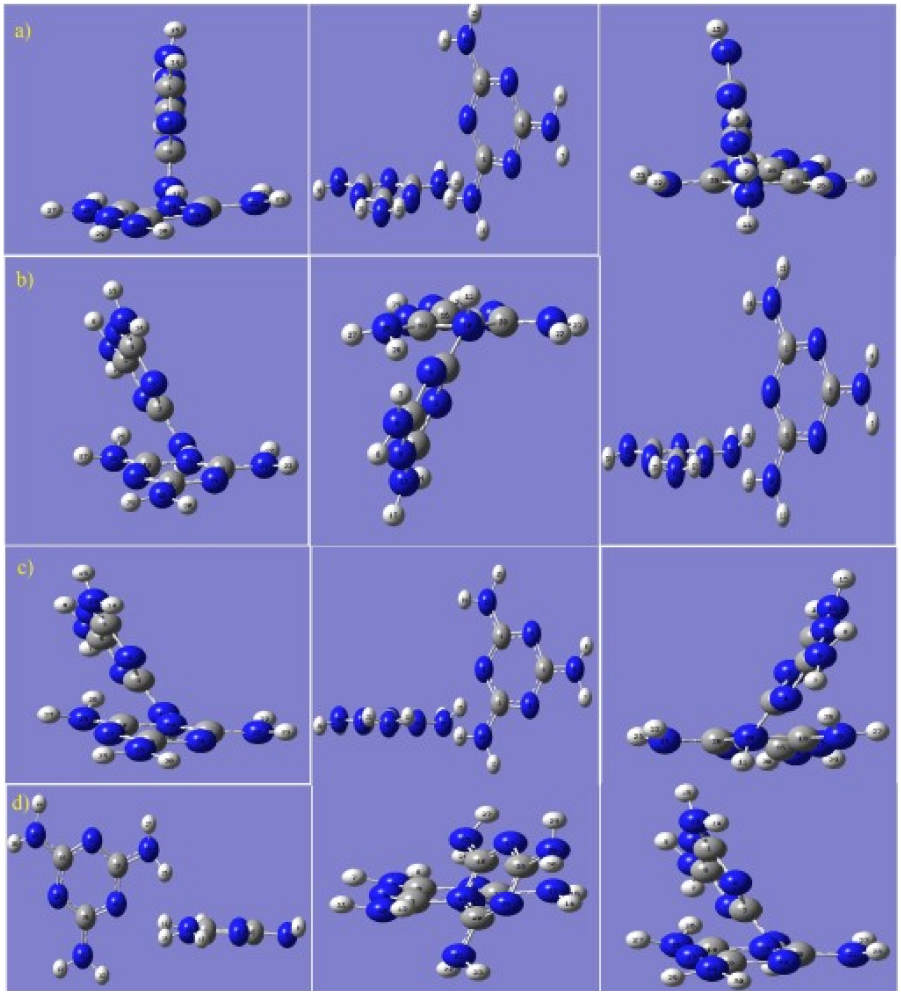

Figure 2a-18. *Structural representations of energetically least favorable conformers by using (a) B3LYPD3/6-311++G(d,p), (b) B97XD/6-311++G(d,p), and (c) B3LYP-D3/6-31G(d,p) and (d) MP2/6-311++G(d,p) functional respectively. In this figure each row represents the differnt portrayals of same configuration.*

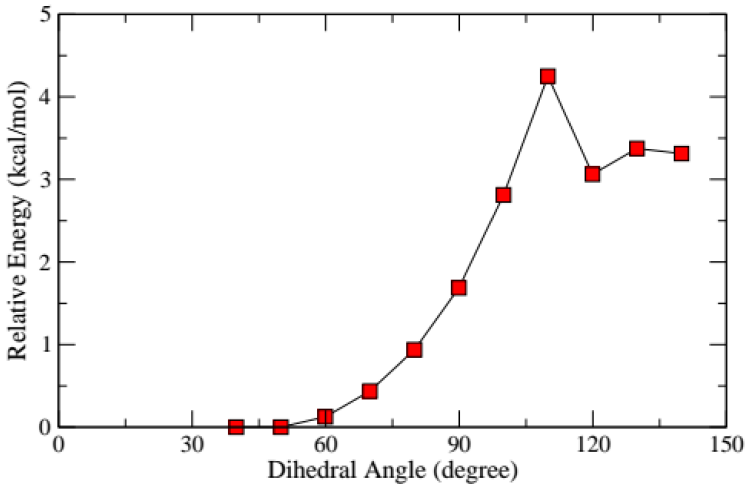

Figure 2a-19. *Potential energy surface of Type-1 complex calculated by using B97XD/6-311++G(d,p) level of theory. The relative energies of different conformations are calculated by rescaling the most stable structure to zero energy.*

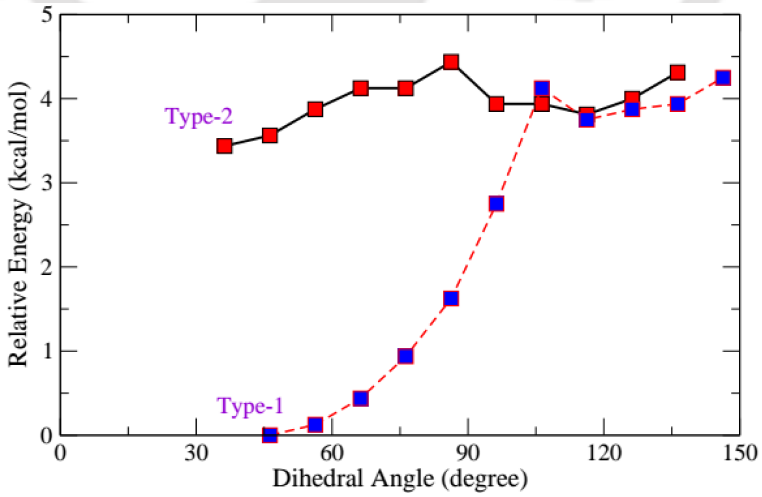

Figure 2a-20. *Potential energy surface of Type-1 (blue square) and Type-2 (red square) complexes calculated by using B3LYP-D3/6-31G(d,p) level of theory. The relative energies of different conformations are calculated by rescaling the most stable structure to zero energy.*

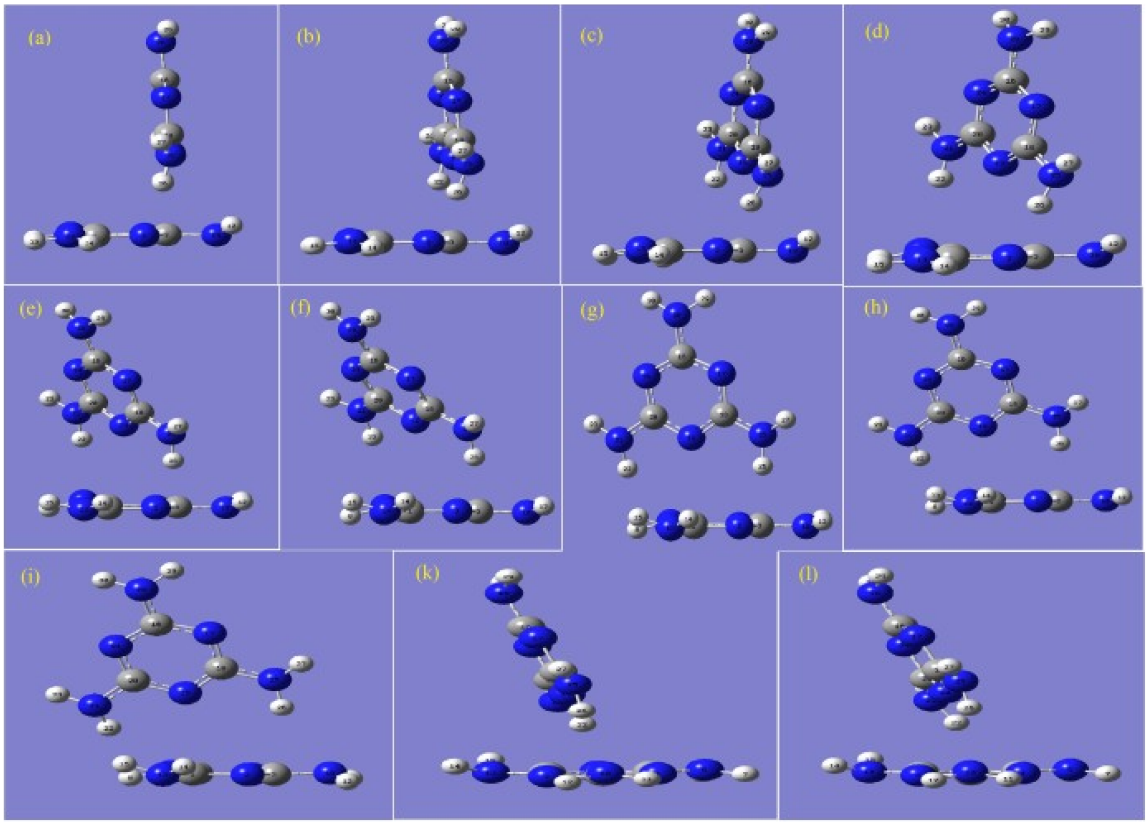

Figure 2a-21. *All the structures from (a) to (l) that are generated during PES scan by B3LYP-D3/6-31G(d,p) level of theory where the angle of the Type-2 structure is varied from lower to higher angle respectively.*

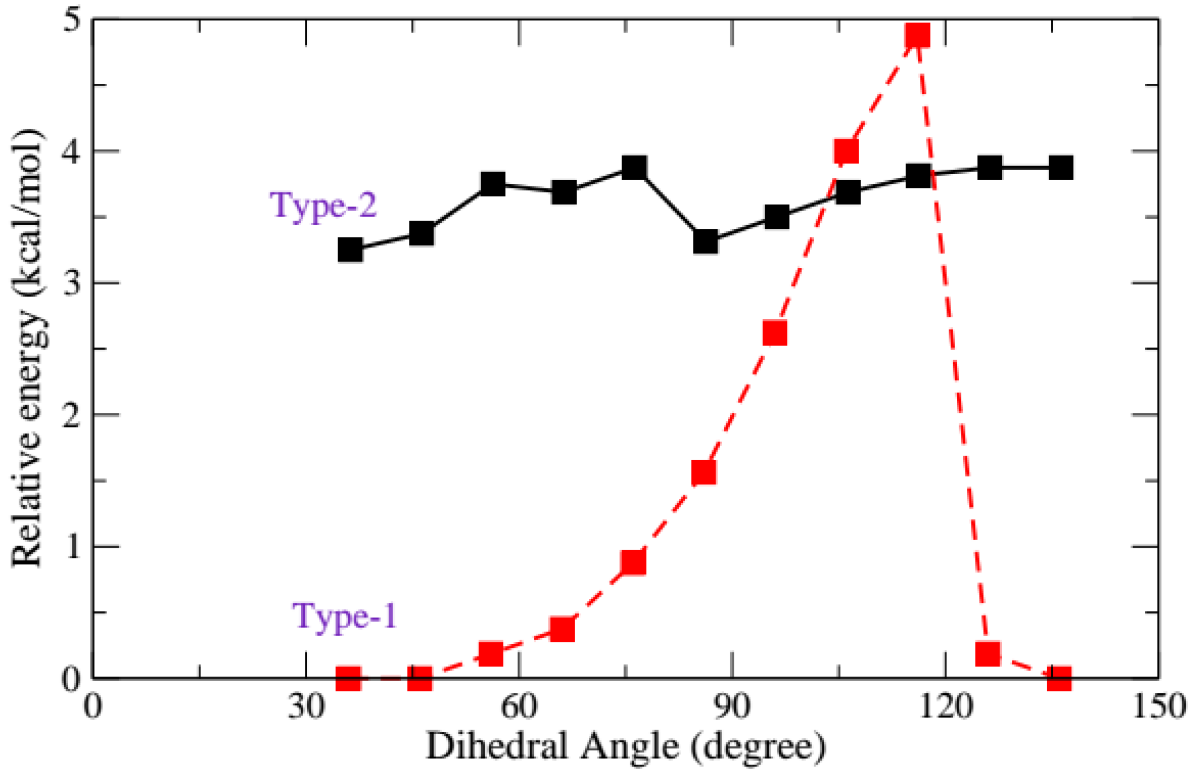

Figure 2a-22. *Potential energy surface of Type-1 (red) and Type-2 (black) complexes calculated by using B3LYP-D3/6-311++G(d,p) level of theory. The relative energies of different conformations are calculated by rescaling the most stable structure to zero energy.*

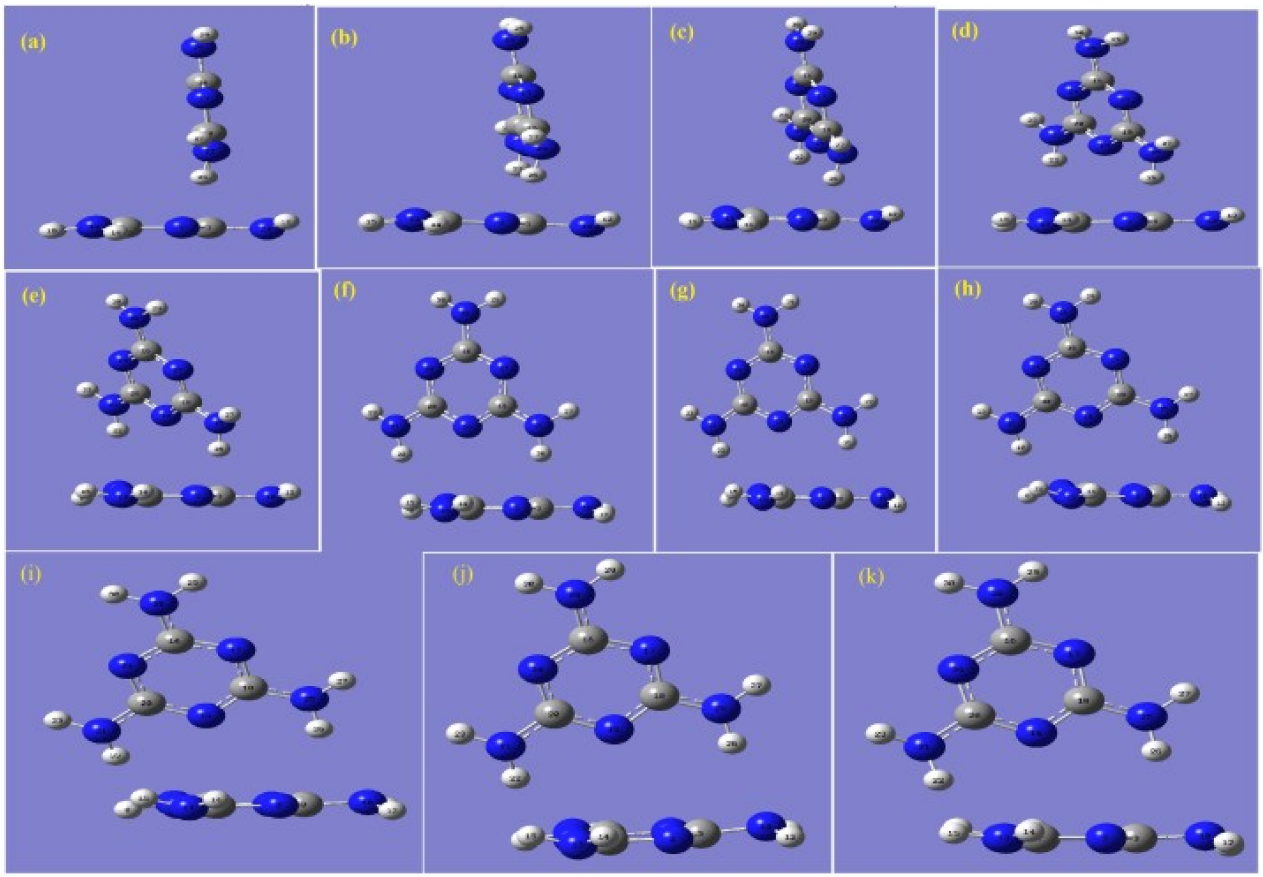

Figure 2a-23. *All the structures that are generated from (a) to (k) during PES scan by B3LYP-D3/6-311++G(d,p) level of theory through the angle variation of the Type-2 structure from lower to higher angle respectively.*

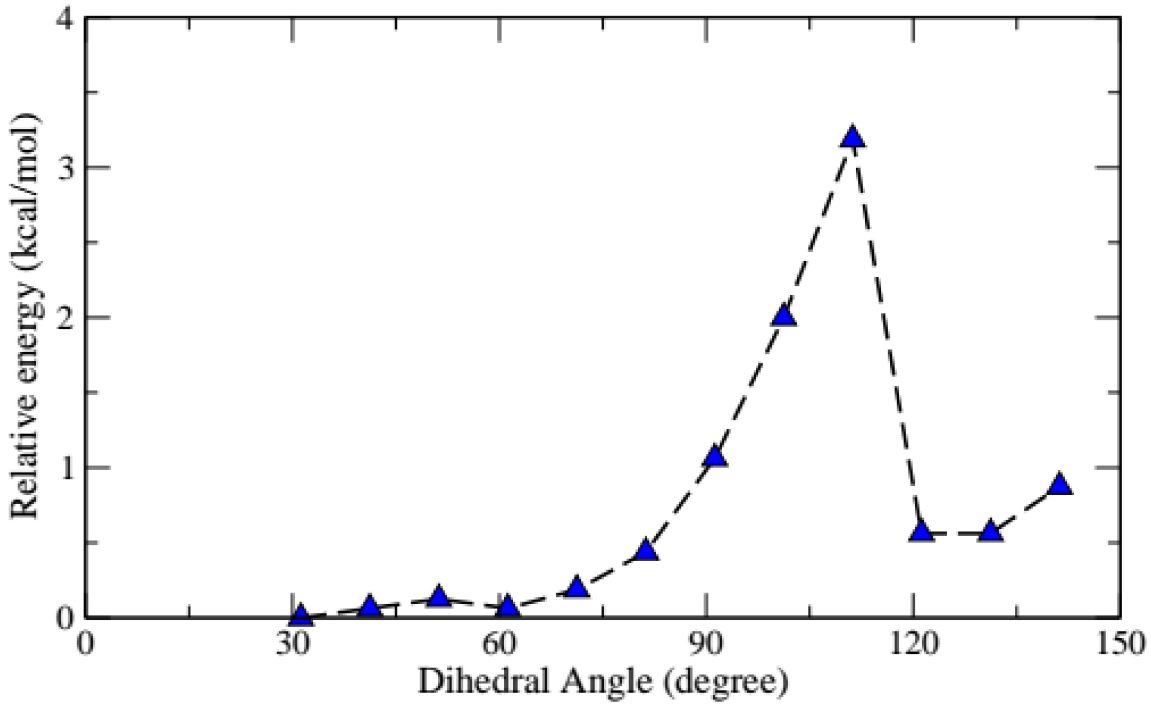

Figure 2a-24. *Potential energy surface of Type-1 complex calculated by using MP2/6-311++G(d,p). The relative energies of different conformations are calculated by rescaling the most stable structure to zero energy.*

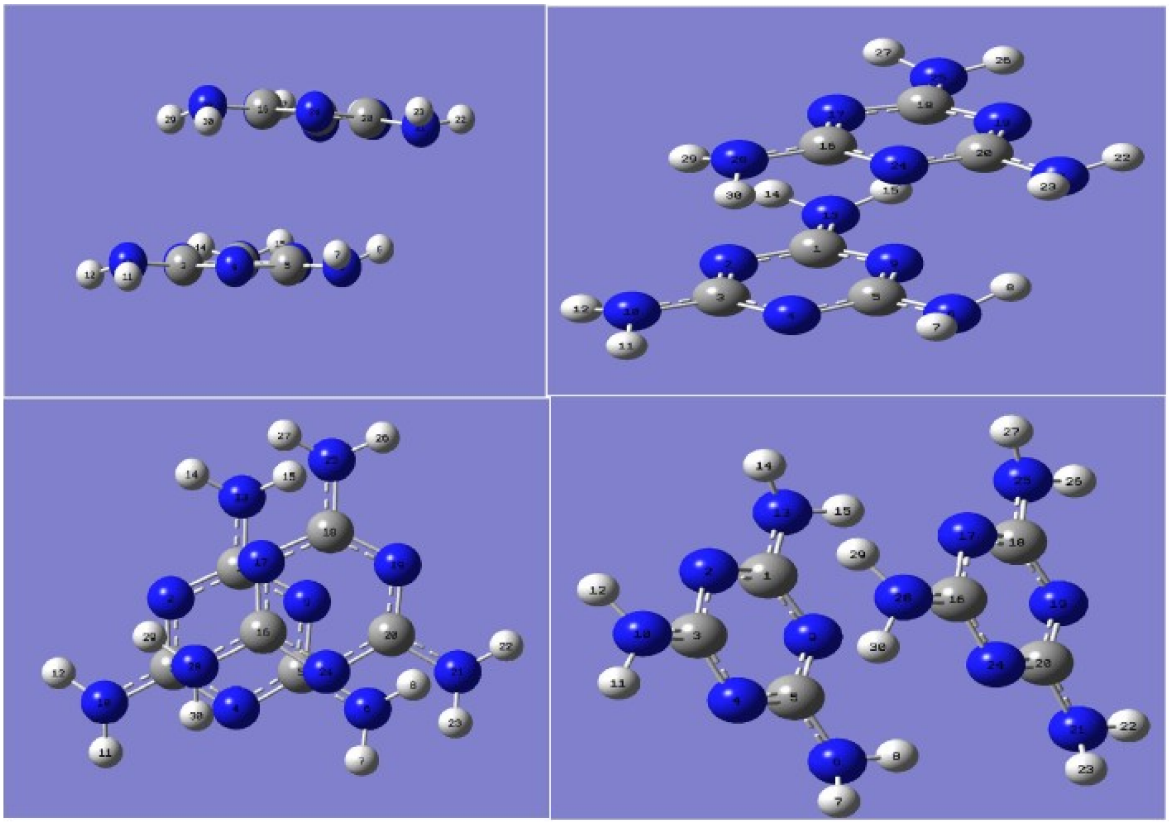

Figure 2a-25. *Layered structures generated from the B3LYP-D3/6-311++G(d,p) level of theory where one MM hovers over the other MM molecule. Here all structures represent different portrayal of same stacked conformation.*

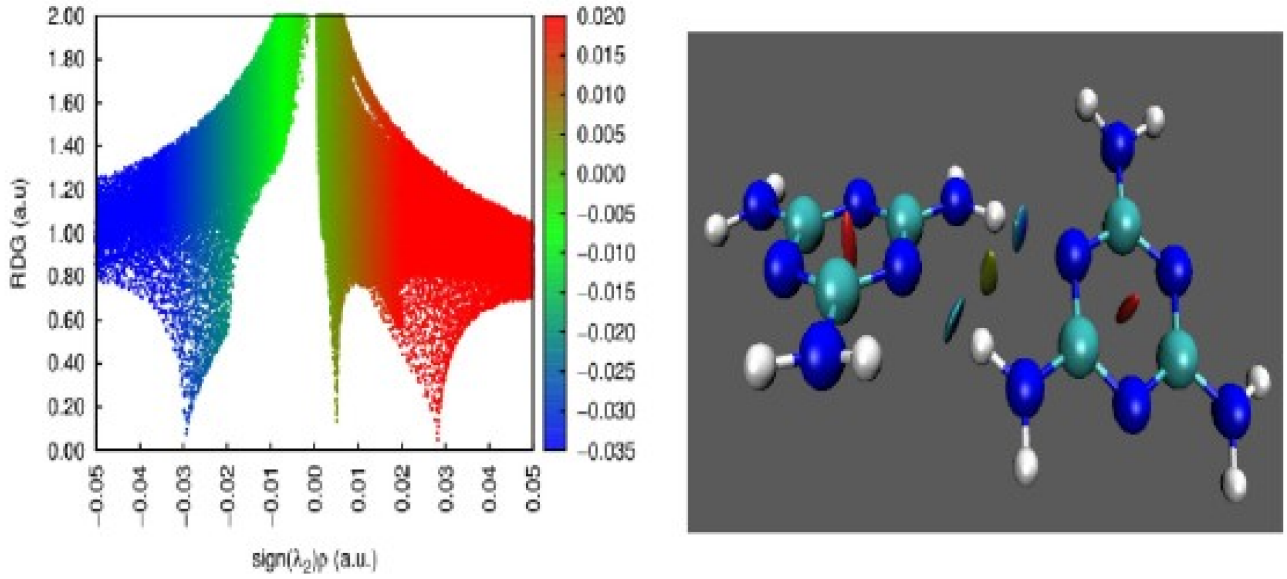

Figure 2a-26. *Reduced Density Gradient (RDG) plot for the nearly coplanar structure that is generated by the optimization using B3LYP-D3/6-311++G(d,p) level of theory between two MMs.*

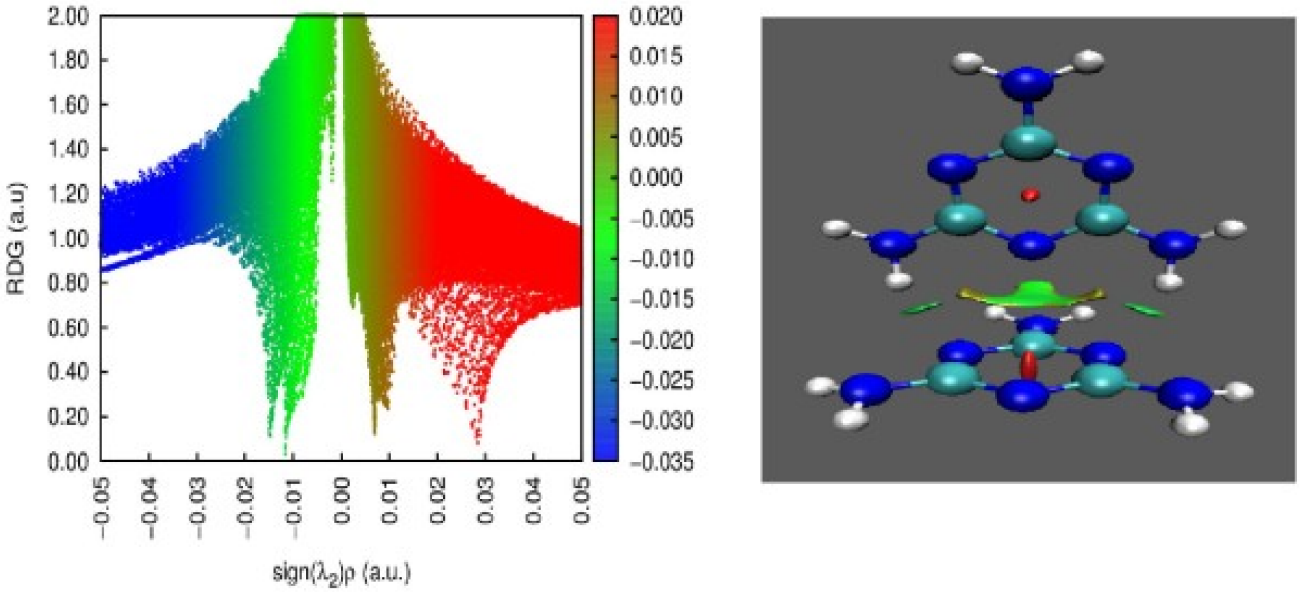

Figure 2a-27. *Reduced Density Gradient (RDG) plot for the almost perpendicular structure that is generated by the optimization using B3LYP-D3/6-311++G(d,p) level of theory between two MMs.*

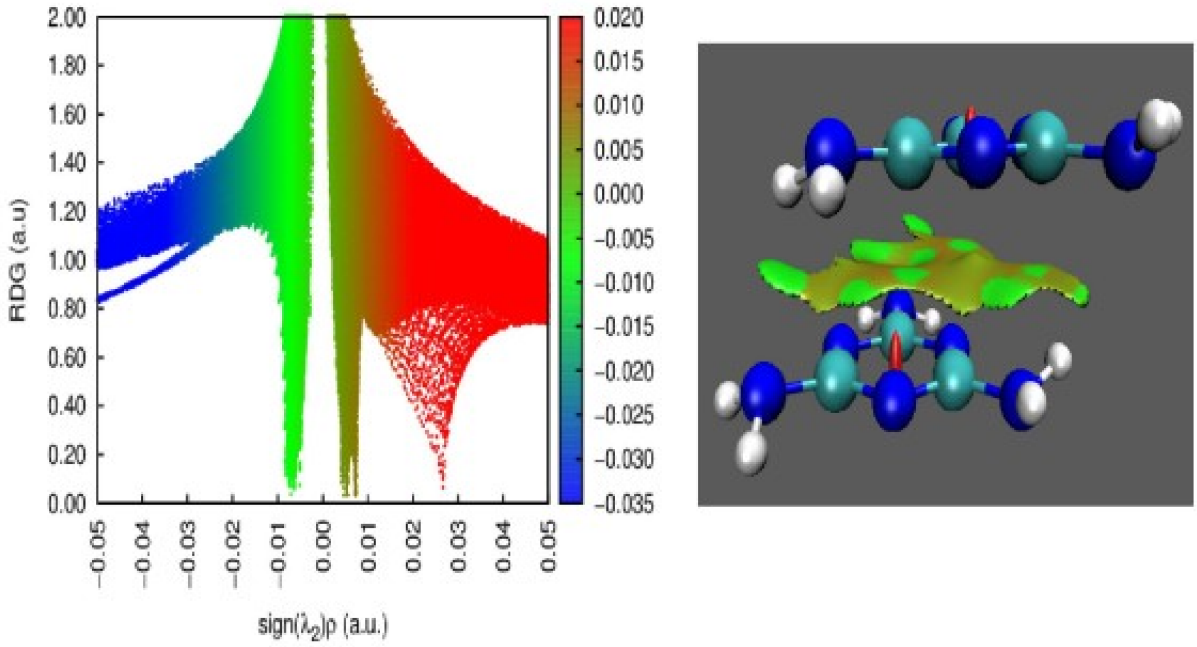

Figure 2a-28. *Reduced Density Gradient (RDG) plot for the stacked structure that is generated by the optimization using B3LYP-D3/6-311++G(d,p) level of theory between two MMs.*

have further performed a PES scan in gas phase only with a different long-range corrected functional namely, ωB97XD functional with triple zeta basis set 6-311++G(d,p). In this case, we get a similar result (Figure 2a-19) where Type-1 is the most stable structure and the most unfavorable one being almost perpendicular can be seen in Figure 2a-18(b). Next taking the Type-2 and Type-1 structures (Figure 2a-16) as initial configurations, we have also performed another two PES scans by B3LYP-D3/6-31G(d,p) level of theory in the gas phase up to 150^o variation by 11 steps with an interval of 10^o degree with respect to the same dihedral angle. Here, this basis set is used to hasten the calculations to cover a wide range of angle variations. In this case, when we start with Type-1 structure, we get the similar trend like the one in the previous scans (Figure 2a-20) with a unfavorable one, in which MM molecule is perpendicular to another as can be seen in Figure 2a-18(c).

But, when we start with the Type-2 structure, we can see that all the structures that are generated are very similar to that of the original Type-2 (see Figure 2a-21) with relatively higher in energy than that of type-1 structure (Figure 2a-20). To verify this result, we again run another PES scan with B3LYP-D3/6-311++G(d,p) level of theory. This scan also shows the similar pattern with that of the B3LYP-D3/6-31G(d,p) (Figure 2a-22). Here, we can also see that, if we consider the Type-2 structure as initial structure, we get all the structures that are very similar to that of the Type-2 (Figure 2a-23) and all the structure have relatively higher in energy than that of Type-1 (Figure 2a-22). Moreover, we have carried a more robust PES scan with MP2/6-311++G(d,p) level of theory starting with Type-1 structure. We find a very similar results with no exceptions (Figure 2a-24) suggesting that the almost perpendicular structure is the most unstable one (Figure 2a-18(d)). We have also calculated the complexation energy for all the conformations using BSSE correction method (Table 2a-7). This complexation energy data further confirms that Type-1 is the most stable conformer over the other structures. From our frequency calculation, we find that there is no imaginary frequency in the optimized structures. Now we consider a layered structure in which one MM hovers over the other (Figure 2a-25) and we calculate the complexation energy with B3LYP-D3/6-311++G(d,p), B3LYP-D3/6-31++G(d,p) and other level of theories. From the energical point of view, we get that the Type-1 is the most stable over all the structures (Table 2a-7). So, from our quantum calculations, it is apparent that hydrogen-bonded nearly coplanar structure between MM molecules with a dihedral angle between 36^o-46^o is the most stable over the other structures, say parallel, anti-parallel or perpendicular. Our findings are in good accordance with the previous quantum chemical calculations reported elsewhere.[129, 130, 163] Moreover, these pieces of literatures did not produce the PES scan result over a wide range of angles in gas phase as well as in liquid phase. Further, the continuum model PES scan of dihedral angle between two MM molecule (carried out in this study) is not reported so far. For all the above quantum calculations, Gaussian09 package is used.[138]

Reduced density gradient (RDG) method is very popular for studying weak interactions. So, we have employed RDG and its color-filled variant to investigate the interaction between two MM molecules. To do so, we take optimized structures from B3LYP-D3/6-311++G(d,p) level of theory and draw a scattered map (color filled isosurface graph) with default isosurface value 0.5 and with default color range from 0.035 to 0.02. From the plots (Figure 2a-26, Figure 2a-27, and Figure 2a-28) we can see that hydrogen bonding

interaction (when two MM molecules are coplanar with each other) predominates over the other interactions such as vdW and $\pi - \pi$ stacking (when two MM molecules are arranged in perpendicular and stacking fashions respectively). This calculation is done by employing Multiwfn software.[164, 165]

Table 2a-7. Calculated complexation energies for all conformations (Type-1, Type-2, A, B, C, D and stacked conformer) using BSSE correction in gas phase. A, B, C and D represent the least favorable conformations among the all structures in a PES scan of dihedral angles using B3LYP-D3/6-311++G(d,p), ωB97XD/6-311++G(d,p), B3LYP-D3/6-31G(d,p) and MP2/6-311++G(d,p) levels of theories respectively. Here, B3LYP-D3/6-31++G(d,p) level of theory is just used for the determination of the complexation energy of Type-1, Type-2 and Stacked conformers only. All energy values are expressed in kcal/mol units.

Conformation	B3LYP-D3/ 6-31G(d,p)	B3LYP-D3/ 6-311++G(d,p)	ω97XD/ 6-311++G(d,p)	MP2/ 6-311++G(d,p)	B3LYP-D3/ 6-31++G(d,p)
Type-1	-14.91	-13.80	-13.48	-10.21	-13.73
Type-2	-9.76	-9.65	-9.96	-7.79	-9.64
A	—	-8.44	—	—	—
B	—	—	-9.46	—	—
C	-11.24	—	—	—	—
D	—	—	—	-7.25	—
stack	-9.70	-9.49	-9.80	-8.51	-9.68

Isothermal Titration Calorimetry (ITC)

According to this experiment, from the fitted curve (Figure 2a-29), we get ΔH = -48960 cal/mol and ΔS = -156 cal/mol at 300K temperature and these give ΔG = -2.16 kcal/mol. So, from the ITC experiment, the MM association by non-covalent interaction in water at 300K is essentially enthalpy driven and the change in free energy for the same is -2.16 kcal/mol.

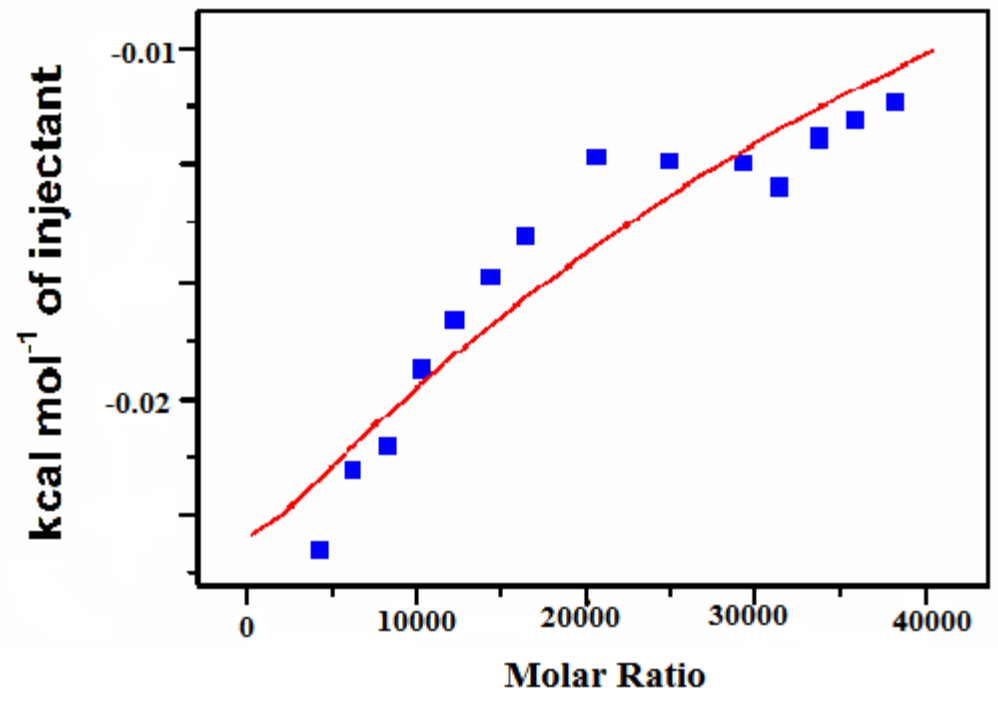

Figure 2a-29. *Isothermal Titration Calorimetry curve for 1:1 binding of MM molecules at 300 K temperature.*

■ SUMMARY AND CONCLUSIONS

Classical molecular dynamics (MD) simulations together with quantum calculations and Isothermal Titration Calorimetry (ITC) experiments are performed to investigate the association of MM molecules in water in a range of MM concentrations at ambient temperature (300 K) and pressure (1 atm) conditions. In order to verify the results obtained, we have further considered high level quantum calculations. The snapshots of different systems reveal that the association propensity of MM molecules in water decreases as MM concentration is decreased. This finding is in accordance with the recent experimental findings.[134] This finding is further confirmed by the contour density maps of water around MM for different systems, which show that as the MM concentration is decreased, the density of water molecules around the MM increases implying more and more hydration of MM molecules. The quantitative estimations of the average number of MM and water

molecules as measured by running coordination numbers, also act as corroborative shreds of evidence of these observations. The coordination number of water molecules around a MM molecule at 3.45 Å (around 4 water molecules) is in good agreement with the experimental results.[136] The analyses of the potential of mean forces confirms the initial probability of the growth of higher order clusters. The analyses of the probability of formation of MM clusters of different sizes for different systems reveal the breaking of higher order MM clusters into smaller sizes as MM concentration is decreased. This is well matched with the recent experimental report.[134] In order to probe the role of $\pi - \pi$ interactions, if any, between the aromatic rings of MM molecules on the association of MM molecules, the probability of orientational preferences between the aromatic rings of two reference molecules are considered for the highest MM concentration. A broad distribution together with the appearance of maximum probability at an angle of 54^o essentially rules out the role of strong $\pi - \pi$ interactions in MM association. These findings are also confirmed by the quantum chemical calculation, which apparently tells that a MM molecule prefers to bind with another MM molecule with a dihedral angle ranging from 36^o to 46^o in a nearly co-planar arrangement between them and the quantum calculations presented here nullifies the possibility of the presence of other conformations. These results match well with the experimental observations.[129, 130, 125, 126]

The analyses of the average number of different hydrogen bonds such as water-water, water-MM and MM-MM for different systems suggest that in the MM-MM hydrogen bonds the hydrogen atoms attached to sp^3 hybridized nitrogen atoms of MM form the significant number of hydrogen bonds with sp^2 hybridized nitrogen atoms of MM. On the other hand, in MM-water hydrogen bonds, the hydrogen bonds involving the atomic sites of sp^3 hybridized nitrogen atoms of MM and water contributes more than that for the atomic sites of sp^2 hybridized nitrogen atoms of MM and water molecules.[135, 136] We have also determined the dimer existence autocorrelation functions to investigate the MM-dimer stability with time in aqueous solution. This analysis of the dynamical nature of dimers as aggregates of MM molecules shows the sharp distinctions over lifetimes between different systems where dimer lifetime gradually decreases with the decrease of MM concentrations. These findings are in accordance with our earlier analyses discussed above. Moreover, as MM concentration is decreased, as expected, the average number of MM-MM hydrogen bonds decreases and MM-water hydrogen bond number is increased. Here, we note that in all the systems the maximum number of hydrogen bonds are observed for water-water. Further,

the decomposition of total MM-MM interactions into electrostatic and vdW components indicate that it is the former interaction which plays a major role in the MM association. With decrease in the MM concentration, these interaction energies become more and more unfavorable. Moreover, from the calculations of enthalpy and entropy contributions towards the association of MM molecules in water, it is found that the association process is essentially enthalpic in nature. And our finding is in line with the experimental finding also. Furthermore, the thermodynamics of MM association reveals that the association process is essentially driven by enthalpy and this enthalpy driven phenomenon is also confirmed by the experimental isothermal titration calorimetry measurements. Findings of this study can serve as theoretical references for future identification and utilization of MM aggregates as well as clusters. Again, the results obtained in this study will prove to be helpful for designing new and effective drugs to prevent MM aggregation in order to eliminate harmful diseases.

2b: How does Temperature Modulate the Structural Properties of Aggregated Melamine in Aqueous Solution?

"Medicine heals doubts as well as diseases."

– Karl Marx

Overview: In the present study, classical molecular dynamics simulation of eight melamine (MM) molecules are carried out in water over a temperature range from 300 K to 380 K at ambient pressure to examine the molecular details of MM aggregation along with the impact of temperature on the aggregated state of MM in water. It is found that the hydrogen bonds formed between sp^3 N-sp^2 N, which is mainly responsible for aggregation over the sp^3 N-sp^3 N, is disturbed mainly by the rise of temperature. These outcomes are complemented by the consideration of average number of hydrogen bonds per MM and preferential interaction parameter calculations. The impact of temperature is negligible on the orientational probability between the two triazine cores. The $\pi - \pi$ stacking interaction between two triazine rings plays less significant role on MM aggregation. Dynamical calculations, by considering the cluster structure analysis and dimer existence autocorrelation function, strengthen the fact of destabilization of aggregated MM in water with the rise of temperature. Free energy of solvation, association constant along with the binding free energy between a MM pair give the thermodynamical points of view about the impact of temperature on MM aggregation. Interestingly, potential of mean force calculation by the use of umbrella sampling explains the reasons, in depth, of how does sp^3 N-sp^2 N interactions confirm the decrease of initial probability of growth of higher order clusters with the increase of temperature.

■ INTRODUCTION

MM (1,3,5-triazine-2,4,6-triamine) is a very stable molecule of s-triazine group. From the structure of MM (Figure 2b-1), it can be easily seen that it contains six nitrogen atoms. These nitrogen atoms form intermolecular hydrogen bonds to like molecules along with other complementary molecules. MM is used widely in industrial purposes like plastic and coating industries. Not only that, it has a broad application in making cements, pastes, laminates, fire retardants etc. as it contains the high percentage of nitrogen by weight. It can be harmful when it is consumed in human as well as non-human body. Nowadays, it is not very unknown to everybody that MM is the main component for the cause of urinary stones. It strongly binds with uric acid in our body to form an insoluble crystals in our unitary tract. Sometimes this urinary inflammation causes death also.[1, 77, 2]

In 1941, Hughes discovered first the crystal structure of MM. Later on, the IR spectroscopy and the theoretical vibrational calculations were made. From these studies the structural phenomenon of MM along with its diverse hydrogen bonding property can be sensed well. From then to till now, MM is a great choice of chemists. In the field of crystallography, various crystals designed by MM-formaldehyde, MM-cyanuric acid etc. encourage the researchers to develop new crystal structures modified by MM. This field of crystallography in chemistry generated the most awaited crystal structure of MM-uric acid after the sudden outbreak of renal calculi in the various part of the universe.[166, 167, 168] In 2007, K. M. Anderson *et. al.* proposed the MM and uric acid crystal structure.[26] Later on, other groups shed lights on this structure carefully and proposed that MM and uric acid forms 1:1 complex. The formation of this complex is responsible for kidney stone.[45, 108] Currently, another research area of supra-molecular chemistry is highly delighted by the use of this molecule. In supra-molecular science, the procedure of self-assembly makes different complex structures. In the course of the most recent couple of years, a developing significance of the gadgets, made of nano-material, has boosted the investigation of intra along with inter-molecular chemical forces like hydrogen bonds. These weak forces have a control to the arrangement of one to three dimensional ordered nanostructures. These nanostructures are built mainly by the self-accumulation of little molecular building blocks with the extensive utilization of hydrogen bonding communications. This field is highly enriched by the wide use of MM due to its structural functionalism.[169, 170]

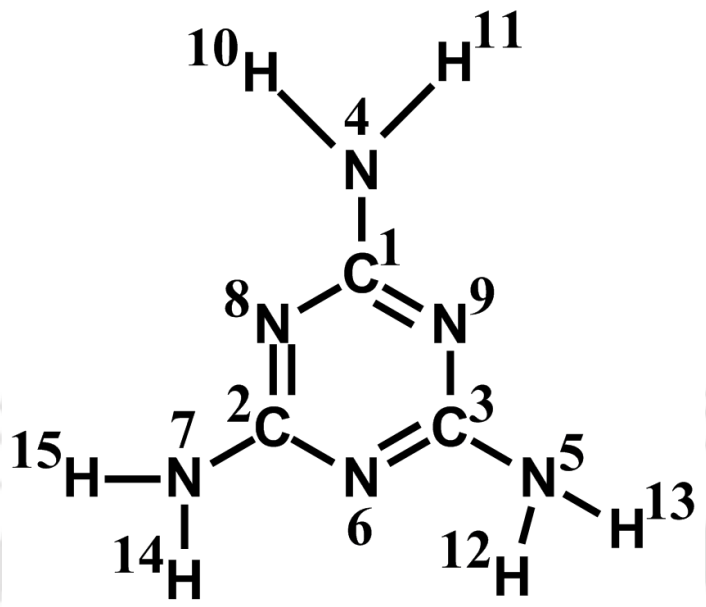

Figure 2b-1. *Structure of MM with atom numbering.*

If the thing is good it will have some negatives also. From the above discussion, it is sure that MM is used in various chemical purposes to shape magical structures by the use of crystallography and supra-molecular chemistry, but unfortunately this exciting property of MM causes lots of loss in the universe. Due to the presence of high percentage nitrogen content in it, people started to mix it with the baby foods to increase the nitrogen content falsely. As a result of these, renal calculi becomes the lead news with a new threat to the world. Some pseudo-medical researches said that, MM itself can aggregate also in our body in absence of uric acid. This self-accumulation causes various urinary along with harmful diseases in human and also in pets like cat, dog etc. So how does MM self-aggregate? Various studies presented in time to time and reported about the fact of aggregation process among MM molecules. This aggregation process may take place in water or it may happen in various solvents. In each and every solvent, it shows different structural pattern. But its main characteristics, that is, hydrogen bonding remains unchanged. The results of various crystallographic and microscopic techniques proposed that at ambient conditions MM forms a crystalline molecular solid. In this crystalline state it shows monoclinic symmetry with P21/a space group. Interestingly, in such structure, N-H$\cdots$ N intermolecular interactions predominates. Similar kind of findings are also said by various groups but presenting all the references is beyond the scope. From these literatures,

it is clear that MM forms hydrogen bond with itself through sp^3 N-sp^3 N and also with sp^3 N-sp^2 N communications.[1, 77, 2, 171, 172, 173] In our previous study[174] we have proposed that how does MM behaves in water with the variation of concentration. In 1943, the solubility change of MM in water over the range of temperature from 0^o-100^o C was studied by R. R. Harris *et. al.*.[124] And they presented the data on MM solubility at these temperature range. They found that with the increase of temperature, solubility of MM increases incredibly. Sadly, though experimental studies although tell about the aggregation process at ambient condition and also presented the solubility of MM in water with the increase of temperature, the atomistic details of how does the arrangement of MM molecules change with the rise of temperature are not reported. Moreover, in experiment it has also been said that the hydrogen-bonding is the main reason for the formation of different sizes of clusters by MM in water at ambient conditions. In another experiment, W. F. Schmidt *et. al.*[171] reported the interruption of consistency of packing of MM molecules with the increase of temperature. An explanation consistent with their results is that with the increase of temperature, the ring structure becomes more inflexible in general, and two of the NH2 sites turn out to be more planar, however one C-N site twists more out of plane. This molecular site turns to be progressively more unequal, i.e., above or below the steady ring plane. The increase with temperature in out-of-plane bending may disturb the packing among MM molecules. Temperature dependent properties may be helpful for phase transitions and may correlate with chemical reactions. Again temperature dependent properties of MM may also be useful for the identification of the environmental contamination made by triazine in soils and fertilizers as recent food and animal feed safety incidents has prompted to an immediate need for rapid and trusted methods for the identification of MM not only in various products of food, but also in environmental samples. As a small contributions have been paid to explore the mechanistic details of interaction mechanism between MM molecules in water, a concluding remarks about the aggregation of MM in water at ambient temperature as well as higher temperatures with atomistic details are yet to be achieved. Therefore, in this work, for the first time, classical MD simulation was carried out by us to examine the self-aggregation of MM in water with a range of temperature at a fixed MM concentration. By this study, we want to achieve the following goals: (a) How does the aggregation pattern of MM change with temperature? (b) What is the change of exact number of hydrogen bonds made by MM with the change of temperature? (c) How does the triazine ring of MM orient themselves

during aggregation with the impact of temperature on the orientational angle? (d) Between the two possibilities i.e., MM sp^3 N-MM sp^3 N ($H_{sp3N-sp3N}$) and MM sp^3 N-MM sp^2 N ($H_{sp3N-sp2N}$) H-bonding, which one predominates with proper explanation and (e) the dynamical properties of MM dimers with the cluster structure analysis of MM molecules to show the impact of temperature of the aggregated structure of MM to increase the solubility as proposed by experimental findings.

Rest of the chapter consist of three sections. The models and simulation details are given in section II. Section III proposes the results with discussion in detail by presenting the related information and lastly summary and concluding remarks are presented in the section IV.

■ MODELS AND SIMULATION METHOD

Classical molecular dynamics (MD) simulations were carried out using 8 MM molecules in water at five different temperatures. The distinctive systems, S0-S4, considered here are outlined in Table 2b-1. For MM, at to begin with, the structural information files were taken from our previous work.[174] In our earlier work,[174] RESP suite of AMBER12 program package[139, 140] was employed to obtain the partial charges of MM and their GAFF force field parameters were used with the help of ANTECHAMBER module built in AMBER12.[141, 142] For all systems, TIP3P water model was used.[143] At first the initial configuration of system S0 was prepared by the use of PACKMOL.[144] The rest of the systems were generated by using the same initial configuration of that of S0. During the course of the simulations, for all systems, we have fixed the temperature at the desired temperature. For each of the systems, a cubic box was used for incorporating all the molecules. For all simulations, at first, energy minimization of 10000 steps were carried out in which first 4000 steps are performed in steepest descent method and for rest 6000 steps the conjugate gradient method was employed. Then the systems were heated up to 480 K starting from 0 K temperature at an interim of 50 K for 20 ps. Such heating benefits to effective unwinding of the systems to surmount the global minimum boundary stature. This is trailed by extinguishing the systems to the coveted temperature with a decrement interim of 25 K in canonical ensemble (NVT) followed by 5 ns equilibration for all systems at isothermal-isobaric (NPT) ensemble. Subsequently simulations were then expanded to 180 ns in NPT ensemble to analyze the diverse contributory properties for all the systems. PBC were applied in all directions. Langevin dynamics[145] method was applied to control

the temperature for all

Table 2b-1. Overview of systems[a]

System	N_{MM}	N_{wat}	Temp.(K)	Box Length (Å)	Conc.(M)
S0	8	1500	300	35.880	0.2876
S0-a	8	1500	300	35.913	0.2897
S0-b	8	1500	300	35.953	0.2858
S1	8	1500	320	36.176	0.2806
S2	8	1500	340	36.324	0.2771
S3	8	1500	360	36.701	0.2687
S4	8	1500	380	36.967	0.2629
S4-a	8	1500	380	36.968	0.2629
S4-b	8	1500	380	37.252	0.2569
S5	8	1500	300	35.738	0.2909
P0	2	2000	300	39.312	0.0547
P1	2	2000	320	39.602	0.0535
P2	2	2000	340	39.897	0.0523
P3	2	2000	360	40.204	0.0511
P4	2	2000	380	40.584	0.0497

[a] N_{MM} and N_{wat} are the number of MM and water molecules respectively. M is the molar concentration of MM.

the systems with 1 ps^{-1} collision frequency. The pressure of the systems (in NPT ensemble) was maintained with Berendsen barostat using a 2 ps relaxation time.[146] For estimating the long-ranged electrostatic interactions, Particle Mesh Ewald (PME) algorithm was applied.[147] All covalent bonds containing hydrogen atoms were constrained by the use of SHAKE algorithm.[148] A 10 Å cut off distance was used to treat the all non-bonding short-ranged interactions. Furthermore, to test the biasness, if any, before summarizing the consequences obtained on this study, two different systems, say S0-a and S4-a, having different initial configurations were tested following the identical manner referred to above. These systems S0-a and S4-a contain identical number of different molecules as that of systems S0 and S4 respectively. These newly generated systems were then subjected to separate 180 ns MD simulation runs. Since, the aggregation could, on a fundamental level, rely upon the decision of the thermodynamic ensemble, we have run additionally a 180 ns NVT reproduction (at pressure of 1 bar and an indistinguishable temperature from in the NPT calculation) for two of the considered systems (S0-b and S4-b). In MD simulation, the usage of NVT ensemble can be successful for the assurance of the aggregation pattern of any molecule (clusterization in particular) in aqueous solvent. For this, these two systems

(S0-b and S4-b) were composed. Those systems were used for the predictions of aggregates of MM clusters. Furthermore, to check the force field dependency for various properties of MM solution, the system S5 was prepared wherein CHARMM general force field (version 3.0.1) [175]was used for MM (Table 2b-2) and TIP3P model was

Table 2b-2. Force field parameters[a]

Atom Name	CGenFF Atom Type	$R_{min}/2$ (Å)	$\epsilon(kcal/mol)$	Partial charge (e)
C1/C2/C3	CG2R64	2.1000	-0.0400	0.849
N6/N8/N9	NG2R62	2.0600	-0.0500	-0.780
N4/N5/N7	NG2S3	1.8500	-0.2000	-0.775
H1-6	HGP4	0.2245	-0.0460	0.353

[a] CHARMM GENERAL FORCE FIELD parameter for different atomic sites of MM molecule with elementary charge.

Table 2b-3. System overview[a]

Systems	Temp.(K)	N_{MM}	N_{wat}	Box Length (Å)	Conc.(M)	$H_{sp3N-sp3N}$	$H_{sp3N-sp2N}$	$total_{m-m}$
S300	300	24	1500	36.350	0.8296	1.18	3.48	4.66
S380	380	24	1500	37.375	0.7632	1.05	2.76	3.81

[a] N_{MM} and N_{wat} are the number of MM and water molecules respectively. M is the molar concentration of MM. $H_{sp3N-sp3N}$, and $H_{sp3N-sp2N}$ represent the MM-MM (per MM through $sp3N$-$sp3N$ N atoms), MM-MM (per MM through $sp3N$-$sp2N$ N atoms of MM), for the distinctive systems. Here, hydrogen bonds are given for last 120ns MD run.

adopted for water. This specific simulation for system S5 was carried out by the usage of the NAMD 2.10 code.[176] At the beginning, the system S5 was energy minimized by using conjugate method. The temperature of the system was continuously increased to 300 K through a quick 20 ps MD run by the use of NVT ensemble. Then the whole system was equilibrated for 1 ns at 300 K temperature and 1 atm pressure in NPT ensemble. The temperature was controlled by the Langevin dynamics with a friction constant of 5 ps^{-1}. Again Langevin piston approach with 100 fs of a piston period, 50 fs damping time regular and a 300 K piston temperature were employed to keep the preferred pressure. At the end of the equilibration step, for the system S5, total 200 ns production run was performed in NPT ensemble with a cut off distance of 12 Å . In addition, to estimate the potential

mean force (PMF) between 2 MM molecules, umbrella sampling[150] was done. For this, five systems (P0 to P4) with two MM molecules in 2000 water were prepared (Table 2b-1). Following an indistinguishable method from the different systems (S0-S4), each system was simulated for 410 ns. The reaction coordinate, which was estimated as a component of a separation amongst N4 and N9 atom of two MM molecules, was differed from 2 to 12 Å by a small increase of 0.25 Å to acquire the PMFs. To get the PMF, the results were then analyzed using the Weighted Histogram Analysis Method (WHAM).[151] In this regard, we need to express that the focus of our study is centered around the systems S0 to S4. We try to demonstrate how structural properties of MM is changed at difference temperatures. Alongside this, S0-a and S4-a systems were utilized for the confirmation of the accuracy of the outcomes originating from the systems i.e S0 and S4. Again with this, the systems S0-b and S4-b were made to ponder the clusterization procedure specifically to confirm the rightness of the outcomes of the cluster structure investigation that were obtained from the systems S0 and S4 respectively. Further, the system S5 was prepared to examine the force field dependency of MM aggregation alongside the orientational probability of the six membered ring in particular. Entirely, orientational probability (mostly $\pi - \pi$ stacking and perpendicular shape between two MM rings) is checked especially with the variety of two diverse force field i.e GAFF and CGenFF. Moreover, the 0.2876 (M) solution of MM at 300 K was chosen to examine the effect of temperature on MM aggregation. Furthermore, a system consisting of 24 MM molecules immersed into 1500 water molecules were also simulated at two different temperatures (Table 2b-3). The consideration of this concentrated system will allow us to cross-check the aggregation of MM molecules of systems with lower MM concentration. Therefore, 17 systems were considered to show the correct impact of temperature on MM aggregation in water.

■ RESULTS AND DISCUSSION

In this section, at first we discuss about the MM aggregation of S0-S4 systems. The snapshots of these systems, contemplated here, are viewed first and these are appeared in Figure 2b-2. The depictions are captured using VMD.[149] For better clarity of these depictions, the water molecules are not shown. Paying attention to the impact of temperature on the self-aggregation of MM molecules, it is observed that the aggregation affinity of the MM molecules diminishes as the temperature is increased and these observation is at per

with the expectation. Here it is important enough to justify that each of these depictions is derived from the single step of simulation and it uncovers the main aspects of MM

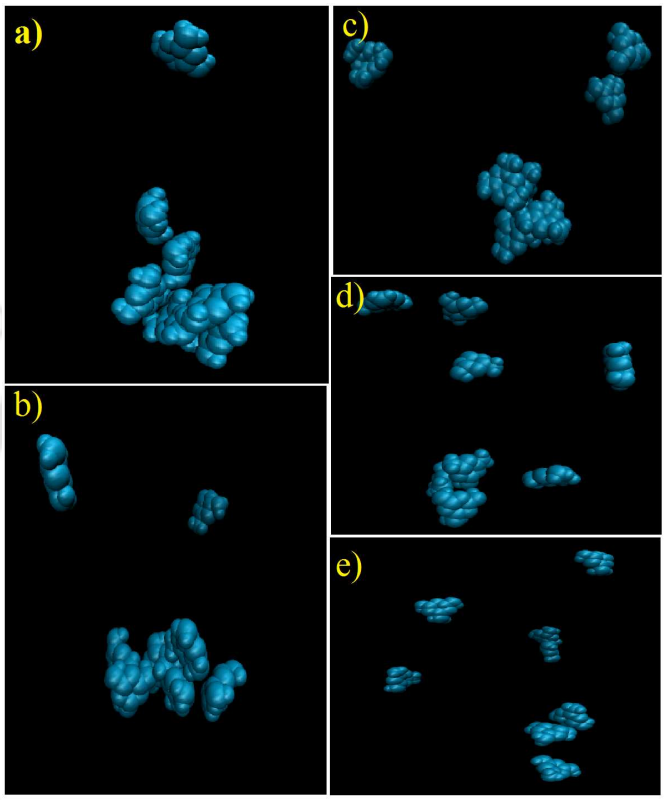

Figure 2b-2. *(a)-(e) represent the snapshots for different systems S0-S4. For clarity, the water molecules are not shown in the snapshots.*

association. Further, it is worth mentioning that as we are fascinated with the interpretation of molecular aggregation of MM in aqueous environment at different temperatures at an ambient pressure condition, the following discussions focus on the structural insights of the self association of MM in water at a range of temperatures by considering the average number of MM-MM hydrogen bonds (per MM), DACF, cluster structure analyses and so on. We will not intricate our discussions on MM-water relationship as it is already discussed somewhere else.[177] To analyze all the systems considered here, we initially look at the MM-MM pair correlation functions (rdfs) which is then multiplied by the number density (ρ) of the observed atom. As the g(r)'s can be deceiving as at a given distance, the peak heights are not identified with the number of chosen atoms, however, it relies principally on the number density (ρ) as the density changes with the increase of

temperature. For that reason g(r)s are multiplied by the (ρ) of that atom which is taken account. In this way, to evaluate the change of the first shell coordination numbers, the g(r)ρ is more suitable as for this, the height of the first peak is specifically identified with the number of molecules present in the first shell. In the first place, we analyze MM-MM g(r)ρ's. For this, following our previous work, N4 along with N9 atoms of MM molecule are considered here.

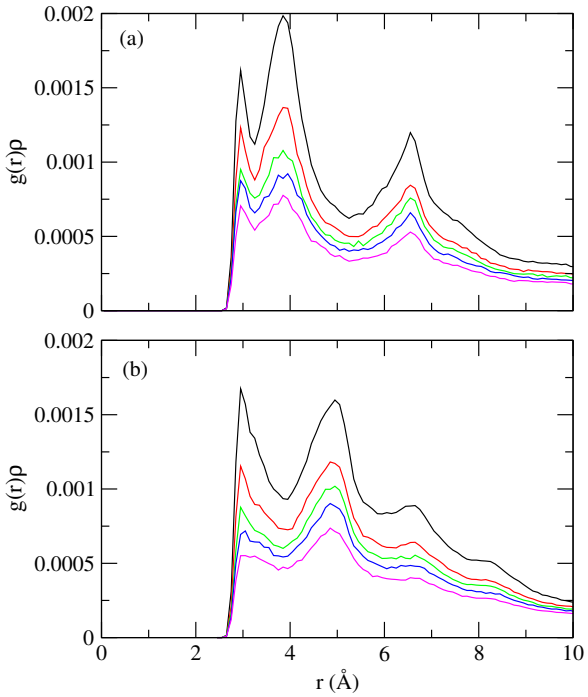

Figure 2b-3. *(a) and (b) refer to N4-N4 and N4-N9 pair distribution functions multiplied by ρ, respectively. Here, black, red, green, blue, and magenta correspond to the systems S0, S1, S2, S3, and S4, respectively.*

As the chemical environments of all sp^3 hybridized nitrogen atoms (N6, N8 and N9) are indistinguishable in MM. In the similar note, the all sp^2 hybridized nitrogen atoms (N6, N8 with N9) are likewise indistinguishable in MM. In the hydrogen bonding association in MM-MM one would predict sp^2 hybridized nitrogen atoms to act as hydrogen bond acceptors. On the other hand, sp^3 hybridized nitrogen atoms can act as both hydrogen bond acceptors as well as donors. So, the consideration of N4-N4 along with N4-N9 g(r)ρ

for assessing MM-MM pair distribution functions is reasonable and these g(r)ρ values for various systems are shown in Figure 2b-3. Additionally, to take a look at the hydration behavior of MM molecules subjectively, as the temperature changes from S0 to S4, it is imperative to ascertain rdfs including N4-Ow and N9-Ow multiplied through ρ. Though we are not interested in the MM-water relationship but these are shown just to obtain a very brief idea on the local arrangement of water surrounding MM for all the systems (discussed later). These two pair correlation functions multiplied by ρ are presented in Figure 2b-4. Focusing on g(r)ρ of N4-N4 first (Figure 2b-3(a)) it is seen that there is a sharp first at 2.95 Å with second peak at around 3.85 Å and the peak heights diminish as the temperature is incremented. The trend of changing the height of g(r)ρ, coming from N4-N9 interaction (Figure 2b-3(b)), is fundamentally the same as that for N4-N4 distribution. Only the positions of the both first and second minima of N4-N9 g(r)ρ are moved towards higher distances. Again, the hydration behavior of solute molecules in solvent gives, yet in a roundabout way, the facts about the self aggregation tendency of the former. Thus, it is vital to compute solute-water pair correlation functions. These rdfs give a subjective view of the dissolvable molecules around a reference solute molecule. These certainties incited us to ascertain N4-Ow along with N9-Ow distribution functions multiplied by ρ for various systems (Figure 2b-4). At around 2.85 Å, a Sharp first peak is seen, succeeded by a considerably little second peak (appears at around 4.05 Å) are seen in the N4-Ow g(r)ρ for S0 (Figure 2b-4(a)). As the temperature goes up, the heights of both the first as well as second peaks are decremented. Figure 2b-4(b) depicts the site-site distribution function including H11 atomic site of MM (hydrogen atom joined to the N4 nitrogen atom present in MM) and oxygen atom of water. From these pair correlation functions, we mention following objectives about the local structures of water around the solute molecules. Since MM has a moderate surface territory with approximately symmetric by structure, it has a strong hydrophilicity and minor dissolvability. Its hydrophilic atomic sites make it a stronger aggregating agent with low dissolvability in water.[174] Figure 2b-4(a) and (c) demonstrate the RDF multiplied by ρ of the nitrogen atoms in MM. As the temperature is increases, g(r)ρ of N4-Ow and N9-Ow suggest that the ordered arrangement of the first hydrated shell is debilitated. The positions of these peaks are well right shifted. This fact tells about the dissemination of water molecules around the nitrogen atoms winds up meager with the increments of temperature, and there is a general propensity for the quantity of hydrogen bonds to diminish, which is predictable and reported in various literatures. The

g(r)ρ of H11-Ow appears in Figure 2b-4(b). The enhancement in the temperature causes a shifts in the positions of appearances of both first and second peaks. Moreover, an examination of the first peak height of g(r)ρ's of N4-N4 and N4-N9 atomic sites, which are the main topics to be discussed, suggests that the interaction amongst the N4 and N9 nitrogen atoms of MM, which cooperates more positively in comparison of N4-N4 nitrogen atoms. This is additionally affirmed by the computations of the average number of MM-MM hydrogen bonds (per MM) for various systems (examined later).

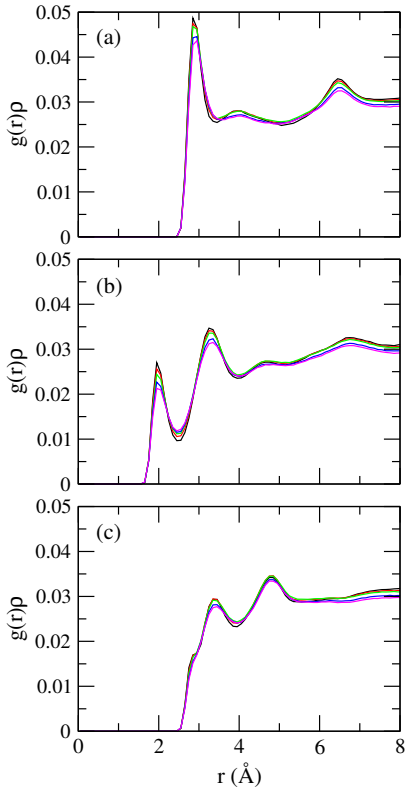

Figure 2b-4. *(a)-(c) refer to N4-Ow, H11-Ow, and N9-Ow pair distribution functions multiplied by ρ, respectively. Here, black, red, green, blue, and magenta correspond to the systems S0, S1, S2, S3, and S4, respectively.*

Again, the running coordination number (RCN) of MM around a reference MM molecule is ascertained. RCN gives the change of coordination number of MM around a reference MM molecule. Following earlier works[174, 178, 179] RCN can be defined as:

$$RCN = 4\pi\rho_\beta \int_0^r r^2 g_{\alpha\beta}(r) dr \tag{2.9}$$

RCN is characterized as the number of atomic sites of type β around the atomic sites of type α in a shell extending from 0 to a separation, r. Here ρ_β represents the number density of β in the system. In Figure 2b-5, we present the RCN of MM around MM vs. distance of separation between them. The distribution function of N4-N9 is utilized to compute the RCNs of different systems. With the decrease of temperature, for a given distance, a significant reduction in the RCN number is evident as one moves from systems S0 to S4. The results are in accordance with that of rdfs coming out of MM-MM interaction, and the snapshots of various systems examined previously.

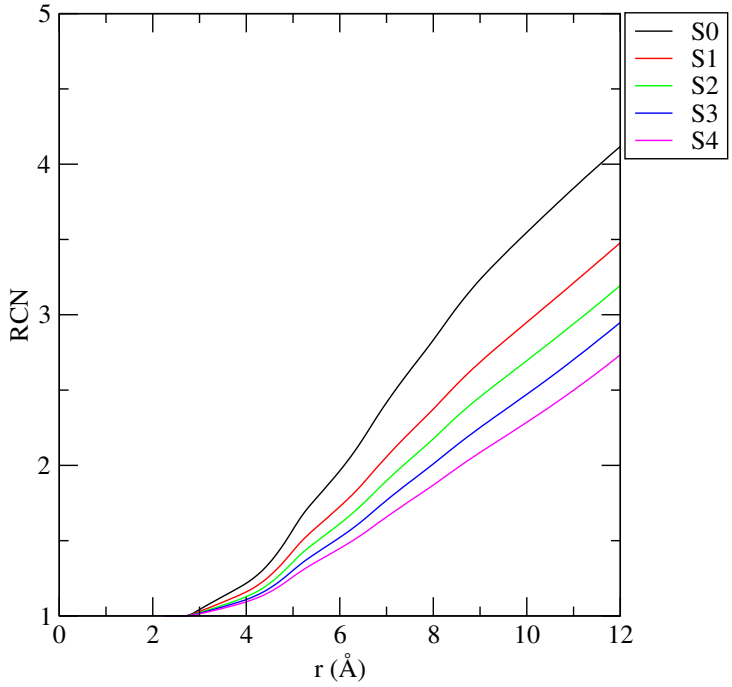

Figure 2b-5. *Running coordination number of MM around a reference MM molecule for S0-S4.*

It is imperative to analyze the water-water g(r) functions with the change of temperature. In Figure 2b-6, the pair correlation functions involving Ow-Ow along with Ow-Hw (Hw represents water hydrogen) are displayed. From the Ow-Ow rdf of system S0 (Figure 2b-6(a)) the appearance of a prominent first peak together with a less pronounced second peak at 2.75 Å and 3.75 Å are noticed. The first peak relates to the hydrogen bonded first neighbor and the second peak is ascribed to the tetrahedrally found second neighbor. With

increasing temperature a reduction in the first peak height is observed together with this the second peak is vanished. A slight shift in the appearance in the first peak can also be noticed. Concentrating on the Ow-Hw rdf (Figure 2b-6(b)), we discover the presence of hydrogen bonding peak at 1.8 Å . As obtained for Ow-Ow rdf, the impact of temperature on the change in Ow-Hw distribution function is also observed. In specific, with the increase of temperature, the first peak height of Hw-Ow diminishes and the valley of first minimum becomes shallower, which demonstrates that the ordered tetrahedral arrangement of water molecules is disturbed at higher temperature.

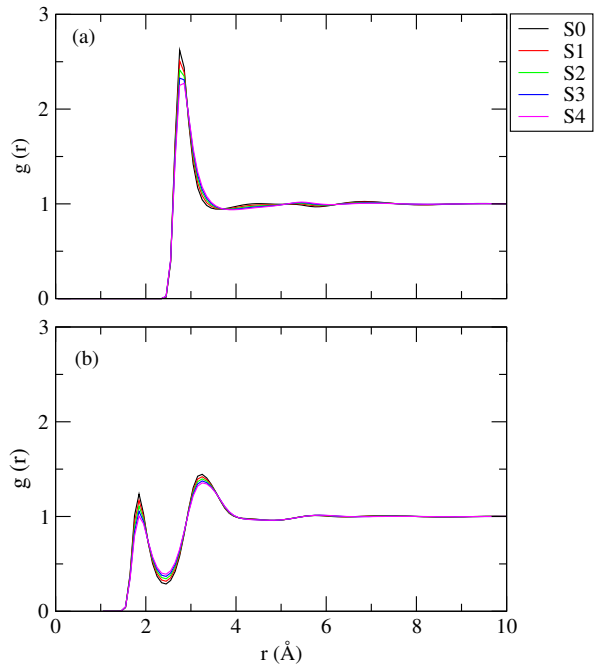

Figure 2b-6. *(a) and (b) refer to Ow-Ow and Hw-Ow distribution functions, respectively, for S0-S4. Here, Ow represents the water oxygen and Hw represents the water hydrogen.*

Hydrogen bond properties

As already specified in our earlier study[174] that MM uses its six hydrogen bonding site during the formation hydrogen bonds with other MM molecules present in the systems. The estimate the average number of hydrogen bonds between, the bonds formed in sp^3 N-

sp^3 N (sp^3 N-H$\cdots$ sp^3 N) along with sp^3 N-sp^2 N (sp^3 N-H$\cdots$ sp^2 N) are considered. In similar manner hydrogen bonds made by water-water interactions are likewise conceivable in where oxygen atom of water can form hydrogen bonds with hydrogen atom of another water molecules in which oxygen atom of water. Thus, in aqueous MM solution, water-water (H_{w-w}), MM sp^3 N-MM sp^3 N ($H_{sp3N-sp3N}$) along with MM sp^3 N-MM sp^2 N ($H_{sp3N-sp2N}$) hydrogen bonds are possible. Besides these, the other possibilities like sp^3 N-H$\cdots$ Ow and sp^2 N-H$\cdots$ Ow are not taken into discussion as these are already discussed somewhere else.

Following previous study,[174] a set of criteria is utilized to characterize a hydrogen bond. Hydrogen bonding is considered between two atoms if D-A $\leqslant$ r_{cut} and, simultaneously $\angle$ D-H$\cdots$ A $\geqslant 120^o$ where the donor atom of one molecule is denoted by D and the A corresponds to an acceptor of another molecule. In the present study, estimation of r_{cut} is obtained from the position of first minimum in the relating rdf. Like in our earlier study[174] as we have also determined the combined angular-radial distribution function of Ow-Ow hydrogen bonds for system S0 that gives the hydrogen bonds criteria where the donor-acceptor separation is plotted against D-H$\cdots$A angle (results are not shown). It is to be noted that the separation and angle cut-off considered in this investigation to characterize a hydrogen bond falls inside the region of high intensity. Further, for various systems (S0-S4 along with S0-a,S4-a and S5), the number of distinctive hydrogen bonds coming from the MM-MM and water-water interactions are displayed in Table 2b-4. It is clear that it is the $H_{sp3N-sp2N}$ hydrogen bond, which contributes on the whole for all systems. These findings are in accordance with the radial distribution functions of MM-MM interaction discussed above. The impact of elevated temperature on these hydrogen bonds, can be noticed in the reduction of MM-MM hydrogen bonds. Besides, not surprisingly, there is also a decrement in the water-water hydrogen bond numbers as temperature is increased.

Here it is worth to specify that the examinations of average number of MM-MM hydrogen bonds for different systems (S0, S0-a, S4 and S4-a) make us to reach to an essential conclusion that distinctive starting structures do not differ a definitive outcomes with the change of temperatures. This is also valid for the use of various of ensembles (NPT and NVT) for the systems S0, S0-b, S4 and S4-b. Further, the average number of different hydrogen bonds for the system S5 matches well with that of the system S0. In spite of the fact that these two systems are prepared with two different models of MM. This clearly suggests model dependency of our findings.

For systems S300 and S380, the average number of MM-MM hydrogen bond is 4.66 and 3.81 respectively (Table 2b-3). Considering the fact of poor aqueous solubility of MM molecules, these average hydrogen bond numbers do not provide any surprising fact. Moreover, the effect of elevated temperature on this hydrogen bond numbers is also quite prominent.

Table 2b-4. Average number of hydrogen bonds[a]

Systems	H_{w-w}	$H_{sp3N-sp3N}$	$H_{sp3N-sp2N}$	total_{m-m}
S0	3.87	0.84	1.18	2.02
S0-a	3.87	0.85	1.15	2.00
S0-b	3.88	0.84	1.17	2.02
S1	3.82	0.51	0.85	1.36
S2	3.76	0.43	0.68	1.11
S3	3.69	0.37	0.56	0.93
S4	3.61	0.30	0.48	0.78
S4-a	3.59	0.30	0.48	0.78
S4-b	3.60	0.31	0.49	0.80
S5	4.34	0.91	1.35	2.26

[a] Average hydrogen bonds number where H_{w-w}, $H_{sp3N-sp3N}$, and $H_{sp3N-sp2N}$ represent the water-water (per water), melamine-melamine (per melamine through $sp3N - sp2N$ N atoms), melamine-melamine (per melamine through $sp3N - sp2N$ N atoms of melamine), for the distinctive systems. Here, hydrogen bonds are given for last 120ns MD run. For the system S5, D-A distance is adapted for the corresponding rdfs (not shown).

Spatial Density Plots

In Figure 2b-7, for all systems (S0-S4) the spatial distribution of solute MM density inside the solvation shell of a reference MM with the isovalue of 0.45 $\mathring{A}^{-3}$ are displayed. For the determination of density distribution[158], last 80ns trajectory is considered. As one continuously moves from S0 to S4 (Figure 2b-7 (a)-(e)) the distribution of density of MM molecules around a reference MM particle is diminished. As we can find that the spatial distribution of MM is the most noteworthy at 300K. At that temperature it can be effortlessly seen that the distribution of MM around a reference MM is more symmetric in nature. In this context we classify the self-association of MM molecules into the parts

emerging from N4-N9 alongside the N4-N4 interactions (Figure 2b-8). One can, without much of a stretch, find that the density distribution of MM around a reference MM is the

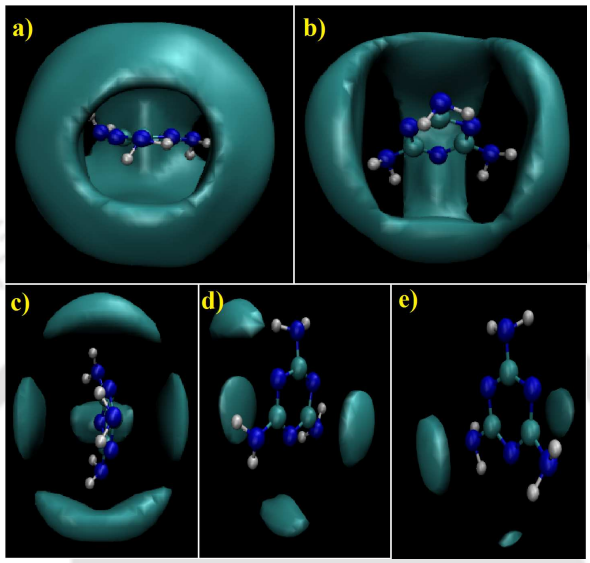

Figure 2b-7. *(a)-(e) represent the spatial density distribution of MM around a reference MM for systems S0, S1, S2, S3, and S4, respectively. These plots are given for the last 80 ns MD run.*

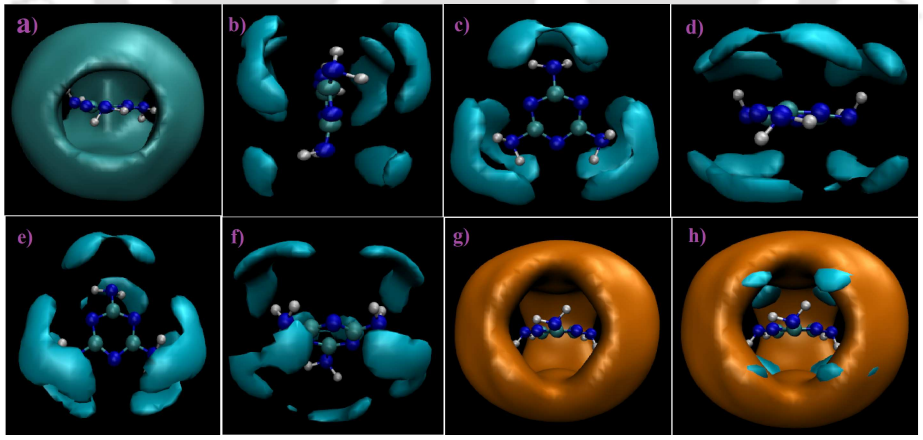

Figure 2b-8. *Spatial density maps for (a) MM around a reference MM molecule for the system S0 (averaged over the last 80 ns of simulated trajectory). [(b)-(f)] Spatial density maps are given for N4-N4 distribution with different portrayals for the system S0. (g) describes the spatial map of N4-N9 distribution for S0. (h) represents N4-N4 and N4-N9 density maps in a single arrangement for the system S0 at 300 K.*

most for the interaction between the N4-N9 atomic sites and this finding go with our prior discussions. This is also true for all the temperature considered in the present study (data not shown). From these facts it is obvious that the aggregation tendency of MM, which mainly due to the N4-N9 interactions, is diminished from system S0 to system S4.

Preferential Interaction Parameters

The molecular level understanding of the propensity of MM aggregation with the other like molecules, as the temperature is increased, can be assessed with the determination of the preferential interaction parameter, τ,.

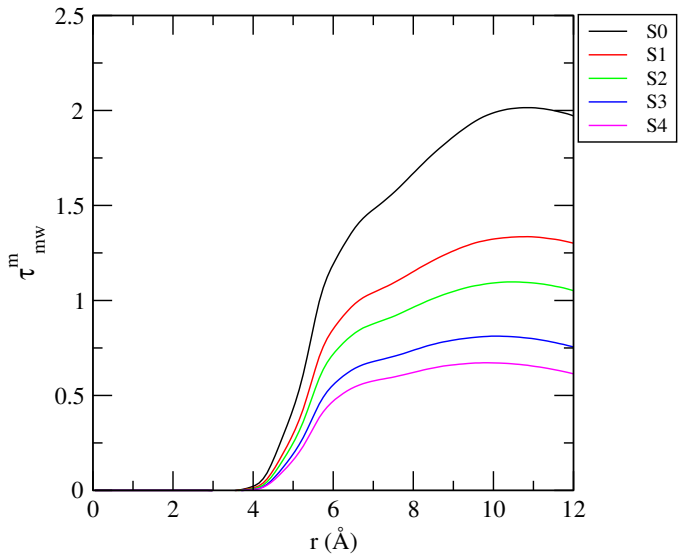

Figure 2b-9. *Preferential interaction parameters of MM for a MM over water for different systems.*

To do so, Kirkwood-Buff theory is applied for the determination of the preferential interaction parameter of solute MM with like molecules over solvent water and this can be estimated as:

$$\tau^m_{mw} = \rho_m(G_{ms} - G_{mw}) \quad (2.10)$$

where m, s and w corresponds to the MM (solute), co-solutes and water, respectively and ρ_m denotes to the number density (N/V) of MM.

G_{ms} i.e. G_{mm} and G_{mw} correspond to Kirkwood-Buff integrals. These integrals are obtained from MM-MM and MM-water rdfs. And for the determination of these distribution functions, we have considered the center of mass of MM and water molecules.[174, 180]

In grand canonical ensemble, G_{ij} (for species i and j) is defined as:

$$G_{ij} = 4\pi \int_0^\infty [g_{ij}(r) - 1] r^2 dr \tag{2.11}$$

In case of a closed system, the above equation can be reduced to:

$$G_{ij} \approx 4\pi \int_0^R [g_{ij}(r) - 1] r^2 dr \tag{2.12}$$

where R refers to the distance at which the above integral

From the above equation (eq. 2.10), it is very clear that the value of τ_{mw}^m is positive when a MM molecule shows more inclination to interact with other MM molecules over water. Note that, its positive value slightly above zero suggests (though non-zero) the hydration of MM molecules preferentially. For various systems, the estimations of τ_{mw}^m are presented in Figure 2b-9. The value of τ_{mw}^m for system S0 is around 2 suggesting a MM molecule preferentially interacts with other MM molecules present in the system over water particles. As the temperature is increased, the value of τ_{mw}^m starts to decrease and for the systems S3 and S4, the values of τ_{mw}^m are slightly over zero and these small positive τ_{mw}^m values imply that MM does not interact substantially with another MM molecule over water molecules. In this manner, the perceptions produced by the above discussions lead us to finish up, rather subjectively, that as the temperature is increased, MM molecules go into more solvation. In the succeeding discussion, the part of stacking interaction between the triazine cores present in MM on the aggregation of MM is investigated. Besides, various sizes of MM clusters in various systems are investigated quantitatively. Therefore, in the latter sections, we try to capture the molecular level picture of MM aggregation and the effect of temperature on to it.

Orientational Preference of MM Aromatic Plane

To examine the temperature effect on the $\pi - \pi$ stacking interactions between the triazine cores present in MM, we have determined the probability of orientational angles

between two MM molecules. To do so, an angle between two vector normals of two triazine cores is taken here (Figure 2b-10). S0, the angle between the vector normals i.e 0^o, 90^o and 180^o corresponds to the parallel, perpendicular and anti-parallel stacking interactions between the two triazine cores respectively. In Figure 2b-11, the probability distribution of angle θ, P(θ) as a component of inter-plane angle (θ) is plotted for all systems S0-S4.

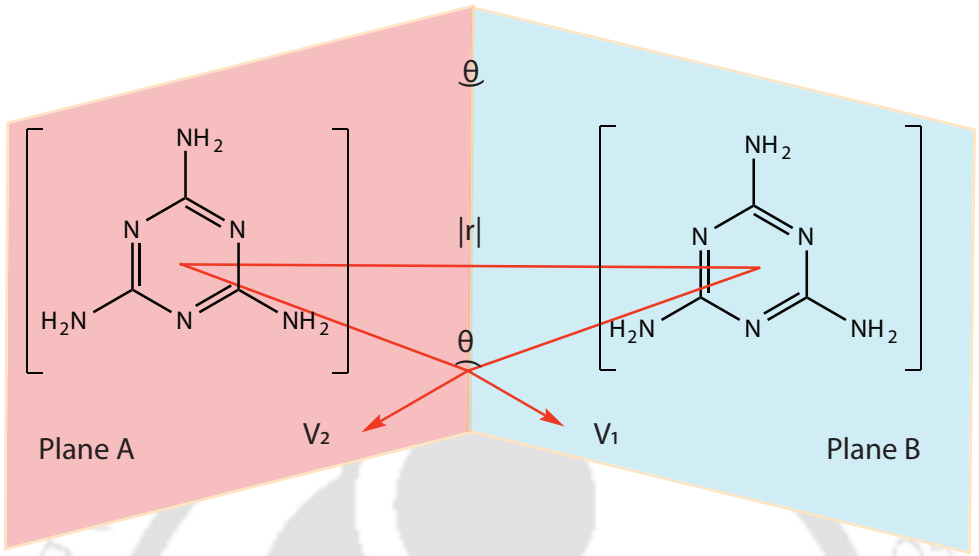

Figure 2b-10. *Schematic representations of the molecular planes of MM molecules inclined at an angle θ.*

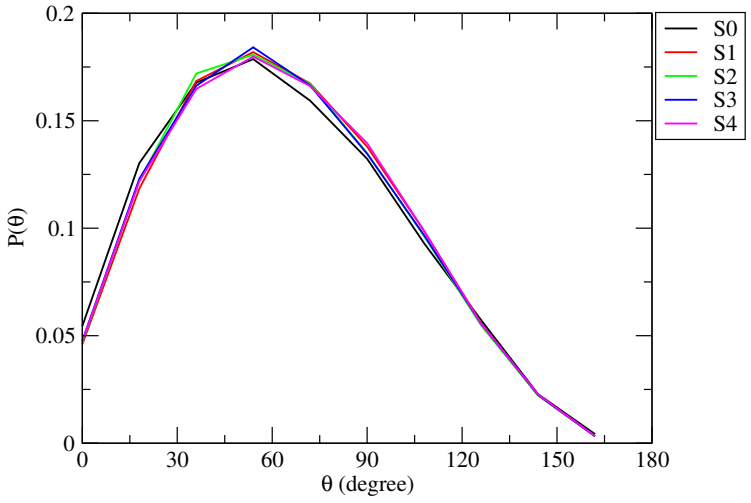

Figure 2b-11. *Probability [P(θ)] of orientational angle (θ) between the two molecular triazine cores of MM for all systems.*

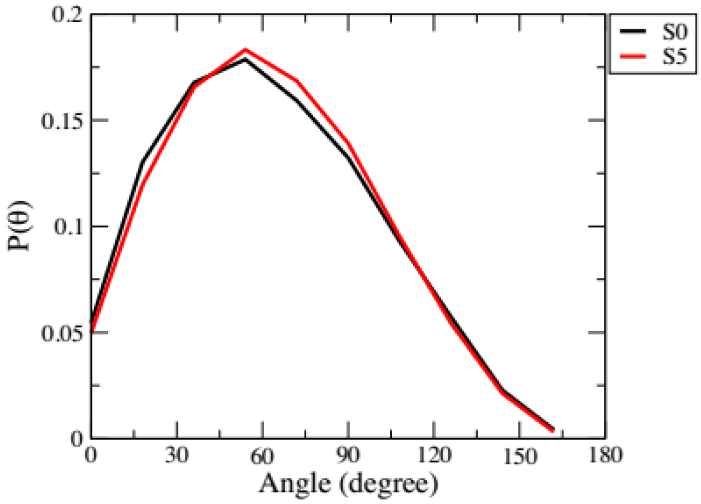

Figure 2b-12. *Probability (P(θ)) of orientational angle (θ) between the two molecular planes of MM for the system S0 and S5 at 300 K.*

Since, for all the systems considered in this study consist of 8 MM molecules, ideally the P(θ) versus θ should be plotted for all combinations of aromatic triazine cores of various MM molecules. Therefore, an aggregate of 28 combinations between the triazine cores of any two MM molecules need to be considered. Again, each of these 28 possibilities generate fundamentally very similar P(θ) versus θ plots. Thus we choose just a single the P(θ) versus θ out of these 28 combinations (Figure 2b-11). For all the systems, the maximum of P(θ) is observed for θ=55^o and remarkably, the temperature values considered in this study, have little very impact on this orientation. Moreover, for the system S5, the maximum value of P(θ) is found when θ=54^o (Figure 2b-12). This, further, confirms that CGenFF and GAFF force field of MM molecules depict very similar orientational patterns of their aromatic rings in the course of self-aggregation.

Cluster Structure Analysis

In this segment, for various systems considered, the clusters of various sizes formed by MM molecules are determined quantitatively. To do so, two distinctive MM say M1 and M2 are first. Now, M1 and M2 can shape a dimer when these two molecules are

locked-in by a hydrogen bond. Essentially, another third MM, say M3, makes a hydrogen

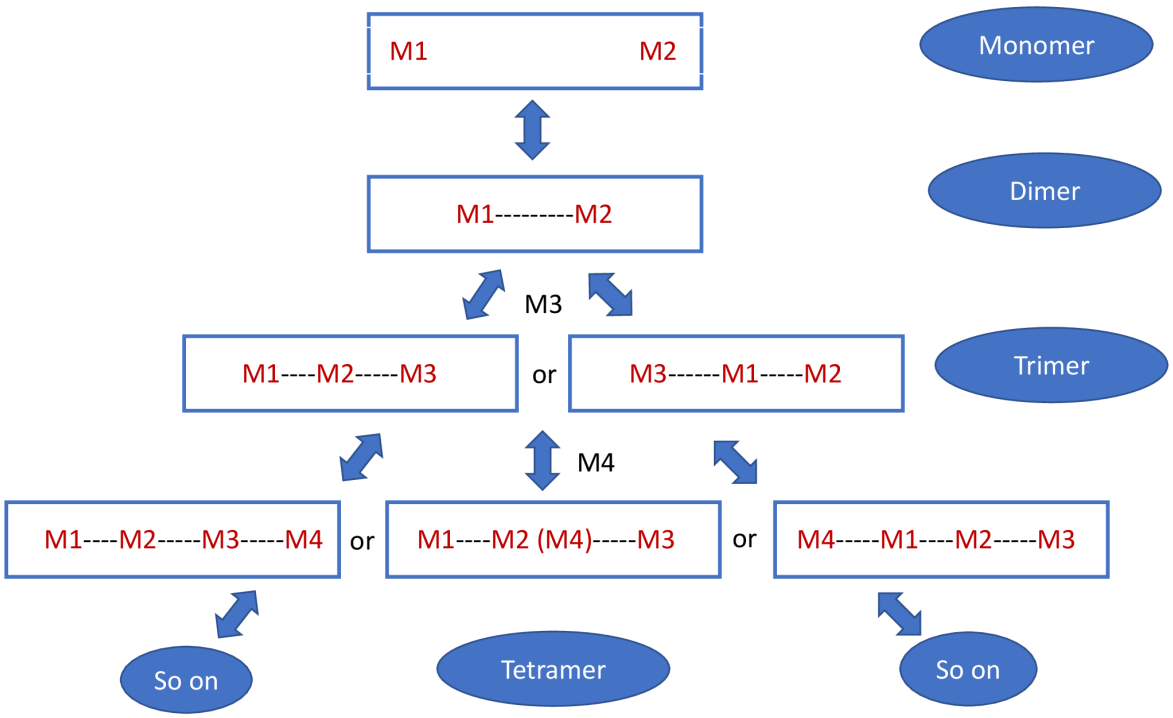

Figure 2b-13. *Schematic portrayal that is utilized for the cluster structure analysis where M1 and M2 relate to the two distinctive MM molecules. Whenever M1 and M2 stay far separated from each other, then they are accepted not to be a piece of any cluster through hydrogen bonds and they are viewed as two monomers. M1 and M2 are considered to shape a dimer in the event that they are bolted in through a hydrogen bond at certain separation (here N4-N9 distance, i.e., 3.95 Å is taken as a most extreme separation). A third MM, M3, will be the bit of a trimer involving M1 and M2 on the off chance that M3 shapes hydrogen bond either with M1 or M2. In a comparable manner, when another MM molecule, say, M4, associates with that of the previously formed trimer, it can tie to this trimer made out of M1, M2, and M3 through the hydrogen bond from any heading. M4 can influence hydrogen bond to cling to any of three MM particles to give a birth of a tetramer. This is valid for higher order clusters too. Furthermore, this goes on up to an octamer as all systems are contained eight MM molecules as it were.*

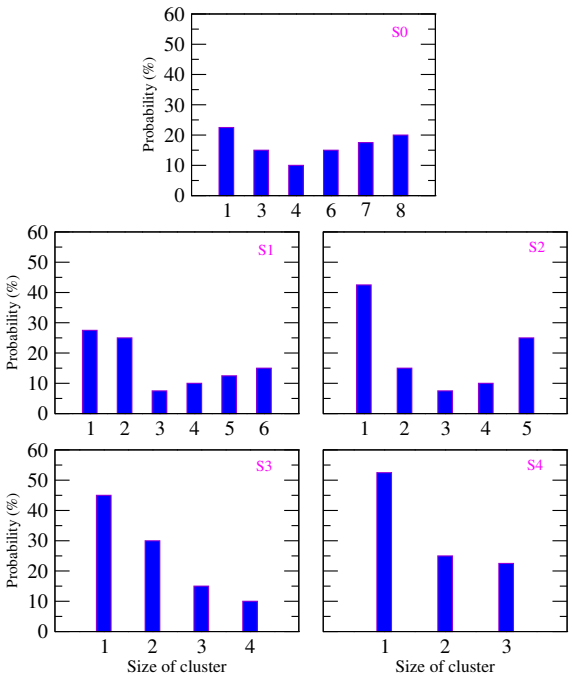

Figure 2b-14. *Probability distributions of clusters of different sizes made by MM for all the systems S0, S1, S2, S3, and S4. In this diagram, 1-8 represent to the monomer, dimer, trimer, tetramer, pentamer, hexamer, heptamer, and octamer, respectively. Distributions are given in percentage.*

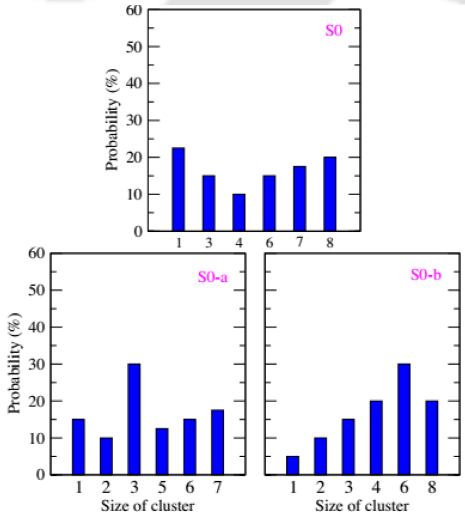

Figure 2b-15. *Probability distributions (in percentage) of MM clusters of different sizes for the systems S0, S0-a and S0-b.*

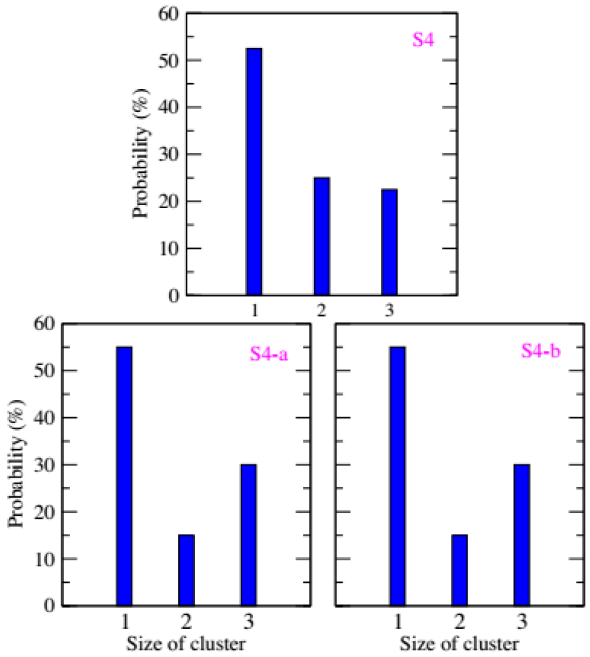

Figure 2b-16. *Probability distributions (in percentage) of MM clusters of different sizes for the systems S4, S4-a and S4-b.*

bond either with M1 or M2 (Figure 2b-13) then a trimer comprising of M1, M2 and M3, is formed. A comparative definition for MM clusters proceeds for the clusters of higher order also. As, in MM aggregation, hydrogen bonds plays the key role predominantly (discussed above), so this definition is exceptionally rational. In Figure 2b-14, for various systems, the probability of arrangement of MM aggregates of various sizes are introduced. To do so, we use last 20 ns trajectories of our MD production run for the determination of cluster structure. It is seen that for S0 at 300 K, the probability of having octamer is 20%. Alongside this, a significant amount of heptamers, hexamers, and tetramers can also be noticed. A moderately low probability of MM monomer (22.5%) is also found. Presently, 22.5% is not low to be sure, however, in comparison to alternate S2, S3 and S4 systems in where 42.5%, 45% and 52.5% monomers can be found respectively. So one can come to a decision that the system S0 is comprised of low probability of monomers.

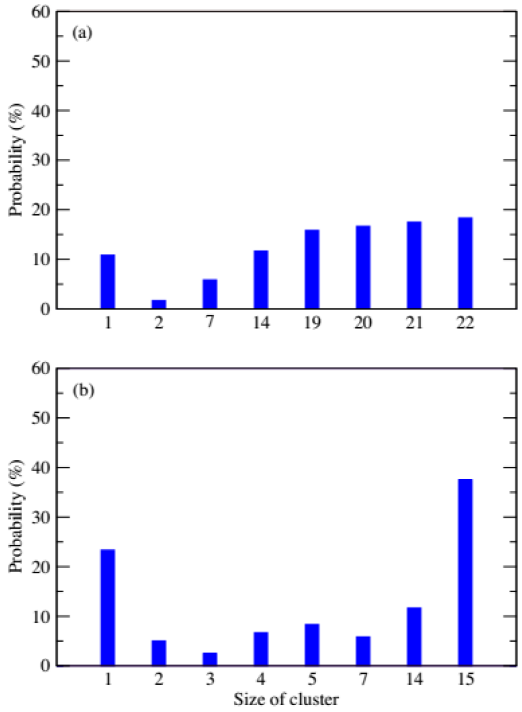

Figure 2b-17. *Probability distributions (in percentage) of MM clusters of different sizes for the systems (a) S300 and (b) S380.*

As the temperature is increased, the probability of lower order clusters formation is increased by the breakage of higher order clusters. For system S4, 52.5% MM monomers with 25% dimers and the rest of trimers are available.

Moreover, on comparing the cluster structures formed by the MM molecules for the systems S0, S0-a, and S0-b, one can find that there is no noticeable difference in the conclusion that have expressed previously (Figure 2b-15). In addition, comparable cluster structures probabilities findings are also seen for the systems S4, S4-a and S4-b (Figure 2b-16).

For the systems S300 and S380 (Table 2b-3) one can easily find that higher concentrations lead to bigger clusters of MM. The clusters that are broken into smaller size of clusters at 385 K. (Figure 2b-17)

Free Energy of Solvation of MM

When simple hydrophobic solutes aggregate in aqueous solutions, their contact-pair is stabilized by the solvent water. The determination of PMF of these hydrophobic molecules shows a high stabilizing (negative) solvent-initiated contribution to the PMF. A recent study reported the contribution of solvent to total PMF of guanidium moieties at different concentration.[161] Here, the PMF values ($W_{total}(r)$) between MM moieties at various temperatures are estimated from the pair correlation function between MM molecules as

$$W_{total}(r) = -k_B T ln g_{cc}(r) \tag{2.13}$$

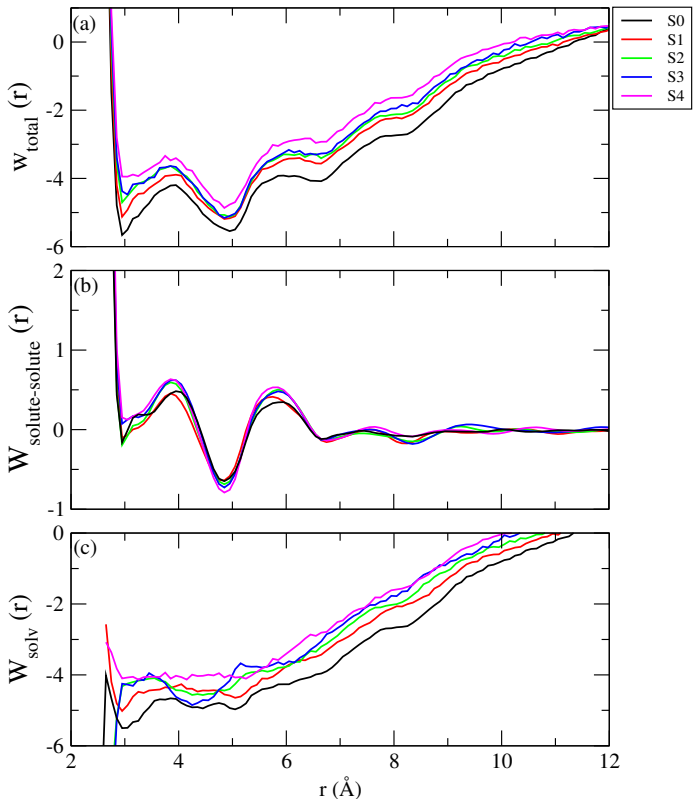

Figure 2b-18. *(a) Potential of mean force values [$W_{total}(r)$] among the MM moieties for different temperatures of MM solution. (b) Direct solute-solute interaction $W_{solu}(r)$ as obtained from vacuum simulations of MM at different temperatures. (c) Solvent-induced contribution, $W_{solv}(r)$, to the PMF at different temperatures of MM solution.*

where k_B is Boltzmann constant and T represents absolute temperature. The difference between the total PMF and PMF due to solute-solute direct interaction, $W_{solu}(r)$, produces solvent contribution, $W_{solv}(r)$, viz.,

$$W_{total}(r) = W_{solu}(r) + W_{solv}(r) \tag{2.14}$$

To evaluate PMF for solute-solute interactions, a vacuum simulation (with no water molecule) of MM is performed at various temperatures. The N4-N9 (of MM moieties) distribution function, calculated from the vacuum simulation, is then used to calculate $W_{solu}(r)$. Finally, $W_{solv}(r)$ is obtained by subtracting $W_{solu}(r)$ from $W_{total}(r)$. These PMFs are appeared in Figure 2b-18. From Figure 2b-18 (c), it can be seen that the solvent initiated contribution is responsible for stabilizing (negative) the contact-pair state. Further, as the temperature is increased, $W_{solv}(r)$ turns out to be less negative, which demonstrates that the contact-pair state is getting weaken from the system S0 to system S4.

Thermodynamics of MM Association

To calculate the distance dependent entropy and enthalpy contributions to the contact pair state and solvent separated state for the temperatures 320 K, 340 K and 360 K, the potentials of mean forces (PMFs), W(r), are estimated as a function of N4-N9 distance of MM, r, using the above equation 2.13. In our previous work, we have already calculated the thermodynamics of MM association at ambient temperature (300 K).[174] The entropy is calculated from the PMFs of the corresponding temperatures by using the finite difference temperature derivative.[174]

$$-\Delta S(r) = 1/2[\frac{\delta W(r, T+\delta T)}{\delta T} - \frac{\delta W(r, T-\delta T)}{\delta T}] \tag{2.15}$$

In the above eq. 2.15, the value of δT is 20 K and the corresponding enthalpy contribution ($\Delta H(r)$) can be determined from the value of $\Delta S(r)$ by

$$\Delta H(r) = W(r) + T\Delta S(r) \tag{2.16}$$

The entropic (-TΔS(r)) and enthalpic (ΔH) contributions to the PMFs at 320 K, 340 K and 360 K temperatures are shown in Figure 2b-19.

The PMF plots show two distinct minima for all temperatures. The first minimum, viz., contact minimum (CM), apprears at 2.95 Å , 2.95 Å , and 3.05 Å for

systems S1, S2 and S3 respectively and the second one, which corresponds to solvent separated minimum (SSM), appears at 4.85 Å , 4.95 Å , and 4.85 Å for the systems S1, S2 and S3 respectively. A small potential barrier positioned at 3.85 Å distance separates these two minima for all these systems.

Concentrating on the contributions of enthalpy and entropy on the PMFs for all temperatures, it very well may be seen that the $\Delta H(r)$ and $-T\Delta S(r)$ act in the opposite way and the estimation of these two parameters rely upon the separation of N4 and N9 atoms of two MM molecules. Besides, for CM, the estimation of $-T\Delta S(r)$ and $\Delta H(r)$ is positive and negative individually for all the systems S1, S2 and S3 recommending that the contact minimum is stabilised exclusively by enthalpy. Thus, it is very obvious that the aggregation of MM molecules in water is enthalpy driven at these temperatures. Just like CM, the contribution of enthalpy on the SSM state can also be noticed. Moreover, as expected, the elevation of temperature makes PMF of CM state more unfavorable. On the other hand, elevated temperatures has negligible influence on the PMF values of the SSM state.

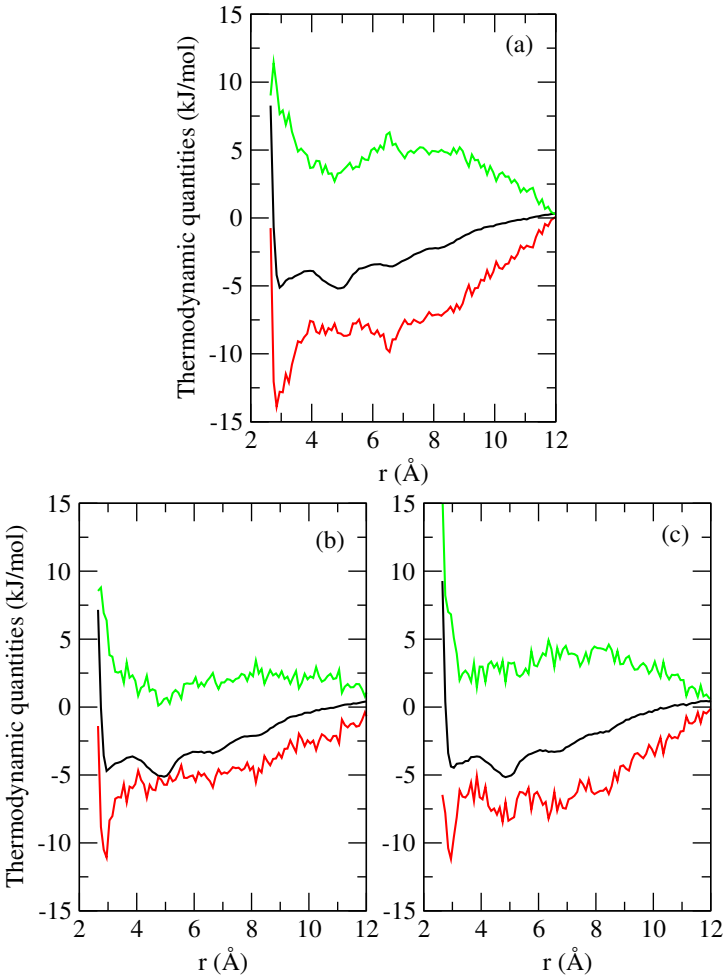

Figure 2b-19. *The distance dependent entropy and enthalpy contribution to the corresponding contact pair state and solvent separated state for the temperatures (a) 320 K, (b) 340 K, and (c) 360 K. Here, black lines correspond to the PMF [W(r)], red lines correspond to the ΔH, and green lines correspond to the -$T\Delta S(r)$. Here, all the values are drawn as a function of the separation between N4 and N9 atoms of MM molecule.*

Dimer existence Autocorrelation Functions

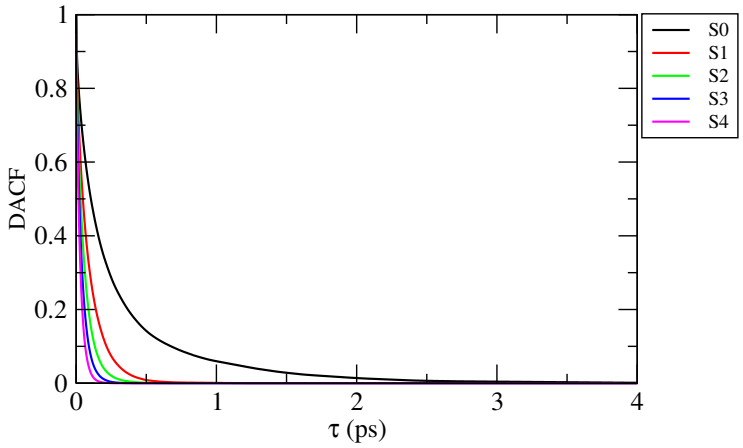

Figure 2b-20. *DACF for the MM dimer present in solution at different temperatures.*

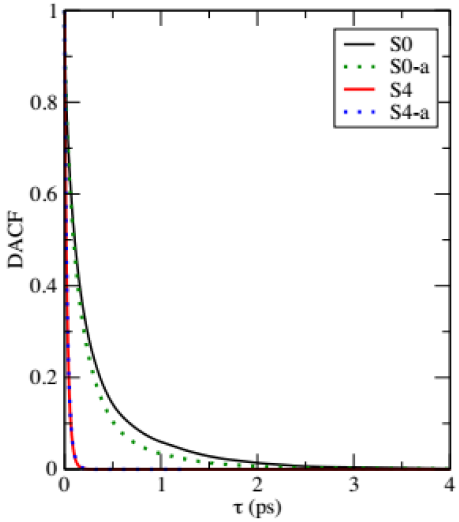

Figure 2b-21. *DACFs for MM dimer present in solution at different temperatures for the systems S0, S0-a, S4 and S4-a.*

In the preceding sections we discussed about the formation of MM clusters and the underlying causes of their formation, in this section we will try to estimate the lifetimes in order to understand the dynamics of them. For this, the dimer existence autocorrelation function (DACF) is considered. For a given set of molecules i, j DACF is characterized as the autocorrelation of a straightforward function β_{ij} , which attains the value 1 until the distance criteria are satisfied, and its value changes to zero when the distance criterion breaks for the first time.[174, 158] Thus,

$$DACF(\tau) = N. < \sum_{t=0}^{T-\tau} \beta_{ij}(t+\tau).\beta_{ij}(t) >_{ij} \tag{2.17}$$

Remember that DACF remains at 0, regardless of whether the criteria are again satisfied later on. In Figure 2b-20, DACFs of MM molecules are compared to five distinct systems.

Here we take the most extreme separation of 3.95 Å between sp^3 N-sp^2 N distance of two MM molecules. From Figure 2b-20, it is obvious that DACF tumbles to zero at various lifetimes for different systems individually. Subsequently, the investigation of the dynamical idea of dimers demonstrates the clear refinements over the lifetimes between the two systems S0 and S1. There on it steadily diminishes from S1 to S4.

In addition to this outcome, it is certain that the τ for the systems S0 and S0-a are very close to each other. This is valid for the other two comparative systems i.e. S4 and S4-a (Figure 2b-21). Values confirms the robustness of the simulations presented here.

Association Constant (K_a)

Table 2b-5. Association constants[a]

Systems	$K_a \times 10^2$ (M^{-1})
S0	105.40
S1	84.63
S2	73.48
S3	66.66
S4	57.58

[a]Association constants (K_a) for MM molecules in water as a function of temperature for all the systems.

To comprehend the impact of temperature on accumulation of MM in water, we have calculated the association constant, K_a. The K_a can be defined as:[181]

$$K_a = 4\pi \int_0^{r_a} r^2 e^{-W(r)/k_B T} dr \tag{2.18}$$

where r_a indicates to the position in where the energy barrier exists in the PMF curve. Higher the value of K_a, more prominent is the association of the solutes in solution. The values of K_a for S0-S4 are introduced in Table 2b-5. It is clear that with the increase of temperature, in water, the aggregation propensity of MM molecules is reduced to a great extent.

Binding free energy between a MM pair (G_b)

Table 2b-6. Binding free energies[a]

Systems	G_b (kJ mol^{-1})
S0	-4.08
S1	-3.53
S2	-3.17
S3	-2.94
S4	-2.57

[a]Binding free energies (G_b) for MM molecules in water as a function of temperature for all the systems.

As per the Kuyucak *et al.*, one can utilize PMF as a tool for the examination of the results got from the classical and ab initio calculations. Yet, PMF can not be utilized to compute the binding free energy between ion pairs. To do as such, one needs to utilize volume integral of PMF;[182]

$$G_b = -k_B T ln[4\pi/V \int_0^{r_a} e^{-W(r)/k_B T} r^2 dr] \tag{2.19}$$

where V=4π r_c^3 is the volume occupied by the ion-pair. Here we have utilized this volume integral of PMF to ascertain the binding free energy of MM pair in water from the PMF esteem acquired from the RDF of MM pair. The bigger the absolute value of G_b, more noteworthy is the propensity for cluster formation. In the present investigation, all the G_b esteems for all the systems are given in the Table 2b-6 where one can find effectively that for the system S0, G_b is higher than the other systems considered.

Umbrella Sampling

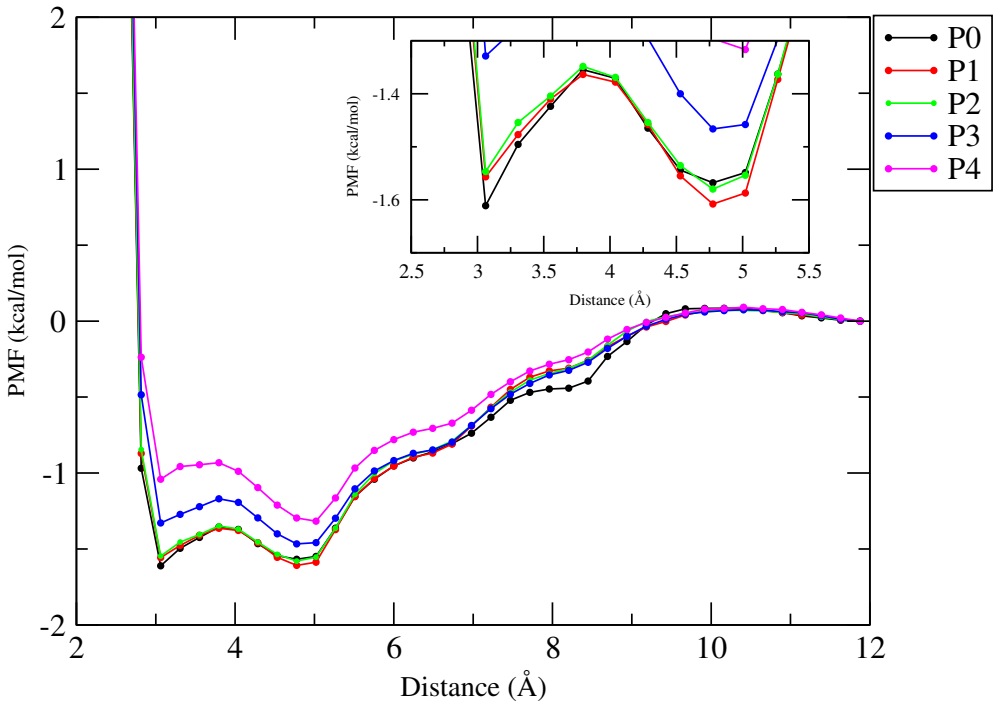

Figure 2b-22. *MM-MM potential of mean forces (PMFs) for all the systems P0 to P4. The magnified PMFs are presented in the inset. Here, the distance is taken as the separation between N4 (mol-1) and N9 (mol-2) in units of Å .*

To investigate the free energy cost of developing higher order clusters from monomers, we perform umbrella sampling. Towards this, we compute the potential of mean forces (PMFs) for MM-MM interaction as a function of separation between N4 and N9 atoms present in two diverse MM molecules at different temperatures. For this, as we discussed above, we consider five systems, P0-P4. For each of systems, PACKMOL is used to prepare the starting configuration. Then a normal MD run is carried out for each of the systems. For every system, the coordinates generated in the ordinary MD simulation run is used for

umbrella sampling. PMF can be utilized to discover how does the free energy change as a function of reaction coordinate. In umbrella sampling, an arrangement of initial setups are created, every one of them corresponding to a location wherein the molecule of intrigue is delicately controlled by increasing N4-N9 distance by employing an umbrella biasing potential. The utilization of restriction enables the molecule to test the configurational space in a characterized region (alongside a reaction co-ordinate) amongst it and the reference particle. It ought to be noted here that the windows must overlap slightly in order to produce a PMF curve in an appropriate way. The PMFs for the systems from P0-P4 are displayed in the Figure 2b-22. From the PMF curve, at 3.06 Å a first minimum is seen. This minimum is ascribed to contact minimum (CM). Again a second shallow well that appears at 4.77 Å . This relates to the solvent separated minimum (SSM) for all systems. Now one little energy barrier (BARR) shows up at 3.79 Å needs to cross to reach CM to SSM state. The effect of increased temperature is quite visible. In particular, the elevation of temperature makes both first and second minima shallower. A close look into the PMF curve reveals that at higher temperature the SSM state is slightly more favorable than CM state.

■ SUMMARY AND CONCLUSIONS

In the present work, classical MD simulation of eight MM molecules is carried out in water over a temperature range from 300 K to 380 K. The snapshots taken from different systems qualitatively imply MM aggregation in water decreases with rise in temperature. This finding is in line with the experimental findings of by Harris *et. al.*.[124] Moreover, these observations are further affirmed from the density distribution maps of MM around a reference MM molecule for different systems. These maps depict that as the temperature is increased, the density of MM molecules around the reference MM molecule in water decreases, which points to preferential hydration of MM molecules. The determination of running coordination number of MM around MM also indicate about the more hydration of MM as the temperature is increased. The evaluation of average number of MM-MM hydrogen bond numbers indicates that the increase of temperature disrupts the aggregated MM structures significantly. From the hydrogen bond counts, it is very clear that out of two possibilities, while making inter-molecular hydrogen bonds between MM molecules in water, it is the MM sp^3 N-MM sp^2 N hydrogen bond, which predominates over the MM sp^3 N-MM sp^3 N hydrogen bonding interaction. Again when we disintegrate the total MM-MM density

distribution into two parts emerging from the sp^3 N-sp^2 N and sp^3 N-sp^2 N interactions, then we find that the maximum accumulation of MM around MM is due to the presence of MM sp^3 N-MM sp^2 N hydrogen bonding interactions over the alternate one. This finding exactly matches with the experimental findings reported elsewhere. The analyses of preferential interaction parameter clearly indicates that as the temperature is increased, the preferential interaction parameter between MM-water predominates over the MM-MM interactions. Cluster structure analyses of eight MM molecules are also determined. It is found that as the temperature increases, the higher order clusters break into the smaller order clusters like trimers, dimers and monomers at higher temperature. The determination of free energy of solvation from PMF suggests that the solvent induced contribution is stabilizing (negative) the contact-pair state. Furthermore, as the temperature is increased, free energy of solvation becomes less negative. This fact implies that the contact-pair state between MM molecules is getting weaken with the increase of temperature. The calculation of dimer existence auto correlation function, which deals with the direct dynamic nature of dimer, indicates that at 300 K, the lifetime of dimer framed by the two MM molecule is the highest. As the temperature is increased, this lifetime gets more and more shorter indicating the instability of formed dimer at higher temperatures. This fluctuating nature of aggregated MM molecules at higher temperature is the main evidence of its increased solubility in water. To examine the role of $\pi - \pi$ stacking interactions between the triazine cores of MM in the time of aggregation in water, the probability of orientational preferences between the triazine core of two reference MM are taken into consideration for all systems. A wide distribution along with the appearance of maximum probability at 54^o-55^o clearly rules out the role of strong $\pi - \pi$ interactions. Moreover, the elevated temperature has negligible influence on this distribution. The analyses of the potential of mean forces confirms the decrease of initial probability of growth of higher order clusters with the increase of temperature.

Chapter 3

Underlying Mechanistic Insights into the Structural Properties of Melamine and Uric Acid Complexes with Compositional Variation under Ambient Conditions

"One of the biggest challenges to medicine is the incorporation of information technology in our practices."

— Samuel Wilson

Overview: The structural properties of melamine (MM)-uric acid (UA) complexes (which are responsible for kidney stones) with compositional variations are examined using a series of classical molecular dynamics simulations. The preferential interaction parameters imply that MM interacts more strongly with UA than with other MM molecules present in the system, whereas UA preferentially interacts with other UA molecules rather than with MM. The stronger interactions among UA molecules produce higher-order UA clusters, which "drag" neighboring MM molecules to be added to a cluster. Determination of orientational preferences between aromatic planes reveals that π-π stacking is responsible for UA self-association but less significant for MM-MM and MM-UA accumulation. Cluster structure analyses suggest that higher concentrations of MM, UA, or both result in a large insoluble MM-UA complex cluster. Molecular mechanics-Poisson Boltzmann surface area calculations give a negative binding energy, indicating favorable complexation between MM and UA molecules. Moreover, the overall complexation energy ($\Delta G^0{}_{(mel\text{-}mel)}+ \Delta G^0{}_{(uri\text{-}uri)}+ \Delta G^0{}_{(mel\text{-}uri)}$) is more negative than the $\Delta G^0{}_{bind}(mel\text{-}uri)$. The lifetime of MM dimers is quite low compared with those of UA-UA and MM-UA dimers, resulting in a low percentage of larger clusters for MM-MM interaction and a significant percentage of higher-order MM-UA and UA-UA clusters with longer lifetimes. Furthermore, MM and UA form strong hydrogen bonds, and MM-MM interactions are dominated by hydrogen bonding, whereas UA forms only a small number of hydrogen bonds with other UA molecules.

■ INTRODUCTION

MM (Figure 3-1), an organic compound containing a high percentage of nitrogen (66% by molecular weight),[2] produces several stable hydrogen-bonded arrays with cyanuric acid and other related compounds.[89, 90, 183, 106] MM is safe when used normally but potentially dangerous when consumed in excess amounts, which can occur when foodstuffs are contaminated. There have been cases of illegal use of MM to adulterate foods in order to falsely elevate the nitrogen content of the constituent proteins, mainly in baby foods. As a result, various food safety incidents have taken place worldwide,[111] including the formation of kidney stones in infants following the ingestion of MM-contaminated foods.[113] Analysis of these kidney stones showed that they were composed of MM and UA (Figure 3-1). As well as the effects on the human body, evidence of MM toxicity, including nephrolithiasis, chronic kidney infection, and bladder cancer, has been found in animals. The risk of kidney stone formation is increased when MM is consumed daily.[2, 1]

The [UA]:[MM] molar ratio measured in kidney stones from infants has varied from 1:2 to 2.1:1, indicating that the composition of MM-UA stones may vary.[1, 24, 47] K. M. Anderson *et al.*[26] first predicted the crystal structure of MM-UA, showing that MM and UA form hydrogen-bonded lattices. These lattices are thought to shape sheet-like structures that are associated by stacking to give a three-dimensional structure held together by hydrogen bonding between the layers. The authors proposed that the hydrogel was composed of two distinct hydrogen-bonding adjustments of complementary donor-acceptor pairs when these are present in equimolar amounts in the body. Furthermore, the results of this study suggested that a 1:1 hydrogen-bonded interaction of the two components is responsible for stone formation. Later, in 2014, Hiroya Asami *et al.*[45] found that a 1:1 complex of UA and MM acquires a non-planar structure in which the UA plane is slightly folded with respect to MM and stabilized by multiple hydrogen bonds. In 2015, D. Chen *et al.*[46] proposed that MM binds more strongly to UA than to cyanuric acid. They studied these interactions through fluorescence quenching of solutions of various concentrations of MM and UA, showing that both hydrogen bonding and π-π stacking are responsible for the tight binding in the complex.[46]

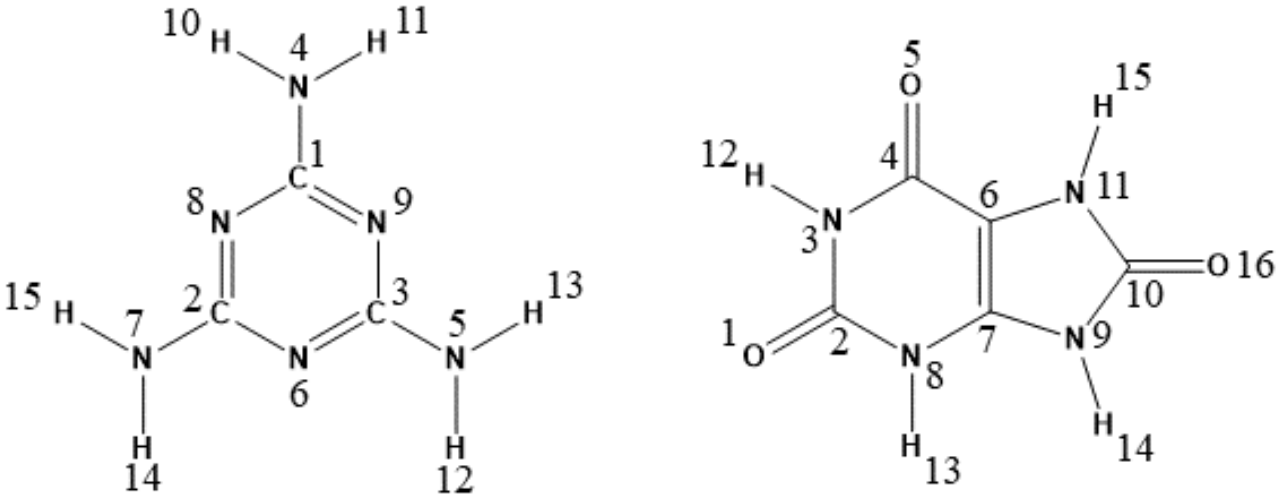

Figure 3-1. *Structure of MM and UA with atom numbering.*

The interactions between MM and UA to form kidney stones indicate that decreasing UA concentration in the kidney could help to prevent the formation of renal stones. As it has been shown that the formation of renal calculi occurs in supersaturated (resulting from excess dosage of MM) urine but not in under-saturated urine, exposure to MM in low concentrations could be a fruitful way to prevent renal calculi.[2, 1] Thus, the concentrations of both MM and UA are important in discussions of MM-UA-related renal calculi. The present study makes a contribution toward this end. Here, motivated by the clinical research described above, the interaction between MM and UA is studied in a concentration-dependent manner. The purpose of this work was to determine the exact underlying mechanism by which the structural properties of MM-UA complexes vary with composition under ambient temperature-pressure conditions; in particular, we addressed the previously unsolved question of whether MM or UA helps to increase the excretion of their solubility of interest (either MM or UA). To the best of our knowledge, this is the first

theoretical study to describe explicitly the mechanism of formation of kidney stones.

The rest of the chapter is organized as follows. In Section II, we discuss the models of MM, UA, and water molecules that are used in this study. Other simulation details are also described in this section. In Section III, the results are presented, together with discussion. In Section IV, our conclusions are briefly summarized.

■ MODELS AND DETAILS OF SIMULATIONS

In the present study, classical molecular dynamics (MD) simulations were performed using different concentrations of MM and UA in water. Representative systems are presented in Table 3-1.

Table 3-1. System overview[a]

System	N_{MM}	$N_{\mathrm{uric\,acid}}$	[MM]:[UA]	N_{wat}	Box length (Å)	C_{MM}(M)	$C_{\mathrm{uric\,acid}}$(M)
S0	5	5	1:1	3000	45.17	0.0901	0.0901
S1	10	10	1:1	3000	45.43	0.1771	0.1771
S2	20	20	1:1	3000	45.76	0.3465	0.3465
S3	30	30	1:1	3000	46.10	0.5084	0.5084
P0	5	10	1:2	3000	45.31	0.0892	0.1785
P1	5	15	1:3	3000	45.43	0.0885	0.2656
P2	10	5	2:1	3000	45.31	0.1785	0.0892
P3	15	5	3:1	3000	45.34	0.2672	0.0891
N0	10	15	2:3	3000	45.46	0.1767	0.2651
N1	15	10	3:2	3000	45.55	0.2635	0.1757
S_u	—	5	—	3000	45.17	—	0.0901

[a] N_{MM}, $N_{\mathrm{uric\,acid}}$, and N_{wat} correspond to the number of MM, UA, and water molecules, respectively. The molar concentrations of MM and UA are represented by M.

Table 3-2. Partial charges of different atomic sites of UA and MM[a]

Molecule	Atom	Charge (e)	Atom	Charge (e)
UA	O1	-0.6540	C6	-0.2259
	C2	0.9763	C7	0.6143
	N8	-0.7968	N9	-0.6466
	H13	0.4496	H14	0.4239
	N3	-0.7868	C10	0.8012
	H12	0.4197	O16	-0.6430
	C4	0.8161	N11	-0.5576
	O5	-0.6064	H15	0.4159
MM	C1/C2/C3	1.3069	N4/N5/N7	-1.2006
	N6/N8/N9	-1.0794	H10-H15	0.4866

[a]e is the elementary charge.

First, the RESP (restrained electrostatic potential)[140] suite of the AMBER12 package[139] was used to obtain the partial charges of different atomic sites of MM and UA molecules (after energy optimization using the *ab initio* HF/6-31+G** method with the help of Gaussian 09[138])(Table 3-2). Next, general AMBER force field[142] parameters were applied, using the built-in ANTECHAMBER module in AMBER12.[141] For all systems, the three-point transferable intermolecular potential[143] water model was chosen to perform the MD simulations. The starting configurations of all systems were constructed using PACKMOL.[144] During the course of the simulations, a final temperature of 300 K was fixed for all systems. For each system, all molecules were incorporated in a cubic box. For each simulation, a 10000-step energy minimization was carried out, of which 4000 steps were performed with the steepest descent method, followed by 6000 steps with the conjugate gradient method. All systems were slowly heated from 0 to 480 K in increments of 50 K for 20 ps, followed by gradual cooling to the final temperature with a decrement interval of 25 K in the canonical ensemble (NVT). Then, each system was subjected to 5 ns equilibration in an isothermal-isobaric (NPT) ensemble at 300 K and 1 atm. Subsequently, simulations were subjected to a 200 ns production run in the NPT ensemble. The last 100 ns of each 200 ns production run were used for data analysis. Periodic boundary conditions were employed in all three directions. Langevin dynamics (with 1 ps^{-1} collision frequency)[145] were used to maintain a temperature of 300 K during the simulation for all systems. To maintain the system

at a pressure of 1 atm (in the NPT ensemble), the Berendsen barostat was used with a 2 ps pressure relaxation time.[146] The particle mesh Ewald algorithm was used to treat long-range electrostatic interactions.[147] The SHAKE algorithm was used to constrain covalent bonds involving hydrogen atoms.[148] Short-range non-bonded interactions were defined using a 10 Å cut-off distance. MD simulation trajectories were analyzed using the CPPTRAJ module in AMBER. Visual Molecular Dynamics [149] was used for visualization of the obtained MD simulation trajectories, including analysis of various properties when required.

The last 20 ns of MD trajectories of all systems were taken to calculate binding free energy or complexation free energy (ΔG^0_{bind}) using the molecular mechanics-Poisson Boltzmann surface area (MM-PBSA) [184] methodology.

The Python script MMPBSA.py in the AMBER package was used for all MM-PBSA calculations. The binding free energy, ΔG^0_{bind}, was estimated as follows:

$$\Delta G^0_{bind} = \Delta E_{vac} + \Delta G_{solv}, \tag{3.1}$$

where ΔE_{vac} corresponds to the energy in the vacuum (gas phase) and the solvation free energy is represented by ΔG_{solv}. [185, 186] ΔE_{vac} can further be decomposed as:

$$\Delta E_{vac} = \Delta E_{ele} + \Delta E_{vdw}, \tag{3.2}$$

where ΔE_{ele} and ΔE_{vdw} refer to receptor-ligand electrostatic and van der Waals interactions, respectively. The solvation free energy (ΔG_{solv}) was calculated as the sum of the electrostatic solvation free energy (ΔG_{PB}) and apolar solvation free energy (ΔG_{NP}):

$$\Delta G_{solv} = \Delta G_{PB} + \Delta G_{NP}. \tag{3.3}$$

ΔG_{PB} was computed in a continuum solvent using the MM-PBSA package of AMBER. On the other hand, ΔG_{NP} was determined from the solvent-accessible surface area (SASA). The SASA was calculated using MSMS [187] for the estimation of ΔG_{NP} as in [188, 189, 190, 191, 192, 193]:

$$\Delta G_{NP} = \gamma(SASA) + \beta, \tag{3.4}$$

where $\gamma = 0.005$ kcal/Å^2 and $\beta = 0.0$.

In the present study, four systems (S0, S1, S2, and S3), with a [MM]:[UA] of 1:1 but different concentrations, were initially prepared. Next, the UA concentration of system S0 was increased gradually. These systems were denoted P0 and P1. The MM concentration of system S0 was also varied with a regular increment; the resulting systems were denoted P2 and P3. Two additional systems (N0 and N1) were prepared, in which the [MM]:[UA] ratios were 2:3 and 3:2, respectively, in order to compare their outcomes with those of the other systems to validate the conclusions. System S_u was prepared to determine the change in structural properties of UA in the presence of MM compared with system S0. Systems P0–P3, N0, N1, and S_u are briefly described in Table 3-1.

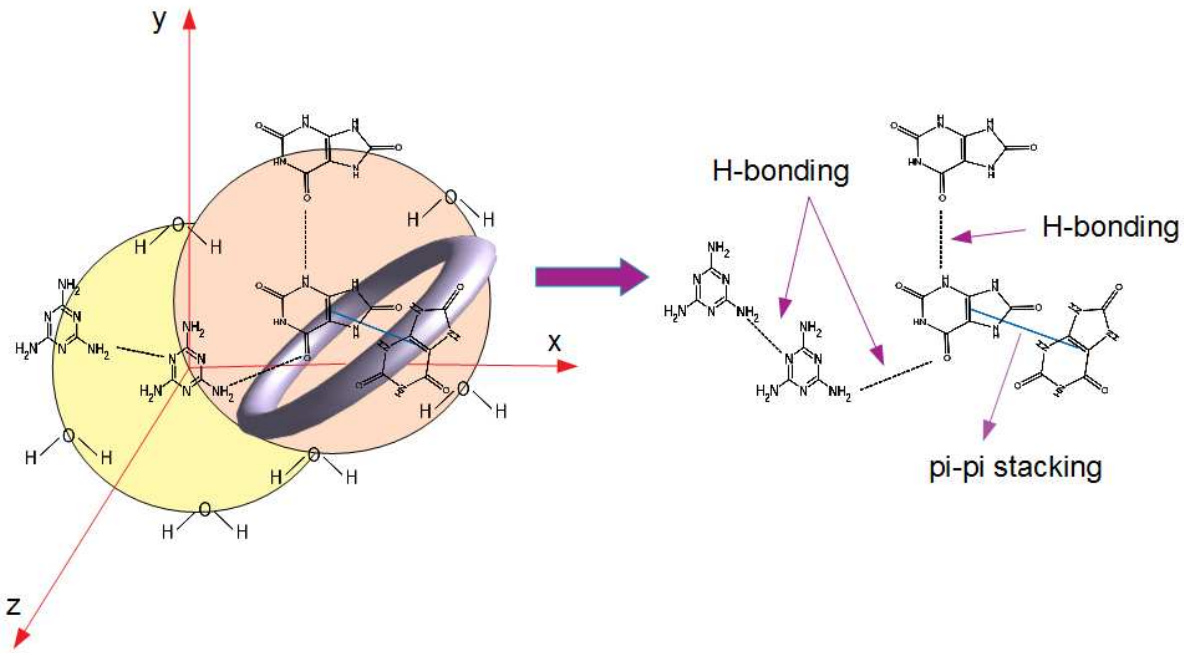

Figure 3-2. *Schematic representation of the first shell coordination number of MM around UA (r_c=7 Å), UA around MM (r_c=7 Å), MM around MM (r_c=5 Å), and UA around UA (r_c=6 Å) in water. Here, MM is attached to other UA molecules predominantly through hydrogen bonding. Similarly, MM is linked to other MM molecules through hydrogen bonding, and UA is coordinated to other UA molecules through both hydrogen bonding and π-π stacking interactions in water.*

■ RESULTS AND DISCUSSION

First shell coordination number

The first shell coordination number (CN) is a measure of the number of molecules of a specific solute that accumulate around a reference solute in a system. In the present study, CN values were determined for MM-UA, UA-UA, and MM-MM interactions using the respective pair distribution functions and the center of mass (COM) of a particular solute by the equation

$$CN = 4\pi\rho_\beta \int_0^{r_c} r^2 g_{\alpha\beta}(r) dr, \tag{3.5}$$

Table 3-3. First shell coordination number of MM around UA (r_c=7 Å), UA around MM (r_c=7 Å), MM around MM (r_c=5 Å), and UA around UA (r_c=6 Å) for all systems. Here, r_c is the position of the first minimum of the respective radial distribution function (not shown).

System	MM around UA	UA around MM	MM around MM	UA around UA
S0	0.97	0.97	0.11	1.04
S1	2.14	2.14	0.45	1.62
S2	2.98	2.98	0.67	1.74
S3	2.78	2.78	0.95	1.98
P0	1.51	3.01	0.18	1.71
P1	1.21	3.36	0.22	1.97
P2	2.28	1.14	0.54	1.66
P3	3.61	1.20	0.77	1.26
N0	1.89	2.83	0.66	1.83
N1	3.40	2.27	0.75	1.36
S_u	—	—	—	1.12

where CN is the number of atoms of type β around the atomic sites of type α in a shell extending from 0 to a separation r_c (Figure 3-2). Here, ρ_β represents the number density of β in the system. In Table 3-3, for the systems, S0–S3, running coordination number values of MM around a reference UA are presented. The CNs of MM around a reference UA were 0.97, 2.14, 2.98, and 2.78 for systems S0, S1, S2, and S3, respectively. For systems

P0 and P1, the CN values of MM around UA are 1.51 were 1.21 respectively, and those for systems P2 and P3 were 2.28 and 3.61, respectively (Table 3-3). On the other hand, for N0 and N1, the CN values were 1.89 and 3.40, respectively (Table 3-3). As the concentration of MM increased, the CN value of MM around UA molecules also increased for systems S0–S3, P2, P3, and N1. Thus, the coordination number of MM around a reference UA varied from 1 to 3. This result is supported by the CN values for systems S0, P0, and P1, which had the lowest concentrations of MM, and also those for systems S3, P3, and N1, in which the maximum number of MM molecules were present in addition to UA. Similarly, the CN values of UA around MM were determined for all systems (Table 3-3). The CN of UA around MM differed in a similar way to that of the CN of MM around UA for systems S0–S3 (Table 3-3). For systems P0 and P1, the CN values of UA around reference MM were 3.01 and 3.36, respectively,

Table 3-4. First shell coordination number of water around MM (r_c=5.25 Å) and UA (r_c=5.25 Å) for all systems. Here, r_c is the position of the first minimum of the respective radial distribution functions (not shown).

System	Water around MM	Water around UA
S0	16.09	11.47
S1	11.64	6.92
S2	9.21	6.42
S3	7.78	5.64
P0	12.29	8.10
P1	11.77	7.42
P2	13.75	7.95
P3	11.75	7.20
N0	8.65	7.04
N1	9.99	6.51
S_u	–	12.15

and those for systems P2 and P3 were 1.14 and 1.20, respectively (Table 3-3). For N0 and N1, the CN values were 2.83 and 2.27, respectively (Table 3-3). In this case, also, the CN of UA around the reference MM varied from 1 to 3. Similarly, the CN of UA around UA ranged from 1.04 to 1.98 (Table 3-3). These values (for UA around UA) can be understood in terms of their π-stacked structure (discussed below). The CN of MM around MM varied from 1 to a maximum value of 0.95 (Table 3-3). These results indicate that in the

presence of UA, MM interacts more with UA than with other MM molecules. Moreover, the comparison between systems S0 and S_u reveals that

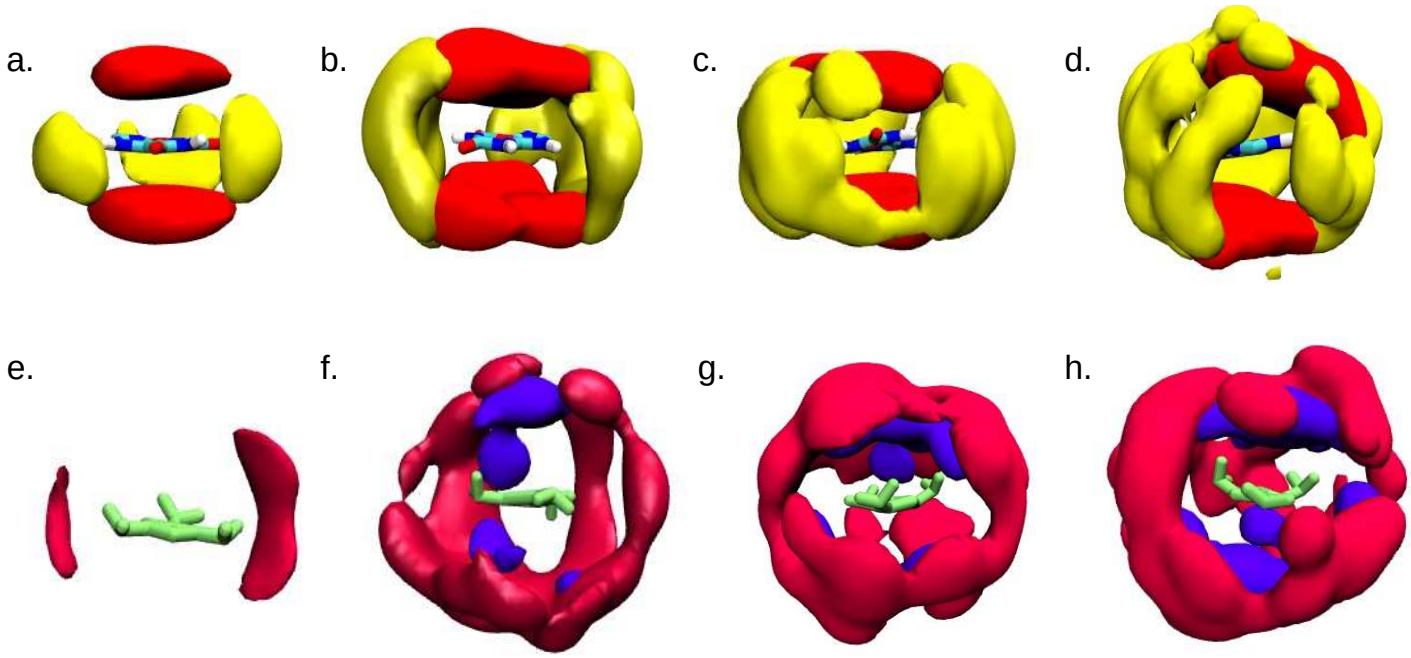

Figure 3-3. *(a)–(d) Spatial density distributions of UA (r_c= 6 Å) and MM (r_c= 7 Å) around a reference UA for systems S0–S3, respectively. Red represents the UA density distribution; yellow represents the density of MM. (e)–(h) Spatial density distributions of MM (r_c= 5 Å) and UA (r_c= 7 Å) around a reference MM for the systems S0–S3, respectively. Dark red represents the UA density distribution and violet the density of MM.*

the coordination number of UA around UA does not change notably in the presence of MM. This suggests that MM does not interfere with UA-UA interactions; rather, it binds to the aggregated UA molecules. Furthermore, the CN of water around MM and UA (Table 3-4) was determined. Clearly, MM accommodated more water around it than UA in all systems (Table 3-4). In particular, for systems S0 and S_u, the CN values of water around a reference UA were 11.47 and 12.15, respectively (Table 3-4). The change in the CN value was due to complexation between MM and UA in water for system S0, in contrast with S_u,

which contained UA in water only.

Spatial density plots

In this section, spatial density distributions of various combinations—including the density of UA and MM around reference UA, and density distributions of MM and UA around a reference MM—were determined. In Figure 3-3(a)–(d), for all systems (S0–S3), the spatial distributions of solute UA and MM density inside the solvation shell of a reference UA are shown. An isovalue of 2.0 $\mathring{A}^{-3}$ was used. For the determination of density distribution,[174, 158] the last 20 ns of trajectory files were used.

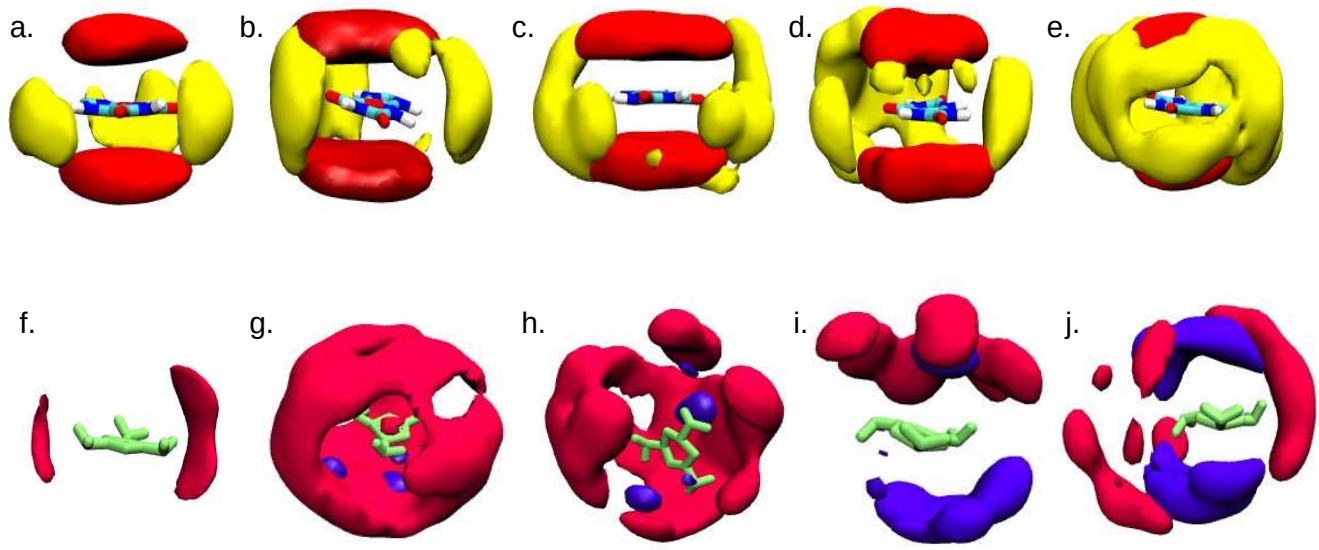

Figure 3-4. *(a)–(e) Spatial density distributions of UA (r_c= 6 Å) and MM (r_c= 7 Å) around a reference UA for systems S0, P0, P1, P2, and P3, respectively. Red represents the UA density distribution; yellow represents the density of MM. (f)–(j) Spatial density distributions of MM (r_c= 5 Å) and UA (r_c= 7 Å) around a reference MM for systems S0, P0, P1, P2, and P3, respectively. Dark red represents the UA density distribution and violet the density of MM.*

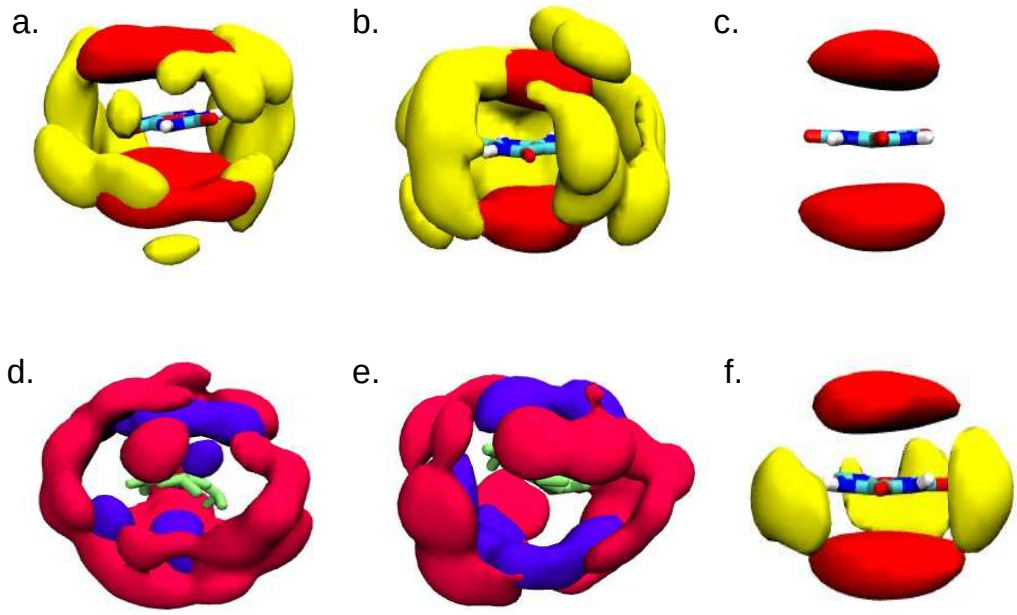

Figure 3-5. *(a)–(c) Spatial density distributions of UA and MM around a reference UA for systems N0, N1, and S_u, respectively. Red represents the UA density distribution; yellow represents the density of MM. (d)–(e) Spatial density distributions of MM and UA around a reference MM for systems N0 and N1. Dark red represents UA density distribution and violet the density of MM. (f) Spatial density distribution of UA and MM around a reference UA for system S0, where red represents the UA density distribution and yellow the density of MM.*

Moving continuously from system S0 to system S3 (Figure 3-3(a)–(d)), the enhanced density of UA molecules around a reference UA molecule can be observed. In addition, the spatial distribution of MM also increased around a reference UA. It can be easily seen that the distribution of UA and MM around a reference UA becomes more compact and symmetric when both molecules are present in a higher concentration in the system. In Figure 3-3(e)–(h), the density of MM and UA molecules around a reference MM molecule is also presented. As shown in Figure 3-3(e), for system S0, the density of MM around a reference MM was negligible but became more prominent at higher MM concentrations. Moreover,

there was a persistent increment of UA distributions around the reference MM from system S0 to system S3 (Figure 3-3(e)–(h)). In this context, we classify the aggregation of MM and UA molecules in terms of the compositional variation of one solute keeping the other one fixed. As shown in Figure 3-4(a)–(e), the density distribution of UA and MM around the reference UA increased when the concentration of one solute was kept fixed and the other continuously increased. This was also true for the density distributions of MM and UA around a reference MM (Figure 3-4(f)–(j)). Interestingly, as shown in Figure 3-4(f)–(h), as the UA concentration increased, with the MM concentration fixed, MM participated more in systems P0 and P1 (Figure 3-4(g)–(h)) than in system S0 (Figure 3-4(f)). This indicates that MM forms more complexes with UA in the presence of a higher concentration of UA molecules, where UA "drags" MM towards itself. Again, comparing the similar distributions of density for systems N0 and N1 (Figure 3-5), a pattern can be seen for these two systems in comparison with the other systems presented earlier. Comparison of systems S0 and S_u shows more clearly that there was no interference of MM with the distribution of UA around a reference UA, as the two systems showed a similar pattern (Figure 3-5(c) and (f)).

Preferential interaction parameters

To draw preliminary conclusions regarding the solute-solute interactions, as well as the interactions between solute and solvent, it is appropriate to calculate their mutual propensities to each other; in this regard, Kirkwood–Buff (KB) solution theory represents a convenient way to determine the preferential interactions between a solute and co-solvent and the preferential solute-solute interactions in presence of solvents. KB theory has a wide range of applications in solvation chemistry; for example, in studies of the association of ions, interactions of solvents with proteins, and the impact of solvent on conformations in protein-peptide chemistry. Principally, this approach involves measuring thermodynamical properties with the assessment of structural changes in solutions, in order to establish a relation of volume integrals over the pair distribution functions for the derivatives of the chemical potentials. According to KB theory, which was originally constructed using the grand-canonical (μVT) ensemble, the associated KB integrals are taken as the volume integrals

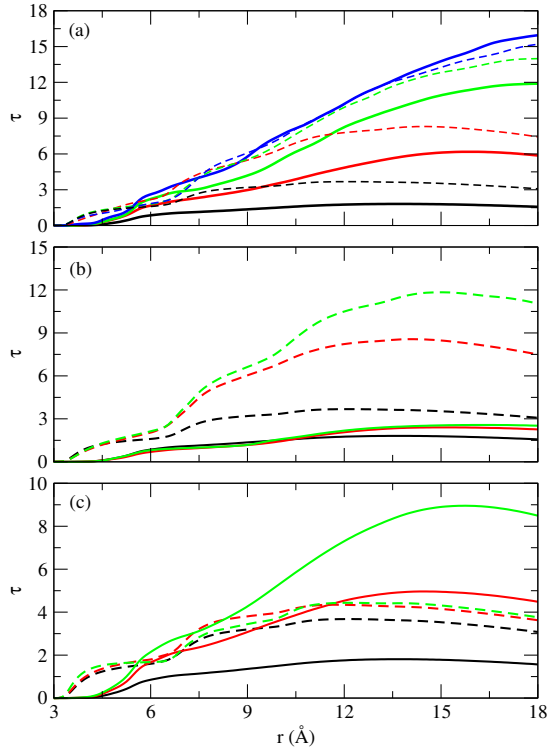

Figure 3-6. *Preferential interaction of MM-MM (solid) and UA-UA (dotted line) interactions over water for systems (a) S0 (black), S1 (red), S2 (green) and S3 (blue), (b) S0 (black), P0 (red) and P1 (green), (c) S0 (black), P2 (red) and P3 (green).*

over the pair distribution function of species i and j present in the systems:[174, 194, 195, 196, 197, 178, 179]

$$G_{ij} = \int [g_{ij}^{\mu VT}(r) - 1] dv, \tag{3.6}$$

where r is the measure of the scalar distance between the COMs of that species, i.e., i and j.

Now, considering a spherical symmetry, this integral over volume in Eq. (3.6) can be written as:

$$G_{ij} = 4\pi \int [g_{ij}^{\mu VT}(r) - 1] r^2 dr. \tag{3.7}$$

Using the isothermal-isobaric (NpT) ensemble under periodic boundary conditions, the following equation can be approximated as:

$$G_{ij} = 4\pi \int_0^R [g_{ij}(r) - 1] r^2 dr, \tag{3.8}$$

where G_{ij}(r) represents the pair correlation functions of a closed ensemble and R is the measure of the upper limit of a correlation region around the center of a particular molecule, below which the pair distribution function is governed by the intermolecular interactions between species i and j.

At a molecular level, the aggregation tendency of MM and UA molecules can be estimated by determining the preferential interaction parameter, τ.

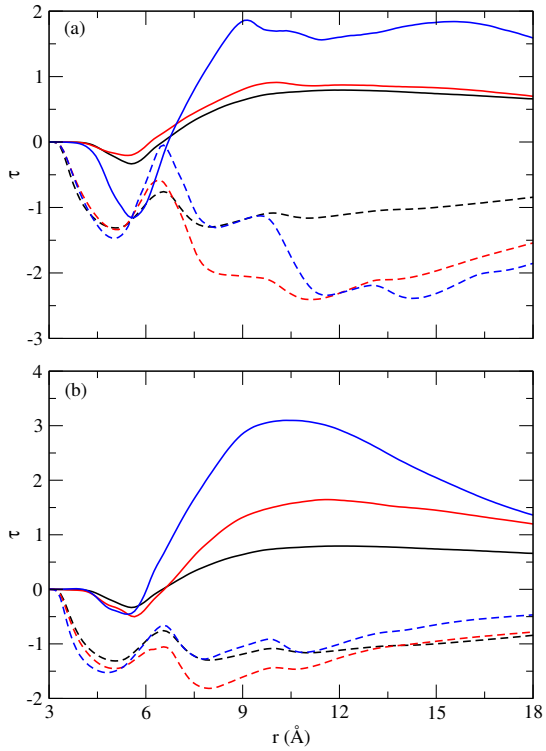

Figure 3-7. *Preferential interaction parameters of MM-UA interaction over MM-MM (solid line) and UA-MM over UA-UA (dotted line) for different systems: (a) S0 (black), P0 (red), and P1 (blue); (b) S0 (black), P2 (red), and P3 (blue).*

Here, KB theory was used to estimate the preferential interaction parameters of solute MM (UA) with like molecules over UA (MM) and solvent water, as follows:

$$\tau_{mw}^{m} = \rho_m (G_{mm} - G_{mw}) \tag{3.9}$$

$$\tau_{uw}^{u} = \rho_u(G_{uu} - G_{uw}) \tag{3.10}$$

$$\tau_{um}^{m} = \rho_m(G_{mu} - G_{mm}) \tag{3.11}$$

$$\tau_{mu}^{u} = \rho_u(G_{um} - G_{uu}) \tag{3.12}$$

where m, u, and w correspond to MM, UA, and water, respectively; and ρ_m and ρ_u denote the number densities of MM and UA, respectively. The positive τ_{mw}^{m} value indicates more favorable MM-MM interactions compared with MM-water interactions, and so on. G_{mm} and G_{mw} reciprocate to KB integrals. These integrals can be obtained the from MM-MM and MM-water rdfs. In the estimation of these distribution functions, COM of MM and water molecules were taken into consideration.[174, 197] Using above equations (Eq. 3.9 and 3.10), the values of τ_{mw}^{m} and τ_{uw}^{u} were determined for systems S0–S3, where the ratio [MM]:[UA] is 1:1 with increasing concentrations of both MM and UA. The change in these values can be seen in Figure 3-6(a). As shown in the figure, both MM and UA interacted preferably with themselves over water, that is, the corresponding preferential interaction parameters had positive values. Furthermore, the preferential interactions among UA molecules were greater than those among MM molecules in water for systems S0–S3. For system S3, the value of τ_{mw}^{m} and τ_{uw}^{u} do not differ as much, possibly owing to the saturation of the solution at this concentration of MM and UA in water. For systems S0, P0, and P1, the MM concentration was fixed while the concentration of UA was increased. In these systems, the value of τ_{mw}^{m} showed almost no change, while the value of τ_{uw}^{u} increased consistently (Figure 3-6(b)). Similar changes were observed for systems S0, P2, and P3, in which the concentration of UA was fixed (Figure 3-6(c)). In these systems, τ_{mw}^{m} changed continuously and showed an increasing trend, whereas the value of τ_{uw}^{u} remained nearly unchanged. These results suggest that MM interacts preferentially with other MM molecules, and UA interacts preferentially with other UA molecules, in all cases. The same was true for the N0 and N1 systems (not shown).

The preferential interaction parameters for MM-UA interaction over MM-MM and UA-MM interaction over UA-UA were also determined, to obtain a better understanding of which interaction predominates when both MM and UA molecules are present in solution. Figure 3-7(a) shows the preferential interaction parameters for MM-UA interaction over MM-MM for systems S0, P0, and P1. Here, MM interacted more with UA than with other MM molecules present in the system. Furthermore, the preferential interaction parameters for MM-UA interactions over UA-UA interactions were negative. These results indicate

that UA preferentially interacts with other UA molecules rather than with MM. This was also the case for systems S0, P2, and P3 (Figure 3-7(b)), and for systems S1–S3, N0, and N1 (not shown).

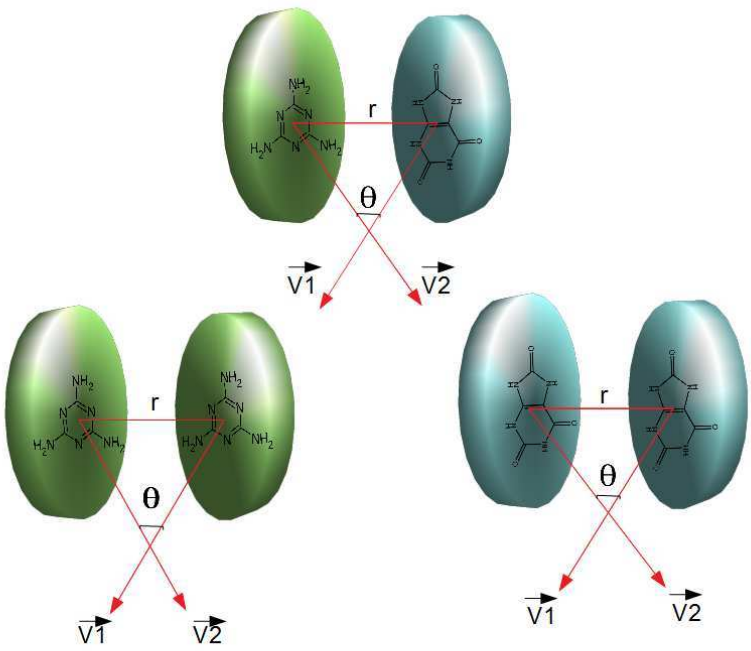

Figure 3-8. *Schematic representations of the vector normals of molecular planes of MM and UA molecules forming an angle θ.*

Orientational preference of aromatic planes

In this section, we examine how UA molecules orient themselves close to another solute, that is, MM. To understand the orientational configuration of UA molecules in solution in the presence of MM, we considered the angle between the molecular planes of these molecules.

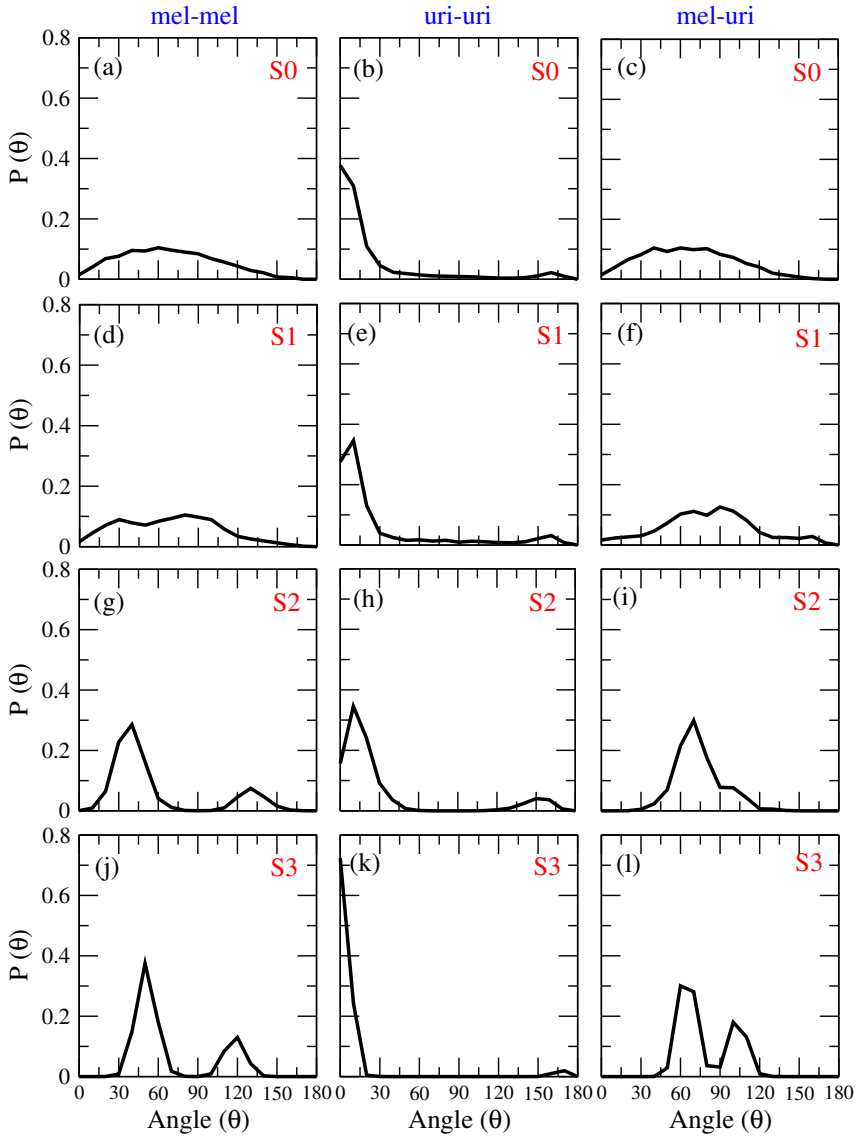

Figure 3-9. *Probability (P(θ)) of orientational angle (θ) between two molecular aromatic planes of MM-MM (first column, (a), (d), (g), (j)), UA-UA (second column, (b), (e), (h), (k)), and MM-UA (third column, (c), (f), (i), (l)) for systems S0–S3 (row-wise).*

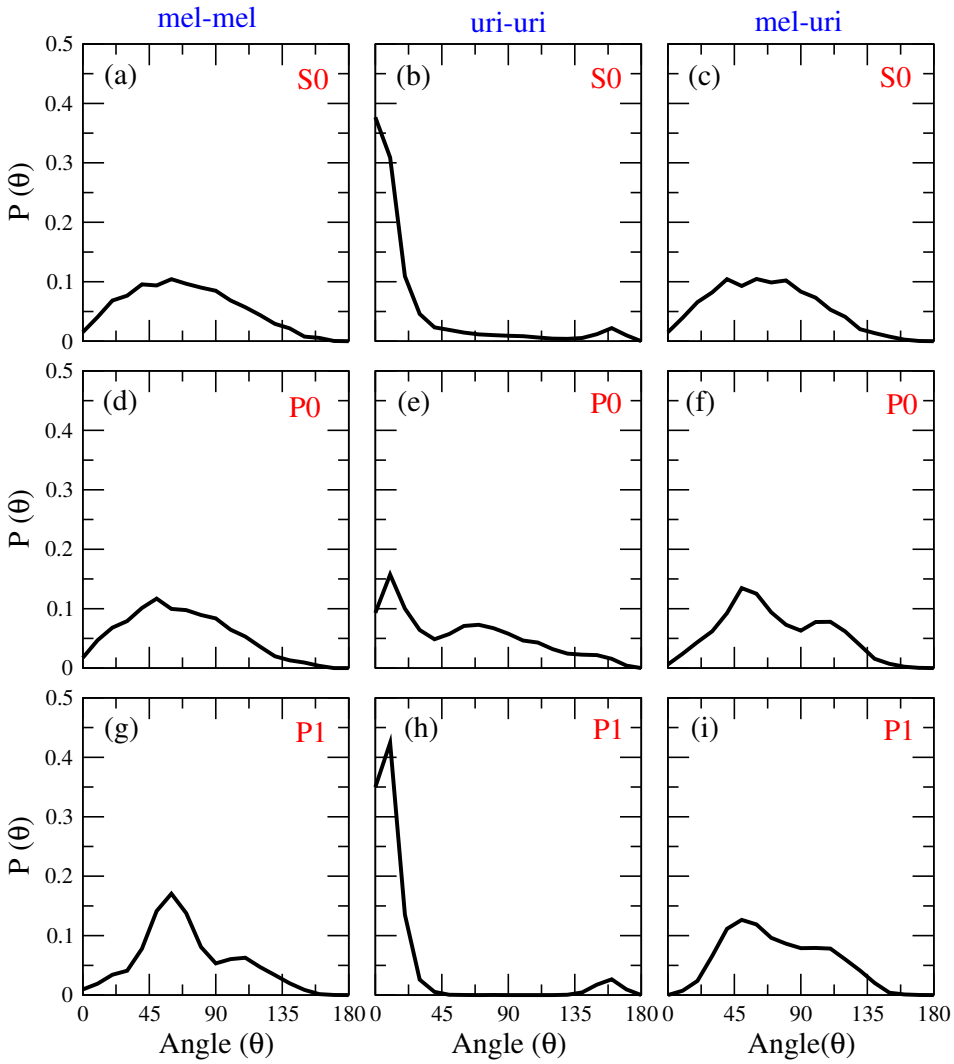

Figure 3-10. *Probability (P(θ)) of orientational angle (θ) between the two molecular aromatic planes of MM-MM (first column, (a), (d), (g)), UA-UA (second column, (b), (e), (h)), and MM-UA (third column, (c), (f), (i)) interactions for systems S0, P0, and P1 (row-wise).*

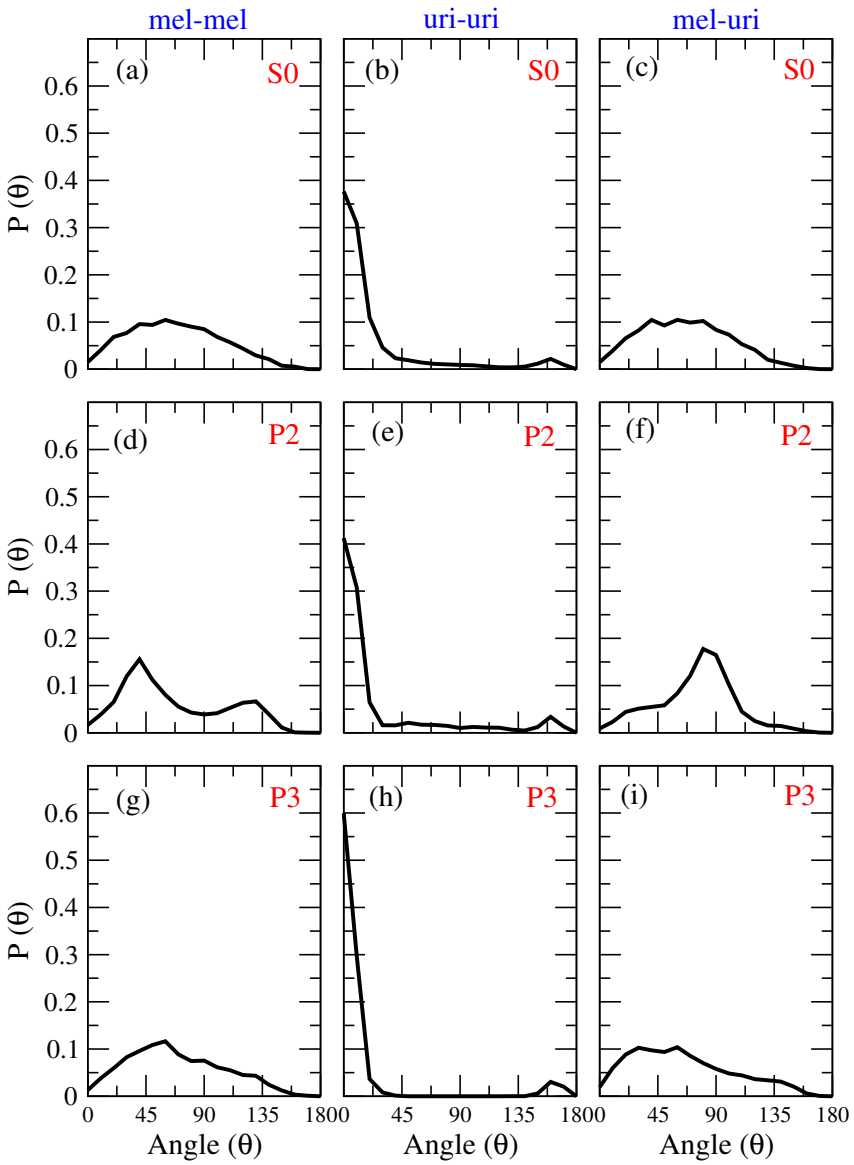

Figure 3-11. *Probability (P(θ)) of orientational angle (θ) between the two molecular aromatic planes of MM-MM (first column, (a), (d), (g)), UA-UA (second column, (b), (e), (h)), and MM-UA (third column, (c), (f), (i)) interactions for systems S0, P2, and P3 (row-wise).*

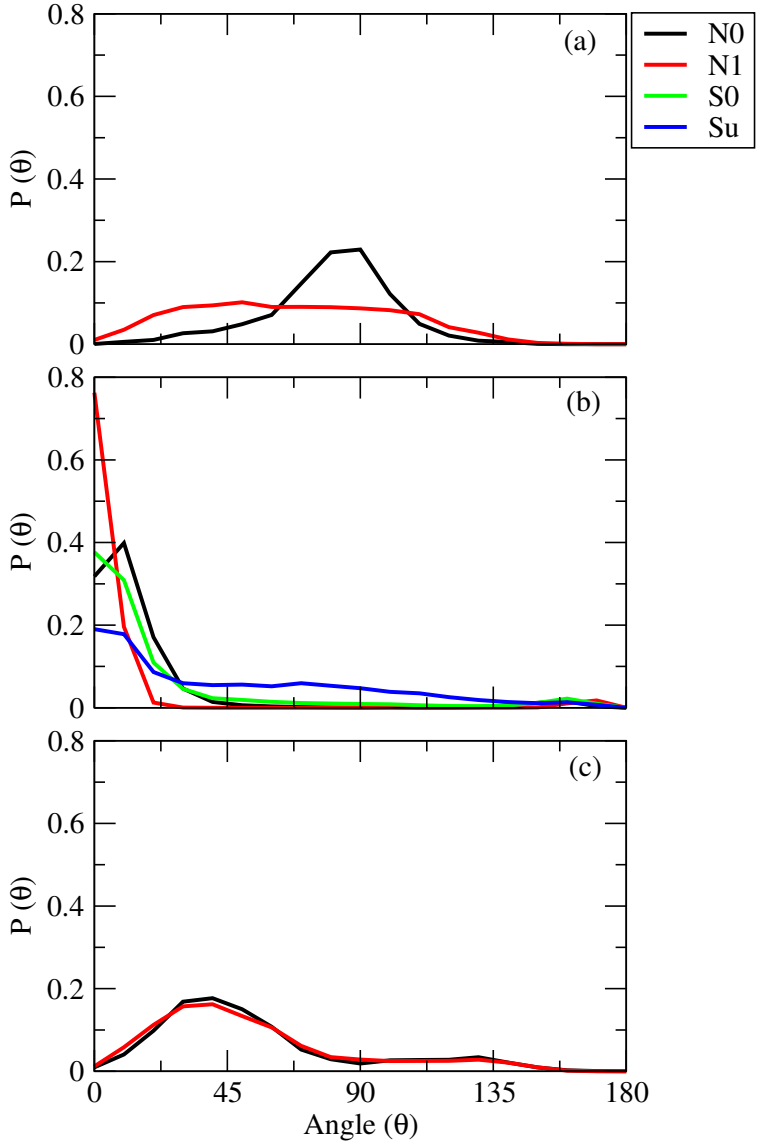

Figure 3-12. *Probability (P(θ)) of orientational angle (θ) between the two molecular aromatic planes of (a) MM-MM, (b) UA-UA, and (c) MM-UA for systems N0, N1, S0 and* S_u.

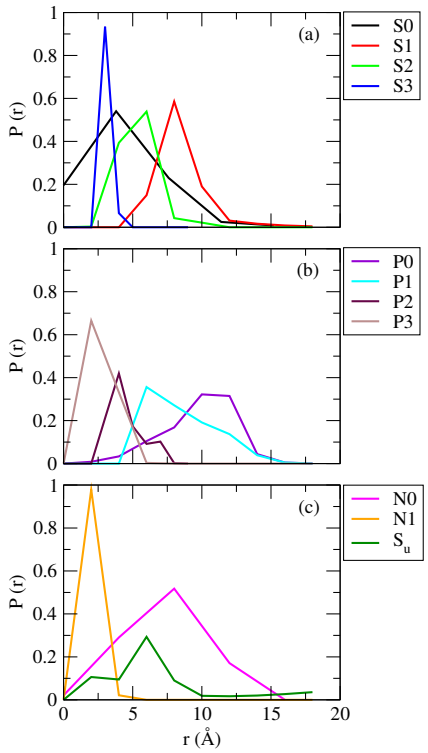

Figure 3-13. *Probability of distance (r) at which π-π stacking exists for all systems.*

To look at the interactions coming from the $\pi - \pi$ stacking between the aromatic planes present in UA and MM, the probability of orientational angles between two UA molecules and two MM molecules is determined separately alongside the interplanar angle between MM and UA molecules. To do so, an angle between two vector normals of any two aromatic planes is considered (Figure 3-8). The angle i.e 0^o, 90^o and 180^o between these vector normals correspond to the parallel, perpendicular along with anti-parallel stacking between the two aromatic planes respectively.[174, 197, 161] In Figure 3-9, the probability distribution of angle θ, P(θ), as a component of the inter-planar angle (θ) is plotted for systems S0–S3. For systems, S0 and S1, a broad distribution of P(θ) was observed, and the maximum of P(θ) was reached at $\theta \simeq 50°$ for MM-MM interactions. Furthermore, for the S2 and S3 systems, two peaks at $\theta \simeq 50°$ and θ=122–135° were apparent. From these angle values (θ), it appears that MM does not interact with other MM molecules through π-π stacking interactions. In the case of UA-UA interactions, one can reasonably suppose that UA molecules to interact with other UA molecules through π-π stacking, as the maximum

value of P(θ) appeared at 20° along with a very small peak at θ=165–175° for systems S0–S3. For MM-UA interactions, the maximum value of P(θ) was observed when $\theta \simeq 60°$. Based on these values of θ, we can conclude that MM molecules associate with other UA molecules in water overwhelmingly through hydrogen-bonding interactions (discussed below), with a very low probability of π-π interactions. As the concentration of MM and UA increased from system S0 to S3, the peak height increased. It is important to note here that π-π stacking made a small contribution to the MM-MM interactions in comparison with the hydrogen-bonding interactions. Interestingly, however, UA molecules self-aggregated with other UA present in the system through π-π stacking in particular, with negligible contributions from hydrogen-bonding interactions (see below). This was the case for all systems S0–S3 at 300 K (Figure 3-9). For systems in which the concentration of MM was fixed and the concentration of UA varied (with an increasing trend for systems S0, P0, and P1), similar orientational preferences were observed for MM-MM, UA-UA, and MM-UA interactions (Figure 3-10). Similar results were obtained for systems S0, P2, and P3 (Figure 3-11), in which the concentration of MM was increased while the concentration of UA was fixed. In systems N0 and N1, where the MM:UA ratios were 2:3 and 3:2, respectively, a similar pattern was produced (Figure 3-12(a)–(c)). In system S_u (free UA in water without MM), UA was shown to form stacking interactions (Figure 3-12 (b)). This reference system was used to determine whether or not the orientational preference of free UA in water was hindered in the presence of a foreign element such as MM. The results showed that MM did not alter the interaction of UAs; rather, MM bound to the stacked UAs through hydrogen bond formation in particular (see below).

These stacking interactions are only meaningful when the two interacting molecules simultaneously maintain a particular angle and meet a particular distance criterion (Figure 3-8). From the results discussed above, it is clear that when two UA molecules are involved in π-π stacking, they maintain the angle (0–20°).[174, 197, 161] It was also important to measure the distance between the UAs to check that they met the distance criterion as well as the specific angle. To do this, the distance between two UA cores was measured for all systems. In Figure 3-13, the probabilities of the distances between two UAs are given. An average distance of 3 Å with a maximum of 7 Å was maintained for all systems considered in the present study. These distance values, together with the angles determined earlier, constitute further evidence of π-π stacking between the aromatic cores of two UA molecules

Cluster structure analysis

The clusters of different sizes that are formed by MM-MM, UA-UA, and MM-UA interactions were determined using a distance criterion between two distinctive solute molecules. Considering MM-MM clusters first, two different MM molecules, say M1 and M2, can form a dimer if the COMs of these two molecules are locked in by a distance of 5 Å (that is, the COM-COM distance between M1 and M2). Now, if the COM of a third MM M3

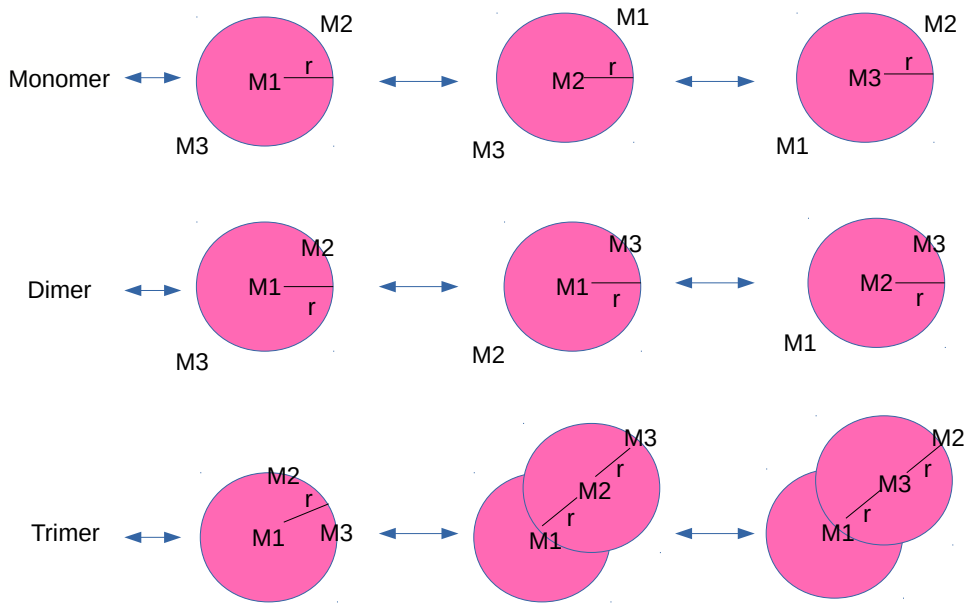

Figure 3-14. *Schematic representation of the cluster structure analysis. Here, M1 and M2 represent two separate molecules, either MM or UA. When M1 and M2 remain far from each other, they are considered not to be a part of any cluster through any interactions such as hydrogen bonds or π-π stacking; instead, they are considered as two monomers. M1 and M2 are considered to form a dimer when they are attached through any kind of interactions at a certain separation (here, COM-COM distances of 5 Å for MM-MM and 6 Å for UA-UA are taken as the cut-off distances). A third MM or UA, M3, is considered to be a part of a trimer with M1 and M2 when it comes within the respective distance range of either M1 or M2. This is also valid for higher-order clusters.*

comes within this distance range, i.e., 5 Å of either M1 or M2 (Figure 3-14), then a trimer (comprising M1, M2, and M3) is formed. A similar definition for MM clusters applies to clusters of higher orders.

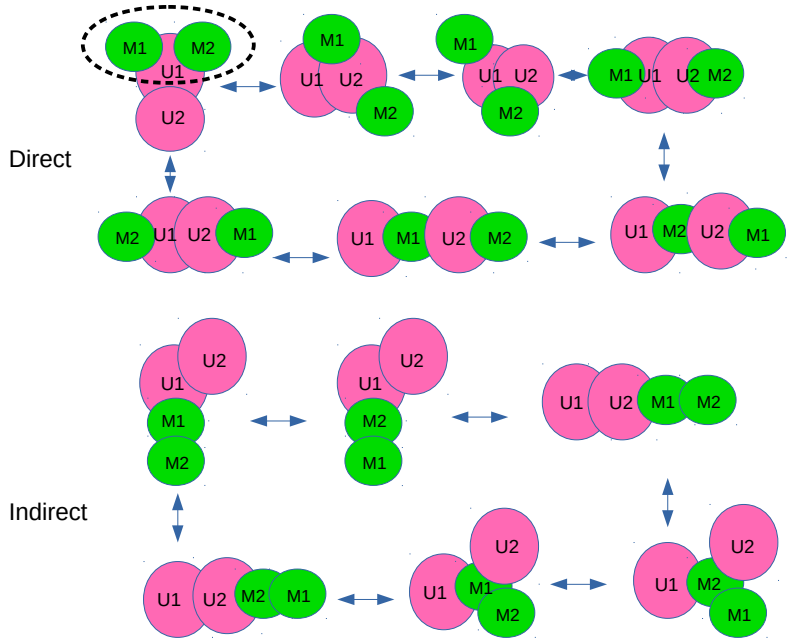

Figure 3-15. *Schematic representation of the analysis of cluster structure for MM-UA complexes. M1 and M2 represent two separate MM molecules, and U1 and U2 are two different UA molecules.*

A similar definition was used for UA-UA clusters. In this case, the COM-COM distance between two UA molecules was taken to be 6 Å (Figure 3-14). For clusters formed by MM-UA interactions, two different approaches were used, involving "direct" and "indirect" contact between MM and UA molecules. In direct contact, two MM molecules, say M1 and M2, are directly attached to two UA molecules U1 and U2, or to one UA molecule, say either U1 or U2. The distance criterion was taken as earlier, with a COM_m-COM_u distance of 7 Å. In the indirect contact approach, the COM_m-COM_m distance (for MM-MM contact) was 5 Å (for MM-MM contact), the COM_u-COM_u distance (UA-UA contact) was 6 Å and the COM_m-COM_u distance (MM-UA contact) was 7 Å. Thus, in the indirect contact approach, two MM molecules can form a cluster with UA in which one of the two

MM molecules is not in contact with UA directly but by bridging through a MM molecule. This is also true in the case of two UA molecules where one is linked through another UA bridge. The results for MM-UA cluster structure formation were obtained through a combination of the two approaches (direct and indirect contact) (Figure 3-15).

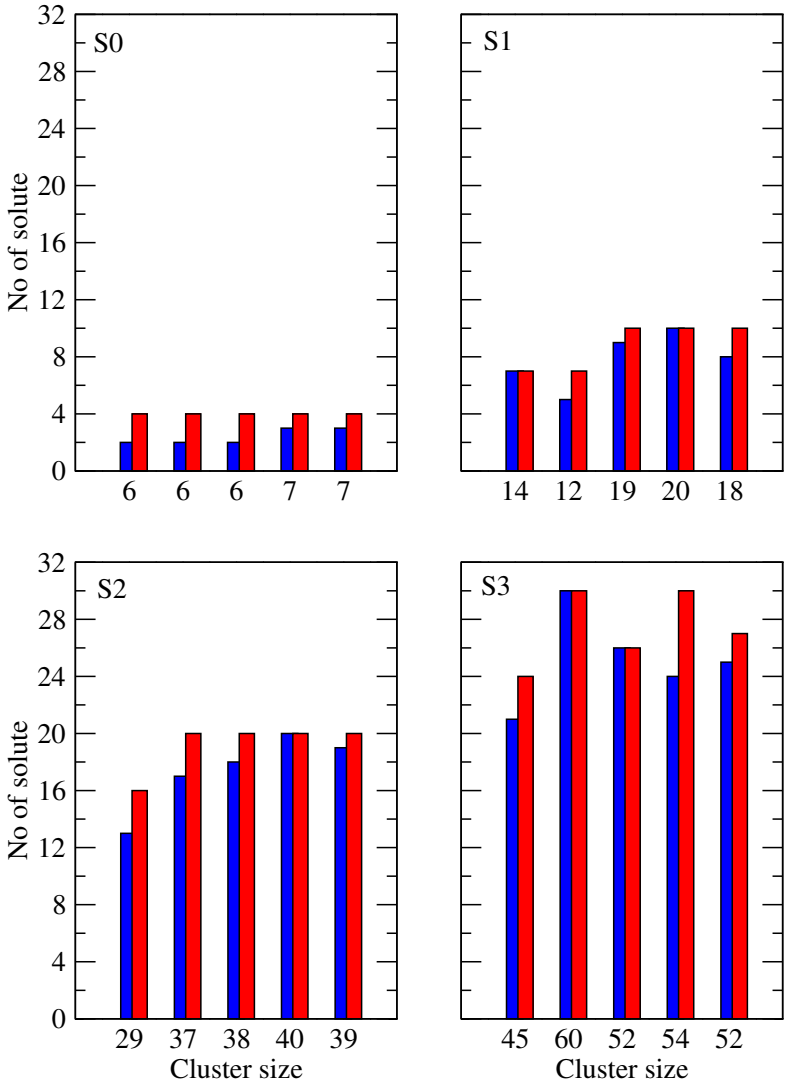

Figure 3-16. *Various clusters of different sizes made by MM-UA for systems S0-S3. Red color represents UA and blue color stands for MM.*

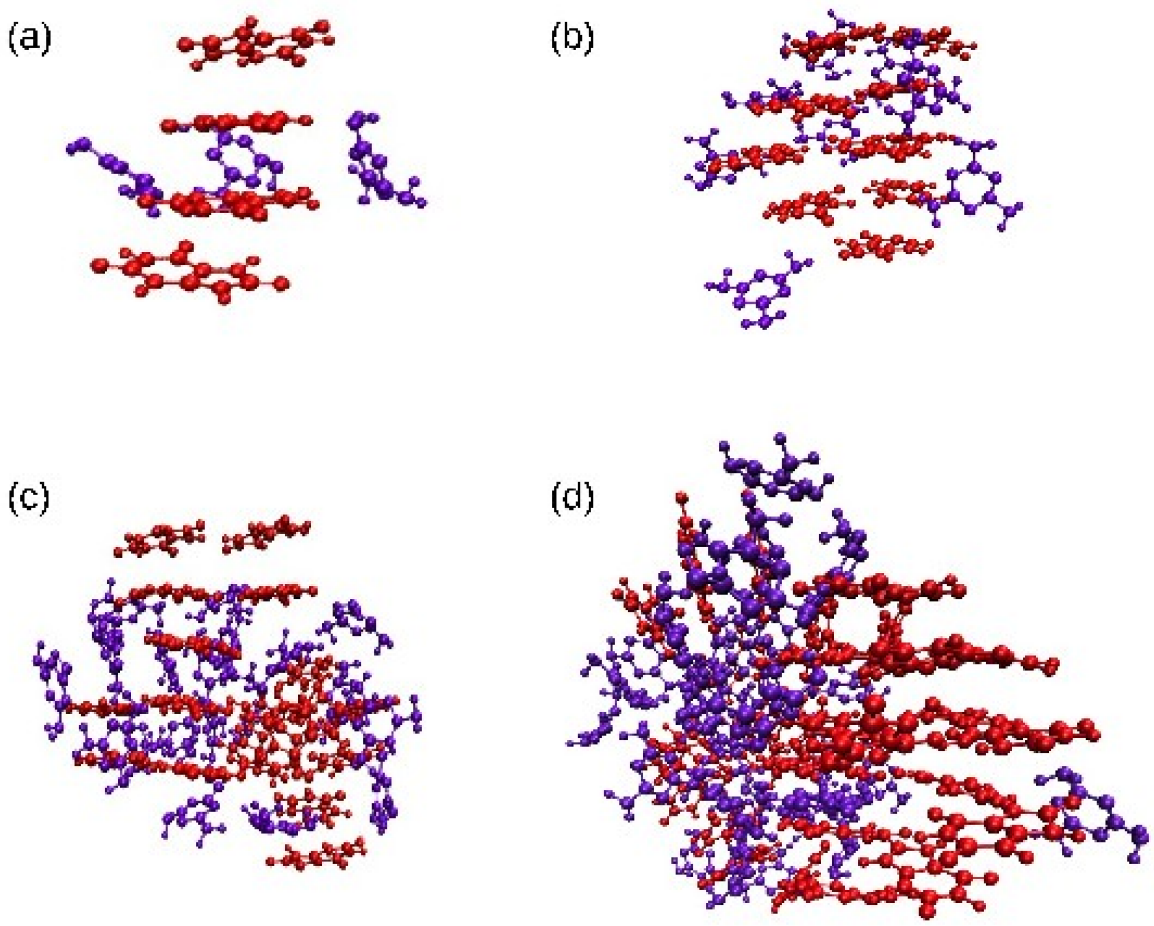

Figure 3-17. *Representative snapshots of clusters formed by MM and UA for systems S0, S1, S2, and S3 at 200 ns.*

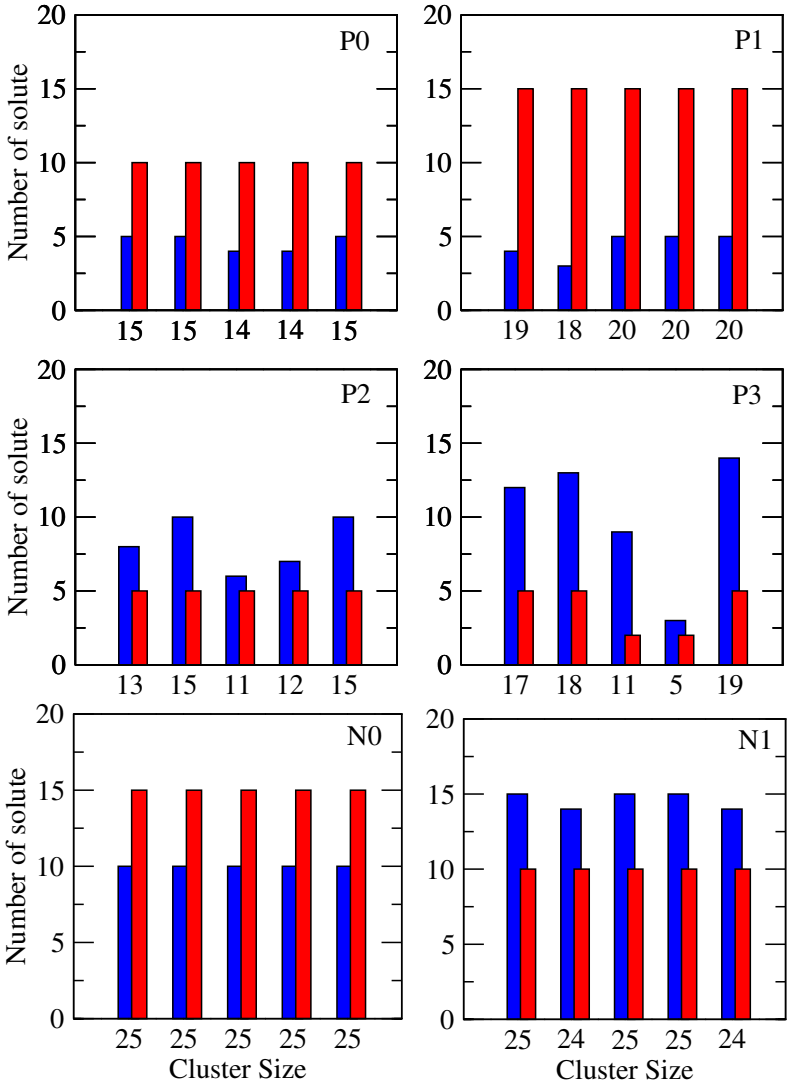

Figure 3-18. *Various clusters of different sizes made by MM and UA for systems P0, P1, P2, P3, N0 and N1. Red color represents UA and blue color stands for MM.*

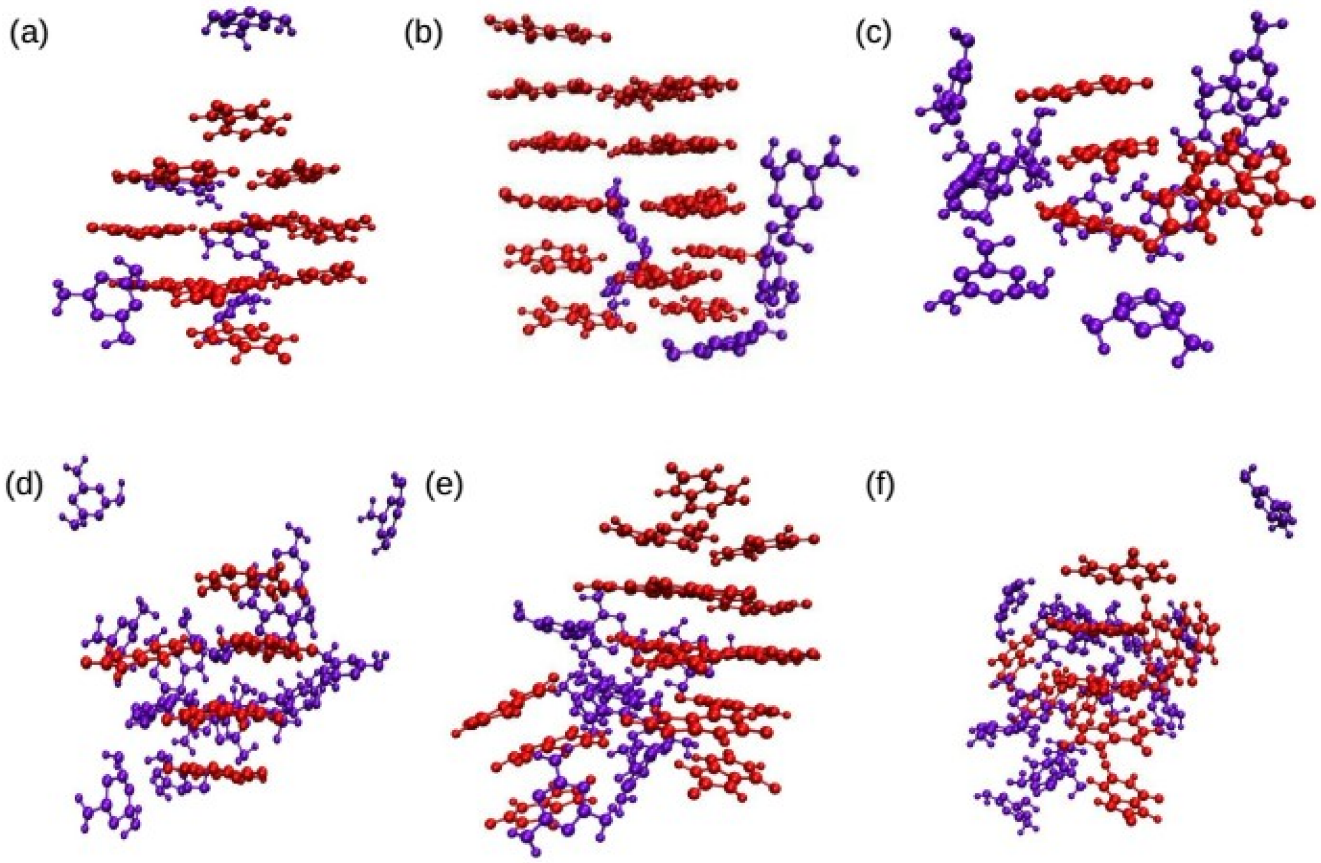

Figure 3-19. *Representative snapshots of clusters formed by MM and UA for systems P0, P1, P2, P3, N0, and N1 at 200 ns.*

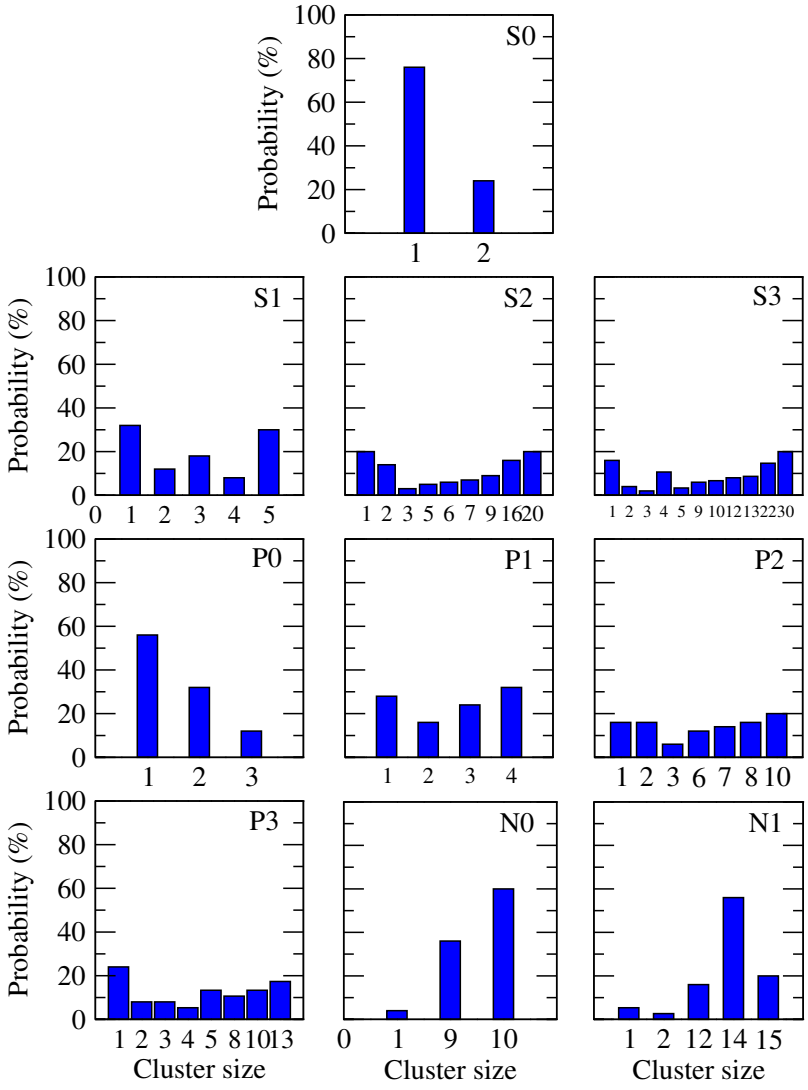

Figure 3-20. *Distributions of various clusters of different sizes made by MM-MM interactions for different systems.*

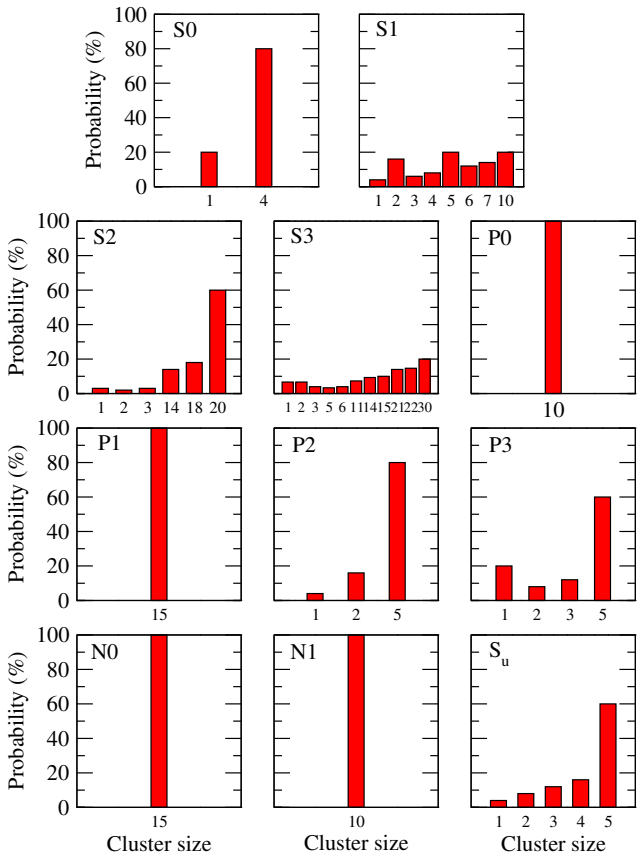

Figure 3-21. *Distributions of various clusters of different sizes made by UA-UA for different systems.*

Figure 3-16 shows the maximum size of MM-UA aggregates determined for systems S0–S3. The last 20 ns trajectories of the total MD production runs were used, and results were obtained over time intervals of 184 ns to 200 ns in 4 ns steps. In the case of system S0, the largest cluster composed of MM and UA was a hexamer or heptamer (Figure 3-16 and Figure 3-17). Moreover, this hexamer/heptamer was an aggregate of two or three MM molecules with four UA molecules. Thus, of the 10 molecules (five molecules each of MM and UA) present in system S0, six or seven are involved in the formation of an aggregate. This suggests that the interaction between MM and UA is quite strong. Furthermore, in all aggregates for system S0, 80% of the UA molecules present came close enough to form a tetramer, whereas 40–60% of the MM molecules present in the system preferentially bound to the UA aggregates. Similarly, for systems S1, S2, and S3, larger clusters were formed with increasing concentration; the cluster size increased from system S0 to S3

(Figure 3-16 and Figure 3-17). This indicates that MM forms a strong complex with UA in water. Interestingly, in systems S0–S3, where the MM: UA ratio was 1:1, the percentage of UA that formed an aggregate with MM was higher than the corresponding percentage of MM in all cases. It was then of interest to determine cluster sizes for different MM: UA ratios. Clusters of various sizes were determined for systems P0 and P1, which had higher concentrations of UA. It was clear that for these systems, 100% of the UA present went into clusters (Figure 3-18 and Figure 3-19). Furthermore, 80– to 100% of the total MM was involved in forming these large clusters. When the concentration of MM was varied in systems P2 and P3, a similar scenario was observed. Interestingly, however, not all MM molecules participated in cluster formation with UA for these systems (Figure 3-18 and Figure 3-19). Similarly, noteworthy complexation was found for systems N0 and N2 (Figure 3-18 and Figure 3-19). These observations clearly show that the self-aggregation tendency of UA is greater than that of MM (discussed below). Furthermore, MM is more "attracted" towards the larger clusters formed by UA. This conclusion was verified by performing cluster size determination for the self-assembly of MM-MM and UA-UA for all systems. Now, considering the MM-MM cluster sizes for all systems, higher-order clusters were observed in substantial quantities for all systems containing a significant percentage of the monomer (Figure 3-20). However, in the case of UA, higher-order clusters were formed in systems with a low percentage of monomer units (Figure 3-21). Again for UA, both the size of the cluster and the probability of formation of higher-order clusters were greater than those of MM-MM clusters in systems S0–S3, in which the concentration ratio was 1:1 (Figure 3-21). A considerable quantity of higher-order clusters was also found for the other systems (Figure 3-21). Moreover, comparing systems S0 and S_u, 80% tetramer and 20% monomer were found in the former, in contrast to 60% pentamer with 4% monomer and the remainder consisting of tetramer, trimer, and dimer for S_u (Figure 3-21). Thus, the presence of MM in S0 did not affect UA aggregation; rather, it bound to pre-existing clusters of UA (Figure 3-21).

MM-PBSA and complexation energy

MM-PBSA is widely used to measure the binding free energies of complexes formed by macromolecules. Free energy perturbation techniques can also be used for this purpose, but the MM-PBSA technique is 10 times faster than conventional methods. MM-PBSA is also computationally less expensive as it uses a continuum solvent model. In the present study,

the binding free energy was calculated by decomposing it into components for specific types of interactions between MM and UA molecules during complexation. We chose UA as the receptor and MM as the ligand, and investigated the driving force for the binding of ligand molecules to receptors, in order to obtain a better understanding of MM-UA complexation.

Table 3-5. All energies derived from the MM-PBSA calculations. Here, ΔE_{vdW}, ΔE_{elec}, ΔG_{PB}, ΔG_{NP}, and $\Delta G^0{}_{bind}$ are the energy of van der Waals interaction, electrostatic energy, Poisson–Boltzmann energy, non-polar energy, and binding free energy, respectively. All energy values are given in kcal/mol.

System	ΔE_{vdW}	ΔE_{elec}	ΔE_{PB}	ΔG_{NP}	$\Delta G^0{}_{bind}$
S0	-7.69	-28.10	26.17	4.86	-5.03
S1	-51.40	-144.87	126.06	26.96	-43.26
S2	-130.52	-429.16	365.77	73.45	-120.46
S3	-207.69	-594.72	487.12	105.70	-209.59
P0	-28.88	-95.76	82.05	14.99	-27.61
P1	-31.58	-117.38	96.35	18.74	-33.87
P2	-25.45	-86.42	75.88	14.41	-21.58
P3	-40.08	-128.30	103.87	20.11	-44.39
N0	-66.89	-199.14	168.42	33.95	-63.66
N1	-71.77	-248.12	195.12	35.34	-89.43

All energy values for the various systems considered in the present study are summarized in Table 3-5. As shown in the table, the total binding free energies ($\Delta G^0{}_{bind}$) were negative for all systems. This indicates that MM-UA complex formation is favorable in water. Again, one would typically expect to find an extremely favorable electrostatic energy (ΔE_{elec}) and an unfavorable solvation free energy ($\Delta G_{sol} = \Delta E_{PB} + \Delta E_{NP}$). This symbolizes the energy required to desolvate the binding particles and to align their binding interfaces. Furthermore, taking the results together, it can be seen that a considerable contribution to the binding free energy is made by the favorable MM-UA van der Waals interactions (ΔE_{vdW}), but the electrostatic energy component (ΔE_{elec}) is the main driving force behind MM-UA complex formation. For systems S0–S3, the $\Delta G^0{}_{bind}$ was more favorable. This indicates that the greater the concentration of MM alongside UA in a system, the stronger the complexation that will occur. Moreover, in systems P2 and P3, in which the MM concentration was increased in comparison with S0, the $\Delta G^0{}_{bind}$ had more negative values.

Similarly, the negative $\Delta G^0{}_{bind}$ for systems P0 and P1 increased when the concentration of UA was increased, while keeping the MM concentration fixed, in contrast to system S0. This trend was also observed for systems N0 and N1. These results indicate that an increase in concentration of either MM or UA in a system is favorable for complexation between MM and UA molecules in water.

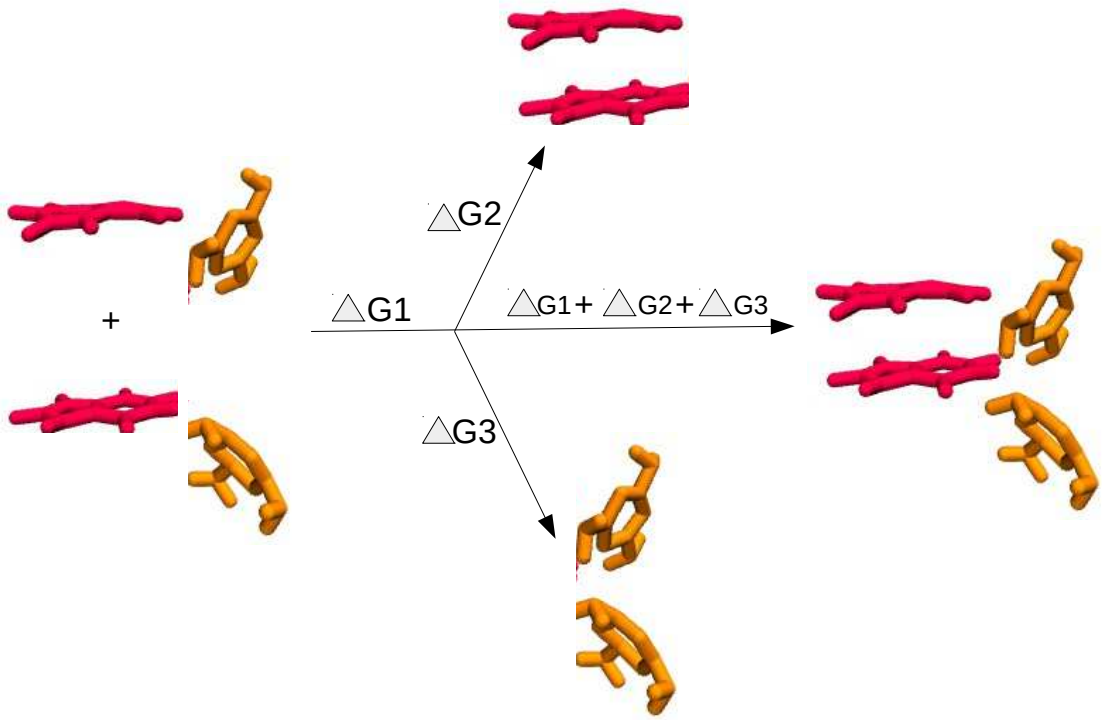

Figure 3-22. *Schematic representation of the complexation energy during the formation of a complex between MM (orange) and UA (red) in system S0. Here, $\Delta G1$, $\Delta G2$, and $\Delta G3$ represent $\Delta G^0{}_{(mel\text{-}uri)}$, $\Delta G^0{}_{(uri\text{-}uri)}$, and $\Delta G^0{}_{(mel\text{-}mel)}$, respectively.*

Note that MM-PBSA only gives the binding free energy when the ligands and receptors are in direct contact. Thus, the total negative binding free energies ($\Delta G^0{}_{bind}$) only correspond to direct contact between MM and UA in water (Table 3-5). In order to compute the total complexation energies, both direct and indirect contacts (as discussed above) should be taken into consideration for all systems. All MM-MM and UA-UA indirect contacts should be added to the MM-UA direct contacts to obtain the total complexation energy. This

complexation energy gives a more accurate picture of the formation of clusters among the MM and UA molecules in water (Figure 3-22). In the present study, the complexation energy for system S0 was determined so that an overall idea and conclusion could be developed and applied to the remaining systems. To do so, $\Delta G^0{}_{bind}$ values for MM-MM, UA-UA, and MM-UA were determined using the last 4 ns trajectories of system S0. In this system, MM-MM direct contacts were missing, but UA-UA direct contacts were present, as were MM-UA contacts. The cluster structure analysis showed that for the last 4 ns, four of the five UAs formed a complex with three of the five MM molecules. However, none of the three MM molecules were in direct contact with each other. This was verified by the cluster structure analysis for MM-MM contacts for the last 20 ns, in which 76% molecules were found to be in monomeric states while the remaining 24% were involved in dimer formation. Thus, it was apparent that no direct contacts could exist among MM molecules in the last 4 ns trajectories. In the determination of total complexation energy for system S0, the $\Delta G^0{}_{bind}$ values for UA-UA and MM-uric acid contacts were added together to give the total binding free energies. As shown in Table 3-6, the overall complexation energy was more negative than the $\Delta G^0{}_{bind}$ for direct MM-UA binding. This indicates that the total complexation through all contact types among MM, UA, and water was favorable in the case of system S0; this may also be true for the remaining systems.

Table 3-6. Complexation energy derived by MM-PBSA calculations. Here, $\Delta G^0{}_{MM\text{-}MM}$, $\Delta G^0{}_{uric\,acid\text{-}uric\,acid}$, $\Delta G^0{}_{MM\text{-}uric\,acid}$, and $\Delta G^0{}_{complex}$ represent the binding free energies of MM-MM interaction, UA-UA interaction, MM-UA interaction, and total complex, respectively. $\Delta G^0{}_{complex}$ is the summation of $\Delta G^0{}_{MM\text{-}MM}$, $\Delta G^0{}_{uric\,acid\text{-}uric\,acid}$, and $\Delta G^0{}_{MM\text{-}uric\,acid}$. All energy values are given in kcal/mol.

System	$\Delta G^0{}_{MM\text{-}MM}$	$\Delta G^0{}_{uric\,acid\text{-}uric\,acid}$	$\Delta G^0{}_{MM\text{-}uric\,acid}$	$\Delta G^0{}_{complex}$
S0	0.0	-1.94	-6.91	-8.85

Umbrella sampling

We used umbrella sampling techniques to calculate the potential of mean force (PMF) values of single MM and UA molecules alongside that of

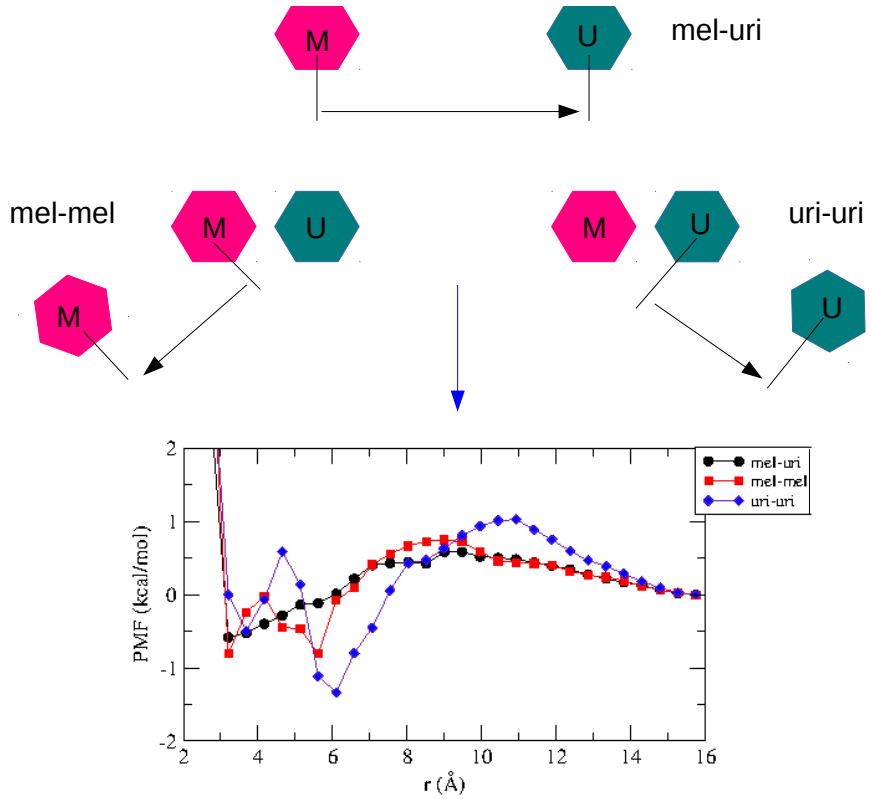

Figure 3-23. *Potential of mean forces for the association of MM-UA (black circle), MM-MM-UA (red square), and UA-UA-MM (blue diamond).*

a MM-UA dimer, in order to determine the possibility of clusters developing from a pre-existing dimer of MM and UA. Three consecutive simulations were performed to determine the PMF using the umbrella sampling method. First, one molecule each of MM and UA was immersed in 3000 water molecules at 300 K. This allowed us to calculate the PMF of MM-UA interaction as a function of the distance between the COMs of these two molecules. In that case, at a distance of 3.2 Å, a minimum was found with an energy value of -0.58 kcal/mol (Figure 3-23). This negative free energy suggests that MM-UA aggregation is quite favorable at 300 K. Next, another two umbrella sampling simulations were performed, in which a second molecule, either MM or UA, was introduced to the pre-existing MM-UA dimer in 3000 water molecules at 300 K. To do so, two separate "springs" were applied. The first spring was used to maintain the pre-existing dimer at a fixed separation. In this case, the equilibrium separation was 3.2 Å. This equilibrium separation was the same for all of

the umbrella windows. The second spring was fixed between the COM of a third molecule and the COM of one of the molecules in the dimer. The equilibrium distance between the second spring of the reference molecule and the third molecule was then varied between 2 to 16 Å in small increments 0.5 Å to obtain the PMFs. This resulted in the formation of two types of trimers: MM-MM-UA and MM-UA-UA. Notably, two further trimers could be formed when starting with a MM-UA dimer: MM-UA-MM and UA-MM-UA. However, these were ignored here, as the MM-PBSA calculations (discussed earlier) showed favorable negative binding energies for MM-UA direct contacts in all systems (S0–S3, P0–P3, N0, and N1). The resulting PMF curves for MM-MM-UA and MM-UA-UA trimer formation in water are shown in Figure 3-23 as a function of the distance between the COMs of the third molecule and the reference molecule. The negative free energy of aggregation in these two cases indicates that as the aggregate increases in size, further aggregation becomes more favorable (more negative PMF values). All simulations for umbrella sampling followed the protocols described in our previous papers.[174, 197]

Dimer existence autocorrelation functions

We also estimated the lifetimes of dimers formed by the association of MM-MM, UA-UA, and MM-UA molecules, in order to understand their dynamics, using the dimer existence autocorrelation function (DACF). The DACF for a pair of molecules i and j is the autocorrelation of a straightforward function β_{ij}, which takes the value 1 while the distance criterion is met, and becomes zero when the distance criterion "breaks" for the first time.[174, 158] Thus,

$$DACF(\tau) = N. < \sum_{t=0}^{T-\tau} \beta_{ij}(t+\tau).\beta_{ij}(t) >_{ij} \tag{3.13}$$

Note that the DACF remains zero even if the criterion is again satisfied later. DACFs for all combinations (MM-MM, UA-UA, and MM-UA) are presented in Figure 3-24.

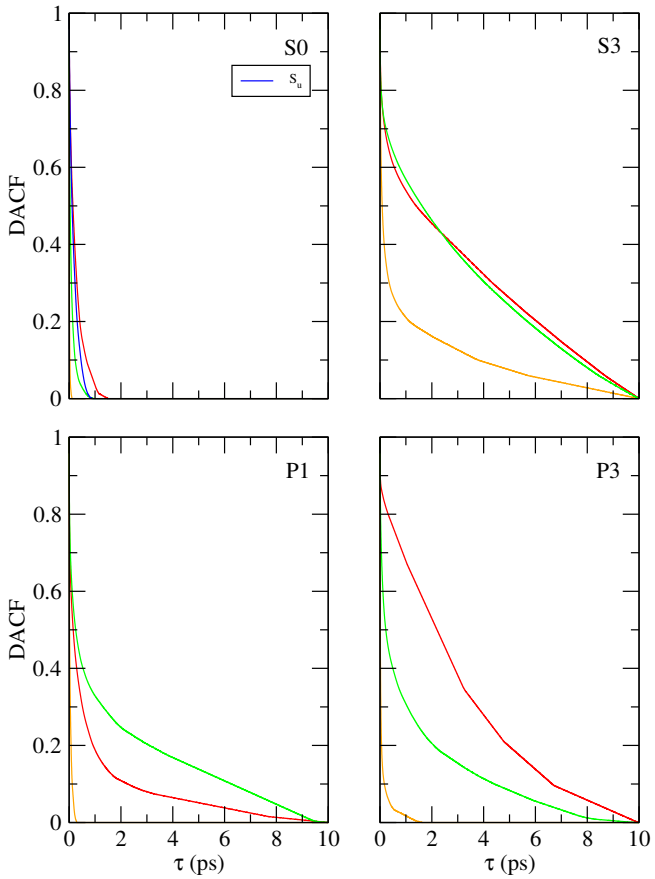

Figure 3-24. *Dimer existence autocorrelation functions (DACFs) for MM-MM (orange), MM-UA (green), and UA-UA (red) dimers for various systems.*

Here, we took the most extreme separation of 5.0 Å as the COM-COM distance between two MM molecules. For UA-UA interactions, a 6.0 Å distance was chosen as the distance cut-off. Similarly, for the MM-UA pair, the COM-COM cut-off distance was set as 7.0 Å. As shown in Figure 3-24, the DACF of the MM-MM pair fell to zero very fast in all systems, suggesting that it has a very short lifetime. However, for the MM-UA and UA-UA interactions, the lifetimes of the dimers were quite long for all systems. As the concentration of MM increased, the lifetime of the MM-MM dimer also increased. For example, comparing systems S0 and S3, there is a marked increase in the lifetime of the MM-MM dimer. The lifetime of the MM dimer was quite short compared with that of the UA-UA dimer in all systems except S3, in which its lifetime was reasonably long; thus, one would expect MM interactions to result in a low percentage of larger clusters. By contrast,

as the lifetime of dimer formation was long for MM-UA and UA-UA interactions, there was a larger percentage of higher-order clusters. This was true for all systems presented in this study.

Hydrogen bond properties

For the various systems, the average number of hydrogen bonds was determined for MM-MM, UA-UA and MM-UA. First, the average number of hydrogen bonds among all the atomic sites of UA (per UA) with the sp^3N atoms present in MM for all systems are given in Table 3-7. No clear trend in these values could be found for any of the systems. All atomic sites of UA produced a nearly equal number of hydrogen bonds with the sp^3N atoms present in MM for a particular system. Similar results (i.e., no obvious trend) were also be observed when average hydrogen bond numbers were determined (Table 3-8) among all the atomic sites of UA (per UA) with the sp^2N atoms present in MM.

Numbers of hydrogen bonds in MM-MM and UA-UA were also determined. As shown in our earlier studies[174, 197], MM utilizes nine hydrogen-bonding sites (6 H-donors and 3 H-acceptors) when forming hydrogen bonds with other MM molecules present in the system. Thus, to determine the average number of hydrogen bonds between two MM molecules, sp^3 N-H$\cdots$ sp^3 N and sp^3 N-H$\cdots$ sp^2 N were taken into account (Table 3-9). As UA-UA interactions involve a very small number of hydrogen bonds in comparison with MM-MM and MM-UA interactions, the total number of hydrogen bonds (per UA) was determined in this case. The site-site number of hydrogen bonds in UA-UA interactions has not opted (Table 3-9). It is clear that MM prefers to interact with other MM through hydrogen-bonding interactions, whereas UA formed a much lower number of hydrogen bonds in all systems. In the comparison between systems S0 and S_u, owing to the interaction between MM and UA molecules, the total number of UA-UA hydrogen bond numbers was reduced in system S0 compared with system S_u.

Similarly, hydrogen bonds may also occur in MM-water, UA-water, and water-water interactions. Thus, in an aqueous MM-UA solution, water-water (H_{w-w}), MM sp^3 N-water O_w N ($H_{sp3N-Ow}$), MM sp^2 N-water O_w N ($H_{sp2N-Ow}$) hydrogen bonds were determined, along with those of UA-water, considering all atomic sites (Table 3-10). MM formed more hydrogen bonds with water through its sp^3N sites than through its sp^2N sites. Moreover, the total number of MM-water hydrogen bonds was much higher than that of UA-water hydrogen bonds (Table 3-10). This was the case for all the systems considered here. Fur-

thermore, these results match well with the CN values of water around MM and UA discussed above. H_{w-w} was similar for all systems. This result confirms that MM-MM, UA-UA, and MM-UA interactions do not influence the water-water hydrogen bonds.

In this regard, it is notable that to determine the number of hydrogen bonds (discussed above) involved in all types of interaction, a set of criteria was chosen to define a hydrogen bond between the donor (D) and acceptor (A) atoms.[174, 197] If D-A $\leqslant$ r_{cut} and, simultaneously, $\angle$ D-H$\cdots$ A $\geqslant$ 120°, then hydrogen bonding was considered to be present. In the present study, the positions of the first minimum in the relating rdfs (not shown) were taken as r_{cut}.

Table 3-7. Average number of hydrogen bonds involving all the atomic sites of UA (per UA) with the sp^3N atoms present in MM for different systems.

System	$H_{O1\text{-}(sp3N)_m}$	$H_{O16\text{-}(sp3N)_m}$	$H_{O5-(sp3N)_m}$	$H_{N8\text{-}(sp3N)_m}$	$H_{N9\text{-}(sp3N)_m}$	$H_{N11-(sp3N)_m}$	$H_{N3\text{-}(sp3N)_m}$
S0	0.36	0.32	0.33	0.12	0.11	0.07	0.07
S1	0.52	0.88	0.64	0.11	0.14	0.12	0.15
S2	0.66	0.88	0.78	0.24	0.21	0.19	0.20
S3	0.74	0.64	0.88	0.19	0.13	0.14	0.16
P0	0.35	0.38	0.38	0.10	0.11	0.09	0.06
P1	0.26	0.66	0.55	0.02	0.12	0.09	0.02
P2	0.72	0.66	0.46	0.25	0.26	0.15	0.13
P3	0.72	1.05	0.90	0.35	0.34	0.20	0.18
N0	0.26	0.70	0.30	0.21	0.16	0.13	0.09
N1	0.90	1.02	0.74	0.19	0.30	0.20	0.14

Table 3-8. Average number of hydrogen bonds involving all the atomic sites of UA (per UA) with the sp^2N atoms present in MM for different systems.

System	$H_{N8\text{-}(sp2N)_m}$	$H_{N9\text{-}(sp2N)_m}$	$H_{N11\text{-}(sp2N)_m}$	$H_{N3\text{-}(sp2N)_m}$
S0	0.09	0.07	0.06	0.09
S1	0.07	0.10	0.12	0.18
S2	0.11	0.15	0.15	0.20
S3	0.19	0.07	0.10	0.18
P0	0.07	0.09	0.05	0.10
P1	0.08	0.02	0.09	0.10
P2	0.18	0.16	0.09	0.16
P3	0.18	0.28	0.21	0.31
N0	0.05	0.16	0.11	0.05
N1	0.18	0.23	0.10	0.25

Table 3-9. Average number of MM-MM (per MM) and UA-UA (per UA) hydrogen bonds involving all their atomic sites for all systems. For the UA-UA (per UA) hydrogen bonds calculation, D-A $\leqslant$ 3.45 and, simultaneously, $\angle$ D-H$\cdots$ A $\geqslant$ 120° are taken.

System	$H_{N(sp3N\text{-}sp3N)}$(mel)	$H_{N(sp3N\text{-}sp2N)}$(mel)	H_{total}(mel)	H_{total}(uric)
S0	0.16	0.79	0.95	0.15
S1	0.30	1.55	1.85	0.92
S2	1.26	1.19	2.45	0.78
S3	0.81	0.93	1.74	0.90
P0	0.22	0.83	1.05	0.86
P1	0.05	0.68	0.73	1.14
P2	0.41	1.75	2.16	0.70
P3	0.52	1.45	1.97	0.21
N0	0.73	1.12	1.85	0.91
N1	0.38	1.68	2.06	0.69
S_u	—	–	–	0.26

Table 3-10. Total number of hydrogen bonds involving all the atomic sites of UA and MM (per atom) with the oxygen atom of water for all systems. Here, sp^3N and sp^2N represent the sp^3N and sp^2N nitrogen atoms of MM, respectively. Ow represents the water-water (per water) hydrogen bonds. The remaining atomic sites belong to UA.

System	*sp3N*	*sp2N*	O1	O16	O5	N8	N9	N11	N3	Ow
S0	12.00	4.92	6.26	7.21	5.50	3.31	3.28	3.11	3.13	3.99
S1	19.03	8.14	10.44	9.81	6.10	6.06	5.44	2.96	4.06	3.98
S2	28.34	11.11	16.25	17.56	13.35	6.86	7.45	7.94	7.16	3.94
S3	41.33	16.65	25.27	25.97	18.16	13.08	10.91	10.32	9.33	3.94
P0	10.79	4.29	11.15	13.07	8.27	6.40	6.13	4.38	4.97	3.98
P1	10.06	3.87	15.39	18.95	12.58	9.21	9.26	7.16	7.31	3.97
P2	20.47	8.30	5.05	6.33	4.42	2.24	2.38	2.59	2.28	3.98
P3	30.59	12.24	4.51	5.93	3.73	2.01	2.06	1.66	2.11	3.97
N0	7.30	16.98	15.14	17.03	11.41	7.85	7.75	6.35	6.50	3.97
N1	26.17	10.30	7.89	10.41	7.21	3.88	4.41	4.18	3.35	3.97
S_u	—	—	6.45	7.70	6.06	3.91	3.91	3.54	3.34	4.00

Quantum chemical calculation

A series of density functional theory (DFT) calculations (complexation energy with BSSE correction after optimization using B3LYP-D3/6-311++G(d,p)) of various combinations of UA-UA and MM-UA interactions have been carried out.[26, 172, 138, 198, 199] Here, the MM-MM interaction was not considered as it had already been discussed in our previous study.[174] First, the complexation energy with BSSE correction using B3LYP-D3/6-311++G(d,p) level theory of all combinations of UA dimers was calculated in the gas phase. A set of structures in which hydrogen-bonding interactions were present (Figure 3-25 (a)–(e), Figure 3-26 (a)–(o) and Figure 3-27 (a)–(j)) along with stacked conformations between two UA molecules (Figure 3-28 (a)–(d)) were considered. These structures, which are presented in Figure 3-26 (b), (c), and (n) and Figure 3-27 (a), are the most stable hydrogen-bonded structures of all the hydrogen-bonded configurations of UA dimers. This would seem to suggest that UA forms long hydrogen-bonded sheets during its self-organization. However, closer examination of these dimer structures reveals that they form

a symmetrical and complementary structure to each other. For this reason, repeating a similar structure to form a large cluster such as a hydrogen-bonded sheet is not possible, as the third UA molecule added to any dimer would not be able to form a similar pattern to that of the pre-existing dimer. Thus, the formation of such structures is possible only when they form discrete dimers or when pre-existing π-stacked structures come into close proximity and form hydrogen bonds between two π-stacked strands. Other stable structures resulting from UA-UA complexation have lower or similar energies (around -16 to -18 kcal/mol) to those of MM-UA structures. MM and UA can form four types of hydrogen-bonded structure (Figure 3–28 (e)–(h)), of which two are non-coplanar (Figure 3-28 (e) and (f)) and the other two are coplanar (Figure 3-28 (g) and (h)). A proper explanation of these structures can be found elsewhere.[26, 172] The MM-UA structure is more symmetric and can be repeated in all directions to create a symmetrical long hydrogen-bonded sheet structure, but this is not possible for the most stable UA-UA dimers. Again, stacking between UA and UA is more probable than MM-UA stacking (Figure 3-28 (a)–(d) and (i)). All these configurations reveal that UA-UA π-π stacking is the more reliable configuration and, as a result, hydrogen bonding between pre-existing π-π stacked structures of UA molecules is quite normal. The DFT and MD simulation results of the present study are also consistent with the experimental crystal structure of UA.[200]

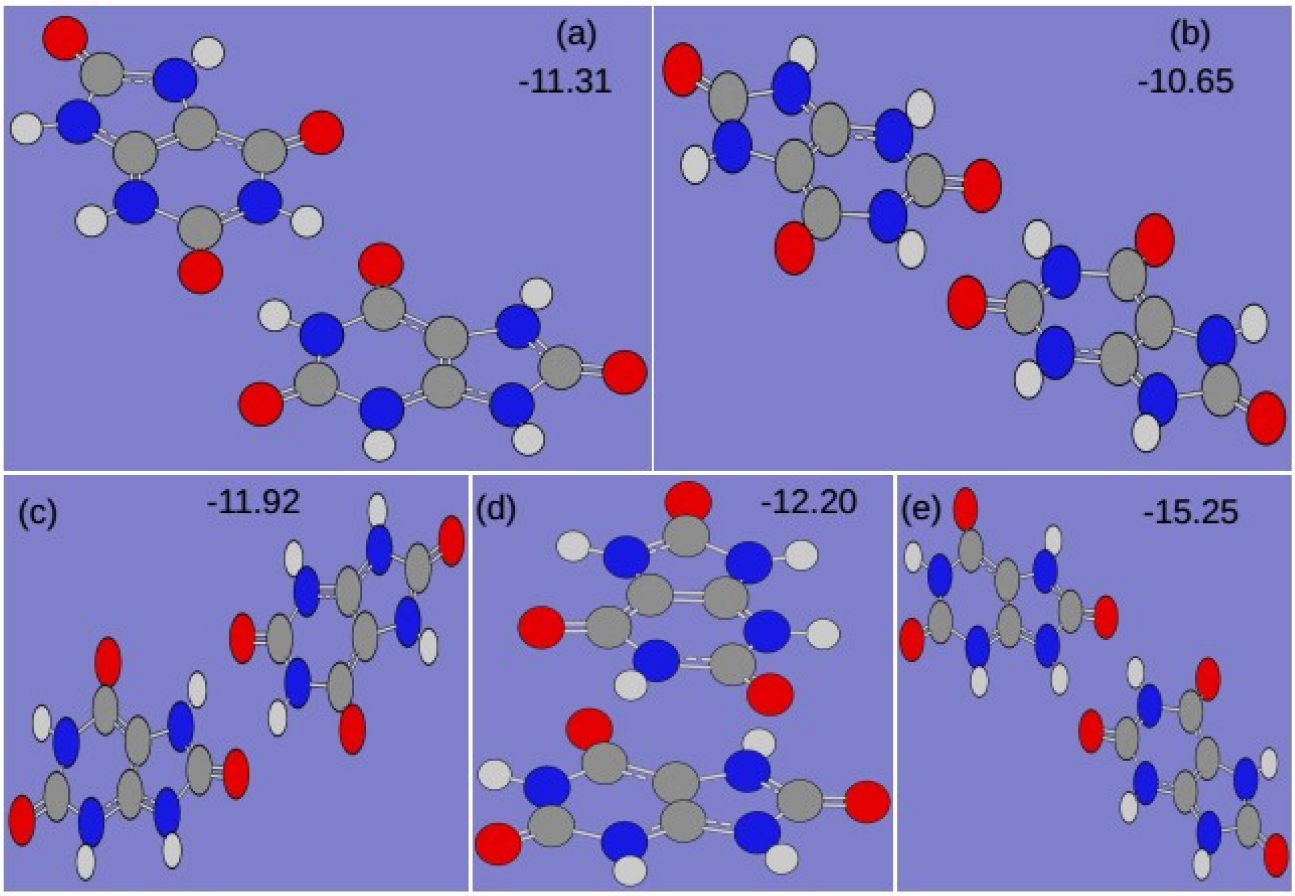

Figure 3-25. *Energy optimized structures of hydrogen bonded UA dimers and their complexation energies with BSSE correction by using B3LYP-D3/6-311++G(d,p) level theory. Here, one particular UA is kept fixed and the rotation of other one is made during the determination of initial structures before optimization. So, there may present some structures that are replica of one another. All energy values are expressed by kcal/mol unit.*

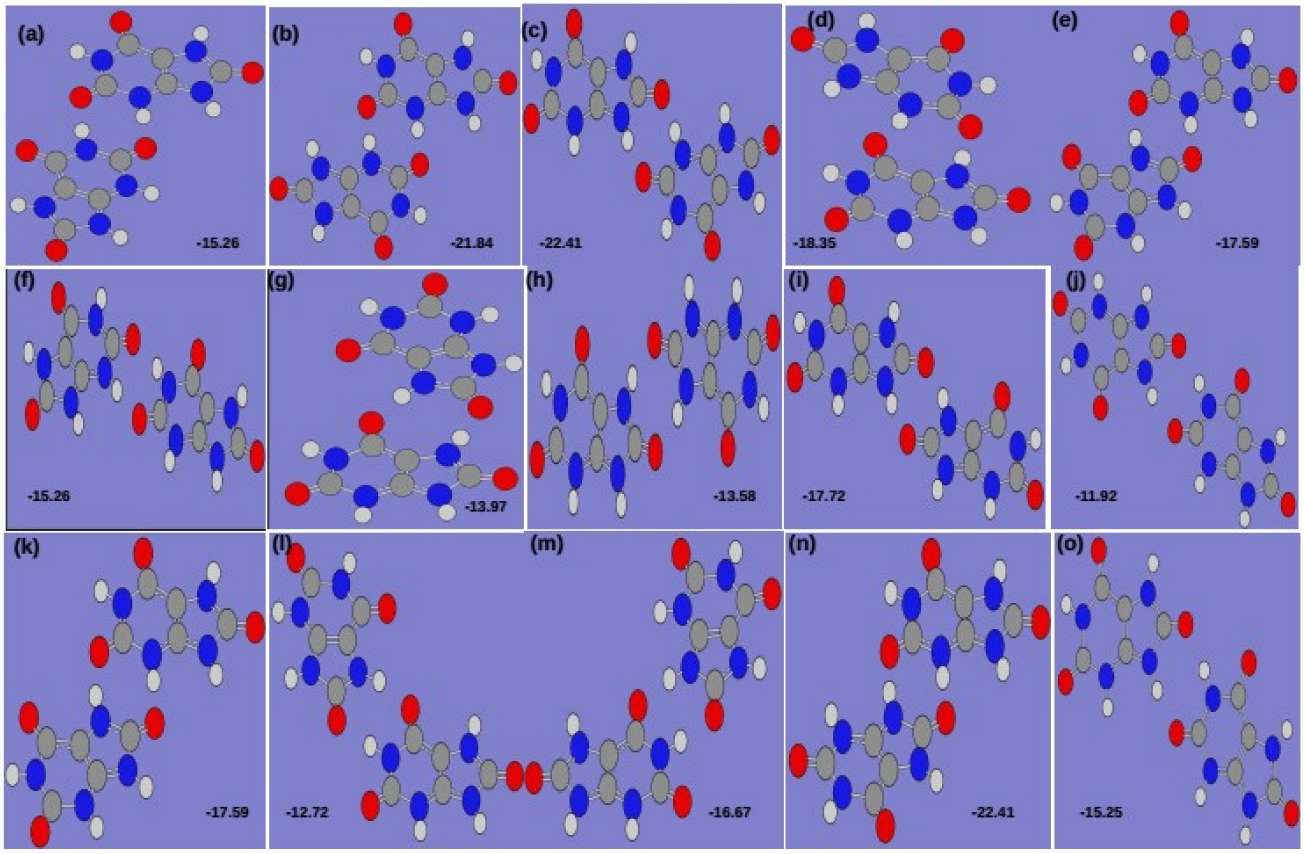

Figure 3-26. *Energy optimized structures of hydrogen bonded UA dimers and their complexation energies with BSSE correction by using B3LYP-D3/6-311++G(d,p) level theory. Here, one particular UA is kept fixed and the rotation of other one is made during the determination of initial structures before optimization. So, there may present some structures that are replica of one another. All energy values are expressed by kcal/mol unit*

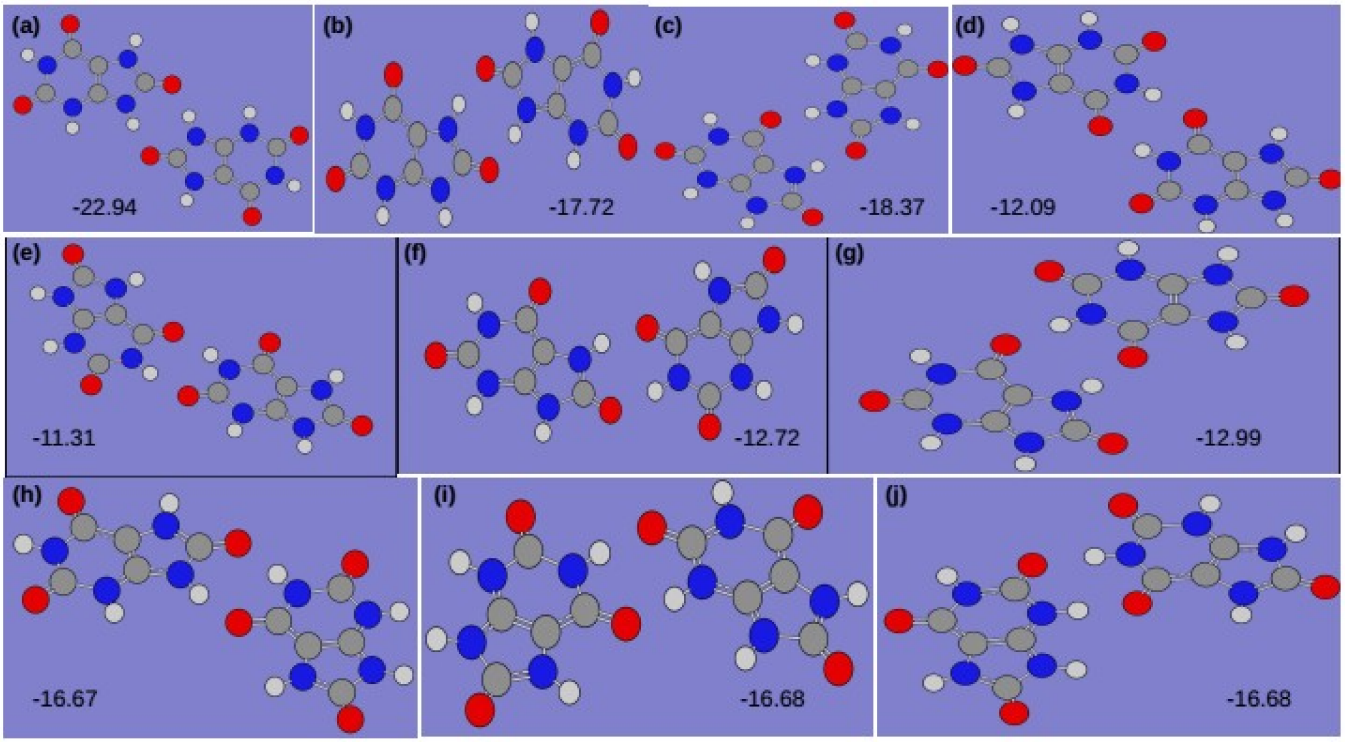

Figure 3-27. *Energy optimized structures of hydrogen bonded UA dimers and their complexation energies with BSSE correction by using B3LYP-D3/6-311++G(d,p) level of theory. Here, one particular UA is kept fixed and the rotation of other one is made during the determination of initial structures before optimization. So, there may present some structures that are replica of one another. All energy values are expressed by kcal/mol unit.*

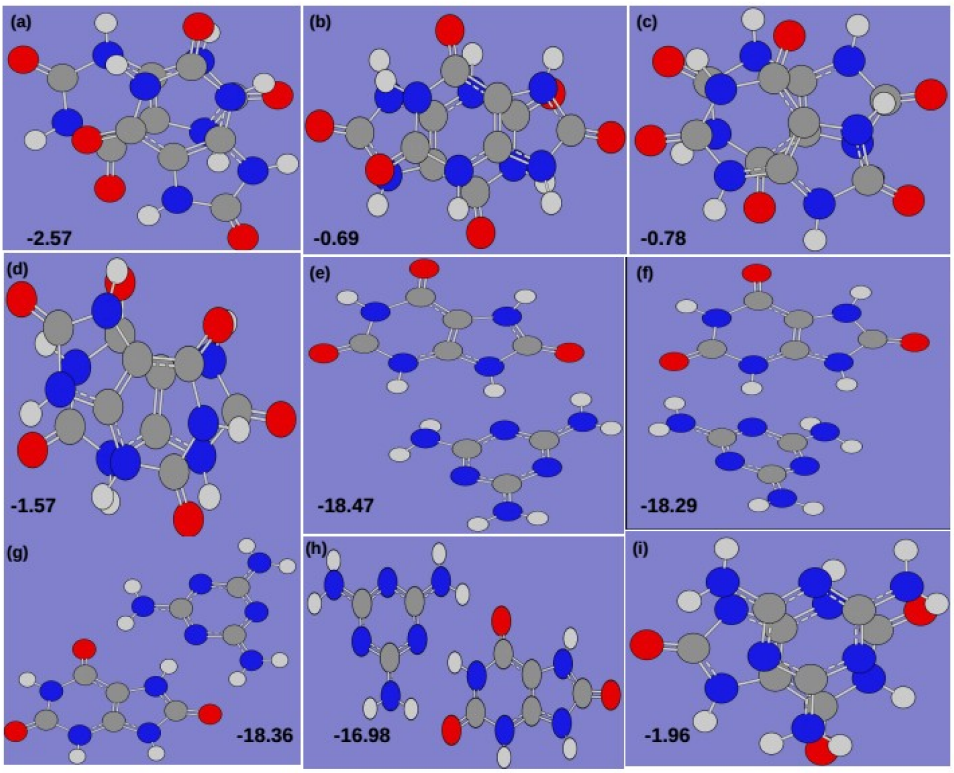

Figure 3-28. *(a)-(d) are energy optimized structures of π-stacked UA dimers, (e)-(h) are energy optimized structures of hydrogen bonded MM and UA complex and (i) represents the energy optimized structure of π-stacked MM-UA dimer and their complexation energies with BSSE correction by using B3LYP-D3/6-311++G(d,p) level theory. All energy values are expressed by kcal/mol unit.*

■ SUMMARY AND CONCLUSIONS

In the present study, the underlying mechanism of the structural properties of MM and UA complex with compositional variation under ambient conditions was investigated thoroughly using a series of classical MD simulations. The CN values of MM around UA and UA around MM were determined. The coordination number of MM around a reference UA varied from 1 to 3, as did that of UA around a reference MM. This result is consistent with experimental data showing that renal stones from infants consuming MM-contaminated formula were composed of UA and MM in a 1:2 to 2.1:1 molar ratio with no cyanuric acid

The determination of spatial density distributions of MM around reference UA and UA around a reference MM clearly showed that the distributions of UA and MM around one another become more compact and symmetric when both molecules are present in higher number in a system. The preferential interaction parameters (based on KB theory) for MM-uric acid interaction over MM-MM and UA-MM interaction over UA- UA were determined. MM interacted more with UA than with other MM molecules present in a system, and UA preferentially interacted with other UA molecules rather than MM. These results imply that in the presence of uric acid, MM interacts more with UA than with other MM molecules. This result was supported by the estimation of spatial density distributions. Again, the CN values of MM around MM varied from 0.12 to a maximum of 1.01, whereas the CN of UA around UA ranged from 1.04 to 1.98. These data also support the notion that in the presence of uric acid, MM interacts more with UA than with other MM molecules.

The calculations of the orientational preference of aromatic planes of MM and UA molecules suggest that π-π stacking interaction plays a key part in UA-UA interactions in water. Similarly, the CNs of UA were explained by their π-stacked structures. MM molecules associated with other UA molecules in water overwhelmingly through hydrogen bonding interactions, with a very low probability of π-π interactions. Furthermore, in MM-MM self-association, π-π interaction plays a less significant part. These results show good consistency with those of previous experimental and theoretical studies. Experimentally, it has been well established that MM can form self-aggregating complexes through hydrogen bonds as well as π-π aromatic ring-stacking interactions with other analogs.[201] These experimental findings match well with the results of the present study. Further, in vitro testing by Grases *etet al.*[36] revealed that at a certain pH value, MM and UA form insoluble compounds with a structure related to that of the insoluble compound of MM and cyanuric acid. Beton *et al.* demonstrated a highly symmetric hydrogen-bonded two-dimensional array of cyanuric acid and MM.[167] Thus, it can be assumed that MM also forms a complex with UA in which hydrogen bonding has a dominant role compared with π-π aromatic ring-stacking interactions. Chen *et al.*[173] reported that carbonyl (-CO) groups and amino groups (-NH2) produce a strong interaction between UA and MM molecules. In a MM-UA system, MM acts as an electron donor, resulting in a more effective interaction with UA, which acts as an electron acceptor. Such donor-acceptor conjugations enable π-π stacking in addition to hydrogen bonding, and these dual interactions cause more compact association between MM and UA. This explains why the complex formed by MM and

UA is more stable than other any complexes formed in the kidney.

Cluster structure analyses of MM-UA interactions suggested that the presence of either MM or UA or the presence of both molecules in higher concentration in a system produces a large insoluble complex cluster. Thus, the higher the concentration, the larger the cluster of MM and UA molecules in water. Chen *et al.*[173] showed experimentally that the fluorescence of MM molecules is quenched with increasing UA concentration. This quenching can be attributed to the interaction of UA with MM particles. Generally, an excessive dosage of MM can cause renal problems in humans owing to the development of insoluble stones. Besides, given the nature of the interaction of MM and UA molecules, it might be possible to rapidly resolve this renal impairment. Again, abnormal metabolism of nucleic acid bases is the cause of the accumulation of UA that results in kidney stone formation. Our MM-PBSA results show that the higher the concentration of MM in the presence of UA in the system, the stronger their complexation. Moreover, this complexation has a favorable negative binding energy, which further demonstrates the stronger interaction of MM and UA. Interestingly, these findings closely resemble those of the experimental studies, in which a higher binding constant with lower binding distance was found, with negative free energy change. This negative sign for free energy change indicates the spontaneity of the binding of UA to MEL molecules. Moreover, the overall complexation energy ($\Delta G^0{}_{bind}$(mel-mel)+ $\Delta G^0{}_{bind}$(uri-uri)+ $\Delta G^0{}_{bind}$(mel-uri)) was more negative than the $\Delta G^0{}_{bind}$ for MM-UA complexation. Thus, the total complexation through all types of contact in MM-UA-water ternary systems is favorable.

The lifetimes of UA-UA and MM-UA dimer were similar and long. The lifetime of a MM dimer was quite short compared with those of UA-UA dimers in all systems. Thus, one can expect a low percentage of the larger clusters resulting from MM-MM interactions, given that strong MM-UA interactions tend to occur rather than MM-MM self-association in water. Furthermore, as the lifetime of dimer formation was long for MM-UA and UA-UA interactions, the percentage of higher-order clusters was high for all systems presented in this study. These findings indicate that the stronger interaction in UA-UA leads to the formation of stable UA clusters; thus, the larger clusters composed only of UA in water "drag" the MM molecules around themselves to form MM-UA clusters of larger sizes. Interestingly, these results are well explained by the preferential interaction parameter values. Moreover, this result is consistent with those of the cluster structure analysis. Hydrogen bond analyses revealed that MM mainly forms hydrogen bonds with UA, whereas

MM forms a hydrogen-bonded complex with UA, using all available sites. This results in stronger complexation between the two molecule types in water. UA predominately interacts with other UA molecules present in a system through π-π stacking rather than hydrogen bonding, as the number of UA-UA hydrogen bonds in water is very low compared with the number of MM-UA and MM-MM hydrogen bonds. Again, MM-MM interaction is dominated by hydrogen bonding in particular; the consequences of this are validated well by our previous studies.[174, 197] Moreover, the hydrogen bonding results of the present studies match well with recent experimental findings.[26, 172] Finally, it is important to note that the MM-MM, UA-UA, and MM-UA interactions do not influence the tetrahedrally coordinated water structure.

Chapter 4

4a: Inclusion of Theobromine Modifies Uric Acid Aggregation With Possible Changes in Melamine-Uric Acid Clusters Responsible for Kidney Stones: The Role of π-Stacking

"Medicine is not only a science; it is also an art. It does not consist of compounding pills and plasters; it deals with the very processes of life, which must be understood before they may be guided."

– Paracelsus

Overview: Theobromine (TB), a naturally occurring substance, can be conceived as a prospective inhibitor for uric acid (UA) clustering. In aqueous solution, aggregates of π-stacked UA molecules with the larger size of clusters are modified into lower-order clusters with a substantial percentage of monomer by the incorporation of TB. The composite made of TB-UA is expected to have enhanced water solubility, allowing stable kidney stones to be excreted through urine. Interestingly, the strategy for the decomposition with feasible modifications in melamine (MM)-uric acid (UA) composites (that are hydrogen-bonded) is developed (by implementing cluster structure analysis technique and binding free energies). The all-atom molecular dynamics (MD) data provides new insights into the structure and dynamics of UA along with MM molecules in the context of aggregation. The simulation in the present study is supported further by structural and dynamical properties calculations. The calculations of hydrogen bond dynamics, the average number of hydrogen bonds, dimer existence autocorrelation functions, umbrella sampling, and coordination number theorize that the incorporation of TB significantly modifies the aggregated structure of UA. The overall complexation energy, along with the quantum chemical calculations, further explain the alternation of aggregated structure. Furthermore, the preferential interaction parameter describes at which concentration TB-UA interaction (which is π-stacked) predominates over UA-UA interactions. Interestingly, the interactions between TB-MM and MM-MM (which are hydrogen-bonded) are not relevant here. Thus, MM-UA cluster size is reduced owing to the disintegration of self-aggregated UA clusters by the involvement of TB. Moreover, an excellent agreement is observed between present MD results and experimentally obtained data.

■ INTRODUCTION

Renal lithiasis may be identified as the abnormal growth in urinary tract crystals, which otherwise small are not of concern to our health. The rate of nucleation and growth in crystals may become so large that the crystals cannot be easily removed. Renal lithiasis, which currently impacts around 10% of the world's people, is a very prevalent disease and is anticipated to affect 30% of the world's population by 2050.[202, 203] Most renal calculi include UA, and till date, no inhibitors have been defined for UA crystallization. Lithiasis of the renal tissue is considered as a multifactorial illness. A precautionary step to avoid kidney stones is to refrain from inappropriate dietary habits.[203, 204] Several etiologic variables can be significantly affected by nutrition, which eventually alters the composition of the urine.[204] F. Grases *et al.* connects the relationship between various nutritional variables (fluid intake, pH, calcium, phosphate, oxalate, citrate, phytate, urates, and vitamins) with distinct types of renal stones.[203] They suggested that specific nutritional balance must be present in the diet to prevent any renal calculus formation. They also advised to take a suitable volume of liquid and to avoid vegetarian diets, excessive protein diets, excessive salt (NaCl) consumption, excessive vitamin C/D, and also to prevent the use of cytotoxic substances.[203, 204]

UA nephrolithiasis accounts for 7-10% of kidney stones. The most common genetic abnormality of UA nephrolithiasis is reduced urinary pH, hyperuricosuria, and poor diuresis. The therapy of individuals who are susceptible to UA stones is dependent on urine alkalinization, and allopurinol is administered to individuals with hyperuricemia because of the absence of UA inhibitors.[203, 205]

Experimental studies discovered that the presence of MM, along with UA (Figure 4a-1) leads to the development of kidney stones.[206, 36] So far, numerous studies on MM related kidney stones have been conducted. The composition of stones made of UA and MM varies between 1.2:1 to 2.1:1.[1, 24, 47] In a recent study of our group, we have devised the exact mechanism of kidney stone formation based on computational studies.[207] The temperature of decomposition of a composite MM-UA complex is higher than that of MM, which indicates that the composite structure is significantly stabilized.[208] It has already been reported that MM combines with UA through both N-H$\cdots$O and N-H$\cdots$N hydrogen bonds, then assembles into a planar supramolecular network structure mediated by the neighboring water molecules.[207, 208] Besides, various studies have focused solely on the formation of UA stone formation and MM detection.[203, 44] However, a minimal number

of studies focused on the underlying mechanism of kidney stone formation and its prevention using therapeutic drugs.

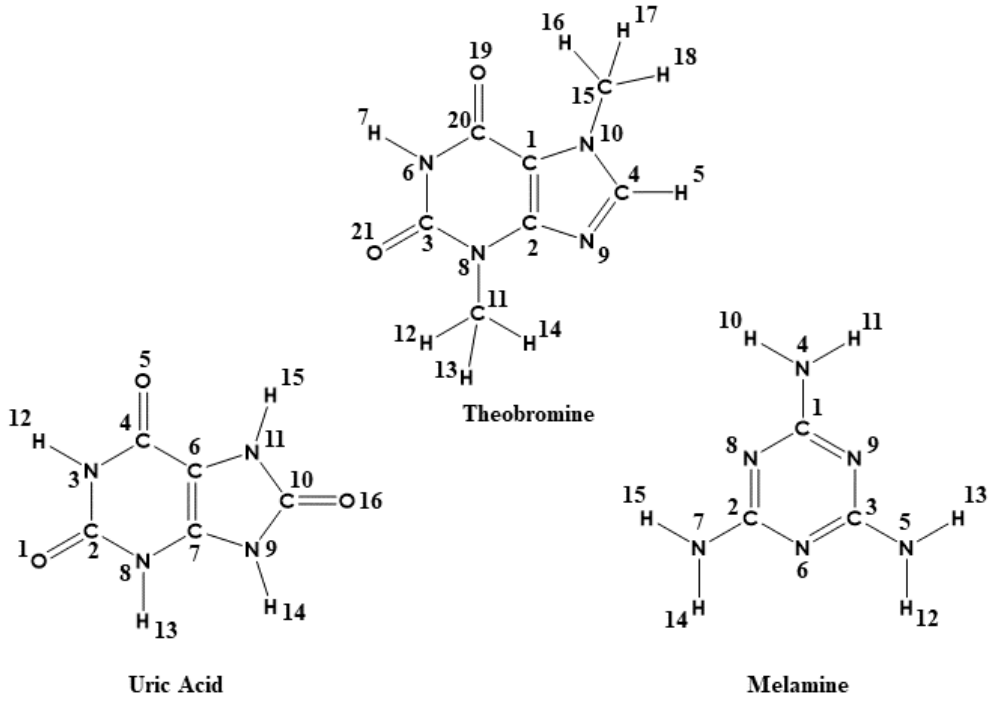

Figure 4a-1. *Structure of UA, TB, and MM with atom numbering.*

MM and associated triazine compounds are the most common building blocks in supramolecular chemistry, primarily due to the reality that MM can behave both as donors and acceptors that are essential in supramolecular chemistry.[209, 210, 211, 212, 213, 214, 215, 216, 217, 218, 219, 220, 221, 222] In MM-UA pair, donor-donor-acceptor arrangement closely resembles with the acceptor-donor-acceptor site. Such conjugation between MM and UA make the giant supramolecular hydrogen-bonded crystals.[26, 45, 2, 113, 1] Moreover, in the formation of MM-UA pair, the self-accumulation of UA plays an important role. A previous computational study reported that higher-order UA cluster drags MM molecules near to them to add to it.[207] Furthermore, a recent experimental study observed that the presence of MM makes UA aggregation more rapid.[208] Unfortunately, there are no such drug that can be used to treat the MM induced UA kidney stones till now.

TB is the primary alkaloids in cocoa beans and green tea containing about 2-5% caffeine by dry weight. These bio-active components are generally present in cocoa beans, coffee beans, tea, and guarana. TB is one of the xanthine products found in more than 60 plants, including leaves and seeds or fruits. TB functions as a diuretic and spasmolytic drug. This drug has been regularly consumed with a lower risk for terminal diseases, including liver, kidney, basal, and colorectal cancers. The impacts of xanthine are considered to affect the living organisms for a long time. These compounds may slow down the Parkinson's and Alzheimer's by preventing neurodegeneration.[223, 224]

Recent studies have shown that UA crystallization can be inhibited by TB (Figure 4a-1), indicating can help avoid UA urolithiasis.[203, 56] TB is, therefore, the first naturally occurring substance which can be used in the therapy of kidney stones that prevent UA's crystallization. Besides, TB is excreted out through urine at levels similar to those required to avoid UA crystallization.[203, 56] Dimethylxanthine (i.e., TB) is an essential component of cocoa products, for example, chocolate. Caffeine consumption can also contribute to TB removal, and approximately 11% of the daily amount of caffeine is excreted as TB owing to metabolism in the liver.[56]

S. Parkin *et al.* proposed that crystals of pure laboratory-grown UA dihydrate are monoclinic[225], P21/c, with a = 7.237 (3), b = 6.363 (4), c = 17.449 (11) Å, [β] = 90.51 (1)° Z = 4, wR2 (all data) = 0.1094, R1 = 0.0406 for data with I > 2σ(I). The crystals exhibit pseudo-orthorhombic twinning with refined twin fractions of 0.89 and 0.11. Within each twin, disorder about a noncrystallographic twofold exists with refined occupancies of 0.83 and 0.17. Packing consists of layers of hydrogen-bonded UA separated by layers of hydrogen-bonded water. F. Grases *et al.* proposed that in the presence of TB, UA crystal growth is inhibited. TB makes the UA crystal thinner and elongated than the previous crystal lattice in the absence of TB. Furthermore, TB, being present in cocoa (as a natural dimethylxanthine) can prevent the early stage nucleation and crystal growth of UA.[203, 56]

The experimental results of TB, however, as a prospective inhibitor of kidney stone, provide no precise mechanism and intimate details as to how inhibition can be made feasible. It is worth noting now that UA accumulation can be prevented by TB. TB, therefore, destructs the early stage of UA's crystal growth based on the experimental results as mentioned above. Now, since the relationship between UA and MM is robust in the kidney, the present study is, therefore, a strategic approach. In the present study, the impacts of TB on MM-UA interactions are being reported. This study, we hope, would

provide information about how does TB act to prevent the formation of the more massive MM-UA cluster. The UA-TB compound is formed by communication between TB and UA. TB is more soluble in an aqueous medium than UA. The addition of TB to the UA cluster, thus, enhances water solubility of the composite. Therefore, to prevent UA accumulation, TB is suitable to be made water-soluble and finally excreted of the body.

The remaining article is arranged in this way. The models of MM, UA, TB, and water molecules used in this study, as well as simulation details, are discussed in Part II. The findings are provided and discussed in Section III. Our results are summarized in Section IV.

■ MODELS AND SIMULATION METHOD

In this study, a series of classical molecular dynamics (MD) simulations are carried out with varying concentrations of UA, TB, and MM in water under ambient conditions. Table 4a-1 presents the representative systems considered in this study. Initially, the RESP (restrained electrostatic potential)[140] suite of the AMBER14 package[226] was used to acquire the partial charges of different atomic sites of UA, TB and MM molecules. In this regard, the energy-optimized structures of these molecules were taken by the use of the *ab initio* HF/6-31+G** method with the help of Gaussian 09[138](Table 4a-2). Then, with AMBER14 built-in module ANTECHAMBER[141], for the atomic sites of these molecules, general AMBER force field[142] parameters were obtained. The TIP3P (three-point transferable inter-molecular potential) water model[143] is selected for all systems to carry out MD simulations. The initial configurations of each system was built with the help of PACKMOL package.[144] All the simulations were performed by using a cubic box containing MM, UA, and TB molecules in desired proportions. A 10000-step energy minimization was performed for each simulation and 4000 steps were taken with the steepest descent method, and 6000 steps were followed with the conjugate gradient method. All systems are then slowly heated by 50 K for 20 ps from 0 K to 480 K. Such heating enables systems to overcome global minimum boundary stature. Subsequently, all systems were cooled down to 300 K (which is the final temperature) in a canonical ensemble (NVT) with a decreased interval of 25 K. Every system was then subjected to a 5 ns equilibration at 300 K and 1 atm, in an isothermal-isobaric (NPT) ensemble.

Table 4b-1. System overview[a]

System	N_{MM}	N_{UA}	N_{TB}	N_{wat}	Box length (Å)	C_{MM}(M)	C_{UA}(M)	C_{TB}(M)
S0	—	16	—	6000	56.932	—	0.1440	—
S1	4	16	—	6000	56.983	0.0359	0.1436	—
S2	4	16	5	6000	57.074	0.0357	0.1429	0.0447
S2-a	4	16	5	6000	57.122	0.0356	0.1425	0.0445
S3	4	16	10	6000	57.168	0.0356	0.1422	0.0889
S4	4	16	20	6000	57.370	0.0352	0.1407	0.1759
S5	4	16	30	6000	57.566	0.0348	0.1392	0.2610
S5-a	4	16	30	6000	57.611	0.0347	0.1389	0.2604
S6	—	10	10	6000	57.026	—	0.0895	0.0895
S7	10	—	10	6000	57.031	0.0895	—	0.0895
S8	2	2	2	3000	45.170	0.0360	0.0360	0.0360
S9	—	5	5	6000	56.920	—-	0.0450	0.0450
S10	—	—	10	3000	45.180	—-	—-	0.1800
P0	—	2	—	1500	35.817	—-	0.0723	—-
P1	—	2	4	1500	36.019	—-	0.0711	0.1421
P2	—	—	2	1500	35.930	—-	—-	0.0715
P3	—	4	2	1500	36.010	—-	0.1421	0.0711
P4	2	—	—	1500	35.890	0.0718	—-	—-
P5	2	—	4	1500	36.020	0.0711	—-	0.1421
P6	1	1	—	1500	35.900	0.0359	0.0359	—-
P7	1	1	4	1500	36.010	0.0356	0.0356	0.1422

[a] N_{MM}, N_{UA}, N_{TB}, and N_{wat} refer to the number of MM, UA, TB, and water molecules, respectively. M represents the molar concentrations of MM, UA and TB.

Table 4a-2. Atomic charges[a]

Molecule	Atom	Charge (e)	Atom	Charge (e)
TB	C1	-0.4788	N6	-0.9072
	N10	0.1335	C3	0.9118
	C4	-0.1647	O21	-0.6589
	H5	0.1656	H7	0.4459
	N9	-0.6182	O19	-0.6574
	C15	-0.4487	C2	0.5695
	H16/17/18	0.1817	N8	-0.3055
	C20	0.9516	C11	0.00534
	H12/13/14	0.0606	—	—

[a]Partial charges of different atomic sites of TB (e is the elementary charge).

Simulations will then be subjected to a production of 200 ns carried out within the NVT ensemble. Data analysis includes the last 100 ns of each 200 ns production run. Periodic boundary conditions were employed in all three directions. For all processes during simulation, the Langevin dynamics (with 1 ps^{-1} collision frequency)[145] was used to keep the temperature fixed at 300 K. The Berendsen barostat was used with a pressure relaxation time of 2 ps[146] to keep the system at a pressure of 1 atm (in the NPT ensemble). In treating long-ranged electrostatic interactions, the particle mesh Ewald algorithm[147] was employed. The SHAKE algorithm was used to restrain the covalent bonds containing hydrogen atoms.[148] A 10 Å cut-off distance distance is used to estimate short-ranged non-bonded interactions. The trajectories of MD simulation are then analyzed using the CPPTRAJ module of AMBER. Visual Molecular Dynamic (VMD)[149] are utilized to visualize acquired MD trajectories.

For the calculation of binding free-energies (ΔG^0_{bind}) for different systems using Boltzmann Surface Mechanism Methodology, last 20 ns of MD trajectories are used.[184, 227] The Python script of the AMBER package, MMPBSA.py, is used in all the MM-PBSA calculations. ΔG^0_{bind} can be estimated as follows:

$$\Delta G^0_{bind} = \Delta E_{vac} + \Delta G_{solv}, \tag{4.1}$$

where ΔE_{vac}, and ΔG_{solv} are the interaction enrgy in the gas phase, and the solvation free energy[220, 586] respectively. ΔE_{vac} can further be decomposed as:

$$\Delta E_{vac} = \Delta E_{ele} + \Delta E_{vdw}, \tag{4.2}$$

where ΔE_{ele} and ΔE_{vdw} are the receptor-ligand electrostatic and van der Waals interaction energy ingredient, respectively. Moreover, (ΔG_{solv}) energy can also be seperated into two energy terms as:

$$\Delta G_{solv} = \Delta G_{PB} + \Delta G_{NP}. \tag{4.3}$$

Here, polar (electrostatic) solvation free energy, and nonpolar solvation free energy are illustrated by ΔG_{PB}, and ΔG_{NP}, respectively. ΔG_{PB} is estimated in a continuum solvent method by the PBSA program of AMBER14. ΔG_{NP} can be computed from the solvent-accessible surface area (SASA). The SASA is calculated using maximal speed molecular surfaces (MSMS)[187] for the estimation of ΔG_{NP} as:[207, 188, 189, 190, 191, 192, 193]

$$\Delta G_{NP} = \gamma(SASA) + \beta, \tag{4.4}$$

where $\gamma = 0.005$ kcal/Å^2 and $\beta = 0.0$.

The potential of mean force (PMF) is estimated using umbrella sampling (US) method.[228] We have assumed the reaction coordinate ξ as the z-component center of mass (COM)-center of mass (COM) distance (r) between two chosen molecules.[207] In the US method, simulations are executed in the presence of a biasing window potential $w(\xi)$, which is induced to enhance the sampling in the neighborhood of a chosen value ξ. A total of 25 biased simulations are carried out with $i = 4, 8, \cdots, 28$, in which ξ is restrained to the values of $\xi_i = i \times 0.5$ Å in the phase space configuration X by a harmonic potential:

$$w_i(\xi) = 1/2K(\xi(X) - \xi_i)^2 \tag{4.5}$$

where K is the force constant for harmonic restraint. A harmonic restraint force along z-coordinate with a force constant of 6 kcal/mol/Å^2 is used for our biased simulation. The initial distance between the two chosen molecules is 2.0 Å , and this distance is gradually increased along the z-coordinate by pulling one molecule from another one. For this purpose, we have considered P0–P7 systems. Final normal MD simulation trajectories for these systems are used as the initial configuration for US method. Then, every system is introduced to 4000 steps minimization (1000 steps in steepest descent method followed by 3000 steps conjugate gradient method), and 1 ns equilibration is performed with the

same procedure as of normal MD simulation (discussed above) for every biased US simulation. Every window is subjected to a 10 ns production run. So, we have performed, additionally, a total of 250 ns production for each system in US method. Simulation data are collected in every 2 fs time interval. Finally, to determine the unbiased position probability distribution P(ξ), the US simulation results are analyzed by employing the Weighted Histogram Analysis Method (WHAM)[229, 230] algorithm. Then we obtain the PMF value from P(ξ) as:

$$PMF = -k_B T \ln P(\xi) \tag{4.6}$$

where k_B is the Boltzmann constant, and T is the absolute temperature of the system.

In the present study, two systems (S0 and S1) are prepared where S0 contains only UA and S1 is made of UA and MM to know the property of aggregation of both of these molecules in that concentration. Next, other four systems (S2, S3, S4, and S5) are made in which TB is introduced at various concentrations keeping the concentration of UA and MM fixed with that of S0 and S1. Thus, systems S0 and S1 that are devoid of TB molecules can be considered as reference systems. Later on, another system, S6 is prepared to compare the results with other systems as well as to verify the aggregation property of UA and TB together without MM. Furthermore, system S7 is taken into consideration to know about the interactions between MM and TB in the absence of UA. MD simulations with the variations of ensembles like NVT or NPT are also performed. Here, NPT simulations with S2-a and S5-a systems are performed to check whether or not the clusterization of TB, UA and MM depend on an ensemble. System S8 is used to determine total complexation energy. Furthermore, one more system, S9, is prepared to confirm the predictions made in this study with different simulation set up. Moreover, a pure system with only TB (S10) is also prepared to examine the aggregation pattern of it in pure water. As stated, the systems P0–P7 are used to perform the umbrella sampling.

■ RESULTS AND DISCUSSION

First shell coordination number

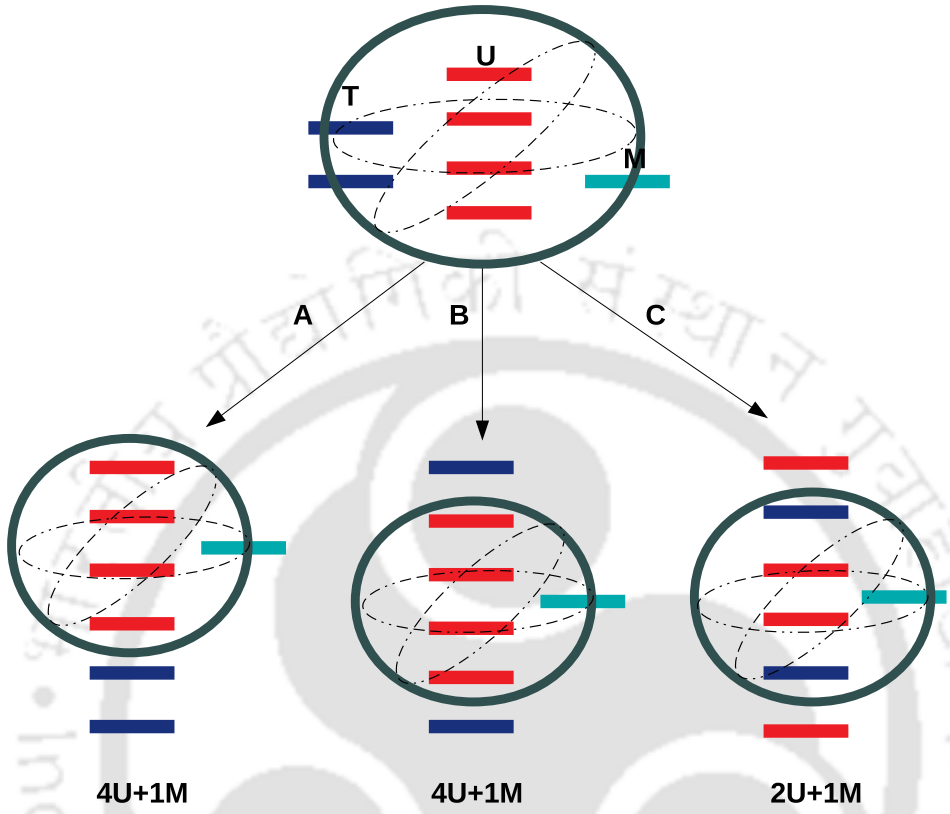

Figure 4a-2. *Schematic representation of MM around uric acid molecules in a random system of MM (M), UA (U), and TB (T). Here, 4U+1M and 2U+1M represent four UA molecules are associated with one MM and two UA molecules are associated with one MM molecule, respectively. In case of 2U+1M, the cluster of four UA molecules is reduced to a dimer comprised of two UA molecules due to the presence of TB molecules in the cluster.*

A measurement of how many molecules of a specific solute or solvent accumulate around a reference solute is the first shell coordination number (CN).[231] CN can be described by the use of the equation as follows:[232, 233, 234, 235, 236, 237, 238, 239, 240, 241, 242, 243, 244]

$$CN = 4\pi\rho_\beta \int_0^{r_c} r^2 g_{\alpha\beta}(r) dr, \tag{4.7}$$

This equation defines the CN of atoms of type β in a solvation shell around the atomic sites of type α from 0 to separation r_c. ρ_β depicts the number density of atom type β in the system.

Here, CN values are determined in the context of interactions between UA-UA, UA-TB, MM-UA, MM-TB, and MM-MM using the relevant pair distribution functions.

Table 4b-3. First shell coordination number of UA around UA (r_c=6 Å), TB around UA (r_c=6 Å), MM around UA (r_c=7 Å), MM around MM (r_c=5 Å), and TB around TB (r_c=6 Å) for different systems. Here, r_c is the position of the first minimum of the respective radial distribution functions (not shown)

System	UA around UA	TB around UA	MM around UA	MM around MM	TB around TB
S0	2.33	—	—	—	—
S1	2.31	—	0.62	0.09	—
S2	1.63	0.53	0.55	0.03	0.46
S2-a	1.74	0.58	0.48	0.08	0.31
S3	1.57	0.73	0.61	0.09	0.95
S4	0.82	1.55	0.30	0.08	1.16
S5	0.62	1.82	0.38	0.03	1.33
S5-a	0.58	1.97	0.36	0.09	1.38
S6	1.38	0.87	—	—	1.06
S7	—	—	—	0.16	1.65

In Table 4a-3, for systems, S0–S6, the first shell CN values for UA-UA interaction are introduced. The CNs of UA around a reference UA are 2.33, 2.31, 1.63, 1.57. 0.82, 0.62, and 1.38 for systems S0, S1, S2, S3, S4, S5, and S6, respectively. Thus, the coordination number of UA around a reference UA varies approximately from 1 to 3. In addition, as the concentration of TB is increased, the co-ordination number of UA around a reference UA decreases. Here, for systems S0 and S1, the CNs of UA around a reference UA have the highest value. However, in system S5, the number is reduced to 0.62. This fact indicates that TB molecules alter the process of self-assembly of UA in water.

The CN of TB around UA differs in a opposite way to that of the CN of UA around UA for systems S2–S6 (Table 4a-3). In this case also, as the number of TB is increased, the CN values of TB around UA are increased. Again, for systems S2–S6, the CN of TB around TB is also increased. Therefore, more TB accumulates around UA. It is to be noted that the self-aggregation of TB also occurs when the number of TB, in a system, increases. The CN values of MM around reference UA are varied from 0.62 to 0.38 for systems S1 to S5. Thus, a noticeable reduction is seen in systems S4 and S5 as compared to the systems S1–S3. At higher concentration of TB, these numbers reduce to a lower number. Thereupon, a question arises as to whether MM-TB interaction reduces these CN values or not. It will, therefore, be fascinating to explore. To counter this, we have

determined, firstly, the CN number for MM-MM interaction. It shows that the CN of MM around MM remains the same for all the systems from S1 to S5. As MM-MM CN remains the same; thus, the reduction in CN values may occur owing to the increasing interaction between MM and TB. To do so, we have prepared the system S7, in which only MM and TB molecules are present. We find that the CN of MM around reference MM is quite high (Table 4a-3). Again, CN of TB around TB has the highest value amongst all the systems. Moreover, the CN of MM around reference TB is low (the value of CN of MM around TB is not mentioned in Table 4a-3). So, the interaction between MM and TB cannot be the case here. As the CN of UA around a reference UA decreases with the increase in the number of TB, the size of clusters made by only UA is also reduced. Therefore, lower-order clusters drag a small number of MM molecules towards themselves to add to it (Figure 4a-2). Thus, the reduction of the interaction between MM and UA plays a predominant role here. Though, it is premature to say here, however, an initial assessment can be made.

When comparing S0 and S1 systems, MM does not change in UA co-ordination number around UA. Though the concentration of MM is minimal, MM does not alter the UA aggregation, as mentioned in a previously reported study.[207] The present results also suggest that MM does not alter with UA-UA aggregation; instead, it prefers to bind to the aggregated UA molecules. Moreover, on comparing system S3 and S6, we find similar results, which reveal that a different initial configuration having a slightly different number of molecules give identical as well as comparable results. Furthermore, the CNs are also determined using the NPT ensemble for systems S2-a and S5-a (Table 4a-3). Here, it can be seen that different ensembles do not bring as such any change in the CN values for all interactions. Thus, the results confirm the reliability and robustness of the simulations presented here.

Spatial density plots

This portion discusses the spatial density distributions for multiple connections such as UA-UA, and UA-TB along with the density distributions of TB around reference TB. In Figure 4a-3(a)–(f), for all systems (S0–S5), the spatial density distributions for UA-UA interaction are displayed. Last 20 ns of MD simulation trajectory files are used to determine the density distribution.[207, 174, 197, 158]

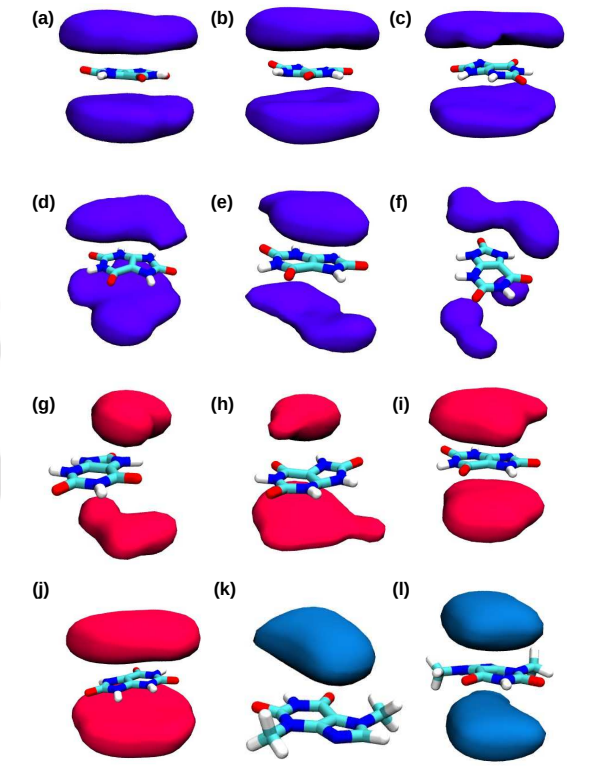

Figure 4a-3. *(a)–(f) Spatial density distributions of UA around a reference UA for systems S0 to S5, respectively. (g)–(j) Spatial density distributions of TB around a reference UA for systems S2, S3, S4, and S5, respectively. (k)–(l) Spatial density distributions of TB around a reference TB for systems S2 and S5.*

The decreased density of the UA molecules around the reference UA molecule is seen on continuously moving from system S0 to System S5 (Figure 4a-3(a)–(f)). Furthermore, the spatial distribution of TB is increased around a reference UA (Figure 4a-3(g)–(j)) for systems S2–S5. In system S0, only UA molecules are present in water. Obviously, the spatial distribution of UA around a reference UA is the highest for this system. Thus, the aggregation tendency among UA molecules is quite strong for this system. A similar density distribution can be seen for system S1 too. As TB is introduced for systems S2–S5, the density distribution of UA around a reference UA is reduced (Figure 4a-3(a)–(f)). In system S5, a very low-density distribution can be observed for UA around UA (Figure 4a-3(f)). Therefore, the presence of TB can influence the aggregation of UA in water significantly. Now, as the density distribution of TB around a reference UA is getting higher in systems S2–S5, one can predict that with the increase of the concentration in

solution, TB is interacting more with UA. In system S5, as the number of TB is higher than other systems, i.e., systems S2–S4, a significant interaction of TB with UA can be observed. Furthermore, looking at the pattern of the spatial density distribution of UA molecules around a reference UA shows a parallel density distribution. So, π-π stacking between UA molecules is quite evident. Interestingly, a similar pattern is also observed in the case of TB during the interaction with UA molecules for systems S2–S4. Therefore, the replacement of UA molecules are seen, and the replacement of UA with TB is occurred with a similar fashion, i.e., via π-π stacking interactions. Moreover, the density distribution of TB around reference TB is also determined for systems S2 and S5 (Figure 4a-3(k) and (l)). From systems S2 to S5, the density distribution of TB around reference TB is increased. The pattern of interactions between the TB molecules in water is similar to that of UA-UA interaction.

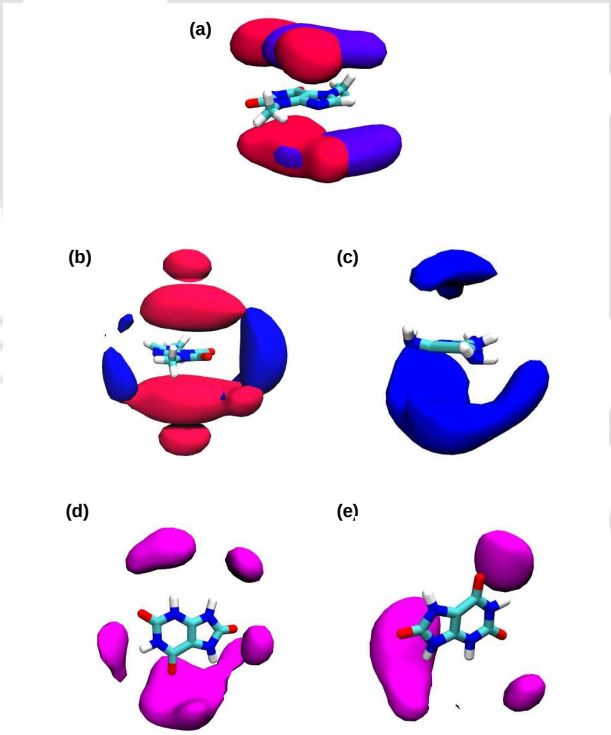

Figure 4a-4. *(a) Spatial density distribution of UA (violet) and TB (deep red) around a reference UA for systems S6. (b) and (c) Spatial density distributions of MM (blue) and TB (dark red) around a reference TB for system S7. (d) and (e) Spatial density distributions of MM around a reference UA for systems S1 and S5, respectively.*

In this context, we have determined the aggregation of UA molecules in terms of density distribution for the systems S0 and S1 as mentioned earlier (Figure 4a-3(a) and (b)). Here, a similar aggregation tendency is observed for the UA-UA density distribution for these two systems, i.e., systems S0 and S1. Thus, the presence of MM does not interfere in the UA-UA aggregation; instead, it binds to the UA aggregate. Now, if we look into the density distribution of UA around reference UA for the system S6, a similar distribution with that of system S3 can be found. For system S6, the density distribution of TB around UA is also determined. Figure 4a-4(a) shows that TB preferentially interacts with UA and a mutual interaction is present among TB and UA. Also, looking into the spatial density distribution of MM around TB for system S7, it is apparent that the distribution of MM around reference TB is not significant, which conveys that MM does not preferentially interact with TB as the way it does with UA (Figure 4a-4(b)). Again, in system S7, TB interacts with the like molecules quite prominently resulting in self-aggregation of TB molecules. The density distribution of TB around a reference TB is quite dense (Figure 4a-4(b)). Moreover, as the MM molecules are not interacting with TB molecules, they also self-aggregate, which can be seen from Figure 4a-4(c). In the context of UA-TB-MM interactions, therefore, MM-TB communication is not so important. Moreover, this result is well comprehended by the determination of first shell co-ordination numbers (discussed above).

Moreover, a considerable decrease of MM density distributions around a reference UA is observed while moving from system S1 to system S5 (Figure 4a-4(d)–(e)). As the aggregation tendency of UA is reduced in system S5, the higher-order clusters among UA molecules are not formed. As a consequence, lower-order clusters made of UA molecules drag MM molecules towards themselves in system S5. As a consequence of this, the total MM-UA cluster size is reduced significantly. Thus, in the present study, a comparatively little tendency to aggregate is observed for MM-UA interactions. As a result, the total MM-UA cluster size is reduced significantly.

Preferential interaction parameters

In order to arrive at conclusions for the solute-solute as well as solute-solvent interactions, the calculation of their mutual interaction propensities should be carried out. The Kirkwood–Buff (KB) theory provides a useful way of determining the solute-solute preferential interactions in the presence of solvents.[245] The KB theory, which is originally

constructed by the use of the grand-canonical (μVT) ensemble, proposes that the related KB integrals are considered as the volume integrals

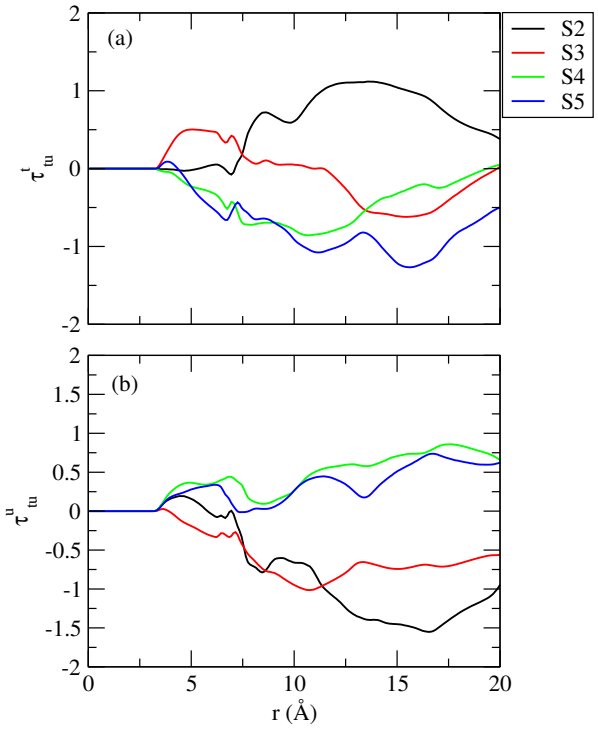

Figure 4a-5. *Preferential interaction of: (a) TB-TB over TB-UA and (b) UA-TB interactions over UA-UA for systems S2–S5.*

over the pair distribution function of species i and j present in the systems:[207, 232, 174, 197, 194, 195, 196, 179]

$$G_{ij} = \int [g_{ij}^{\mu VT}(r) - 1] dv, \tag{4.8}$$

where r is the distance between the center of mass (COM) of the species, i.e., i and j, and G_{ij} referes to KB integral.

Now, in the context of a spherical symmetry, this integral over volume in Eq. (8) can be written as:

$$G_{ij} = 4\pi \int [g_{ij}^{\mu VT}(r) - 1] r^2 dr. \tag{4.9}$$

The above equation can be estimated by the use of the isothermal-isobaric (NpT) ensemble under periodic boundary conditions as:

$$G_{ij} = 4\pi \int_0^R [g_{ij}(r) - 1] r^2 dr, \tag{4.10}$$

where g_{ij}(r) refers to the distribution functions, and R is the distance at which integral approaches to zero.

The aggregation tendency of UA and TB molecules can be measured by the determination of the preferential interaction parameter, τ. The preferential interaction parameters of TB-TB over TB-UA (τ_{tu}^t) and UA-TB over UA-UA interactions (τ_{tu}^u) in solvent water, are as follows:

$$\tau_{tu}^t = \rho_t (G_{tt} - G_{tu}) \tag{4.11}$$

$$\tau_{tu}^u = \rho_u (G_{ut} - G_{uu}) \tag{4.12}$$

where t and u correspond to TB and UA respectively; and ρ_t and ρ_u refer to the number densities of TB and UA, respectively. The positive value of τ implies that one interaction prevails over other interaction and the former aggregates well over the later. As stated above, G_{tt}, G_{tu}, G_{ut}, and G_{uu} reciprocate to KB integrals. The corresponding radial distribution functions are used to obtain these integrals. COM of TB and UA molecules are taken into account during the estimation of these distribution functions.[174, 197]

Using the above equation, the values of τ_{tu}^t are determined for systems S2–S5, where the concentration of UA is kept fixed, and the concentration of TB is increasing. The change in the τ_{tu}^t values can be seen in Figure 4a-5(a). The positive τ_{tu}^t value for system S2 indicates more favorable TB-TB interactions compared to TB-UA interactions. For system S2, TB does not preferentially interact with UA, and instead, they show significant interactions towards themselves. Therefore, the corresponding preferential interaction parameter becomes positive for this system, S2. Furthermore, the preferential interactions between TB molecules are lower than the interaction between TB and UA molecules in water for systems S3–S5. For system S3, the value of τ_{tu}^t is negative, owing to more attractions between TB and UA molecules over TB self-aggregation in water. A similar scenario can be seen for systems S4, and S5 where the interaction between TB and UA molecules predominates over the TB aggregation. These results (for systems S2–S5) suggest that the increase of TB concentration makes stronger TB-UA interaction. As a result of this, TB molecules replace UA molecules from the self-aggregated clusters of UA and forms TB incorporated

TB-UA clusters in water. For system S5, a significant breakage of UA clusters is evident from the higher negative values of τ_{tu}^{t} as the TB-UA interaction is robust here. Thus, these results (for the S2–S5 systems) allow us to understand that TB can alter the formation of UA clusters in water.

Similarly, the value of τ_{tu}^{u} is determined, and the values are presented in Figure 4a-5(b) for systems S2–S5. It is observed that for systems S2 and S3, in which UA does not preferably interact with TB, instead it involves in interacting with like molecules cause self-aggregation of TB. However, in the case of systems S3 and S4, τ_{tu}^{u} shows a different trend, in specific, the value of τ_{tu}^{u} becomes positive for these two systems. These positive values of τ_{tu}^{u} is indicative of the fact that TB interacts preferentially with UA molecules, and simultaneously UA does not interact with other UA molecules present in the system. Moreover, as the number of TB is increased, the values of τ_{tu}^{u} move towards positive values from systems S2–S5. For the system S5, the value of τ_{tu}^{u} is slightly lower than that of system S4. This is, possibly, owing to self-aggregation of TB molecules in water as the number of TB is relatively higher than that of the number present in system S4.

The preferential interaction parameters, τ_{tu}^{t}, and τ_{tu}^{u}, for TB-UA interactions, give a better insight into which interaction predominates when both are present in solution. Figure 4a-5(a) and Figure 4a-5(b) depict that the preferential interaction parameters for UA-UA interaction are quite active at low TB concentration. That is the reason behind the stronger aggregation among UA molecules in water under ambient conditions. Moreover, these figures also reveal that TB is very efficient to break the UA clusters when present in a sufficient number in a system alongside UA molecules. Here it is to be noted that the preferential interaction parameters do not provide the exact size of clusters made of these components. Moreover, the structural changes that happen for UA aggregates when TB interacts considerably with UA in the water should be discussed. Therefore, the cluster structure analysis (presented later) needs to be performed.

Orientational preference of aromatic planes

This section examines the orientation of UA and TB molecules when they are close together. The angle between the vector normals of the molecular planes of these molecules (i.e., UA and TB) is considered for the determination of the orientational configurations of UA and TB molecules in solution when MM is present.

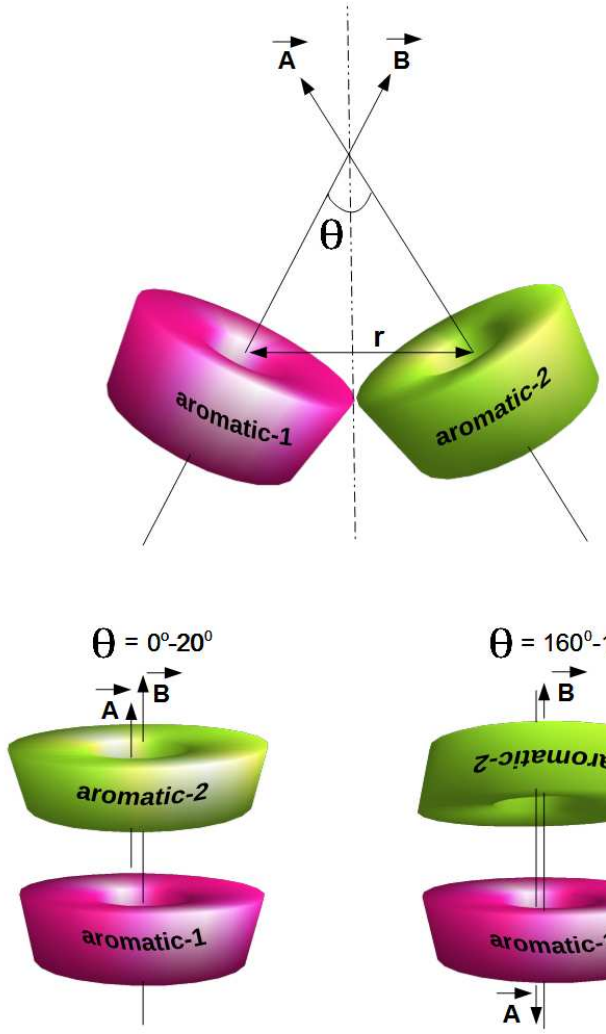

Figure 4a-6. *Schematic representations of the vector normals of any two aromatic molecular planes of MM, TB, and UA molecules forming an angle θ.*

Orientational preference of aromatic planes

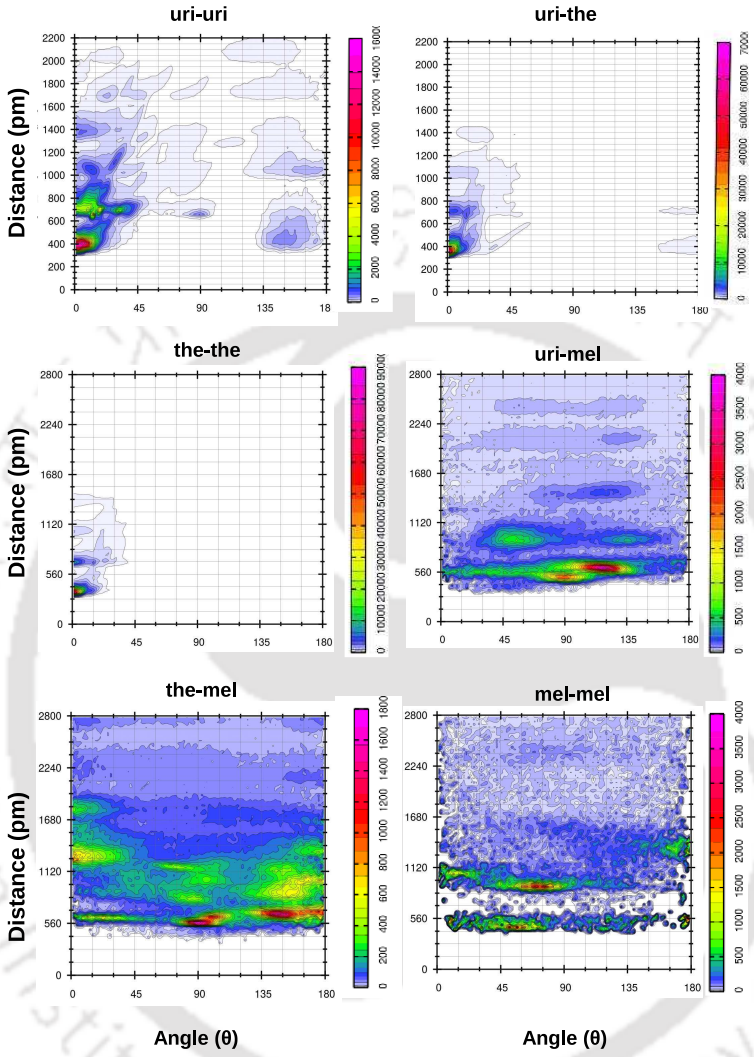

Figure 4a-7. *Probability of orientational angle (θ) at various distance between any two aromatic planes of MM, TB, and UA molecules for system S5.*

To know about the preferred orientations owing to the interactions between the aromatic cores of UA, MM, and TB, the probability of orientational angles between two UA molecules, two MM molecules, and two TB molecules is assessed comprising the inter-planar angle between UA and TB, MM and UA molecules, and MM and TB. To do so, an angle between two vector normals of any two aromatic planes is considered (Figure 4a-6). Now, the angles, i.e., 0°-20° or 160°-180°, between these vector normals indicate the possibility of the presence of π-π stacking interactions between the two molecules.[207, 174, 197, 161] However, with this angle, a certain distance criterion also needs to check to confirm

whether or not the π-π stacking between the two aromatic planes exists. Because, at a certain angle, the distance between two interacting aromatic planes is essential to know as the π-π stacking is only possible when these two criteria, angle and distance, are simultaneously satisfied. Now, along with the angle, mentioned above, if the distance between two aromatics planes lies within 3-5 Å , then one can conclusively say that these two aromatic moieties involve in strong π-π stacking interactions.

In Figure 4a-7, the distribution of angle, θ, as a component of the inter-planar distance r_{A-B} is plotted for system S5. The distribution with high intensity for θ is observed at an angle θ=45–60° for MM-MM interactions. It seems from these angle values (θ) that MM does not communicate through π-π stacking interactions with other MM molecules (and UA molecules). For the interaction between UA and UA, UA can fairly be assumed to communicate with other UA molecules by π-π stacking as in system S5, the value of θ lies within 0°–10°. The maximum intensity of θ is developed when $\theta \simeq 130°$ for the interactions between MM and UA. Based on these values of θ, one can conclude that the MM molecules interact overwhelmingly with other molecules of UA through hydrogen-bonding interactions in water (discussed below), with a very low probability of π-π stacking interactions.

As the TB is introduced with MM and UA for system S5, it is important to investigate whether or not the π-π stacking between the UA molecules (that were present in the absence of TB) are getting affected or not. Interestingly, UA molecules self-aggregate with other UA present in the system through π-π stacking interactions in particular, with negligible contribution from hydrogen-bonding interactions (see below) for system S5. TB molecules also involves in π-π stacking (θ = 0°–10°) interactions during their self-aggregation. Interestingly, the UA-TB interaction occurs predominantly by π-π stacking (θ = 0°–10°) over hydrogen bonding (which has a small contribution) as the number of TB molecules is increased from systems S2–S5. It implies that they replace the UA molecules and occupy the position of UA molecules (that were involved in UA-UA interactions) through π-π stacking interaction. Moreover, MM also interacts with TB molecules through hydrogen bonding interactions over π-π stacking (θ = 130°–145°) (discussed later).

These stacking interactions are only significant if the two interacting molecules retain an orientation and satisfy a certain distance criterion at the same time. From the above outcomes, it is evident that if two UAs, two TBs or one TB and one UA molecule are engaged in π-π stacking, the angle (0–10°) is retained. Thus, the distance between these molecules also needs to be measured to ensure that they meet both the criterion

for distance and the specific angle. In Figure 4a-7, the distances between two aromatic cores are presented for system S5. For all cases considered in the present study, an average distance of 4 Å with a maximum of 5 Å is retained. These distance values along with the angles established earlier, further demonstrate the π-π stacking between the aromatic cores of any two molecules, i.e., UA and TB molecules in water. Note that, a similar angle distribution at a preferred distance for various pairs are seen for all other the systems considered in the present study (data not shown) along with the system S5 for which we present all data.

Cluster structure analysis

This portion of discussion includes the clusters of various sizes produced due to UA-UA, TB-TB, TB-UA, MM-MM, MM-UA, and MM-TB interactions. To define the clusters of different sizes for UA-UA and TB-TB, we have considered two criteria and these are as follows: 1) $r_{COM-COM} \leqslant 6$ Å and the two interacting moieties should be hydrogen-bonded simultaneously, 'or' 2) $r_{COM-COM} \leqslant 6$ Å and the two interacting moieties should be in π-π stacking conformation simultaneously. Here, $r_{COM-COM}$ referes to the center of mass distance between two molecules that we are intended to study. A schematic representation that represents the definition of cluster considered in this study is shown in Figure 4a-8. In Set-1, no UA or TB molecules are hydrogen-bonded though they fall within the distance cut-off. Thus, in Set-1, UA-UA interaction produces the only monomer, and the same is applicable for TB-TB interaction. Similarly, according to the criteria mentioned above, a trimer is formed among UA molecules, while TB forms only a dimer in Set-2. Furthermore, Set-3 (a trimer for both molecules), Set-4 (a trimer for both molecules), Set-5 (two monomer and one dimer for TB molecules as well as one monomer and one dimer for UA molecules), and Set-6 (all molecules are in monomeric state) clearly depict all possible scenarios for the determination of cluster sizes formed by UA-UA and TB-TB interactions in water.

The cluster sizes for the remaining interactions, i.e., TB-UA, MM-MM, MM-UA, and MM-TB interactions, the "direct" and "indirect" approaches are taken into consideration following our previous publication.[207] The "direct" and "indirect" approaches are based on only the distance criteria ($r_{COM-COM} \leqslant 6$ Å for TB-UA, $r_{COM-COM} \leqslant 7$ Å for TB-MM, $r_{COM-COM} \leqslant 7$ Å for UA-MM, and $r_{COM-COM} \leqslant 5$ Å for MM-MM), and according to such criteria, in Set-1, Set-2, Set-3, and Set-4 presented in Figure 4a-8, produces a hexamer TB-UA composite. Similarly, in Set-5, and Set-6, a heptamer is formed for

TB-UA interactions.

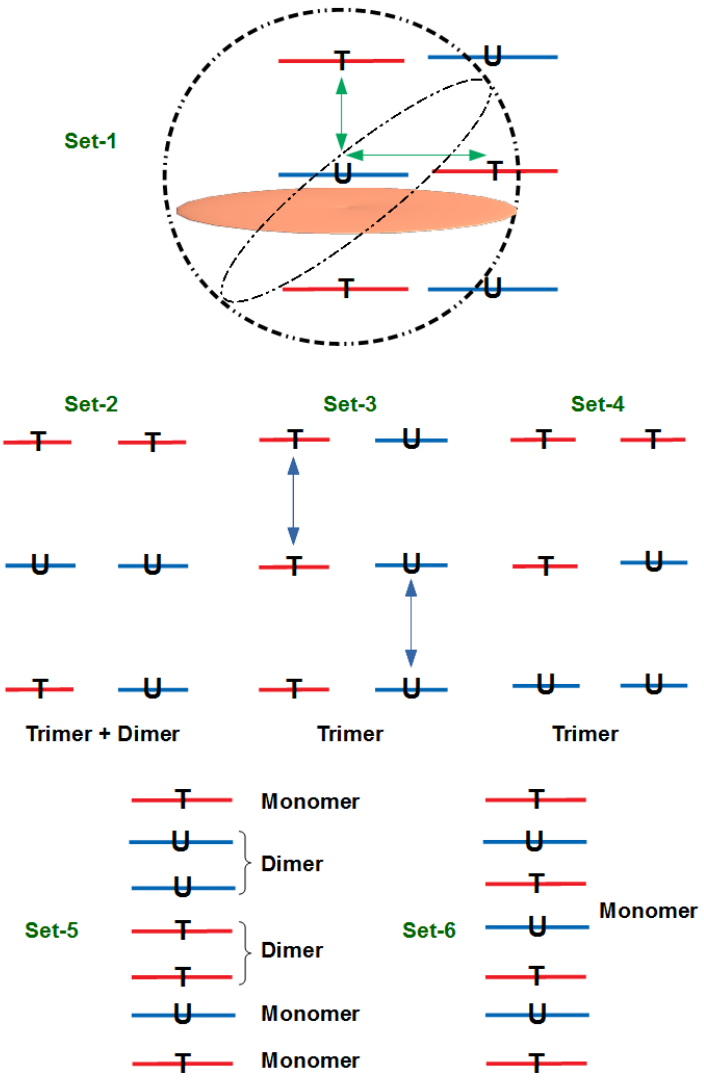

Figure 4a-8. *Schematic representation of the cluster structure interpretation for TB-TB, UA-UA, and TB-UA. Here, T and U represent TB and UA respectively.*

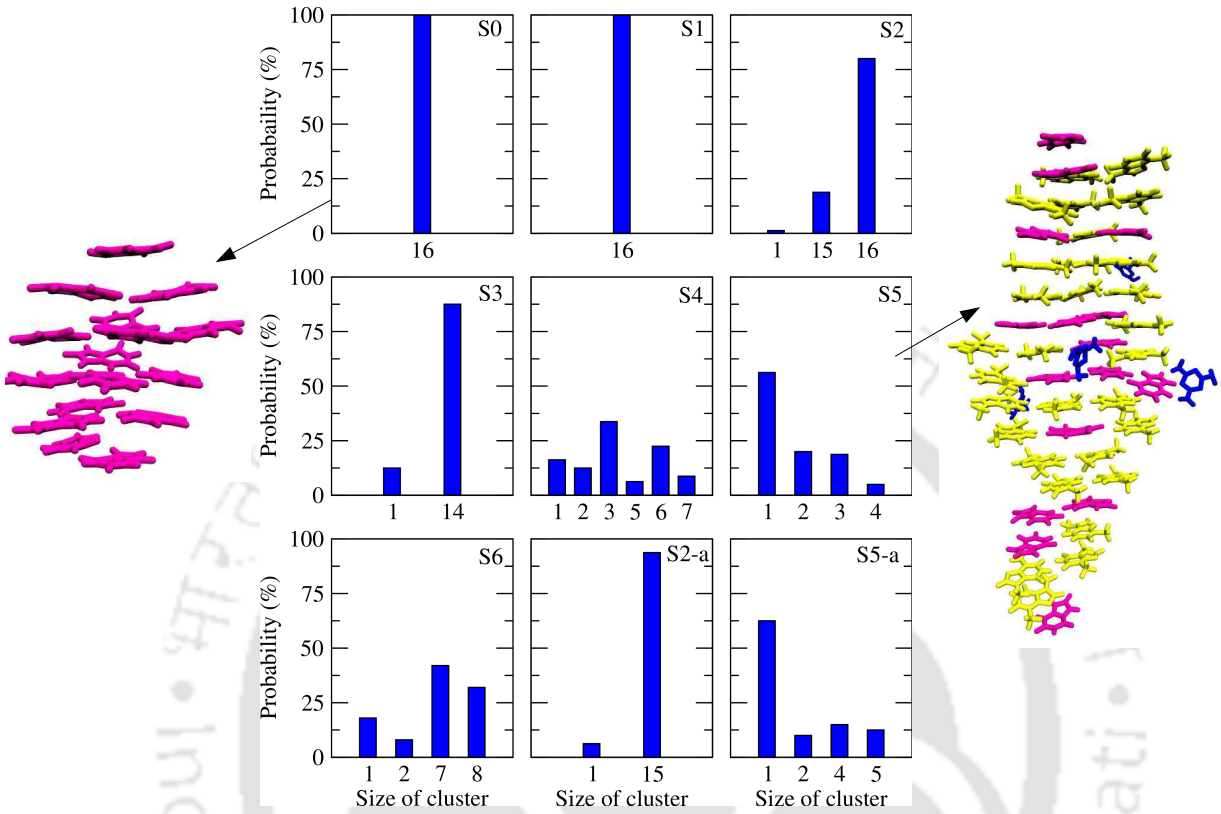

Figure 4a-9. *Distributions of clusters of various sizes resulting from UA-UA interactions for different systems along with the snapshots taken for systems S0, and S5 at 200 ns. Here, UA, MM, and TB are presented by magenta, blue, and yellow color, respectively.*

Firstly, UA-UA interactions that lead to the UA cluster are considered (Figure 4a-9). For system S0, all UA molecules come close to each other and form a large cluster comprised of sixteen UA molecules. In a similar note, it is found that an aggregate of sixteen UA molecules is formed in system S1. Now, system S1 contains a small amount of MM which does not alter the UA aggregation at all. Thus, it will be interesting to see, whether or not, TB can alter the cluster size of UA in water. When a small amount of TB is added to the system S1, a very negligible change with a meager percentage of monomer (1.25%) can be seen in system S2. A moderate increase of monomer percentage with a reduction in the cluster size of UA can be seen for system S3. Now, as the concentration of TB increases gradually from systems S3–S5, a noticeable change with a considerable reduction in cluster size of UA can be seen. In systems S4 and S5, the percentage of monomer is 16.25% and 55.21% respectively. Though the percentage of the monomer in system S4 is not as high as

compared to system S5, however, the higher-order clusters that are present in systems S2 and S3, now break into the lower order clusters like heptamer (8.75%), hexamer (22.5%) and so on in system S4. In case of system S5 in which the concentration of TB is the highest, UA forms tetramer and trimer with 5% and 18.75%, respectively. For systems S4 and S5, a significant change is thus visible. A similar scenario can also be observed for system S6 in which the presence of TB alters the aggregation of UA in water. Moreover, the use of different ensembles can affect the clusterization of solute molecules in water.[258] However, similar results are observed on comparing systems S2 and S2-a or systems S5 and S5-a. The choice of ensemble, therefore, produces comparable results that again confirm the robustness of current simulations.

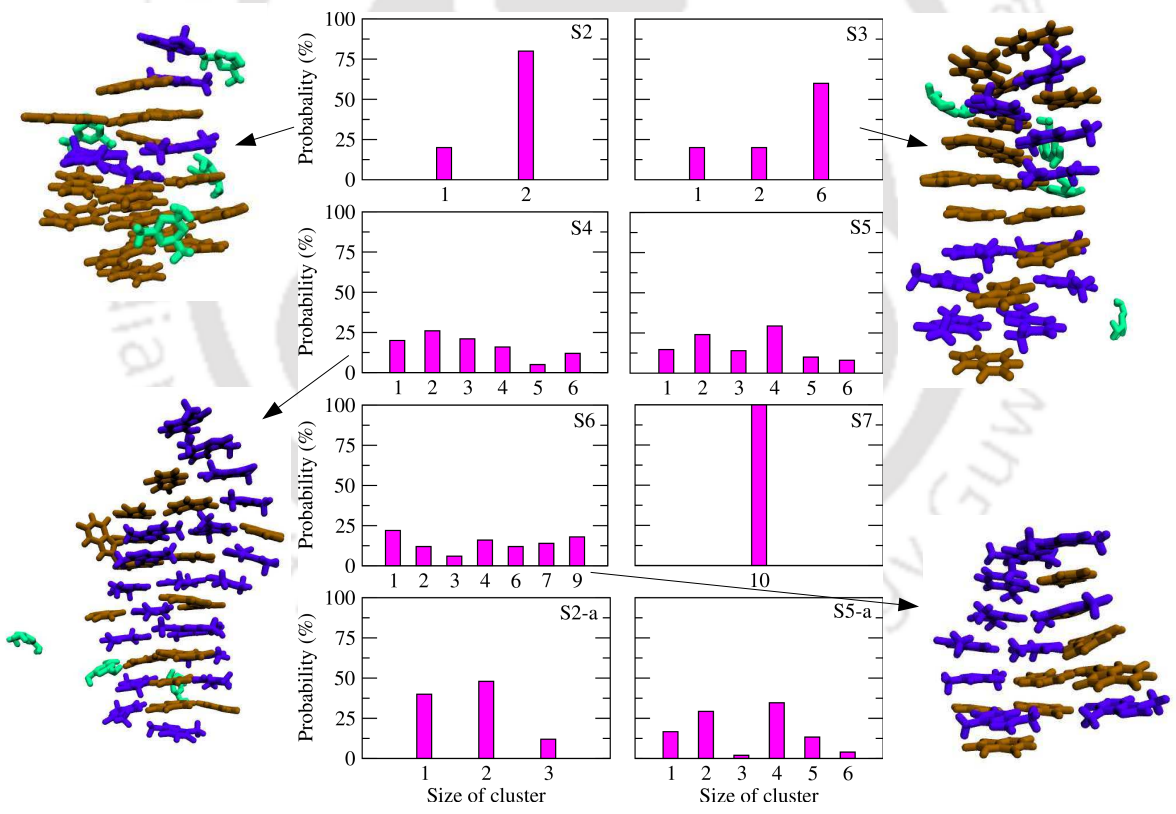

Figure 4a-10. *Distributions of clusters of various sizes resulting from TB-TB interactions for different systems along with the snapshots taken for systems S2, S3, S4, and S6 at 200 ns. Here, UA, MM, and TB are presented by orche, green, and violet color, respectively.*

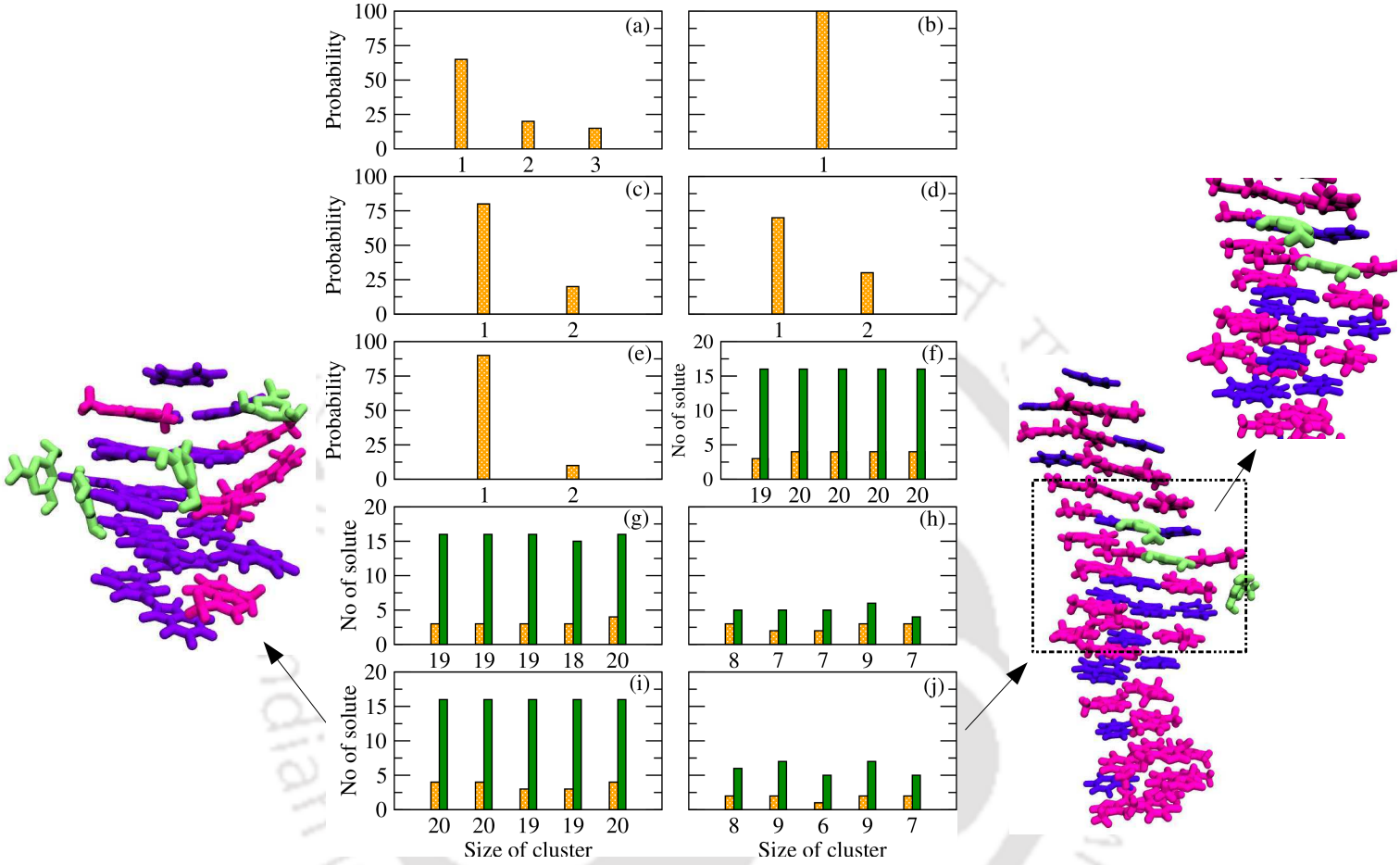

Figure 4a-11. *Distributions of clusters of various sizes resulting from MM-MM interactions for systems (a) S1, (b) S2, (c) S5, (d) S2-a, and (e) S5-a. (f)–(j) represent the maximum size of MM-UA cluster for S1, S2, S5, S2-a, and S5-a, respectively along with the snapshots taken for systems S2-a, and S5-a at 200 ns. Here, UA, MM, and TB are presented by violet, lime, and magenta color, respectively.*

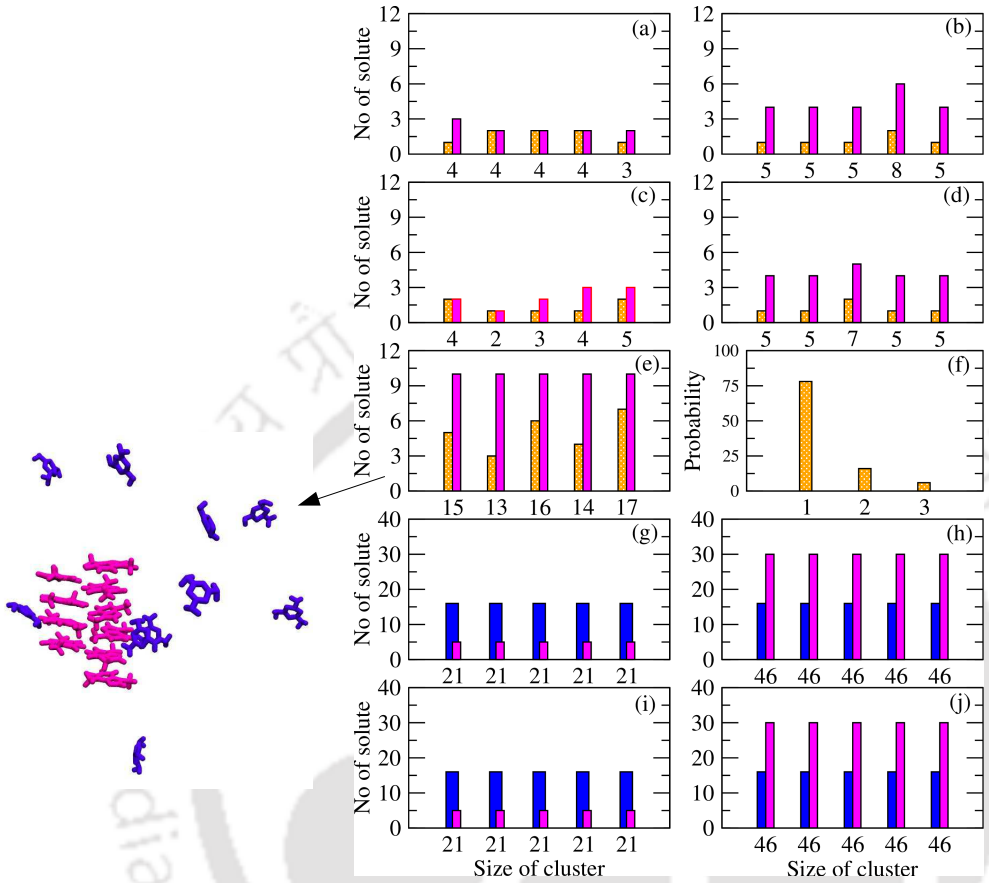

Figure 4a-12. *Distributions of the maximum size of clusters resulting from TB-MM interactions for systems (a) S2, (b) S5, (c) S2-a, (d) S5-a, and (e) S7. (f) represents the MM-MM distribution of cluster of various sizes for system S7. (g)–(j) presents the maximum size of clusters resulting from TB-UA interaction for S2, S5, S2-a, and S5-a respectively along with the snapshots taken for system S7 at 200 ns. Here, MM, and TB are presented by blue, and magenta color, respectively.*

We have further investigated the cluster structure of TB to check how does TB change its aggregation properties during the alternation of UA aggregation in water. From Figure 4a-10, it can be seen that for systems S3–S5, an aggregation among TB molecules takes place. At higher concentration, i.e., in systems S4 and S5, TB makes higher-order clusters such as hexamer, pentamer, tetramer, and so on. Now, it is interesting to note that from systems S2–S5, monomer percentage is nearly the same for all these systems. However, the maximum size of the cluster (i.e., hexamer) is the same for systems S3–S5. Only S2 differs from other systems due to having a lower number of TB molecules. Therefore, it can be expected that in the presence of UA, TB aggregates but not like UA, rather TB binds to

the UA cluster to break them. A similar observation can also be made for system S6. Now, looking at the system S7, it can be found that all TB molecules aggregate in the presence of MM. Thus, MM does not alter the TB aggregation. However, a comparison of cluster structure between systems S6 and S7 shows that TB tends to interact more favorably with UA than with MM molecules. Figure 4a-10 (systems S2-a and S5-a) reveals that NPT and NVT ensembles with different initial configurations produce a very similar results.

Considering the MM-MM clusterization in various systems, we have found that most of the MM molecules remain in the monomeric state (Figure 4a-11 (a)–(e)). Thus, in present systems, MM molecules do not tend to self-aggregate. In the context of MM-UA interaction, MM forms cluster of larger sizes in systems S1 and S2 in which the number of TB is either nil or very small (Figure 4a-11 (f) and (g)). However, the MM-UA composite cluster is reduced significantly in system S5 in which the concentration of TB is reasonably high (Figure 4a-11 (h)). It is interesting to note that MM is tightly bound to the UA molecules in all systems, but the overall cluster size is reducing as TB breaks UA clusters of higher order to a smaller size cluster. Therefore, the reduction in the overall MM-UA cluster is a consequence of UA clusterization, which is initiated by the presence of TB. Moreover, all outcomes for MM-MM (Figure 4a-11 (d) and (e)) and MM-UA (Figure 4a-11 (i) and (j)) clusterization processes are independent of ensemble variation as NPT along with NVT simulations produce similar results for all the systems considered in the present study.

Furthermore, MM-TB cluster size is small as compared to MM-UA for all systems S2–S5 irrespective of the use of different ensembles ,i.e., NPT or NVT (Figure 4a-12 (a)–(d)). However, in system S7, where only MM and TB are present, the cluster sizes are relatively large as there MM-UA interaction is absent (Figure 4a-12 (e)). Thus, there is a little increase of MM-TB interaction, although not all MM molecules come close to TB in system S7. Therefore, it can be concluded that the interaction between MM and UA is more favorable than that of made by MM-TB interaction. In system S7, MM self-aggregates, however, the self-aggregation is not very strong as the concentration of MM is low in system S7 (Figure 4a-12 (f)). Moreover, the TB-UA interaction is robust for all cases as all TB, and UA molecules come close to each other to make large clusters irrespective of the ensemble alternation (Figure 4a-12 (g)–(j)). Such, a strong interaction produces a large cluster of TB and UA in system S5 (Figure 4a-12 (h) and (j)). As a result of this, the breakage of UA by TB is very significant in this system.

A reference system, S9, has been prepared to verify the cluster structure analysis more conveniently. In this system, five TB molecules, which are initially π-stacked to each other, are taken with five UA molecules (which were also initially π-stacked) into 6000 water molecules. A moderately weak force constant is applied to maintain such stacking conformation of UA and TB molecules. Further, 200 ns simulation is performed in the NVT ensemble to check whether or not the initial self-assembled π-stacking structures that involve separate π-stacking between UA-UA and TB-TB undergo some rearrangement. Here, initially, π-stacked pentamer of UA rearranges and breaks into various lower order clusters (32% tetramer, 12% trimer, 32% dimer, and 24% monomer) by the involvement of TB molecules (these results are not shown in the figure). Thus, a similar scenario can also be observed for TB molecules. For TB, the initially π-stacked pentamer produces 12% trimer, 64% dimer, and 24% monomer in water. Now, from the system with pure UA molecules (S0) provides information about the nature of π-stacking of UA. Thus, the question arises, whether or not TB possesses π-stacking in its pure state. To verify this, a system, S10, containing ten TB molecules in pure water, is prepared. The simulation of system S10 reveals that TB also produces π-stacked decamer with 100% aggregation of all ten molecules in pure water (this result is not shown in the figure). Thus, by examining these two systems, S9 and S10, it can be implied that TB forms complex with UA in a π-stacked manner.

MM-PBSA and complexation energy

The Molecular Mechanics Poisson-Boltzmann Surface Area (MM-PBSA) is commonly used for measuring the binding free energy of macromolecular compounds.[246, 247, 284] For this purpose, other methods such as free energy perturbation techniques, linear response approximation (LRA) method (microscopic all-atom method), the linear interaction energy (LIE) method and the double-coupling method can be used, but MM-PBSA method is faster than any of these standard methods. Computationally, MM-PBSA also costs less because it uses a continuum solvent model. Moreover, MM-PBSA makes a high correlation with experiment. For specific interactions between TB and UA molecules during complexation, binding free energy has been calculated in the present study by decomposing it into various components of interaction present. It is to be noted that we have chosen UA as the receptors and TB as the ligand and have studied how the ligand molecules associated with the receptors so that the complexation between TB-UA is better

understood.

Table 4a-4. All energies derived from the MM-PBSA calculations. Here, ΔE_{vdW}, ΔE_{elec}, ΔG_{PB}, ΔG_{NP}, and $\Delta G^0{}_{bind}$ are the energy of van der Waals interaction, electrostatic energy, Poisson–Boltzmann energy, non-polar energy, and binding free energy, respectively. All energy values are expressed in kcal/mol.

System$_{ligand-receptor}$	ΔE_{vdW}	ΔE_{elec}	ΔE_{PB}	ΔG_{NP}	$\Delta G^0{}_{bind}$
S2$_{the-uri}$	-89.38	-52.18	73.63	-3.38	-74.31
S3$_{the-uri}$	-133.57	-135.84	143.20	-10.01	-136.22
S4$_{the-uri}$	-220.77	-195.30	222.50	-17.70	-211.27
S5$_{the-uri}$	-275.53	-151.11	231.25	-20.69	-216.08
S1$_{mel-uri}$	-13.40	-34.73	35.71	-1.95	-14.37
S5$_{mel-uri}$	-13.63	-37.03	37.23	-2.35	-15.78
S6$_{the-uri}$	-102.87	-119.32	120.41	-7.94	-109.73
S7$_{the-mel}$	-5.56	-9.60	11.14	-0.87	-4.89

Table 4a-4 summarizes all of the energy values for different systems (S2—S5) regarded in the present study. The total binding free energies ($\Delta G^0{}_{bind}$) are negative for all systems. This shows that TB-UA complex formation in water is beneficial. Interestingly, an extremely favorable van der Waals energy (ΔE_{vdW}), as well as an unfavorable solvation free energy ($\Delta G_{sol} = \Delta E_{PB} + \Delta E_{NP}$) for all systems can be found. The unfavorable solvation energy means that the energy needed for the binding parts to dissolve and to align its binding interfaces. In addition, the results show that the favorable TB-UA electrostatic interactions (ΔE_{elec}) make an significant contribution to the free energy of binding, but the van der Waals energy component (ΔE_{vdW}) is the main driving force behind the TB-UA complex formation. As we move from the system S2 to S5, the $\Delta G^0{}_{bind}$ becomes more favorable. This fact shows that the higher concentration of TB in a system, the greater the complexity between UA and TB. Moreover, a comparison of systems S2, S4, and S5 indicates that the ΔE_{vdW} significantly predominates over ΔE_{elec} in system S5. This fact signifies that with the increase of TB concentration, UA clusters break into lower-order clusters. As a result, the surface area of the receptors, i.e., UA molecules increases significantly, and along with the surface area, ΔE_{vdW} becomes more favorable from systems S2 to S5. This fact also signifies the destabilization of UA aggregates. We have also estimated $\Delta G^0{}_{bind}$ for MM-UA complexes. Here, MM is considered as the ligand. The comparable

$\Delta G^0{}_{bind}$ signifies that the way MM binds to the UA in system S0, in a similar way, it binds to the system S5. So, all four MM molecules are interacting in a similar way as they do in system S0. The only difference is that, in system S5, the total cluster size of UA-MM is lower than that of system S1. Furthermore, the comparison of $\Delta G^0{}_{bind}$ for systems S6 and S7 depicts that MM-TB binding is not that significant as the value of $\Delta G^0{}_{bind}$ is very small, i.e., the system S6 gives similar results with that of system S2 for $\Delta G^0{}_{bind}$ between UA and TB. So, it can be concluded that TB binds preferably with UA molecules rather MM molecules. Again, for system S7, ΔE_{elec} predominates over ΔE_{vdW}. This fact symbolizes that a small binding between MM and TB occurs with the small number of hydrogen bond formation. These results also indicate that the complexation between MM and TB molecules in water is favorable only when hydrogen bonds attach them.

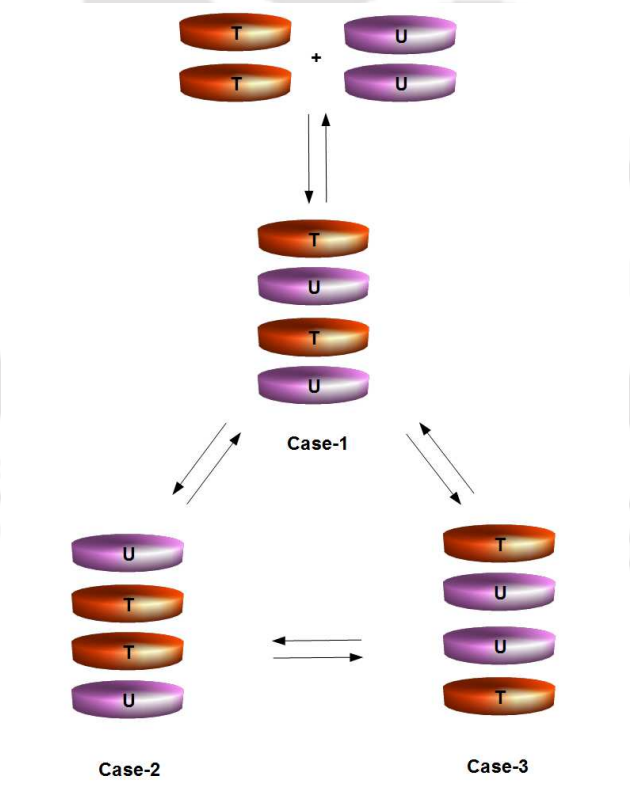

Figure 4a-13. *Schematic representation of the complexation during the formation of a complex between TB (whitish red) and UA (whitish pink) in system S8.*

MM-PBSA provides favorable binding free energy when the ligand, as well as the receptor, binds appropriately to each other. Thus, the total negative binding free energies

($\Delta G^0{}_{bind}$) only correspond to preferable contact between the ligand (TB) and the receptor (UA) in water (Table 4a-4). All the ligand-ligand contacts, the receptor-receptor contacts, as well as ligand-receptor contacts, should be taken together for all systems to determine the total complexation energies. In the present study therefore, in order to gain complete complexation energy, all TB-TB, and UA-UA interactions are to be combined to the TB-UA contacts. The complexation energy provides more accurate information about the clusterization between TB and UA molecules in water (Figure 4a-13). Here to determine the complexation energy, a specific system, S8, is prepared so that an overall idea, as well as a conclusion, can be drawn for all the remaining systems. In system S8, $\Delta G^0{}_{bind}$ values for various combinations are determined using the last 4 ns of a total of 200 ns MD trajectories. From the cluster structure analysis of system S8, it is seen that all UAs form a complex with all TB molecules. Now, we have chosen the last 4 ns trajectories where two UA molecules, as well as two TB molecules, are in the monomeric states. We have considered the last 4 ns as for the last 16 ns of the simulation these molecules remain in the similar conformations (Case-1). So it is a quite stable structure. Both the number of TB and UA molecules are minimal in the system, S8. Thus, randomness can be observed. In spite of having considerable randomness of these four molecules in water, over the last 16 ns, they have not changed the conformation (Case-1). Furthermore, we have chosen another two possible structures from the last 60 ns of total 200 ns trajectories. The structures (Case-2 and Case-3) are given in Figure 4a-13. Now for Case-2, we have estimated the $\Delta G^0{}_{complex}$ following the same procedure mentioned above. The value of $\Delta G^0{}_{complex}$ is given in Table 4a-5. In Case-3, the value of $\Delta G^0{}_{complex}$ is -9.75 kcal/mol. Now from Table 4a-5, the binding of TB with UA is energetically favorable irrespective of the mode of binding between them. Note that, Case-2 is more stable conformation over Case-3. Though it is true for system S8, however, the facts may also be actual for all the remaining systems considered in the present study. Interestingly, for all cases, it is evident from the free energy values ($\Delta G^0{}_{(uri\text{-}uri)}$) that the breaking of UA clusters (Case-1 > Case-2 > Case-3) is quite feasible as well as the formation of UA-TB is inevitable ($\Delta G^0{}_{(uri\text{-}the)}$ is a significant negative for all cases). Moreover, all four molecules are making the complex. This is only possible when they are attached similar to that presented in Figure 4a-13. In this case, we determine the $\Delta G^0{}_{complex}$, and these values are shown in Table 4a-5. Thus, the $\Delta G^0{}_{complex}$ for TB-UA binding is more favorable than the $\Delta G^0{}_{bind}$ of them. This fact indicates that the total complexation through all contact types between TB and UA in water is desirable.

Table 4a-5. Complexation energy derived by MM-PBSA calculations. Here, $\Delta G^0{}_{TB\text{-}TB}$, $\Delta G^0{}_{uric\,acid\text{-}uric\,acid}$, $\Delta G^0{}_{TB\text{-}uric\,acid}$, and $\Delta G^0{}_{complex}$ represent the binding free energies of TB-TB interaction, UA-UA interaction, TB-UA interaction, and total complex, respectively. $\Delta G^0{}_{complex}$ is the summation of $\Delta G^0{}_{TB\text{-}TB}$, $\Delta G^0{}_{uric\,acid\text{-}uric\,acid}$, and $\Delta G^0{}_{TB\text{-}uric\,acid}$. All energy values are expressed in kcal/mol.

System	$\Delta G^0{}_{TB\text{-}TB}$	$\Delta G^0{}_{uric\,acid\text{-}uric\,acid}$	$\Delta G^0{}_{TB\text{-}uric\,acid}$	$\Delta G^0{}_{complex}$
Case-1	-0.64	-0.59	-17.30	-18.53
Case-2	-4.09	-0.85	-14.30	-19.24
Case-3	-0.67	-2.83	-9.75	-13.25

Umbrella sampling

The potentials of mean force (PMF) simulations reveal how the energy of an system changes along a defined reaction coordinate.[249] We use umbrella sampling techniques to estimate PMFs of different molecular pairs in water such as UA-UA, TB-TB, MM-UA, and MM-MM.

To assess the PMFs of different clusters in the presence and absence of TB, the UA-UA dimer is taken into 1500 water at 300 K (Figure 4a-14). Here, all PMFs are calculated as a function of the distance between the COMs of any two molecules.[207, 249] The minimum energy value for the P0 system is -4.8 kJ/mol at a distance of 3.15 Å. This negative free energy means that the aggregation of UA-UA at 300 K is very favorable. Another umbrella sampling simulation is performed in order to evaluate whether there is a possibility of the formation of the UA dimer in 1500 water molecules at the same temperature using two UA molecules with four TB. In this case, a minimum energy value of -4.43 kJ/mol is found at the same equilibrium separation of 3.15 Å (Figure 4a-14). Thus, an increase of free energy under the same conditions implies that the presence of TB molecules disturbs UA dimerization in system P1. Thus, the formation of further clusters from the existing UA dimer becomes energetically unfavorable in the presence of TB. It is now apparent from the calculations of MM-PBSA that the binding free energies between UA and TB are increasing (more unfavorable) with the increase of TB molecules. But, MM-PBSA does not survey which molecule prefers to whom most. Preference interaction parameter

calculations show that UA preferentially interacts with TB in high TB concentrations. Therefore, in the existence of UA molecules, it is essential to verify whether TB dimer formation is interrupted.

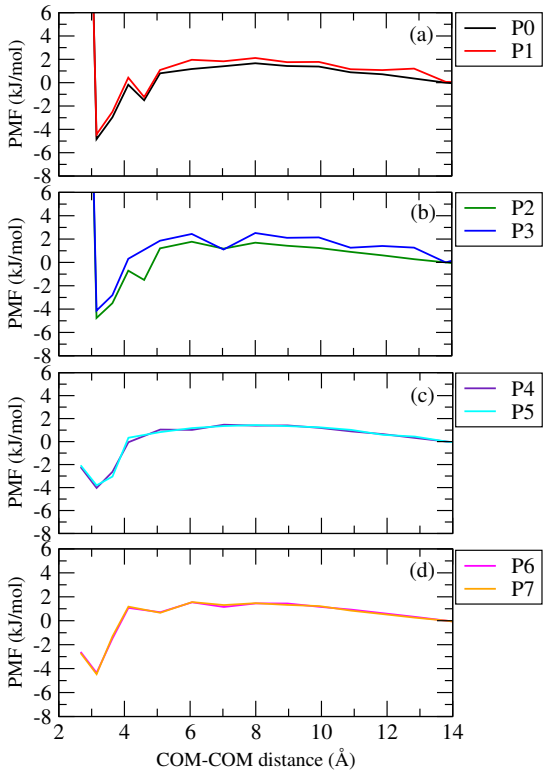

Figure 4a-14. *Potential of mean forces for the association of all systems P0–P7. Standard errors of all data points (calculated using block average method) fall within ± 0.07 kJ/mol.*

For this purpose, we have carried out two more umbrella sampling simulations with TB dimer in the presence (Figure 4a-14 (system P2)) and absence of UA (Figure 4a-14 (system P3)). Figure 4a-14 shows, at 3.15 Å two minima exist with negative energies of -4.75 kJ/mol and -4.13 kJ/mol each for the P2 and P3 systems, respectively. In the presence of UA, TB dimer formation is altered by PMF value. This fact implies that TB interacts preferentially with UA in water. The preferential interaction between UA and TB allows the UA clusters to be destroyed. Interestingly, the presence of TB does not change MM-MM interactions (Figure 4a-14 (system P4) and (system P5)). This fact suggests that the interactions between TB and MM are not essential for destabilizing UA aggregation. A comparison between P6 and P7 systems (Figure 4a-14) also indicates that the presence of

TB does not influence the relationship between MM and UA. As TB interrupts the UA clusters rather than the UA-MM dimer, it can be concluded that the presence of TB will reduce the size of overall MM-UA clusters.

Dimer existence autocorrelation functions

The lifetimes of dimers formed by the association of UA-UA in the presence and absence of TB are assessed by estimating the dimer existence autocorrelation function (DACF). It is useful for the determination of the dynamic nature of UA aggregation. DACF is autocorrelation of the simple function, β_{ij}, for the pair of molecules i and j, which takes the value 1 while fulfilled by the distance criterion and becomes zero when for the first time the distance criterion breaks off. The DACF is determined by using the following equation:[207, 174, 197, 158]

$$DACF(\tau) = N. < \sum_{t=0}^{T-\tau} \beta_{ij}(t+\tau).\beta_{ij}(t) >_{ij} \tag{4.13}$$

Note that, although the distance criterion is met later, DACF will remain zero. Figure 4a-15 (a) presents the DACFs for the dimer of UA-UA in existence of TB and also without TB for systems S0–S5. Here we have chosen a distance of 6.0 Å from the COMs of the two molecules of UA for all systems. The objective of our present study is to determine if TB can break the aggregation of UA in water or not.

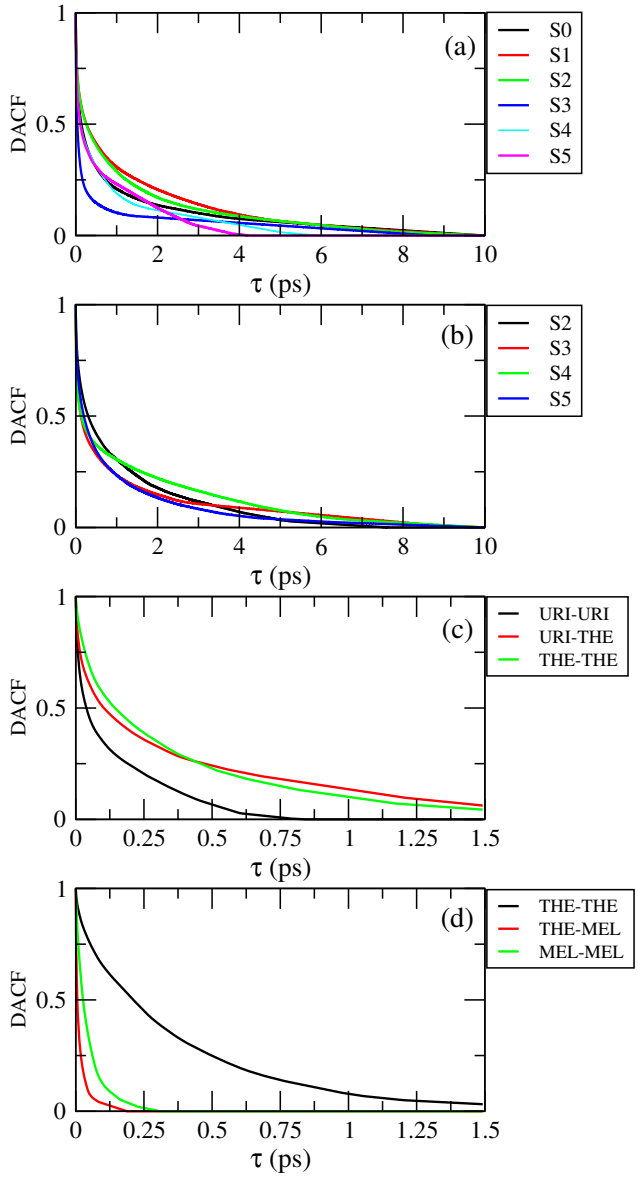

Figure 4a-15. *Dimer existence autocorrelation functions (DACFs) for (a) UA-UA, (b) TB-UA pairs (with a distance of 6.0 Å), along with various pairs of systems (c) S6 and (d) S7.*

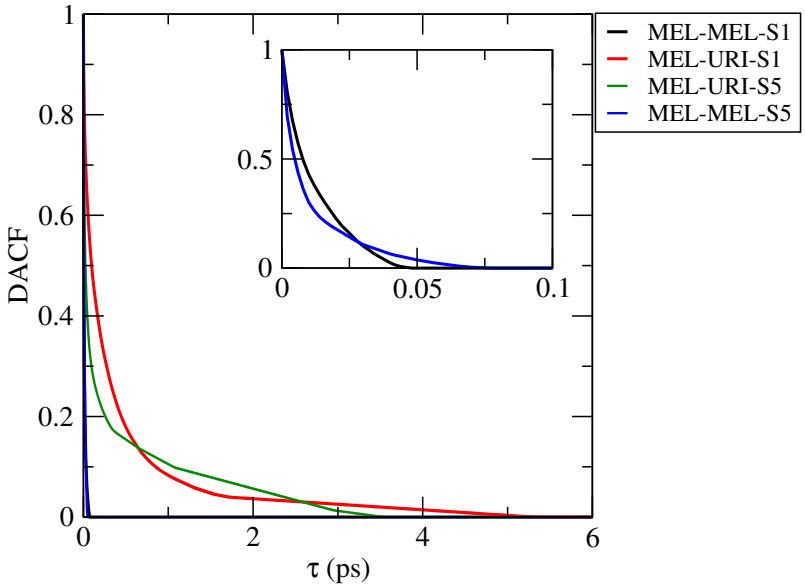

Figure 4a-16. *Dimer existence autocorrelation functions (DACFs) for MM-MM (with a distance of 5.0 Å) and MM-UA (with a distance of 7.0 Å) dimers for systems S1 and S5. The magnified figure is given in the inset.*

This is why, at first, we consider UA-UA over other combinations like UA-TB, UA-MM, and MM-TB. The DACF for the UA-UA dimer is very progressively decreased for systems S0 and S1, indicating that its lifetime is very higher. Similarly, the UA dimer is made with a higher lifetime in S2 system as well. Now, although the S2 system contains a small number of TB, it does not interfere with the formation of UA pair. This is, therefore, indirect evidence of the fact that a small number of TB can not modify the accumulation of UA in water. However, as we move onto the following three consecutive systems, i.e., systems S3, S4, and S5, a noticeable change is observed in the lifetimes of the UA dimer. The lifetime of the UA dimer is too short for the S5 system. The lifetime of the UA-UA dimer is also decreased as the concentration of TB is increased for systems S3–S5. The lifetime of UA dimer for the S5 system is much shorter when compared to the system S0. To sum up, S5, TB molecules significantly break the aggregation of the UA dimer to a high

percentage of monomer.

Figure 4a-15 (b) shows the TB-UA dimer lifetimes for systems S2–S5. As the concentration of TB increases from system S2 to S5, the dimer lifetime of TB-UA pair increases. This signifies that the larger the number of TB in a system, the more UA-TB interaction will be. Moreover, the lifetime of the UA-TB dimer is higher than the UA-UA dimer. The calculation of DACF, for system S6, strengthens this fact. In system S6 (Figure 4a-15 (c)), the lifetime order for the respective pairs is as follows: UA-TB > TB-TB > UA-UA. Furthermore, the determination of DACF for various combinations of pairs present in system S7 reveals that TB does not interact profoundly with MM as Figure 4a-15 (d) shows the order of lifetimes as follows: TB-TB > MM-MM > TB-MM. As a result, the self-aggregation of MM molecules is seen for system S7 along with the substantial clusterization among TB molecules. Thus, MM-UA interactions do not get hindered by the presence of TB. Figure 4a-16 shows that MM-UA lifetime, in system S1, is higher than in system S5. The decrease in lifetime owing to the breakage of higher-order clusters made of UA into the lower-order clusters as TB is involved in that event in system S5. Thus, the maximum size of the UA-MM cluster is reduced. However, for systems S1 and S5, the MM-MM interactions are similar in the presence of UA molecules, as MM does not want to self-aggregate in water in presence of UA.

Hydrogen bond properties

Next, for the various systems considered in the present study, the average number of hydrogen bonds is determined for multiple interactions like UA-UA, UA-MM, UA-TB, MM-MM, MM-TB, TB-TB, and water-water (Table 4a-6). It is seen that the average number of hydrogen bonds between UA molecules decreases from systems S0 to S5. In system S0, only UA is present. The total average number of hydrogen bonds for this system is 23.05. In system S1, MM is brought into, a negligible change in hydrogen bond number between UA molecules is observed. Thus, a very low concentration of MM does not change the UA-UA interactions. From systems S2 to S5, TB is introduced in the manner of increasing concentration of it. In all systems, the average number of hydrogen bonds between UA molecules are 20.39, 16.16, 11.21, and 9.93 for systems S2, S3, S4, and S5, respectively. Thus, in presence of TB, as expected, a substantial decrease in UA-UA hydrogen bond number is observed. Now, considering UA-TB hydrogen bond (H_{u-t}), it is found that as the above shift from system S2 to S5, the number of hydrogen bonds also increases.

So, the values of H_{u-t} reveals that with the increase of TB molecules, the UA starts to interact more with TB rather than themselves. As a result, a very negligible assembly among UA molecules is found in system S5 in which H_{u-t} possesses the highest value. A similar trend can be observed while calculating the hydrogen bonds between MM and TB as well as TB-TB. So, higher the number of TB present in a system, more significant is the interaction between MM-TB, UA-TB, and TB-TB and lower is the interaction between UA-UA.

Furthermore, the average hydrogen bond numbers for the UA-MM pair is also determined. UA forms hydrogen bonds with MM by the use of its all atomic sites, as stated in our previous study.[207] Here, it can be seen that as the number of MM and UA is same for systems S2 to S5, the MM-UA hydrogen bond numbers (H_{u-m}) gets reduced from systems S2 to S5. Now, if we look into the Table 4a-6 carefully, we can find that for systems from systems S2 to system S5, UA makes a less significant number of hydrogen bonds with MM in system S5 compared to system S2. As we stated in our previous study[207] that higher-order UA clusters drag MM to themselves to add to it. Now, as the UA clusters get reduced to lower-order clusters from system S2 to S5 due to the introduction of TB, lower-order UA clusters do not make substantial interactions with MM molecules in system S5. As a result, there is a decrease in hydrogen bonds between MM and UA.

A comparable trend can also be noticed in the calculation of hydrogen bond lifetime (Figure 4a-17). Note that faster the decay of hydrogen bond autocorrelation function (c(t)) lower will be the lifetime. In this case, it is seen that for the system S5, $(\tau_{hb})_{S5}$ is decreased and reduced to zero rapidly as compared to systems S1 and S2. Moreover, for system S1 $(\tau_{hb})_{S1}$ has the higher value than the $(\tau_{hb})_{S2}$ of system S2 as system S1 contains only UA and MM while in system S2, TB is now introduced. Thus, a considerable but not dramatic change of hydrogen bond lifetime can be observed due to the reduction of overall UA-MM cluster size. It is to note that during the calculation of hydrogen bond dynamics, MM is considered as the donor, and UA is chosen as acceptor, and we followed the procedure mentioned elsewhere.[250, 251, 252]

Moreover, MM-MM hydrogen bond numbers remain the same for systems S1–S5. From the cluster structure analysis, it is evident that MM remains in solution predominantly as the monomer (the monomer percentage is higher for all systems for MM-MM interactions). All four MM molecules either attached with UA or TB cluster (with weak interaction) or fully dissolved in water. It is to be noted that along with UA cluster, TB can also

make hydrogen bonds with MM and can attract MM towards themselves. However, the interaction of MM with UA is stronger than TB in solution. Furthermore, a comparison between systems S6 and S7 makes the above facts more evident. In system S6, MM makes more hydrogen bonds with UA rather than with TB like in system S7.

Furthermore, hydrogen bond analysis is also carried out for system S10 in which only TB is present in pure water. Here, the total number of hydrogen bonds between TB-TB pair is very less, i.e., 1.85 (this result is not mentioned in the table). Thus, TB also makes a minimal number of hydrogen bonds with themselves. Thus, the interaction between a TB pair is dominated by $\pi - \pi$ stacking (as discussed above) just like UA pair.

Table 4a-6. Average number of hydrogen bonds (total) involving all possible pairs for different systems.

System	H_{u-u}	H_{u-m}	H_{u-t}	H_{m-m}	H_{m-t}	H_{t-t}	H_{w-w}
S0	23.05	—	—	—	—	—	3.69
S1	23.02	8.54	—	0.81	—	—	3.70
S2	20.39	8.69	5.46	0.43	2.39	1.003	3.69
S2-a	21.38	7.57	7.11	0.39	2.57	1.001	3.70
S3	16.16	10.87	14.57	0.49	3.33	0.97	3.69
S4	11.21	6.12	21.62	1.03	3.65	5.95	3.69
S5	9.93	3.61	24.27	0.37	4.27	11.26	3.67
S5-a	8.68	4.67	24.62	0.88	5.22	12.35	3.70
S6	8.17	—	12.65	—	—	0.90	3.70
S7	—	—	—	1.95	1.92	1.29	3.69

We have also determined the water-water hydrogen bond numbers (H_{w-w}), which describes whether or not the bulk water structure is disturbed in the presence of UA, TB, and MM molecules. As H_{w-w} remains unchanged for all systems (Table 4a-6); thus, it can be suggested that the tetrahedral structure of water is not hindered at all. Moreover, NPT and NVT simulation give similar results for those two systems (S2-a and S5-a).

A set of criteria is chosen for the hydrogen bond definition between donor (D), and accepters (A) to determine the number of hydrogen bonds (discussed above) involved for all types of interactions.[207, 174, 197, 253, 254, 255] If the distance D-A $\leqslant$ 3.5 Å and, simultaneously, angle $\angle$ D-H$\cdots$ A $\geqslant 120^{\circ}$, then hydrogen bonding is considered to be present.

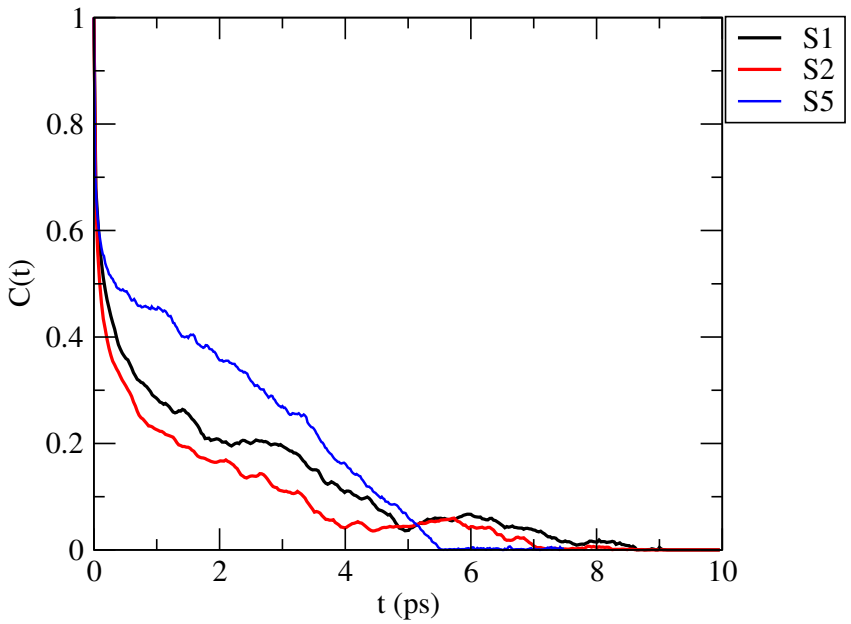

Figure 4a-17. *HB autocorrelation functions for MM-UA interactions for systems S1, S2, and S5.*

Quantum chemical calculation

To validate our simulation results from various interactions such as TB-TB, TB-UA, and UA-UA, we have performed a series of DFT calculations in the gas phase and determined complexation energies between these pairs. It should be noted that only π-stacked structures are taken into account, no hydrogen-bonded structures are prepared as the results of the present MD simulation show predominant $\pi - \pi$ staking over hydrogen-bonded structures among UA and TB molecules (discussed above). Also, the interactions that include MM are excluded as in our previous publications,[207, 174] MM-UA and MM-MM interactions are shown. The other remaining pair, i.e., MM-TB, is not chosen as the interaction between MM and TB is very weak, regardless of any interactions such as π-stacking or hydrogen bonding.

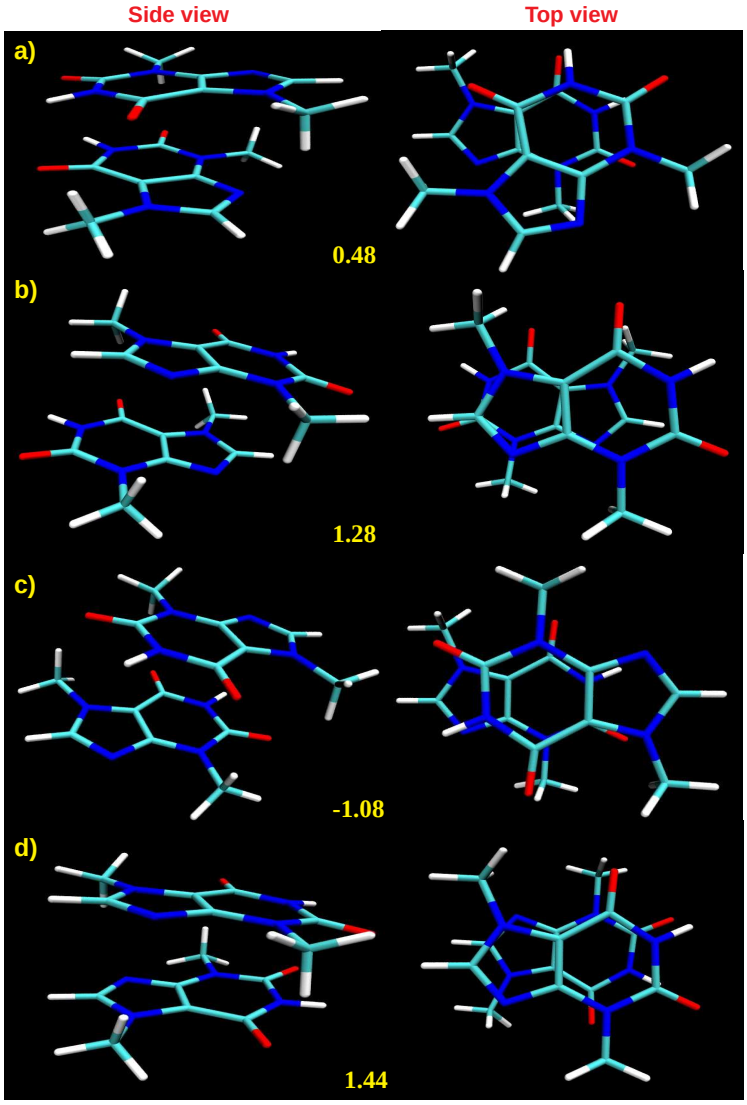

Figure 4a-18. *DFT optimized structures of a TB-TB pair with all possible conformations as well the complexation energies (in kcal/mol unit) using B3LYP-D3/6-311++G(d,p) level theory.*

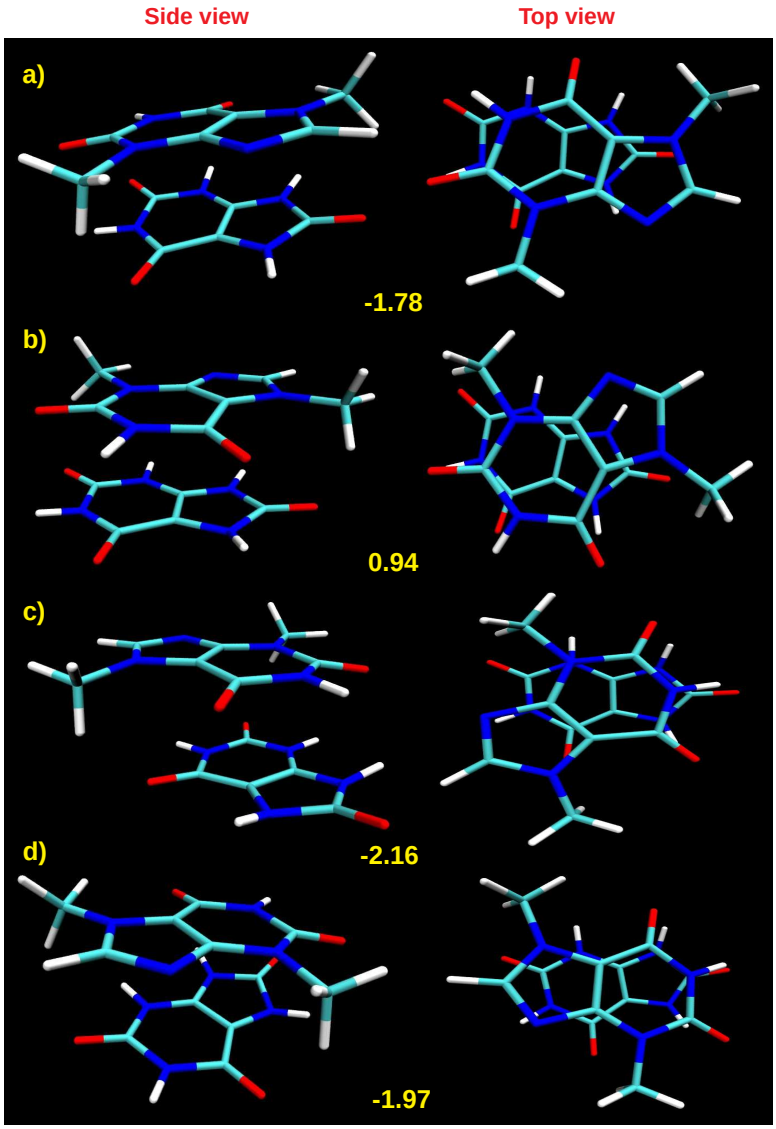

Figure 4a-19. *DFT optimized structures of a TB-UA pair with all possible conformations as well the complexation energies (in kcal/mol unit) using B3LYP-D3/6-311++G(d,p) level theory.*

Therefore, our present quantum calculation focuses mainly on UA-TB interactions. Firstly, with B3LYP-D3/6-311++G(d,p) level theory, we have optimized the various possible structures. The TB-TB dimers are represented in Figure 4a-18 (a)-(d). Of four probable structures between a TB pair, one structure is seen as being the most stable (Figure 4a-18 (c)) from the complexation energy calculations with BSSE corrections using the same level theory. Our present simulation result also shows a similar structure. Furthermore, between

TB and UA molecules, we have adopted all possible arrangements (Figure 4a-19 (a-d)). All structures indicate that TB preferably forms $\pi - \pi$ stacked structures with UA. Moreover, UA-UA $\pi - \pi$ stacked structures are evident from our previously reported results.[207] TB also shows, in the present study, strong π-stacking interactions with UA with high negative and comparable energy value with the UA-UA pair.

Our simulation results, from the present study, precisely match the quantum results. The following results are presented in our simulation: 1. The interaction between a UA pair is dominant when present either as a pure substance or with a small number of TB. 2. Interactions between TB and UA become predominant over UA-UA for systems containing high TB concentration. 3. In comparison to TB-TB, TB-UA contact is preferable in water.

We deduce a very similar conclusion from the present quantum calculations, particularly for TB-UA and TB-TB interactions. Here, $\pi - \pi$ stacking is comparatively less preferable between the TB pairs than UA-TB or UA pair. In addition, the interaction between UA and TB is similar or more prominent than that of UA-UA pair.

SUMMARY AND CONCLUSIONS

In this study, a series of classical MD simulations have been thoroughly examined for the effect of TB on the UA aggregation along with possible changes in the size of the MM-UA cluster. The CN numbers of UA around a reference UA is approximately 1 (at an elevated concentration of TB), and it becomes 3 when the concentration of TB is low. The determination of CN, therefore, suggests that the accumulation of UA changes dramatically in the presence of TB. This result is consistent with the recent experimental findings. It was proposed that TB inhibits UA crystallization in a concentration-dependent manner. Furthermore, the number of TB around UA is increased by replacing other UA molecules. It should be noted that the CN of MM around a reference UA is substantially reduced in the presence of TB. Furthermore, such a noticeable decrease in the CN of MM around UA can be found at a higher level of TB. The increase in TB, thus, reduces the CN of UA around a reference UA along with the CN of MM around UA in the quaternary system of MM-TB-UA-water. Further, the determination of spatial density distribution (SDF) shows the very same scenario in which the density of UA and MM around the reference UA is reduced with increasing TB concentrations. Thus, CN and SDF determination demonstrates that the association between MM-UA is reduced, and the interaction of TB-MM plays a less MM-UA aggregation, while the interaction of TB-UA is the key factor.

In an attempt to examine the solute-solute preferential interaction, the preferential interaction parameters are considered. The determination of preferential interaction parameter shows that TB, at its elevated concentration, interacts preferentially with UA over self-aggregation. Thus, UA-UA interaction is quite strong at low TB concentration, which enables UA to be aggregated under ambient conditions. Moreover, when it is present enough in a system along with UA, TB efficiently breaks the UA clusters.

Orientational preferences of different pairs made of aromatic planes of TB, UA, and MM show that UA-UA, UA acid-TB, and TB-TB interactions prefer π–stacking interactions over the hydrogen-bonded interactions, whereas the remaining combinations like UA-MM, TB-MM, and MM-MM interact profoundly via hydrogen bonds between them.[207, 256, 257] Our previous studies also showed that MM-MM and UA-MM pairs produce a stable hydrogen bonding structure, where UA molecules interact with the like molecules via π–stacking.[207] The inclusion of TB does not alter the scenario; rather, it binds to UA π–stacked manner. Such interaction facilitates UA's replacement by TB molecules, in a system in which UA-UA interaction is less conducive, to form a framework of TB-UA.

Cluster structure analyses of MM-UA-TB ternary solution suggest that in the absence of TB, UA molecules self-assemble with the formation of larger clusters. However, the presence of a moderate amount TB in a system can destroy the higher-order UA clusters into a high percentage of monomers. In addition, the UA-TB cluster size improves with increasing the concentration of TB. The intense interaction between UA and TB allows, therefore, the breaking of large insoluble UA clusters. Moreover, with the increase of the number of TB, UA starts to disaggregate, and as a consequence, MM-UA clusters that cause the formation of kidney stones breaks. Experimentally it has been reported that UA crystals become thinner and longer in the presence of TB than in the absence of the same, and the inhibited crystal face is (210).[203] TB alters the structure of UA clusters and makes them longer and thinner, which indicates that the cluster size of UA is evidently changing alongside the UA-MM in a roundabout way.

Our findings from MM-PBSA calculations reveal that TB makes the binding energy of UA-TB favorable and thus, loosen the UA-UA binding. The energy of complexation of TB-UA is highly negative, while the UA-uric acid complexation energy is close to positive. These facts further demonstrate that TB replaces UA out from its own cluster in order to form the TB-UA composite. Interestingly, these findings are in good accordance with recent experimental results. It has been suggested that TB prevents the growth at only one side

of the crystal, (210), but not on other, (001) and (201). Since UA and TB molecules have very comparable structural properties, TB can be accepted in the relevant UA clusters as a replacement of UA molecules. Adding this molecule (i.e., TB) to the UA crystal lattice will alter the structure of certain layers that will thus increase their energy, therefore, decreasing their growth rate. Thus, it is very probable that TB in UA crystal impacts on the face (210)[203]

Similar outcomes are achieved in the calculation of PMF of the distinct molecular pairs in water. PMF demonstrates that the presence of TB greatly influences UA-UA dimerization. Similarly, if UA is present, the TB pair becomes energetically unfavorable. Now, the interaction between UA and TB enables for the destruction of the UA clusters. As a result, in the existence of TB, the formation of further a cluster from the existing UA alters the MM-MM as well as MM-UA dimerization processes.

As TB interrupts the formation of UA clusters rather than UA-MM dimer, it can be stated that the presence of TB will reduce the size of overall MM-UA clusters. It is expected that the increase of the amount of MM in a systems with higher TB concentration, would results in more MM-MM aggregation in the presence of TB as MM-TB interaction is not very significant. However, MM-UA cluster size is reduced as TB-UA interaction is more favorable than UA-UA interaction that ultimately causes the reduction in UA cluster size. The overall aggregate of UA-MM is, therefore, reduced to smaller size clusters, which confirms the decrease in the size of kidney stones.

The lifetime of the UA dimer is higher in a system where no TB is present. However, the presence of TB in a substantial quantity significantly reduces the lifetime of UA pair. Furthermore, UA-TB pair lifetime is improved considerably with the increase of TB concentration. Again, MM-UA lifetime is reduced when the TB is available in sufficient amount. However, the lifetime of MM-TB pair is very low. Hydrogen bond analyses reveal that in the presence of TB, as expected, a substantial decrease in UA-UA hydrogen bond number is observed. Similarly, UA-MM hydrogen bond number is also reduced in the presence of TB. The total number hydrogen bonds for UA-UA and UA-TB, however, is not that high but significant. Furthermore, MM-MM hydrogen bond number in all system is low that conveys that in the presence of UA, MM does not self-aggregate; preferably binds to the UA aggregate. Again, the increase of TB concentration leads to a rise of UA-TB and TB-TB hydrogen bond numbers. MM does not make a hydrogen bond with TB predominately but forms with UA in a system. Moreover, we do not notice any noticeable change

in the tetrahedrally coordinated water structure. The hydrogen bond dynamics estimated by the calculation of auto-correlation function shows that in the presence of a moderately high concentration of TB, UA-MM correlation is diminished owing to the reduction of the cluster size of UA self-aggregates. Thus, the dynamical calculation correlates well with that of the hydrogen bond numbers. Since in principle, the accumulation can be dependent on the thermodynamic ensembles[258], we have also performed a 200 ns test NPT simulations at the same temperature as we did for NVT calculation. Both in NVT and NPT ensembles, the molecules are aggregating in a similar fashion. The impact of the ensemble is, therefore, presumed to be minimal. Furthermore, *ab initio* calculation of TB-UA pair along with TB dimer proves that TB and UA preferentially interacts with each other by π–stacking interaction and this interaction is more favorable than TB-TB π–stacking. Lastly, we perform high level quantum calculations to validate the simulation results of the present study wherever applicable.

4b: The Underlying Mechanisms of Allopurinol in Eliminating Renal Toxicity Induced by the Melamine-Uric Acid Complex Formation: The Role of π-Stacking

"We know from our clinical experience in the practice of medicine that in diagnosis, prognosis, and treatment, the individual and his background of heredity are just as important, if not more so, as the disease itself."

– Paul Dudley White

Overview: We address uric acid (UA) replacement using molecular dynamics by a model small molecule inhibitor allopurinol (AP) from their aggregated cluster in a columnar fashion. Experimentally it is affirmed that AP is efficient in preventing UA-mediated renal stone formation. However, no study presents the underlying mechanisms yet. Hence, a theoretical approach is presented for mapping the AP, which binds to melamine (MM) and UA clusters. In AP's presence, the higher-order cluster of UA molecules now turns into a lower order cluster, which "drags" fewer MM to them. Consequently, the MM-UA composite structure gets reduced. It is worth noting that the UA-AP and AP-MM hydrogen bonding interactions often play an essential role in reducing the UA-MM cluster size. Interestingly, an AP around UA makes a pillar-like structure affirmed by defining the point-plane distribution function (pldf). The decomposition of the preferential interaction by Kirkwood-Buff (KB) integral into different angles like 0°-30°, 30°-60°, and 60°-90° firmly establish the phenomenon mentioned above. However, the structural order for such π-stacking interaction between AP and UA molecules is not hierarchical but rather more spontaneous. The driving force behind UA-AP-MM composite formation is the favorable complexation energy that can be inferred by computing pairwise binding free energy for all possible combinations. The dependence of cluster size on UA-MM composite structure can be accomplished utilizing the potentials of mean force, cluster structure analysis, dimer existence autocorrelation function (DACF), and MM-PBSA results. The performance of enhanced sampling and quantum calculations further confirms the evidence of UA degradation.

■ INTRODUCTION

The epidemic of kidney stones and renal failure in baby children in China in September 2008 triggered a global health panic. This disease was attributed to the contaminated powdered infant formula containing melamine (MM, Figure 4b-1 (a)). Melamine, which includes 66% nitrogen, a synthetic material, and a cyanamide trimmer that shapes formaldehyde resins, is used in laminates, glues, adhesives, plastics, and some fertilizers. It should not be used for human or animal use as a food additive. To increase the apparent protein level, MM had been intentionally added to the diluted raw milk since nitrogen-based methods typically assess this. Two cases of acute renal failure in South Korean and American cats and dogs were recorded earlier in 2004 and 2007 in association with pet food, tainted by MM and cyanuric acid.[259, 260, 261] However, MM applied to infant formula in mainland China in September 2008 to increase the protein content, leading to a significant MM-associated urinary stones outbreak among infants.[1, 2, 262, 202, 263, 264, 265] The stones' study shows that these compounds consist of MM and UA (Figure 4b-1 (b)) in almost equimolar quantities and indicated a probability for the stone formation of 1:1 hydrogen-bonded interaction of both components.[26, 45] UA and MM stones' composition may range from 1.2:1 to 2.1:1, respectively.[24, 266, 47] The urine is mostly excreted with MM, but not contaminated. Whereas MM is known to be low toxic when consumed in low doses alone, the MM-UA crystals can form in the kidney in combination with very low solubility. We have established the exact mechanism for developing kidney stones based on theoretical studies in recent research.[207] The decomposition temperature of a hybrid MM-UA complex is greater than that of MM, suggesting a substantial stabilization of the composite material. MM has also been documented to integrate with UA through N—H$\cdots$O and N—H$\cdots$N hydrogen bonds and then form a planar supra-molecular network structure via the adjacent water molecules.[26, 45, 207] Furthermore, though some experiments were explicitly based on the causes of the development and identification of pure UA blocks, the fundamental reason for kidney stone development and avoidance using prescription medications is limited to only a handful of studies.[267, 268, 269, 270, 271, 272, 273, 274, 275, 276, 277, 278]

Allopurinol (AP, Figure 4b-1 (c)) is an inhibitor of xanthine oxidase[279] and is currently the only small molecule inhibitor capable of significantly decreasing UA intake. AP can lower UA's blood and urine levels by blocking the xanthine and hypoxanthine oxidation process to treat primary gout. AP can also be used for treating chronic cardiac loss and risk of tumor lysis. AP is, however, a polar compound with good inter-molecular

hydrogen bonds. Nephrolithiasis of uric acid constitutes 7-10% of stones in the kidney. UA nephrolithiasis has a lower urinary pH, hyperuricosuria, and poor diuresis as the most common genetic abnormalities.

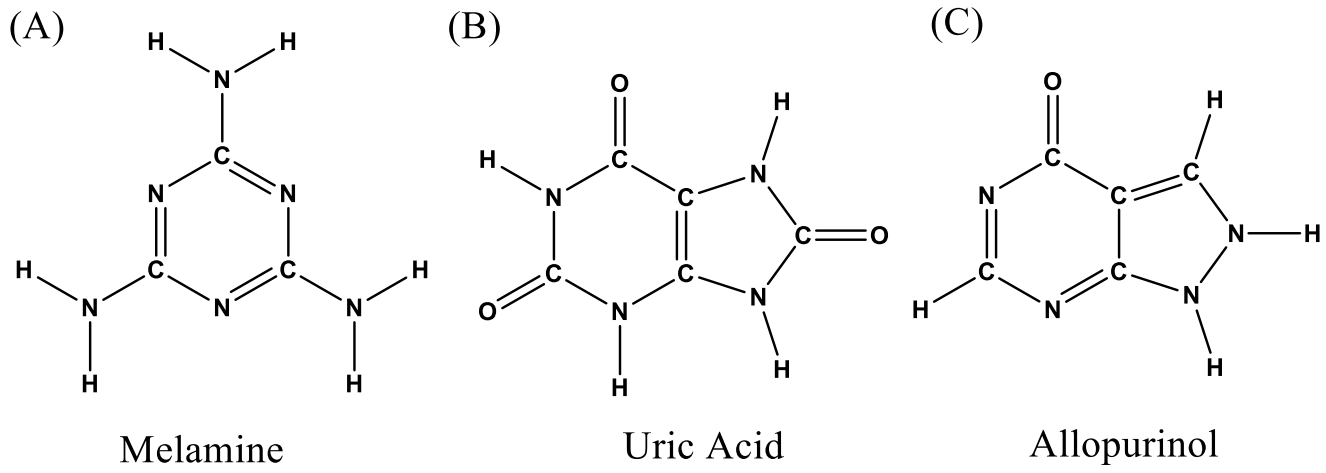

Figure 4b-1. *Structure of (a) MM (melamine), (b) UA (uric acid), and (c) AP (allopurinol).*

Therapy is based on urinary alkalinization of individuals vulnerable to UA stones, and AP is offered to people with hyperuricemia because of the lack of UA inhibitors. Experimental studies indicate that the reduction in new stone formation by chronic AP administration will significantly alter this path. AP decreases the urinary content of undissociated UA, thus immediately modifying the disease's pathogenetic pathways.[267, 268, 269, 270, 271, 272, 273, 274, 275]

The experimental effects of AP do not, however, provide a particular mechanism or information about how inhibitions can be made viable as a prospective inhibitor of kidney stones. It should now be remembered that AP will avoid the formation of UA aggregates. AP then prevents the early stage of UA crystal formation based on the above experimental findings. The current research is, therefore, a proactive approach, as the association between UA and MM are high in the kidney. In empirical research, it has been shown that

AP substantially forms hydrogen bonds with UA as well as MM. This research will, we hope, include details about how AP acts to stop the development of the broader cluster of MM-UA.

The following provision is rendered for the rest of the paper. Part II describes the simulation models and protocols used for MM, UA, AP, and water molecules. The results are addressed in Section III. Section IV summarises our findings.

■ MODELS AND DETAILS OF SIMULATIONS

In this study, a series of classical molecular dynamics (CMD) simulations are performed considering the different UA, MM, and AP concentrations in the water at ambient pressure-temperature conditions. Table 4b-1 presents the model systems proposed here. First, all of the molecules are charged by the RESP (restrained electrostatic potential[140]) method using the ANTECHAMBER[141] module of the AMBER14 package.[226] Besides, to evaluate the RESP charge, an energy-optimized structure is used, and optimization is carried out by Gaussian 09[138], with the aid of the HF/6-31+G** QM calculation. The General AMBER force field[142] is used at all atomic sites in UA, MM, and AP.

All the molecules were immersed in TIP3P (three-point transferable inter-molecular potential) water solvent to conduct MD simulations.[143, 367] The initial configurations of each system were generated using the PACKMOL package.[144] A cubic box containing both solute and solvent molecules in desired concentrations was used for the simulations. Energy minimization was then achieved using two stages. The First 4000 steps (out of the 10,000-step energy minimization process) were performed with the steepest descent method, and the remaining 6,000 steps proceeded with the method of the conjugate gradient. In all three directions, PBC (periodic boundary conditions) was employed. All systems were then heated steadily from 0 K to 480 K with a 40 K rise after minimization. Such rising to a higher temperature might aid to surpass the minimum global boundary status. Finally, each system was cooled down to the final temperature, i.e., 300 K using canonical ensemble (NVT). With a decrement interval of 20 K, the 5 ns simulation was run for equilibrating each system in isothermal-isobaric (NPT) ensemble at 300 K and 1 atm pressure. Simulations in the NVT ensemble were consequently subjected to a production run of 200 ns. The last 100 ns for every 200 ns production run is included in the statistical analyses. For all simulation protocols, Langevin dynamics (with 1 ps^{-1} collision frequency) was used to retain a temperature at 300 K.[145] The Berendsen barostat was used in the NPT ensemble to stabilize pressure at 1 atm, with a pressure relaxation time period of 2 ps.[146] The particle

mesh Ewald (PME) algorithm was used to handle long-ranged nonbonded electrostatic interactions.[147] With the input of the SHAKE algorithm, the covalent bonds comprising hydrogen atoms are restricted.[148]

Table 4b-1. System overview[a]

System	N_{AP}	N_{UA}	N_{MM}	N_{wat}	Box length (Å)	C_{MM}(M)	C_{UA}(M)	C_{AP}(M)
S0	5	16	4	6000	57.059	0.0357	0.1428	0.0447
S0-a	5	16	4	6000	57.062	0.0357	0.1428	0.0446
S1	10	16	4	6000	57.082	0.0357	0.1428	0.0893
S2	20	16	4	6000	57.205	0.0355	0.1420	0.1774
S3	30	16	4	6000	57.387	0.0351	0.1404	0.2635
S3-a	30	16	4	6000	57.398	0.0351	0.1404	0.2634
S4	10	10		6000	56.966	—	0.0898	0.0898
S5	10	—	10	6000	56.978	0.0898	—	0.0898
S6	10	—	—	3000	45.242	—	—	0.1793
S7	5	5	—	6000	57.505	—	0.0437	0.0437
S8	5	5	—	6000	57.480	—	0.0437	0.0437
S9	5	5	—	6000	57.265	—	0.0442	0.0442
S10	—	16	16	6000	57.080	0.1428	0.1428	—
S11	30	16	16	6000	57.479	0.1399	0.1399	0.2623
U5M1	—	5	1	6000	56.843	0.0090	0.0452	—
U10M1	—	10	1	6000	56.857	0.0090	0.0903	—
S12	2	2	2	3000	45.210	0.0359	0.0359	0.0359
P0	—	1	1	1500	35.899	0.0359	0.0359	—
P1	4	1	1	1500	36.018	0.0355	0.0355	0.1421
P2	—	2	—	1500	35.832	—	0.0722	—
P3	4	2	—	1500	36.011	—	0.0711	0.1422
P4	2	—	—	1500	35.893	—	—	0.0718
P5	2	4	—	1500	36.017	—	0.1421	0.0711

[a] N_{MM}, N_{UA}, N_{AP}, and N_{wat} refer to the number of melamine, uric acid, allopurinol, and water molecules, respectively. C represents the molar concentrations of melamine (MM), uric acid (UA), and allopurinol (AP).

A cut-off interval of 10 Å was used to measure short-range nonbonded interactions. The trajectories of the MD simulation were analyzed via the CPPTRAJ module built-in AMBER.[376] For the depiction of the acquired MD simulation trajectories, Visual Molecular Dynamics (VMD)[377] was used, including assessment of different properties when needed.

For the last 20 ns of MD trajectories, the binding free energy is calculated for various systems using the molecular mechanics-Poisson Boltzmann surface area (MM-PBSA) methodology. The calculations of the MM-PBSA are based on a python-based AMBER script, MMPBSA.py.[184, 227] The binding free energy change ΔG^0_{bind} can be determined:

$$\Delta G^0_{bind} = \Delta E_{vac} + \Delta G_{solv}, \tag{4.14}$$

where ΔE_{vac}, and ΔG_{solv} are the interaction energy in the gas phase, and the solvation free energy,[185, 186] respectively. ΔE_{vac} can further be decomposed as:

$$\Delta E_{vac} = \Delta E_{ele} + \Delta E_{vdw}, \tag{4.15}$$

where ΔE_{ele} and ΔE_{vdw} measures the receptor-ligand electrostatic and van der Waals interaction energy ingredient, respectively. Moreover, (ΔG_{solv}) energy can also be divided into two energy terms as:

$$\Delta G_{solv} = \Delta G_{PB} + \Delta G_{NP}. \tag{4.16}$$

Here, polar (electrostatic) solvation free energy, and non-polar solvation free energy are shown here by ΔG_{PB}, and ΔG_{NP}, respectively. ΔG_{PB} is determined in a continuum solvent method by the PBSA program of AMBER14. ΔG_{NP} can be measured from the solvent-accessible surface area (SASA). In order to estimate ΔG_{NP}, SASA is determined using Maximal Speed Molecular Surface (MSMS)[187] as:[269, 192, 193]

$$\Delta G_{NP} = \gamma(SASA) + \beta, \tag{4.17}$$

where $\gamma = 0.005$ kcal/Å^2 and $\beta = 0.0$.

For estimating the potentials of mean forces (PMFs)[228], the umbrella sampling (US) approach is applied. The reaction co-ordination ξ has been described as the z-component center of mass (COM)-center of mass (COM) distance (r) between two selected molecules. In the US method, calculations are carried out with a biasing window potential $w(\xi)$ that increases the sampling around the chosen values of ξ. A total of 81 biased simulations with I = 16, ..., 96 are completed, during which the values of ξ are constrained to $\xi_i = i \times 0.15$ Å within the phase space X by a harmonic potential:

$$w_i(\xi) = 1/2K(\xi(X) - \xi_i)^2 \tag{4.18}$$

where K is known as the force constant for harmonic restraint. For these biased simulations, a harmonic restraint force along the z-coordinate of 6 kcal/mol/Å^2 force constant is assumed. The first separation is 2 Å , and this distance is extended by taking one molecule from another in the z-direction. For this, we have considered P0–P5 systems. For these systems, for an initial US process setup, final standard MD simulation trajectories are used. Each model is subjected to 4000 steps minimization (1000 steps from the steepest descent method and the remaining 3000 steps from the conjugate gradient method), and equilibration of 1 ns is obtained for any US-based simulation, in the same way as the standard MD simulation (discussed earlier). Every window has a production run of 10 ns. In reality, we have generated 490 ns trajectories for each system in the US process. Simulation data is obtained at a 2 fs time interval. Using the Weighted Histogram Analysis Method (WHAM)[229, 230], the US simulations' results are eventually estimated for the non-biased P(ξ) distribution of probabilities. Then the PMF value from P(ξ) is obtained as:

$$PMF(\xi) = -k_B T \ln P(\xi) \tag{4.19}$$

where k_B is the Boltzmann constant, and T is the absolute temperature.

In the current study, system S0 is set up in which UA and MM are taken with a modest number of AP to determine the aggregation preferences of UA and MM within that concentration of AP. Three different systems are then prepared (systems S1, S2, and S3), with AP at various concentrations, keeping the number of UA and MM particles fixed to system S0. Accordingly, these systems are adequate to check the impact of AP in MM-UA conglomeration. MD simulations are likewise performed with various ensembles, for example, NVT or NPT. NPT simulations are performed utilizing systems S0-a and S3-a to test if AP, UA, and MM aggregation depend upon the ensemble chosen. Several controlled systems S4–S11, U5M1, and U10M1 are selected to establish the accumulation properties of various pairs like UA-UA, UA-AP, AP-AP, AP-MM, MM-MM, and UA-MM. System S12 is prepared to decide the complexation energy among AP, UA, and MM molecules in water. Finally, systems P0–P5 are considered to carry out the umbrella sampling.

■ RESULTS AND DISCUSSION

HOW DO UA, MM, AND AP AGGREGATE?

First shell coordination number

The first shell coordination number (CN) provides an assessment of the accumulated number of molecules of a given species (say *b*-type) in the shell from 0 to a distance r_{cut}, around a reference atom (say *a*-type). Therefore, CN can be defined as follows:[240, 241, 242, 280]

$$CN = 4\pi\rho_b \int_0^{r_{cut}} r^2 g_{ab}(r) dr, \tag{4.20}$$

Here, ρ_b is the number density of the atom type *b*. First shell CNs are calculated using specific radial distribution functions, considering the center of mass (COM) of those molecules in the form of interactions between UA-UA, UA-MM, MM-MM, AP-UA, AP-MM, and AP-AP (Figure 4b-2).

For systems S0–S3, the first shell CNs for UA-UA interactions are considered first. It can be seen that the CNs of UA around UA are 2.07, 1.69, 1.46, and 1.24 for systems S0, S1, S2, and S3, respectively. Thus, with the increase of AP from system S0–S3, UA's CN around UA is decreased. Furthermore, the CN of the same for system S3 is reduced significantly to 1.24. Such a decrease in CN value indicates that the assembly process alters among UA molecules in a higher AP in system S3. It is to be noted that the change in the volumes is negligible as one moves from system S0 to system S3, which further suggests a minimal effect of volume change in the "CN" values. In the case of UA-MM interaction, an intriguing scenario can be seen, in where, the CNs for MM around UA are decreased when AP molecules are introduced with an increasing manner of concentrations from system S0 to system S3. The CN for MM around UA in system S0 is 0.68, which is reduced to 0.29 in system S3. Furthermore, the CN of MM around MM decreases from 0.14 (in system S0) to 0.04 (in system S3). It indicates that AP interacts concurrently with the two molecules, i.e., MM and UA, thus interrupting UA-MM interaction and their self-aggregation process. However, the decrease in CNs for UA-MM interaction is prominent. AP disrupts the UA-aggregation (as indicated by CN of UA around UA), which reduces MM's small aggregated UA cluster (discussed later). Not only that but also with

the help of AP, the MM-MM interaction is reduced, thus, prevent from producing kidney stones. This concurrent AP-UA-MM communication can also be viewed concerning the CNs' estimation for MM-AP and UA-AP pairs. The CN of AP around UA is 0.45 for system S0, which is 1.84 for system S3.

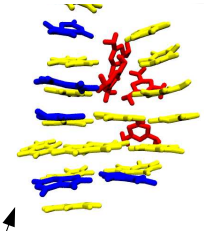

System (Conc. of AP (M))	UA around UA	MM around UA	MM around MM	AP around UA	AP around MM	AP around AP
S0 (0.0447)	2.07	0.68	0.14	0.45	0.35	0.18
S0-a (0.0446)	2.04	0.65	0.14	0.46	0.31	0.15
S1 (0.0893)	1.69	0.53	0.12	0.95	0.59	0.82
S2 (0.1774)	1.46	0.32	0.06	1.53	1.03	1.12
S3 (0.2635)	1.24	0.29	0.04	1.84	1.35	1.57
S3-a (0.2634)	1.24	0.29	0.04	1.81	1.34	1.58

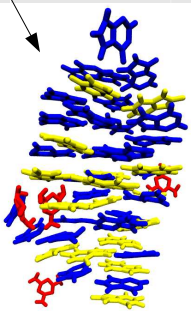

Figure 4b-2. *First shell coordination numbers of UA around UA (r_c=6 Å), MM around UA (r_c=7 Å), MM around MM (r_c=5 Å), AP around UA (r_c=5.95 Å), AP around MM ((r_c=6.95 Å), and AP around AP (r_c=6 Å) for different systems. Here, r_c depicts the first minimum of the respective radial distribution functions considering the center of mass (COM) of each molecule (not shown). Standard errors of all data points (calculated using the block average method) fall within ± 0.03. Here, the AP concentration in each system is presented to better understand the effect of AP on agglomeration. Snapshots (in which UA, AP, and MM molecules depicted in yellow, blue, and red in color, respectively) for systems (i.e., systems S0 and S3) are also presented.*

Therefore, higher the number of AP present in a system, the more likely the commu-

nication between UA and AP is. Similarly, as one moves from system S0 to system S3, the CN of AP around MM is also increased from 0.35 to 1.35. Such an increase in the CN values of AP around both MM and UA molecules suggests that AP interacts with UA and MM, resulting in the accumulation of AP surrounding UA and MM to protect both their self-assembly and inter-accumulation. It is interesting to note that AP tends to self accumulates too. In system S0, the AP's CN around AP is 0.18, which is increased to 1.57 in system S3. Therefore, close accumulation of AP around UA and MM increases the CN of AP around AP also.

Above all, the results of the systems S0 and S3 in the NVT ensemble resemble that of the NPT ensemble for systems S0-a and S3-a in the present study. Though in principle, the aggregation properties can be dependent on the choice of thermodynamic ensembles.[258] In (Figure 4b-2), the CNs of system S0 (in NVT ensemble) is compared with that of S0-a (in NPT ensemble), and similarly, the CNs of systems S3 (in NVT ensemble) and S3-a (in NPT ensemble) are compared. The very similar CN values of systems S0 and S0-a and S3 and S3-a reveal that a different initial configuration with various ensembles produces identical and comparable results. Therefore, a conclusion can be drawn that the CN values for all interactions considered here are similar for these two ensembles chosen. Thus, the present results that are presented here are very robust.

Spatial density plots

This section discusses the spatial density distributions for different interactions such as UA-UA, UA-AP, UA-MM, AP-MM, MM-MM, and AP-AP. In Figure 4b-3, for systems S0 and S3, UA's spatial density distributions around a reference UA are presented. Last 20 ns of MD simulation trajectory files are used to determine these density distributions.[281, 158] It can be seen that the density distribution of UA around a reference UA is decreased from system S0 to S3. Note that a few AP molecules are accessible in system S0. This suggests that UA-UA interaction is prevailing in the presence of a very small AP (in system S0). However, UA-UA interactions are considerably hindered in the presence of a higher number of AP molecules (in system S3). AP, accordingly, restrains the aggregation of UA-UA, keeping it from framing an enormous self-aggregated structure. Also, AP density around a reference UA is enhanced from system S0 to S3 (Figure 4b-3 (c) and (d)). As the density of AP around UA is increased and as a result of such an increase, the density of MM around a reference UA is decreased along with the depletion of UA-UA self-accumulation (Figure 4b-

3 (e) and (f)). Not just that, but the density of AP is likewise increased around a reference MM (Figure 4b-3 (g) and (h)). In this way, a considerable AP accumulation around both molecules, specifically MM and UA, actuates an interruption in the higher-order clusters, including MM and UA molecules, which, therefore, transforms into lower-order clusters (discussed later). It is currently evident that MM-UA composite's dismantling is essential to disassemble the improvement of more giant kidney stones. The importance of a third molecule in the degradation of the Mel-UA cluster is, therefore, peremptory.

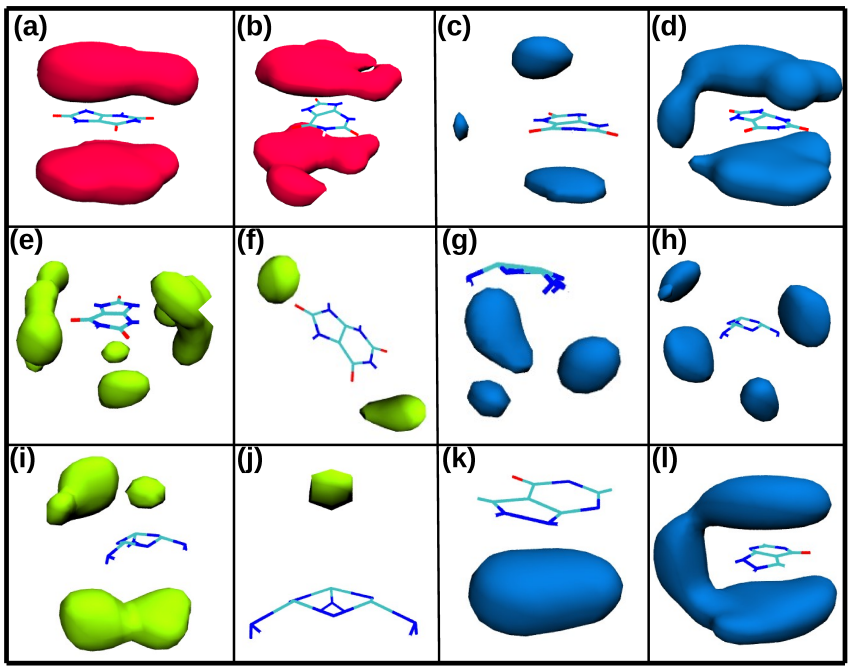

Figure 4b-3. *(a)–(b) Spatial density distributions of UA around a reference UA (with isovalue of 2 $Å^{-3}$) in system S0 and system S3, respectively. (c)–(d) Spatial density distributions of AP around a reference UA (with isovalue of 2 $Å^{-3}$) in system S0 and system S3, respectively. (e)–(f) Spatial density distributions of MM around a reference UA (with isovalue of 2 $Å^{-3}$) in system S0 and system S3, respectively. (g)–(h) Spatial density distributions of AP around a reference MM (with isovalue of 2 $Å^{-3}$) in system S0 and system S3, respectively. (i)–(j) Spatial density distributions of MM around a reference MM (with isovalue of 1 $Å^{-3}$) in system S0 and system S3, respectively. (k)–(l) Spatial density distributions of AP around a reference AP (with isovalue of 2 $Å^{-3}$) in system S0 and system S3, respectively.*

The third molecule must be bound with either MM or UA or both to disrupt the renal stones. However, the spatial density of MM around a reference MM is also determined,

and it is seen that MM density is decreased around a reference MM in system S3 due to an increase in the concentration of AP (Figure 4b-3 (i) and (j)). Therefore, it is confirmed by the SDF calculation that the higher number of AP well surrounds UA and MM. It is interesting to note that AP molecules tend to self-accumulate also as indicated by the somewhat increase of AP around a reference AP when the number of AP is high (Figure 4b-3 (k) and (l)), though the accumulation is not significant.

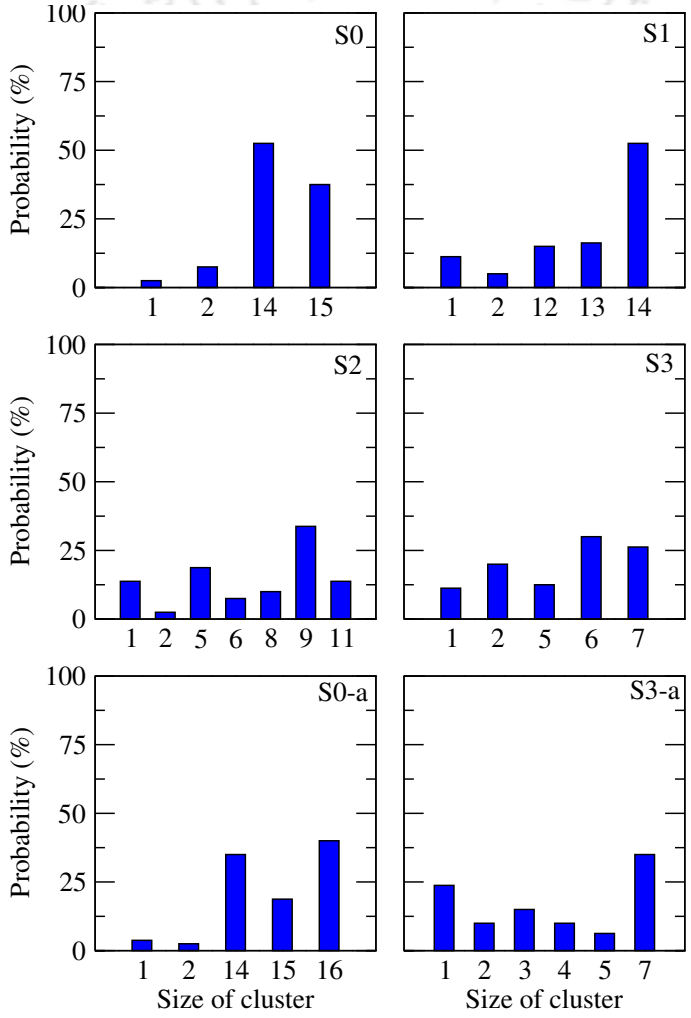

Figure 4b-4. *The probability of maximum sizes of the UA-UA clusters for the last 20 ns out of total 200 ns for systems S0—S3. It is to be noted that the system S0-a and S3-a present the results that are calculated from NPT ensemble.*

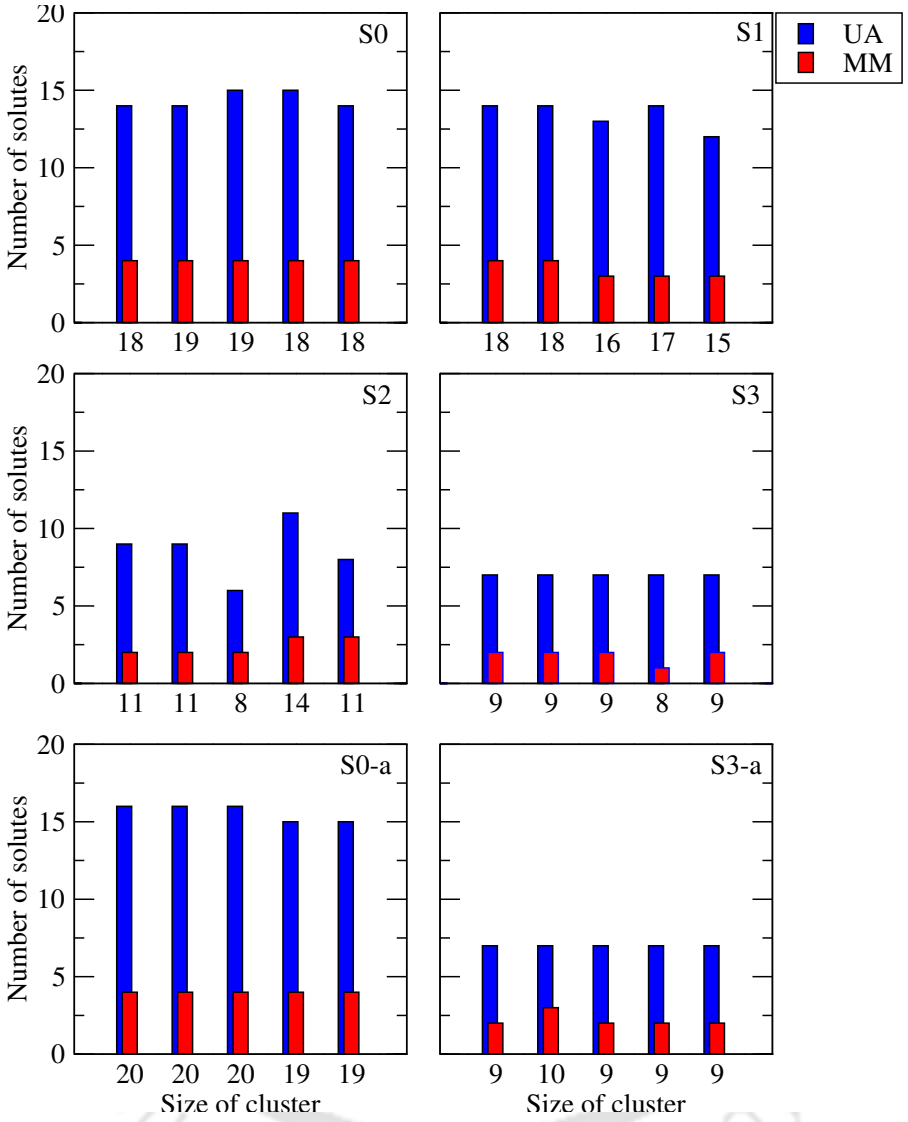

Figure 4b-5. *The distributions of clusters of various sizes resulting from MM-UA interactions for systems S0–S3 for the last 20 ns out of total 200 ns at each 4 ns time interval. Here, NPT and NVT ensemble produce similar results which can be compared for systems S0, S0-a, S3, and S3-a.*

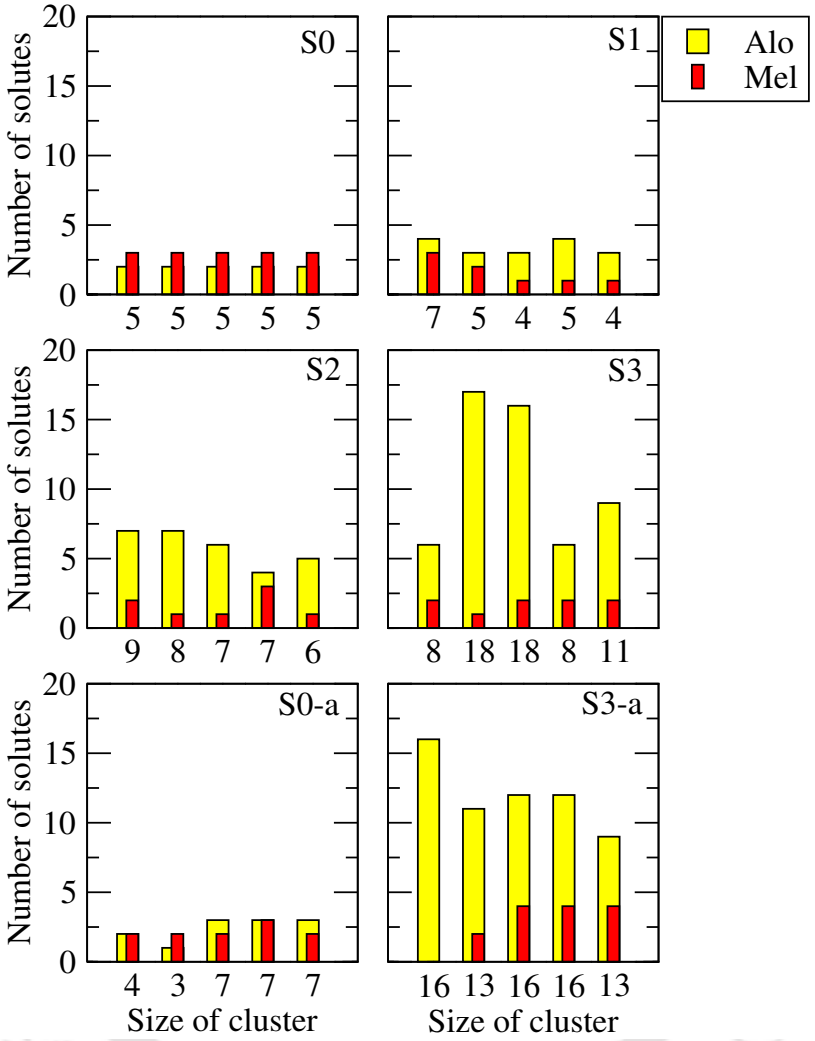

Figure 4b-6. *Distributions of clusters of various sizes resulting from AP-MM interaction for systems S0–S3 for the last 20 ns out of total 200 ns at each 4 ns interval. Here, systems S0-a and S3-a represent the results calculated from NPT ensemble. It is interesting to note that NPT and NVT ensemble simulation results are closely resembled.*

Cluster structure analysis

This portion explores how various interacting molecules, such as MM, UA or AP, produce different size clusters. The assessment of different size clusters or changes in the size of the clusters is important to establish the effect of AP on the UA-UA and UA-MM

 Now, to determine the UA-UA cluster size, a similar systematic approach

is taken here into consideration following our previous study[207, 282] in which two UA molecules can make a cluster called dimer, only when they are attached either by hydrogen bonding or π-stacking. Similarly, when 3 UA molecules come close and associate either by making hydrogen bonding interaction or π-stacking, then a trimer is formed. An exactly same definition also goes for the higher order clusters for UA molecules. Moreover, for AP-AP and AP-UA, the cluster structure definition also follows the same interpretation. However, in case of UA-MM, MM-MM, and AP-MM, the combination of "direct" and "in-direct" approach[207, 282] is taken together and to do so only hydrogen bonding interaction between them is taken as a criterion to follow. Moreover, for all types of interactions, a definite distance criterion is considered and the same is as follows:

1. r_{COM}^{UA}—$r_{COM}^{UA} \leqslant 6$ Å
2. r_{COM}^{UA}—$r_{COM}^{AP} \leqslant 5.95$ Å
3. r_{COM}^{AP}—$r_{COM}^{AP} \leqslant 6$ Å
4. r_{COM}^{UA}—$r_{COM}^{MM} \leqslant 7$ Å
5. r_{COM}^{MM}—$r_{COM}^{MM} \leqslant 5$ Å
6. r_{COM}^{AP}—$r_{COM}^{MM} \leqslant 6.95$ Å

Cluster formed by UA-UA interaction is taken first in this section (Figure 4b-4). It can be seen that as one moves from systems S0 to S3, the higher order clusters are transformed into lower order clusters. In system S0, larger clusters is formed due to UA self-assembly wherein 15 UA molecules come close to form a giant cluster. However, in system S3, maximum heptamer (i.e., 7 UA molecules are closely associated to form UA cluster) can be found along with higher percentage of monomer and dimers in comparison of S0. Thus, as the concentration of AP is increased, UA-UA self-association is reduced significantly. Moreover, NVT and NPT simulation produce similar results which further confirms the robustness of the simulations presented here (Figure 4b-4).

A similar finding can also be observed in case of UA-MM cluster size (Figure 4b-5). One can easily see that in system S0, the size of total cluster made of UA-MM is higher in which almost 14 to 15 UA molecules bind to all four MM molecules. However, in system S3, seven UA molecules bind with maximum two MM molecules which, thus, results in lowering maximum cluster size. Therefore, it is evident that AP can effectively reduce MM-UA cluster size. Now, the question is whether the reduction in UA-MM cluster size is due to lowering of UA-UA cluster or for the reducing of MM-AP interaction which can

also play an crucial role. Therefore, it will be wise to check MM-AP cluster size to make conclusion.

Cluster structure analysis for controlled systems

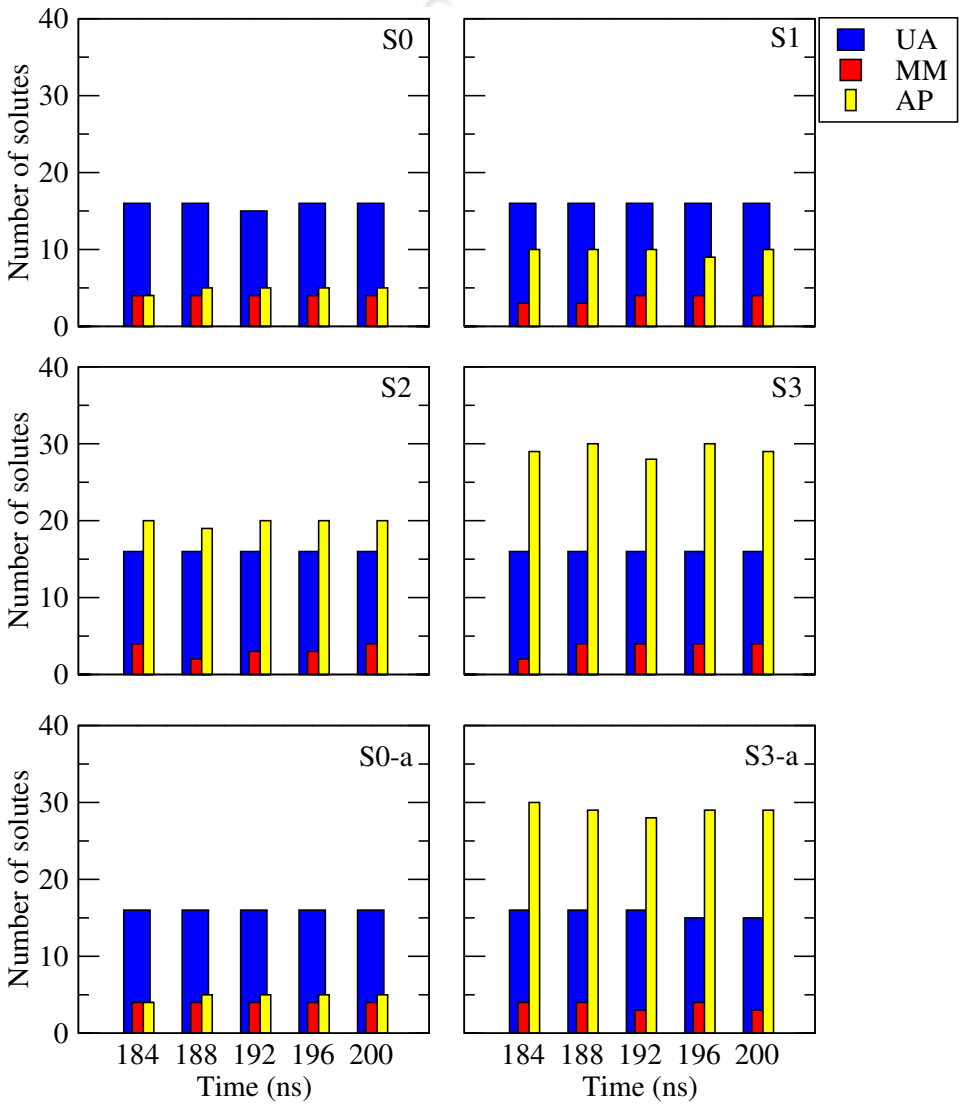

Figure 4b-7. *The maximum sizes of the MM-UA-AP clusters for the last 20 ns out of total 200 ns at each 4 ns interval for systems S0-S3.*

From the (Figure 4b-6), it is evident that AP is attracting MM but not like UA. It can be easily seen that the overall cluster size for MM-AP interaction is not so high as compared to UA-MM. Thus, MM shows considerable inclination towards AP, however, the interaction is much smaller in comparison to that of UA-MM clusterization. Therefore, it will be safe

to say that a moderate but not significant attraction between AP-MM is present which can help somewhat to prevent the UA-MM aggregation. Moreover, breaking of UA-UA cluster by AP predominates over AP-MM interaction through AP-UP interaction. To check the AP-UP interaction, total AP-UA-MM cluster size (which is calculated by the summation of number of AP, MM and UA attached by direct and indirect approach) is determined and it is seen as the number of AP is increased, most of the AP is now interacting with all UA which enables UA-UA disassembly to produce discrete UA-MM clusters (Figure 4b-7).

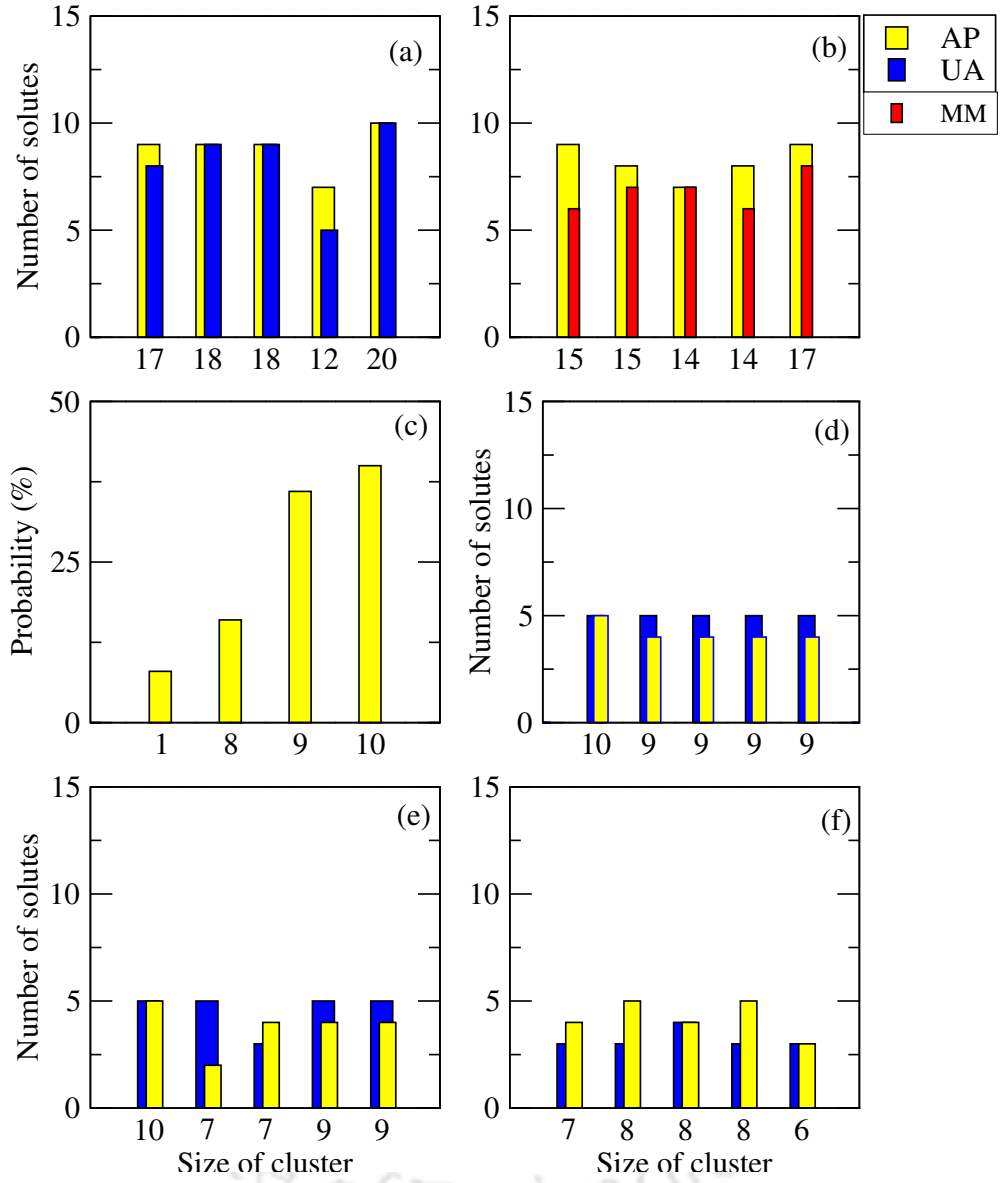

Figure 4b-8. *(a) represents the maximum sizes of the UA-AP clusters for system S4, (b) represents the maximum sizes of the AP-MM clusters for system S5, (c) represents the maximum sizes of the AP-AP clusters for system S6, (d)-(f) represents the maximum sizes of the UA-AP clusters for system S7–S9, respectively. Here the cluster structure is determined for last 20 ns out of total 200 ns at each 4 ns interval.*

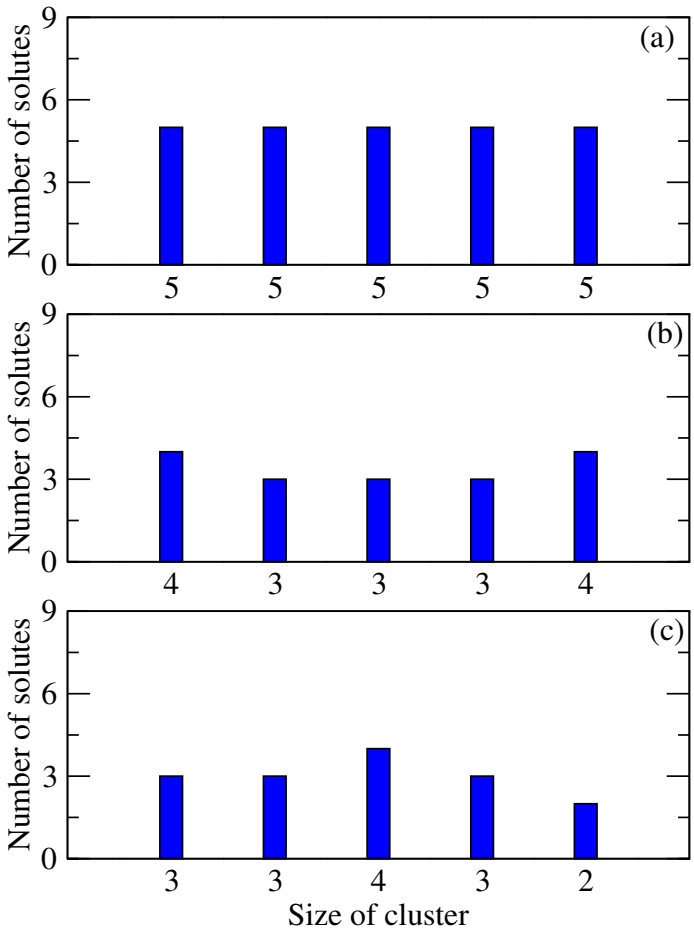

Figure 4b-9. *(a)–(c) presents the maximum sizes of the UA-UA clusters for last 20 ns out of total 200 ns at each 4 ns interval for systems S7, S8, and S9, respectively.*

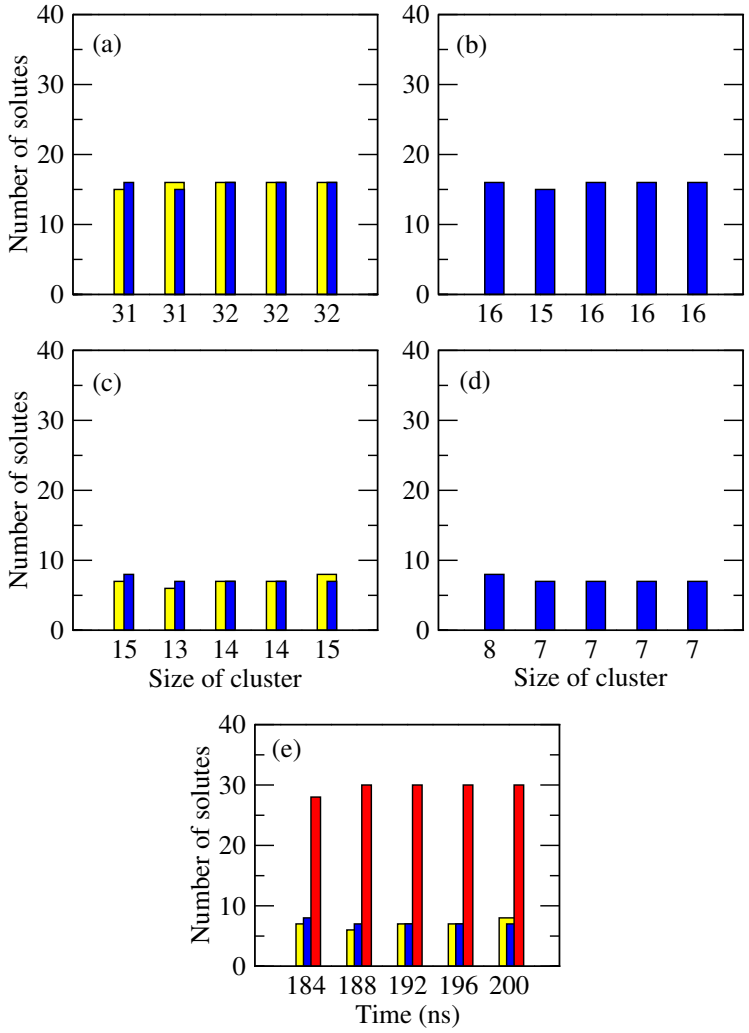

Figure 4b-10. *(a) represents the maximum sizes of the UA (blue)-MM (yellow) clusters for system S10 for last 20 ns out of total 200 ns at each 4 ns interval, (b) represents the maximum sizes of the UA-UA clusters for system S10 for last 20 ns out of total 200 ns, (c) represents the maximum sizes of the UA-MM clusters for system S11 for last 20 ns out of total 200 ns at each 4 ns interval, (d) represents the maximum sizes of the UA-UA clusters for system S11 for last 20 ns out of total 200 ns, and (e) represents the maximum sizes of the UA (blue)-MM (yellow)-AP (red) clusters for system S11 for last 20 ns out of total 200 ns at each 4 ns interval.*

Now, we have determined the cluster structure for controlled systems too. Firstly, the cluster structure for AP-UA is determined for system S4 (Figure 4b-8(a)). Here, we can

see the similar phenomenon in which AP-UA interaction is quite strong. Almost 9 to 10 UA molecules attach with 9 to 10 number of AP molecules. Next, we have determined that AP-MM cluster size for system S5. In this case, it is noticed that AP-MM is strong in the absence of UA. Around 7 to 8 MM molecules interact with 8 to 9 AP molecules (Figure 4b-8(b)). Next, a system with only AP is taken to see how it aggregates for system S6. We found that AP is a quite strong aggregating agent as the percentage of higher order cluster is high (Figure 4b-8(c)). Therefore, when we compare system S4 and system S6, we can see that in absence of UA, AP makes higher order cluster, however, in presence of UA, it is very prone to interact with UA (Figure 4b-8(a) and (c)). Now, a few more controlled systems are made keeping in mind the π-stacking nature either of AP or UA. First of all, we have made one system in which initially stacked AP and stacked UA is taken, and after that, followed by 5 ns equilibration run, an 80 ns MD production run is performed, releasing UA keeping AP in a stacked position. After 80 ns, a further 120ns NVT run is done releasing all molecules for system S7. It is found that after releasing them, AP and UA are making strong interaction (Figure 4b-8(d)). Mostly, all UA and AP molecules are now interacting togetherly. Therefore, UA and AP molecules are very prone to interact with themselves rather than self-aggregation. Similarly, when AP is released after equillibrium keeping UA in stacked position upto 80 ns and thereafter releasing all molecules for system S8 give similar result for AP-UA as that of system S7 (Figure 4b-8(e)). Another approach is made in which randomly AP is taken with initially stacked UA and after equlllibrium all are released for system S9. It is found that AP-UA interaction is quite strong here too (Figure 4b-8(f)). It is to be noted that for UA-AP cluster size determination, the total number of UA and AP molecules are taken into consideration by taking direct and indirect approach. For these all systems from S7–S9, we have also calculated the UA-UA self-assembly (which is determined by the number of UA molecules that are attached to each other directly). It is found that initially released AP molecules produce maximum trimer for self-assembly for systems S8 and S9 except S7 in where AP molecules are released after quite sometime. Therefore, the pentamer, which forms in system S7 for UA self-assembly, is now reduced to trimer in systems S8 and S9 by the presence of randomly placed AP after equilibration. The Figure 4b-9(a)–(c) represent the exact scenario. Thus, AP is quite prone to interact with UA which therefore enables UA to disintegrate onto lower order cluster.

Next, we have considered more two systems i.e., systems S10 and S11. In system S10, first MM and UA molecules are closely attached to each other (Figure 4b-10(a)).

These MM and UA molecules form cluster by direct as well as indirect approach. However, if we look into the UA self-assembly only for system S10, then it can be observed that all UA molecules come together to form a giant cluster which drags almost all MM molecules to add to it (Figure 4b-10(b)). Therefore, in the absence of AP, MM-UA aggregation is quite strong. Now, in case of system S11, the MM-UA cluster size is reduced significantly (Figure 4b-10(c)), whereas, UA-UA self-aggregated cluster size is also hindered to form large cluster (Figure 4b-10(d)). Therefore, AP inhibits UA-UA self-assembly which, thus, causes less aggregation between MM and UA. As a result, the growth of kidney stone is hampered. Moreover, the attraction of AP towards UA and MM cluster can be seen in Figure 4b-10(e). Almost, all AP bind to them to form AP-MM-UA conjugate which in turn degrade the UA self-assembly.

Dimer existence autocorrelation functions

In this section, dimers' stability involving different solution species in the presence and absence of AP is determined. To do so, the dimer existence autocorrelation function (DACF) is evaluated by the use of the following equations:[158]

$$DACF(\tau) = N. < \sum_{t=0}^{T-\tau} \beta_{ij}(t+\tau).\beta_{ij}(t) >_{ij} \tag{4.21}$$

Here, DACF is considered autocorrelation of a simple function, β_{ij}, for the pair of molecules say, i and j, that can have value 1 when maintaining a preset distance criterion, and it goes to zero if the distance criterion is lost for the first time.[158] It is worth noting that, even if the criterion of distance is met later, DACF will remain zero. The total DACF is the average over all different pairs i,j. As per the description, DACFs start with the value 1 and then decline to 0 with increasing τ. The statement included in the resulting function DACF(τ) is as follows: "How large is the probability of the criteria still fulfilled (without interruption) at a given time τ when they were fulfilled at time 0?" It is to be noted here that we have considered only two systems to provide the dynamic nature of all kinds of dimers in two extreme conditions. Figure 4b-11 (a) depicts the DACFs for the dimer formed by the interaction between two UA molecules in systems S0 and S3 (i.e., in the presence and absence of AP, respectively). The DACF for UA-UA interaction is higher in system S0 than system S3. In this context, we have chosen a distance of 6.0 Å as a distance criterion, which comes from the COM-COM rdf of these two molecules (i.e., UA

and UA). Therefore, UA-UA dimer formation, i.e., aggregation, is lowered immensely by the presence of AP in system S3. The inhibition of the self-aggregation of UA molecules only can take place in the presence of AP if AP interacts significantly with UA molecules in system S3. The exact nature of AP molecules' inhibition can be found in Figure 4b-11 (b), in which DACF for UA-AP interaction (in system S3) is significantly increased. Thus, it is confirmed that AP is prone to interact with UA molecules.

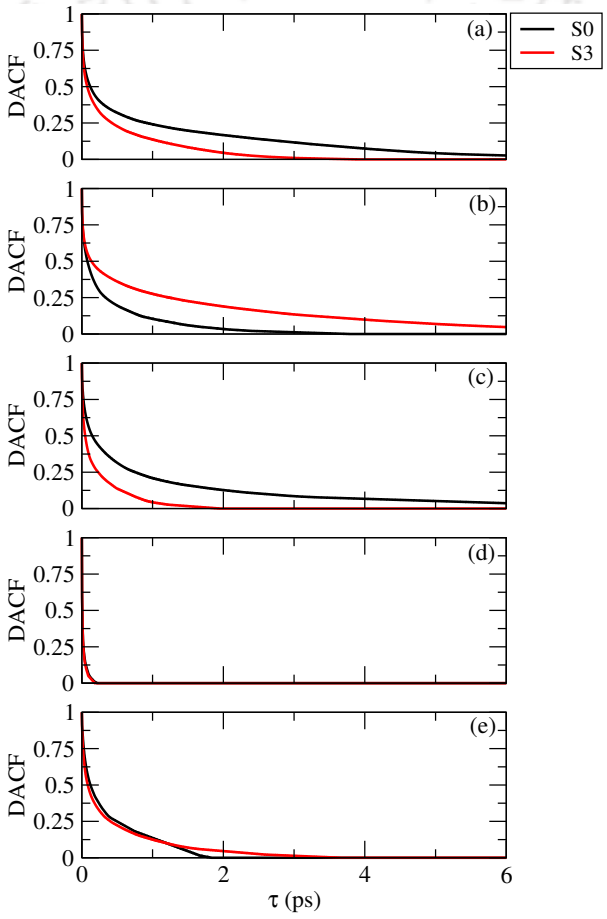

Figure 4b-11. *Dimer existence autocorrelation functions (DACFs) for (a) UA-UA for systems S0 (black) and S3 (red), with a distance of 6.0 Å , (b) UA-AP for systems S0 (black) and S3 (red), with a distance of 5.95 Å , (c) UA-MM for for systems S0 (black) and S3 (red), with a distance of 7 Å , (d) MM-MM for systems S0 (black) and S3 (red), with a distance of 5 Å , (e) MM-AP for systems S0 (black) and S3 (red), with a distance of 6.95 Å .*

In system S0, though, the AP number is lower; however, a somewhat lower interaction can also be observed. Furthermore, this weak interaction is greatly improved when AP is present in a

higher number and effectively inhibits the UA-UA aggregation. Next, DACF is determined for UA-MM interaction, and it is found that UA-MM interaction is inhibited in system S3 (Figure 4b-11 (c)). Therefore, AP can be considered as a potent inhibitor as it can significantly reduce UA-MM interaction. Now, if we look into the MM-MM interaction, then it is evident that this interaction is very week in both the systems S0 and S3 (Figure 4b-11 (d)). Therefore, MM-MM interaction cannot be the case behind the reduction of UA-MM dimer formation. The MM-AP interaction plays a significant role in the interruption of UA-MM interaction as MM-AP interaction is much improved in system S3 (Figure 4b-11 (e)). As a combination of MM-AP interaction along with strong UA-AP interaction, UA-MM dimer formation is weakened. This is what is needed to disrupt kidney stone formation. Thus, AP does not only inhibits the UA-MM aggregation but also interrupts the self-aggregating of UA-UA and MM-MM pairs.

Effect of UA cluster size on Mel-UA aggregation

In this section, we include an overview of how different sizes of UA clusters influence the MM-UA aggregation. An observation of the composition of the clusters illustrates (discussed above) that the prevalence of AP molecules induces a substantive change of the MM-UA cluster. Now to support this fact, here, we have derived the effect of UA cluster size on UA-MM aggregation by means of preferential interaction parameter (Γ_{mu}) and the potentials of mean force, W(r).

The determination of cluster structure analysis indicates that in system S0, most UA molecules (i.e., 15 UA molecules) form a more significant size cluster. In contrast, in system S3, the occurrence of a maximum of heptamer can be achieved as inhibitor AP's presence perturbs the aggregation of UA. Therefore, it will be interesting to see the interaction pattern between MM and different sizes of UA clusters. We intend is to examine the change of interaction in MM-$(UA)_{15}$ and MM-$(UA)_7$. Thus, the prediction of the preferential interaction parameter between MM-$(UA)_{15}$ and MM-$(UA)_7$ would be sufficient to judge the effect of the presence of AP. Figure 4b-12 displays the preferential interaction parameters for MM-$(UA)_{15}$ and MM-$(UA)_7$. The result presented in Figure 4b-12 demonstrates that MM-$(UA)_{15}$ is more potent than MM-$(UA)_7$. Thus, the effect of cluster size on UA on MM aggregation is evident. Therefore, the larger the cluster size more is the UA-MM interaction. Here, the presence of AP results in the lowering of UA cluster size, which in turn weakens the UA-MM interaction to form a large kidney stone. To explore more about

the aforementioned occurrence, the potentials of mean forces, W(r), as a function of COM-COM distance between MM and UA, r, are determined by using the equation:[283, 284]

$$W(r) = -k_B T ln\, g_{mn}(r) \tag{4.22}$$

where k_B and T are the Boltzmann constant and absolute temperature, respectively, and $g_{mn}(r)$ is the pair distribution function between MM and UA. Figure 4b-13 shows that W(r) for MM-$(UA)_{15}$ in system S0 is energetically more favorable. In contrast, the cluster size is reduced in system S3 due to AP's presence. The contact minimum between MM-$(UA)_7$ gets energetically unfavorable, thus clearly predicting that the aggregation tendency gets lowered between UA and MM when UA's cluster size receives reduced. It is to be noted that in Figure 4b-12 and Figure 4b-13, $(UA)_{16}$ presents all UA molecules considered in system S3. This shows that overall UA molecules in system S3 are more attractive towards MM than the discrete $(UA)_7$-MM interaction. Thus, UA's heptamer drags less MM towards themselves, which is much lower than all UA molecules, and the following trend goes as per expectation.

Moreover, to prove the fact mentioned above, we have prepared two more systems, i.e., system U5M1 and U10M1 (Table 4b-1). The cluster structure for UA-MM interaction for these two systems is predicted. In system U5M1, the overall cluster size for UA-MM interaction is 2 with no MM present in that cluster except UA molecules, whereas the cluster's maximum size for the same interaction is 11 (which contains 10 UA and 1 MM molecules) in system U10M1 (Figure 4b-14). Therefore, it is observed that the large UA attracts the single MM molecule present in the system U10M1. However, the single MM molecules are not dragged by the UA dimer present in system U5M1.

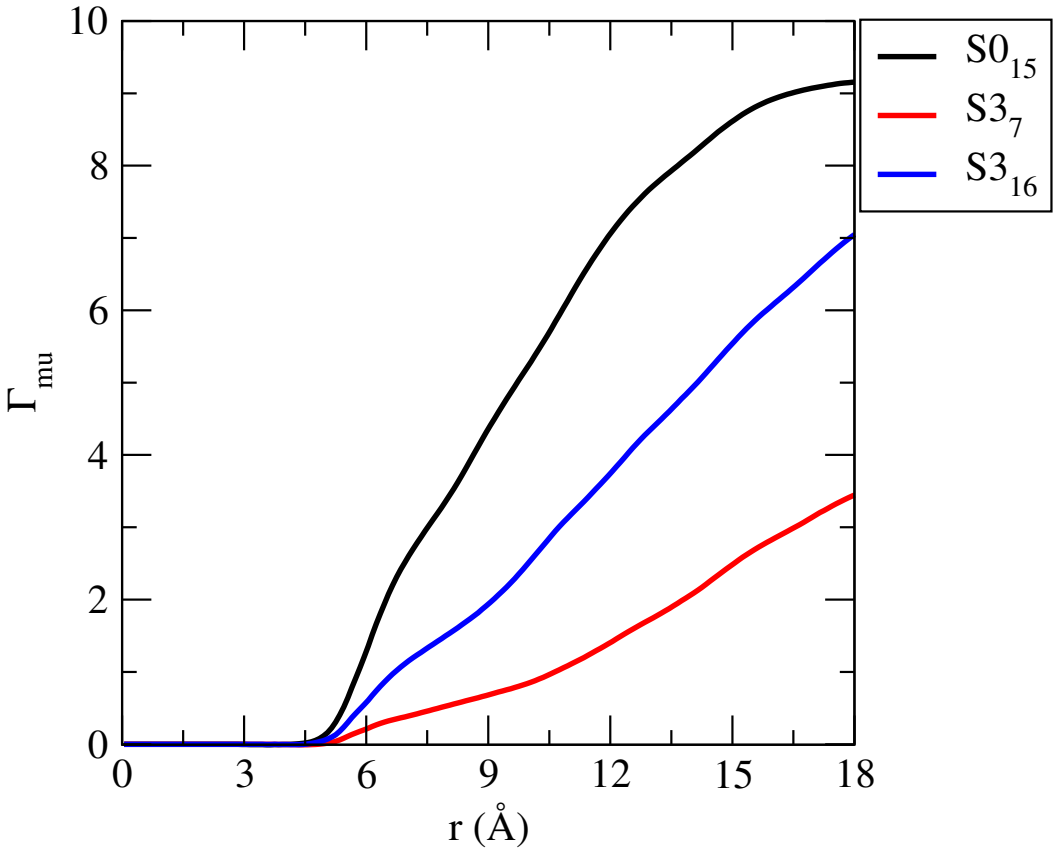

Figure 4b-12. *Preferential interaction parameters for $(UA)_{15}$-MM interaction in system S0, $(UA)_7$-MM interaction in system S3, and $(UA)_{16}$-MM interaction in system S3. Here, $(UA)_{16}$ presents all UA molecules in system S3.*

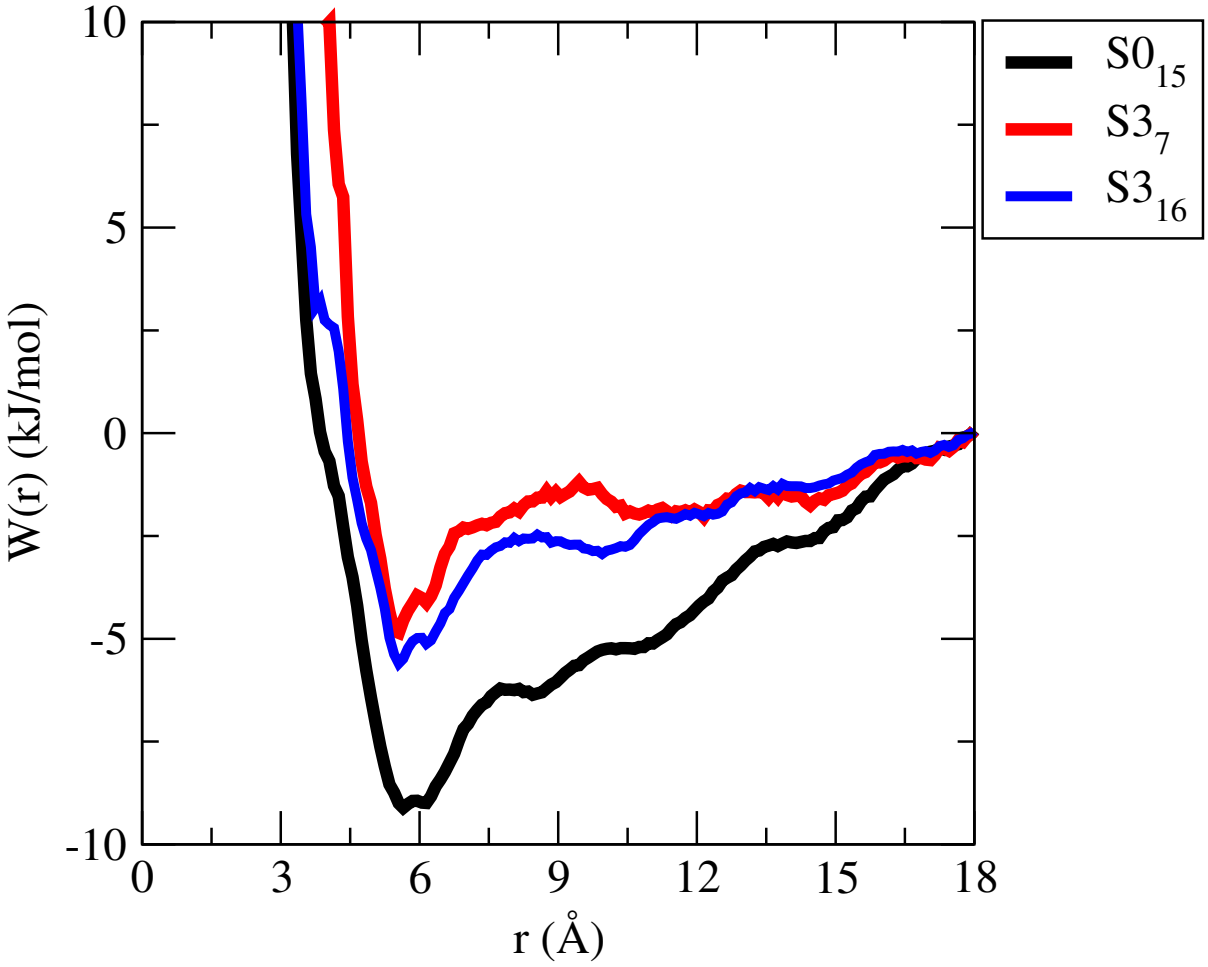

Figure 4b-13. *Potential of mean forces (W(r)) for the $(UA)_{15}$-MM, $(UA)_{7}$-MM, and $(UA)_{16}$-MM for systems S0 and S3.*

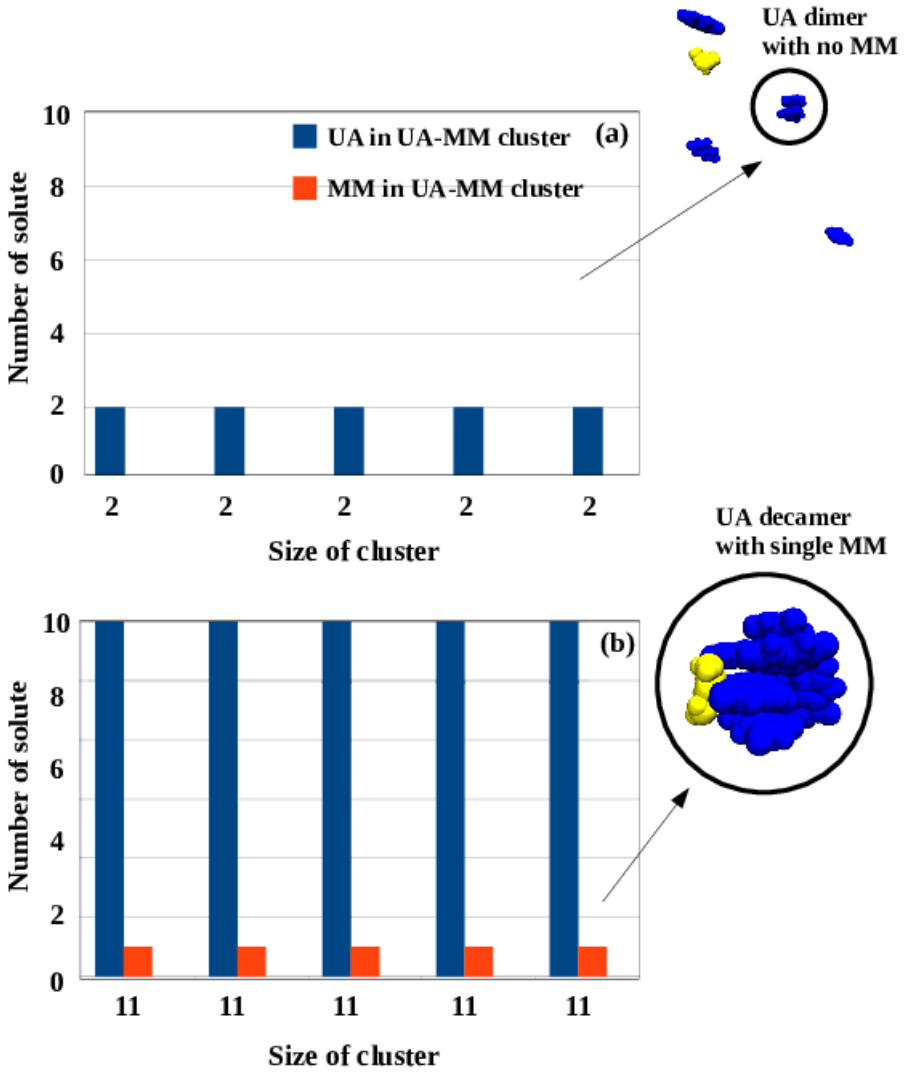

Figure 4b-14. *The overall cluster size for the interaction between UA and MM in systems (a) U5M1 and (b) U10M1. Here,the cluster sizes are given for last 20 ns out of total 200 ns at each 4 ns interval. In each system, representative snapshots are presented. Here, UA molecules are shown in blue color and MM molecule is shown in yellow color.*

Free Energy Landscape (FEL)

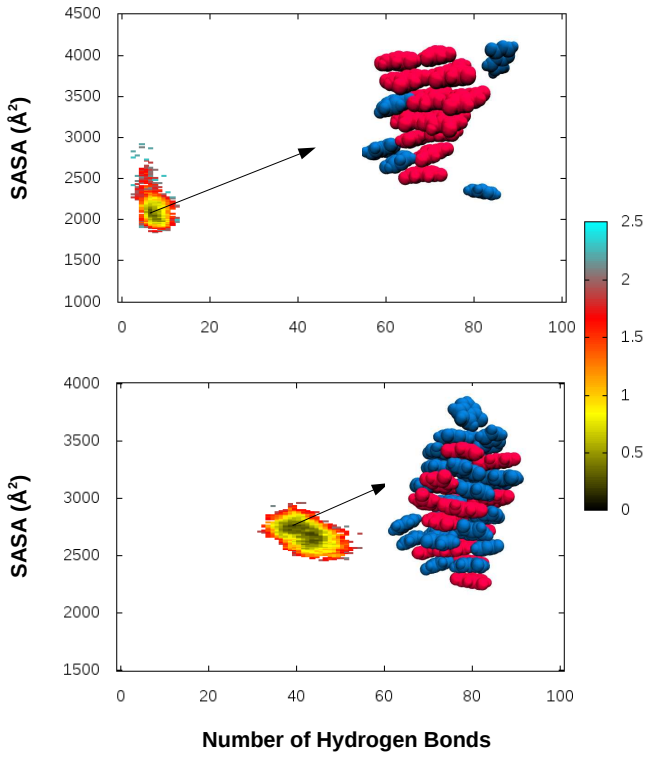

Figure 4b-15. *Free energy landscape (SASA (Å^2) for UA-UA pair vs number of hydrogen bonds between UA-AP pair) for systems S0 (top panel) and S3 (bottom panel). Simulation snapshots of these systems are also attached with the corresponding FELs where UA is represented in dark red and AP is presented by dark blue in color. Here, the side color bar represents the free energy in kcal/mol unit.*

To determine the free energy landscape (FEL) of UA-UA association, in various AP concentrations in water, two reaction coordinates, i.e., solvent accessible surface area (SASA) for UA-UA interaction and hydrogen bond between UA and AP, are chosen to describe the effect of AP on UA aggregation. The FEL is determined by using the following equation:[253]

$$\Delta G(V) = -k_B T[\ln P(V) - \ln P_{max}], \tag{4.23}$$

where P (V) portrays the probability of coordinate (V) calculated from the last 20 ns trajectory path, and it is deducted by P_{max}, which is the maximal distribution such that ΔG (V) gets zero for the minimum free energy. Figure 4b-15 (top panel) provides that the average intermolecular hydrogen bonding between UA and AP is small in the FEL. Again,

the SASA for the UA-UA aggregation in S0 is minimal. Therefore, a stronger UA-UA self-aggregation is proposed by the minimum free energy in system S0. Therefore, a smaller area is available for AP to counteract UA-UA self-aggregation. However, the greater SASA and very high hydrogen-bonding connections between AP and UA in system S3 produce minimal free energy, which implies that the UA-UA accumulation is lower in system S3 than in system S0 (bottom panel of Figure 4b-15). Thus, the presence of AP molecules in system S3 disrupts UA-UA aggregation by forming UA-AP hydrogen bonding (the exact number of average hydrogen bond numbers are discussed later).

WHY DO UA, MM, AND AP AGGREGATE?

Preferential interaction parameters

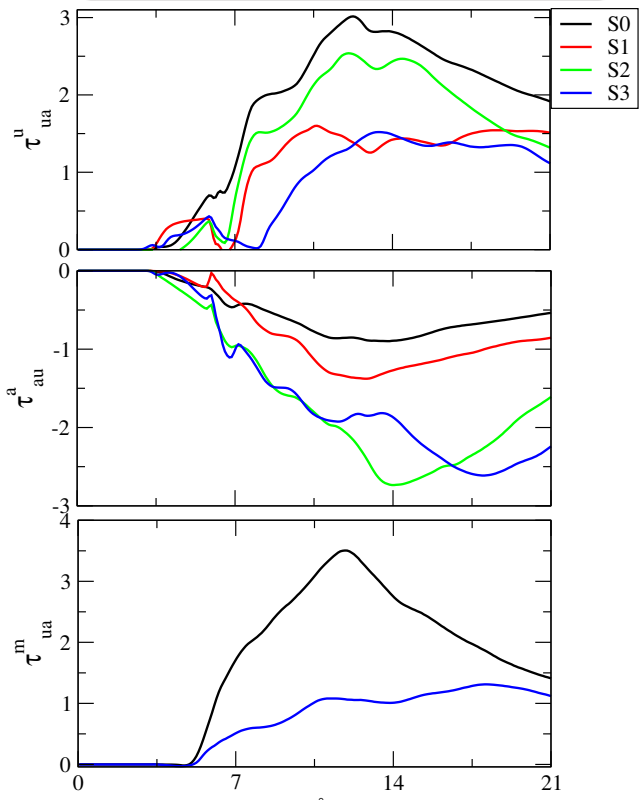

Figure 4b-16. *The preferential interaction parameters for UA-UA over UA-AP interaction (top panel), AP-AP over AP-UA interaction (middle panel), and MM-UA over MM-AP interaction (bottom panel) for respective systems.*

In the current study, the preferential interaction parameters, τ_{ua}^{u} (UA-UA over UA-AP), τ_{au}^{a} (AP-AP over AP-UA), and τ_{ua}^{m} (MM-UA over MM-AP) are determined, and these are generated for systems S0—S3 following the equations mentioned below:[282, 285, 194, 195, 196, 179, 286]

$$\tau_{ua}^{u} = \rho_u(G_{uu} - G_{ua}) \tag{4.24}$$

$$\tau_{au}^{a} = \rho_a(G_{aa} - G_{au}) \tag{4.25}$$

$$\tau_{ua}^{m} = \rho_u(G_{mu} - G_{ma}) \tag{4.26}$$

where a, m, and u denote AP, MM, and UA molecules, respectively; and ρ_u and ρ_a represent the number density of UA and AP molecules, respectively. The preferable interaction between any two molecules (say i and j) can be indicated with the higher positive value of τ than any other interactions. Here, G_{ua}, G_{uu}, G_{aa}, G_{mu}, G_{ma}, and G_{au} correspond to Kirkwood–Buff (KB) integrals, and these integrals can be accessed following earlier studies.[282, 285, 194, 195, 196, 179, 286] It ought to be referenced that these integrals can be accomplished with the accompanying radial distribution functions. The center of masses (COMs) of any two molecules are considered for appraising these distribution functions.

From systems S0 to S3, the number of AP increases. Therefore, if it is true that AP reduces the UA aggregation, then there should be the presence of higher UA-AP preferential interaction over UA-UA interaction, and such strong interaction could lead to massive destruction of UA aggregates. A similar phenomenon can be observed in Figure 4b-16 (top panel). Eq. 9 depicts the values of τ_{ua}^{u} for systems S0–S3. As the AP number is increased from systems S0-S3, the preferential interaction between AP and UA is also improved over UA-UA interaction. As a result, τ_{ua}^{u} tends to go towards zero. In system S3, AP molecules destruct the UA aggregation significantly and produce partial UA-UA self-aggregated clusters. It is interesting to note that AP is quite prone to interact with UA. Such a propensity for AP-UA interactions results in the lowering of UA clusters (discussed earlier). The determination of τ_{au}^{a} values show that AP prefers to interact with UA instead of themselves. Such AP-UA conjugation results in the replacement of UA molecules from their self-aggregated clusters (i.e., UA-UA clusters), and therefore, the continuity of UA-cluster formation gets interrupted. Figure 4b-16 (middle panel) shows that in system S3, AP-UA interaction is relatively high compared to AP-AP self-aggregation, thus disintegrating the UA self-accumulation to form UA-AP conjugate. Therefore, due to such preferential interaction, lower-order clusters of UA molecules are included in the presence of AP. Such

smaller clusters of UA drag a lower number of MM to form UA-MM conjugate in system S3 compared to system S0 (Figure 4b-16, (bottom panel)). As a consequence, the formation of kidney stones gets disrupted.

Hydrogen bond properties

For the systems considered in this study from S0 to S3, the average number of hydrogen bonds for several interactions is then determined, including UA-UA, UA-MM, MM-MM, UA-AP, MM-AP, AP-AP, and water-water (Ow-Ow) (Table 4b-2). The average number of UA-UA hydrogen bonds is shown to be decreasing between systems S0 to S3. From Table 4b-2, it can be seen that UA-UA interaction forms 16.55 number of hydrogen bonds in the presence of a small AP in system S0. As we move from S1 to S3, the average number of hydrogen bonds between UA and UA molecules is 15.57, 13.25, and 10.22, respectively. Thus, a substantial decrease in the number of hydrogen bonds is observed in the presence of AP. Now, if we look into the UA-MM hydrogen bond (H_{u-m}), it can be seen that as one moves from systems S0 to S3, there is also a decline in the number of hydrogen bonds. Therefore, UA continues to communicate with AP molecules instead of either itself or with MM with the rise in AP molecules. A typical pattern is identified when MM-MM hydrogen bonds are calculated for the S0–S3 systems. The hydrogen bond interactions between UA-UA, UA-MM, and MM-MM are significantly decreased as the number of AP molecules increases. However, the rise in AP concentration from system S1 to system S3 improves the hydrogen connections between UA-AP and MM-AP (Table 4b-2). The hydrogen bond numbers of AP-AP[287] also increase from S1–S3 systems. The water-water hydrogen binding (H_{w-w}) numbers have also been calculated to determine whether UA, AP, and MM molecules disrupt the bulk water structure. Since H_{w-w} remains unchanged in all systems (Table 4b-2), it can therefore be stated that the tetrahedral network of water is not perturbed at all. Furthermore, simulations of NPT and NVT ensembles give similar results for these two systems (S0-a and S3-a).

Table 4b-2. Average number of hydrogen bonds (total) involving all possible pairs for different systems. Here, the concentration of AP in each system is provided to better understand the effect of AP on agglomeration. Statistical uncertainties in the results are ±0.07 to ±0.47.

System (Conc. of AP (M))	H_{u-u}	H_{u-m}	H_{m-m}	H_{u-a}	H_{m-a}	H_{a-a}	H_{w-w}
S0 (0.0447)	16.55	12.09	2.04	7.24	1.03	0.18	3.69
S0-a (0.0446)	18.51	12.80	1.94	7.14	1.75	0.12	3.70
S1 (0.0893)	15.57	9.46	1.81	17.93	1.61	3.71	3.68
S2 (0.1774)	13.25	5.66	0.80	28.28	3.19	8.22	3.67
S3 (0.2635)	10.22	5.26	0.34	41.90	4.33	18.95	3.67
S3-a (0.2634)	9.48	5.88	0.25	36.22	5.43	16.67	3.68

To determine the number of hydrogen-bonds (discussed above) involved in all forms of connections, a series of criterion is used to describe the hydrogen bonds between the donor (D) and acceptor (A).[207, 253, 288, 289, 290] If the distance D-A $\leqslant$ 3.5 Å and, simultaneously, angle $\angle$ D-H$\cdots$ A $\geqslant 120^{\circ}$ are fulfilled, hydrogen bonding is then considered to be present.

π-stacking interaction and orientational preference

It is worth exploring whether π-stacking interactions in UA-UA, UA-AP, AP-AP, UA-MM, AP-MM, and MM-MM are taking place. This section explores the same where one might find how all interacting species communicate. Hence, in the presence and absence of AP molecules, their orientational preference should be reviewed for further analysis, and in this regard, we choose system S3. In deciding the orientation criterion, the angle between the vector normals of the molecular planes of any two interacting species is, therefore, taken into consideration. To determine the preferred orientation owing to their associations, the probability of orientation angles is estimated. An angle (θ) between two vector normals of two aromatic planes may be regarded for this purpose. The angle of such vector normals, either 0°-20° or 160°-180°, indicates the propensity for π-π stacking interactions between two molecules considered.[161] A specific distance criterion is also often needed next to the angle to determine whether two aromatic planes of two molecules communicate, as π-π stacking association is only possible if they are all achieved, namely angle and distance at

the same time. Then it can be inferred, in addition to the angle, that these two aromatic planes have strong associations with π-stacking interactions if the distance between two substances is less than 5 Å. In Figure 4b-17, θ is assessed against the distance between two normal vectors. The association between UA-UA is predominantly π-stacked with the maximum probability of angle 0°-20° (Figure 4b-17 (a)). A similar pattern can also be identified with the interaction of UA-AP (Figure 4b-17 (b)), and AP-AP[287] (Figure 4b-17 (c)) with a maximum angle is either at 0°-20° or 160°-180°. Nevertheless, the interactions between MM-UA (Figure 4b-17 (d)), AP-MM (Figure 4b-17 (e)), and MM-MM (Figure 4b-17 (f)) are primarily regulated by hydrogen bonding (the precise measurement of the hydrogen bond number is discussed above) with minimal π-π stacking involvement as the angle probability is high with a maximum of $\theta \approx$45°-135°. Apart from these angle requirements, distance is also assessed, and UA and AP molecules tend to keep between 3–5 Å distances in system S3 during their π-stacking interactions. In addition to the angle, thus, distance requirement is also established to maintaining effective π-π stacking of UA and AP molecules.

Now from the vector normal approach, it is not sufficient to claim the relationship between UA-MM, AP-MM, and MM-MM as hydrogen bondings at angles other than 0°-20° or 160°-180°. Another specific approach for such interactions is then proposed by considering two-point vector methods, thereby enabling us to conclude that hydrogen-bonding interactions are prevalent. In such a scenario, an angle is determined between the two vectors, connecting D (donor), H (hydrogen), and A (acceptor), and if the angle is 160°-180°, one may infer that perfect hydrogen bonds are formed between them. Figure 4b-18 indicates that all these interactions come within the scope of specific angles. Therefore, hydrogen bonding interactions are indeed maintained between them.

It is evident from the above discussions that the π-stacking interaction between UA-AP is significant. Therefore, communication between UA-UA in system S3 is now substituted by contact between UA and AP. The determination of the combined distribution function employing two separate rdfs will be conceivable to establish if the stacking interaction is adequate or not. In Figure 4b-19, for systems S2 and S3, two rdfs from two distinct distances are measured for UA-AP interaction. It is seen that at a certain point, these two rdfs firmly conjugate, which thus shows how intense the UA-AP association is (Figure 4b-19). Not just that, the estimation of the preferential interaction parameter is often regarded at various angles between the pair UA-AP with the other two pairs (UA-UA and AP-AP).

From Figure 4b-20, it can be seen that the preferential interaction between UA-UA, UA-AP, and AP-AP pairs at angle 0°-30° is higher than that of 30°-60° and 60°-90°. Here, the angles are measured between two vector normals of any two interacting aromatic rings. Thus, UA-AP, along with UA-UA and AP-AP interactions, are quite firmly attached at 0°-30° through efficient π-stacking. These intense interactions contribute to the alternation of the UA-UA self-assembly by the substitution of UA by AP to form UA-AP clusters in the process of inhibition.

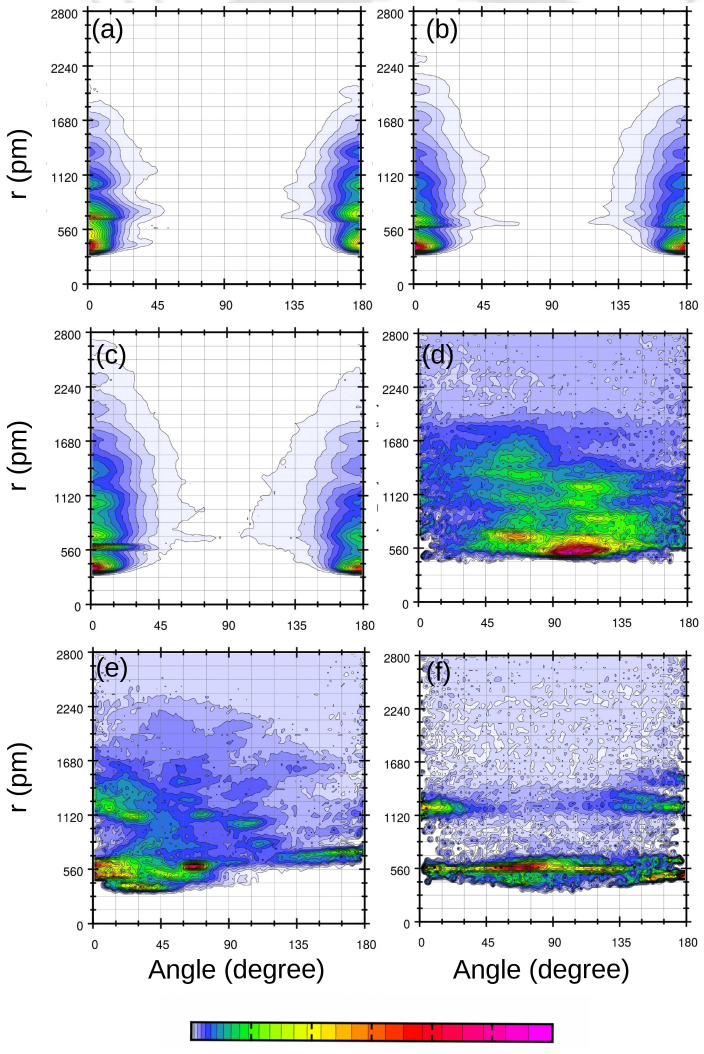

Figure 4b-17. *The distribution of angle between two vector normals of any two aromatic rings as a function of r (pm) for (a) UA-UA, (b) UA-AP, (c) AP-AP, (d) UA-MM, (e) AP-MM, and (f) MM-MM interactions for system S3.*

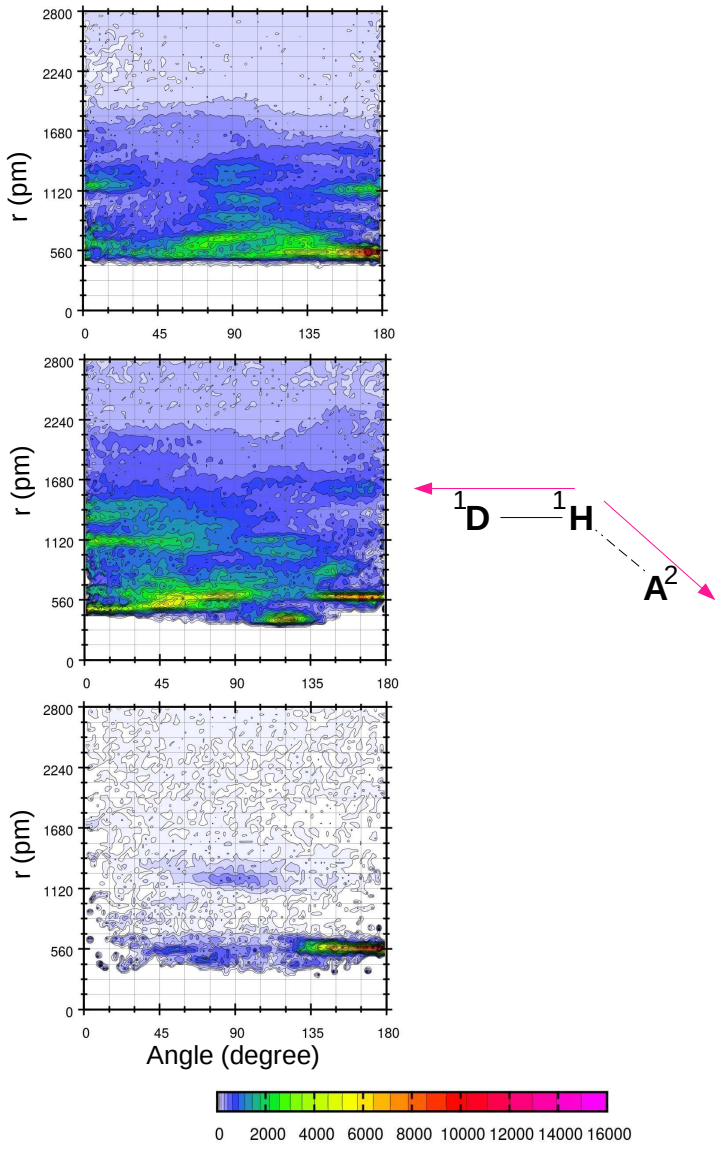

Figure 4b-18. *The distribution of angle considering two-point vectors of any two molecules as a function of r (pm) for (d) UA-MM, (e) AP-MM, and (f) MM-MM interactions for system S3. Here, one point vector is considered taking donor (D), and hydrogen (H) atoms of molecule-1, and the other point vector is taken considering hydrogen (H) atom of molecule-1 and acceptor (A) atom of molecule-2.*

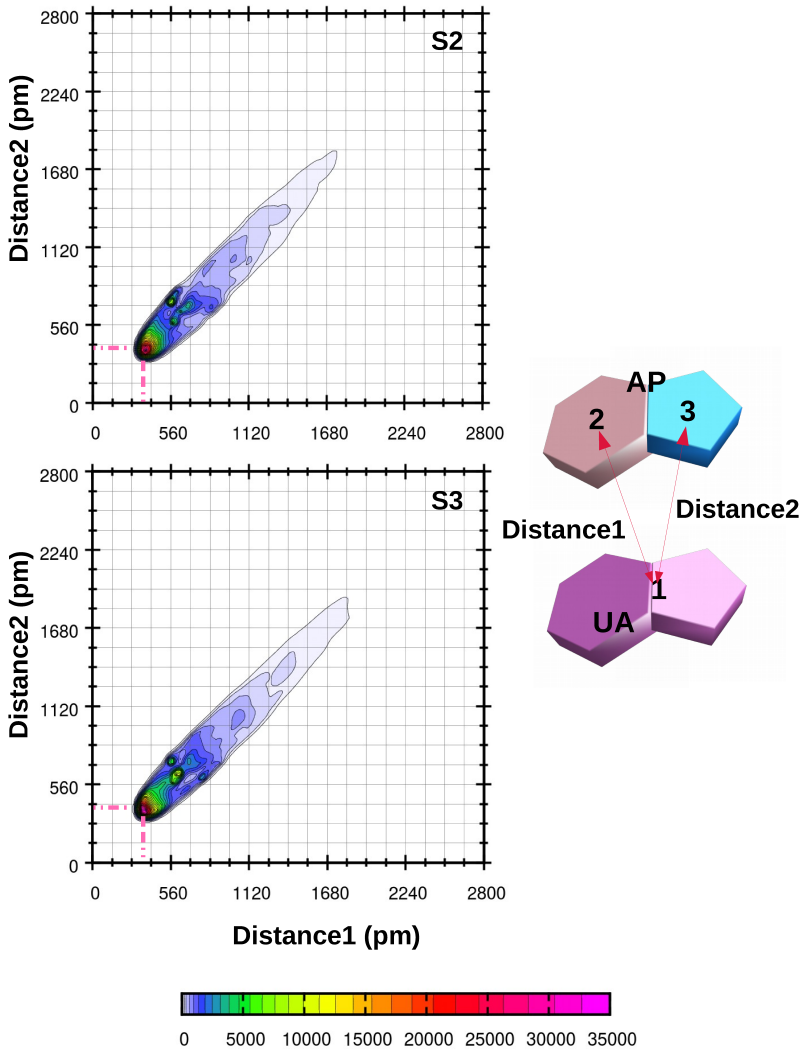

Figure 4b-19. *Combined distribution function of two different distances between any two aromatic rings for systems S2 and S3. The first distance is taken between the COM of UA and the COM of 6-membered ring of AP and the second distance is taken between the COM of UA and the COM of 5-membered ring of AP.*

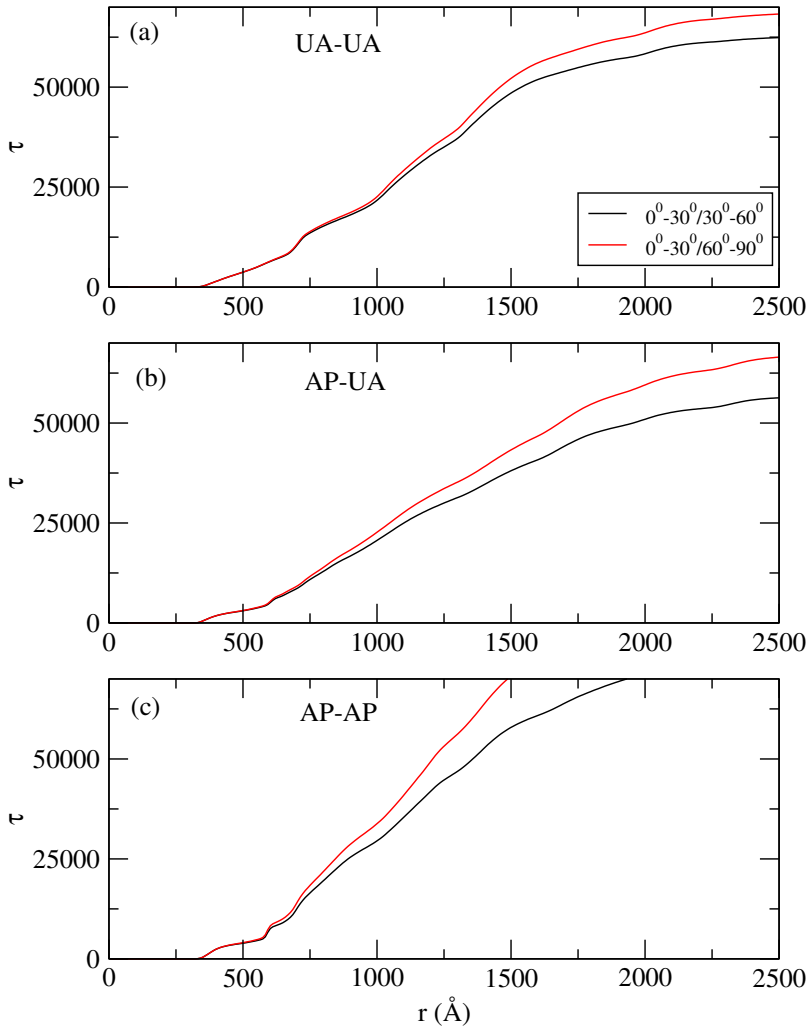

Figure 4b-20. *Preferential interaction parameter for various combinations like UA-UA, UA-AP, and AP-AP at various angles i.e.,* 0°-30°, 30°-60°, *and* 60°-90°. *Here, black line presents the preferential interaction parameter for the interaction between any two aromatic ring at an angle ranges* 0°-30° *over* 30°-60°. *Similarly, the red line presents the preferential interaction pram for the interaction between any two aromatic ring at an angle ranges* 0°-30° *over* 60°-90°.*It is to be noted that the angle is considered between two vector normals of any two aromatic planes.*

Quantum calculation

 From the above discussions, it is fortified that UA-AP interaction is dominated by π-

stacking and hydrogen-bonding interactions. To provide more evidence, we have estimated quantum calculations between UA-AP pairs to present the nature of π-stacking and hydrogen bonding interactions. To do so, we have determined their optimized π-stacked as well as hydrogen-bonded structures with dispersion-corrected DFT method using the B3LYP-D3/6-311++G(d,p) level of theory.[138] From these optimized structures, the complexation energies with BSSE correction are determined. Besides, we apply a quantum-based non-covalent interaction-reduced density gradient (NCI-RDG) technique with the same basis set for each type of interaction. This scatter map's default isosurface value (color-filled isosurface chart) is 0.5, and the default color is between -0.035 and 0.020. It is a meaningful approach to describe and visualize weak associations. Strong repulsive nonbonded steric interactions are represented in red, and attractive hydrogen bonding and van der Waals interactions are shown blue and green. The assessment is carried out with the aid of Multiwfn tools[165, 164]. The weak nonbonded interaction isosurface and the 2D plot for the π-stacked AP-UA pair are shown in Figure 4b-21 (a)-(b). It is seen that an energetically favorable π-stacking interaction is present between AP and UA with the complexation energy of -2.61 kcal/mole. Similarly, a favorable hydrogen-bonding interaction can be observed between the same pair in Figure 4b-21 (c)-(d) with the complexation energy -24.39 kcal/mole. Thus, in the complex formation between AP-UA pair, both π-stacking and hydrogen bonding interactions can be apparent. Furthermore, similar calculations are also accomplished for the AP-MM pair. It is seen that AP-MM interaction can be dominated by hydrogen bonding interactions with complexation energy of -11.97 kcal/mole (Figure 4b-21 (e)-(f)). Thus, the quantum results resemble the molecular dynamics simulation outcomes presented earlier. Moreover, the present force field can achieve the real situation between all these pairs conferred in this study.

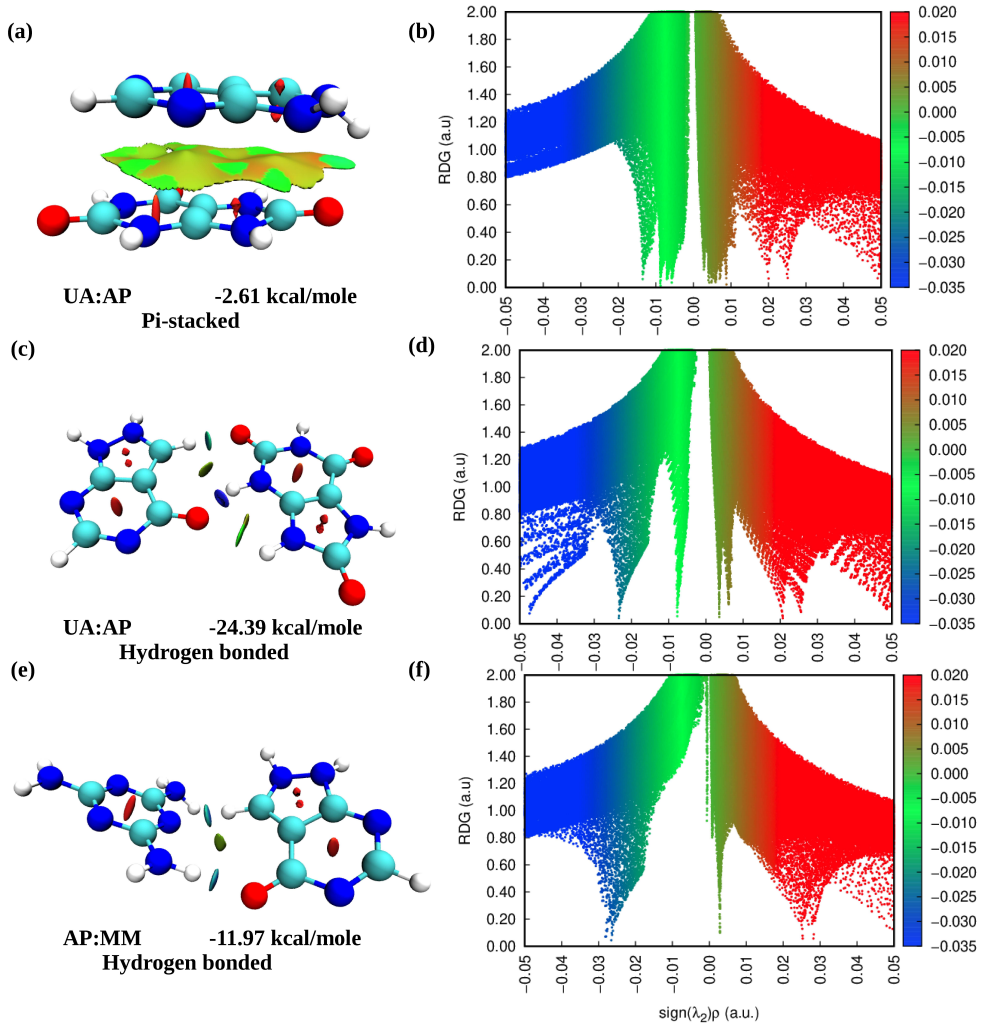

Figure 4b-21. *(a)-(b) Color-filled RDG isosurface delimitate noncovalent interaction (NCI) regions for π-stacked UA-AP interaction with the dispersion-corrected DFT method using the B3LYP-D3/6-311++G(d,p) level of theory along with the complexation energies with BSSE correction, (c)-(d) color-filled RDG isosurface delimitate noncovalent interaction (NCI) regions for hydrogen-bonded UA-AP interaction with the dispersion-corrected DFT method using the B3LYP-D3/6-311++G(d,p) level of theory along with the complexation energies with BSSE correction, and (e)-(f) color-filled RDG isosurface delimitate noncovalent interaction (NCI) regions for hydrogen-bonded AP-MM interaction with the dispersion-corrected DFT method using the B3LYP-D3/6-311++G(d,p) level of theory along with the complexation energies with BSSE correction.*

Table 4b-3. All energies derived from the MM-PBSA calculations. Here, ΔE_{vdW}, ΔE_{elec}, ΔG_{PB}, ΔG_{NP}, and $\Delta G^0{}_{bind}$ are the energy of van der Waals interaction, electrostatic energy, Poisson–Boltzmann energy, non-polar energy, and binding free energy, respectively. All energy values are expressed in kcal/mol. Statistical uncertainties in the results are ±0.08 kcal/mol to ±0.16 kcal/mol.

System$_{receptor-ligand}$	ΔE_{vdW}	ΔE_{elec}	ΔG_{PB}	ΔG_{NP}	$\Delta G^0{}_{bind}$
S0$_{UA-MM}$	-17.70	-56.21	55.55	-2.90	-21.26
S3$_{UA-MM}$	-14.13	-36.96	37.72	-2.24	-15.62
S0$_{UA-AP}$	-54.99	-62.02	75.85	-4.98	-46.14
S1$_{UA-AP}$	-100.11	-251.94	226.22	-9.04	-134.86
S2$_{UA-AP}$	-175.55	-327.76	318.53	-14.46	-199.24
S3$_{UA-AP}$	-209.27	-388.31	369.18	-16.69	-245.09
S0$_{AP-MM}$	-7.53	-26.80	28.29	-1.73	-7.76
S3$_{AP-MM}$	-8.60	-35.85	35.05	-2.27	-11.68

Table 4b-4. All energies derived from the MM-PBSA calculations. Here, ΔE_{vdW}, ΔE_{elec}, ΔG_{PB}, ΔG_{NP}, and $\Delta G^0{}_{bind}$ are the energy of van der Waals interaction, electrostatic energy, Poisson–Boltzmann energy, non-polar energy, and binding free energy, respectively. All energy values are expressed in kcal/mol. Statistical uncertainties in the results are ±0.003 kcal/mol to ±0.10 kcal/mol.

System$_{receptor-ligand}$	ΔE_{vdW}	ΔE_{elec}	ΔG_{PB}	ΔG_{NP}	$\Delta G^0{}_{bind}$
S12$_{AP-AP}$	-0.07	-0.18	2.45	-0.26	-0.05
S12$_{AP-MM}$	-1.11	-5.02	12.57	-0.34	-1.76
S12$_{MM-MM}$	-0.95	-3.25	51.03	-0.69	-1.16
S12$_{UA-AP}$	-7.49	-8.05	0.87	-0.08	-5.87
S12$_{UA-MM}$	-3.50	-14.50	0.72	-0.52	-5.42
S12$_{UA-UA}$	-6.98	0.61	2.97	-0.72	-4.11

Complexation Energy

For systems S0 and S3, MM-PBSA results[291, 292] are accessed in this section for all interactions that include UA-MM, UA-AP, and AP-MM (Table 4b-3). Both systems are selected so that the effect of AP (at low and high concentrations of it, respectively) on

UA and MM interactions can be addressed. From Table 4b-3, it can be found that UA-MM interaction of the system S3 becomes less favorable than system S0.

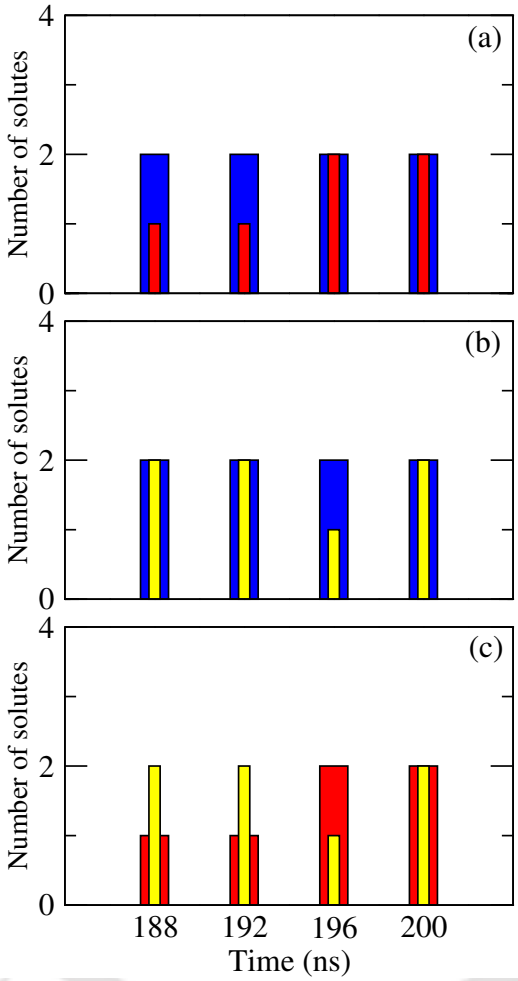

Figure 4b-22. *The distribution of clusters of various interactions like (a) UA (blue)-AP (red), (b) UA (blue)-MM (yellow), and (c) AP (red)-MM (yellow) for system S12.*

Interestingly, UA-AP interaction gets more promising as we from system S0 to system S3. Therefore, in the system S3, UA molecules are now surrounded by AP molecules. Moreover, in system S3, AP-MM interaction is also somewhat higher (more favorable) than any other system. Thus, AP attracts MM when it is present in a higher number. It is to be noted that two consecutive interactions (UA-AP and AP-MM interactions) work togetherly to reduce the UA-MM interaction, mostly in system S3. However, UA-AP interaction is predominant over all other interactions. Therefore, it can be concluded that aggregated UA in system S0 is [illegible] aggregated UA-AP conjugate, which protects to form kidney stones induced

by MM and UA.

Next, the complexation energy for the formation of UA-AP-MM conjugates is determined. To do so, a specific system S12, is considered. In this system, two of each type of molecules (say, MM, UA, and AP) are taken together, and the $\Delta G^0{}_{bind}$ is determined for all combinations (Table 4b-4). It is found that the total complexation energy is favorable. Therefore, it can be concluded that AP interacts with UA and MM to destroy their combination. In this regard, cluster structure analysis is also performed taking system S12 (Figure 4b-22). It is observed that all UA and AP molecules bind together to form a UA-AP cluster (Figure 4b-22 (a)). Again, all UA and MM molecules come together to form UA-MM conjugate cluster (Figure 4b-22 (b)). Moreover, AP-MM interaction also strong (Figure 4b-22 (c)). Thus, all AP molecules bind with UA-MM conjugate (Figure 4b-22 (a), (b), and (c)). Such complexation is responsible for disrupting the UA-UA as well as UA-MM interactions.

Potential of mean force (PMF)

For numerous interactions, such as UA-UA in presence of AP, AP-AP in presence of UA, and UA-MM in AP, potentials of mean forces are estimated by using umbrella sampling.[293, 294, 295, 296, 297] By assessing these three interactions, one can expect the facts involved with UA-MM interaction in presence of AP, which will further strongly suggest the significant decrease or elimination of MM-UA mediated kidney stones. From Figure 4b-23(a) , it is clear that UA-MM interaction is reduced in presence of AP. Hence it is apparent that in a ternary mixture of UA-MM-AP, AP interferes with UA as well as MM. Now, if one looks into the UA-UA interaction in presence of AP, it can be found that the UA-UA interaction gets reduced (Figure 4b-23(b)). Thus, the presence of AP evidently produces the smaller size of UA-UA clusters, thus, dragging a minimal number of MM molecules towards them to form an MM-UA composite. It is to be noted that in presence of AP, the contact minimum of UA-UA interactions becomes unfavorable. However, the solvent separated minimum at 6.78 Å attains more stability. Thus, UA molecules remain stabilized at long separations between them. The existence of AP, therefore, decreases the size of UA-induced kidney stones. Now, if we look at the interaction between AP molecules in presence of UA, then it can be seen that the interaction AP-AP is less beneficial (Figure 4b-23(c)). Thus, AP appears to associate more with UA than with itself. As a result, the

AP-UA composite begins to develop, allowing the UA-UA aggregation to decrease. In conclusion, it does seem that in presence of AP, the lower order cluster of UA can be assumed to minimize the composite structure of MM-UA.

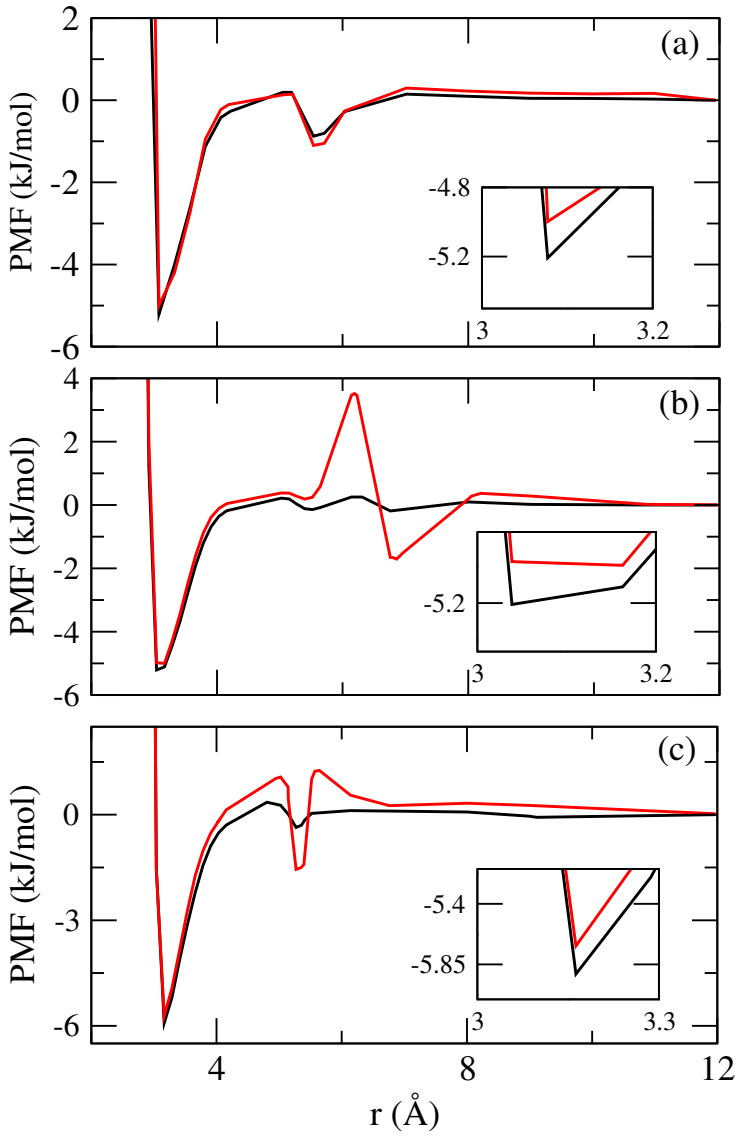

Figure 4b-23. *potential of mean forces of numerous interactions for systems (a) P0 (black solid line), P1 (red solid line), (b) P2 (black solid line), P3 (red solid line), (c) P4 (black solid line), P5 (red solid line). Here, insets figures depict the magnified portion of the corresponding graphs. Standard errors of all data points (calculated using the block average method) fall within ± 0.08 kJ/mol.*

STRUCTURAL ARRANGMENT DURING THE AGGREGATION AMONG UA, AP, AND MM

Probability of Columnar structure

The point-plane distance distribution (pldf) between two aromatic moieties are calculated here for different interacting pairs like UA-UA, AP-AP, and UA-AP for system S3 to determine the columnar structure[158, 298] (Fig. S12, Supporting Information). The determination of angle probability as mentioned earlier, confirms that UA and AP are very prone to interact with each other and π-stacking interaction plays a dominant role. Therefore, the determination of point-plane distance distribution between above-mentioned pairs provides the information about the columnar pillar like structures during their interaction (Figure 4b-24). It is to be noted here that the columnar structure is possible for a set of molecules when they are stacked in a pillar like structure. Now, the molecules are arranged one after one in almost equispaced during their π-stacking. Importantly, in case of UA-AP interaction, there are several possibilities of their arrangements like A–B–A–B, A–A–A–A–B–B–B, A–A–B–B, or A–A–B–A–A–B etc. However, in the present case, it is not found any systematic order of their arrangement, rather a random stacking can be observed. As a consequence, the pillar like columnar structure of only UA gets hindered by the presence of AP and thereafter, UA-AP pillar is formed. Thus, the calculation of pldf for UA-UA interaction shows that UA molecules forms nearly equispaced orderly stacked pillar like structure through π-stacking as indicated by the angle criterion (Figure 4b-25 (a)). A similar situation can also be observed for AP-AP (Figure 4b-25 (b)) as well as UA-AP interactions (Figure 4b-25 (c)). Therefore, it is confirmed that UA and AP molecules forms pillar like columnar structure (as indicated by angle criteria) in the process of aggregation.

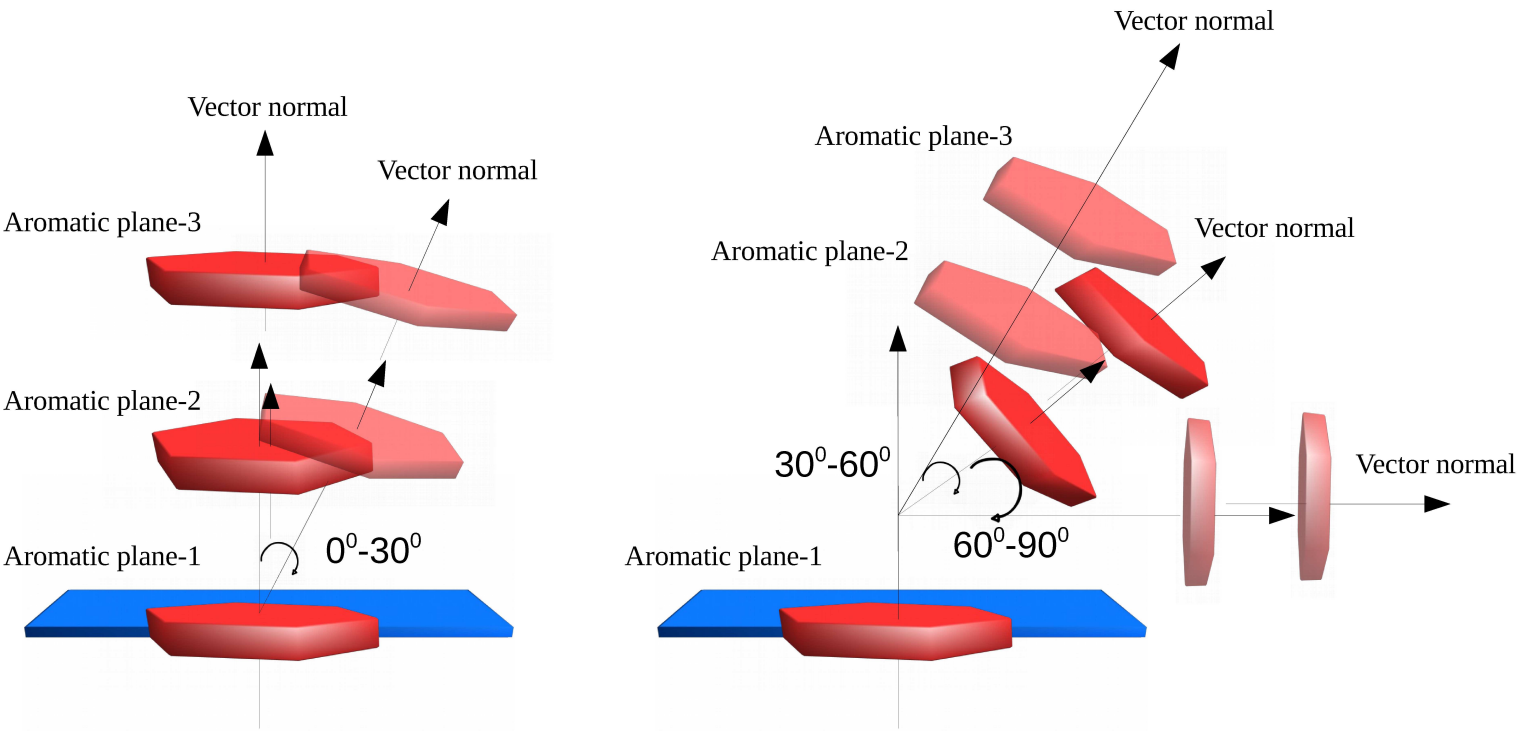

Figure 4b-24. *Schematic representation for the determination of point-plane distance distribution. The pictorial representation clearly depicts the inclination of aromatic rings at various angle ranges (i.e.,* 0°-30°, 30°-60°, *and* 60°-90° *) in where* 0°-30° *angle range provide the* π*-stacking scenario.*

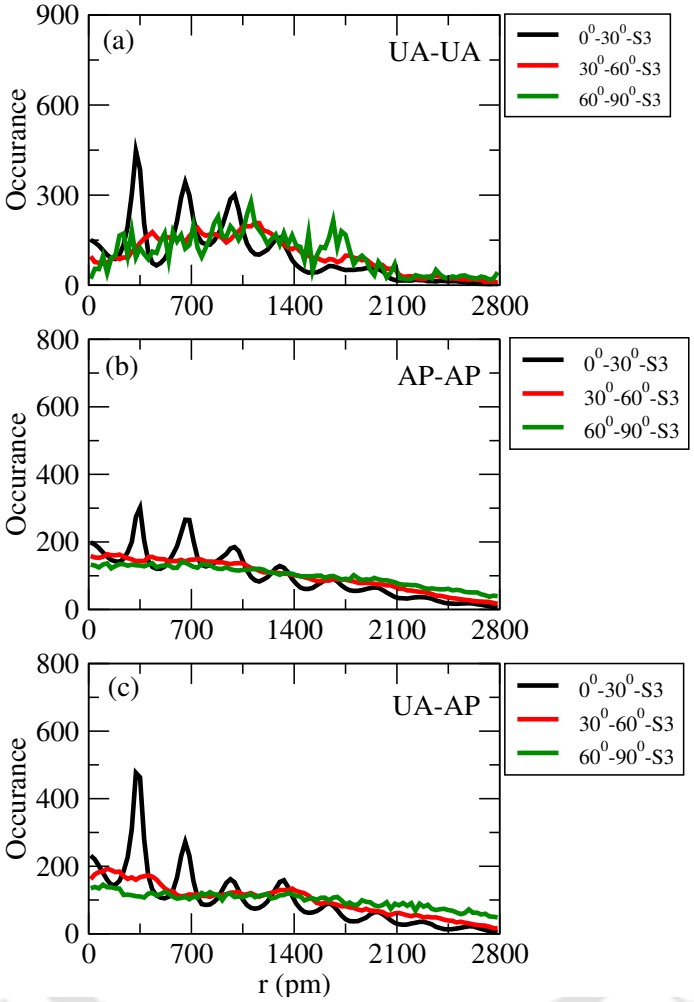

Figure 4b-25. *The point-plane distance distribution (pldf) between two aromatic rings for various interactions like UA-UA, AP-AP, and UA-AP for system S3. Here, three angle ranges are chosen i.e.,* 0°-30°, 30°-60°, *and* 60°-90°. *The angle range between* 0°-30° *can depict the* π*-stacking properly.*

■ SUMMARY AND CONCLUSIONS

With the best available sources and shreds of evidence in human and animal studies, it can be inferred that a high-dosage of MM contributes to urinary stones and acute renal dysfunction in both humans and animals. The composition of kidney stones is found to be a combination of MM and UA. In the present study, we have established a theoretical

model for investigating the prevention of renal stones' development and have described potential pathways for inducing adverse effects on the formulation of a model small molecule inhibitor, AP, in MM-UA crystal. Previous experimental trials have demonstrated that AP can successfully suppress kidney stone deposition, thereby hemming renal failure. In this work, several systems are considered, among which four systems contain AP with a manner of increasing concentration of it keeping the number of MM and UA molecules fixed, which shows that AP inhibits the formation of MM and UA clusterization by making hydrogen bonds with MM and breaking the more prominent size clusters of UA into smaller ones. To introduce how do AP, UA, and MM aggregate, the first shell CN is determined. It is found that the increase in AP concentration has resulted in a reduction in UA-MM interaction, along with the relationship between UA-UA and MM-MM interactions. This is triggered by the rise in the number of AP around UA and MM. The assessment of spatial density plots for numerous interactions is also in line with the CN. The calculation of cluster structure analysis provides that in systems with AP in increasing quantities, UA-UA interaction is eased. Hence, the smaller order cluster, like heptamer or pentamer, is identified relative to the system where the AP amount is less, with approximately 14 to 15 UA molecules forming a higher-order cluster. The involvement of AP also interferes with the MM-MM interactions. As a result, the presence of AP affects the UA-MM cluster size significantly. Almost all UA and MM molecules from large clusters in the appearance of a limited number of AP, while the UA-MM cluster size is substantially reduced to lower order in the presence of a large number of AP. Therefore, the emergence of kidney stones can be avoided by applying AP by reducing its cluster size. Intriguingly, more significant UA clusters are dragging more MM to create larger renal stones. Therefore, the association of UA molecules increases the size of the UA-MM cluster. However, when AP inhibits UA's self-aggregation to form a more significant proportion of the lower order cluster, it receives fewer MM than the higher-order cluster. Consequently, the UA-MM kidney stone size decreases, thus, avoid renal insufficiency by applying model pharmaceutical inhibitor, AP. The DACF is determined to demonstrate that the UA-MM dimer lifetime is more significant when the amount of AP is less than the lifespan of the dimer they generate when the amount of AP is higher. The free energy landscape (SASA ($\mathring{A}^2$) versus hydrogen bond number) also reveals that UA-UA aggregation is hindered with more UA-AP hydrogen bond numbers in the presence of a higher AP. Thus, the SASA value for UA-UA aggregation increases. Therefore, a more surface area is exposed to AP. However, the determination

of CN, SDF, cluster structure, and FEL does not produce any substantial mechanisms for why AP molecules meddle with UA molecules' aggregation. It just shows the statistical circumstances within AP's presence without any particular mechanistic point of view on UA-UA disintegration. Therefore, the estimation of the preferential interaction parameter, hydrogen bond numbers, and binding free energy should be performed to present why do AP, UA, and MM aggregate. The preferential interaction parameter demonstrates that UA-AP interaction becomes prevalent over UA-UA interaction with AP's increasing concentration. Besides, the determination of potentials of mean forces employing umbrella sampling, calculating the average number of hydrogen bonds, and the estimation of binding free energy often anticipate similar data and thus endorse the process as mentioned above. Therefore, the favorable interaction energy among these solute molecules with preferable hydrogen bonding and hydrophobic interaction like π-stacking interaction is the driving force for the intense complexation among UA, AP, and MM, thus, resulting in disrupting the UA aggregation and UA-MM conjugate cluster formation. It is interesting to note that during the interaction between UA and AP, the latter substitutes the former from their self-aggregated clusters. Surprisingly, UA and AP develop a pillar-like columnar structure during π-stacking interaction. However, the structure order for stacking between UA and AP molecules is not hierarchical, more spontaneous.

Following this study, AP's preventive ability for mitigating increased risks associated with the intake of MM in the presence of UA is demonstrated. AP should also be prescribed for the treatment of UA stones affected by MM, which will attract attention to a broader approach to the medication in renal diseases.

Chapter 5

Investigation on the Mechanisms of Synchronous Interaction of K_3Cit with Melamine and Uric Acid That Avoids the Formation of Large Clusters: The Role of Hydrogen Bonding

"Medicine is the restoration of discordant elements; sickness is the discord of the elements infused into the living body."

— Leonardo da Vinci

Overview: Uric acid (UA) has an enormous competence to aggregate over melamine (MM), producing large UA clusters that "drag" MM to it. Such a combination of donor-acceptor pairs provides a robust MM-UA composite, thereby denoting a high complexity. Thus, a straightforward but pragmatic methodology might indeed require either destroying the aggregation of UA or impeding a hydrogen-bonded cluster of MM and UA. Here, potassium citrate (K_3Cit) is used as a potent inhibitor for the significant decrease of large UA-MM clusters. The underlying mechanisms of synchronous interaction between K_3Cit and MM-UA pair are examined by the classical molecular dynamics simulation coupled with the enhanced sampling method. K_3Cit binds to MM-UA pair profoundly to produce MM-UA-K_3Cit complex with favorable complexation energy (as indicated by the reckoning of pairwise ΔG^0_{bind} employing MM-PBSA method). The strength of interaction goes according to the order: UA-K_3Cit > MM-K_3Cit > MM-UA, thus clearly demonstrating the instability by upsetting π-stacking of UA and hydrogen bonding of MM-UA simultaneously. A comprehensive, strategically designed "direct approach" and "indirect approach" cluster structure analysis shows that K_3Cit reduces the "direct approach" MM-UA cluster size significantly irrespective of ensemble variation. Furthermore, the estimation of potential of mean forces (PMFs) reveals that $(UA)_{decamer}$-MM interaction prevails over $(UA)_{tetramer}$-MM. The dynamic property (Dimer existence autocorrelation functions) proves the essence of dimerization between MM and UA in the absence and presence of K_3Cit. Moreover, the calculation of the preferential interaction parameter provides the concentration in which interactions between MM-K_3Cit and UA-K_3Cit over the interaction of MM and UA are predominant.

■ INTRODUCTION

The kidney stones are thin, urinary-tract crystals that are found in the kidneys. Back or abdominal discomfort and urinary bleeding are the most common symptoms of kidney stones. While attacks on kidney stones can be excruciating and kidney stone pain is usually caused if the stone goes through and obstructs the ureter. The ureter is a long tube that connects the kidney to the bladder and drains urine. The typical symptoms are generally identical, despite gender when this tube is blocked. In the Western world and beyond, nephrolithiasis has a high prevalence, and its occurrence is increasing in every demographic group. Besides the morbidity of the acute case, stone diseases also develop into a lifetime issue that needs preventive therapy to minimize continuous incidence. Nephrolithiasis is often a chronic and long-term disorder, with repeated stone cases suggesting more significant recurrences and worse clinical outcomes for the future. Due to a very high recurrence risk, medication to avoid stone-forming is essential to decrease patient morbidity and costs.[299, 300]

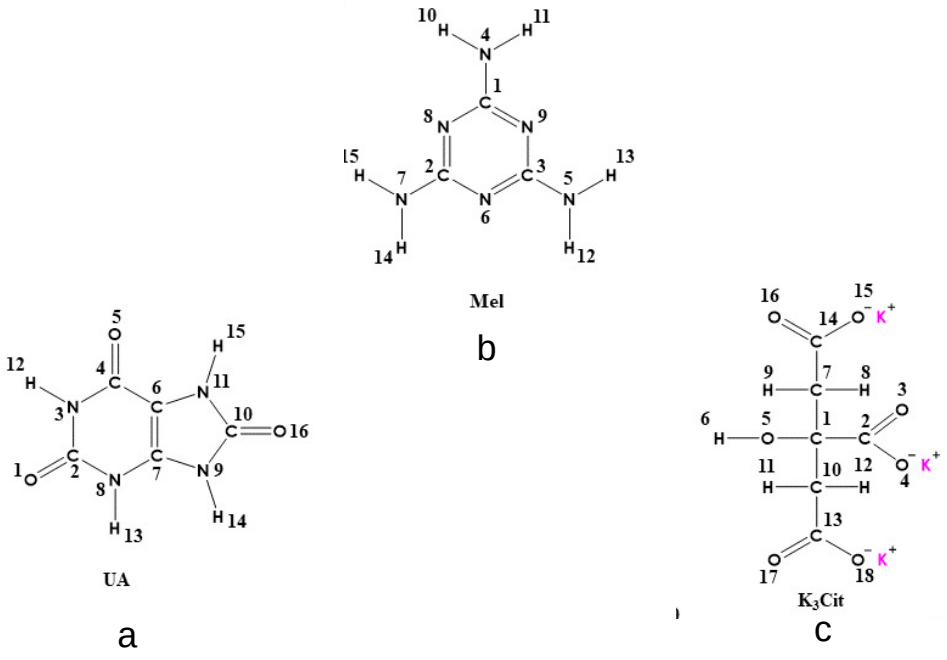

Figure 5-1. *Structures of (a) UA, (b) MM, and (c) K_3Cit with atom numbering.*

 Renal dysfunction due to urinary tract calculi is seldom reported in children. How-

ever, scandals in 2007 in North America and a dairy controversy in 2008 in China also drawn significant public interest in this issue. 25 Chinese people between 6 to 36 months of age were diagnosed at Beijing Children's Hospital in a 2008 trial to more accurately diagnose and treat these specific cases because of melamine-mediated kidney stones exacerbated by severe renal obstruction. A history of feeding, clinical presentation, ultrasound results, treatment, and effects had been summarized. Examination of ultrasounds revealed that there were calculi on the kidney and ureters. Uric acid (UA, Figure 5-1a) and MMamine (MM, Figure 5-1b) were made of the stones in the 1.2:1 to 2.1:1 molar ratio.[24, 202, 1, 2] The most stable structure with equimolar proportions of MM and UA was formed where two atomic sites CO and NH of UA were held by MM by hydrogen bonding.[26] Several research works on MM-related kidney stones have been performed.[1, 266] Several experiments were also dealing with the origins of UA pure stones and the identification of MM.[301, 302, 303, 304, 305] Few have fully explored the formation process and microstructure of infant stones without mentioning preventive and therapeutic drugs.[208, 44, 45, 207] UA is a waste byproduct. It is created when body breaks down purines that are found in some foods. MM is an organic-based, nitrogen-rich compound. The fundamental mechanistic study of UA and MM complexes at different concentrations revealed that the number of coordination of MM around a reference UA varies between 1 and 3, and vise Versa. MM associates more intensely with UA over self-assembly, and UA prefers to interact with other UA molecules rather than MM. Higher-order UA clusters result from intense interactions within UA molecules, that "drag" the surrounding MM molecules to bind to them. The UA-MM complex has a non-planar structure that conforms to the most stable structure, as stabilized by several H-bonding interactions.[207] π-stacking is accountable for the self-association of UA.[207, 306] Therefore significant π-stacking interactions, together with multiple associations with hydrogen bonding, inevitably play a very vital and perhaps decisive role in the MM and UA assembly and thus implies a high complexity.[207] A straightforward yet realistic approach may indeed entail either devastation of UA aggregation or an impediment of a MM and UA hydrogen-bonded cluster. If both methods can be achieved, it will be beneficial. In a recent study, Dong *et al.* assumed that the microstructure of MM-UA frameworks continue with the removal of hydrogen ties or the occupation of the hydrogen bonds by both inhibiting the stone growth as well as removing the stones created.[44] The reduction of stones can also be made by layered peeling or alkalinization. They finished by claiming that potassium citrate (K_3Cit, Figure 5-1c) is

the inhibitor and remover by far the most effective.[44] Therefore, K_3Cit is ideal for use in the primary prevention of stone formation. The binding force order was shown to be as follows: K_3Cit-UA > K_3Cit-MM > MM-UA.[44] K_3Cit is better bound with both MM and UA than MM with UA so that K_3Cit can be used as an inhibitor and an eliminator both. The K_3Cit includes -OH group. The electronegativity of the oxygen atom is higher than that of the nitrogen atom. Thus, K_3Cit has a high hydrogen bonding capability. Before forming stones, if K_3Cit attaches to MM or UA, the aggregation of MM and UA will be avoided, and the inhibitory effect accomplished. In brief, K_3Cit plays a double role in inhibiting and removing stones and is expected to be an advantageous medication to inhibit and remove MM-UA stones.

Inspired by the above study, by incorporating K_3Cit with diverse concentrations, we have investigated the inhibitive influence of K_3Cit towards the elimination of kidney stones (which is quite challenging) by disrupting the conjugation of MM-UA employing the classical molecular dynamics simulation. However, this study explores the exact nature of the relationship among K_3Cit, MM, and UA, and also gives a deeper understanding of the degradation of the more massive MM-UA clusters in aqueous media. In this regard, a comprehensive, strategically designed "direct approach" and "indirect approach" for cluster structure analysis are considered, and we have revealed how K_3Cit deals with the "direct approach" to prevent the initial growth of MM-UA cluster. Moreover, it has been anticipated that since UA tends to aggregate higher than MM, the aggregated UA cluster "drags" MM molecules to form a large insoluble cluster. The present study deals with the estimation of the impact of the UA cluster on MM with the conjugation of PMF and preferential interaction parameter (based on Kirkwood–Buff theory). Therefore, for the first time, the theoretical perspective clarifies the molecular mechanisms of K_3Cit's synchronous association with MM and UA to repress the development of MM-UA induced kidney stones.

The rest of the chapter comprises of three sections: Models and details of simulations (Section II), Results and Discussions (Section III) and Conclusions (Section IV).

■ MODELS AND SIMULATION METHOD

A series of classical molecular dynamics (MD) simulations are conducted in this study taking into account different concentrations of UA, MM, and K_3Cit in water under ambient pressure-temperature conditions. The representative systems considered here are presented

in Table 5-1. Firstly, the RESP (restrained electrostatic potential)[140] charge is employed for all molecules (Table 5-2) and this is generated with the help of ANTECHAMBER[141] module present in AMBER14 package.[226] Moreover, to determine the RESP charge, an energy optimized structure is used and the optimization is done with the help of Gaussian 09[138] with the use of *ab initio* HF/6-31+G** method. For all the atomic sites of UA, MM, and K_3Cit, general AMBER force field[142] is employed. In order to carry out MD simulations, all molecules were immersed into TIP3P (three-point transferable inter-molecular potential)[143, 367] water. The PACKMOL[144] package was used to generate the initial configurations of each system. During the simulations, a cubic box containing solute as well as solvent molecules in desired proportions was employed. Thereafter, minimization was carried out using two methods. First 4000 steps (out of 10000-step energy minimization process) were performed with the steepest descent method, and the remaining 6000 steps were followed with the conjugate gradient method. PBC (periodic boundary conditions) were employed along all three directions. After minimization, all systems were then heated slowly from 0 K to 480 K with an increase of 50 K. Such heating up to a higher temperature may help in overcoming the global minimum boundary status. Finally, each system was cooled down with a decrement interval of 25 K to the final temperature, i.e., 300 K using canonical ensemble (NVT). After that, an equilibration of 5 ns at 300 K and 1 atm was performed for all systems in an isothermal-isobaric (NPT) ensemble. Simulations are subsequently subjected to a production run of 200 ns in the NVT ensemble. The last 100 ns for every 200 ns production run are included in the data analysis. The Langevin dynamics (with 1 ps^{-1} collision frequency) was used for all simulation procedures to sustain a temperature at 300 K.[145] The Berendsen barostat was used for maintaining pressure at 1 atm with a pressure relaxing time span of 2 ps in the NPT ensemble.[146] The Particle mesh Ewald (PME) algorithm was used in treating long-ranged non-bonded electrostatic interactions.[147] The covalent bonds containing hydrogen atoms were constrained with the aid of the SHAKE algorithm.[148] For estimating short-ranged non-bonded interactions, a cut-off distance of 10 Å was utilized. The MD simulation trajectories were then analyzed via the AMBER CPPTRAJ module.[376] Visual Molecular Dynamics (VMD) is used to perceive the MD trajectories acquired.[149]

In order to carry out MD simulations, all molecules were immersed into TIP3P (three-point transferable inter-molecular potential)[143, 367] water. The PACKMOL[144] package was used to generate the initial configurations of each system. During the simulations, a

cubic box containing solute as well as solvent molecules in desired proportions was employed. Thereafter, minimization was carried out using two methods. First 4000 steps (out of 10000-step energy minimization process) were performed with the steepest descent method, and the remaining 6000 steps were followed with the conjugate gradient method. PBC (periodic boundary conditions) were employed along all three directions. After minimization,

Table 5-1. Overview of systems[a]

System	N_{MM}	N_{UA}	N_{K_3Cit}	N_{wat}	Box length (Å)	C_{MM}(M)	C_{UA}(M)	C_{K_3Cit}(M)
S0	10	10	—	5000	53.620	0.1077	0.1077	—
S0-a	10	10	—	5000	53.637	0.1076	0.1076	—
S1	10	10	5	5000	53.783	0.1067	0.1067	0.0534
S1-a	10	10	5	5000	53.726	0.1071	0.1071	0.0535
S2	10	10	10	5000	53.751	0.1069	0.1069	0.1069
S3	10	10	20	5000	53.956	0.1057	0.1057	0.2114
S4	10	10	30	5000	54.143	0.1046	0.1046	0.3138
S4-a	10	10	30	5000	54.193	0.1043	0.1043	0.3129
S5	—	5	—	2500	42.502	—	0.1081	—
S6	—	5	10	2500	42.702	—	0.1066	0.2132
S7	5	—	—	2500	42.477	0.1083	—	—
S8	5	—	10	2500	42.693	0.1067	—	0.2134
S9	—	—	10	2500	42.621	—	—	0.2144
S10	10	20	—	5000	53.801	0.1066	0.2132	—
S11	10	20	30	5000	54.287	0.1038	0.2076	0.3113
S12	10	30	—	5000	53.911	0.1059	0.3179	—
S13	10	30	30	5000	54.461	0.1028	0.3083	0.3083
S14	20	10	—	5000	53.690	0.2146	0.1072	—
S15	20	10	30	5000	54.264	0.2078	0.1039	0.3117
S16	30	10	—	5000	53.886	0.3188	0.1062	—-
S17	30	10	30	5000	54.367	0.3099	0.1033	0.3099
S18	2	2	2	1500	35.860	0.0720	0.0720	0.0720
P0	1	1	—	1500	37.993	0.0303	0.0303	—
P1	1	1	5	1500	38.126	0.0299	0.0299	0.1498
P2	1	—	1	1500	38.000	0.0303	—-	0.0303
P3	—	1	1	1500	38.060	—	0.0301	0.0301

[a] N_{MM}, N_{UA}, N_{K_3Cit}, and N_{wat} refer to the number of melamine, uric acid, potassium citrate, and water molecules, respectively. C represents the molar concentrations of melamine (MM), uric acid (UA) and potassium citrate (K_3Cit).

all systems were then heated slowly from 0 K to 480 K with an increase of 50 K. Such heating up to a higher temperature may help in overcoming the global minimum

boundary status. Finally, each system was cooled down with a decrement interval of 25 K to the final temperature, i.e., 300 K using canonical ensemble (NVT). After that, an equilibration of 5 ns at 300 K and 1 atm was performed for all systems in an isothermal-isobaric (NPT) ensemble. Simulations are subsequently subjected to a production run of 200 ns in the NVT ensemble. The last 100 ns for every 200 ns production run are included in the data analysis. The Langevin dynamics (with 1 ps^{-1} collision frequency) was used for all simulation procedures to sustain a temperature at 300 K.[145] The Berendsen barostat was used for maintaining pressure at 1 atm with a pressure relaxing time span of 2 ps in the NPT ensemble.[146] The Particle mesh Ewald (PME) algorithm was used in treating long-ranged non-bonded electrostatic interactions.[147] The covalent bonds containing hydrogen atoms were constrained with the aid of the SHAKE algorithm.[148] For estimating short-ranged non-bonded interactions, a cut-off distance of 10 Å was utilized. The MD simulation trajectories were then analyzed via the AMBER CPPTRAJ module.[376] Visual Molecular Dynamics (VMD) is used to perceive the MD trajectories acquired.[149]

Last 20 ns of MD trajectories are used for estimating the binding free energy for different systems using Boltzmann Surface Mechanism Methodology.[184, 227] The Molecular Mechanics Poisson-Boltzmann Surface Area (MM-PBSA) measurements are made based on a Python script of AMBER software, MMPBSA.py. ΔG^0_{bind} can be determined as follows:

Table 5-2. Partial charges of different atomic sites of K_3Cit. The partial charges for MM and UA molecules are taken from previous simulation studies.[174] The charge for K+ ion is obtained from Joung and Cheatham force-field parameter already present in AMBER, which is TIP3P specific.[307] e is the elementary charge.

Molecule	Atom	Charge (e)
K_3Cit	C1	0.8643
	C2	0.8144
	O5	-0.9005
	H6	0.4551
	O15/16/17/18	-0.8909
	H8/9/11/12	0.0087
	C13/14	0.9388
	C7/10	-0.4009
	O3/4	-0.8901
	K	1.0000

$$\Delta G^0_{bind} = \Delta E_{vac} + \Delta G_{solv}, \tag{5.1}$$

where ΔE_{vac}, and ΔG_{solv} depicts the interaction energy in the gas phase, and variation of solvation energy during binding process,[185, 186] respectively. ΔE_{vac} can further be decomposed as:

$$\Delta E_{vac} = \Delta E_{ele} + \Delta E_{vdw}, \tag{5.2}$$

where ΔE_{ele} and ΔE_{vdw} measures the receptor-ligand electrostatic and van der Waals interaction energy ingredient, respectively. Moreover, (ΔG_{solv}) energy can also be divided into two energy terms as:

$$\Delta G_{solv} = \Delta G_{PB} + \Delta G_{NP}. \tag{5.3}$$

Here, polar (electrostatic) solvation free energy, and non-polar solvation free energy are shown here by ΔG_{PB}, and ΔG_{NP}, respectively. ΔG_{PB} is determined in a continuum solvent method by the PBSA program of AMBER14. ΔG_{NP} can be measured from the solvent-accessible surface area (SASA). In order to estimate ΔG_{NP}, SASA is determined using maximal speed molecular surfaces (MSMS)[187] as:[207, 192, 193]

$$\Delta G_{NP} = \gamma(SASA) + \beta, \tag{5.4}$$

where $\gamma = 0.005$ kcal/Å^2 and $\beta = 0.0$.

Umbrella sampling (US) method is used in order to estimate the potential of mean force (PMF).[228] The reaction coordination ξ has been defined as the z-component center of mass (COM)-center of mass (COM) distance (r) between two selected molecules. In the US process, simulations are conducted with a biasing window potential $w(\xi)$, which is prompted to improve the sampling in the vicinity of the selected value ξ. A total of 25 biased simulations are performed with $i = 4, 8, \cdots, 28$, in which ξ is restrained to the values of $\xi_i = i \times 0.5$ Å in the phase space configuration X by a harmonic potential:

$$w_i(\xi) = 1/2K(\xi(X) - \xi_i)^2 \tag{5.5}$$

where K is defined as the force constant for harmonic restraint. A harmonic restraint force along z-coordinate with a force constant of 6 kcal/mol/Å^2 is employed for these biased simulations. The initial separation between the two molecules is 2 Å , and that distance is increasingly expanded by drawing one molecule from another in the z-direction. We take into account for this reason. Final normal MD simulation

 P0–P3 systems

trajectories are used for these systems as the initial US method configuration. Each system is subjected to a minimization of 4000 steps (1000 steps of the steepest descent method, accompanied by 3000 steps of the conjugate gradient method), and an equilibration of 1 ns for each US-based simulation is accomplished in the same manner as the usual MD simulation (discussed above). The production run for each window is performed for 10 ns. In fact, in US method, we have conducted a total production run of 250 ns for each system. In every 2 fs time interval, simulation data is collected. Ultimately, the results of the US simulation are assessed using the Weighted Histogram Analysis method (WHAM)[229, 230] to determine the unbiased position probability distribution P(ξ). Then the PMF function from P(ξ) is obtained as:

$$PMF(\xi) = -k_B T \ln P(\xi) \tag{5.6}$$

where k_B is the Boltzmann constant, and T is the absolute temperature of the system.

In the present study, system S0 is prepared in which only UA and MM are taken to establish the aggregating propensities of both these molecules within that concentration. Four additional systems are then developed (systems S1, S2, S3, and S4), with K_3Cit at different concentrations, keeping the number of molecules of UA and MM to that of system S0. Thus, system S0 can therefore be seen as a reference system, which does not have K_3Cit molecules. Later on, another two systems, S5 and S6 are prepared to verify the aggregation of UA molecules in the presence and absence of K_3Cit molecules. Similarly, the aggregation properties of only MM molecules are also verified from systems S7 and S8. To know the properties of pure K_3Cit molecules, system S9 is prepared. MD simulations are also performed with the combinations of different ensembles such as NVT or NPT. NPT simulations are performed here using systems S0-a, S1-a, and S4-a to test if K_3Cit, UA and MM clustering depends on ensemble employed. Furthermore, systems S10-S17 are established to check the inhibitory effect of K_3Cit as the concentrations of either MM or UA is increased. System S18 is prepared in order to determine the complexation energy among K_3Cit, UA and MM molecules in water. Lastly, systems P0–P3 are prepared to perform the umbrella sampling.

■ RESULTS AND DISCUSSION

5.1 First coordination number

The first shell coordination number (CN) is an estimate of how many molecules of a given species accumulate around a reference atom in a shell extending from 0 to a distance r_c. CN can be defined as follows:[240, 241, 242, 280]

$$CN = 4\pi\rho_\beta \int_0^{r_c} r^2 g_{\alpha\beta}(r) dr, \tag{5.7}$$

The CN of β-type atoms are determined by this formula in a solvation shell around the atomic sites of α, between 0 and separation r_c. ρ_β defines the number density of atom type β in the system. Here, first shell CNs are determined in the context of interactions between MM-UA, UA-UA, MM-MM, UA-MM, MM-K_3Cit, and UA-K_3Cit using the relevant radial distribution functions considering the center of masses (COM) of these molecules.

Table 5-3. First shell coordination numbers (CNs) of MM around UA (r_c=7 Å), UA around UA (r_c=6 Å), MM around MM (r_c=5 Å), MM around K_3Cit (r_c=5.45 Å), and UA around K_3Cit (r_c=5.45 Å) for different systems. Here, r_c is the position of the first minimum of the respective radial distribution functions considering the center of mass (COM) of each molecule (not shown).

System	MM around UA	UA around UA	MM around MM	MM around K_3Cit	UA around K_3Cit
S0	2.17	1.78	0.62	—-	—-
S0-a	2.22	1.77	0.66	—-	—-
S1	1.72	1.83	0.80	0.32	0.09
S2	1.27	1.40	0.38	0.52	0.20
S3	0.40	1.12	0.18	0.83	0.35
S4	0.22	0.87	0.11	0.97	0.44
S4-a	0.26	0.99	0.08	0.95	0.39

In Table 5-3, for systems S0–S4, the first shell CNs for MM-UA interaction are taken first. The CNs of MM around UA are 2.17, 1.72, 1.27, 0.40, and 0.22 for systems S0, S1, S2, S3, and S4, respectively. Note that, the system S0 comprises MM and UA only, while K_3Cit of different concentrations are included in other systems (from systems S1 to S4). As the number of K_3Cit is increased from system S1–S4, the CN of MM around UA decreases. Thus, for S0 system, the CN of MM around a reference UA has the highest value since in the absence of K_3Cit, the maximum aggregation emerges. In addition, the CN for system S4 is reduced to 0.22 significantly. Such a decrease in CN value suggests that the alternation in the assembly process among MM and UA molecules in presence of K_3Cit. Note that there

is a negligible change in volumes as one moves from system S0 to system S4 which suggests a minimum effect of volume change in the "CN" values. In the context of UA self-assembly, a similar scenario can also be observed, in which UA molecules self-aggregate, which results in the highest CN for system S0, where no K_3Cit molecules are available. However, the CNs for UA are decreased subsequently when the K_3Cit molecule is introduced with an increase of concentrations from system S1 to S4. The CN for UA accumulation in system S0 is 1.78 which decreases to 0.87 in system S4. Furthermore, the CN of MM around MM decreases from 0.62 (in system S0) to 0.11 (in system S4). It indicates that K_3Cit interacts concurrently with the two molecules i.e., MM and UA. In fact, this concurrent K_3Cit-UA-MM interaction can also be viewed with regard to the estimation of the CNs for MM-K_3Cit and UA-K_3Cit pairs. The CN of K_3Cit around MM is 0.32 for system S1, which is 0.95 for system S4. Therefore, higher the number of K_3Cit present in a system, the more likely the communication is. In addition, as one moves from system S1 to system S4, the CN of K_3Cit around UA is increased by 0.09 to 0.39. Such increase in the CN value of K_3Cit for both MM and UA molecules demonstrates that K_3Cit coordinates with them in order to protect both their self-assembly as well as inter-accumulation.

Moreover, the findings from two separate ensembles (NPT and NVT) for systems S0 and S4 are compared in the present study. In principle, the aggregation properties can be dependent on the choice of thermodynamic ensembles.[258] In Table 5-3, the CNs of system S0 (in NVT ensemble) are compared with that of S0-a (in NPT ensemble) and similarly, the CNs of systems S4 (in NVT ensemble) and S4-a (in NPT ensemble) are compared. The very similar CN values confirm the robustness of the current simulations.

Spatial density plots

This section discusses the spatial density distributions for different interactions such as MM-UA, UA-K_3Cit, and MM-K_3Cit. In Figure 5-2 (a) and (b), for systems S1 and S4, the spatial density distributions for MM around a reference UA is presented. Last 20 ns of MD simulation trajectory files are used to determine these density distributions.[158] It can be seen that the density distribution of MM around a reference UA is decreased from system S1 to S4. Note that, a small number of K_3Cit molecules is available in system S1. This implies MM-UA interaction is prevalent in presence of very low concentration of K_3Cit (in system S1). However, MM-UA interactions are significantly reduced in the presence of higher number of K_3Cit molecules (in system S4). K_3Cit, therefore, inhibits

the aggregation of MM-UA, preventing it from forming a large aggregated structure. In addition, K_3Cit density around a reference UA is increased from system S1 to S4 (Figure 5-2(c) and (d)). Not just that but the density of K_3Cit is likewise increased around a reference MM (Figure 5-2(e) and (f)). Thus, excessive K_3Cit aggregation around both molecules, namely MM and UA, induces a disruption in the higher order clusters involving MM and UA molecules, which, thus, turns into lower order clusters. It is now evident that the destruction of MM-UA conjugate is necessary to dismantle the development of larger kidney stones. The role of a third molecule in the degradation of MM-UA cluster is therefore imperative.

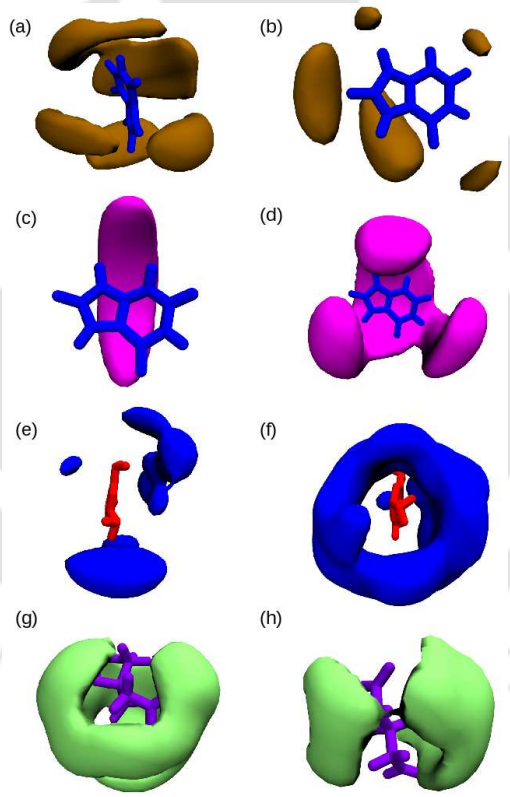

Figure 5-2. *(a)–(b) Spatial density distributions of MM around a reference UA in system S1 and system S4, respectively. (c)–(d) Spatial density distributions of K_3Cit around a reference UA in system S1 and system S4, respectively. (e)–(f) Spatial density distributions of K_3Cit around a reference MM in system S1 and system S4, respectively. (g)–(h) Spatial density distributions of water around a reference K_3Cit in system S1 and system S4, respectively. Here, isovalue of 2 $Å^{-3}$ is used for all cases.*

Similarly, third molecule has to enable conjugation with either MM or UA or any molecule

during the solubilization of renal stones, it is, therefore, important to check the overall water accessibility of such conjugates. Moreover, the water accessibility of the total conjugates should be increased by the third molecule in the context of solubilization. If not, the third molecule should not be an alternative for breaking the kidney stones. Therefore, to check the water accessibility of overall MM-UA-K_3Cit conjugate, we have determined the water density around a reference K_3Cit. It is observed that in system S4 like system S1, K_3Cit molecules are exposed to water. In system S1, the conjugation between MM and UA is high and renders a larger cluster (discussed later). Three or four K_3Cit molecules out of five K_3Cit now come closer to the aggregated MM–UA cluster to include it in system S1. However, the amount of K_3Cit molecules to sever the MM-UA cluster is not adequate. As a result, the MM-UA cluster stays surrounded by these K_3Cit molecules. Consequently, K_3Cit molecules are likely to be exposed to water. Thus, the water density of K_3Cit molecules is indeed very high (Figure 5-2(g)). In system S4, about twenty five out of thirty K_3Cit molecules are engaged in smaller MM-UA clusters (discussed later).

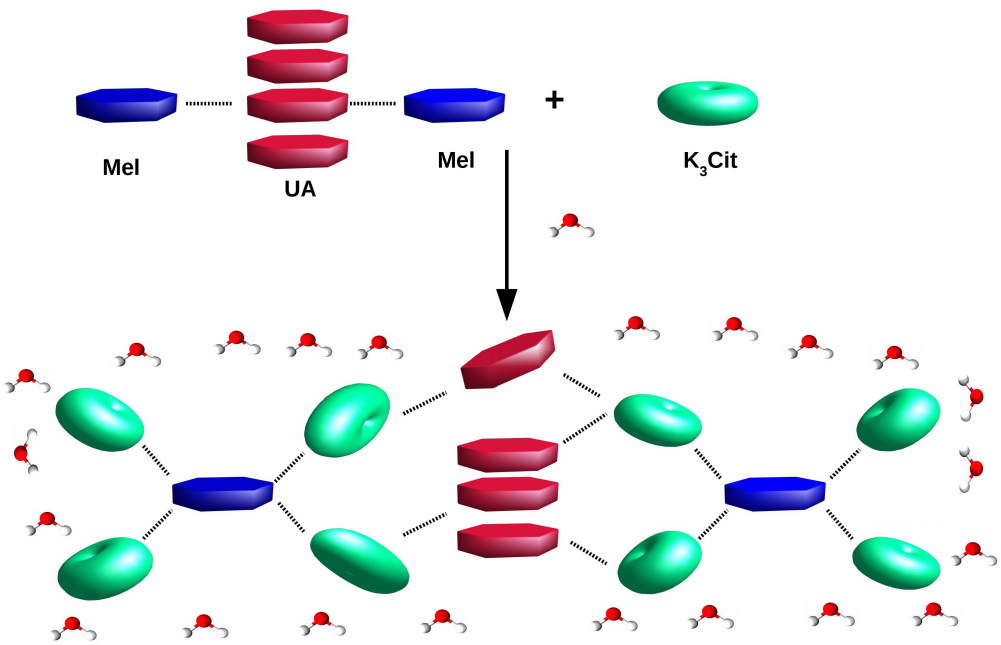

Figure 5-3. *Schematic representation of co-ordination of K3Cit (green) with MM (blue) and UA (red) molecules. Here, K_3Cit molecules are interspersed in and outside the MM and UA molecules results in lower order MM-UA clusters. Overall MM-UA-K_3Cit conjugate is surrounded by water molecules.*

Now, these K_3Cit molecules will be interspersed "in and outside" the MM and UA molecules result in lower order MM-UA clusters (Figure 5-3). K_3Cit molecules are therefore subjected to water in system S4 as well. Nevertheless, the MM and UA molecules of system S4 are symmetrically rounded by a significant amount of K_3Cit molecules. A significant water density is therefore accessible in system S4 around K_3Cit molecules (Figure 5-2(h)). Thus, the cumulative MM-UA-K_3Cit cluster is highly accessible to water. The presence of K_3Cit molecules in the MM-UA system, thus, is conducive to the degradation of entire cluster.

Free Energy Landscape (FEL)

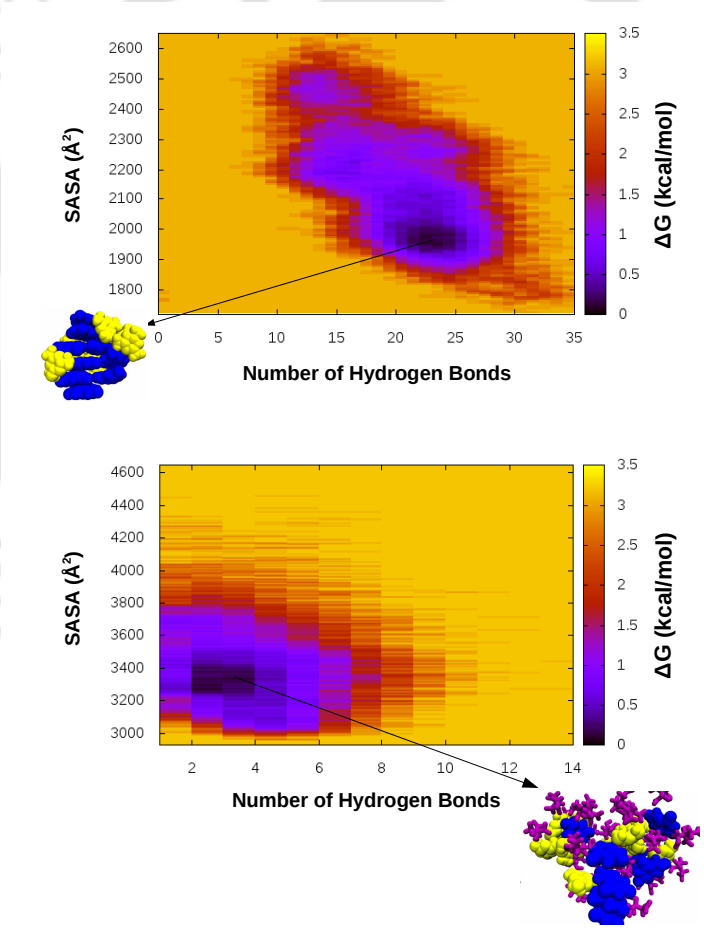

Figure 5-4. *Free energy landscape (SASA ($Å^2$) vs number of hydrogen bonds) for systems S0 (top panel) and S4 (bottom panel) for MM-UA pair. Simulation snapshots of these systems are also attached with the corresponding FELs where MM is represented in blue color, UA is presented by yellow color, and K_3Cit are presented by pink color.*

In order to build the free energy landscape (FEL) of MM-UA aggregation, in

different inhibitor solutions in water, two appropriate reaction coordinates (viz. hydrogen bonds between MM and UA and solvent accessible surface area (SASA) in the present study) are chosen to explain the imminent aggregation dynamics. The FEL is constructed in accordance with the following formula:[253]

$$\Delta G(V) = -k_B T[\ln P(V) - \ln P_{max}], \tag{5.8}$$

where P(V) means the probability of coordinate (V) that is computed from the last 100 ns trajectory path and it is subtracted by P_{max} which is the maximum of the distribution so that ΔG becomes zero for the minimum free energy. It should be noted that the area that is accessible to water in system S0 is specified by SASA, whereas for system S4, it is accessible for inhibitors as well as water.

Figure 5-4 (top panel) reveals that in the free energy landscape, the average intermolecular hydrogen bonding between MM and UA is very large. Therefore, the SASA in S0 is minimal. Moreover, the minimum free energy in this system discloses a stronger aggregation between MM and UA molecules, which engenders smaller areas available for water. On the other hand, the greater SASA produces minimal free energy, in which very little hydrogen bonding connections are formed between MM and UA which implies that the accumulation/aggregation is very poor in system S4 (bottom panel of Figure 5-4) as opposed to the other system S0. Thus, the participation of K_3Cit molecules in system S4 impedes mostly with MM-UA aggregation.

The individual states of energy landscape depict various intermediates during the simulation. In order to verify the convergence of the simulation run, we have compared FELs for different time frames. The last 100 ns are divided into four (i.e., 25ns each) windows and FEL for each of these 25 ns window is calculated. Figure 5-5 reveals that for each window in system S0, the FELs with an almost equal number of hydrogen bonds with the corresponding SASA values closely resemble each other. Not only that, it is possible to identify the MM density around a reference UA for each window of the same system without having much differences. Furthermore, FELs in system S4 (Figure 5-6) as well as the density distribution of MM around a reference UA reveal exactly similar behavior in each window. Thus, these two systems, considered in the present study, are converged as the sampling of convergence for the simulation run matches well in terms of FELs over the time.

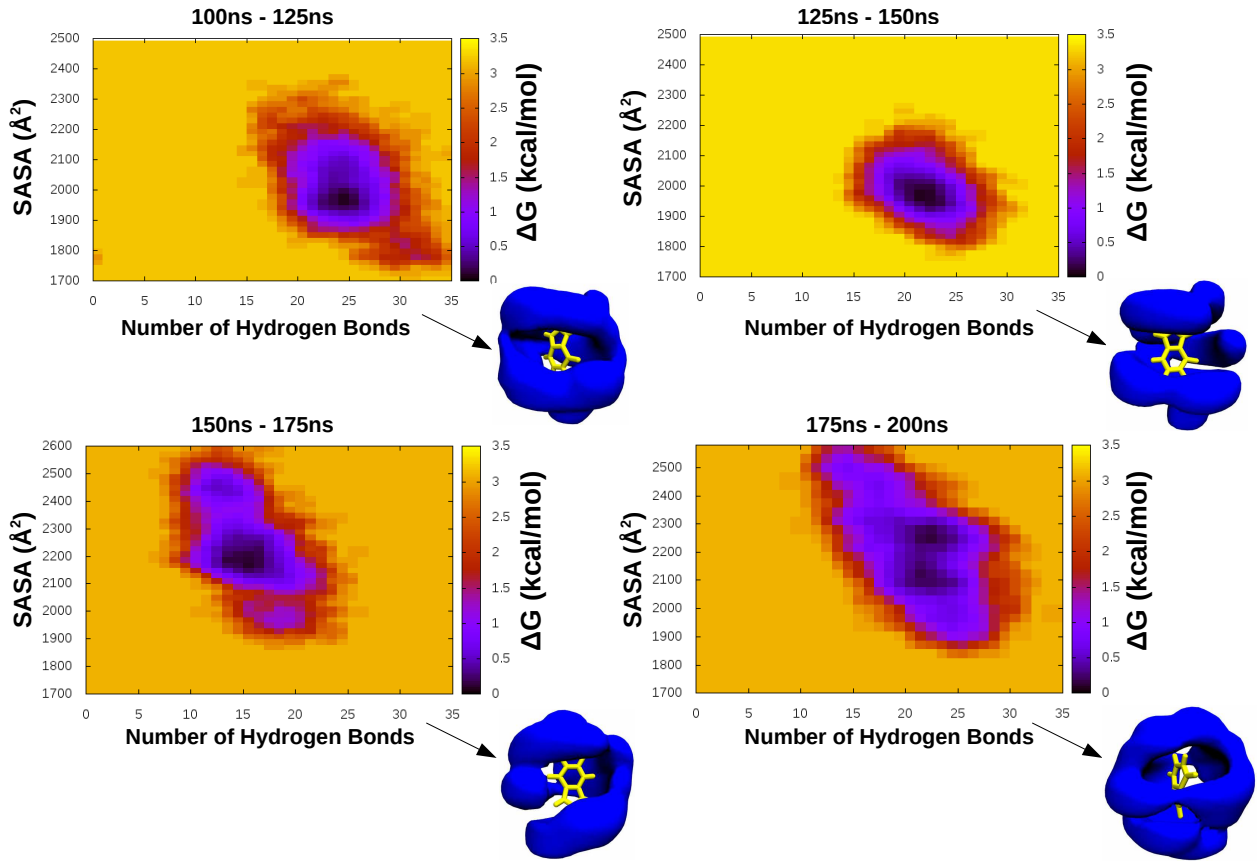

Figure 5-5. *Convergence of simulation is presented by FEL for system S0 in multiple time steps. The corresponding density distribution of MM around a reference UA is also presented over each time frame for each 25 ns.*

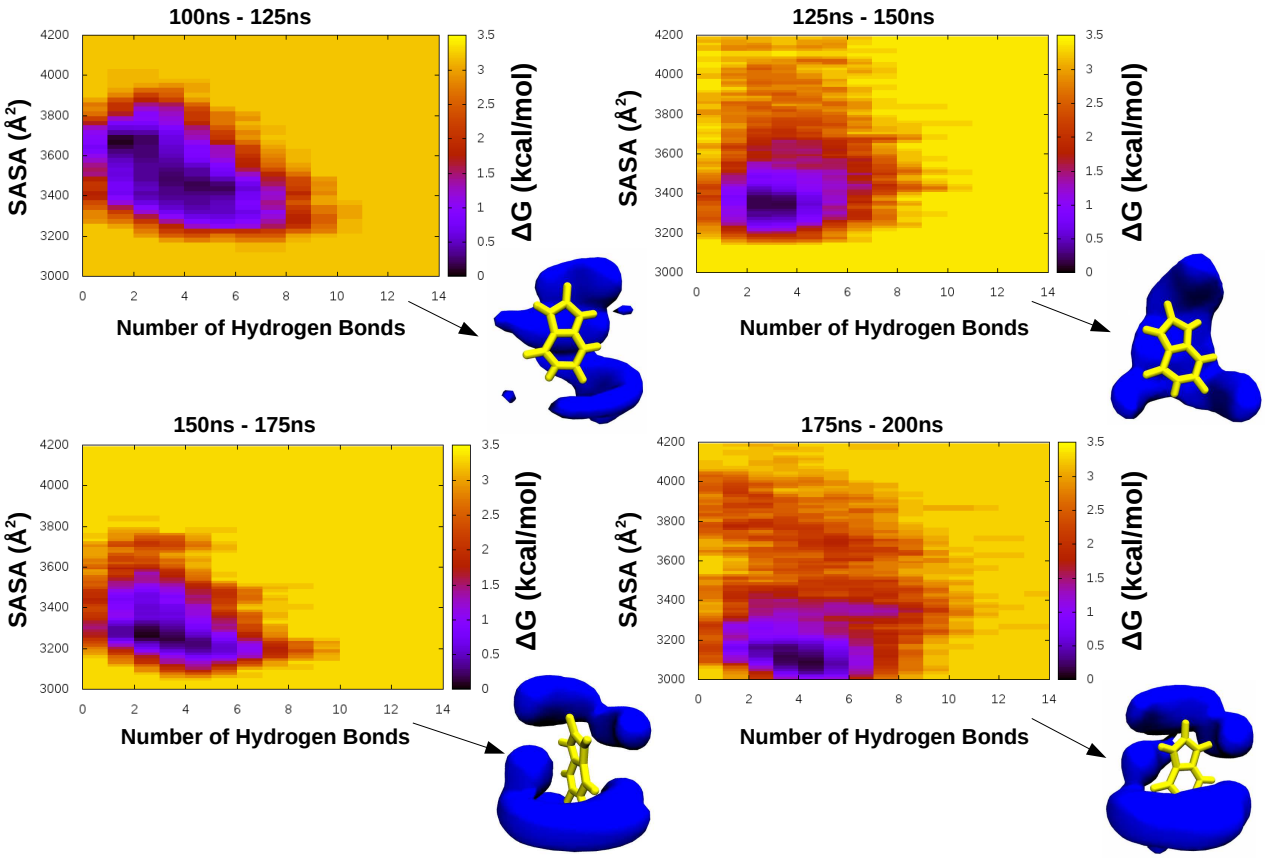

Figure 5-6. *Convergence of simulation is presented by FEL for system S4 in multiple time steps. The corresponding density distribution of MM around a reference UA is also presented over each time frame for each 25 ns.*

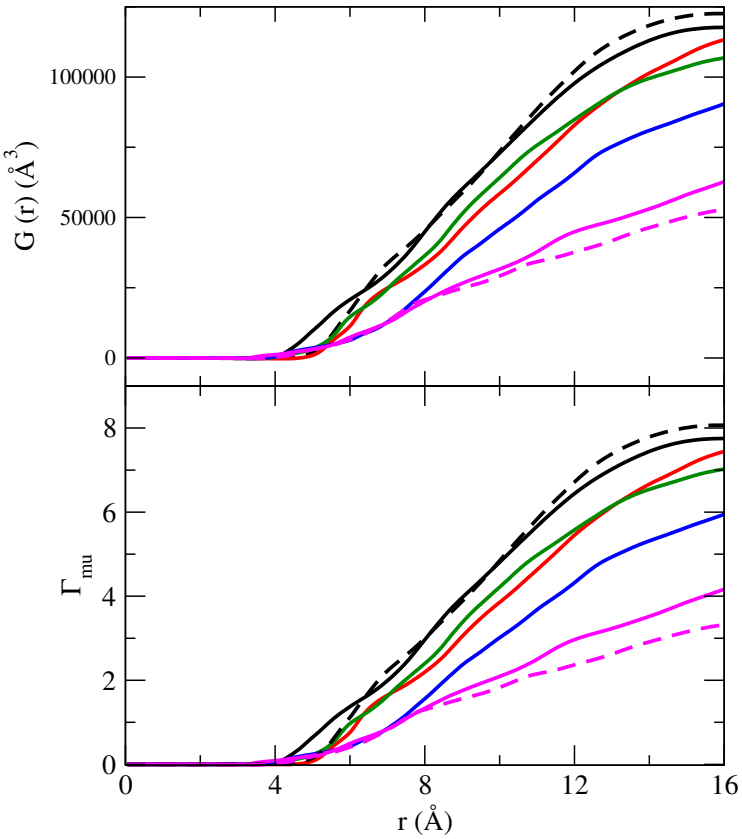

Figure 5-7. *Kirkwood–Buff integrals (top panel) and preferential interaction parameters (bottom panel) of MM-UA interactions for systems S0 (black), S0-a (dashed line of black), S1 (red), S2 (green), S3 (blue), S4 (magenta), and S4-a (dashed line of magenta).*

In the present study, for MM-UA pair of various solutions, the preferential interaction parameter, Γ_{mu}, is determined. The determination of Γ_{mu} ensures the preferential interaction of MM molecules with UA molecules for systems S0—S4. Γ_{mu} is constructed according to the following equation:[285, 194, 195, 196, 179, 286, 282]

$$\Gamma_{mu} = \rho_m(G_{mu} - G_{mw}) \tag{5.9}$$

where m and u denotes to MM and UA molecules,respectively; and ρ_m corresponds to the number density of MM molecules. The preferable interaction between any two molecules

can be indicated with the positive value of Γ. Here, G_{mu} and G_{mw} reciprocate to Kirkwood–Buff (KB) integrals and these integrals can be obtained following previous studies.[285, 194, 195, 196, 179, 286, 282] It should be mentioned that these integrals can be achieved with the corresponding radial distribution functions. Center of masses (COMs) of MM and UA molecules are considered to estimate these distribution functions. The values of G_{mu} are shown in Figure 5-7 (top panel). It is to be noted that the symbol Γ is similar with that of symbol τ (ussed in the other chapters).

Above equation points out the values of Γ_{mu} for systems S0–S4, where both MM and UA are maintained at a fixed concentration. From systems S1–S4, the concentration of K_3Cit is increased. Figure 5-7 (bottom panel) presents the change in Γ_{mu}. The positive values of Γ_{mu} for all systems indicate a favorable MM-UA interaction in these systems. However, it is intriguing to note that, the value of Γ_{mu} gradually decreases from system S0–S4. The reduced values in Γ_{mu} demonstrate that, in the presence of K_3Cit molecules, MM looses its preferred interaction with UA molecules. Moreover, system S4, which shows a lowest Γ_{mu} value in all systems, has the highest number of K_3Cit molecules, while system S0, where no K_3Cit molecule is available, has the highest Γ_{mu} value. The presence of the K_3Cit molecule in the MM–UA mixture, therefore, profoundly disrupts the interaction between MM and UA and, thus, prohibits the formation of an extensive cluster of MM and UA molecules in water. Moreover, similar results for S0 and S0-a systems together with systems S4 and S4-a, are obtained through the NVT and NPT simulations and which, therefore, demonstrates the robustness of the results of the simulation conducted.

The preferential interaction parameters, Γ_{mu} for MM-UA interaction, do not provide any substantial mechanism in the way K_3Cit molecules interfere with the aggregation of MM-UA. It offers just statistical circumstances in the presence and absence of the K_3Cit, without any specific mechanistic perspective on MM-UA dissolution and aggregation, respectively, in water. Therefore, the analysis like the cluster structure analysis, binding free energy calculation along with enhanced sampling (addressed below) should be carried out.

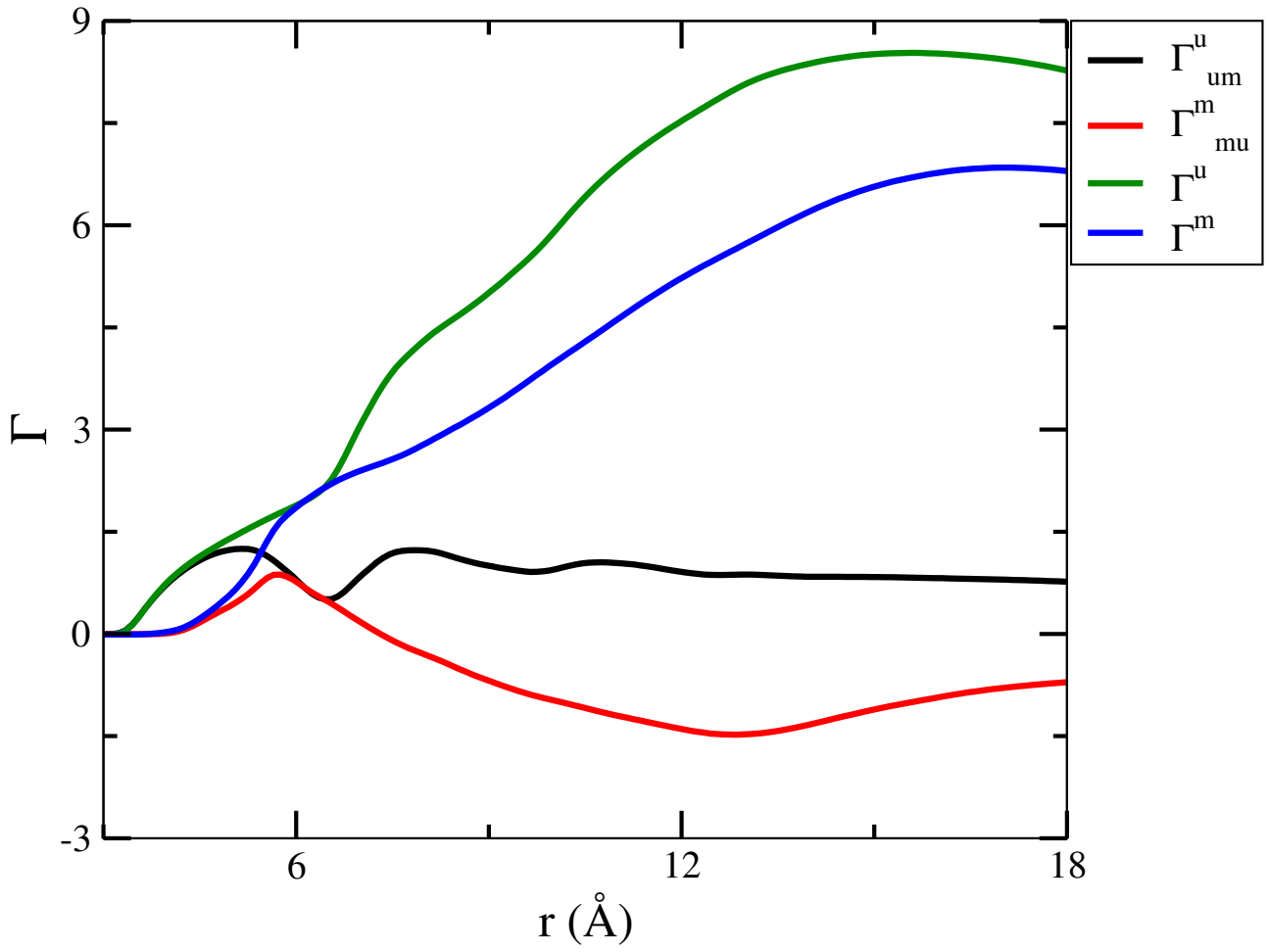

Figure 5-8. *Preferential interaction parameters for UA-UA over UA-MM (Γ^u_{um}), MM-MM over MM-UA (Γ^m_{mu}), UA-UA over UA-water (Γ_{uu}), and MM-MM over MM-water (Γ_{mm}) for system S0.*

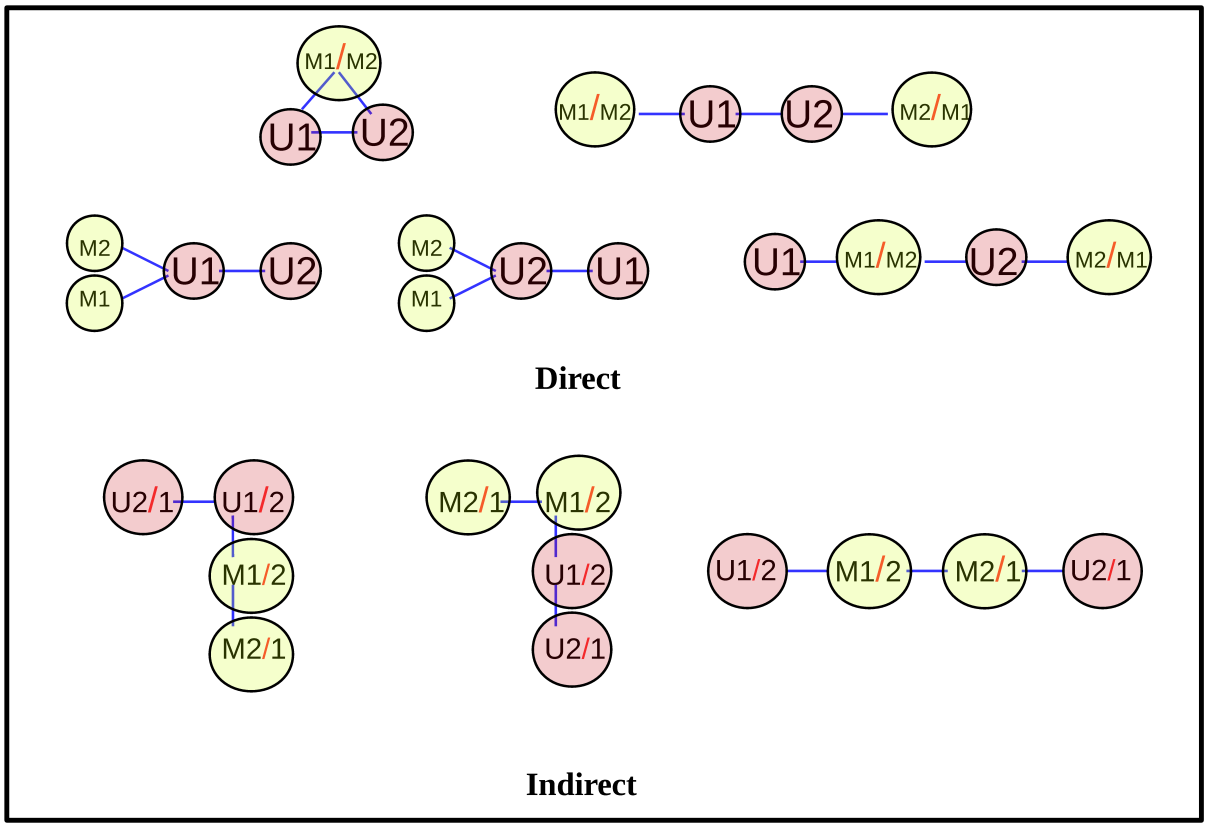

Figure 5-9. *Schematic representation of MM-UA cluster. Here, when MM (M1/M2) directly attaches with UA (U1/U2) then it is called "direct approach". Similarly, when MM and UA are attached through any bridges made of MM or UA, then it is referred as "indirect approach".*

This section discusses the variation of different clusters produced due to MM-UA interactions both in presence and absence of K_3Cit molecules. To determine the effect of K_3Cit on MM-UA pair, a strategic approach is made in order to establish the cluster size. The cluster size for the MM-UA pair is determined by estimating the number of melamine molecules attached to the highest order UA cluster to form the biggest MM-UA cluster other than any discrete clusters in each system and subsequently add this total of MM and UA molecules. The estimation of preferential interaction parameter provides the best explanation for deciding such an approach for cluster structure. For system S0, we have taken 157 MM as UA molecules without the presence of any K_3Cit molecules. It is seen that

the preferential interaction parameter for UA-UA over UA-MM (Γ^u_{um}) has positive value (Figure 5-8). Moreover, the preferential interaction parameter for MM-MM over MM-UA (Γ^m_{mu}) shows negative value (Figure 5-8). Therefore, it is assumed that UA molecules aggregate (with like molecules) more preferably over MM molecules in system S0. In our previous study, it was defined that UA molecules aggregate into larger clusters which then drags MM molecules towards themselves to add to the cluster.[207] Not only that UA-UA aggregation is more preferable than MM-MM pair formation as it is shown in Figure 5-8 by means of Γ_{mm} and Γ_{uu} values. Here, Γ_{uu} predominates over Γ_{mm}. In this regard, Γ^u_{um}, Γ^m_{mu}, Γ_{uu}, and Γ_{mm} are determined by the following equations:[285, 194, 195, 196, 179, 286, 282]

$$\Gamma^u_{um} = \rho_m(G_{uu} - G_{um}) \tag{5.10}$$

$$\Gamma^m_{mu} = \rho_m(G_{mm} - G_{mu}) \tag{5.11}$$

$$\Gamma_{uu} = \rho_m(G_{uu} - G_{uw}) \tag{5.12}$$

$$\Gamma_{mm} = \rho_m(G_{mm} - G_{mw}) \tag{5.13}$$

Therefore, in the presence and absence of K_3Cit molecules, it is ideal to define the cluster size on number of melamine molecules that are attached with the largest cluster of UA to form the biggest cluster of them and then add the total number of MM and UA molecules. To define the clusters of different sizes for UA-UA interaction, we have considered two criteria in accordance with our previous studies[207, 282] and these are as follows: 1) $r_{COM-COM}$ $\leqslant$ 6 Å and the two interacting moieties should be hydrogen-bonded simultaneously; 'or' 2) $r_{COM-COM} \leqslant$ 6 Å and the two interacting moieties should be in π-π stacking conformation simultaneously. Here, $r_{COM-COM}$ refers to the center of mass-center of mass distance between two UA molecules. For MM-UA interactions, cluster size is defined as follows: $r_{COM-COM} \leqslant$ 7 Å and the two interacting moieties should be hydrogen-bonded simultaneously and the same definition goes for MM-MM, UA-K_3Cit, MM-K_3Cit and, K_3Cit-K_3Cit clusters too, however, the cut off distances for these cases are defined as $r_{COM-COM} \leqslant$ 5 Å , 5.45 Å , 5.45 Å , and 7 Å , respectively.

In this regard, it is to be noted that for MM-UA interaction, only the "direct approach" is taken into account following our previous study[207, 282] along with the conditions mentioned above to describe the total size of the biggest cluster made by the pair. Here, the other option, i.e., "indirect approach" is discarded (Figure 5-9).[207, 282] This is done from the strategic point of view. Here, "direct approsch" depicts when one MM and UA in

each are directly attached. In case of "indirect approach" in where MM and UA molecules can form a cluster in which they are not directly attached but by bridging through MM or UA molecule. The "indirect approach" does not deal with the inhibition of kidney stones properly as the growth of renal stone is occurred due to the interaction between MM and UA directly. Therefore, only the "direct approach" deals with the direct combination of MM and UA perfectly. Now, a potent inhibitor should be able to counteract with the direct combination of MM-UA pair. The "indirect approach" can also be considered from a tactical perspective where an expanded cluster is generated in this situation. However, we are concerned about the prevention of growth of kidney stones rather than the overall size of them.

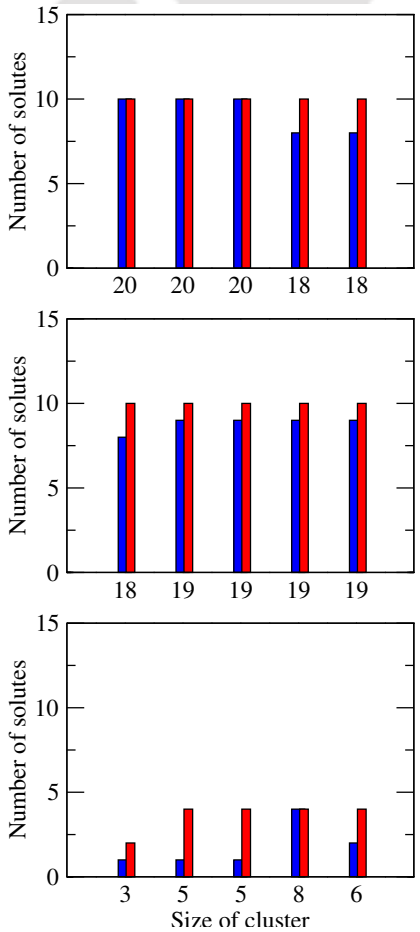

Figure 5-10. *The maximum sizes of the MM (blue)-UA (red) clusters for the last 20 ns out of total 200 ns at each 4 ns interval for systems S0 (top panel), S1 (middle panel), and S4 (bottom panel).*

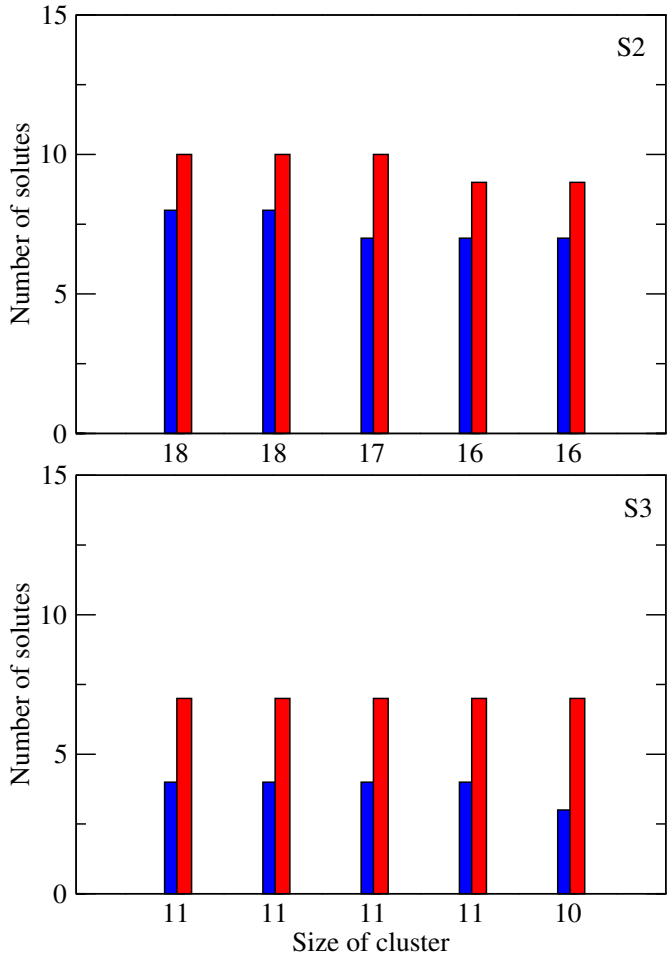

Figure 5-11. *The maximum sizes of the MM (blue)-UA (red) clusters for the last 20 ns out of total 200 ns at each 4 ns interval for systems S2 and S3.*

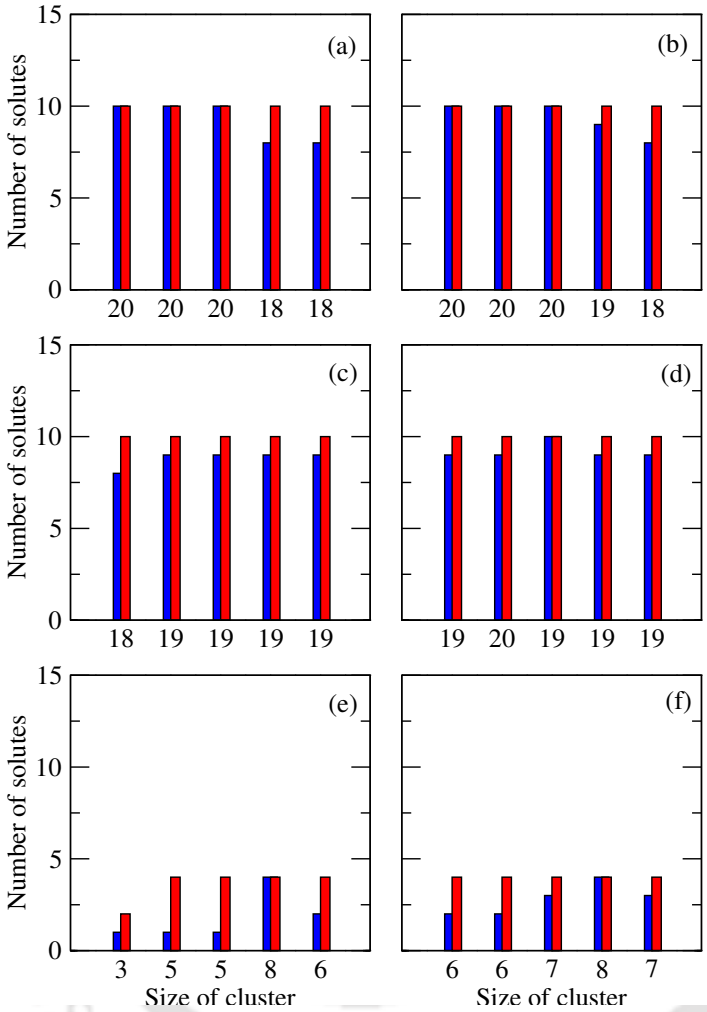

Figure 5-12. *(a)-(f) presents the maximum sizes of the MM (blue)-UA (red) clusters for the last 20 ns out of total 200 ns at each 4 ns interval for systems S0, S0-a, S1, S1-a, S4, and S4-a, respectively.*

Firstly, MM-UA cluster is considered for systems S0–S4 (Figure 5-10). For system S0, all UA molecules together form a large cluster with the incorporation of all 10 UA molecules (Figure 5-10 (top panel)). Now, this decamer formed in system S0 then drags almost 8 to 10 MM molecules to add to it (Figure 5-10 (top panel)). Therefore, the aggregation is very strong in case of system S0. A similar trend can also be found in system S1 in which a small number of K_3Cit molecules is present (Figure 5-10 (middle panel)). Thus, the lower concentration of inhibitor does not effectively disrupt the MM-UA cluster. However, as the number of K_3Cit increases, MM-UA cluster starts to disintegrate. In system S2, a small fluctuation in the UA cluster as compared to system S1 is observed (Figure 5-11). Though,

the size of the UA cluster is higher, however, a very less number of MM molecules are being attached to it due to the presence of K_3Cit molecules in system S2. Therefore, the interference by K_3Cit molecules occurs in system S2. If we move to system S3, a severe destruction of UA self-aggregated cluster can be seen (Figure 5-11). The overall cluster made of MM and UA is now reduced to lower order cluster. Therefore, the lower order UA cluster now drags small number of MM molecules to add to it. This occurs because there are an adequate number of K_3Cit molecules in system S3. Furthermore, it can now be seen the impact of K_3Cit molecules on system S4 in which a much lower order cluster of MM and UA is found by the incorporation of smaller number of MM as well as UA molecules (Figure 5-10 (bottom panel)). Thus, K_3Cit simultaneously interacts with MM and UA molecules, thus, reduces the cluster size (discussed later). Moreover, NPT and NVT simulations produce comparable results for these systems (i.e., S0, S0-a, S4, and S4-a) as shown in Figure 5-12. In principle, ensemble can have an effect on the size of the cluster.[258] However, the present simulations deal with the minimal effect on cluster size with the variation of ensembles, which, thus proves the robustness of the presented results.

Now, if we look into the behaviour of K_3Cit molecules in destabilization of these clusters made of MM-UA (Figure 5-13), it can be found that 3 to 4 molecules out of total five K_3Cit molecules add to the MM-UA cluster in systems S1 and S1-a (Figure 5-13(c)-(d)). But in case of systems S4 and S4-a, around 25 molecules or more than that are involved with MM-UA cluster (Figure 5-13(e)-(f)). Thus, K_3Cit breaks the direct contact of UA and MM, whereas it is attached with all MM and UA molecules to form a overall larger MM-UA-K_3Cit conjugate (which contains MM, UA, and K_3Cit in where K_3Cit are interspersed in and outside the MM and UA molecules). Therefore, K_3Cit molecules disrupt the MM-UA cluster and the overall larger MM-UA-K_3Cit conjugate becomes more accessible to water. Again, it is also confirmed that NPT and NVT simulations produce similar results.

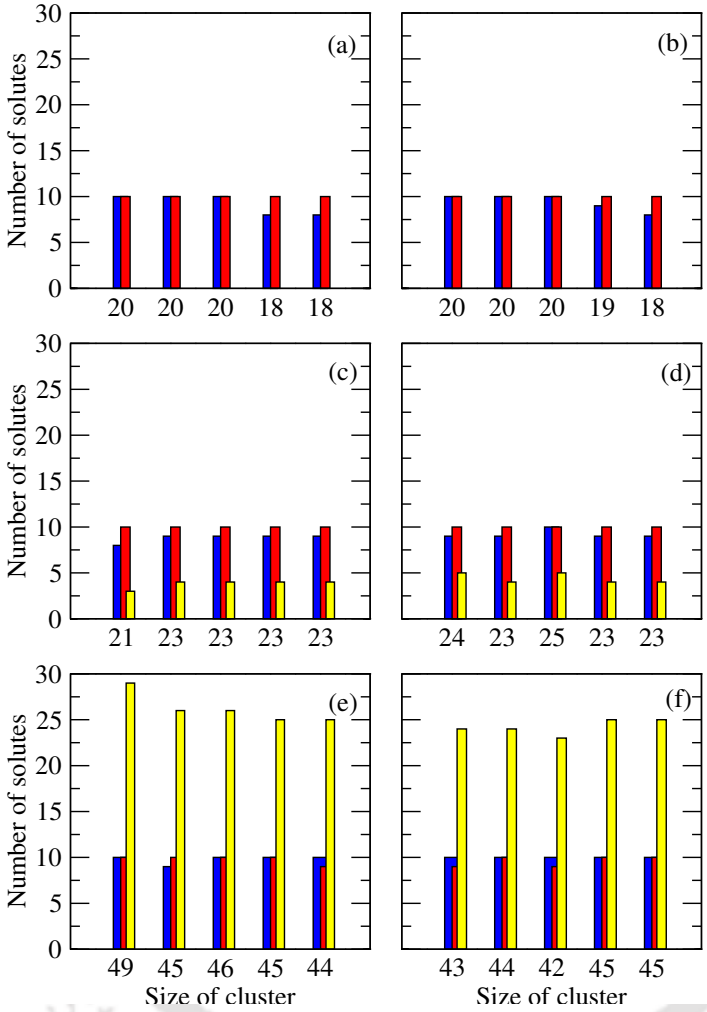

Figure 5-13. *(a)-(f) Distributions of clusters of various sizes resulting from MM (blue)-UA (red)-K3Cit (yellow) interactions for systems S0, S0-a, S1, S1-a, S4, and S4-a, respectively. Here, the size of the conjugate of MM-UA-K_3Cit is calculated by the number of K_3Cit molecules that are attached with MM and UA molecules by direct as well as indirect approach.*

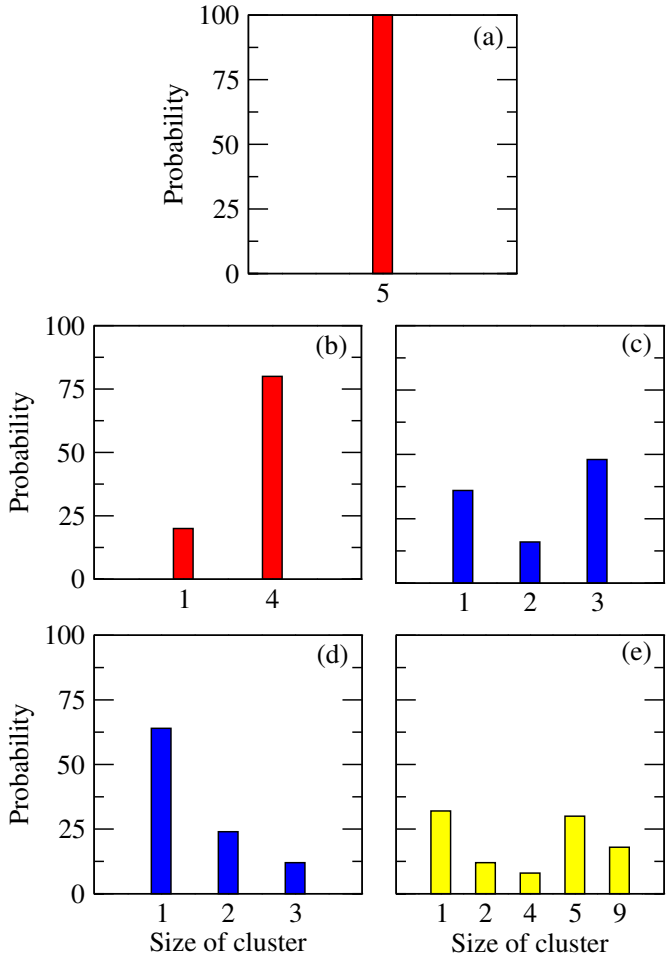

Figure 5-14. *Distributions of clusters of various sizes resulting from UA-UA (a-b), MM-MM (c-d), and K_3Cit-K_3Cit (e) interactions for corresponding systems (a) S5, (b) S6, (c) S7, (d) S8, and (e) S9, respectively.*

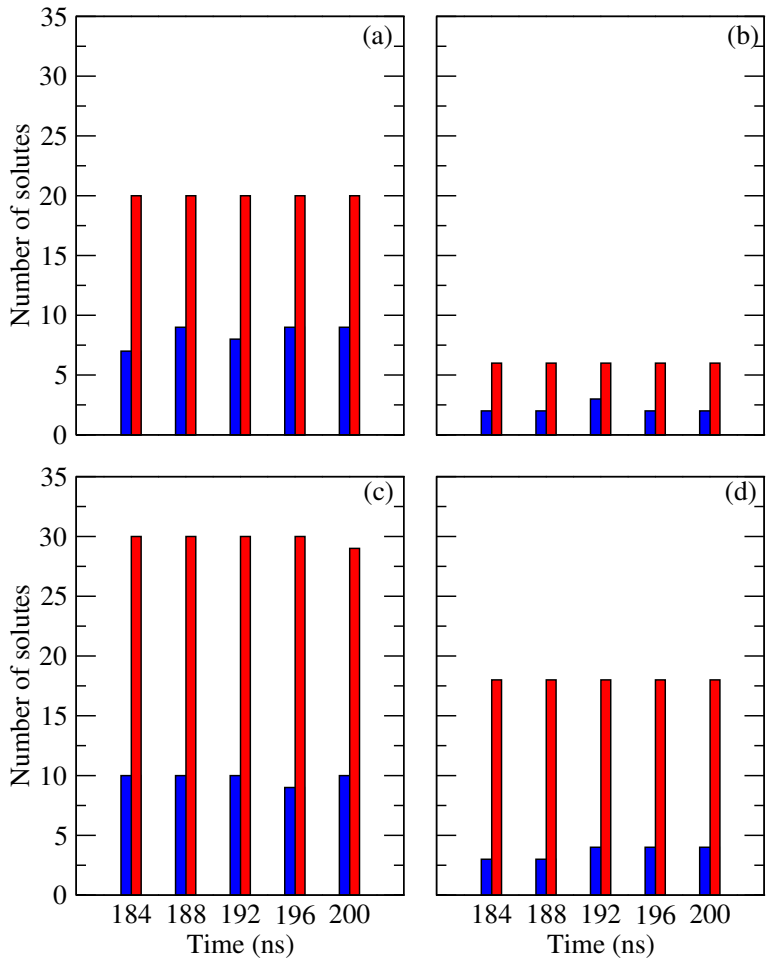

Figure 5-15. *(a)-(d) presents the maximum sizes of the MM (blue)-UA (red) clusters for the last 20 ns out of total 200 ns at each 4 ns interval for systems S10, S11, S12, and S13, respectively.*

Now, it will be intriguing if we look on how K_3Cit molecules interact with UA molecules in the absence of MM molecules. To do so, we have made two control systems (i.e., systems S5 and S6). Here, in system S5, five UA molecules are taken in pure water where in system S6, five UA molecules are immersed into same number of water molecules, but in presence of 10 K_3Cit molecules. It is found that, in system S5, pentamer (100%) is formed for last 20ns trajectory (Figure 5-14(a)). Thus, the aggregation of uric acid molecules is quite strong. However in case of system S6, 80% tetramer and remaining 20% is present as monomer (Figure 5-14(b)). Thus, K_3Cit molecules bring a change in UA clustering. Now, as 100% pentamer is formed in system S5, thus it can be assumed that aggregation of UA molecules

is quite strong. Thus, the formation of tetratmer(80%) in presence of K_3Cit molecules proves that K_3Cit molecules interact well with UA molecules. Similar systems are made for MM molecules too. In case of system S7, 48% trimer, 16% dimer and remaining 36% monomer (Figure 5-14(c)) are found for MM molecules. Therefore, in that concentration, MM molecules aggregate but not as much as like UA molecules. Furthermore, in the presence of K_3Cit molecules (system S8), MM molecules are significantly disrupted as like UA molecules. In system S8, 12% trimer, 24% dimer and 64 % monomer are formed (Figure 5-14(d)). Therefore, the interaction between K_3Cit and MM is also preferable. As, K_3Cit interacts with both molecules (i.e., MM and UA) in quite fascinating manner, thus, it is confirmed that the reduction in cluster size of MM-UA pair is occurred due to interaction with both molecules with K_3Cit simultaneously. In contrast, K_3Cit molecules do not adequately aggregate in pure water, although K_3Cit produces larger order clusters, however the percentage is not that high (18% nonamer, 30% pentamer, and 8% tetramer) as shown in Figure 5-14 (e) for system S9. Furthermore, there are considerable amounts of lower order clusters (32% monomer together with 12% dimer in Figure 5-14(e)) present in system S9. The aggregation trend of K_3Cit molecules is therefore not as high as compared to MM or UA molecules in pure water.

We have further investigated the cluster structures of MM-UA with varying concentration of MM and UA molecules to validate the alterations to the aggregation properties of MM and UA by K_3Cit when higher number of MM or UA is present in a system. To do so, we have prepared eight more control systems (S10-S17) as presented in Table 5-1. For systems S10 to S13, the concentration of MM is kept fixed, where the concentration of UA is varied. It is to be noted that along with this, 30 K_3Cit molecules are added in systems S11 and S13. This is done to verify the effect of K_3Cit on higher number of UA, when it is taken with similar concentration as like in system S4. It is found that the presence of sufficient number of K_3Cit molecules in a system is able to disrupt the kidney stones. Here, in case of system S10, 20 UA molecules make a cluster with al least 7 to 9 MM molecules in the absence of K_3Cit (Figure 5-15(a)). However, in presence of K_3Cit, the higher order clusters made in system S10 is now broken into lower order cluster in system S11 which contains a hexamer of UA molecules that drags 2 to 3 MM molecules towards themselves (Figure 5-15(b)). Thus, K_3Cit effectively disrupts the MM-UA cluster. In a similar note, K_3Cit induces disruption in MM-UA cluster when compared the cluster sizes in these two systems namely S12 and S13. In system S12, around 29 to 30 molecules of UA come into

play to make a large cluster with MM (Figure 5-15(c)). However, in the presence of K_3Cit in system S13, the higher order clusters of UA now turns into lower order clusters containing 18 of UA molecules which thus attracts lower number of MM molecules as compared to system S12 (Figure 5-15(d)). Thus, it can be concluded that the incorporation of K_3Cit in MM-UA cluster can break MM-UA composite profoundly and can be considered as a potent inhibitor in kidney stone formation.

Furthermore, similar testing is also made on two other systems (i.e., systems S14 and S15). In this case, MM concentration keeps changing where the concentration of UA is kept fixed. For system S14, all UA molecules make a decamer with 100% aggregation which thus drags about 14 to 16 of MM molecules (Figure 5-16(a)). Therefore, the aggregation between MM and UA is quite strong. As K_3Cit is introduced in system S15, the cluster size of UA is reduced to hexamer which in turn attracts less number of MM molecules (around 6 to 7) to add to the cluster (Figure 5-16(b)). This indicates that the presence of K_3Cit reduces the cluster size effectively. This is also true for systems S16 and S17. The higher order cluster of 10 UA molecules with 18 to 20 MM molecules in system S16 is now transformed into lower order cluster in which 6 UA molecules are associated directly with 6 to 7 MM molecules in system S17 (Figure 5-16(c)-(d)). Thus, although the concentration of MM is increased in system S17 from system S16, however overall MM-UA cluster size is not increased in presence of K_3Cit. Therefore, K_3Cit acts as an inhibitor perfectly. In this regard, it is to be noted that nearly all the K_3Cit molecules bind together with MM and UA molecules in systems S11, S13, S15, and S17 to form a large aggregate of MM-UA-K_3Cit (Figure 5-17). As the overall cluster size of MM-UA-K_3Cit is increased in comparison to the cluster comprised of only MM and UA in these same systems, thus, it can be concluded that MM as well as UA binds simultaneously to K_3Cit to produce a large cluster which thus breaks the MM-UA pair in a roundabout way.

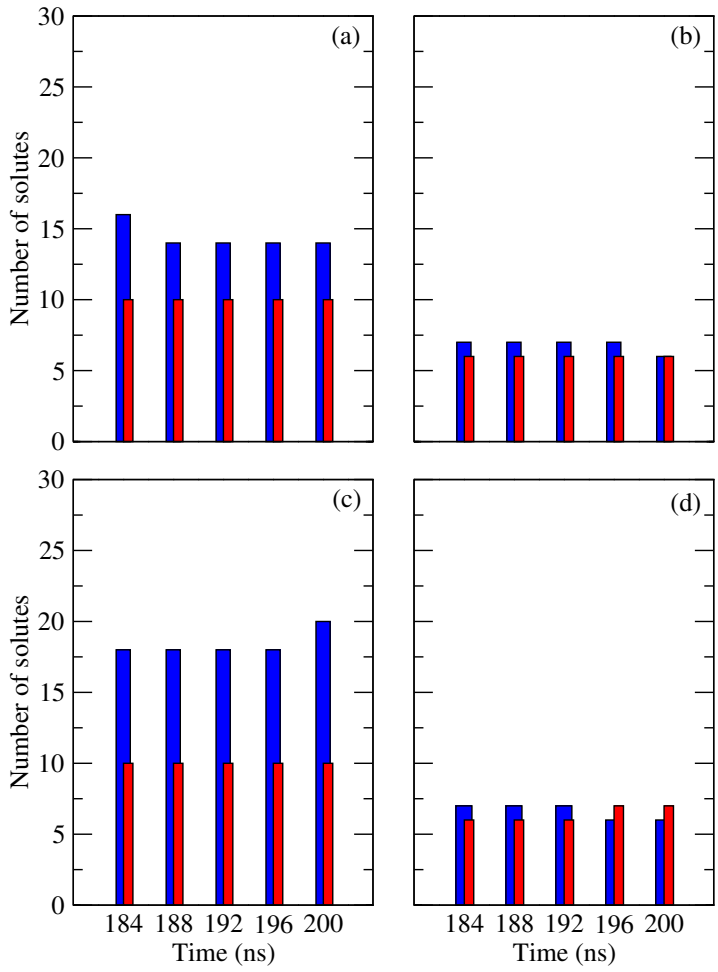

Figure 5-16. *(a)-(d) presents the maximum sizes of the MM (blue)-UA (red) clusters for last 20 ns out of total 200 ns at each 4 ns interval for systems S14, S15, S16, and S17, respectively.*

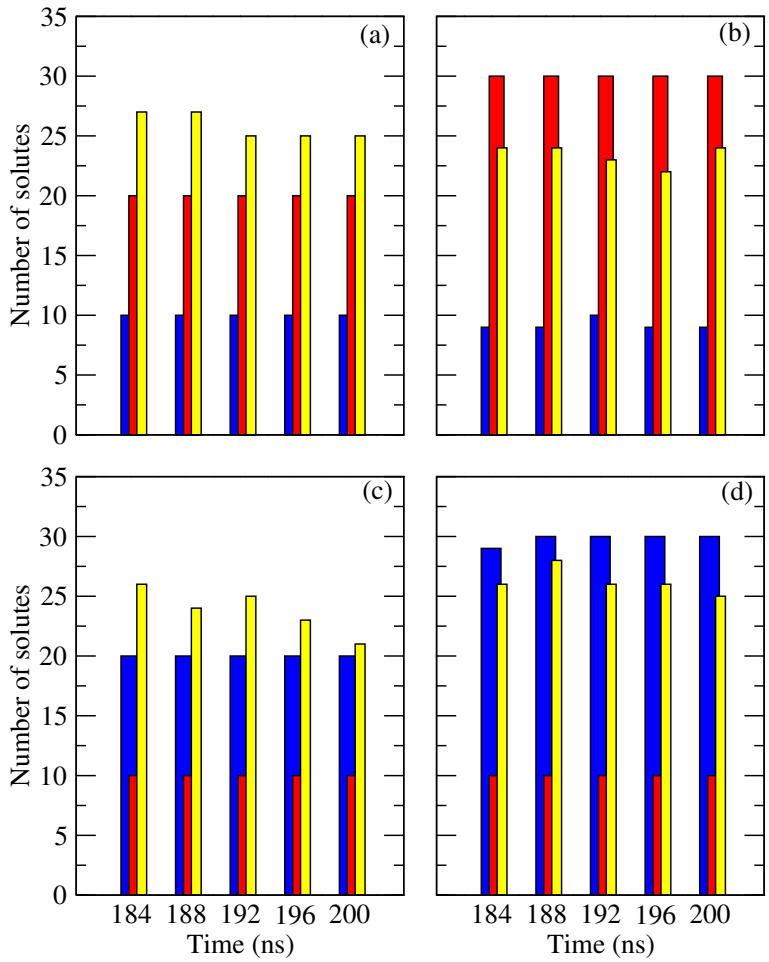

Figure 5-17. *(a)-(d) presents the maximum sizes of the MM (blue)-UA (red)-K_3Cit (yellow) clusters for last 20 ns out of total 200 ns at each 4 ns interval for systems S11, S13, S15, and S17, respectively. Here, the size of the conjugate of MM-UA-K_3Cit is calculated by the number of K_3Cit molecules that are attached with MM and UA molecules by direct as well as indirect approach.*

To determine the cluster structure, we impose the conditions where UA can make π stacking as well as hydrogen bonding during the interaction with UA, and hydrogen bonding with MM. Again, in case of MM-MM interaction, it is considered that they are hydrogen bonded. Thus, it is necessary to check their orientational preference in the presence and absence of K_3Cit molecules to validate the above-mentioned conditions. Therefore, the orientation of UA and MM molecules are analyzed when they are close enough during UA-UA, MM-MM and UA-MM interactions. Thus, the angle between the vector normals of the

molecular planes of any two interactions is taken into account for the establishment of the orientational preference criterion. The probability of orientation angles of two interacting molecules is estimated to assess the preferable orientation due to the correlations between them. For this, an angle is considered between two normal vectors of any two aromatic planes. The angle between these vector normals, that is, 0°-20° or 160°-180°, indicate a possibility that two molecules considered may have π-π stacking interactions.[161] Alongside this angle, a certain distance criterion must now also be checked in order to confirm whether or not there is π-π stacking interaction between the two aromatic planes of two respective molecules since the π-π stacking is only feasible if both of these conditions are concurrently satisfied, namely angle and distance. So, in addition to the angle if the distance between two aromatic planes falls below 5 Å , then it is possible to conclude that these two aromatic moieties have good associations with π-stacking interactions. In Figure 5-18, the probability of angle θ between two vector normals is plotted against θ. In system S0, UA-UA interaction is dominated by π-π stacking as the probability of angle θ shows maximum at angle 0°-20° (Figure 5-18(a)). However, MM-UA and MM-MM interactions are predominately governed by hydrogen bonding (the calculation of exact number of hydrogen bonds are addressed later) with minimal contribution from π-π stacking as the probability of angle θ presents a broad peak with a maximum at $\theta\approx$45°-120° (Figure 5-18(a)). Moreover, this is also true for the system S4 in which maximum concentration of K_3Cit is present (Figure 5-18(b)). Therefore, K_3Cit does not alter the orientational preference of MM as well as UA. In addition to this angle criteria, probability of distance (P(r)) is also measured and it is found that in both systems, i.e., S0 and S4, UA molecules prefers to stay around 3–5 Å distance (Figure 5-18(c)–(d)). Thus, along with the angle, distance criteria is also maintained, which ensures that UA molecules are engaged in strong π-π stacking. Note that the corresponding angle distribution at a preferred angle is not considered in the present study for various pairs involving K_3Cit since they lack an aromatic core which makes sure that K_3Cit is able to interact with itself or other molecules such as MM and UA by interactions of any kind excluding π-π stacking.

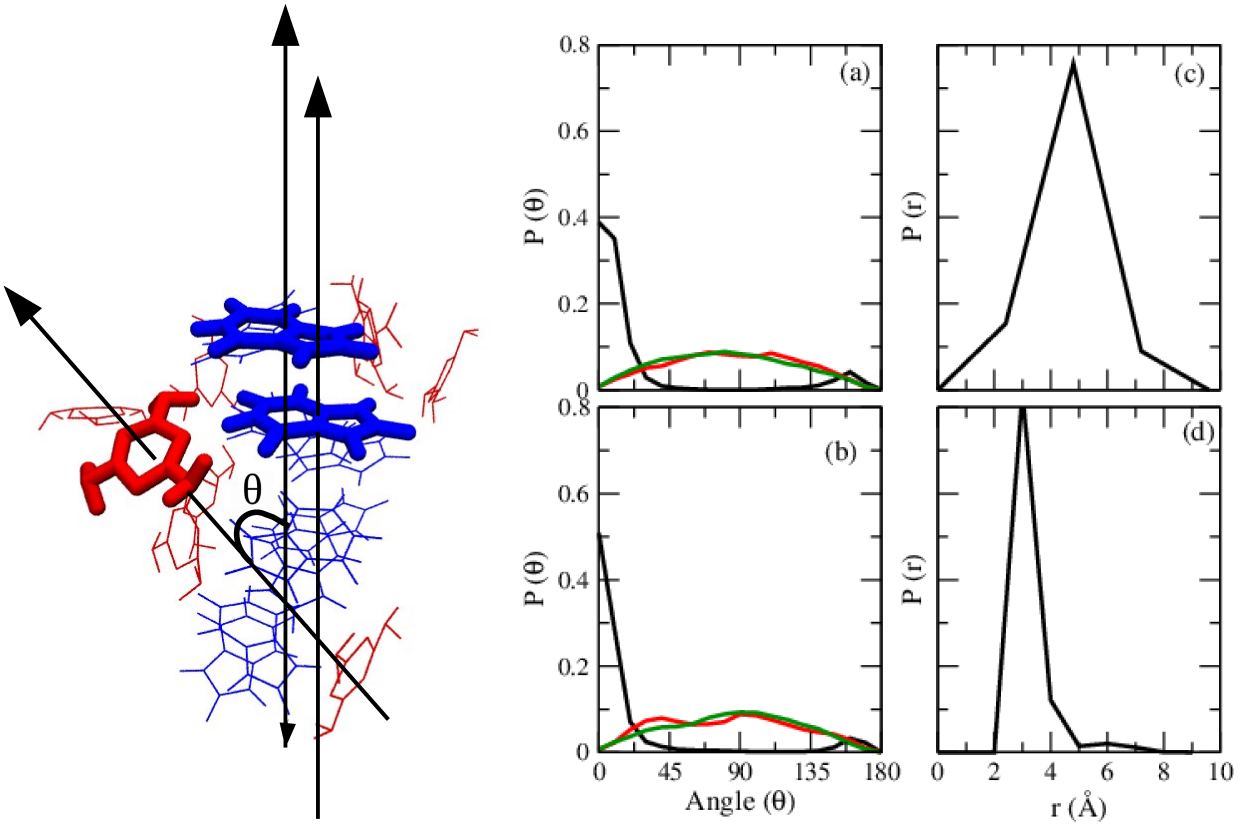

Figure 5-18. *(a)-(b) Probability of orientational angle (θ) at various angles (θ) between the vector normals of two aromatic planes for UA-UA (black), MM-UA (red), and MM-MM (green) interactions for system S0 and S4, respectively. (c)-(d) Probability of distance at various distances r (distance between COM-COM of two UA molecules) for systems S0 and S4, respectively.*

Effect of UA cluster size on MM-UA aggregation

A description of how various cluster sizes of UA actually influence the MM-UA aggregation is given in this section. An assessment of the cluster structure reveals that a substantial alteration in the MM-UA cluster as well as their individual aggregation results in the presence of K_3Cit molecules. In our earlier study, it has been anticipated that since UA tends to aggregate higher than MM, the aggregated UA cluster draws MM molecules to

form a large insoluble cluster named kidney stone.[207] The present study deals with similar facts. The estimation of the impact of the UA cluster on MM is, therefore, appropriate in the absence and presence of an inhibitor.

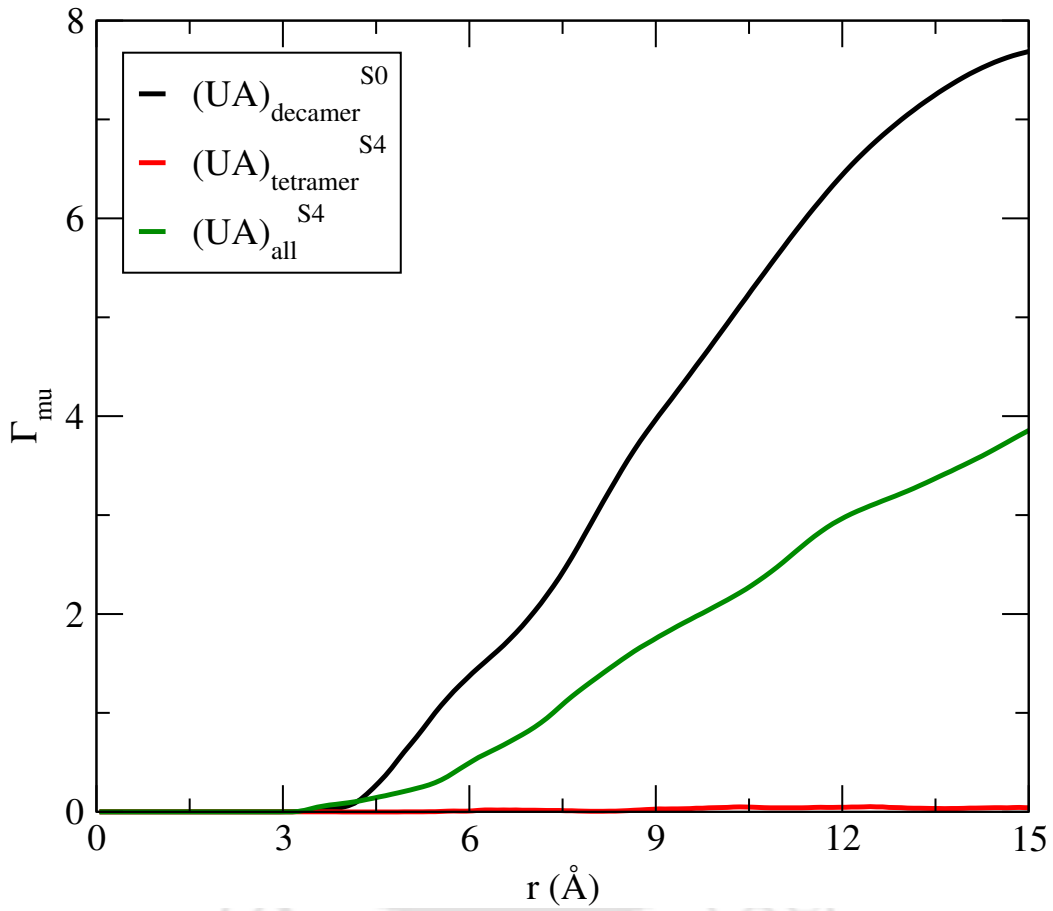

Figure 5-19. *Preferential interaction parameters for $(UA)_{decamer}$-MM interactions in system S0, $(UA)_{tetramer}$-MM interactions in system S4, and $(UA)_{all}$-MM interactions in system S4.*

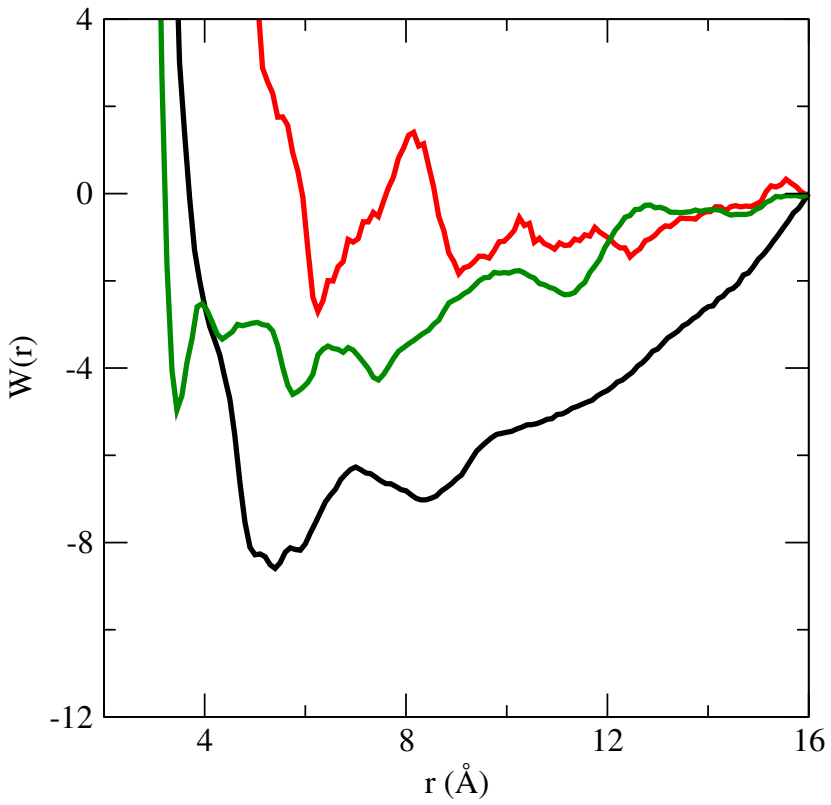

Figure 5-20. *Potentials of mean force (W(r)) for the $(UA)_{decamer}$-MM (black), $(UA)_{tetramer}$-MM (red), and $(UA)_{all}$-MM (green) interactions for systems S0, S4, and S4, respectively.*

It is apparent that all UA molecules in system S0 are aggregated in order to form a decamer as found in the cluster structure analysis. However, once K_3Cit is introduced as an inhibitor, the decamer produced by UA molecules is turned into a tetramer in system S4. The comparison of the preferential interaction between $(UA)_{decamer}$ and all MM molecules in system S0 with the preferential interaction between $(UA)_{tetramer}$ and MM in system S4, therefore, provides a perfect idea behind the introduction of a third molecule as an inhibitor for MM-UA composites. Thus, the preferential interaction parameter is determined for both systems (i.e., S0 and S4). Figure 5-19 shows that the interaction between $(UA)_{decamer}$-MM (in system S0) is stronger as compared to the other system, i.e., $(UA)_{tetramer}$-MM (in system S4). Thus, the larger cluster of UA interacts more with MM. In system S0, no K_3Cit molecules are present. Thus, all ten UA molecules aggregate in system S0, while in

system S4, the inclusion of appropriate K_3Cit molecules puts the large UA cluster into a smaller size cluster which eventually induces poor association with MM molecules present in that system. In order to explore more about the aforementioned occurrence, the potential of mean forces, W(r), as a function of COM-COM distance between MM and UA, r, are determined by using the equation as follows:[283]

$$W(r) = -k_B T ln\, g_{mn}(r) \tag{5.14}$$

where k_B and T are the Boltzmann constant and absolute temperature, respectively, and $g_{mn}(r)$ is the pair distribution function between MM and UA. W(r) values of system S4 are shown to be more positive than the values of system S0. Therefore, the addition of K_3Cit molecules into the MM-UA mixture makes the contact minimum (CM) more energetically unfavorable for the MM-UA pair. Moreover, of system S4, CM (first minimum) as shown in PMF shifts towards higher r-value than that of system S0. It symbolizes the fact that the contact between MM-UA is shielded by K_3Cit molecules around MM and UA. The use of K_3Cit molecules as an inhibitor of MM-UA aggregation is therefore adequate, because it breaks both the UA as well as MM clusters (as previously mentioned). It is to be noted that in Figure 5-19 and Figure 5-20, preferential interaction parameter and W(r) are introduced for $(UA)_{all}$-MM interaction in system S4. This is because the comparison between the impact of all UA molecules present in that system to that of UA in tetrameric form (i.e., $UA_{tetramer}$). Clearly, the overall UA interaction is greater than $UA_{tetramer}$ interaction with MM molecules. Here, the difference between $(UA)_{all}$ and $UA_{tetramer}$ is due to fact that total UA molecules develop tetrameric cluster along with other discrete clusters present in system S4. Thus, in conjunction with the tetramer, all distinct clusters certainly show a somewhat stronger preference for MM molecules than for just tetrameric UA (i.e., $UA_{tetramer}$), and this goes with as per expectation. However, the interaction between MM and UA, considering various combinations of clusters, does not show as much interaction as $(UA)_{decamer}$ does for MM molecules in system S0. K_3Cit is, therefore, a potent inhibitor against MM-UA aggregation, which readily breaks up the kidney stone.

Decomposition of total energy, MM-PBSA, and complexation energy

In this section, total interaction energy between MM-UA, MM-K_3Cit, and UA-K_3Cit is decomposed into van der Waals (vdW) as well as electrostatic interaction energy. To do so,

we have used the NAMD energy plugin built in VMD package.[149] In this regard, a 10 Å cut off for the nonbonding interactions is chosen. Thereafter, periodic boundary conditions are applied by the inclusion of periodic cell information. Moreover, we have turned off the switching and run the energy calculation with PME to create the bulk phase properties with an appropriate mesh density. These conditions applied above allow one to calculate the full electrostatics. In this scheme, the cut off parameter has slightly different meaning for electrostatic interactions. It represents the local interactions distance, or distance within electrostatic pairs will be directly calculated at every time steps. Outside of this distance, interactions will be calculated only periodically using PME by using a multiple time-step integration scheme.

Table 5-4. elec, vdW, and total are the electrostatic energy, van der Waals interaction, and total energy for MM-UA, respectively[a]

System	elec	vdW	total
S0	-185.67	-57.96	-243.63
S0-a	-171.16	-53.16	-224.32
S1	-117.80	-43.65	-161.45
S2	-71.10	-36.62	-107.72
S3	-16.06	-32.94	-49.00
S4	-10.20	-38.48	-48.68
S4-a	-16.06	-33.97	-50.04

[a]All energy values are expressed in kcal/mol.

Table 5-5. elec, vdW, and total are the electrostatic energy, van der Waals interaction, and total energy, respectively.[a]

System	elec	vdW	total
$S0_{MM-water}$	-390.09	-18.42	-408.51
$S0_{UA-water}$	-397.67	-29.14	-426.81
$S0_{K_3Cit-water}$	——	——	——
$S4_{MM-water}$	-162.18	-19.04	-181.22
$S4_{UA-water}$	-85.63	-50.65	-136.28
$S4_{K_3Cit-water}$	-12082.81	276.65	-11806.16

[a]All energy values are expressed in kcal/mol.

Now looking at the interaction energies for MM-UA pair (Table 5-4), the electrostatic as well as the vdW energy are found to be the highest (most favorable) for system S0 among all the systems. Moreover, electrostatic interaction energy contributes more to the

total interaction energy than vdW counter part does for the MM-UA pair in system S0. Now, since, inhibitor is introduced in system S1, the total interaction energy along with the electrostatic and vdW energy decreases (less favorable). Such reduction in interaction energy portrays about the lower interaction between MM and UA in the presence of K_3Cit molecules. Thereafter, since K_3Cit is increased from systems S1–S3, the interaction energy also reduces (less favorable) to smaller values. Furthermore, in system S4, the total interaction energy is minimal among all the systems (i.e., systems S0–S4) considered in the present study. Moreover, in system S4, vdW energy predominates over electrostatic energy. It suggests that the presence of K_3Cit as an inhibitor reduces the MM-UA interaction profoundly. Thus, the insoluble MM-UA composite in water is now disintegrated due to the lowering in interaction among them. Moreover, if we look into the MM-water, UA-water, and K_3Cit-water interaction energy, then we can find that in system S4, K_3Cit is interacting more with water than that of MM-wat or UA-wat in system S4 (Table 5-5). Thus, it can be said that the presence of K_3Cit disrupts the MM-UA conjugation by making a strong interaction with them along with water molecules, which enables the whole composite made of MM-UA-K_3Cit to be accessible to water. Now, in systems S0 and S4, the total MM-water and UA-water interaction energies are also significantly favorable (Table 5-5). Furthermore, K_3Cit is making strong connection with water, MM, and UA. Thus, one can conclude that K_3Cit does not only break the MM-UA cluster but also preferentially makes accessible to water of this disaggregated MM-UA composite. Therefore, the mechanism of K_3Cit on the inhibition of MM-UA pair formation is the indirect desolvation of kidney stones. It makes a strong interaction with MM and UA with the inclusion of water molecules from the outer surface of MM-UA complex and surrounds MM and UA molecules with the preservation of more water surrounding the overall MM-UA-K_3Cit cluster. Now, if we look at the MM-K_3Cit and UA-K_3Cit interaction energies for each system, then a clear picture will be portrayed about their nature of interaction with the variation of K_3Cit concentration, which acts as an inhibitor.

Table 5-6. elec, vdW, and total are the electrostatic energy, van der Waals interaction, and total energy for MM-K_3Cit interaction, respectively.[a]

System	elec	vdW	total
S1	-144.81	-8.14	-152.95
S2	-192.89	-13.30	-206.19
S3	-388.74	-36.38	-425.12
S4	-404.36	-45.12	-449.48
S4-a	-445.87	-44.59	-490.47

[a]All energy values are expressed in kcal/mol.

Table 5-7. elec, vdW, and total are the electrostatic energy, van der Waals interaction, and total energy for UA-K_3Cit interaction, respectively.[a]

System	elec	vdW	total
S1	-229.26	-9.45	-238.71
S2	-392.58	-13.05	-405.63
S3	-361.72	-42.39	-404.11
S4	-507.45	-45.18	-552.63
S4-a	-531.99	-41.38	-573.37

[a]All energy values are expressed in kcal/mol.

From Table 5-6 and Table 5-7, it clear that MM and UA strongly interact with K_3Cit molecules and this interaction energy increases with the increasing concentration of K_3Cit from system S0 to system S4. Furthermore, from the decomposed electrostatic and vdW energy, it is clear that UA strongly interacts with K_3Cit than that of made by MM. Again, in both cases, i.e., for both molecules MM and UA, electrostatic energy predominates over vdW energy. Thus, MM and UA predominantly interacting with K_3Cit molecules by hydrogen bonds preferably and this is obvious from their chemical structural point of view. Furthermore, in system S4, MM-K_3Cit and UA-K_3Cit interaction energies predominates over MM-UA interaction energies which clearly depicts that MM-UA composite is energetically less favorable in the presence of sufficient number of K_3Cit as K_3Cit molecules are now included in between the MM-UA cluster. Thus, the overall cluster made of MM-UA-K_3Cit is produced which again more water soluble as predicted earlier because K_3Cit interacts with water more strongly than the way MM or UA does.

Table 5-8. elec, vdW, and total are the electrostatic energy, van der Waals interaction, and total energy, respectively.[a]

System	elec	vdW	total
$S18_{MM-UA}$	-2.30	-1.24	-3.54
$S18_{MM-K_3Cit}$	-13.36	-1.08	-14.44
$S18_{UA-K_3Cit}$	-69.76	-1.13	-70.89
$S18_{MM-MM}$	-0.79	-0.23	-1.02
$S18_{UA-UA}$	5.43	-0.04	-5.39
$S18_{K_3Cit-K_3Cit}$	2.57	-5.60	-3.03
$S18_{total}$	-78.21	-9.32	-87.53

[a]All energy values are expressed in kcal/mol.

Since, it is evident that K_3Cit molecules comes together with MM and UA to form a large aggregate with an indirect solubilization of MM-UA cluster in water, hence it will be better to examine whether or not the total complexation energy among MM-UA-K_3Cit provides stabilization. In order to do so, a specific system S18 is prepared taking two molecules of each of MM, UA, and K_3Cit and the system is described in Table 5-1. Now, considering this system, we have derived first the cluster structure analysis (by employing the conditions as prescribed above) and it is seen that for last 20ns, maximum cluster size of MM-UA is trimer (dimer for UA and monomer for MM) as shown in Figure 5-21. Now, if one looks into the cluster size of MM-UA-K_3Cit, it can be found that all six molecules come close to form an aggregate of hexamer in system S18 (Figure 5-21). Therefore, overall cluster involves all molecules present in system S18. Now, if one calculates the total complexation for last 20ns taking this particular system, then energy coming from MM-UA, MM-K_3Cit, UA-K_3Cit should be added up to the MM-MM, UA-UA and K_3Cit-K_3Cit to get the total complexation energy. From the Table 5-8, it is confirmed that the total complexation energy is negative. Thus, total complexation is energetically favorable which enables K_3Cit molecules to add to the MM-UA cluster. As a result, MM-UA cluster formation gets weaker in the presence of K_3Cit.

From MM-PBSA calculation (which is mostly used to determine the complexation energy for macromolecular compounds)[291, 292], total binding free energy for MM-UA interaction is diminished (less favorable) from system S0–S4 (Table 5-9). Thus, it is confirmed that the presence of K_3Cit molecules in a sufficient number in a system can disrupt the MM-UA interactions profoundly and this happens due to the preferable interaction between MM-K_3Cit and UA-K_3Cit over MM-UA. Here also, electrostatic energy predominates over

vdW energy in system S0 and the opposite trend is true for system S4, which reveals that hydrogen bonded MM-UA interaction in system S0 is drastically reduced (less favorable) in system S4. Moreover, changes in ensemble, i.e., NPT and NVT do not produce any noticeable difference in results for system S0 and S0-a and the same is true for S4 and S4-a systems. Thus, the effect of ensemble on the clusterization is minimal. It is to be noted that in MM-PBSA calculation, we have chosen UA as the receptors and MM as the ligand and have studied how the ligand molecules can be associated with the receptors so that the complexation between MM-UA is better understood.

Table 5-9. All energies derived from the MM-PBSA calculations. Here, ΔE_{vdW}, ΔE_{elec}, ΔG_{PB}, ΔG_{NP}, and $\Delta G^0{}_{bind}$ are the energy of van der Waals interaction, electrostatic energy, Poisson–Boltzmann energy, non-polar energy, and binding free energy, respectively.[a]

System$_{ligand-receptor}$	ΔE_{vdW}	ΔE_{elec}	ΔG_{PB}	ΔG_{NP}	$\Delta G^0{}_{bind}$
S0$_{MM-UA}$	-59.01	-185.63	155.96	-6.30	-94.99
S0-a$_{MM-UA}$	-54.25	-171.15	138.97	-5.42	-91.85
S1$_{MM-UA}$	-44.77	-117.79	114.46	-5.12	-53.22
S2$_{MM-UA}$	-37.41	-71.11	95.57	-5.48	-18.42
S3$_{MM-UA}$	-33.96	-16.06	44.84	-5.16	-10.34
S4$_{MM-UA}$	-36.92	-9.02	50.22	-5.37	-1.10
S4-a$_{MM-UA}$	-28.05	-6.37	34.30	-3.96	-4.10

[a]All energy values are expressed in kcal/mol.

Table 5-10. All energies derived from the MM-PBSA calculations. Here, ΔE_{vdW}, ΔE_{elec}, ΔG_{PB}, ΔG_{NP}, and $\Delta G^0{}_{bind}$ are the energy of van der Waals interaction, electrostatic energy, Poisson–Boltzmann energy, non-polar energy, and binding free energy, respectively.[a]

System$_{ligand-receptor}$	ΔE_{vdW}	ΔE_{elec}	ΔG_{PB}	ΔG_{NP}	$\Delta G^0{}_{bind}$
S18$_{MM-UA}$	-1.11	-1.64	2.45	-0.26	-0.86
S18$_{MM-K_3Cit}$	-1.002	-12.56	12.57	-0.34	-1.33
S18$_{UA-K_3Cit}$	-0.92	-58.77	51.03	-0.69	-9.34
S18$_{MM-MM}$	-0.23	-0.79	0.87	-0.08	-0.23
S18$_{UA-UA}$	-5.08	2.44	0.72	-0.52	-2.45
S18$_{K_3Cit-K_3Cit}$	-0.04	171.63	-169.37	-0.0048	2.21

[a]All energy values are expressed in kcal/mol.

In case of complexation energy also, MM-PBSA provides favorable complexation energy. From Table 5-10, it can be seen that UA interacts more favorably with K_3Cit molecules than MM does. Moreover, ΔG^{O}_{bind} for MM-UA pair is more positive than that of MM-K_3Cit or UA-K_3Cit. Therefore, it is obvious that K_3Cit molecules interact with MM and UA simultaneously to disrupt the MM-UA cluster.

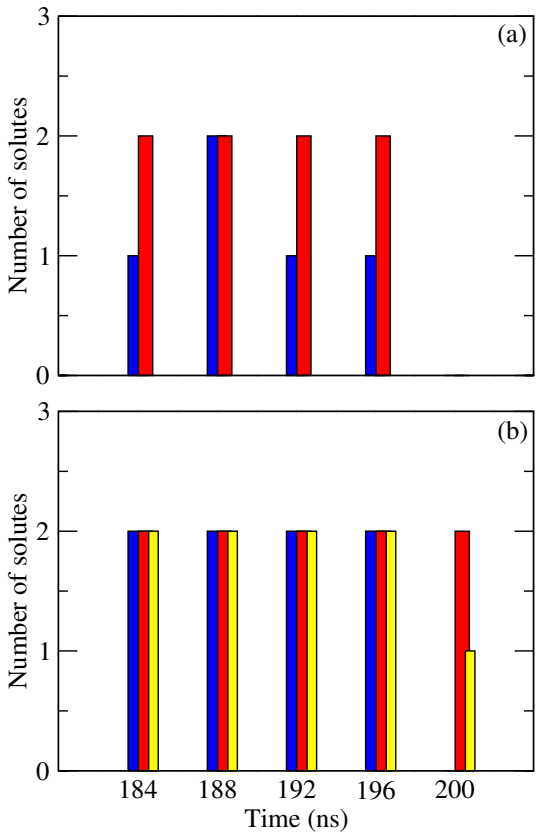

Figure 5-21. *Maximum sizes of the (a) MM (blue)-UA (red) and (b) MM (blue)-UA (red)-K_3Cit (yellow) clusters for the last 20 ns of total 200 ns at each 4 ns interval for system S18.*

Umbrella sampling

The potential of mean forces (PMFs) represent the changes in the free energy of a system along a certain reaction coordinate.[293, 294, 295] Moreover, for crystal nucleus appearance, umbrella sampling method is employed.[296, 297] In the present study, umbrella sampling

technique is used to evaluate the PMFs of various combinations like MM-UA in the presence and absence of K_3Cit, MM-K_3Cit, and UA-K_3Cit in water.

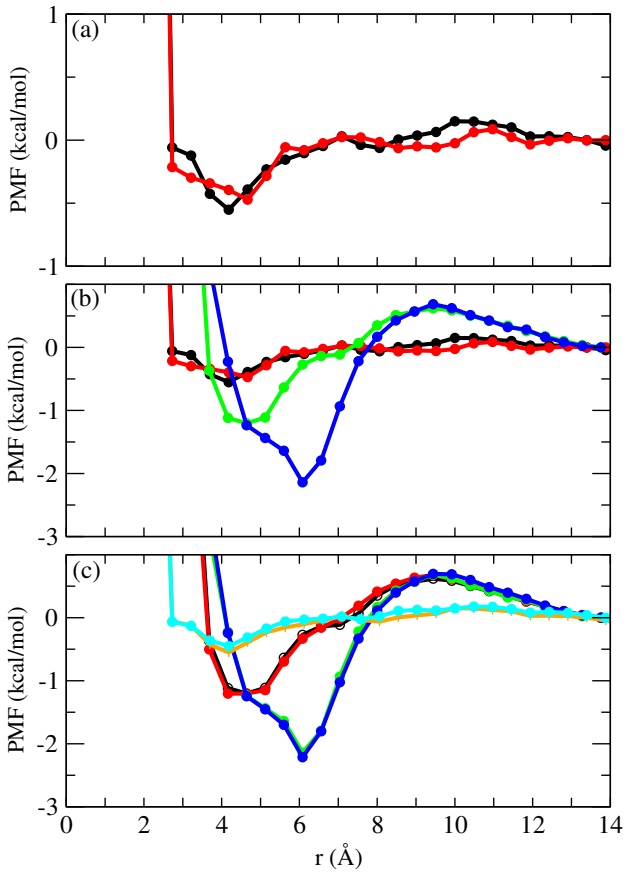

Figure 5-22. *Potential of mean forces for the association of all systems P0–P3. (a) PMFs for MM-UA interaction in systems P0 (black) and P1 (red), (b) PMFs for MM-UA interaction in systems P0 (black), P1 (red), MM-K_3Cit in P2 (green), and UA-K_3Cit in P3 (blue), (c) PMFs for MM-UA interaction in systems P0 (orange, 10 ns), P0 (cyan, 50 ns), MM-K_3Cit interaction in systems P2 (black, 10 ns), P2 (red, 50 ns), and UA-K_3Cit interaction in systems P3 (green, 10 ns), and P3 (blue, 50 ns). Standard errors of all data points (calculated using the block average methode) fall within ± 0.02 kcal/mol.*

Firstly, MM and UA pair is considered for two different conditions. The pair is taken in pure 1800 water at 300 K in one system. In other system, the same molecular pair is immersed in the same number of water molecules but, here, five K_3Cit molecules are present. From Figure 5-22 (a), it is seen that MM-UA pair in pure water is more stable as the minimum between this pair is more favorable than that of MM-UA pair in the

presence of K_3Cit molecules. Moreover, the contact minimum between MM-UA pair in the presence of K_3Cit moves towards higher r value. Thus, the presence of K_3Cit molecules in MM and UA mixture destabilizes the interaction between them.

The question now is whether the anticipation of the interaction between MM and K_3Cit plays an important role in minimizing the interactions between MM and UA molecules or whether the same is true due to the prerequisite of UA-K_3Cit interaction in water. Therefore, we have determined the two different interactions and found that MM-K_3Cit is much weaker than that of UA-K_3Cit (Figure 5-22 (b)).

Recent experimental results proposed that the order of interactions are as follows: UA-K_3Cit > MM-K_3Cit > MM-UA interaction.[44] Similar findings are also shown in the present study. Furthermore, to convey the convergence of these interactions, a different umbrella sampling simulation is run over 50 ns production run for each window. In these simulations, not only this but a different initial configuration is also considered. It is found that in all types of interactions, all simulations are well-converged (Figure 5-22 (c)). The PMF plot generated in each window by the 10 ns production run corresponds perfectly with that generated in each window by the PMF values from the 50 ns production run. This convergence of various initial configurations displays that the pair UA-K_3Cit is the most stable of all interactions. In addition, it is apparent that K_3Cit simultaneously interacts with MM and UA. The MM-UA pair is, thus, disrupted by such simultaneous interaction.

Dimer existence autocorrelation functions

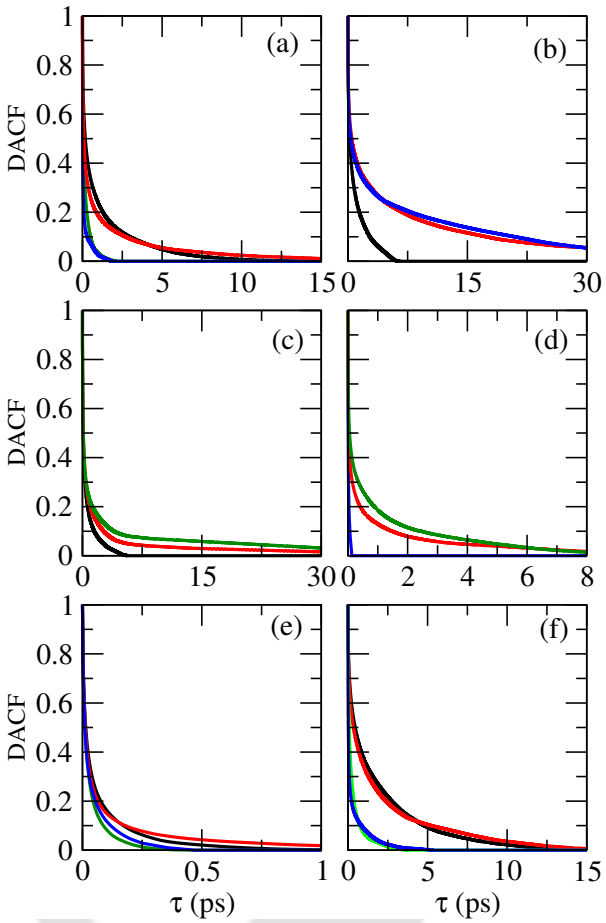

Figure 5-23. *Dimer existence autocorrelation functions (DACFs) for (a) UA-MM for systems S0 (black), S0-a (red), S4 (green), and S4-a (blue), with a distance of 7.0 Å , (b) MM-K_3Cit for systems S1 (black), S4 (red), and S4-a (blue), with a distance of 5.45 Å , (c) UA-K_3Cit for systems S1 (black), S4 (red), and S4-a (green), with a distance of 5.45 Å , (d) K_3Cit-K_3Cit for systems S1 (blue), S4 (red), and S4-a (green), with a distance of 7 Å , (e) MM-MM for systems S0 (black), S0-a (red), S4 (green), and S4-a (blue), with a distance of 5 Å , (f) UA-UA for systems S0 (black), S0-a (red), S4 (green), and S4-a (blue), with a distance of 6 Å .*

The lifetime of dimers formed in the presence and absence of K_3Cit molecules by the interaction of UA-UA pair are evaluated by estimating the dimer existence autocorrelation function (DACF). The dynamic nature of MM-UA aggregation can be defined usefully by this approach. DACF is defined as an autocorrelation of a simple function, β_{ij}, for the pair of molecules, i and j, that can have value 1 when maintaining a preset distance criterion

and finally zero if the distance criterion is lost for the first time. The DACF is constructed by the use of the equation as follows:[158]

$$DACF(\tau) = N. < \sum_{t=0}^{T-\tau} \beta_{ij}(t+\tau).\beta_{ij}(t) >_{ij} \quad (5.15)$$

It is worth noting that, even if the criterion of distance is met later, DACF will remain zero. Figure 5-23 (a) shows the DACFs for the dimer of UA-MM in the presence and absence of K_3Cit for systems S0 and S4. In this regard, we have chosen only two systems just to convey the dynamic nature UA-MM dimer in two adverse conditions. In system S0, no inhibitor is present to disrupt the UA-MM conjugation, where as system S4 contains the highest number of K_3Cit molecules. In this context we have chosen a distance of 7.0 Å which comes from the COM-COM rdf of these two molecules (i.e., MM and UA). Our present study intends to assess whether or not K_3Cit inhibits MM and UA aggregation. For this reason, at first, we consider MM-UA over other combinations like MM-K_3Cit, UA-K_3Cit, K_3Cit-K_3Cit, MM-MM, and UA-UA. The DACF for the MM-UA dimer is very readily reduced for systems S4 (with a high concentration of K_3Cit in all systems) as opposed to system S0 (in which no K_3Cit molecules are present), suggesting a much lower lifetime. Thus, with the increase of concentration of K_3Cit, lifetime of MM-UA dimer decreases significantly. Moreover, this fact also applies to all systems in this study (data not shown). Furthermore, NPT and NVT simulation produces similar outcomes in these two systems. Afterwards, it is confirmed why the development of MM-UA dimer is impeded by the rupture of large order clusters to produce a high percentage of monomer.

DACF is therefore calculated for the MM-K_3Cit as well as the UA-K_3Cit pair for S1 and S4 systems (Figure 5-23(b)-(c)). The interaction of MM with Cit is significant in system S4 compared to system S1. The concentration of K_3Cit is higher in system S4 than in system S1. As the number of K_3Cit increases, the more interaction with MM can be observed. Such intense interaction between MM-K_3Cit contributes to the breakdown of the MM-UA cluster in lower order clusters. A similar trend can also be seen for UA-K_3Cit pair in these two systems. MM and UA then associate well with K_3Cit molecules, rendering K_3Cit an effective inhibitor (Figure 5-23(c)). Next, DACF for K_3Cit-K_3Cit is determined for these two systems (i.e., systems S1 and S4). Figure 5-23(d) shows that K_3Cit does not interact well with itself in system S1 as compared to system S4. However, K_3Cit-K_3Cit dimer lifetime is low in comparison of MM-K_3Cit or UA-K_3Cit dimer lifetimes. Thus, it can be concluded that K_3Cit molecules do not self-aggregate well in presence of MM and UA;

rather it binds either to UA or MM or with both UA and MM molecules to inhibit their aggregation. Furthermore, to strengthen the above facts, MM-MM dimer lifetime along with dimer lifetime of UA-UA pair are determined. It can be seen that MM-MM dimer formation tendency is low as compared to UA-UA pair since in the presence of UA, MM tends to associate with UA molecules instead of MM-MM self-aggregation. Not only that, DACF for both pair, i.e., MM-MM and UA-UA is rapidly decreased to zero in presence of higher number of K_3Cit in system S4. Therefore it can be inferred that MM-UA pairing is weakened by the presence of K_3Cit, which impairs the self-aggregation of the MM-MM and UA-UA in a system that is required in all for the repair of kidney stone.

Hydrogen bond properties

The average number of hydrogen bands is then ascertained for the various systems considered in this study for systems S0–S4 for numerous interactions, such as MM-UA, UA-UA, MM-MM, MM-K_3Cit, UA-K_3Cit, K_3Cit-K_3Cit, and water-water interactions (Table 5-11). A set of criteria is used to define the hydrogen bond connections between donor (D), and accepters (A) to assess the number of hydrogen bonds (discussed above) involved for all types of interactions.[207, 253, 288, 289] If the distance D-A $\leqslant$ 3.5 Å and, simultaneously, angle $\angle$ D-H$\cdots$ A $\geqslant 120^{\circ}$, then hydrogen bonding is considered to be present. It is observed that the average number of hydrogen bonds between MM-UA interactions declines from systems S0 to S4. In system S0, only MM and UA are present without any presence of K_3Cit molecules. Therefore, it can be seen that MM and UA pair forms 26.72 number of hydrogen bonds in the absence of K_3Cit in system S0. There is a small change in the number of hydrogen bond between MM and UA molecules when K_3Cit is introduced in system S1. Therefore, a lower concentration of K_3Cit does not bring as such alternations in the MM-UA hydrogen bonding. For systems S2 to S4, the average number of hydrogen bonds between MM and UA molecules are 17.54, 7.05, and 3.63, respectively. Thus, a substantial decrease in the numbers of hydrogen bonds is observed in the presence of K_3Cit. Now, if we consider the UA-UA hydrogen bond (H_{u-u}), it is seen that as we move from systems S0 to S4, the number of hydrogen bonds is also decreased. Thus, it depicts that with the increase of K_3Cit molecules, UA commences to interact with K_3Cit molecules rather than with itself. A similar tendency is seen when determining MM-MM hydrogen bonds for systems S0–S4. Thus, the lower the amount of K_3Cit molecules in the systems, the hydrogen bonding

interactions between MM-UA, UA-UA and MM-MM are reduced significantly. Moreover, with the increase in K_3Cit concentration from system S1 to system S4, MM-K_3Cit and UA-K_3Cit hydrogen bonds are increased which is very obvious (Table 5-11). Again, K_3Cit-K_3Cit hydrogen bonding is also increased form systems S1–S4. However, the number of K_3Cit-K_3Cit hydrogen bonds are smaller than UA-K_3Cit as well as MM-K_3Cit interactions as shown in Table 5-11. Thus, K_3Cit interacts more with MM and UA molecules rather than with itself which causes disruption in MM-UA interactions. The water-water hydrogen binding (H_{w-w}) numbers have also been calculated to determine whether or not UA, K_3Cit, and MM molecules disrupt the bulk water structure. Since H_{w-w} remains unchanged in all systems (Table 5-11), it can therefore be stated, that the tetrahedral network of water is not perturbed at all. Furthermore, simulations of NPT and NVT ensembles give similar results for these two systems (S0-a and S4-a).

Hydrogen bonds for systems S5–S9 are also determined. This is done solely to verify the nature of aggregation of UA and MM in pure water as well as in presence of K_3Cit. Not only that, it is also possible to find out, by detecting the hydrogen bonds between K_3Cit-K_3Cit in a pure solution, how do K_3Cit molecules aggregate in pure water. It is found that in system S5, UA-UA aggregation is quite strong and the number of H_{u-u} is 0.66 which is then reduced to 0.02 in the presence of K_3Cit in system S6 (Table 5-12). Therefore, pure UA aggregation in system S5 is affected by the incorporation of K_3Cit in system S6 (Table 5-12). A similar trend is also observed for system containing MM molecules in pure water. In system S7, H_{m-m} is 0.75 which is thus reduced to 0.32 in system S8 (Table 5-12). Therefore, it is confirmed that pure UA aggregation or pure MM aggregation is impeded by the presence of K_3Cit which reveals that K_3Cit can be used as an effective inhibitor against MM-UA clustering.

Furthermore, hydrogen bond analysis is also performed for system S10 in which 10 of MM molecules are present with 20 of UA molecules in pure water. Here, the total number of hydrogen bonds between MM-UA is 23.52 (Table 5-13). However, in the presence of sufficient amount of K_3Cit with these number of molecules in system S11 brings a change in the H_{m-u} number. Now, total number of hydrogen bonds between MM-UA pair goes down to 14.87. Therefore, K_3Cit molecules disrupt the MM-UA interaction effectively. Not only that there is a reduction in H_{m-m} and H_{u-u} numbers also in system S11 as compared to S10. Thus, self-aggregation of MM as well as UA molecules also interrupted in the presence of K_3Cit. A similar trend can also be observed when one compares the various hydrogen

bond numbers between systems S13 and S14 (Table 5-13). Therefore, it is confirmed that K_3Cit alters the MM-UA pair even in the presence of higher number of UA molecules along with the destruction of their self-aggregation. Now, it will be intriguing to see, when the concentration of MM molecules increases keeping the number of UA fixed, whether or not K_3Cit alters the MM-UA composite. Interestingly, we have found no exceptions in case of systems S14-17 (Table 5-13). Therefore, it is seen that the application of K_3Cit molecules disrupts the MM-UA clusterization.

Table 5-11. Average number of hydrogen bonds (total) involving all possible pairs for different systems.

System	H_{m-u}	H_{u-u}	H_{m-m}	H_{m-c}	H_{u-c}	H_{c-c}	H_{w-w}
S0	26.72	8.16	14.28	—	—	—	3.77
S0-a	25.88	8.63	16.39	—	—	—	3.76
S1	20.69	8.04	12.92	13.17	14.15	4.50	3.74
S2	17.54	8.49	9.80	16.39	21.92	8.76	3.73
S3	7.05	0.49	5.22	30.68	30.28	17.06	3.71
S4	3.63	0.04	4.96	36.27	32.30	25.66	3.68
S4-a	4.78	0.02	5.15	32.09	31.83	26.81	3.69

Table 5-12. Average number of hydrogen bonds (total) involving all possible pairs for different systems.

System	H_{u-u}	H_{m-m}	H_{m-c}	H_{u-c}	H_{c-c}
S5	0.66	—	—	—	—
S6	0.02	—	—	15.42	8.97
S7	—	0.75	—	—	—
S8	—	0.32	14.53	—	8.80
S9	—	—	—	—	9.33

Table 5-13. Average number of hydrogen bonds (total) involving all possible pairs for different systems.

System	H_{m-u}	H_{m-m}	H_{u-u}	H_{m-c}	H_{u-c}	H_{c-c}
S10	23.52	8.35	31.04	—	—	—
S11	14.87	7.63	5.38	27.41	54.84	26.54
S12	35.52	10.61	39.39	—	—	—
S13	18.08	5.79	7.35	22.57	75.08	25.24
S14	35.67	36.58	8.16	—	—	—
S15	23.47	16.96	0.20	60.51	24.94	25.58
S16	55.17	76.47	5.13	—	—	—
S17	34.69	34.69	0.13	81.71	27.07	23.80

■ SUMMARY AND CONCLUSIONS

Kidney stones are very prevalent in all age groups around the world, and their prevalence is rising. A change in food habits and pharmacological therapies are the possible treatment options for preventing stone recurrences. Therefore, the treatment of chronic stone disease demands a multifaceted lifestyle and pharmacological strategy. Consequently, it is imperative to develop preventive and therapeutic drugs for kidney stones. Classical molecular dynamics simulation, MM-PBSA, and biased umbrella sampling method examine the synchronous interaction of K_3Cit with MM along with UA. In brief, the inhibitory effect of K_3Cit for MM-UA complexation, which makes kidney stones, is identified. Hydrogen bonding interaction with both MM and UA allows the deterioration of the composite of MM-UA concurrently. From the determination of first shell CN and SDF, we can state that with the increase of K_3Cit concentration, the interaction of K_3Cit with MM and UA increases. Therefore, more the number of K_3Cit present in a system, the more inhibition in MM-UA conjugation. Furthermore, the symmetric distribution of K_3Cit around MM as well as UA provides that K_3Cit molecules are interspersed "in and outside" the MM and UA molecules, which, thus, results in lowering the aggregation between MM and UA molecules. The determination of the preferential interaction parameter also reflects similar results with that of CN and SDF. However, the preferential interaction parameter does not provide any substantial mechanism in which way K_3Cit molecules degrade the MM-UA assembled clusters. The performance of cluster structure analysis suggests that K_3Cit molecules preferentially bind to the MM-UA clusters, which in turn produces the lower order clusters m1de of MM and UA molecules, and this is determined by inducing "direct approach" for cluster structure analysis. Furthermore, K_3Cit also reduces the self-aggregation of MM and UA, as indicated by cluster structure analysis. As a result lower-order UA clusters in the presence of K_3Cit "drags" a smaller number of MM to add to it. The estimation of the potential of mean forces (PMFs) reveals that $(UA)_{decamer}$-MM interaction prevails over $(UA)_{tetramer}$-MM. Again, the decomposition of total energy, MM-PBSA analysis say that the binding of MM and UA becomes less favorable in the presence of a higher number of K_3Cit. Moreover, MM-UA-K_3Cit complexation energy is favorable, which proves that K_3Cit attaches with MM-UA conjugate profoundly. The complexation energy for MM-UA-K_3Cit composite by the reckoning of pairwise $\Delta G^0{}_{bind}$ employing the MM-PBSA method. The performance of umbrella sampling provides information about how K_3Cit interacts with UA significantly than MM which has higher interaction energy

than MM-UA interaction again. Thus, the interaction energy follows the order: UA-K_3Cit > MM-K_3Cit > MM-UA. This order exactly (qualitatively) matches with experimental findings.[44] Therefore, K_3Cit simultaneously interacts with MM as well as UA, and this simultaneous interaction reduces the MM-UA clusters by upsetting π-stacking of UA and impeding the hydrogen-bonded cluster of MM and UA simultaneously. Dynamic property like DACF also proves the essence of dimerization between MM and UA in the absence and presence of K_3Cit. Moreover, K_3Cit molecules coordinate with MM and UA by making a higher number of hydrogen bonds with the lowering of MM-UA hydrogen bond numbers. Thus, these stronger hydrogen bonding interactions break the MM-UA complexation, which avoids the introduction of large clusters. Moreover, both the previous simulation as well as DFT studies validate the emergence of theoretical models of MM and UA interms of force field.[207, 174, 282, 197] Therefore, this study uses molecular dynamics simulations to characterize more real molecular models of MM-UA-drug complexes with the aim of understanding and revealing the details of the effect of drug loads on the structural character of MM-UA clusters.

Chapter 6

6a: The Miscibility and Solubility of Uric Acid and Vitamin C in the Solution Phase and Their Structural Alignment in the Solid-Liquid Interface

"It is easy to get a thousand prescriptions, but hard to get one single remedy."

— Chinese Proverb

Overview: Crystallization of uric acid (UA) in human is correlated with unpropitious medical predicaments, including gout and kidney stone germination. Its comparatively low solubility in physiologic solutions is a significant contributory factor to UA biomineralization. The inhibition of UA aggregation is pondered by the reasonable approach for contending kidney and gout-related problems. Therefore, we examine the role of vitamin-C (Vit-C), a water-soluble vitamin, in the aggregation of UA, which has confirmed its potency in solubilizing UA experimentally. We notice that Vit-C encapsulates the aggregated UA. Moreover, it can dismantle the assemblies of UA. We have proffered comprehensive molecular mechanisms of the interplay between the aggregated UA and Vit-C. Vit-C molecules are interspersed in solution due to its non-aggregating nature. We perceive that through hydrogen bonding and aromatic stacking interactions, Vit-C molecules interact with UA molecules. The determination of the Flory-Huggins interaction parameters suggests that the appearance of Vit-C enhances the solubility of UA aggregates. Besides, UA molecules are conformed on a monolayer graphene sheet, where they are significantly assembled to create a 2D self-assembly. Vit-C, however, encompasses and disseminates itself within the aggregated UA molecules on the surface. Therefore, the molecular mechanisms of the impact of Vit-C on UA aggregation can render relevant shrewdness into drug design against chronic diseases.

■ INTRODUCTION

The gout disorder is the most prevalent type of arthritis globally, characterized by uric acid (UA, Figure 6a-1 (a)) accumulation in joints. The comparatively low solubility in physiological solutions is a significant factor leading to UA biomineralization, i.e., the deposition of pathogenic UA crystals.[57, 58] Gout is triggered by a disorder called hyperuricemia, whereby too much UA is found in the bloodstream. The disease is often, though not always, related to undue serum UA levels. Clinical manifestations involve severe and persistent arthritis, tophi, interstitial renal disease, and UA nephrolithiasis.[57, 58] The treatment is based on identifying UA crystals in the joints, tissue, or body fluid. Furthermore, UA nephrolithiasis is characteristically an expression of systemic metabolic disease. UA nephrolithiasis is the third most prevalent type of kidney stone, with a prevalence of about 10% among all stone formers. The UA stones mostly form due to excessive acid urine; less deciding factors are hyperuricosuria and a low urine volume. The immense majority of UA stone formers have metabolic dysfunction, and not uncommonly; clinical gout is present as well.[57, 58, 59]

For individuals suffering from cancers to a common cold, vitamin C (Vit-C, Figure 6a-1 (b)) has been regarded as a preventative medication. But can you benefit from gout by daily consumption of Vit-C supplements? If an adult consumes more Vit-C, the probability of having gout will be less. The chance of gout is decreased by 17%, with every 500-milligrams consumption of Vit-C. The case is even reduced by 45% if more than 1500 mg of Vit-C is consumed daily by patients. Vit-C is believed to be protective against gout by minimizing serum UA levels. However, the effect of Vit-C on people with gout is not as evident as Vit-C consumption, but the risk of acquiring gout is lower. A moderate dosage of Vit-C can not reduce UA to a clinically relevant degree in patients with proven gout. In addition to knowing the actual value of gout patients, it is essential to assess the amount of Vit-C, which is best beneficial, without having the negative side effect of unnecessary Vit-C (e.g., kidney stones).[60] The endogenous generation of UA is mainly from the liver, intestines, and different tissues like muscles, kidneys, and the vascular endothelium. Therefore, Vit-C is expected to have been caused by a more significant elimination of UA from the kidney.

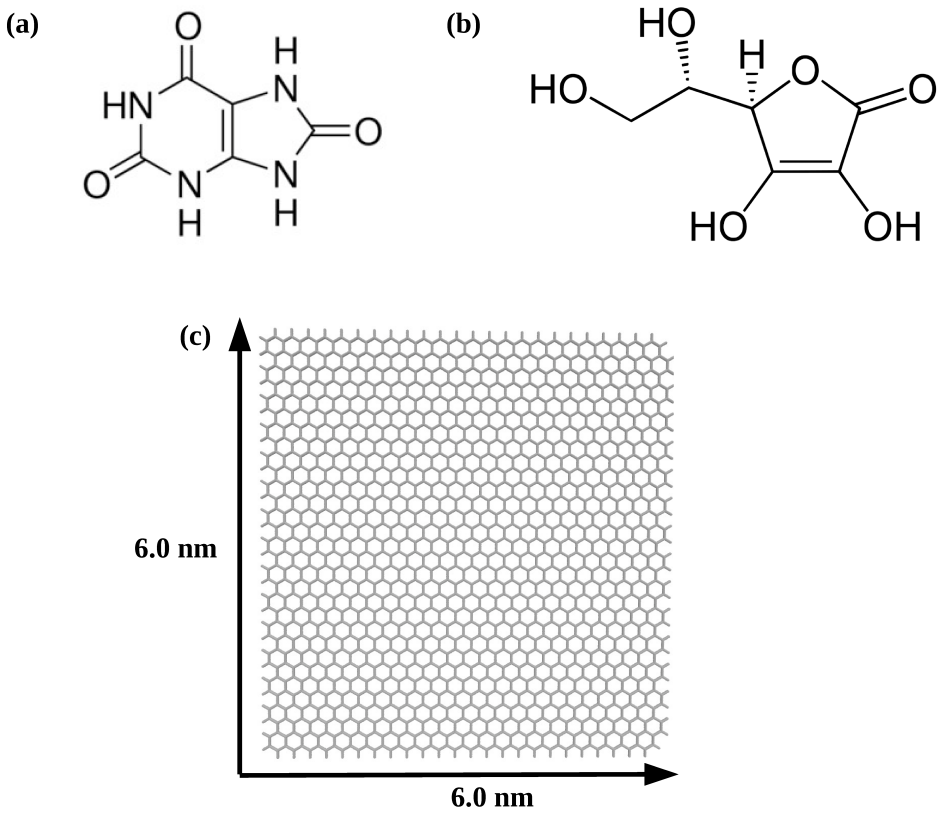

Figure 6a-1. *The chemical structures of (a) uric acid (UA), (b) vitamin C (Vit-C), and (c) monolayer graphene sheet.*

In non-gout cases, the results of high oral doses of Vit-C on renal clearance and excretion of UA had been examined as Vit-C improved the renal UA clearance. The findings showed that 4 or 12 gm Vit-C in divided doses did not affect the concentration of serum UA or UA excretion and release from the kidney.[61] Vit-C was analyzed in the serum and urinary UA. The fractional release of UA was improved to 202% ± 41% of the control value after ingesting 4.0 g of Vit-C. The ingestion of 8.0 g of Vit-C for 3 to 7 days had reduced the serum UA by 1.2 to 3.1 mg/dl due to a sustained uricosuria. These outcomes propose that Vit-C can refute studies involving the measurement of UA and disguise gout diagnosis in some cases. Theoretically, it might precipitate attacks of gouty arthritis or renal calculi in predisposed individuals.[60, 62] These findings suggest a pharmacologic influence of megadoses of a vitamin. There are several other reports of the effect of Vit-C

on the UA.[63, 64, 65, 66]

Crystal precipitates are kidney stones identified free or attached to renal papillae in the renal calyx and pelvis. Organic and crystalline segments produced by supersaturation of urine are also included. On renal papillary facades, the most common type of kidney stone is formed. The growth of stone is achieved by aggregating preformed crystals or secondary crystal nucleation on the matrix-coated surface. Substances are inhibitors that reduce the initiation of supersaturation, nucleation, crystal expansion, rate of aggregation, or processes of stone-forming. Inhibitors may have an undeviating effect on urinary conditions or behave obliquely by feuding with crystals. There is, hence, an imperative mechanism for the development and preservation of the deposition of kidney stones and the adsorption to the crystal surface of antibodies.[67, 68, 69, 70] The ultimate degradation product of purine metabolism is UA, which is excreted into the urine. In the diagnosis, surveillance, prevention, and treatment of illnesses, UA identification and characterization are relevant. Therefore identifying this species is essential for clinical and therapeutic study, not just in medicinal chemistry and neurochemistry. Different graphene platforms are also seen for detecting and quantifying UA. Positively charged PDDA-AuNPs/graphene hybrids had been developed and used to draw UA molecules by electrostatic interactions.[308] The graphene sheet for UA sensing polymers such as poly(acridine red)[309] and poly(acridine orange)[310] with acceptable results had also been introduced. In another work, the surface of a glassy carbon electrode (GCE) was changed by electropolymerization of acridine red followed by drop-coating of graphene. The morphology was identified by scanning electron microscopy. UA was adequately accumulated on the surface of the modified electrode and produced a sharp anodic peak in solutions of pH 6.5. Differential pulse voltammetry was employed to assess the electrochemical response of the modified GCE to UA. Compared to the bare GCE, the GCE modified with acridine red, and to the graphene-modified electrode, the new GCE revealed high electrochemical activity in providing an oxidation peak current that was proportional to the concentration of UA in the range from 0.8 to 150 μM, with a detection limit of 0.3 μM.[311] The neutral red (NR) was recently anchored in graphene sheets at the edges of graphene sheets. The application of NR also accelerated the electron transfer in neutral red covalently-functionalized graphene nanosheets (NR-FGN), improving the solubility and stability of graphene. Due to the synergic effect between GN and NR, the nanocomposite displayed remarkable electrocatalytic activity toward UA oxida-

tion. The conjunction of dye molecule and graphene through covalent bond would serve as a

stepping stone to synthesize other multifunctional graphene materials with excellent photochemical or electrochemical characteristics, as the authors suggested.[311] Furthermore, in a recent work, an electrode modification of Pt/PFIL/GS (Pt nanoparticles/polyelectrolyte-functionalized ionic liquid/graphene) sheets was configured to evaluate Vit-C. Besides, in human urine samples, the proposed sensor was also used to determine Vit-C and UA.[312]

Throughout this study, the detailed molecular mechanisms of the interactions between Vit-C and UA have been investigated. UA molecules can make substantial π-stacking and hydrogen bonding in the aqueous solution.[58, 207] Its accumulation leads to high-risk circumstances in the human body. Thus the role of Vit-C in the removal of UA can be discussed in this model simulation. Simultaneously, a mono-layer graphene sheet is also included in the analysis to clarify the impact of UA adsorption and also the effect of Vit-C on the adsorbed UA. Here, the incorporation of graphene sheet is done to simulate kidney stone adsorption in the human body. Though comprehensive modelization of actual kidney stone is challenging, however, the present study provides a theoretical perspective towards the aggregation, adsorption, and elimination of UA in the presence and absence of Vit-C to give a kidney stone formation mechanism.

The following sections are presented for the rest of the paper. Part II describes the simulation models and protocols used for the systems made of UA, Vit-C, and water molecules. The results are addressed in Section III. Section IV summarises our findings.

■ MODELS AND SIMULATION METHOD

In the current work, atomistic classical molecular dynamics (MD) simulation was carried out to interpret the solution attributes of UA–Vit-C–water ternary mixtures. Firstly, the geometry of Vit-C solute molecule was optimized with the help of Gaussian 09[138] utilizing HF/6-31G* basis set. After that, the charges of the Vit-C molecule were produced with the RESP[140] module of AMBER14.[226] The allocation of force field parameters for all atomic sites was accomplished using the general AMBER force field (GAFF)[142] of the ANTECHAMBER[141] suite of AMBER14. The force field parameters and the charges for all atomic sites of UA were taken from our previous publication.[207] In the current study, numerous systems are prepared, and these are presented in Table 6a-1. The TIP3P water model[143, 367] was utilized for systems. With the PACKMOL package[144], the initial configurations for each of the simulated systems were prepared. All the simulations were performed at 300 K of temperature and 1 atm pressure using

the AMBER14 package. All molecules were primarily put in a cubic simulation box on arbitrary initial positions, and periodic boundary conditions were also introduced in all three directions. Energy minimization was done for 10000 steps (out of which 4000 steps of steepest descent method followed by 6000 steps of conjugate gradient method). The temperature of minimized structures was increased gradually from 0 K to 300 K in a canonical ensemble (NVT). The systems were then equilibrated for 5 ns at 300 K temperature and 1 atm pressure in isothermal-isobaric (NPT) ensemble. The simulations were then extended further for 200 ns production runs in NPT ensemble with the temperature and pressure maintained at 300 K and 1 atm, respectively. With a pressure relaxation time of 2 ps, Berendsen barostat[146] was used to control the pressures of all the systems. The simulation temperature was regulated by the Langevin dynamics method[145] with a collision frequency of 1 ps^{-1}. The SHAKE algorithm[148] was used to constrain all covalent bonds involving hydrogen atoms, and also the simulation time step of 2 fs was used for all the simulations. All MD simulations were run with a 10 Å cutoff for the calculation of all nonbonding short-ranged interactions. The particle mesh Ewald (PME)[147] method was utilized for adequate treatment of long-ranged nonbonding electrostatic interactions.

Table 6a-1. System overview[a]

System	N_{UA}	N_{Vit-C}	N_{wat}	Box lengths (x×y×z) (Å)
V0	8	–	4000	49.687×49.687×49.687
V4	8	4	4000	49.772×49.772×49.772
V8	8	8	4000	49.868×49.868×49.868
V16	8	16	4000	50.063×50.063×50.063
V24	8	24	4000	50.206×50.206×50.206
V40	8	40	4000	50.600×50.600×50.600
V_o8	–	8	4000	49.722×49.722×49.722
V_o24	–	24	4000	50.101×50.101×50.101
V16-a	8	16	6000	57.131×57.131×57.131
V16-b	8	16	8000	62.718×62.718×62.718
U16V32	16	32	6000	57.553×57.553×57.553
U16G	16	–	8000	67.048×67.048×57.470
U16V32G	16	32	8000	67.135×67.135×57.631
U25V40G	25	40	10000	69.072×69.072×69.072

[a] N_{UA}, N_{Vit-C}, and N_{wat} refer to the number of uric acid (UA), vitamin C (Vit-C), and water molecules,

respectively.

To study the self-assembly of small molecules on the graphene surface, a non-charged graphene monolayer with a dimension of 6.0 nm × 6.0 nm in the XY plane (Figure 6a-1 (c)) was built in VMD.[149] It was positioned at the center of a simulation box. Periodic boundary conditions were applied in all three directions so that the periodic images do not overlap. All atomic sites of the graphene surface were allocated with the general AMBER force field (GAFF).[142] The systems were equilibrated for 10 ns at 300 K temperature and 1 atm pressure in isothermal-isobaric (NPT) ensemble in these simulations. The simulations were then extended further for 200 ns production runs in NVT ensemble with the temperature and pressure maintained at 300 K and 1 atm, respectively. Here, MD simulations were run with a 12 Å cutoff to calculate all nonbonding short-ranged interactions. The trajectories of the MD simulation were analyzed via the CPPTRAJ[376] module built-in AMBER.

Flory-Huggins (FH) theory, although the principle was initially derived for smaller molecules, provides a fundamental thermodynamic equation for mixing polymer systems to interpret their non-ideal behavior.[313, 314] FH theory, based on the lattice model, suggests that the molecules are dispersed randomly. In compliance with this principle, the mixing of polymers is predominantly based on (i) repeating monomers for a polymer chain can be subjected to a highly disordered state from a perfectly ordered state, and this is accompanied by (ii) spontaneous mixing of polymer monomer units and solvent molecules. The Flory-Huggins interaction parameter (χ_{FH}) is another concept that requires consideration and is used to describe the relationship between the polymer and solvent molecules. The critical value of χ_{FH} for phase separation of a polymer-solvent mixture can be obtained from

$$\chi_{FH} = 1/2 + 1/2x + 1/\sqrt{x} \tag{6.1}$$

Thus, the above equation reveals that for a monomeric mixture (x = 1), χ_{FH} becomes 2 and when x $\rightarrow \infty$, χ_{FH} becomes 0.5. Therefore, the critical value of χ_{FH} is less than 0.5 for polymer solubility, i.e., polymer-solvent miscibility.

The modified version of FH theory is also extended to systems consisting of small molecules.[315] Following previous researches,[192, 191] an updated FH theory is used to study the solubility of UA molecules. Here, we can see no intermolecular interaction between molecules in the original FH theory. Flory-Huggins interaction parameter is also

composition independent in the original FH theory. However, in contradiction to FH theory, the modified FH theory considers the intermolecular interactions between molecules, and it also enables the measurement of the concentration-dependent χ_{FH}.[316] In our present study, we also consider the modified FH theory to measure UA solubility. The modified FH theory was used previously to predict the solubility of small molecules with the help of the MD simulation technique.[192, 191] χ_{FH} is a quantity without dimension and it is defined as[315]

$$\chi_{FH} = V_{ref}\Delta E_{mix}/RT \tag{6.2}$$

where V_{ref} represents the reference volume, i.e., the smaller volume between the molar volumes of UA and Vit-C. ΔE_{mix} refer to the energy of mixing of UA and Vit-C molecules. The volume change upon mixing is negligible, thus ΔE_{mix} can be successfully replaced by enthalpy of mixing ΔH_{mix}.[317] ΔH_{mix} can be directly determined from the enthalpy of binding, ΔH_{bind}, of pure UA molecules ($(\Delta H_{bind})_{UA}$), pure Vit-C molecules ($(\Delta H_{bind})_{Vit-C}$), and the UA–Vit-C mixture ($(\Delta H_{bind})_{UA-Vit-C}$), with the help of the following equation,

$$\Delta H_{mix} = (\Delta H_{UA-Vit-C}/V)_{UA-Vit-C} - \phi_{UA}(\Delta H_{bind}/V)_{UA} - \phi_{Vit-C}(\Delta H_{bind}/V)_{Vit-C} \tag{6.3}$$

where the volume fractions of UA and Vit-C in a mixed system are ϕ_{UA} and ϕ_{Vit-C} respectively and V is representing the overall system volume.

Following earlier works,[192, 191] we have considered two independent UA–Vit-C simulation systems to study the miscibility of UA and Vit-C mixtures. In the first combination, the simulation was done with 24 Vit-C and 1 UA molecules (in 24:1 ratio). In the second one, simulation was carried out with 24 Vit-C and 4 UA molecules (in 6:1 proportion). These molecules were initially placed randomly in both systems. We had equilibrated each mixture in a vacuum to obtain initial compactness. A 12 ns simulation was carried out in AMBER14 at 300 K for both these mixtures in a cubic box. A small number of water molecules, primarily at the cubic box corner, were included in 24:1 and 6:1 combinations. After that, energy minimization of 10000 steps was performed, out of which the first 4000 steps were in the steepest descent method followed by 6000 steps in the conjugate gradient method. In the canonical ensemble (NVT), the temperature was increased steadily from 0 to 300 K. A 4 ns equilibrium process was carried out with 300 K temperature and 1 atm pressure in an isothermal-isobaric (NPT) ensemble so that the

system relaxes into its equilibrium structure. These two simulations were expanded using periodic boundary conditions in all three directions for another 20 ns in the NPT ensemble (at 300 K and 1 atm pressures). The AMBER14 package was used in all MD simulations at a time step of 2 fs. SHAKE algorithm restricts the bonds involving hydrogen atoms. For all short-range nonbonded interactions, a 10.0 Å cut-off distance was used. For the treatment of long-range nonbonding electrostatic interactions, the particle mesh Ewald (PME) was used.

The MM-GBSA[184] approach enables ΔH_{bind} to be measured, and the last 4 ns of simulation trajectories were considered for the same. The python script MMPBSA.py of MM-PBSA, in the AMBER14 software, was used for each MM-GBSA estimation. ΔH_{bind} was determined according to

$$\Delta H_{bind} = \Delta E_{vac} + \Delta G_{solv}, \tag{6.4}$$

where ΔE_{vac}, and ΔG_{solv} were the energy in vacuum (gas phase), and the solvation free energy,[227, 291] respectively. ΔE_{vac} can further be decomposed as:

$$\Delta E_{vac} = \Delta E_{ele} + \Delta E_{vdw}, \tag{6.5}$$

where ΔE_{ele} and ΔE_{vdw} measures the receptor-ligand electrostatic and van der Waals interaction energy components, respectively. Moreover, (ΔG_{solv}) energy can also be divided into two energy terms as:

$$\Delta G_{solv} = \Delta G_{GB} + \Delta G_{NP}. \tag{6.6}$$

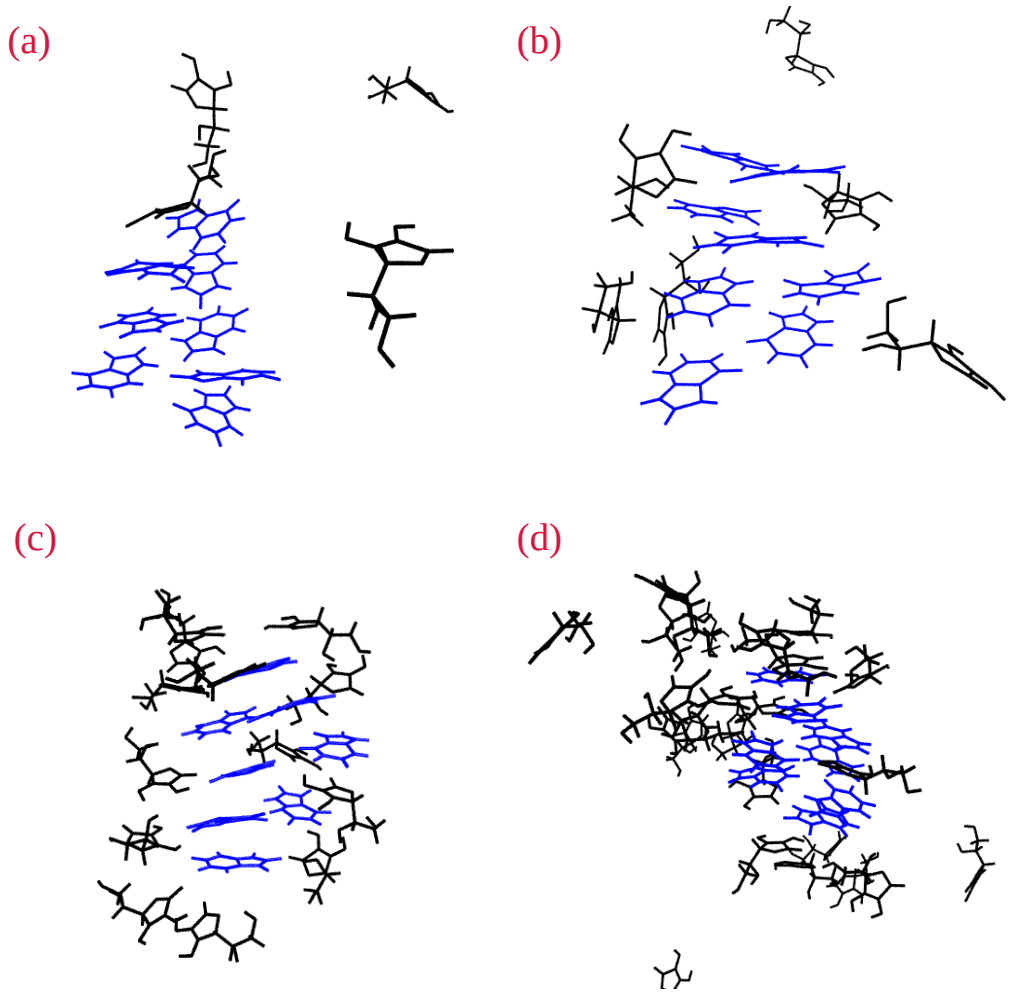

Figure 6a-2. *The snapshots of an aggregated UA molecules (blue in color) surrounded by Vit-C molecules (black in color) in systems (a) V4, (b) V8, (C) V16, and (d) V24.*

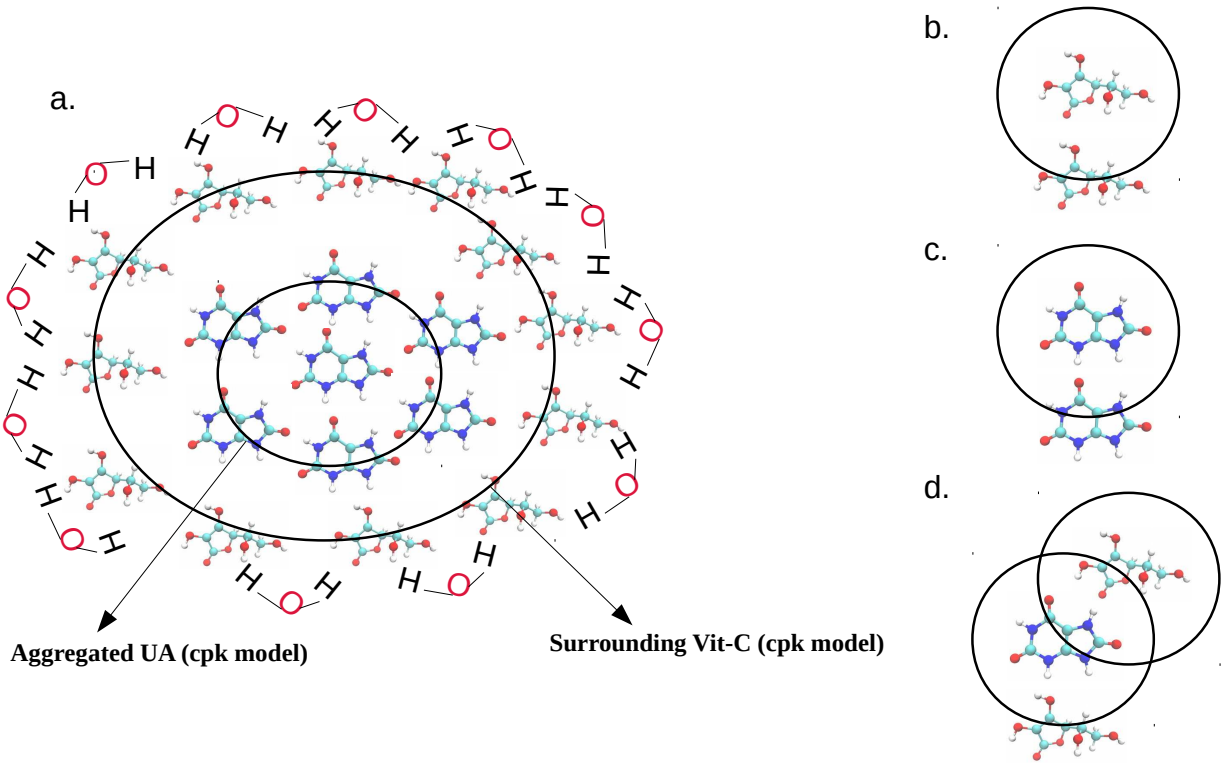

Figure 6a-3. *(a) In the UA–Vit-C mixture, aggregated UA molecules are surrounded by Vit-C molecules. Schematic representation of cluster structure determination for the (b) Vit-C–Vit-C, (c) UA-UA, and (d) UA–Vit-C interactions. When two molecules satisfy a distance criterion, we can determine the size of the cluster structure. Here, the minimum distances for these interactions are 6 Å, 5.30 Å, and 5 Å for UA-UA, UA–Vit-C, and Vit-C–Vit-C interactions. In the case of self-aggregation like UA-UA and Vit-C–Vit-C interactions, if the respective pair maintains the distance criteria, we can say they are forming a dimer. The same definition goes for higher-order clusters also. In the conjugated cluster for UA–Vit-C interactions, self, and intermolecular interactions are also considered. Therefore, the conjugate cluster is determined by combining all possible pairs like UA-UA, UA–Vit-C, and Vit-C–Vit-C with their respective distance criteria.*

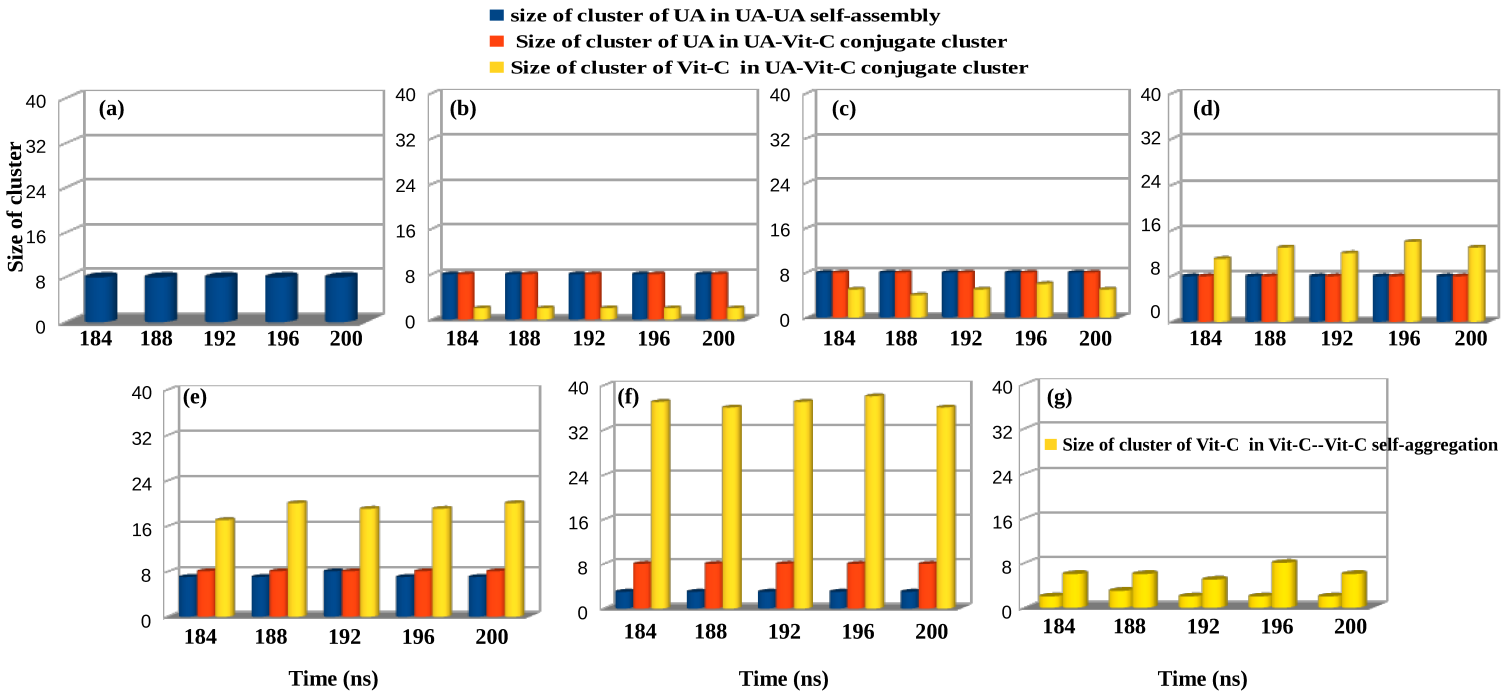

Figure 6a-4. *(a)-(f) The size of clusters produced by UA due to UA-UA self-aggregation (blue), UA due to UA–Vit-C conjugate cluster (red), Vit-C due to UA–Vit-C conjugate cluster (yellow) for systems (a) V0, (b) V4, (c) V8, (d) V16, (e) V24, and (f) V40. (g) represents the size of clusters produced by Vit-C due to Vit-C–Vit-C aggregation in systems V_o8 (first 3D cylinder representation at each interval) and V_o24 (second 3D cylinder representation at each interval). Here, cluster sizes are given at each 4 ns time interval for the last 20 ns trajectory out of a total 200 ns simulation run for all systems.*

Here, polar component, ΔG_{GB}, was calculated using generalized-Born (GB) approach[292] and the nonpolar contribution, ΔG_{NP}, of the solvation free energy ΔG_{solv} was determined as follows:[291, 292, 193]

$$\Delta G_{NP} = \gamma(SASA) + \beta, \tag{6.7}$$

where $\gamma = 0.005$ kcal/Å^2 , $\beta = 0.0$, and SASA was the solvent accessible surface area.

■ RESULTS AND DISCUSSION

CLUSTER STRUCTURE

Aggregation of UA molecules in the presence and absence of Vit-C

As per the VMD snapshots, an aggregated UA molecules are surrounded by Vit-C molecules (Figure 6a-2). The cluster structure determination (Figure 6a-3) illustrates the prevailing circumstances of how well ordered UA molecules are impeded in the presence of an inhibitor (here, Vit-C) at higher concentration based on divergence from coherently adorned structures. UA aggregates and forms a stable octamer in system V0 in pure water (Figure 6a-4(a)). 100% aggregation of UA molecules will thus be observed (in system V0). Inhibitor Vit-C is eventually applied to the UA molecules from system V4 to V40. It can be seen that UA molecules ultimately aggregate from system V4 to system V24 without any exception with that of system V0 (Figre 6a-4(b)-(e)). Consequently, Vit-C does not break UA clusters into tiny fragments. However, in system V40, where the quantity of Vit-C is comparatively more extensive, the UA cluster is shattered (Figre 6a-4(f)). It can be seen that the UA cluster is now transformed into a trimer in system V40 (Figre 6a-4(f)). Therefore, a moderately large number of Vit-C turns UA clusters into lower-order clusters to inhibit the accumulation of UA. As compared to UA, Vit-C does not accumulate among itself. In a pure Vit-C system (i.e., system V_o8), a maximal trimer with a high dimer percentage is undoubtedly present (Figre 6a-4(g)). Therefore, it is evident that the percentage of monomer is relatively high in system V_o8. A similar observation can also be revealed for system V_o24, where the number of Vit-C is high. In brief, a maximum cluster size of octamer can also be found with a predominant percentage of hexamer (Figre 6a-4(g)). Thus, the self-aggregation of Vit-C is not seen in an aqueous medium. A recent study with perturbed-chain statistical associating fluid theory (PC-SAFT) shows that Vit-C (as an acidic vitamin) is the most soluble in aqueous medium over other amphoteric vitamins.[318] Therefore, UA molecules can attract Vit-C to create a higher-order UA-Vit-C conjugate cluster because of the lower aggregation propensity of Vit-C (discussed later).

Conjugation of Vit-C molecules with UA cluster and overall UA-Vit-C cluster

From the previous section, it is evident that UA cluster size remains same with 100% octamer in almost all systems except system V40 wherein the concentration of Vit-C is relatively high. Again, the aggregation propensity of Vit-C is very negligible. Thus, these scattered Vit-C in all systems must accumulate around the aggregated UA molecules if Vit-C shows favorable interactions with UA. Therefore, the investigation of UA-Vit-C conjugate cluster size may significantly contribute to the prediction of encapsulation along with the breaking of UA cluster by Vit-C. In system V4, an octamer of UA molecules is attached with 2 to 3 Vit-C molecules (Figure 6a-4(b)). As the concentration of Vit-C is increased from systems V4 to V40, the number of Vit-C molecules attached with aggregated UA molecules is increased (Figure 6a-4(c)-(f)). It is evident from these numbers that almost 80 to 90% of all Vit-C molecules present in each system come near to the aggregted UA cluster. Therefore, strong encapsulation of UA molecules can be observed as the number of Vit-C is increased. Moreover, one can see the UA cluster impediment at a substantially higher concentration of Vit-C. It is to be noted that the conjugate cluster for UA–Vit-C interaction is assessed by the criteria introduced earlier (Figure 6a-4 (d)).

Therefore, it is evident that Vit-C encapsulates the UA clusters (at a range of concentrations) and further hinders the UA cluster by turning them into lower-order clusters at a higher concentration. In the present manuscript, the system with a higher concentration of Vit-C (i.e., system V40) is not considered in all analyses except cluster structure analysis and hydrogen bonding calculation (discussed in the next subsection). Though the higher concentration of Vit-C is apparently breaking the UA cluster, experimentally, it is seen that higher concentration can also accelerate kidney stone formation induced by Vit-C itself.

WHY IS Vit-C ATTRACTED TOWARDS THE UA CLUSTER?

Hydrogen bond:

During the clusterization between UA and Vit-C, the hydrogen bonding interaction plays a significant role. Vit-C forms substantial hydrogen bonds with UA, which is also apparent from the snapshots (Figure 6a-2). It is seen that the number of Vit-C–UA hydrogen bonds is gradually increased from system V4 to V24 (Table 6a-2). Thus, as the number

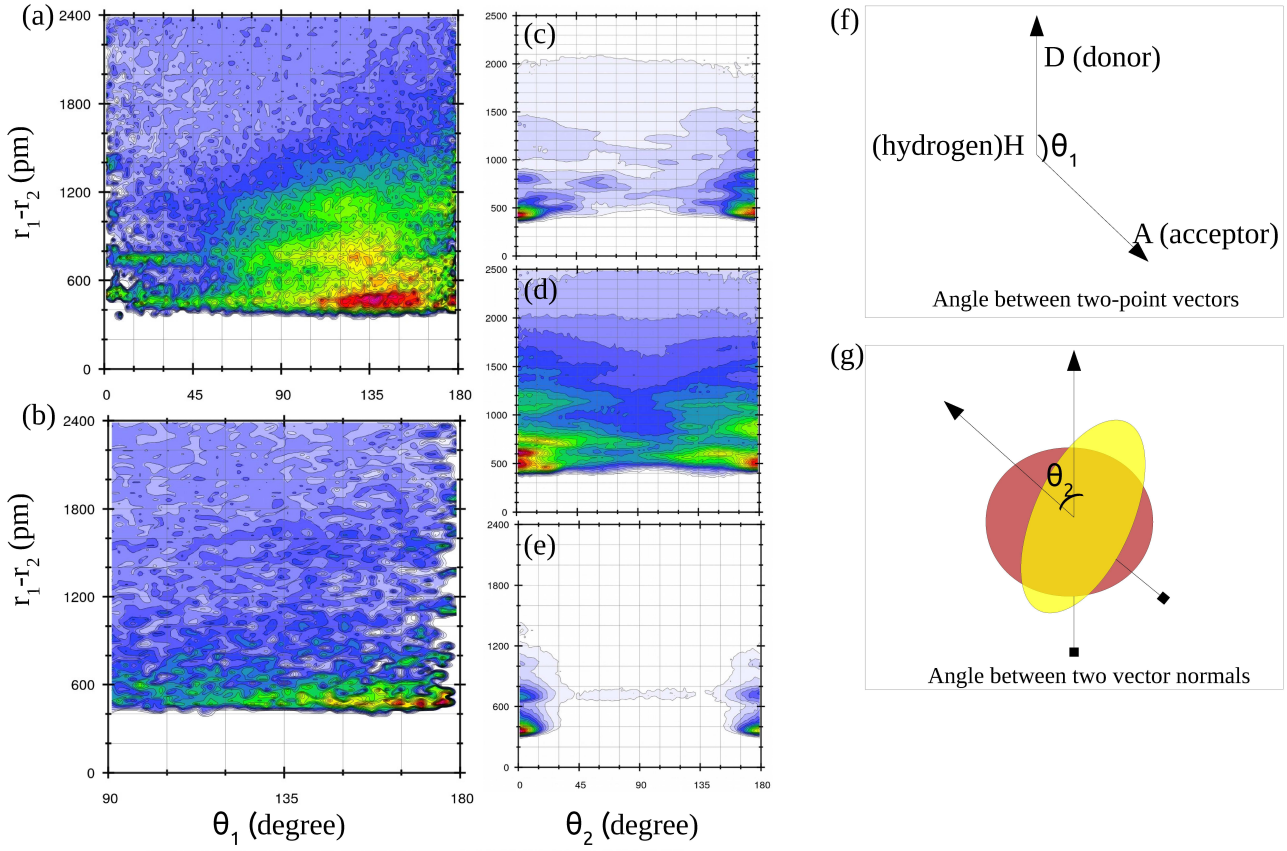

Figure 6a-5. *The distribution of orientational angle between (a) UA and Vit-C molecules, (b) Vit-C and Vit-C molecules considering two-point vectors of these two molecules. The angle between two vector normals is shown for (c) UA–Vit-C, (d) Vit-C–Vit-C, and (e) UA–UA interactions. (f) represents an angle between two-point vectors and (g) represents the approach of an angle between two vector normals. Here, both angles θ_1 and θ_2 are plotted against the COM-COM (center-of-mass) distance between any two molecules.*

of Vit-C is increased, more interaction between them can be also be observed. However, UA-UA aggregation is not perturbed by the presence of a moderately higher number of Vit-C molecules, as can be seen by hydrogen bond number (Table 6a-2). The UA-UA hydrogen bond number does produce a negligible change in the presence of Vit-C. However, a higher number of Vit-C can reduce the UA-UA hydrogen bonding interaction prominently by making strong UA-Vit-C hydrogen bonding interactions (in system V40, Table 6a-2). The same is inferred by the previous cluster structure analysis too. Interestingly, the Vit-

C–Vit-C hydrogen bond number is not as significant as UA–Vit-C (Table 6a-2). Therefore, an aggregated UA can drag more Vit-C towards itself.

Moreover, hydrogen bonding interactions between UA–Vit-C and Vit-C–Vit-C can also be established by the determination of orientational angle (Figure 6a-5 (a) and (b)) as in these figures; it is evident that the probability of D-H$\cdots$A angle lies within 135°-180° which implies the hydrogen bonding interaction.

To delimit the number of hydrogen-bonds implicated in all forms of possible pairs, a set of a criterion is applied to define the hydrogen bonds between the donor (D) and acceptor (A).[207, 253, 288, 289, 290] If the distance D-A $\leqslant$ 3.5 Å and, simultaneously, angle $\angle$ D-H$\cdots$ A $\geqslant$ 120° are met, hydrogen bonding is then deemed to be present.

Table 6a-2. Total number of hydrogen bonds for UA-UA, UA-Vit-C, and Vit-C-Vit-C interactions.

System	UA—UA	UA—Vit-C	Vit-C—Vit-C
V0	6.92	—	—
V4	7.05	1.41	1.32
V8	6.62	8.00	3.46
V16	6.05	17.32	11.08
V24	7.59	23.56	20.16
V40	4.12	35.31	56.42
V_o8	—	—	2.77
V_o24	—	—	12.42

π-stacking:

Visualization of trajectories for all systems (Figure 6a-2), it can be assumed that π-π stacking interaction between UA–Vit-C and Vit-C–Vit-C interactions may also be possible. Therefore, the determination of the orientational angle between these interacting species provides enough evidence of π-π stacking interaction. To do so, the angle between two vector normals between any two interacting aromatic rings is determined, and it can be seen that angle θ_2 lies within 0°-20° and 160°-180° for UA–Vit-C (Figure 6a-5 (c)) and Vit-C–Vit-C (Figure 6a-5 (d)) interactions. This angle range well depicts the criterion for π-π stacking interaction.[207, 161] Thus, we can say that UA–Vit-C and Vit-C–Vit-C interactions may also involve π-π stacking interaction. It is interesting to say that UA-UA

interaction is predominantly dependent on π-π stacking interaction (Figure 6a-5 (e)), and such findings match with that of the previous studies[207].

It is to be perceived that schematic illustrations (in Figure 6a-5 (f)-(g)) are presented for the hydrogen bonding (among donor, acceptor, and hydrogen atoms as mentioned in the last subsection) and π-stacking interactions (between the vector normals of two interacting pairs possessing aromatic rings). The two-point vectors among donor, acceptor, and hydrogen atoms can precisely delineate the hydrogen bonding situation (Figure 6a-5 (f)). In contrast, the angle between the vector normals can define the π-stacking interaction explicitly (Figure 6a-5 (g)).

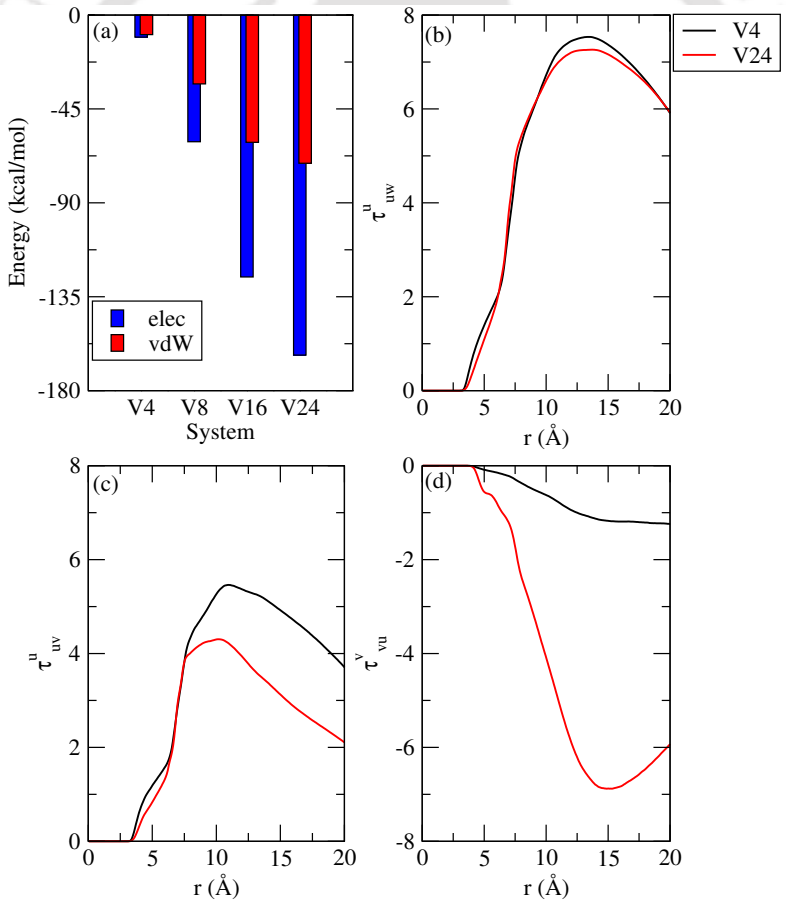

Figure 6a-6. *(a) The components (electrostatic and van der Waals energy) of total energy between UA and Vit-C from system V4 to system V24. The preferential interaction parameters of (b) UA-UA interaction over UA-water, (c) UA-UA interaction over UA–Vit-C, and (d) Vit-C–Vit-C over Vit-C–UA are presented here.*

Interaction energy:

From the Figure 6a-6 (a), it can be easily seen that as the number of Vit-C is increased from system V4 to system V24, the aggregated UA interacts more favorably with Vit-C molecules. Furthermore, in UA–Vit-C interactions, electrostatic energy predominates over van der Waals interactions in all cases. Therefore, a strong hydrogen bonding interaction can be estimated by such interactions. However, negative van der Waals interaction energy also indicates of having energitically favorable hydrophobic (like, π-π stacking) interactions. Thus, the determination of components of total interaction energy provides the same informations as metioned earlier.

Preferential interaction:

The estimation of preferential interaction parameter[285, 194, 195, 196, 179, 286, 282] of UA-UA interaction over UA-water evidently shows that UA-UA aggregation is preferable in water in presence of Vit-C (Figure 6a-6 (b)). However, if we consider the UA-UA interaction over UA–Vit-C, then the interaction among UA molecules is a slightly less favorable in system V24 as the concentration of Vit-C is increased from system V4 to V24. Nevertheless, it is definitely more than the interaction between UA–Vit-C pair in these systems (Figure 6a-6 (c)). Thus, at that concentration range, the aggregation of UA predominates over UA–Vit-C interaction. As a consequence, a higher-order cluster is produced (discussed earlier). Interestingly, Vit-C does not want to aggregate; instead, it is attracted by the UA cluster. This is confirmed by estimating preferential interaction parameters for Vit-C–Vit-C interaction over Vit-C–UA interaction (Figure 6a-6 (d)). Therefore, encapsulation of UA aggregates by Vit-C molecules can be achieved at this concentration range.

The preferential interaction parameters, τ^u_{uw} (UA-UA over UA-water), τ^u_{uv} (UA-UA over UA–Vit-C), and τ^v_{vu} (Vit-C–Vit-C over Vit-C–UA) are determined for respective systems following the equations mentioned below:[285, 194, 195, 196, 179, 286, 282]

$$\tau^u_{uw} = \rho_u(G_{uu} - G_{uw}) \tag{6.8}$$

$$\tau^u_{uv} = \rho_u(G_{uu} - G_{uv}) \tag{6.9}$$

$$\tau^v_{vu} = \rho_v(G_{vv} - G_{vu}) \tag{6.10}$$

where u, v, and w denote UA, Vit-C, and water molecules, respectively. ρ_u and ρ_v represent the number density of UA, and Vit-C molecules, respectively. The preferable interaction

between any two molecules (say i and j) can be indicated with the higher positive value of τ. Here, G_{uu}, G_{uv}, G_{vv}, and G_{vu} correspond to Kirkwood–Buff (KB) integrals, and these integrals can be accessed following earlier studies.[285, 194, 195, 196, 179, 286, 282] It ought to be referenced that these integrals can be accomplished with the accompanying radial distribution functions. The center of masses (COMs) of any two molecules are considered for appraising these distribution functions.

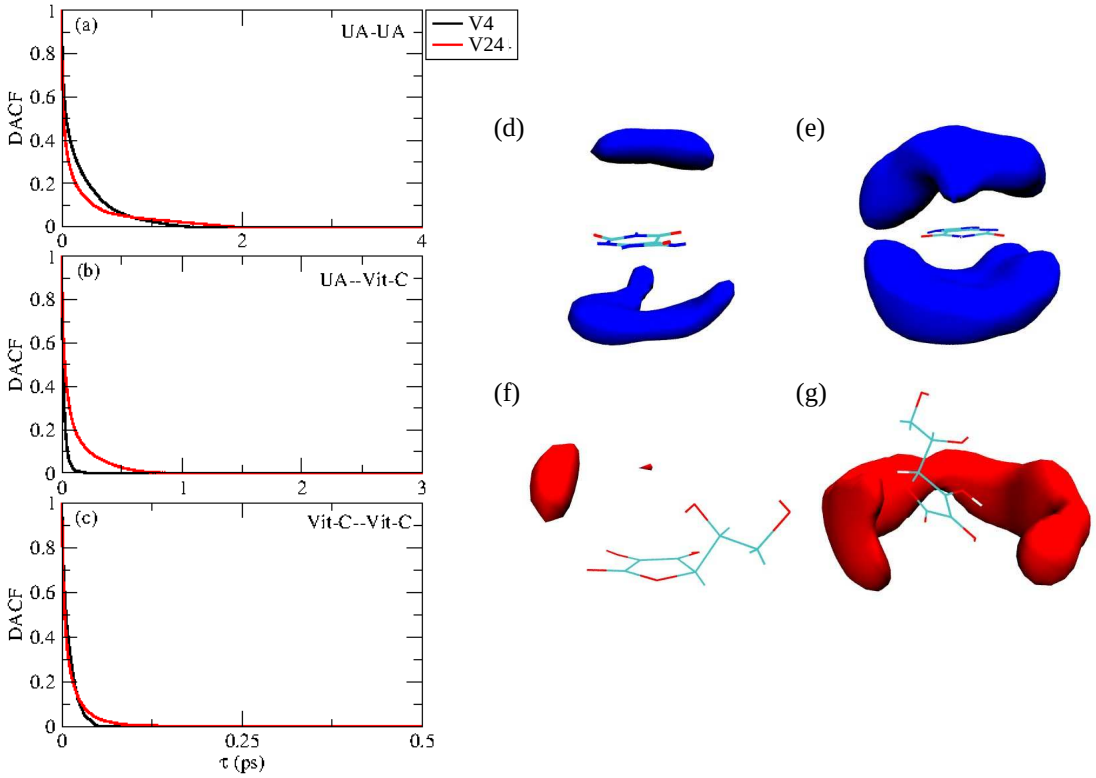

Figure 6a-7. *Dimer existence autocorrelation functions (DACF) for (a) UA-UA, (b) UA–Vit-C, and (c) Vit-C–Vit-C interactions for systems V4 and V24. Here, the minimum distances for these interactions are 6 Å, 5.30 Å, and 5 Å for UA-UA, UA–Vit-C, and Vit-C–Vit-C interactions. For UA-UA interaction, DACF is calculated at an angle* 0°-20° *(considering the vector normals of aromatic rings) as the maximum density of UA around a reference UA can be seen here compared to other angles like* 30°-60° *and* 60°-90° *(not shown). The spatial density functions (SDF) (at an iso-value of 2* $Å^{-3}$*,) for UA–Vit-C interaction is presented for systems (d) V4 and (e) V24. The spatial density functions (SDF) (at an iso-value of 2* $Å^{-3}$*,) for Vit-C–Vit-C interaction is presented for systems (f) V4 and (g) V24.*

STABILITY OF UA–Vit-C CONJUGATE CLUSTER

Dimer existence autocorrelation function (DACF) and spatial density function (SDF)

By employing DACF for UA-UA, UA-Vit-C, and Vit-C–Vit-C interactions, the stability of different dimers is calculated for two systems V4 and V24. The dimer existence autocorrelation function (DACF) is evaluated by the use of the following equation:[158]

$$DACF(\tau) = N. < \sum_{t=0}^{T-\tau} \beta_{ij}(t+\tau).\beta_{ij}(t) >_{ij} \tag{6.11}$$

Here, DACF is considered autocorrelation of a simple function, β_{ij}, for a pair of molecules say, i and j, that can have value 1 when they are maintaining a preset distance criterion, and it goes to zero if the distance criterion is lost for the very first time.[158] It is worth noting that, for a given pair of molecules even if the criterion of distance is met later, DACF will remain zero. One can find a detailed explanation of DACF elsewhere.[158] It is to be noted here that we have considered only two systems to provide the dynamic nature of all kinds of dimers in two extreme conditions. It is observed that, regardless of the amount of Vit-C present in a system, the dimer produced by two UA molecules exhibits almost similar stability (Figure 6a-7 (a)). Therefore, UA preserves its cluster size by strong self-aggregation at this concentration range of Vit-C. In contrast, UA–Vit-C interaction becomes higher in system V24 than system V4 (Figure 6a-7 (b)). It is, therefore, apparent that in the presence of Vit-C, the encapsulation of the UA octamer is occurred. Again the interaction of Vit-C–Vit-C is not as intense as UA-Vit-C, even at higher Vit-C concentration (Figure 6a-7 (c)). Therefore, Vit-C stays distributed in a system, so the aggregated UA clusters attract them to bind it. A similar finding can also be seen if we analyze the spatial density plot for these two interactions, such as UA–Vit-C and Vit-C–Vit-C. It is undoubtedly apparent that the accumulating propensity of Vit-C around a reference UA (Figure 6a-7 (d) and (e)) is much more than Vit-C-Vit-C aggregation preference (Figure 6a-7 (f) and (g)). The Vit-C–Vit-C aggregation in system V24 is not as large as in UA-Vit-C (Figure 6a-7 (e) and (g)).

Free energy landscape and potentials of mean forces

Solvent-accessible surface area (SASA ($\mathring{A}^2$)) for UA-UA aggregation versus UA–

Vit-C hydrogen bonding for both V4 and V24 systems is considered for the assessment of free energy landscape (FEL). The FEL is determined by:[253]

$$\Delta G(V) = -k_B T[\ln P(V) - \ln P_{max}], \tag{6.12}$$

where P(V) portrays the probability of coordinate (V) calculated from the last 20 ns trajectory path, and it is deducted by P_{max}, which is the maximal distribution such that ΔG gets zero for the minimum free energy. For both systems, it is observed that the SASA value is nearly equal. For these two systems thus, the propensity for UA-UA aggregation or the cluster size of UA-UA interaction is identical (Figure 6a-8 (a) and (b)). UA–Vit-C interaction is high for the V24 system as the number of hydrogen bonds at system V24 is more significant than that at system V4 at a point where there is a minimum of free energy (Figure 6a-8 (a) and (b)). Therefore, the aggregated UA cluster in system V24 interacts prominently with the Vit-C present in that system. As a result, the Vit-C molecules encapsulate the UA cluster (here an octamer). In comparison, in system V24, the UA-Vit-C association is energetically more advantageous than V4, which can be concluded by comparing the potentials of mean forces[283, 284] for these two systems (Figure 6a-8 (c)). Thus, inevitably, the presence of Vit-C will wrap up the aggregated cluster of UA. It is to be noted that potentials of mean forces are assessed with the use of the following equation:

$$PMF_{ij}(r) = -k_B T \ln(g_{ij}(r)), \tag{6.13}$$

where $PMF_{ij}(r)$ presents the potential of mean force for the interaction between i and j. $PMF_{ij}(r)$, which provides the information on effective intermolecular interactions between two moieties present in the system as a function of separation distance, is calculated from the intermolecular pair correlation function $g_{ij}(r)$.[283, 284]

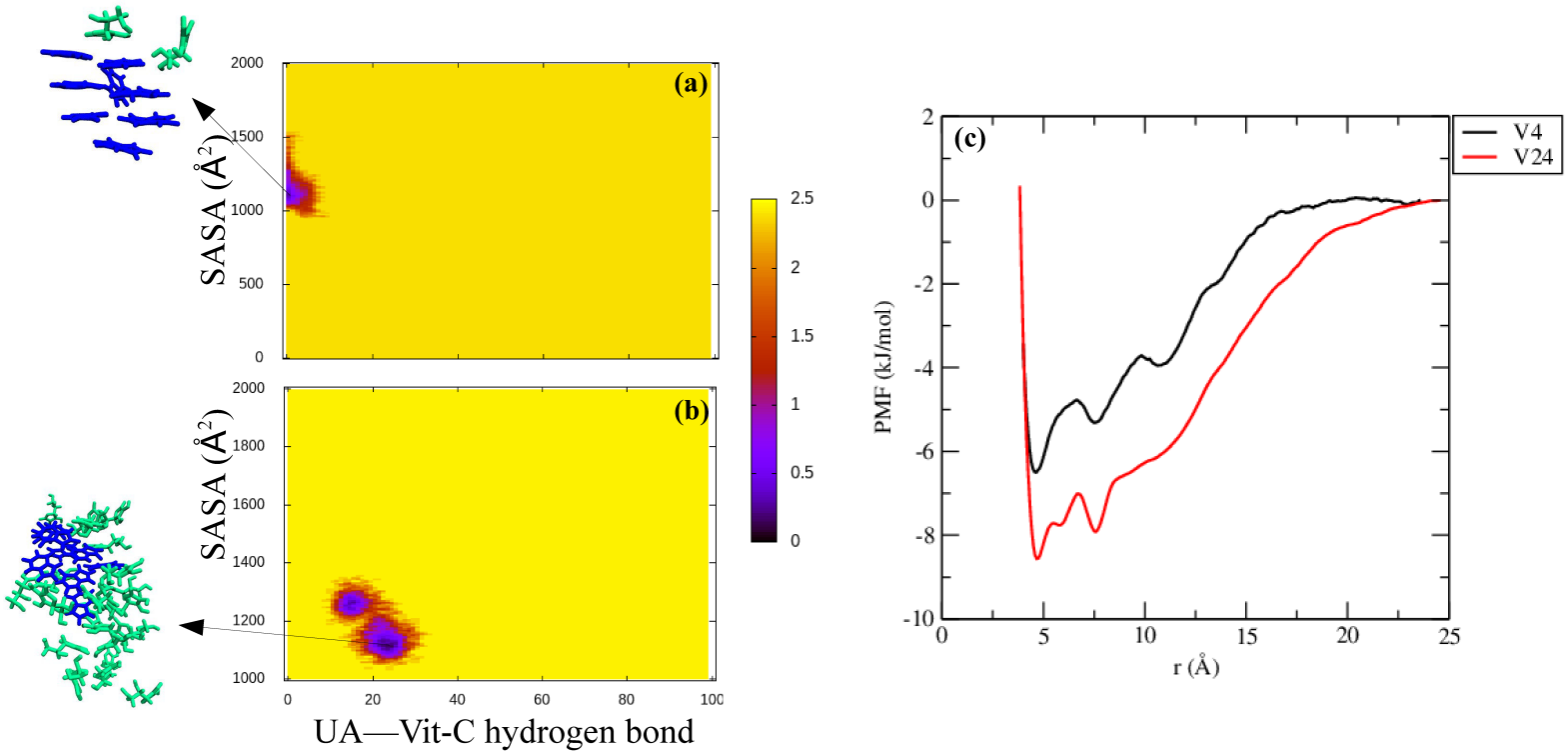

Figure 6a-8. *Free energy landscapes for the solvent-accessible surface area (SASA (Å²)) for UA-UA aggregation versus UA–Vit-C hydrogen bonding for systems (a) V4 and (b) V24. The free energy in the color bar on the right side is manifested in kcal/mol unit. The analogous snaps are also conferred for UA (blue)—Vit-C (green) conjugate assemblages for these two systems. (c) presents the potentials of mean forces for UA–Vit-C interaction for systems V4 and V24.*

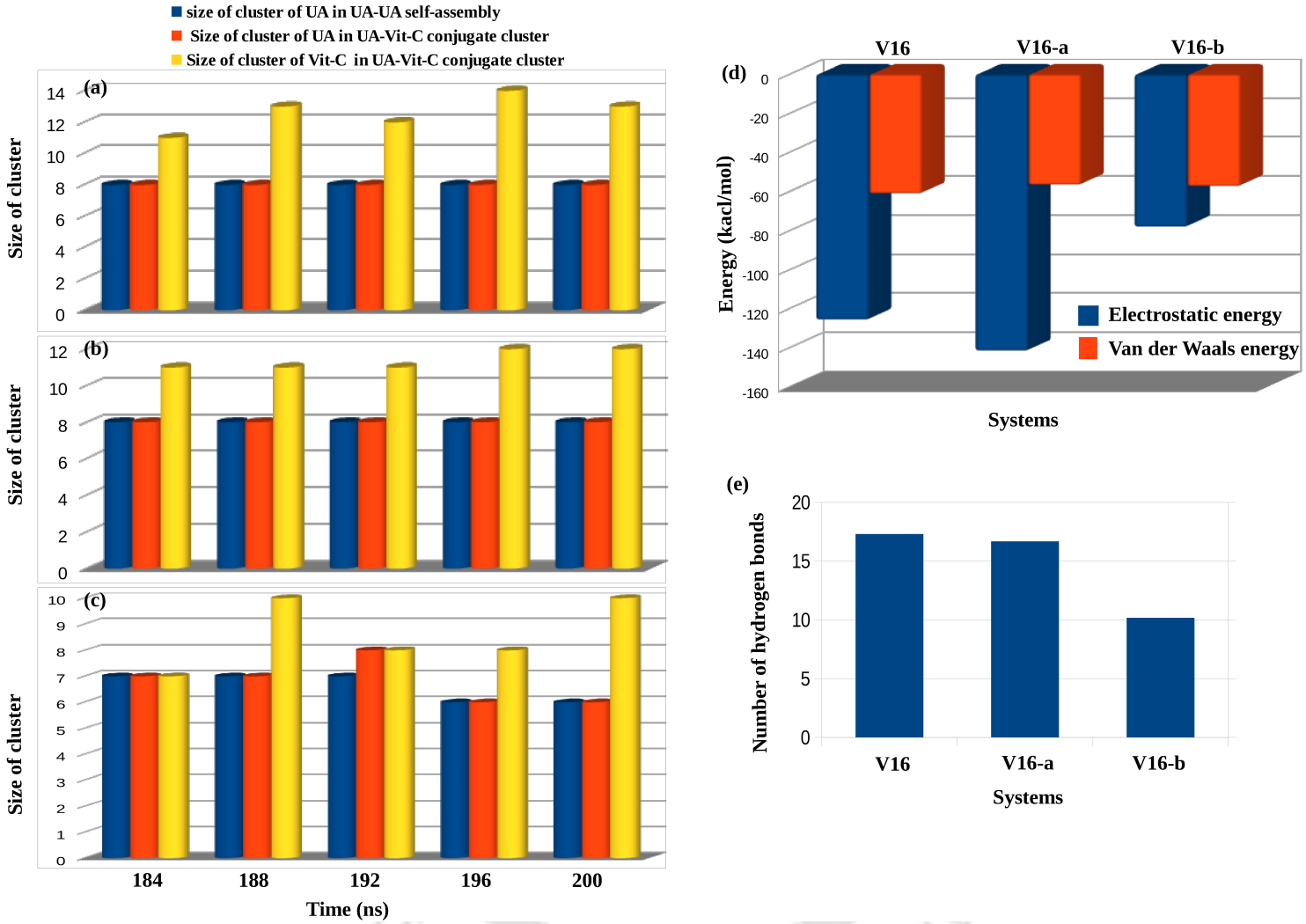

Figure 6a-9. *The different cluster sizes for systems (a) V16, (b) V16-a, and (c) V16-b. (d) presents the decomposition of total energy into its electrostatic and van der Waals energy components for systems V16, V16-a, and V16-b. (e) presents the total hydrogen bond numbers for UA–Vit-C interaction.*

(a)

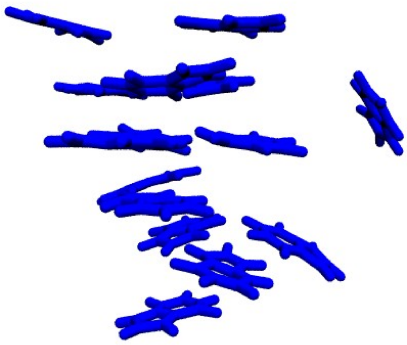

(b)

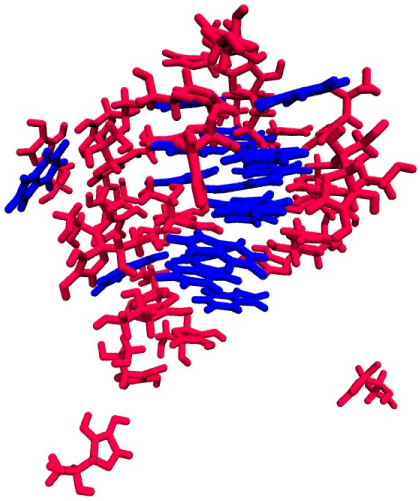

(c)

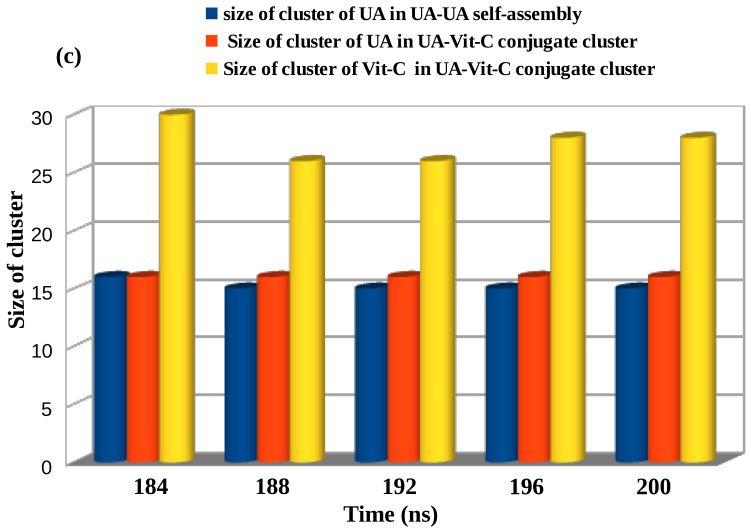

(d)

System	Elec.	vdW
U16V32	-386.35	-173.05

System	Hydrogen bond number
U16V32	50.69

Figure 6a-10. *(a) Elongated UA cluster of UA molecules in system V16V32, (b) the conjugate cluster of UA (blue)–Vit-C (red) for system V16V32, (c) the various sizes of clusters for UA-UA self-assembly and also for UA–Vit-C interaction, and (d) energy components (in kcal/mol unit) and hydrogen bond numbers for UA–Vit-C interaction in that system.*

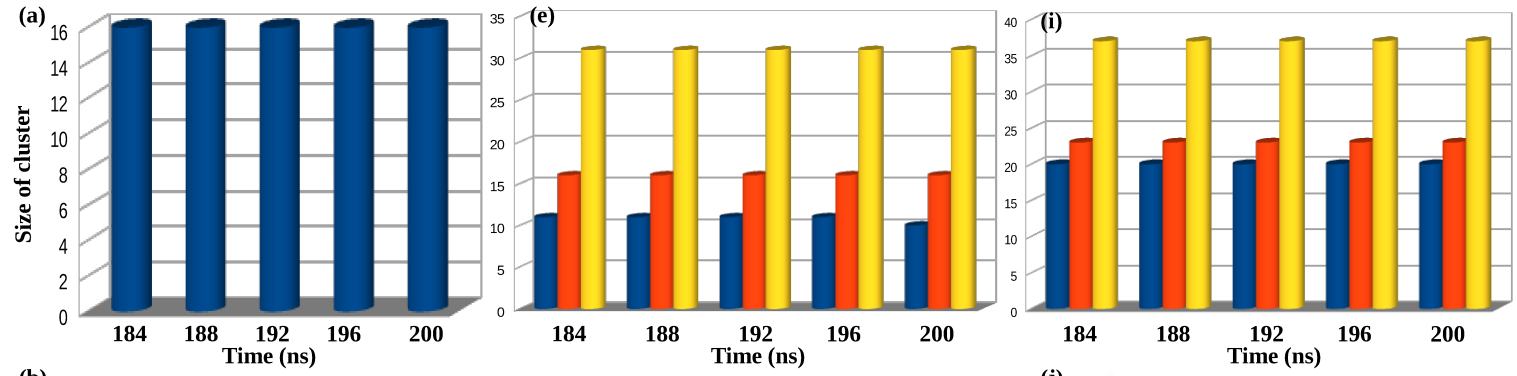

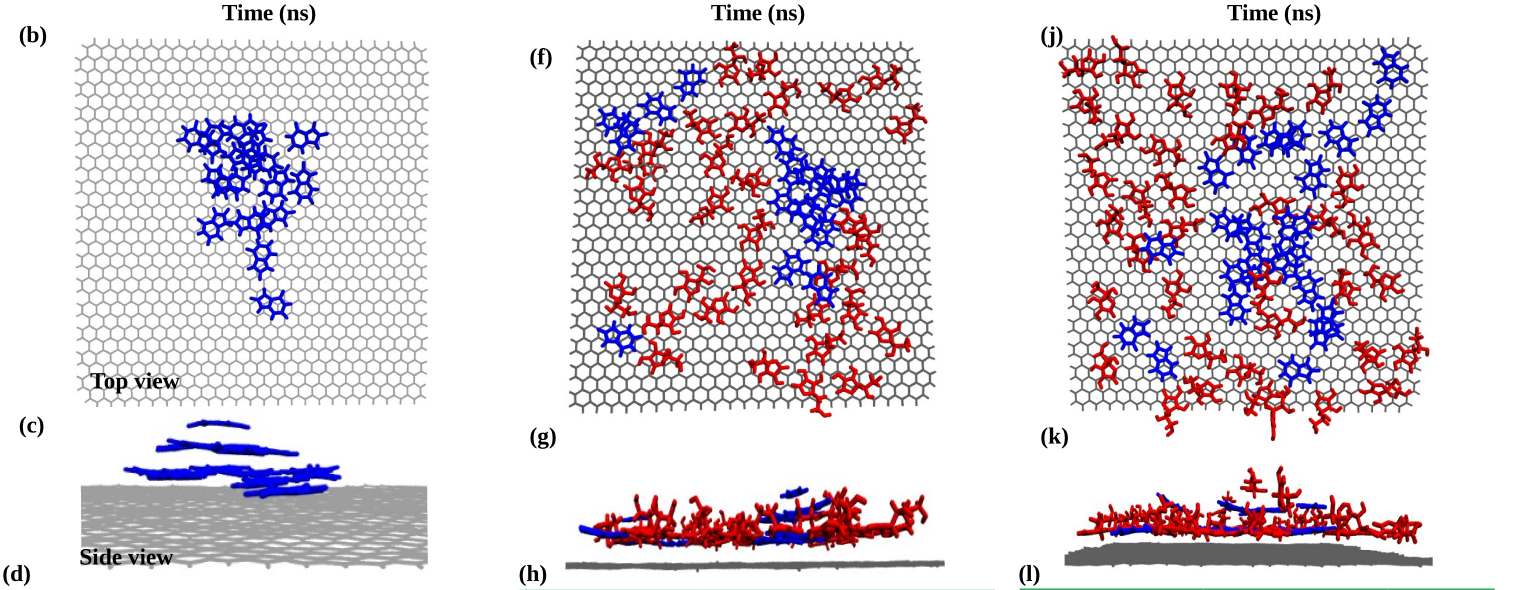

(d)

System	U16V32G	U25V40G
Hydrogen bonds	29.68	46.41

(h)

System	Elec.	vdW
U16V32G	-230.17	-32.71

(l)

System	Elec.	vdW
U25V40G	-361.22	-65.37

Figure 6a-11. *(a) Cluster structure for UA self-assembly in system U16G, (b) and (c) present the adsorbed UA molecules on the graphene sheet, (d) a total number of hydrogen bonds between UA and Vit-C molecules, (e) cluster structure for UA-UA and UA–Vit-C interactions in system U16V32G, (f) and (g) present the adsorbed UA and Vit-C molecules over the graphene surface for system U16V32G, (h) decomposition of total energy (in kcal/mol unit) into its various components, (i) cluster structure for UA-UA and UA–Vit-C interactions in system U25V40G, (j) and (k) present the adsorbed UA and Vit-C molecules over the graphene surface for system U25V40G, and (l) decomposition of total energy (in kcal/mol unit) into its various components for system U25V40G.*

EFFECT OF DILUTION ON THE UA–Vit-C CONJUGATE CLUSTER

The influence of dilution on the UA–Vit-C conjugate cluster can be propitious to procure enough confirmation on the stability of UA–Vit-C interaction. Thus, two more systems (systems V16-a and V16-b) are taken considering the system V16 as a reference system (Table 6a-1). It can be seen that despite increasing water content from system V16 to V16-b, there is no significant reduction in cluster size made by UA and Vit-C molecules (Figure 6a-9 (a)-(c)). There is a notable attraction between UA and Vit-C, despite having a sufficient dilute system, i.e., system V16-b. This implies that the interaction between UA and Vit-C is robust. More significantly, it can be said that UA molecules interact with each other to form a large cluster (here, an octamer) that attracts Vit-C to itself. Such attraction is sturdy and enduring in dilute solutions also. Furthermore, we assess and analyze the interaction energy and hydrogen bond numbers between UA and Vit-C of these three systems (Figure 6a-9 (d)-(e)). There are no such differences present in these systems in terms of hydrogen bond numbers and interaction energies. Hence, in these cases, a strong interaction between them becomes more apparent.

EFFECT OF Vit-C ON THE ELONGATED OF UA CLUSTER

A recent study observed that the large elongated cluster of UA was turned into small thin clusters in presence of theobromine.[282] Therefore, it will be interesting to examine whether Vit-C can provide a comparable impact on the UA cluster or not. Thus, a system (i.e., system U16V32, Table 6a-1) with higher UA molecules is considered, and it is seen that an elongated UA cluster is present in that system (Figure 6a-10 (a)). However, Vit-C cannot produce any such inhibitory effect on UA clusterization to inhibit their elongated aggregation (Figure 6a-10 (b)). It is found that almost all UA molecules appear close to each other to form a giant self-assembled UA cluster (Figure 6a-10 (c)). Interestingly, most of the Vit-C molecules are now attached to that of the UA elongated cluster to form a UA–Vit-C conjugate cluster (Figure 6a-10 (c)). The prediction of hydrogen bond number between UA and Vit-C, along with the decomposition of total energy into electrostatic and vdW energy, demonstrate that Vit-C interaction with the elongated UA cluster is substantial (Figure 6a-10 (d)). As a consequence, the composite UA-Vit-C cluster size is very high. Thus, encapsulation is still present seemingly without any change of UA self-aggregation in system U16V32. Therefore, it can be inferred that Vit-C does not possess any cluster breaking ability on UA self-accumulation in that system; instead, it encloses

the aggregated UA molecules.

SURFACE MEDIATED UA–Vit-C CONJUGATE CLUSTER

Kidney stones, which are ascertained free or appended to renal papillae, are crystal precipitates in the renal calyces and pelvis. They contain organic and crystalline constituents produced by the supersaturation of the urine. The most familiar type of kidney stone is formed on the renal papillary surfaces. Urinary crystals stick to create a tiny hard mass of stone known as crystal growth. The growth of stone is achieved on the matrix-coated surface with the aggregation of preformed crystals or secondary nucleation of crystal. Substances are inhibitors that minimize supersaturation initiation, nucleation, crystal expansion, the aggregation rate, or stone-forming processes. Inhibitors may either directly affect the urinary environment by interfering with crystal or they can act indirectly. There is, therefore, an essential mechanism for the development and protection of kidney stone deposition and adsorption of antibodies to the crystal surface.[67, 68, 69, 70]

In the present work, a graphene sheet is contemplated to provide a surface-mediated UA adsorption. After that, the inclusion of Vit-C onto adsorbed UA molecules illustrates the inhibitory mechanisms of Vit-C on UA self-aggregation. It is found that UA molecules are well adsorbed on the surface of the graphene. Therefore, it infers the surface-mediated UA aggregation to form a kidney stone, unlike pure solution-phase accumulation. Once Vit-C is introduced into the surface adsorbed UA molecules, it can be seen that there is a somewhat change of UA self-aggregation in the presence of Vit-C. However, Vit-C molecules are placed surrounding the aggregated UA molecules over the graphene surface. In system U16G system, all UA molecules are well adsorbed and arranged accordingly through hydrogen bonding and π-stacking interactions with like molecules to produce a large cluster (Figure 6a-11 (a)-(c)). Next, Vit-C is introduced in system U16V32G, and it is found that Vit-C is adsorbed surrounding the aggregated UA molecules. The same mechanism can also be achieved in system U25V40G. There is a strong interaction between UA and Vit-C molecules that can be assumed by estimating the total number of hydrogen bonds and various components of interaction energies for the UA–Vit-C pair (Figure 6a-11 (d)-(l)). Moreover, in all systems, a large UA cluster size can be seen (Figure 6a-11 (a), (e), and (i)) where the composite cluster of UA–Vit-C combination is usually more substantial for a pairing of the two (Figure 6a-11 (e) and (i)). Thus, the encapsulation property of Vit-C is being revealed obviously.

(a)

System	UA-UA	UA—Vit-C	Vit-C--Vit-C	UA-water	Vit-C--water
V0	1.60	--------	--------	9.55	--------
V4	1.59	0.17	0.02	9.25	32.59
V24	1.55	0.30	0.22	4.86	28.24

(b)

System	UA-water	Vit-C--water	water-water
V0	65.99	----------	3.75
V4	63.04	40.65	3.74
V24	37.13	201.50	3.71

(c)

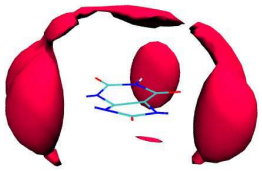

(d)

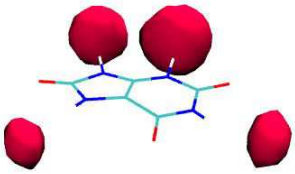

(e)

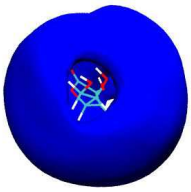

Figure 6a-12. *(a) The first shell coordination number (CN) of various pairs, (b) the total number of hydrogen bonds for numerous couples, (c) the spatial density function of water around UA in system V0, (d) the spatial density function of water around UA in system V24, and (e) the spatial density function of the water around Vit-C in system V24.*

It is seen that well-controlled, low toxicity and extremely effective delivery methods for anti-cancer medicines are a severe hurdle for developing a new class of cancer chemotherapy nanoparticle drug delivery systems. The large surfaces with nontoxicity have been designed as a nanocarrier for anti-cancer medications; however, there is limited knowledge of chemistry at the interface. A recent study reported that doxorubicin is loaded and controlled efficiently with the tunable graphene mediated surface. The non-covalent interactions and π-π stacking are confirmed between the drug and carriers.[319, 320] As a consequence, Vit-C could improve the doxorubicin supply from the graphene mediated surface. Again, stable graphene aqueous dispersions can be readily produced through the chemical reduction of graphene oxide by l-ascorbic acid with l-tryptophan as a stabilizer.[321] Therefore, the ad-

sorption of Vit-C on graphene can be made quickly to mimic the inhibitory mechanism of kidney stone formed by the crystal deposition of UA on the surface in the kidney.

WATER SOLUBILIZATION OF UA–Vit-C CONJUGATE CLUSTER

First shell coordination number (CN)

It can be easily seen that the first shell coordination number (CN)[240, 241, 242, 280] for UA-UA interactions remains almost similar from system V0 to system V24 (Figure 6a-12 (a)). Thus UA-accumulation is not getting hindered in the presence of Vit-C. Simultaneously, the CN of Vit-C around UA increases with the increase of Vit-C number from system V4 to system V24 (Figure 6a-12 (a)). Therefore, UA–Vit-C interaction is getting more favorable as the number of Vit-C is increased. In contrary, the CN of Vit-C around Vit-C does not show drastic change, thus, depicting no self-aggregation among Vit-C molecules (Figure 6a-12 (a)). Consequently, the water CN around UA molecules becomes low compared to the CN of water around Vit-C molecules (Figure 6a-12 (a)). Thus, more water molecules get accumulated around the UA–Vit-C clusters. Therefore, it can be assumed that the UA–Vit-C conjugate cluster gets solubilized in the aqueous medium. A similar observation can also be seen in the case of hydrogen bond numbers in which Vit-C makes more hydrogen bonds with water than UA when the number of Vit-C is higher, and this can be ascertained from the water-water hydrogen bond numbers (Figure 6a-12 (b)). Furthermore, water-water interaction is not hampered in the presence of Vit-C or UA as the water tetrahedral structure is retained for all systems (Figure 6a-12 (b)). Moreover, the determination of spatial water density (at isovalue 20 $\mathring{A}^{-3}$,) around the UA and Vit-C molecules strengthens the water solubility phenomenon of UA by Vit-C (Figure 6a-12 (c)–(e)). In system V0, it can be seen that water is well surrounding the UA molecules (Figure 6a-12 (c)). However, water density around UA gets reduced in system V24 (Figure 6a-12 (d)). This is because Vit-C molecules now surround the UA molecules in system V24. Interestingly, these Vit-C molecules, which produce large clusters with UA molecules, are now covered by many water molecules (Figure 6a-12 (e)). The SDF[281] of water around Vit-C in system V24 is very high. Thus, it can be assumed that the conjugate cluster made of UA–Vit-C interactions is highly solubilized by water. Though, direct solubilization of

UA–Vit-C cannot be predicted by the determination of CN, hydrogen bond, and SDF

plots. Therefore, Flory-Huggins (FH) interaction parameters for UA–Vit-C interactions need to be calculated to predict the solubility.

Flory-Huggins (FH) Interaction Parameters for UA–Vit-C interactions

We have calculated the Flory-Huggins interaction parameters between UA and Vit-C molecules to investigate the miscibility of their mixtures. Two separate UA–Vit-C combinations with different molar ratios are used for this measurement as described above. The enthalpy of mixing (ΔH_{mix}) and Flory-Huggins interaction parameter (χ_{FH}) values are -13.35 cal cm^{-3}, and -2.02, respectively, for the UA : Vit-C ratio of 1:24; -31.21 cal cm^{-3} and -4.72 for the ratio of 1:6, respectively. Therefore, in both combinations, we observe that the χ_{FH} is negative, which recommends that the UA and Vit-C associations are favorable, and the miscibility of them is conceivable.

■ SUMMARY AND CONCLUSIONS

This study examines the influence of Vit-C on the aggregation of UA through all-atom MD simulation. We observe that Vit-C immerses itself with the aggregated UA molecules; hence, it encapsulates UA clusters. The more Vit-C is present in a system, the more extensive interaction between the aggregated UA cluster and the Vit-C molecules. Besides, through the development of significant hydrogen bonding, hydrophobic, and π-stacking interactions, Vit-C combines itself nicely with the UA molecules to form an overall extensive conjugate UA-Vit-C cluster. It is also perceived that Vit-C interacts mainly with the aggregated UA molecules instead of self-aggregation among themselves. Thus, randomly dispersed Vit-C molecules are readily attracted by the large UA clusters in a system. The determination of the cluster structure explicates that Vit-C molecules form a lower-order self-aggregated cluster while UA forms a giant cluster. Also, the determination of average number of hydrogen bonds between the solution species implies that the self-aggregation of Vit-C is negligible suggesting that it can act as a potent inhibitor in the human body against kidney stone and gout. The preferential interaction parameter also explains that the interaction of Vit-C–Vit-C is less significant than the interaction between Vit-C and UA, which again illustrates that UA clusters can be extracted from our body by applying Vit-C. In the presence of higher number of UA molecules in a system, they form elongated UA clusters.[207, 282] Further, the use of the inhibitor in the extended UA cluster produces a comparatively thinner UA cluster.[282] However, in the present case, by blocking

the formation of elongated cluster of UA, Vit-C is unable to generate thinner aggregated UA molecules. Preferably, they firmly bind to the extended cluster. Moreover, the existence of relatively higher Vit-C concentrations can repress the self-assembly of UA from forming a higher-order UA cluster. A reasonable Vit-C concentration thus encapsulates the UA cluster, whereas a comparatively higher Vit-C concentration can intrude the UA cluster. The above fact is profoundly demonstrated by the determination of cluster structure, dimer stability (using DACF), free energy (using the calculation of the free energy surface between SASA (for UA-UA aggregation) versus hydrogen bond (between UA–Vit-C)) and the potentials of mean forces for interaction between UA and Vit-C. Besides, if the total interaction energy between UA and Vit-C is decomposed, electrostatic interaction energy predominates over vdW interaction energy. Crystal precipitates in the renal calyces and pelvis are kidney stones found free or attached to renal papillae. They include organic and crystalline segments formed by urine supersaturation. The most common type of kidney stone is developed on the renal papillary.[67, 68, 69, 70] The growth of stone is achieved on the matrix-coated surface through the aggregation of preformed crystals or secondary crystal nucleation.[67, 68, 69, 70] Substances are inhibitors that reduce supersaturation initiation, nucleation, expansion of crystals, accumulation rate, or stone-forming processes. By conflicting with crystals, inhibitors can undeviatingly affect the urinary circumstances or act obliquely. There is, therefore, an indispensable mechanism for the production and protection of kidney stone deposition and adsorption of antibodies to the crystal surface.[67, 68, 69, 70] In the present work, a graphene sheet is pondered to implement a surface-mediated UA adsorption. Subsequently, the influx of Vit-C into adsorbed UA molecules illustrates the variation in the self-aggregation of UA along with the encapsulation, thus, rendering the inhibitory mechanism of Vit-C in UA accumulation. UA molecules are found to be well-adsorbed on the graphene surface as they form a large cluster through hydrogen bonds and π-stacking interaction among themselves. It then recommends UA aggregation to form a kidney stone. Once Vit-C is included in the surface-adsorbed UA molecules, it can be comprehended that UA aggregation changes significantly. Vit-C molecules, however, are positioned over the graphene surface around the aggregated UA molecules to compose a comprehensive conjugate cluster. Hence, the absorption of Vit-C on the graphene surface can be achieved rapidly to emulate the inhibitory function of kidney stone by the crystal deposition on the surface of kidney. Furthermore, an inhibitor is suitable when it can repress as well as solubilize the solute molecules prominently. In

the present study, it is discerned that the overall conjugate cluster made by UA and Vit-C is highly water-soluble (from the determination of first shell CNs, hydrogen bonds, and density distributions of water around UA and Vit-C molecules). Moreover, the calculations of the Flory-Huggins interaction parameters further establish the evidence that the correlations between UA and Vit-C are affirmative and the miscibility of them is convincing. Christoph Held *et al.*, in a recent work[322], unveiled that Vit-C (as a covitamin) could increase the solubility of other vitamins. Moreover, it has also been reported that the addition of covitamins at low concentrations essentially influences the solubility by a pH change. However, at a particular covitamin concentration specific for each vitamin covitamin system, the molecular interactions predominate over the pH. Thus, prophesying the solubility in a broad range of concentrations needs to consider both molecular interactions and pH effects.[322] Again it has also been revealed that Vit-C is highly soluble in an aqueous medium.[318] Therefore, with a thorough study, our work features the inhibitory and eliminating function of UA by Vit-C. This research provides useful knowledge of inhibitory role of small molecules with UA aggregation and can be expanded to study other small molecule inhibitors.

6b: Appraising the Potency of Small Molecule Inhibitors and Their Graphene Surface-Mediated Organizational Attributes on Uric Acid-Melamine Clusters

"Poisons and medicine are often the same substance given with different intents."

— Peter Mere Latham

Overview: Uric acid (UA) and melamine (MM) crystallization in humans are associated with adverse medical conditions, including the germination of kidney stones, because of their low solubility. The growth of kidney stone usually formed on renal papillary facades is accomplished on the matrix-coated surface by aggregating preformed crystals or secondary crystal nucleation. Therefore, the effects of inhibitors such as theobromine (TB) and allopurinol (AP) on the MM-UA aggregation are investigated by employing classical molecular dynamics simulation on the graphene surface. It impersonates the exact essence of precipitation of kidney stone. The interaction between MM-UA is very intense, thus forming a large cluster on the surface. The presence of TB and AP will, however, substantially inhibit their aggregation. TB and AP significantly impede UA aggregation in particular. Therefore, lower-order UA clusters are formed. Such smaller UA clusters then pull the lower number of MM towards themselves, resulting in a smaller order UA-MM cluster. MM and UA aggregation on a 2D surface is found to be spontaneous. There is no difference in these molecules' adsorption with a change in graphene surface size and force field parameters (i.e., GAFF and OPLS-AA). The greater the surface area of graphene, the more molecules are absorbed. The solute-surface van der Waals interaction energy plays as driving force for solute molecules' adsorption on the surface. Besides, interactions like hydrogen bonding and π-stacking over the graphene surface involve binding all like molecules. These aggregated solute molecules strongly attract more like molecules until all solute molecules are adsorbed on the graphene surface as estimated by the enhanced sampling. The molecular origin of graphene exfoliation by MM is also described here. The present work helps to design novel kidney stone inhibitors.

■ INTRODUCTION

The study that concentrates on the mass processing, characterization, and real-world applications of ultra-thin carbon films, the thinnest of which is graphene (Figure 6b-1 (a) and (b)), is currently engulfing the world of materials research.[323] There have been more inquisitions about requisite strategies for transmitting small molecules of drugs/nucleotides/peptides to specific tissues in medicine. In this sense, many studies have used graphene to deliver chemotherapeutics for cancer treatment. In this way, for potential photothermal therapy, small-size graphene sheets demonstrate high near-infrared (NIR) light absorbance and biocompatibility.[324, 325, 326, 327, 328, 329, 330] However, our lack of perception of the basic principle of the interplay between biomolecules and carbon nanomaterials has become a challenge to the further production of biosensors based on carbon. The first two-dimensional (2D) crystal is known to be a single layer called "graphene". The π-π interactions can include the exfoliation (which is a promising method for producing graphene from graphite)[331, 332, 333, 334] of graphite and stabilizing graphene nanostructures. There are two prevalent conditions for π-π interactions. The first is the nature of π structures, and the second is related to the interacting species' geometry. The overlap must occur between the two components to have a noticeable interaction, and the planarity of the two components strongly favors this.[324, 335, 336, 337] The usefulness of graphene nanostructures as platforms for stabilizing and distributing organic molecules used as drugs in therapeutic protocols is an important application. Two critical conditions of graphene nanostructures are required for this specific role: a covalent or non-covalent interaction with organic molecules and the requisite hydrophilicity that facilitates the hybrid's dispersion in water or biological fluids. In certain situations, non-covalent interactions such as π-π stacking are advantageous concerning the molecules' immobilization. The release of molecules is much simpler to control than covalently bound molecules on the graphene surface.[324] Besides, there are many benefits to liquid-phase peeling techniques because stable graphene suspensions can be applied for different material processing steps, such as film deposition, surface modification, and chemical functionalization. Breaking the van der Waals-like forces between graphite layers demands the exfoliation of graphene into solution.[338, 339, 340, 341] Moreover, graphene layers tend to accumulate to re-establish the graphitic structure and reduce surface free energy. This can be avoided by covalent functionalization or non-covalent contact with stabilizers, such as surfactants, polymers, and aromatic molecules. The non-covalent interactions with graphene

is a fascinating topic.[342, 343, 344, 345, 346] Some researchers have lately insinuated an excellent method for obtaining high-quality graphene from graphite with melamine (MM, Figure 6b-1 (c)) as a non-covalent exfoliating agent. The exfoliated graphene layers can be separated into organic solvents (such as DMF) or aqueous solutions after ball-milling graphite and MM. MM can be washed out easily with water, leaving aqueous dispersions of stable graphene. It emerges from these experiments that MM plays a pivotal role in stabilizing graphene dispersion in water.[347, 348] Moreover, there are numerous experimental shreds of evidence where the adsorption of MM on graphene has been shown in detail. It has been demonstrated that MM can appear as a 2D supramolecular array on the surface.[349, 350, 351, 352, 353, 354, 355]

In human beings, purine bases are found, especially in the liver and kidney's inner organs. The degradation products of purine metabolism in human beings are xanthine (XA) and uric acid (UA, Figure 6b-1 (d)). Responsive measures of such disorders, including perinatal asphyxia, cerebral ischemia, hyperuricemia, gout, and a beneficial effect on the cardiovascular system, are their concentration levels. Therefore, accurate measurements of XA and UA are essential for food, biochemistry, and clinical diagnosis. A recent paper illustrated that it is conceivable to adsorb XA and UA molecules stably on graphene. Amidst these molecules and graphene, the π-π interaction emerges.[356, 357, 358] In this paper, the adsorption properties of MM, UA, TB (xanthine alkaloid), and AP (xanthine oxidase inhibitor) on a monolayer graphene surface are presented. Moreover, the exfoliation of graphene sheets in the presence of MM is also described. In earlier studies, it has been shown that MM and UA make an insoluble complex that causes kidney stones.[1, 207, 1, 45, 359] Chen *et al.* suggested that MM is tied to UA more strongly than cyanuric acid. They investigated these interactions using fluorescence quenching of MM and UA solutions of varying concentrations, demonstrating that hydrogen bonding and π-stacking are responsible for the complex's tight binding.[359] Now, crystal precipitates are kidney stones identified free or attached to renal papillae in the renal calyx and pelvis. Organic and crystalline segments produced by supersaturation of urine are included. On renal papillary facades, the most common type of kidney stone is formed. The stone's growth is achieved by aggregating preformed crystals or secondary crystal nucleation on the matrix-coated surface. Substances are inhibitors that reduce the initiation of supersaturation, nucleation, crystal expansion, rate of aggregation, or processes of stone-forming. Inhibitors may have

a beneficial effect on urinary conditions or behave obliquely by feuding with crystals.

There is, hence, an imperative mechanism for the development and preservation of the deposition of kidney stones and the adsorption to the crystal surface of antibodies.[67, 68, 69, 70] Thus, a detailed study of the adsorption nature of UA and MM-UA composite on a monolayer graphene surface would be beneficial to undestand the molecular nature of kidney stones developed in humans. Theobromine (TB, Figure 6b-1 (e)) and allopurinol (AP, Figure 6b-1 (f)) are applied to the MM-UA mixture on the graphene surface to verify their inhibitory effect on kidney stones. It has been reported that TB could inhibit UA crystallization.[203] TB is the first natural product classified to inhibit the crystallization of UA. It has the potential to be used in the treatment of renal stone formation. Furthermore, TB is excreted in urine at concentrations comparable to those required to prevent UA crystallization.[256, 257, 56] A similar outcome is also recommended by a theoretical study where TB inhibits UA aggregation and hinders MM-UA cluster formation.[282] Again, AP serves as a potent inhibitor against UA nephrolithiasis. Moreover, AP can decrease UA production. Furthermore, AP is efficient in regulating serum and urinary UA. Therapy is based on urinary alkalinization of individuals exposed to UA stones. AP is administered to people with hyperuricemia because of the lack of UA inhibitors. Experimental studies show the reduction in new stone formation by chronic AP administration significantly. AP decreases the urinary content of undissociated UA, hence rapidly altering the diseases pathogenetic pathways.[51, 52, 53] Therefore, the present study elaborately describes the nature of kidney stones in the presence and absence of inhibitors in a surface's appearance, impersonating kidney stone precipitation's exact nature. Not only that, from this study, one can estimate the effectiveness of an inhibitor against kidney infection. Moreover, this is the first theoretical study in which MM and UA's adsorption is presented in detail via molecular dynamics simulation. It also explores the mechanism of self-assembly of conjugate MM and UA. To determine the thermodynamic preference of 2D lattice formation, detailed free energy calculations are conducted. It is shown that the impact of surface size has a moderate effect on the assembly process.

The following provision is rendered for the rest of the paper. Part II describes the materials and methods used for MM, UA, TB, AP, graphene, and water molecules. The results are addressed in Section III. Section IV summarises our findings.

■ MATERIALS AND METHODS

The underlying mechanisms of MM, UA, TB, and AP assembly on a monolayer graphene surface are studied throughout this study. MM (Figure 6b-1 (c)) is an N-heterocycle that

contains 67% nitrogen by mass. Moreover, due to its structural features, it can form extended hydrogen-bonded supramolecular array with like molecules.[360, 361, 362] UA (Figure 6b-1 (d)) is a heterocyclic organic compound composed of nitrogen, carbon, oxygen and hydrogen with a chemical formula C5H4N4O3 (7,9-dihydro-1H-purine-2,6,8(3H)-trione). The solubility of UA in water is low, and in humans, the average concentration of UA in blood is close to the solubility limit (6.8 mg/dL). When the level of UA is higher than 6.8 mg/dL, crystals of UA form. Crystalline UA deposited under low-pH conditions typically exists either in an anhydrous phase (UA) or as a dihydrate (UAD).[363, 364] The strucral features of crystalline UA can be found elsewhere.[363] TB (Figure 6b-1 (e)) is a dimethylxanthine having two methyl groups. A purine alkaloid derived from the cacao plant is found in chocolate and several other foods and is a vasodilator, diuretic, and heart stimulator.[203] It has been reported that TB may be considered as a candidate for the treatment of COVID-19.[365] AP (1,5-dihydro-4H-pyrazolo[3,4-d]pyrimidin-4-one, Figure 6b-1 (f)) is a structural isomer of hypoxanthine. AP inhibits xanthine oxidase, an enzyme that converts oxypurines to UA. By blocking the production of UA, this agent decreases serum and urine concentrations of UA.[366]

A series of atomistic classical molecular dynamics (MD) simulations is carried out to present the adsorption properties of various small molecules like MM, UA, TB, and AP over a monolayer graphene surface in the presence of water molecules. Firstly, the geometries of these solute molecules (i.e., MM, UA, TB, and AP) were optimized with the help of Gaussian 09[138] utilizing HF/6-31+G** basis set. After that, the charges of solute molecules were produced with the RESP module[140] of AMBER14[226]. The allocation of force field parameters for all atomic sites was accomplished using the general AMBER force field (GAFF)[142] of the ANTECHAMBER[141] suite of AMBER14. The TIP3P water model[143, 367] was utilized. In order to study the self-assembly of small molecules on the graphene surface, two types of hydrogen-terminated graphene monolayers with a dimension of 2.5 nm $\times$ 2.0 nm and 6.0 nm $\times$ 6.0 nm in the XY plane were built by VMD[149], and they are positioned at the centre of a simulation box. Periodic boundary conditions were applied in all three directions so that the periodic images do not overlap. All atomic sites of the non-charged graphene surface were allocated with the general AMBER force field (GAFF)[142] and OPLS-AA[368] force fields. Several reports show the use of GAFF and OPLS-AA force field parameters with the compatible TIP3P water model.[369, 370, 371, 372, 373, 374, 375] In this study, numerous systems were prepared, and these are presented in Table

6b-1. With the PACKMOL package[144], the beginning configurations for each of the simulated systems were prepared. All the simulations were performed at 300 K of temperature and 1 atm pressure using the AMBER14 package.

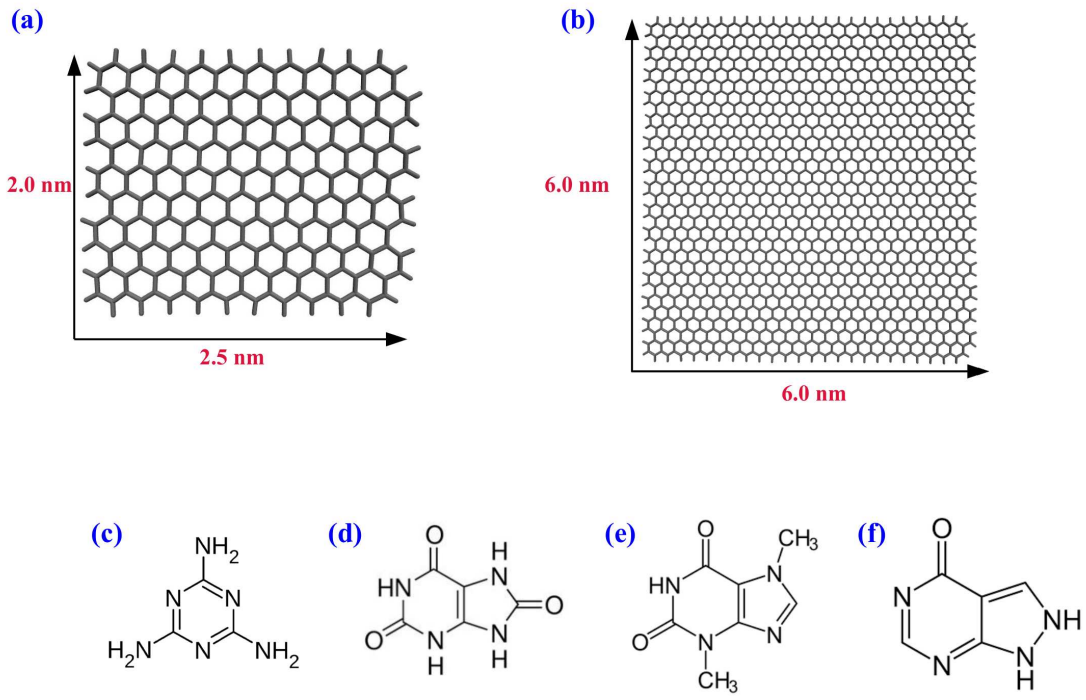

Figure 6b-1. *The chemical structure of (a) small graphene sheet, (b) big graphene sheet, (c) melamine (MM), (d) uric acid (UA), (e) theobromine (TB), and (f) allopurinol (AP).*

All molecules were put in a cubic simulation box on arbitrary initial positions, and periodic boundary conditions were also introduced in all three directions. Energy minimization was done for 10000 steps (out of which 4000 steps of steepest descent method followed by 6000 steps of conjugate gradient method). Initially, the energy minimized structures' temperature was increased gradually from 0 K to 300 K in a canonical ensemble (NVT). The systems were then equilibrated for 5 ns at 300 K temperature and 1 atm pressure in an isothermal-isobaric (NPT) ensemble. The simulations were then extended further for 100 ns production runs in NVT ensemble with temperature and pressure were maintained at 300 K and 1 atm, respectively. With a pressure relaxation time of 2 ps, Berendsen barostat[146] was used to control all the systems' pressures. The simulation temperature was regulated by

using the Langevin dynamics[145] method with a collision frequency of 1 ps^{-1}. The SHAKE algorithm[148] was used to constrain all covalent bonds involving hydrogen atoms, and also the simulation time step of 2 fs was used for all the simulations. All MD simulations were run with a 12 Å cutoff to calculate all short-ranged nonbonding interactions. The particle mesh Ewald (PME) method[147] was utilized for adequate treatment of long-ranged nonbonding electrostatic interactions. The trajectories of the MD simulation were analyzed via the CPPTRAJ module built-in AMBER.[376]

A particular form of simulation is also considered to investigate the exfoliation of graphene nanosheets in the presence of MM molecules. Initially, two hydrogen-terminated non-charged graphene monolayers with a dimension of 2.5 nm × 2.0 nm were placed at a separation of 1 nm, and 40 MM molecules are placed randomly using PACKMOL. Then, following the previous protocols, simulations were extended further for 60 ns production runs in the NVT ensemble with the temperature and pressure maintained at 300 K and 1 atm where these two graphene sheets were harmonically constrained with force constant of 100 kcal/mol/Å so that MM molecules can intercalate in between the graphene sheets. After that, further 440 ns production runs in NVT ensemble were performed at 300 K; where one graphene sheet could travel easily when the other was harmonically restricted with constant force of 100 kcal/mol/Å. For this simulation, the nonbonded interactions were calculated, setting a cutoff distance of 12 Å. A similar graphene exfoliation is also performed considering the big graphene sheets (with a dimension of 6.0 nm × 6.0 nm) with 100 MM molecules. The graphene bilayer simulations are conducted with a vertical separation of 1 nm between the two layers to obtain a better understanding of the position of MM molecules in exfoliation phase. The interlayer binding of graphene is decreased by the molecular level, and MM molecules will intercalate between the layers. This distance reproducing the molecular state is necessary. One graphene layer has been set while the other layer is free to switch. Although it is preferable to understand the results of several layers of graphene sheets, the greater system size makes exfoliation at reasonable time scales appealing. Therefore, we use the two-layer graphene nanosheet concept, which is considered the static graphene layer, to be a multilayer model's terminal sheet. In the literature, such a technique was previously tested.[377, 378]

Table 6b-1. System overview[a]

System	N_{MM}	N_{UA}	N_{TB}	N_{AP}	N_{wat}	Box length (Å)	Force field
M15G1	15	–	–	–	10000	67.597	GAFF
M75G2	75	–	–	–	10000	68.943	GAFF
M1G1	1	–	–	–	3000	45.498	GAFF
M10G1	10	–	–	–	3000	45.594	GAFF
M15G1-a	15	–	–	–	10000	67.544	OPLS-AA
M75G2-a	75	–	–	–	10000	69.004	OPLS-AA
M1G1-a	1	–	–	–	3000	45.425	OPLS-AA
M10G1-a	10	–	–	–	3000	45.574	OPLS-AA
M40G12	40	–	–	–	10000	67.900	GAFF
M40G12-a	40	–	–	–	10000	67.937	OPLS-AA
M100G22	100	–	–	–	10000	70.316	GAFF
M100G22-a	100	–	–	–	10000	70.363	OPLS-AA
M0G14	–	–	–	–	20000	85.179	GAFF
M200G14	200	–	–	–	20000	86.102	GAFF
M0G14-a	–	–	–	–	20000	85.207	OPLS-AA
M200G14-a	200	–	–	–	20000	86.064	OPLS-AA
U75G2	–	75	–	–	10000	69.133	GAFF
U1G1	–	1	–	–	3000	45.470	GAFF
U10G1	–	10	–	–	3000	45.658	GAFF
U75G2-a	–	75	–	–	10000	69.183	OPLS-AA
U1G1-a	–	1	–	–	3000	45.474	OPLS-AA
U10G1-a	–	10	–	–	3000	45.660	OPLS-AA
T0	30	30	–	–	10000	68.812	GAFF
T15	30	30	15	–	10000	69.181	GAFF
T40	30	30	40	–	10000	69.448	GAFF
T0-a	30	30	–	–	10000	68.989	OPLS-AA
T15-a	30	30	15	–	10000	69.204	OPLS-AA
T40-a	30	30	40	–	10000	69.459	OPLS-AA
U2T1G1	–	2	1	–	3000	45.950	GAFF
U2T1G1-a	–	2	1	–	3000	46.012	OPLS-AA
A15	30	30	–	15	10000	69.074	GAFF
A40	30	30	–	40	10000	69.228	GAFF
A15-a	30	30	–	15	10000	69.151	OPLS-AA
A40-a	30	30	–	40	10000	69.305	OPLS-AA
U2A1G1	–	2	–	1	3000	45.873	GAFF
U2A1G1-a	–	2	–	1	3000	45.837	OPLS-AA

[a] N_{MM}, N_{UA}, N_{TB}, N_{AP}, and N_{wat} refer to the number of melamine, uric acid, theobromine, allopurinol, and water molecules, respectively. G1 represents the systems comprised of a small graphene sheet, and G2 refers to the systems consisting of a large graphene sheet. G12 and G22 represent two small and big graphene sheets present in the respective systems. G14 represents four small graphene sheets present in the respective systems.

For estimating the potentials of mean forces (PMFs)[228], the umbrella sampling (US) approach is applied. For these biased simulations, a harmonic restraint force of 1 kcal/mol/Å^2 force constant is assumed. The first separation is 2 Å, and this distance is extended by taking one molecule from another by 1 Å in each step up to 20 Å. For this, we have considered several systems. For these systems, for an initial US process setup, final standard MD simulation trajectories are used. Each model is subjected to 4000 steps minimization

(1000 steps from the steepest descent method and the remaining 3000 steps from the conjugate gradient method), and equilibration of 1 ns is obtained for any US-based simulation, in the same way as the standard MD simulation (discussed earlier). Every window has a production run of 10 ns. In reality, we have generated 190 ns trajectories for each system in the US process. Simulation data is obtained at a 2 fs time interval. Using the Weighted Histogram Analysis Method (WHAM)[229, 230], the US simulations' results are eventually estimated.

The first shell coordination number (CN) provides an assessment of the accumulated number of molecules of a given species (say b-type) in the shell from 0 to a distance r_{cut}, around a reference atom (say a-type). Therefore, CN can be defined as follows:[240, 241, 242, 280]

$$CN = 4\pi\rho_b \int_0^{r_{cut}} r^2 g_{ab}(r) dr, \tag{6.14}$$

Here, ρ_b is the number density of the atom type b. First shell CNs are calculated from the distance cut off at first minimum (r_{cut}) using specific radial distribution functions, considering the center of mass (COM) of those molecules in the form of interactions between the respective pairs.

The dimer existence autocorrelation function (DACF) is evaluated by the use of the following equations:[158]

$$DACF(\tau) = N. < \sum_{t=0}^{T-\tau} \beta_{ij}(t+\tau).\beta_{ij}(t) >_{ij} \tag{6.15}$$

Here, DACF is considered as autocorrelation of a simple function, β_{ij}, for the pair of molecules say, i and j, that can have value 1 when maintaining a preset distance criterion, and it goes to zero if the distance criterion is lost for the first time.[158] It is worth noting that, even if the criterion of distance is met later, DACF will remain zero. Here, the distance criterion is set according to the first minimum distance cut off (r_{cut}) using specific radial distribution functions, considering the center of mass (COM) of those molecules in the form of interactions between the respective pairs.

The free energy landscape (FEL) is determined by using the following equation:[253]

$$\Delta G(V) = -k_B T[\ln P(V) - \ln P_{max}], \tag{6.16}$$

where P(V) portrays the probability of coordinate (V) calculated from the last 20 ns trajectory path, and it is deducted by P_{max}, which is the maximal distribution such that ΔG gives us the minimum free energy.

In the current study, the preferential interaction parameters, τ_{ut}^{u} (UA-UA over UA-TB), τ_{tu}^{t} (TB-TB over TB-UA), τ_{ua}^{u} (UA-UA over UA-AP) and τ_{au}^{a} (AP-AP over AP-UA), are determined, and these are generated for respective systems following the equations mentioned below:[285, 194, 195, 196, 179, 286, 282]

$$\tau_{ut}^{u} = \rho_u(G_{uu} - G_{ut}) \tag{6.17}$$

$$\tau_{tu}^{t} = \rho_t(G_{tt} - G_{tu}) \tag{6.18}$$

$$\tau_{ua}^{u} = \rho_u(G_{uu} - G_{ua}) \tag{6.19}$$

$$\tau_{au}^{a} = \rho_a(G_{aa} - G_{au}) \tag{6.20}$$

where t, a, and u denote TB, AP, and UA molecules,respectively; and ρ_u, ρ_t, and ρ_a represent the number densities of UA, TB, and AP molecules, respectively. The preferable interaction between any two molecules (say i and j) can be indicated with the higher positive value of τ than any other interactions. Here, G_{ut}, G_{tt}, G_{tu}, G_{ua}, G_{uu}, G_{aa}, and G_{au} correspond to Kirkwood–Buff (KB) integrals, and these integrals can be accessed following earlier studies.[285, 194, 195, 196, 179, 286, 282] It ought to be referenced that these integrals can be accomplished with the accompanying radial distribution functions. The center of masses (COMs) of any two molecules are considered for appraising these distribution functions.

The reduced density gradient (RDG) is typical for the study of weak associations. Therefore, we have used RDG and its colorful variant to analyze how numerous solute molecules interact with the graphene surface. To do so, optimized structures are attained from the theory level M06-2X/6-31G+(d,p) with the default isosurface value of 0.5 and the default color scale from 0.035 to 0.02 and we have drawn the scattered maps (i.e., color-filled isosurface graphs). Note that, instead of graphene, a coronene is employed as a small graphene sheet to save the computational time cost. Coronene, C24H12, is a D6h symmetric polycyclic compound consisting of one central and six adjacent C6 rings. Coronene maps on the base planes of graphite and graphene can be used as a finite model for 2D extended structural carbon allotropes.[379]RDG assessment is conducted using tools from Multiwfn.[165, 164]

To determine the average number of hydrogen-bonds formed by different solution species, a series of criterion is used to describe the hydrogen bonds between the donor (D) and acceptor (A).[253, 282, 288, 289, 290] If the distance D-A $\leqslant$ 3.5 and, simultaneously, angle

$\angle$ D-H$\cdots$ A $\geqslant 120^{\circ}$ are fulfilled, hydrogen bonding is then considered to be present.

■ RESULTS AND DISCUSSION

■ MM ON A MONOLAYER GRAPHENE SURFACE

■ Adsorption of MM on a monolayer graphene surface

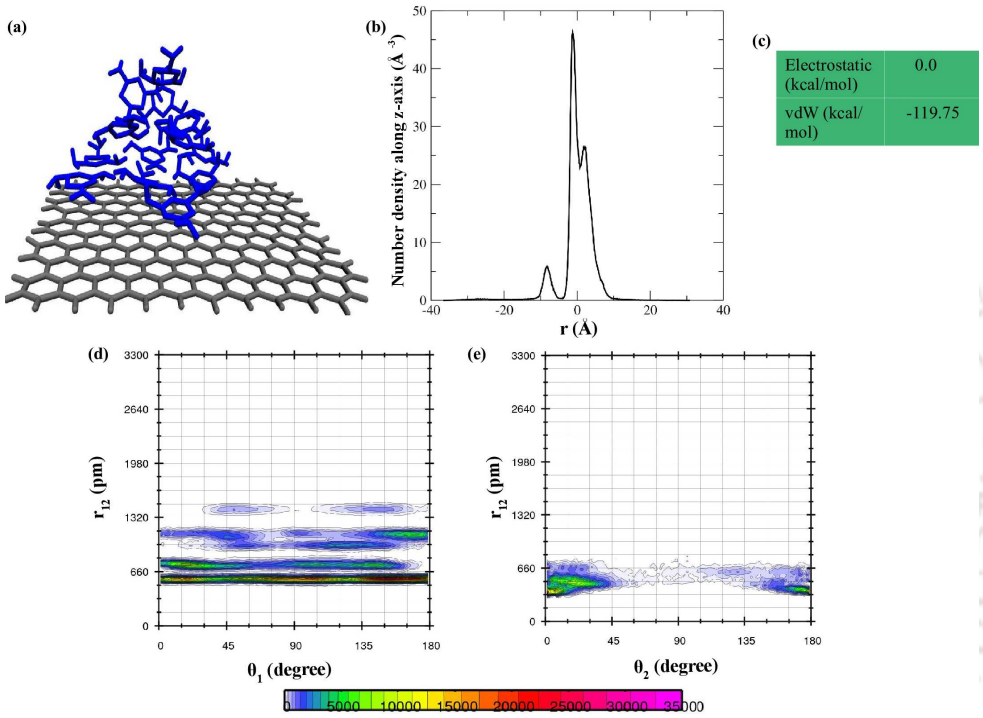

Figure 6b-2. *(a) In system M15G1, 13 out of 15 MM molecules are adsorbed on the graphene surface. Again, 7 MM molecules are adsorbed in the first layer of graphene. The remaining molecules are adsorbed over the first layer. Here, two molecules can form a dimer over the graphene surface during the cluster structure analysis only when they are attached by either hydrogen bonding or π- stacking interactions. The first layer of graphene surface is considered as a surface that at 4 Å of distance from that monolayer graphene surface, (b) the number density of MM molecules over the graphene along the z-direction in system M15G1, (c) the decomposition of total energy into its two components (i.e., electrostatic and vdW energies). The energy is expressed in kcal/mol unit, (d) the distribution of orientational angle (θ_1) between two MM molecules considering two-point vectors (i.e., the vector connected by a donor (D), hydrogen (H), and acceptor (A) atoms of these two molecules) to describe the hydrogen bonding phenomenon, and (e) the angle between two vector normals (θ_2) between two aromatic rings is shown to present the π-stacking. Here, r_{12} refers to the center of mass (COM)- center of mass (COM) distance between the individual molecules.*

In recent experimental works, it has been revealed that MM molecules can be adsorbed on a graphene sheet composing a 2D structure, and these MM molecules are associated with each other by hydrogen bonding networks.[347, 348] In the present work, we have also proposed wherewith MM molecules are adsorbed over a monolayer graphene surface in the presence of water molecules. In system M15G1, 13 out of 15 MM molecules are adsorbed on the graphene surface (Figure 6b-2 (a)). Again, 7 MM molecules are adsorbed in the first graphene layer (Figure 6b-2 (a)). The remaining molecules are adsorbed over the first layer. This distribution can be observed by determining the number density of these molecules over the graphene along the z-direction (Figure 6b-2 (b)). Furthermore, these MM molecules possess a strong van der Waals interaction energy with the graphene surface (Figure 6b-2 (c)). Here, MM molecules are attached by hydrogen bonding (which is assumed to be formed when the angle between vectors connected among donor (D), hydrogen (H), and acceptor (A) atoms of two interacting molecules lies 135° to 180°) as well as π-stacking (which is supposed to be formed when the angle between vector normals of two interacting aromatic rings lies either 0° to 20° or 160° to 180°[161]) interactions (Figure 6b-2 (d) and (e)). The total number of hydrogen bonds formed by MM molecules over the graphene surface is 44.83.

■ **Impact of the size of monolayer graphene surface on the adsorption of MM**

(a)

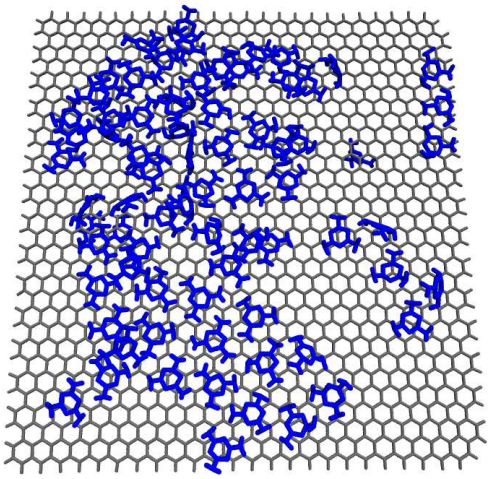

(b)

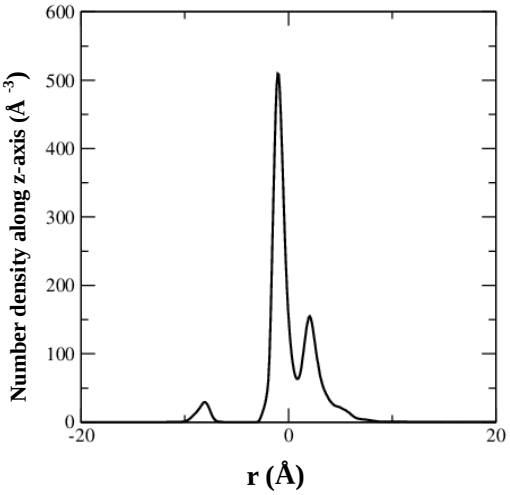

(c)

Electrostatic (kcal/mol)	0.0
vdW (kcal/mol)	-240.88

Figure 6b-3. *(a) In system M75G2, 53 MM molecules are adsorbed in the first layer of graphene, whereas 72 out of 75 MM molecules are adsorbed in all layers in total. Here, during the cluster structure analysis, two molecules can form a dimer over the graphene surface only when they are attached by either hydrogen bonding or π- stacking interactions. The first layer of graphene surface is considered a surface at 4 Å of distance from that monolayer graphene surface, (b) the number density of MM molecules over the graphene along the z-direction in system M75G2, and (c) the decomposition of total energy into its two components (i.e., electrostatic and vdW energies). The energy is expressed in kcal/mol unit.*

A similar system, i.e., system M75G2, is prepared where 75 MM molecules are initially distributed randomly over a graphene surface with a large surface area. It is perceived that 53 MM molecules are adsorbed in the first layer of graphene, whereas 72 out of 75 MM molecules are adsorbed in all layers in total (Figure 6b-3 (a)). The number density calculation provides the distribution of all adsorbed MM molecules along the z-direction (Figure 6b-3 (b)). Moreover, as like system M15G1, hydrogen bonding and π-stacking interaction can be regarded during their adsorption over the graphene surface in system M75G2 (not shown). The MM molecules adsorbed in the first layer make a strong van der

Waals (vdW) interaction with the graphene surface (Figure 6b-3 (c)). Therefore, there is no change in MM molecules' adsorption with a shift in the graphene surface size. The more is the surface area of the graphene, the more molecules are adsorbed.

■ Pattern of adsorption of MM on a monolayer graphene surface

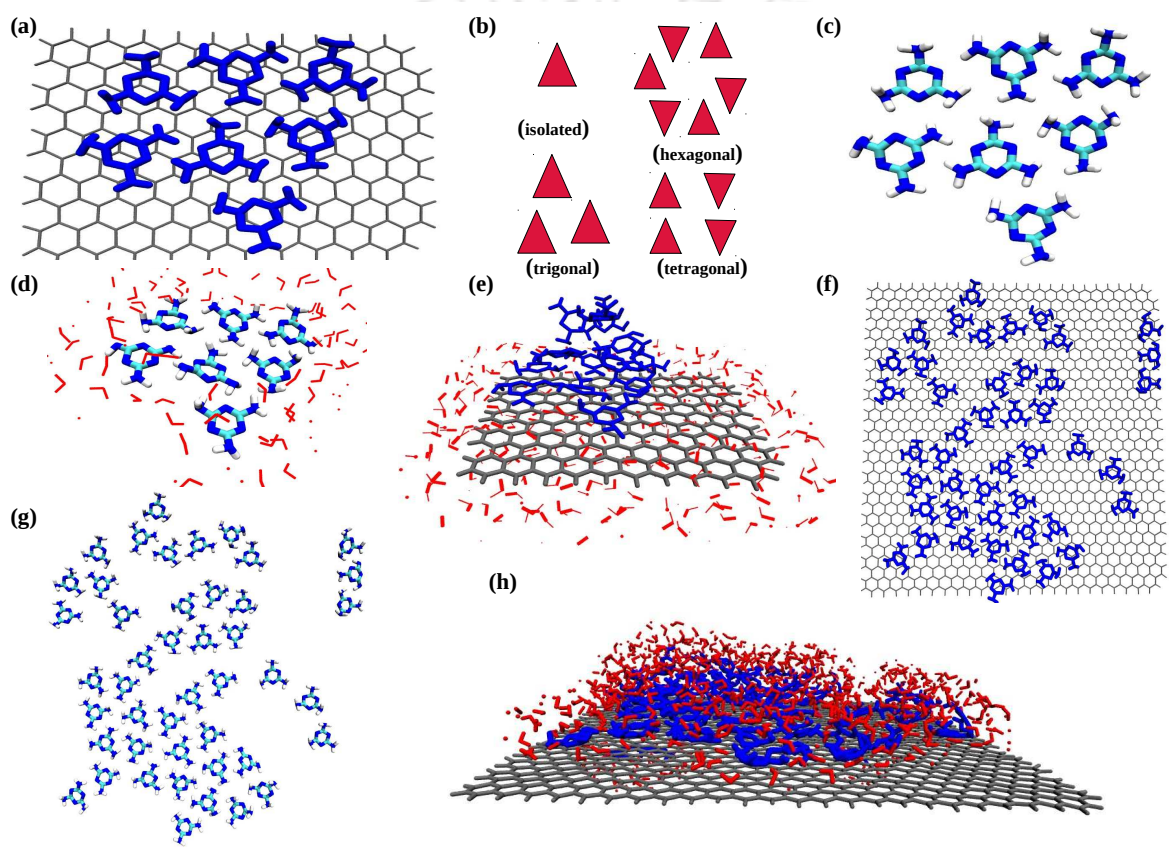

Figure 6b-4. *(a) The first layer of adsorption by MM molecules over a monolayer graphene surface in system M15G1, (b) during the adsorption of MM molecules over a single layer graphene surface, they can form various patterns (i.e., single-molecule adsorption, trigonal, hexagonal, and tetragonal patterns with the increase of surface area coverage) to form large 2D supermolecular shape, (c) hydrogen-bonded MM molecules over the graphene surface in system M15G1, (d)-(e) surface adsorbed water molecules surround MM molecules within 3.5 Å from MM and 5 Å from the graphene surface in system M15G1, (f)-(g) in system M75G2, in the first layer of adsorption by MM molecules and it can be seen that the surface coverage is not extensive as MM molecules are associated with water molecules, and (h) surrounding water molecules over and around the graphene and MM molecules in system M75G2.*

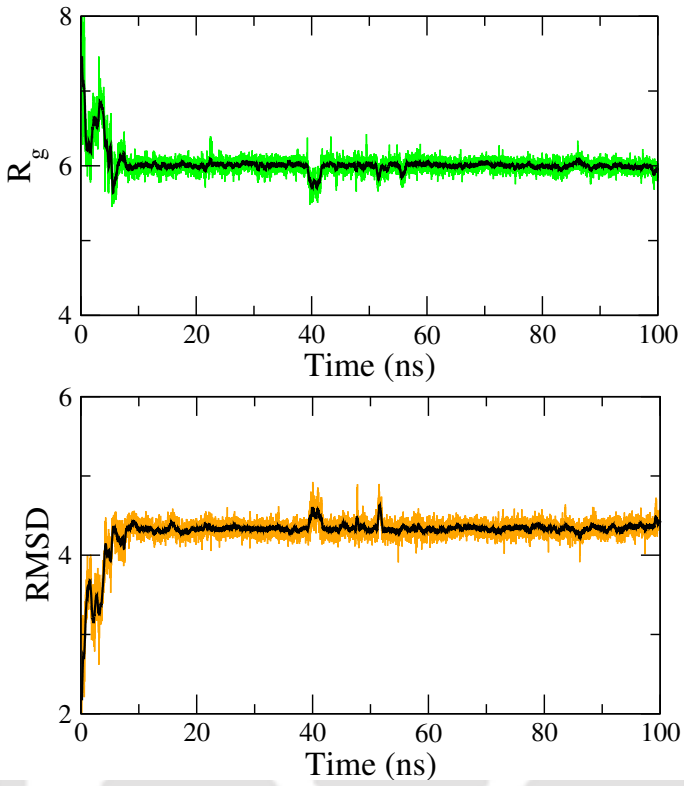

Figure 6b-5. *The radius of gyration (R_g (Å), upper panel) and root means square deviation (RMSD (Å), lower panel) of MM molecules adsorbed in the first layer for system M75G2.*

During the adsorption of MM on a monolayer graphene surface, they are involved in hydrogen bonding and π-stacking interactions with each other, as mentioned earlier. Now, if we look into the first layer of adsorption frugally, it can be seen that MM molecules form a pattern in system M15G1 (Figure 6b-4 (a)). The surface adsorption experiment findings have illustrated that MM can create several 2D supermolecular shapes (Figure 6b-4 (b)).[355] Though extensive surface coverage by MM molecules cannot be observed due to the presence of water molecules, however, the pattern of adsorption is similar (Figure 6b-4 (c)-(e)). In system M75G2, in the first layer of graphene surface, a similar structure by MM molecules can be seen with no definitive extensive surface coverage (Figure 6b-4 (f)-(h)). Moreover, the determination of the radius of gyration (R_g) and root means square deviation (RMSD) of adsorbed MM molecules (in the first layer) shows that the MM molecules promptly arrange themselves over the graphene surface (Figure 6b-5). Thus, it can be concluded that the aggregation tendency of MM molecules over a graphene surface

is high as the cluster size made of adsorbed MM molecules becomes large. However, a definitive compact surface coverage made by MM molecules is not found over the graphene surface in the presence of water molecules (Figure 6b-4 (h)).

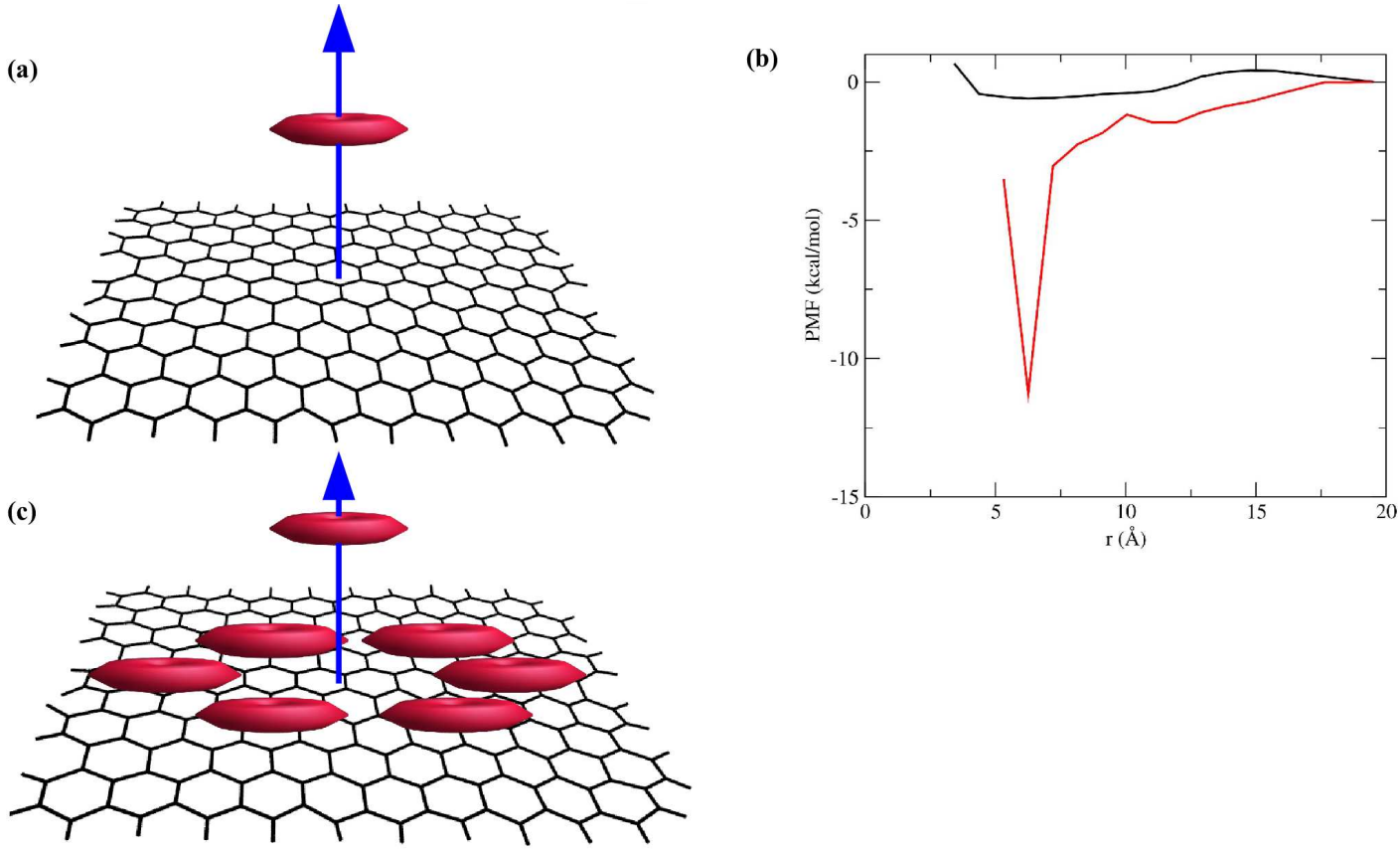

Figure 6b-6. *(a) Schematic representation of umbrella sampling where one MM molecule is pulled up from a monolayer graphene surface, (b) potentials of mean forces for systems M1G1 (black) and M10G1 (red), and (c) schematic representation of umbrella sampling where one MM molecule is pulled up from an aggregated MM molecules on a monolayer graphene surface.*

■ Aggregation tendency of MM on a monolayer graphene surface employing enhanced sampling

 We have considered two more systems, i.e., M1G1 and M10G1, to study MM

molecules' aggregation tendency over graphene. Firstly, we have performed umbrella sampling to calculate potential of mean forces (PMFs) between one MM and graphene surface in system M1G1 (Figure 6b-6 (a)). It is seen that the interaction between the MM and graphene surface is quite strong and energetically favorable (Figure 6b-6 (b)). However, once MM molecules are adsorbed over the graphene surface, these aggregated MM molecules attract other MM molecules more strongly towards them to be adsorbed on the graphene surface (Figure 6b-6 (c)). For system M10G1, it is evident that the previously adsorbed 9 MM molecules that attract the 10th MM molecules towards themselves to be adsorbed on the surface. Therefore, the potential of mean force becomes energetically more favorable compared to system M1G1 (Figure 6b-6 (b)). Thus, the aggregation of MM over graphene surface is 'spontaneous'.

■ Comparison of GAFF and OPLS-AA force field parameters regarding the adsorption of MM on a monolayer graphene surface

The aggregation and adsorption properties of MM molecules over a graphene surface are compared using two different force-field parameters (i.e., GAFF and OPLS-AA). Therefore, two systems, M15G1 and M75G2 (with GAFF force field parameters), are compared with the other two systems M15G1-a and M75G2-a (with OPLS-AA force field parameters). It is found that the number of adsorbed MM molecules over the graphene surface is almost similar. In M15G1-a system, 7 MM molecules are adsorbed at the first layer of graphene while a total of 11 MM molecules are attached with the graphene surface in all layers (Figure Sb-7 (a)). Moreover, in system M15G1-a, MM molecules also produce a strong vdW interaction with the graphene surface (Figure 6b-7 (b)). Like system M15G1, in M15G1-a also, no definite extensive assembly over the graphene surface is formed (Figure 6b-7 (c)-(d)). In systems M75G2 and M75G2-a, an equivalent number of adsorbed MM molecules can be found over the graphene surface (Figure 6b-7 (e)). Moreover, the composition and the pattern of adsorption of the adsorbed MM molecules are also same in these two systems (Figure 6b-7 (f)-(g)). Hereabouts, even a strong vdW interaction can be found for both systems (Figure 6b-7 (h)). Conceding two systems M1G1-a and M10G1-a, an umbrella sampling is performed using the OPLS-AA force field parameters. It is seen that the MM molecule confers a fancied interaction with the graphene sheet in system M1G1-a (Figure 6b-8). Hence, MM molecules aggregate over the graphene surface to accommodate more MM molecules (Figure 6b-8) to form a self-assembled MM cluster in system M10G1-a.

Thus, the results obtained from OPLS-AA and GAFF force field parameters quite resemble each other.

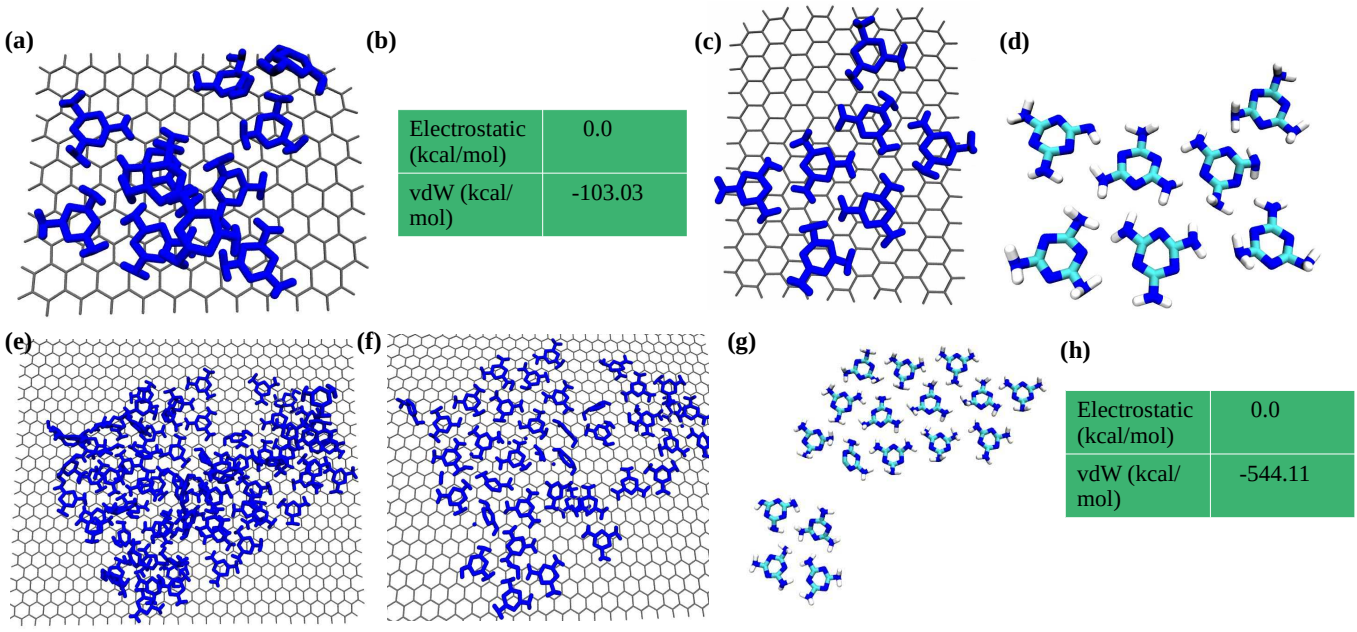

Electrostatic (kcal/mol)	0.0
vdW (kcal/ mol)	-103.03

Electrostatic (kcal/mol)	0.0
vdW (kcal/ mol)	-544.11

Figure 6b-7. *(a) 7 MM molecules are adsorbed at the first layer of graphene. In comparison, a total of 11 MM molecules are attached with the graphene surface in all layers in system M15G1-a, (b) MM molecules produce a strong vdW interaction with the graphene surface, (c)-(d) In the unit cell pattern, here in system M15G1-a, a similar way with no definite large assembly over the graphene surface is formed as like system M15G1, (e) Like the M75G2 system, in system M75G2-a, an equivalent number of adsorbed MM molecules over the graphene surface can be found, (f)-(g) the composition of the adsorbed MM molecules in the first layer and their adsorption pattern in system M75G2-a, and (h) the decomposition of total energy into its two components in system M75G2-a (i.e., electrostatic and vdW energies). The energy is expressed in kcal/mol unit.*

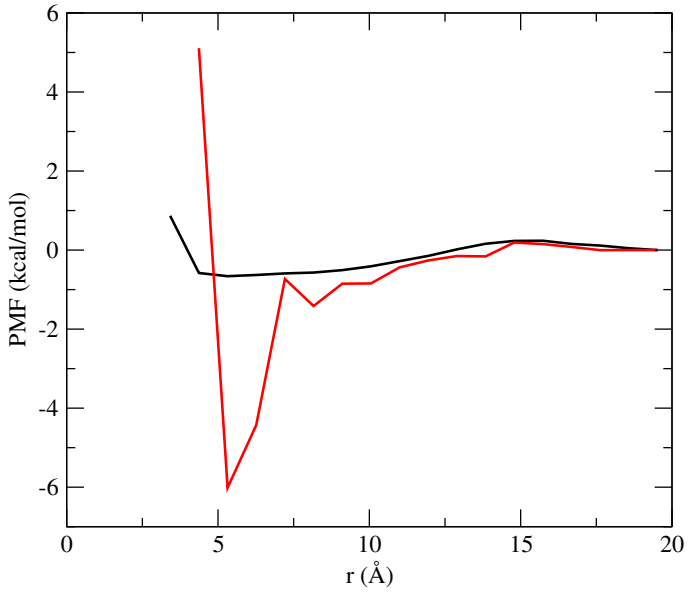

Figure 6b-8. *The potentials of mean forces for systems M1G1-a (black) and M10G1-a (red).*

■ Quantum calculation for the adsorption of MM on coronene

Next, we want to look at the forms of non-bonded interactions that render the stable MM-graphene complexes. To do so, a noncovalent interaction-reduced density gradient (NCI-RDG) technique[165, 164] is applied. The strong repulsive non-bonded steric interaction is observed in the red, and attractive interactions like the hydrogen bonding and van der Waals are blue and green. Figure 6b-9 indicates the weak non-bonded interaction isosurface and 2D plot for the MM-coronene system. Repelling (red) interactions in each system are not attributable to intermolecular MM and coronene-steric interactions. However, the steric repulsion comes from individual intramolecular steric repulsions present in MM and coronene. The vital stabilizing variables in these MM-coronene complexes are vdW and hydrogen-bonding interactions. The vdW interaction is the pioneer in the stabilization of these adsorbed MM molecules (Figure 6b-9 (a)-(c)). Even hydrogen bonding among the MM molecules is a stabilizing factor to form a self-assembled 2D structure (Figure 6b-9 (d)-

(f)) over the surface. However, owing to significant vdW interaction, π-stacking between two MM molecules is also plausible (Figure 6b-9 (g)-(i)).

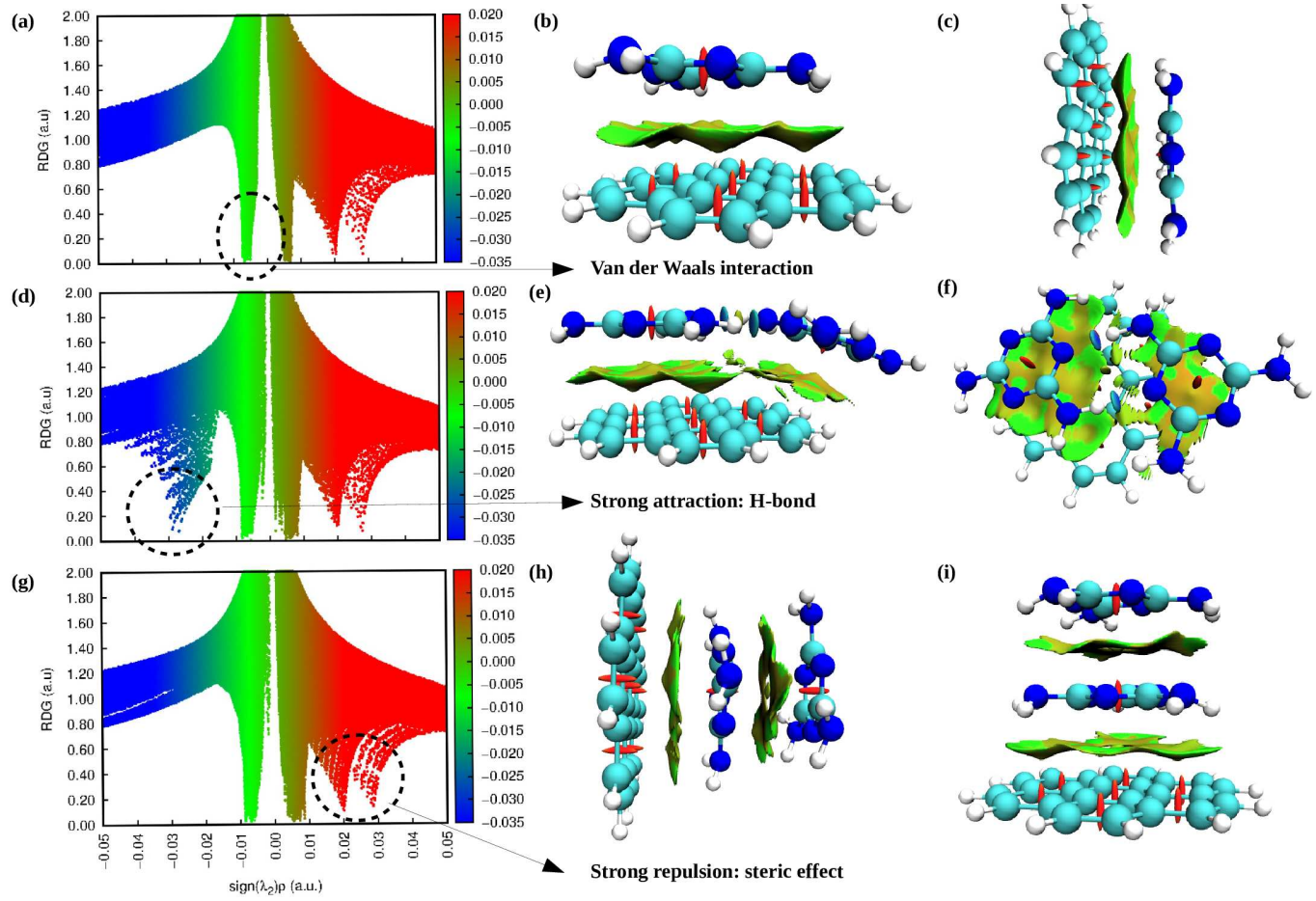

Figure 6b-9. *Color-filled RDG isosurface reciprocates noncovalent interaction (NCI) regions for various interactions between MM and coronene system. (a)-(c) A single MM molecule is adsorbed over a coronene surface, (d)-(f) two hydrogen-bonded MM molecules are adsorbed over a coronene surface, and (g)-(i) two π-stacked MM molecules are adsorbed over a coronene surface. The vertical axis of these plots (a, d, and g) are the reduced density gradient (RDG), and the horizontal axis is the sign of the second largest eigenvalue of the electron density Hessian matrix at position r (sign($\lambda_2(\rho)$). Here, the strong repulsive non-bonded steric interaction is observed in the red, and attractive interactions like the hydrogen bonding and van der Waals are blue and green.*

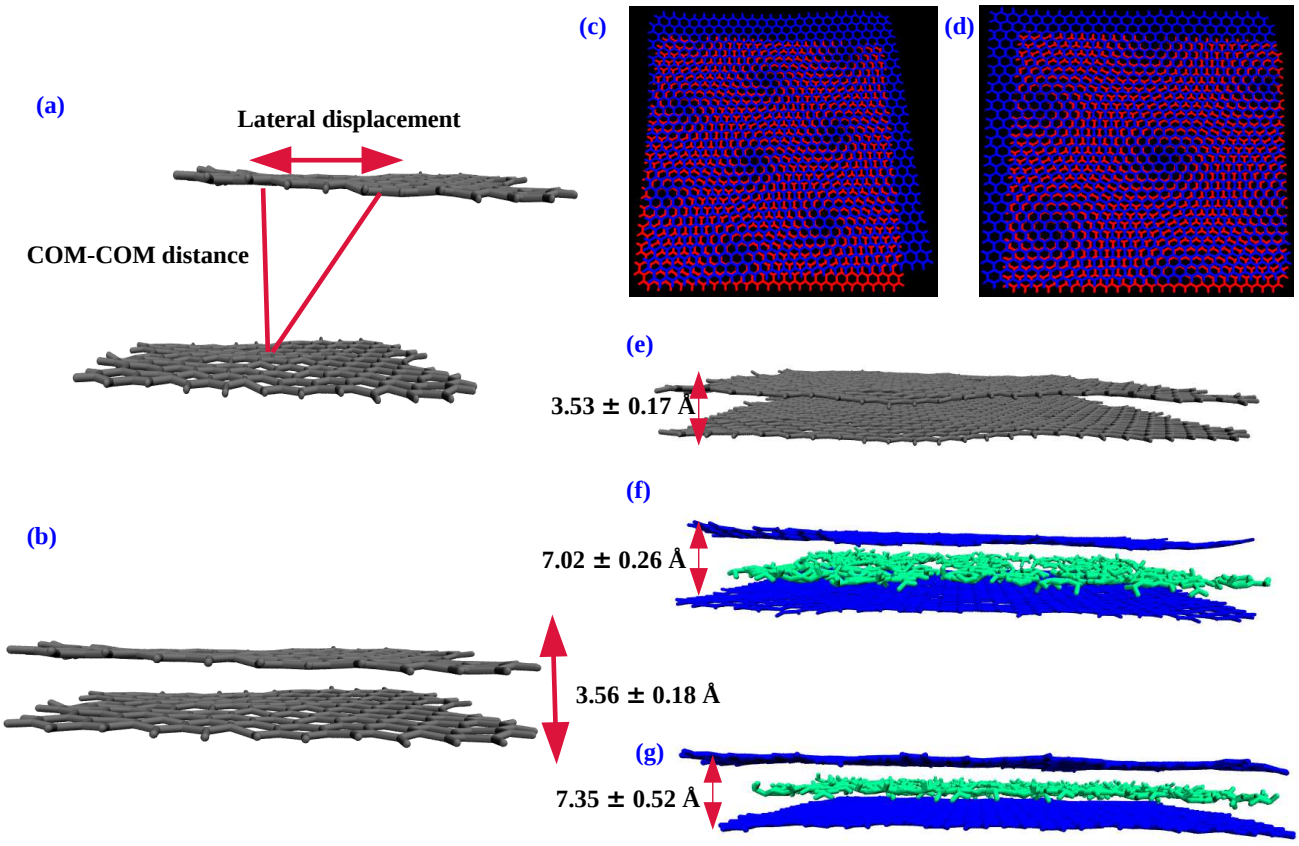

Figure 6b-10. *(a) Schematic representation of lateral displacement in the xy direction of graphene flakes, (b) equilibrium gas phase seperation between two graphene sheets using GAFF parameters, (c) laternal displacement of graphene sheets in system M100G22, (d) laternal displacement of graphene sheets in system M100G22-a, (e) equilibrium gas phase seperation between two big graphene sheets using GAFF parameters, (f) perpendicular displacement of graphene sheets in the presence of MM molecules (green) in system M100G22, and (g) perpendicular displacement of graphene sheets in the presence of MM molecules (green) in system M100G22-a. Here, the equilibrium gas phase seperation between two graphene sheets using OPLS-AA parameters is not presented in the figure.*

Recent experimental studies showed that the adsorption of MM on a graphene surface can cause exfoliation of graphene sheets.[347, 348] In the present study, we have studied the efficacy of MM molecules to induce the exfoliation of graphene sheets. Therefore two systems are prepared, i.e., system M40G12 (which is built by a GAFF force field parameters), and the other one is system M40G12-a (which is produced using OPLS force field parameters). It is seen that a lateral displacement of the graphene sheet (in the xy direction) of about 1.28 ± 0.58 Å and 1.36 ± 0.59 Å takes place for systems M40G12 and M40G12-a, respectively (Figure 6b-10 (a) and Figure 6b-11 (a)-(b)). However, a perpendicular distortion is also present. In both scenarios, initially, two graphene sheets are placed at a separation of 10 Å (Figure 6b-11 (c)). As the simulation progresses, a few MM molecules get adsorbed in between the graphene surfaces, and a small amount of water surrounds MM molecules (Figure 6b-11 (d)-(g)). It is seen that once the force constant is removed from the one graphene surface, the equilibrium distance between the graphene sheets become 6.98 ± 0.08 Å and 7.10 ± 0.09 Å for systems M40G12 and M40G12-a, respectively (Figure 6b-11 (d) and (g)). The eqilibrium gas phase seperations between two graphene sheets are 3.56 ± 0.18 Å (for GAFF parameters) and 3.60 ± 0.27 Å (for OPLS-AA parameters) (Figure 6b-10 (b)) which resemble with the realistic distance present in experimental graphene sheet. Therefore, due to the presence of MM molecules in between the graphene sheets, actual equlibrium distance is now changed. Further, the vdW interaction energies between two graphene sheets are -21.08 kcal/mol and -19.82 kcal/mol for systems M40G12 and M40G12-a, respectively. Due to low vdW interaction, perpendicular displacement becomes plausible. However, extensive hydrogen-bonded MM molecules are now strongly adsorbed between the graphene sheets by vdW interaction (Figure 6b-11 (e) and (f)). The vdW interaction energies between MM and graphene sheets are -383.77 kcal/mol and -344.49 kcal/mol for systems M40G12 and M40G12-a, respectively. Therefore, the presence of MM molecules in between the graphene sheet can displace the graphene surface.

Similarly, the graphene exfoliation is also shown considering two big graphene sheets in the presence of 100 MM molecules in between the sheets, and these are presented by two systems, i.e., systems M100G22 and M100G22-a. In this case, also, a lateral displacement of the graphene sheet (in the xy direction) of about 1.11 ± 0.48 Å (Figure 6b-10 (c)) and 1.18 ± 0.49 Å (Figure 6b-10 (d)) is observed for systems M100G22 and M100G22-a, respectively. The equilibrium distances between the big graphene sheets in the gas phase are 3.56 ± 0.17 Å (in GAFF parameters) and 3.58 ± 0.19 Å (in OPLS-AA parameters) (Figure

6b-10 (e)). However, in the presence of 100 MM molecules in between them, the equilibrium distance between the graphene sheets become 7.02 ± 0.26 Å (Figure 6b-10 (f)) and 7.35 ± 0.52 Å (Figure 6b-10 (g)) for systems M100G22 and M100G22-a, respectively. Thus, MM molecules can exfoliate the graphene sheets in parallel and perpendicular directions significantly.

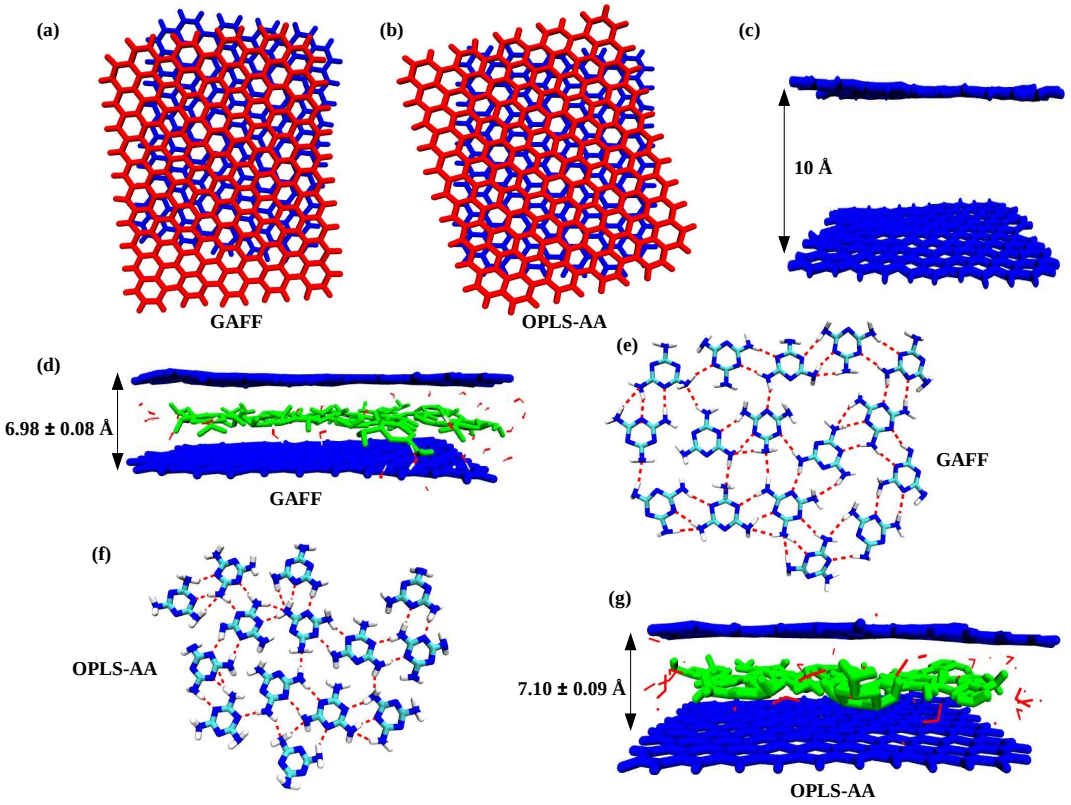

Figure 6b-11. *The lateral displacement of the graphene sheet (in the xy direction) present in system (a) M40G12 and (b) M40G12-a, (c) intial graphene sheet seperation, (d) displacement of the movable graphene sheet in the presence of MM molecules (green) in system M40G12, (e) pattern of adsorption of MM molecules in between two graphene sheets in system M40G12 (red lines represent h-bonding), (f) pattern of adsorption of MM molecules in between two graphene sheets in system M40G12-a (red lines represent h-bonding), (g) displacement of the movable graphene sheet in the presence of MM molecules (green) in system M40G12-a. Here, red lines represent water molecules.*

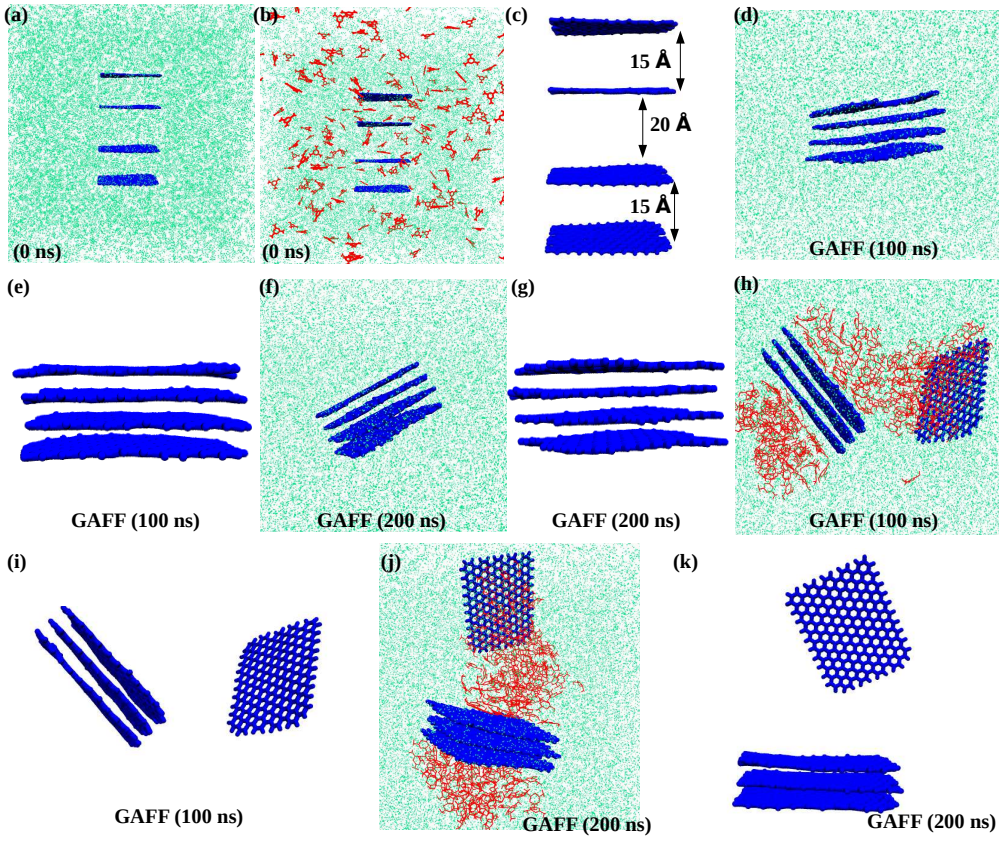

Figure 6b-12. *(a) Initial configuration of graphene sheets surrounded by water (green) in system M0G14, (b) initial configuration of graphene sheets surrounded by water (green) in the presence of MM in system M200G14, (c) the initial separations among graphene sheets in systems M0G14 and M200G14, (d) the aggregated graphene nanosheets in solution at 100 ns simulation run in system M0G14, (e) the aggregated graphene nanosheets at 100 ns simulation run in system M0G14 (water molecules are left out for better visual clarity), (f) the aggregated graphene nanosheets in solution at 200 ns simulation run in system M0G14, (g) the aggregated graphene nanosheets at 200 ns simulation run in system M0G14 (water molecules are left out for better visual clarity), (h) the aggregated graphene nanosheets surrounded by water (green) in the presence of MM at 100 ns simulation run in system M200G14, (i) the aggregated graphene nanosheets at 100 ns simulation run in system M200G14 (water and MM molecules are left out for better visual clarity), (j) the aggregated graphene nanosheets surrounded by water (green) in the presence of MM at 200 ns simulation run in system M200G14, (k) the aggregated graphene nanosheets at 200 ns simulation run in system M200G14 (water and MM molecules are left out for better visual clarity).*

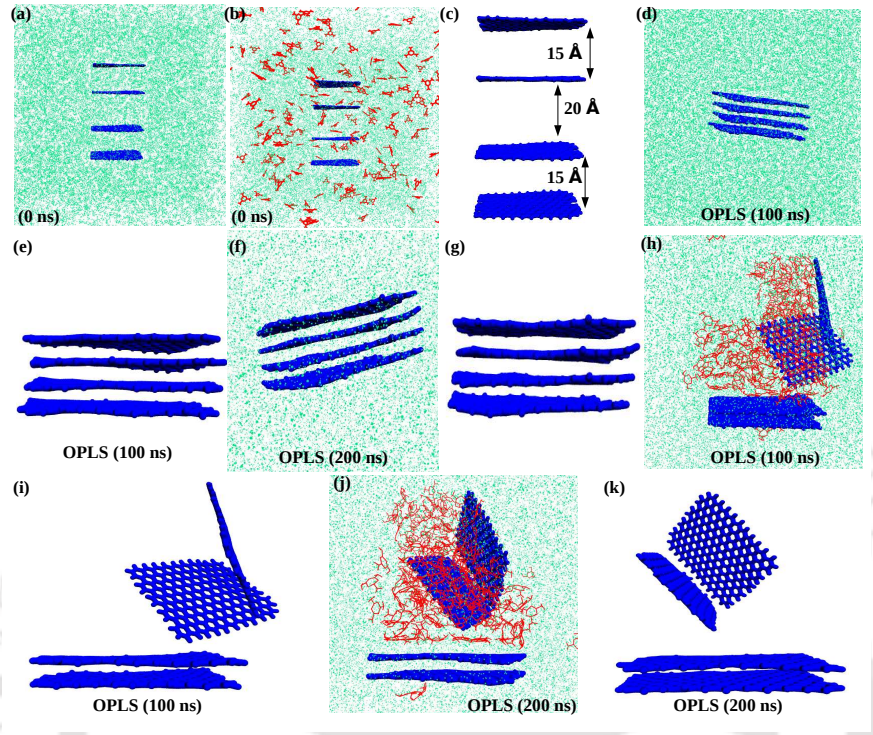

Figure 6b-13. *(a) Initial configuration of graphene sheets surrounded by water (green) in system M0G14-a, (b) initial configuration of graphene sheets surrounded by water (green) in the presence of MM in system M200G14-a, (c) the initial separations among graphene sheets in systems M0G14-a and M200G14-a, (d) the aggregated graphene nanosheets in solution at 100 ns simulation run in system M0G14-a, (e) the aggregated graphene nanosheets at 100 ns simulation run in system M0G14-a (water molecules are left out for better visual clarity), (f) the aggregated graphene nanosheets in solution at 200 ns simulation run in system M0G14-a, (g) the aggregated graphene nanosheets at 200 ns simulation run in system M0G14-a (water molecules are left out for better visual clarity), (h) the aggregated graphene nanosheets surrounded by water (green) in the presence of MM at 100 ns simulation run in system M200G14-a, (i) the aggregated graphene nanosheets at 100 ns simulation run in system M200G14-a (water and MM molecules are left out for better visual clarity), (j) the aggregated graphene nanosheets surrounded by water (green) in the presence of MM at 200 ns simulation run in system M200G14-a, (k) the aggregated graphene nanosheets at 200 ns simulation run in system M200G14-a (water and MM molecules are left out for better visual clarity). Here, in the case of OPLS-AA parameters, both systems' (i.e., systems M0G14-a and M200G14-a) initial configurations are the same as that of the systems made of GAFF parameters (i.e., systems M0G14 and M200G14).*

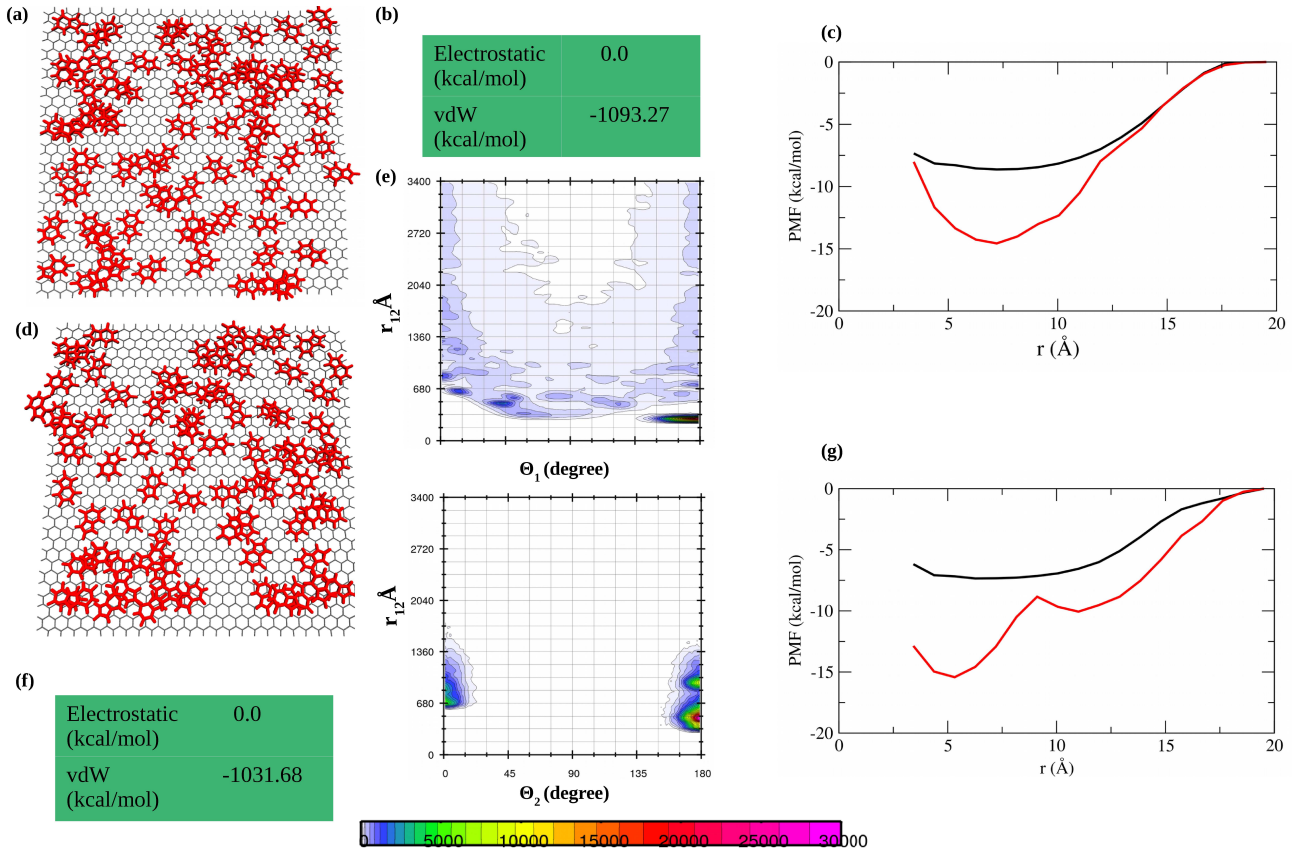

Figure 6b-14. *(a) In system U75G2, 74 out of 75 UA molecules form a large cluster over the graphene sheet, where 54 UA molecules are directly appended to the graphene surface. Here, the cluster structure defination for UA is similar to MM, (b) the decomposition of total energy into its two components (i.e., electrostatic and vdW energies), (c) potentials of mean forces for systems U1G1 (black) and U10G1 (red), (d) the cluster size of the aggregated UA molecules resembles each other in system U75G2-a, (e) the distribution of orientational angle (θ_1, upper panel) between two UA molecules considering two vector points (i.e., the vector connected by a donor (D), hydrogen (H), and acceptor (A) atoms of these two molecules) to describe the hydrogen bonding phenomenon. The angle between two vector normals (θ_2, lower panel) between two aromatic rings is shown to present the π-stacking. Here, r_{12} refers to the center of mass (COM)-center of mass (COM) distance between the individual molecules in system U75G2-a, (f) the decomposition of total energy into its two components in system U75G2-a, and (g) PMFs for systems U1G1-a (black) and U10G1-a (red).*

Table 6b-2. Exfoliation diffusion coefficients ($\times 10^{-9}$ m^2/s) of graphene sheet in the presence of MM for systems M40G12 and M40G12-a.

system	unconstrained exfoliating graphene
M40G12	0.03
M40G12-a	0.04

Moreover, four more systems are considered to study graphene sheets' aggregation in the presence and absence of MM molecules. The systems are (i.e., M0G14, M200G14, M0G14-a, and M200G14-a) presented in Table 6b-1. Here all graphene sheets are free for moving, and their translational and rotational movements are not restricted by employing any constant force throughout the simulation. Furthermore, all these four systems are subjected to 200ns MD simulation run in NVT ensemble following the other usual protocols mentioned in MATERIALS AND METHODS section. From these systems, a deeper understanding of the effect of MM on the separation of graphene nanosheets can be achieved. In M0G14 and M200G14 systems, four small graphene sheets are estimated in the absence and presence of MM molecules, respectively (Figure 6b-12 (a) and (b)). The graphene sheets are well separated initially in both these two systems, and the MM molecules are randomly distributed in system M200G14 (Figure 6b-12 (c) and (b), respectively). At 100 ns simulation, all graphene sheets are well aggregated in the absence of MM molecules in system M0G14 (Figure 6b-12 (d) and (e)). Moreover, at 200 ns also, there is no change in the scenario of the graphene aggregation (Figure 6b-12 (f) and (g)). Therefore, all graphene sheets are aggregated without the presence of any perturbation in pure water. However, in the presence of MM molecules, all graphene sheets are not aggregated even after 100 ns MD simulation run in system M200G4-a (Figure 6b-12 (h)). It can be seen that though three graphene sheets are aggregated, one single graphene is far apart from them (Figure 6b-12 (i)), and this graphene sheet is well surrounded by MM molecules in system M200G14 (Figure 6b-12 (h)). The same condition of the graphene aggregation is seen after a 200 ns simulation run (Figure 6b-12 S9 (j) and (k)). To prevent accumulation, MM hence plays a crucial part in altering the exfoliated graphene sheets. A similar observation can be encountered with the use of OPLS-AA force-field parameters in systems M0G14-a and M200G14-a (Figure 6b-13 (j) - (k)). Thus, in both force field parameters, graphene nanosheets are departed in the

presence of MM, which confirms that MM is considerably effective in exfoliating graphene by rendering a strong interaction between graphene and MM.

Following previous studies,[380, 381] we included the self-diffusion constants for unconstrained exfoliating graphene in systems M40G12 and M40G12-a. The diffusion coefficient was defined from the 12 ns trajectory in the NVE ensemble after the 100 ns of the production run. The diffusion coefficients of unconstrained exfoliating graphene sheets are 0.03 $\times 10^{-9}$ m^2/s and 0.04 $\times 10^{-9}$ m^2/s (Table 6b-2). Note that, the self-diffusion coefficient of graphene sheet in the presence of MM is still to be experimentally determined. However, in comparison to the self-diffusion coefficient of graphene of the previous study[380], the present study proves that in the presence of MM, the exfoliation diffusion of graphene sheets is prominent.

■ UA ON A MONOLAYER GRAPHENE SURFACE

■ Aggregation tendency of UA on a monolayer graphene surface

Initially, randomly placed UA molecules distribute themselves over the graphene sheet along the z-direction in system U75G2. During their distribution, UA molecules form a giant cluster by making hydrogen bonding and π-stacking (discussed later) among themselves. 74 out of 75 UA molecules form a large cluster over the graphene sheet, where 54 UA molecules are directly attached to the graphene surface (Figure 6b-14 (a)) by substantial vdW interaction (Figure 6b-14 (b)). From the aggregation of UA molecules, it can be easily seen that no regular pattern of adsorption of them with the graphene sheet is present; instead, a random orientation can be observed (Figure 6b-14 (a)). Moreover, it can be noted that unlike MM molecules, UA molecules cover the surface area more appropriately, which suggests that UA can make more substantial interaction with that of the graphene surface (Figure 6b-14 (a)).

Furthermore, the determination of UA molecules' adsorption tendency over the graphene surface by determining the potential of mean forces for two systems U1G1 and U10G1 shows that UA molecules promptly aggregate over the graphene surface. The UA assembly is energetically more favorable than a single UA molecule's adsorption over the graphene surface (Figure 6b-14 (c)).

■ Comparison of GAFF and OPLS-AA force filed parameters regarding the adsorption of UA on a monolayer graphene surface

The comparison between GAFF and OPLS-AA force field parameters regarding UA's adsorption on a monolayer graphene surface shows that the cluster size of the aggregated UA molecules (in system U75G2-a) resembles with that of system U75G2 (Figure 6b-14 (d)). Moreover, in the case of the OPLS-AA force field parameter, similar hydrogen bonding and π-stacking interaction can be found like system U75G2 (Figure 6b-14 (e)). Furthermore, strong vdW interaction is also present in the OPLS-AA force field between the adsorbed UA and graphene sheet (Figure 6b-14 (f)). Besides, the PMF estimation employing umbrella sampling conceding two systems, U1G1-a and U10G1-b, unveils that pre-assembled UA molecules on a monolayer graphene surface drag more UA molecules to append to them to be adsorbed preferably over the adsorption of a single UA molecule (Figure 6b-14 (g)). It is to be perceived that in PMFs, GAFF and OPLS-AA force fields resemble each other.

■ Quantum Calculation for the adsorption of UA on coronene

As with MM-coronene interaction, the non-bonded interactions that render the stable complexes between UA and graphene are established. Figure 6b-15 (a)-(c) indicates the weak non-bonded interaction isosurface and 2D plot for the UA-coronene systems. The vital stabilizing force in single UA-coronene complexes is vdW interaction. However, two UA molecules can interact through hydrogen bonding while adsorbed on a surface by strong vdW interaction (Figure 6b-15 (d)-(f)). The vdW interaction is the pioneer in the stabilization of the π-stacking interaction between two adsorbed UA molecules (Figure 6b-15 (g)-(i)). Therefore, owing to significant vdW interaction, π-π stacking, and hydrogen bonding among UA molecules over a graphene surface can be plausible.

■ GRAPHENE SURFACE MEDIATED AGGREGATION OF UA AND MM IN PRESENCE OF TB

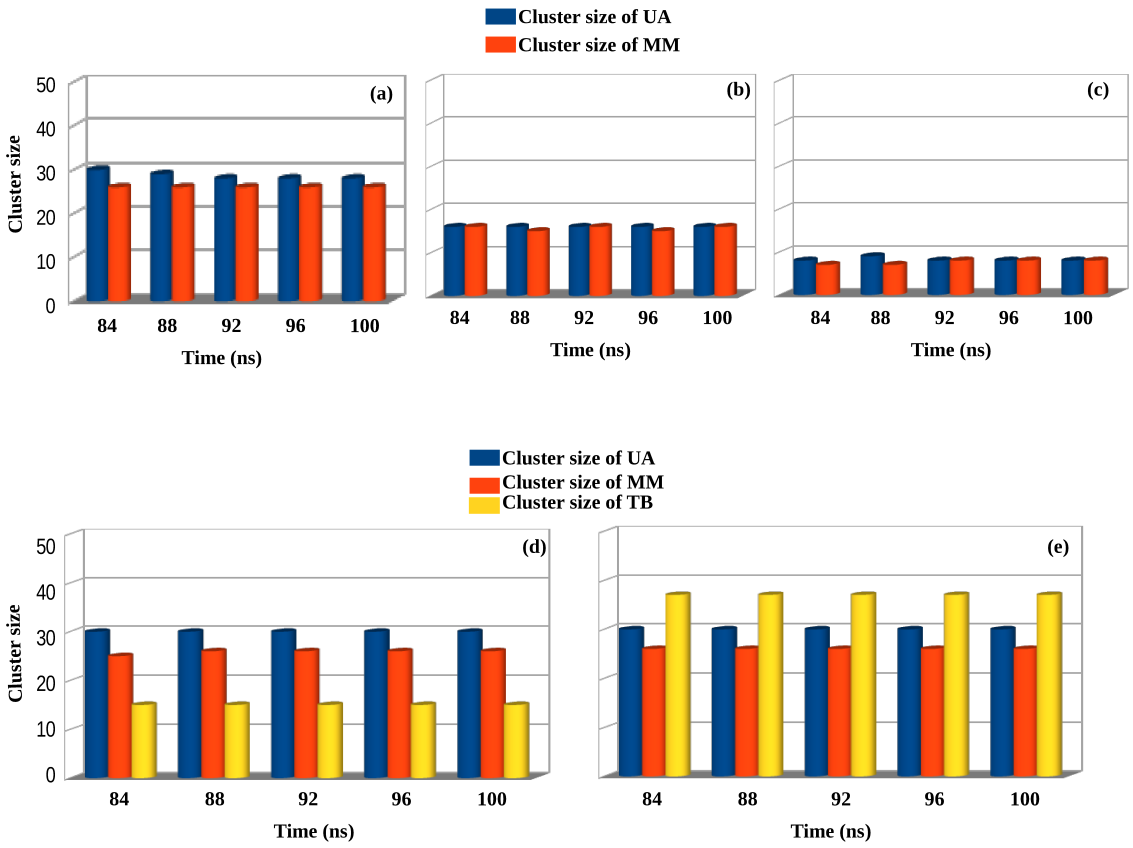

Figure 6b-16. *The different cluster sizes between MM and UA molecules for systems (a) T0, (b) T15, and (c) T40. The conjugate cluster size among MM, UA, and TB molecules for systems (d) T15 and (e) T40. Here, two molecules can form a dimer over the graphene surface during the cluster structure analysis only when bound by either hydrogen bonding or π-stacking interactions. The same definition goes for higher-order clusters also.*

■ Cluster structure of conjugate UA-MM molecules

The previous studies indicate that the size of an aggregated UA cluster and hence the coupled UA-MM cluster size can be decreased obviously by TB.[203, 282] Besides, theobromine is commonly available in coffee, tea, cocoa, energy drinks, etc.[382] Graphene oxide (GO) and reduced graph oxide (RGO) have gained prominence in the past decade, mostly due to π-stacking interactions as components of sensors (chemical and electrochemical,

and biosensors).[383] A recent experimental study showed that TB molecules and related compounds such as caffeine and theophylline are essential for pharmacology, toxicology, and biochemistry.[384] The advent of chirality is vital in this area. Due to surface adsorption, chirality can arise. The chiral adsorption of TB on the surface can also be observed.[385] In a recent experiment, a comparative study of TB monolayers on Au(111) and on few-layer graphene on SiC(0001) is explored.[385] In the present study, TB is used to search for the impact of it on UA clustering in the MM-UA mixture over a graphene monolayer. Thus, multiple different systems with a monolayer graphene sheet that differ in TB concentration in the MM-UA mixture are compared. The UA-MM pure mixture (in system T0) over the graphene sheet does have an acceptable aggregation. A large cluster of approximately 28 UA molecules with 26 MM molecules is formed (Figure 6b-16 (a)). The clusters are very stable over time, which means that the aggregation is significant. Thus, it is apparent that a giant cluster can be developed over a monolayer graphene sheet. Once TB has been added (in system T15), the UA and MM conjugate clusters are severely diminished. In system T15, 16 UA molecules are appended with 15 to 16 MM molecules (Figure 6b-16 (b)). Therefore, the cluster size is greatly reduced in the presence of a small number of TB molecules. When the number of TB is enhanced further in system T40, the clusters of UA and MM molecules are diminished drastically compared to system T0. In system T40, 8 to 9 UA molecules are connected with 7 to 8 MM molecules, thereby conceding a lower order conjugate cluster of MM and UA (Figure 6b-16 (c)). In a previous study, it was clarified that TB substantially interacts with UA molecules compared to MM molecules.[282] Therefore, TB molecules efficiently reduce UA molecules' self-aggregation, which further diminishes the UA-MM overall cluster size.[282] The determination of hydrogen bond numbers between all possible pairs for system T40 also fortifies the aforementioned fact. In this system, the average number of hydrogen bonds between UA-MM, UA-TB, TB-MM, TB-TB, and MM-MM pairs are 47.07, 24.55, 28.21, 10.22, and 34.23, respectively (Table 6b-3). Thus, it reveals that MM-MM aggregation is preferable over TB-MM interaction. Concurrently, UA-MM aggregation propensity is more prominent over TB-MM aggregation. Thus, MM allows preferable interaction towards UA rather than TB. Again, from a comparison of the average hydrogen bond numbers between UA-TB and TB-TB pairs, it is apparent that TB is more inclined towards UA for hydrogen bonding interaction instead of themselves. Hence, TB preferentially interacts more with UA rather than itself (addressed later). Furthermore, (for system T0) the UA-UA, UA-MM, and MM-MM hydrogen bond numbers

are 43.48, 75.93, and 43.21 (Table 6b-3), which is adequately higher than that of system T40 wherein these numbers are 29.11, 47.07, and 34.23, respectively. Thus, TB's appearance reduces the aggregation of UA, which then reduces the UA-MM conjugate cluster size. The disintegration of total energy into electrostatic and van der Waals energy components further reinforces the stated aspect. It is discerned that the electrostatic and van der Waals energies for UA-MM, UA-TB, and TB-MM pairs are reduced (more unfavorable) adequately from system T0 to T40 (Table 6b-4). Furthermore, the UA-MM pair's energy values are much higher (more favorable) than that of the TB-MM pair for systems T15 and T40. Thus, it can be assumed that TB does not efficiently lessen the UA-MM interaction; instead, it confronts with UA-UA pair interaction profoundly.

Table 6b-3. The total number of hydrogen bonds between various pairs in the respective systems.

system	UA-UA	UA-MM	UA-TB	TB-MM	TB-TB	MM-MM
T0	43.48	75.93	—	—	—	43.21
T40	29.11	47.07	24.55	28.21	10.22	34.23

Table 6b-4. The decompostion of total energy into its two components (i.e., electrostatic and vdW energies) for numerous pais. The energy is expreseed in kcal/mol unit.

Energy	UA-MM	UA-MM	UA-TB	TB-MM	UA-MM	UA-TB	TB-MM
electrostatic	-438.84	-367.94	-204.67	-92.02	-288.75	-222.67	-161.03
vdW	-109.16	-54.84	-47.68	-24.87	-54.32	-188.24	-71.95

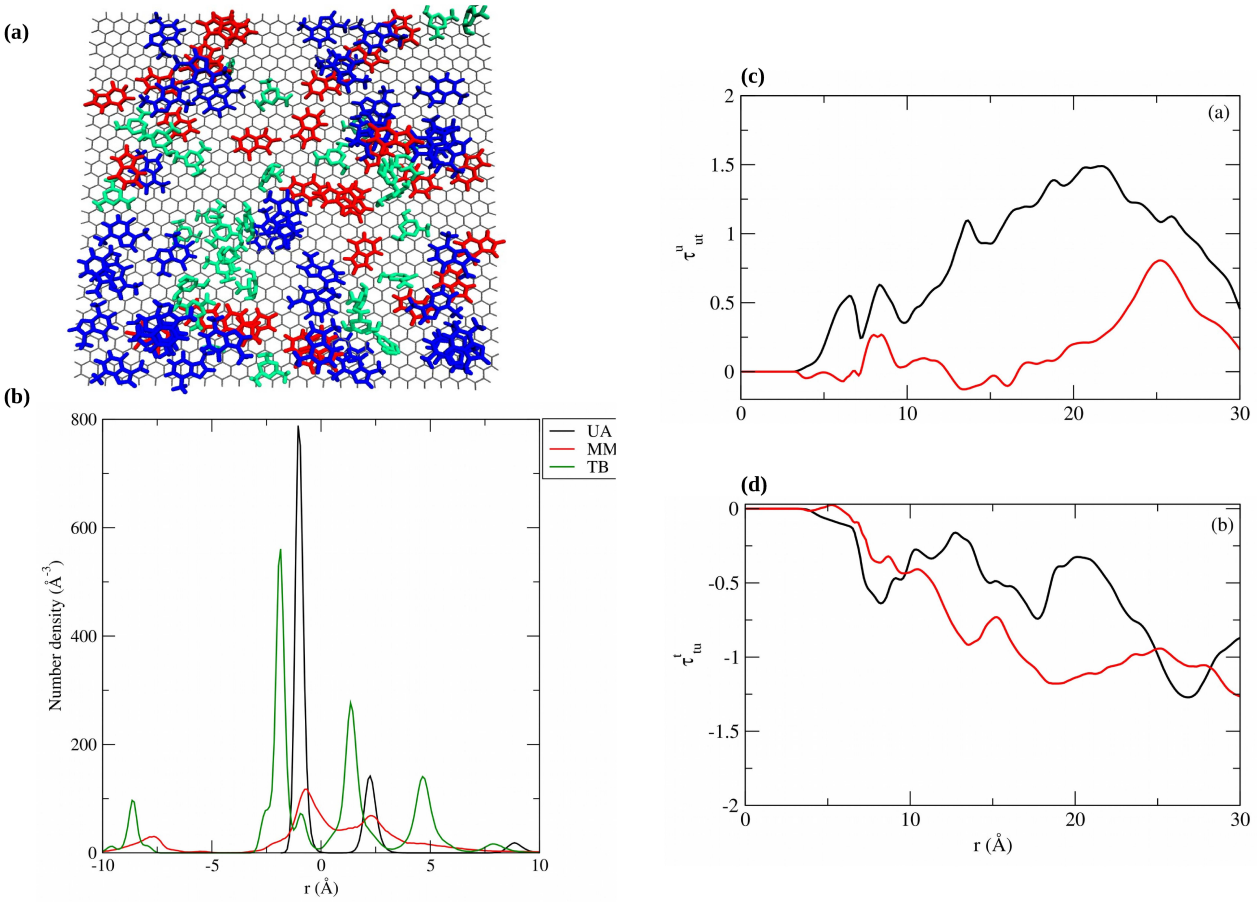

Figure 6b-17. *(a) TB (blue) molecules are well distributed between the UA (red) and MM (green) molecules to interrupt UA aggregations continuity and the UA-MM clusterization in system T40, (b) the number density along the z-axis over the graphene surface of MM, UA, and TB molecules in system T40, (c) the preferential interaction parameter for UA-UA interaction over UA-TB (τ^u_{ut}) for systems T15 (black) and T40 (red), and (d) the preferential interaction parameter for TB-TB interaction over TB-UA (τ^t_{tu}) for systems T15 (black) and T40 (red).*

If we define the overall cluster size among TB, UA, and MM molecules, then it can be seen that all TB molecules are associated with almost all UA and MM molecules in all systems (Figure 6b-16 (d)-(e)). Therefore, the overall cluster size is high in these systems. Consequently, it can be assumed that TB molecules are well distributed between the UA and MM molecules to interrupt UA aggregation's continuity and the UA-MM clusterization (Figure 6b-17(a)). Moreover, the distribution of these three types of solutes over the

monolayer graphene surface can be observed by determining the number density along the z-axis over the graphene surface (Figure 6b-17 (b)).

In the light of the perception of the preferential interaction parameter for UA-UA interaction over UA-TB (τ_{ut}^{u}), for systems T15 and T40, it can be perceived that UA-UA interaction gets reduced in presence of TB; therefore, UA-TB interaction gets surpassed UA-UA interaction in system T40 (Figure 6b-17 (c)). Furthermore, TB-TB interaction is lower than TB-UA (τ_{tu}^{t}) interaction in system T40, which proves that TB interacts more preferably with UA molecules over itself (Figure 6b-17 (d)). Accordingly, UA-TB interaction lowers the cluster size of UA aggregation. The above observation can also be further ascertained by the determination of dynamic properties like DACF. For system T40, the dimer lifetime of the UA-UA pair is decreased considerably in presence of TB as compared to system T0, where TB is absent (Figure 6b-18 (a)). Thus, UA aggregation ability is disengaged with the increase of TB molecules. Moreover, the dimer lifetime of UA-TB pair is increased from system T15 to system T40 (Figure 6b-18 (b)). Consequently, a lower-order UA cluster is conceived, combining less with MM molecules present in that system, thus forming a lower-order UA-MM conjugate cluster. Next, the first shell coordination number (CN) is determined to gain some idea about the aggregation propensity of UA molecules. It is seen that the first shell CN of UA around a reference UA is 1.54, 0.82, and 0.37 for systems T0, T15, and T40, respectively. Thus, TB's presence reduces UA's appearence around other UA molecules, thus reducing the aggregation of UA molecules in the system T40 significantly. Simultaneously, the accumulation of TB molecules around a reference UA molecule is increased, and this can be discerned by the determination of CN of TB molecules around the reference UA molecules. The first shell CNs for TB around UA molecule are 0.15 and 0.68 for system T15 and T40, which validates the fact mentioned above.

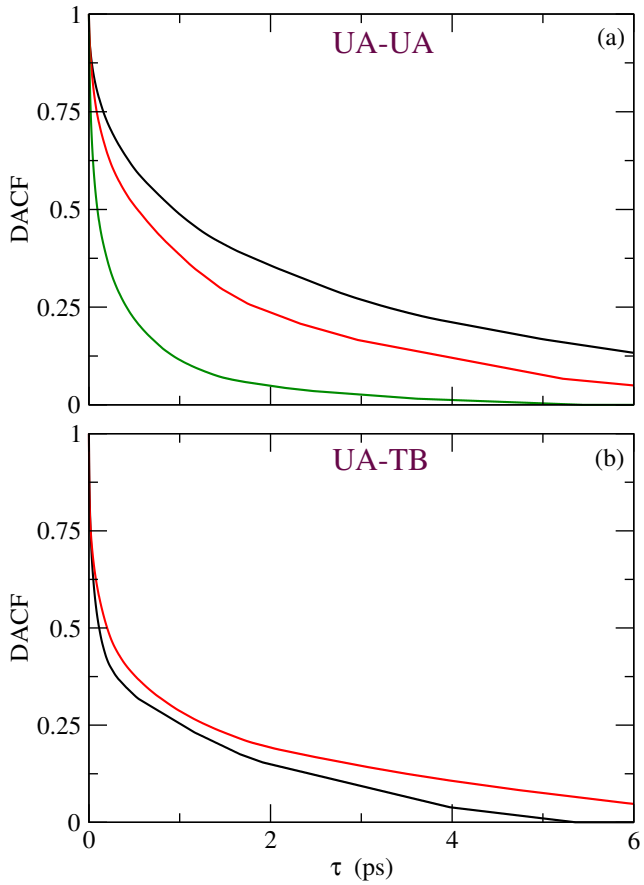

Figure 6b-18. *DACF for (a) UA-UA (upper pannel) pair for systems T0 (black), T15 (red), and T40 (green) and (b) DACF for UA-TB (lower pannel) pair for systems T15 (black) and T40 (red).*

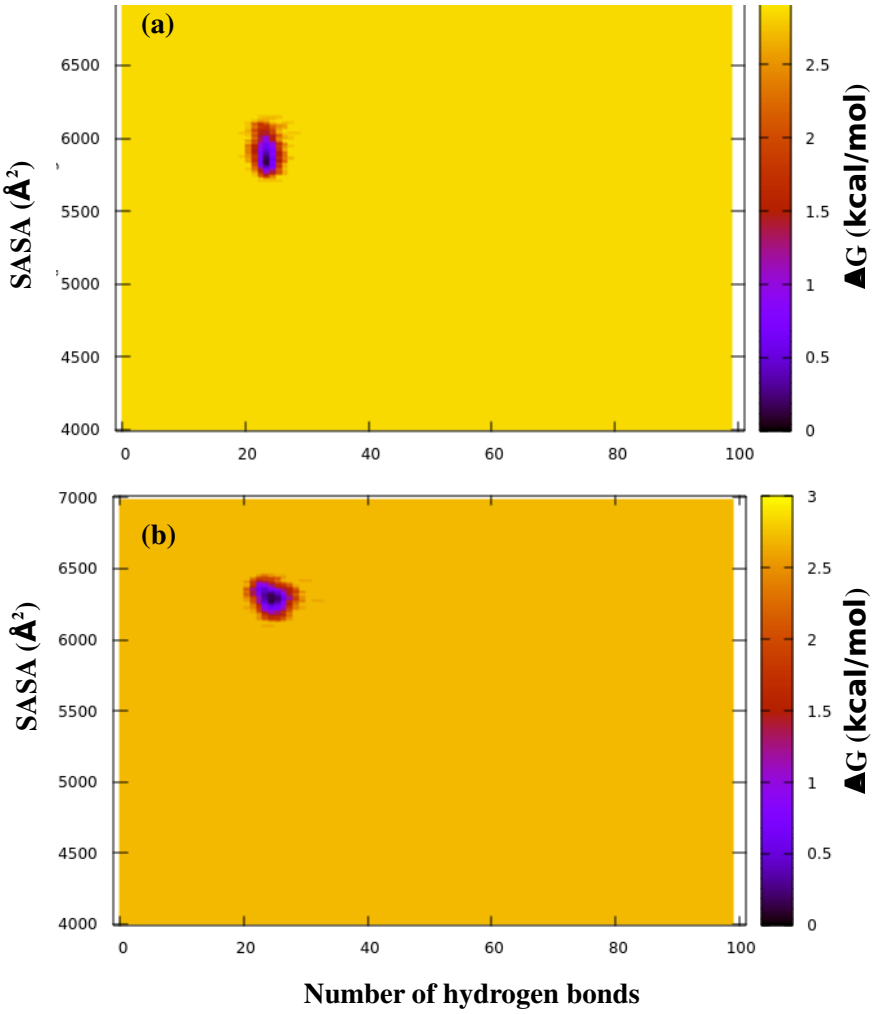

Figure 6b-19. *Free energy landscape for the solvent-accessible surface area (SASA (Å²)) for UA-UA aggregation versus UA-TB hydrogen bonding for systems (a) T15 and (b) T40. The free energy in the color bar on the right side is manifested in kcal/mol unit.*

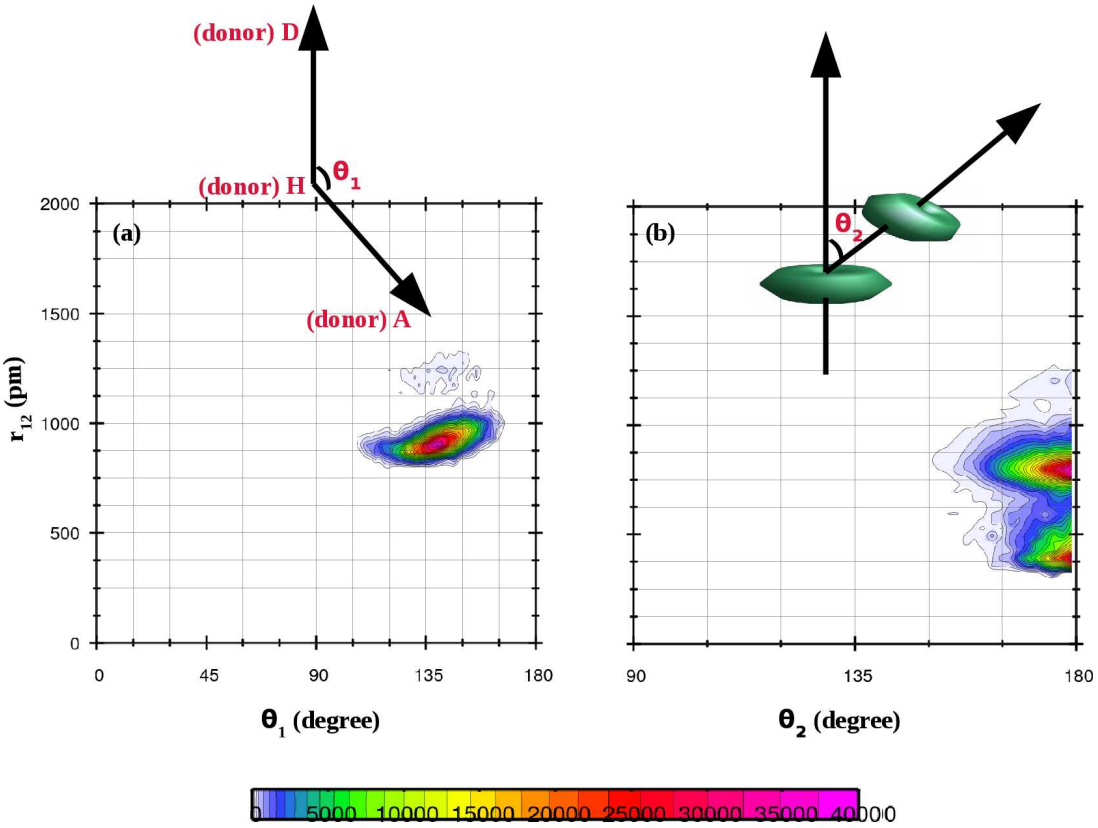

Figure 6b-20. *In system T40, the distribution of orientational angle (θ_1) between UA and TB molecules considering two-point vectors (i.e. the vector connected by donor (D), hydrogen (H), and acceptor (A) atomes of these two molecules) to describe the hydrogen bonding phenomenon, and (e) The angle between two vector normals (θ_2) between two aromatic ring is shown to present the π-stacking. Here, r_{12} refers to the center of mass (COM)-center of mass (COM) distance between the respective molecules.*

By using the solvent-accessible surface area (SASA ($\mathring{A}^2$)) for UA-UA aggregation versus UA-TB hydrogen bonding for both T15 and T40 systems, the free energy landscape is illustrated here (Figure 6b-19 (a)-(b)). It is observed that the hydrogen bond numbers are nearly equal for both the systems as most of the interaction between UA and TB is reliant on π-stacking interaction (discussed later). However, in system T40, the SASA value for UA-UA aggregation is increased (Figure 6b-19 (b)). Note that an extreme difference is not observed in SASA value as the molecules are adsorbed over a graphene surface. Therefore,

UA-TB interaction is high for T40 system as SASA value at system T40 is more evident (Figure 6b-19 (b)) than that at system T15 (Figure 6b-19 (a)) at a point where the free energy is minimum. Hence, the UA cluster's aggregation in system T40 is depreciated in the presence of TB.

The preceding revelations show that UA molecules predominantly interact by π-stacking with other TB molecules over hydrogen bondings.[282] Hereabouts, we also confront similar interactions over the monolayer graphene surface. Nevertheless, UA-TB interaction proffers both hydrogen bonding (Figure 6b-20 (a)) and π-π stacking interactions (Figure 6b-20 (b)) in MM-UA-TB mixture over graphene sheet. Hence, TB molecules break UA clusters by producing the π-stacking and hydrogen-bonding simultaneously.

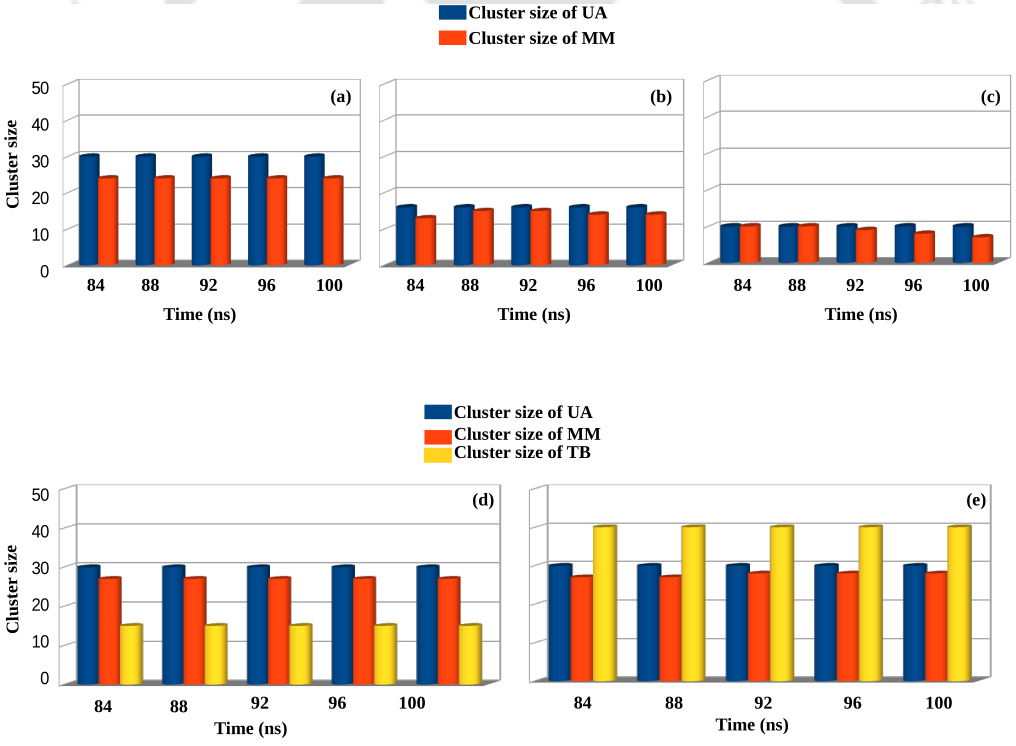

Figure 6b-21. *The different cluster sizes between MM and UA molecules for systems (a) T0-a, (b) T15-a, and (c) T40-a. The conjugate cluster size among MM, UA, and TB molecules for systems (d) T15-a and (e) T40-a. Note that, two molecules can form a dimer over the graphene surface during the cluster structure analysis only when bound by either hydrogen bonding or π-stacking interactions. The same definition goes for higher-order clusters also.*

■ Comparison between GAFF and OPLS-AA foce field parameters regarding the effects of TB on MM-UA interaction

Here, we compare how does the change in the force field parameters of all atomic sites of graphene surface affect its adsorption properties. In case OPLS-AA force field parameter, a similar scenario can be observed in system T0-a, where all UA molecules are attributed with 24 MM molecules (Figure 6b-21 (a)). These clusters are very enduring over a period, which implies a notable aggregation. Since it is apparent that most of the molecules are accumulating; hence, a colossal cluster can be assembled over a monolayer graphene sheet. As TB is introduced in system T15-a, the cluster of UA and MM conjugate is lessened considerably (Figure 6b-21 (b)). In system T15-a, 16 UA molecules are appended with 15 to 16 MM molecules (Figure 6b-21 (b)). Subsequently, the cluster size is reduced in the contiguity of a small number of TB. Moreover, when the number of TB is enhanced further in system T40-a, the cluster of UA and MM molecules is degraded drastically. In system T40-a, 10 UA molecules are united with 7 to 10 MM molecules, whereby gaining a lower order MM and UA conjugate cluster (Figure 6b-21 (c)). A precise result can also be accomplished in the instance of overall cluster size among MM-UA-TB combination (Figure 6b-21 (d)-(e)). OPLS-AA and GAFF force field parameters results resemble each other well in all cases. Besides, in the comparison between the first shell CN for mixed pairs for all systems, it is observed that the results emanating out from these two force field parameters (i.e., OPLS-AA and GAFF) harmonize each other. The first shell CN for the UA-UA pair is 1.61, 0.74, and 0.40 for systems T0-a, T15-a, and T40-a. Similarly, for the UA-TB pair, these are 0.19 and 0.68 for systems T15-a and T40-a, respectively. Moreover, the free energy for these two force fields matches well among these systems T15, T15-a, T40, and T40-a (Figure 6b-22 (a)-(d)).

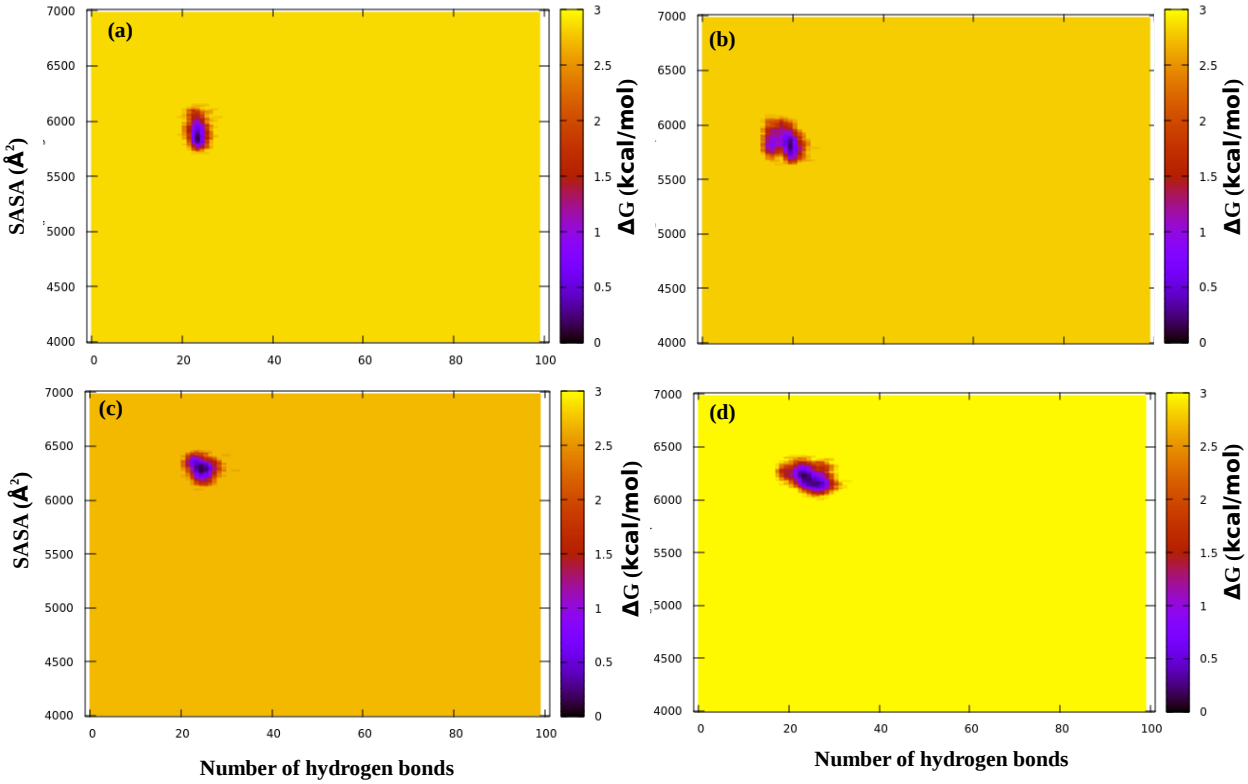

Figure 6b-22. *Free energy landscape for the solvent-accessible surface area (SASA (Å²)) for UA-UA aggregation versus UA-TB hydrogen bonding for systems (a) T15, (b) T15-a, (c) T40, and (d) T40-a. The free energy in the color bar on the right side is manifested in kcal/mol unit.*

■ Quantum Calculation for the adsorption of UA and TB on coronene

The non-bonded interactions that render the stable complexes among UA-TB-graphene are established. Figure 6b-23 (a)-(f) depicts the weak non-bonded interaction isosurface and 2D plot for the UA-TB-coronene systems. Here, UA and TB molecules are strongly hydrogen bonded while they are adsorbed on a surface by strong vdW interaction (Figure 6b-23 (a)-(c)). The van der Waals interaction is the pioneer in the stabilization of the π-stacking between UA and TB molecules (Figure 6b-23 (d)-(e)). Therefore, owing to

significant vdW interaction, π-π stacking, and hydrogen bonding between UA and TB molecules over a graphene surface can be plausible.

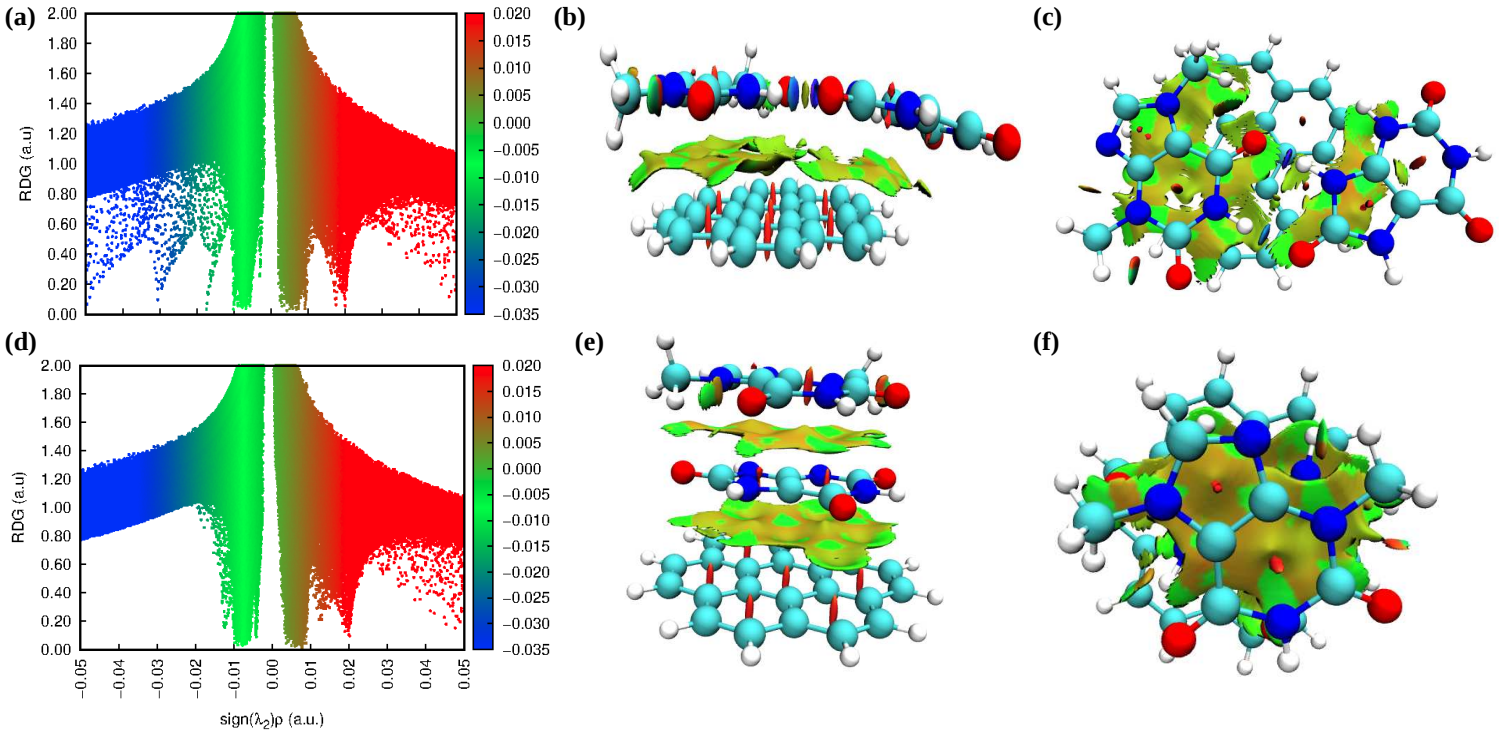

Figure 6b-23. *Color-filled RDG isosurface reciprocates noncovalent interaction (NCI) regions for various interactions among UA, TB, and coronene system. (a)-(c) two hydrogen bonded UA and TB molecules are adsorbed over a coronene surface, and (d)-(f) two π-stacked UA and TB molecules are adsorbed over a coronene surface. The vertical axis of this plot is the reduced density gradient (RDG), and the horizontal axis is the sign of the second largest eigenvalue of the electron density Hessian matrix at position r (sign($\lambda_2(\rho)$)). Here, the strong repulsive non-bonded steric interaction is observed in the red, and attractive interactions like the hydrogen bonding and van der Waals are blue and green.*

■ Umbrella sampling for UA and TB interaction on a graphene surface

For two systems, U2T1G1 and U2T1G1-a (Table 6b-1), the potentials of mean forces (PMFs) for UA and TB interaction on a monolayer graphene surface are determined. For system U2T1G1, we have taken two UA molecules with one TB molecule on a graphene

surface (Figure 6b-24 (a)). The TB molecule is then pulled from the UA molecules to verify whether the UA and TB association is favorable (Figure 6b-24 (b)). The correlation between UA and TB is found to be promising on a graphene surface (Figure 6b-24 (c)). For system U2T1G1-a, the same procedure is followed (Figure 6b-24 (d)-(e)), and it is seen that the interaction is favorable independent of the use of any force field parameter (Figure 6b-24 (c)). TB can also be well adsorbed with UA to prevent UA molecules' aggregation on a monolayer graphene surface to avoid kidney stones.

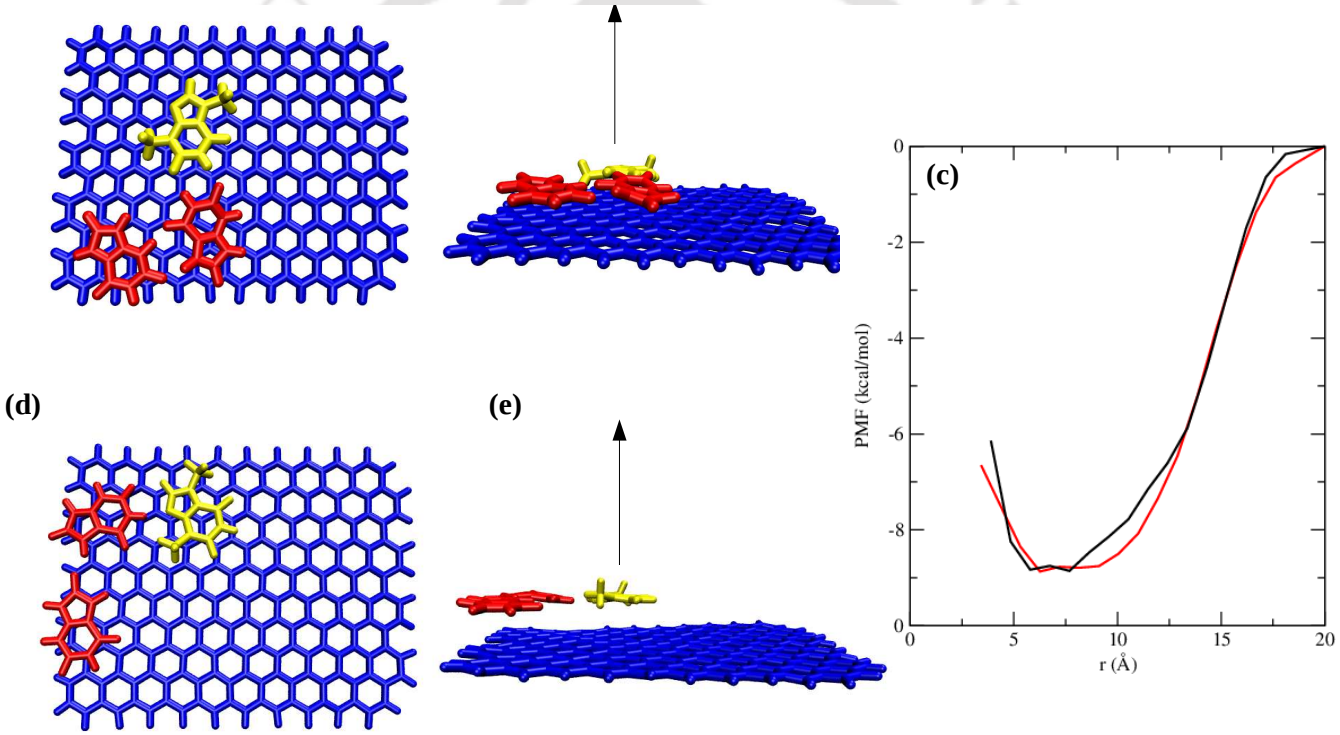

Figure 6b-24. *(a) UA (red) and TB (yellow) molecules are adsorbed on a graphene surface in system U2T1G1, (b) TB molecule is pulled up from UA molecules in system U2T1G1, (c) PMFs for UA and TB interaction in systems U2T1G1 (black) and U2T1G1-a (red), (d) UA (red) and TB (yellow) molecules are adsorbed on a graphene surface in system U2T1G1-a, and (e) TB molecule is pulled up from UA molecules in system U2T1G1-a.*

■ GRAPHENE SURFACE MEDIATED AGGREGATION OF UA AND MM IN PRESENCE OF AP

■ Interaction of AP with UA-MM conjugate cluster

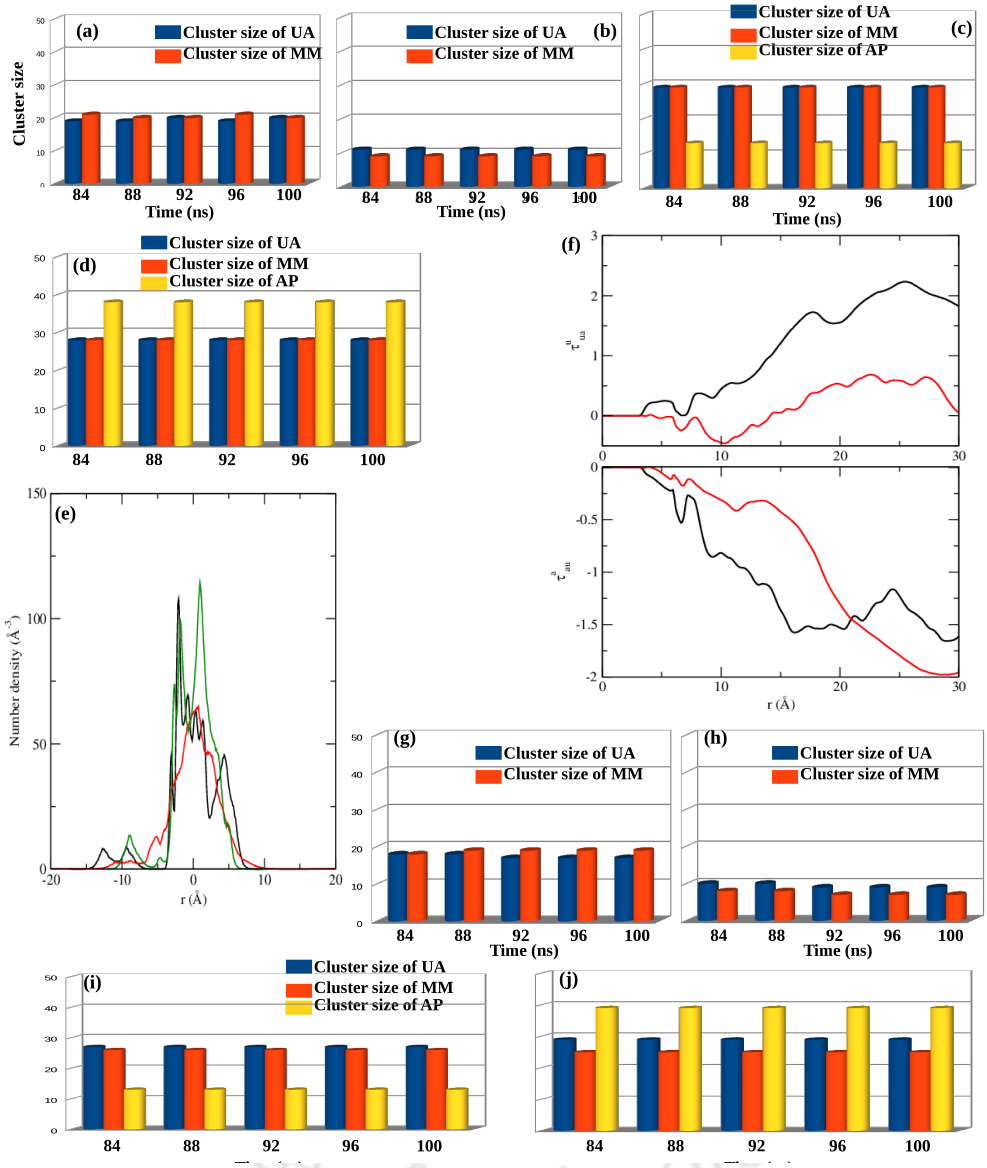

Figure 6b-25. *The different cluster sizes between MM and UA molecules for systems (a) A15, (b) A40, the conjugate cluster size among MM, UA, and AP molecules for systems (c) A15 and (d) A40, (e) the number density along the z-axis for system A40, (f) the preferential interaction parameter for UA-UA interaction over UA-AP (τ^u_{ua}) (upper panel) for systems A15 (black) and A40 (red), and the preferential interaction parameter for AP-AP interaction over AP-UA (τ^a_{au}) (lower panel) for systems A15 (black) and A40 (red), the different cluster sizes between MM and UA molecules for systems (g) A15-a, (h) A40-a, and the conjugate cluster size among MM, UA, and AP molecules for systems (i) A15-a and (j) A40-a. Note that, the cluster structure definition is similar to TB.*

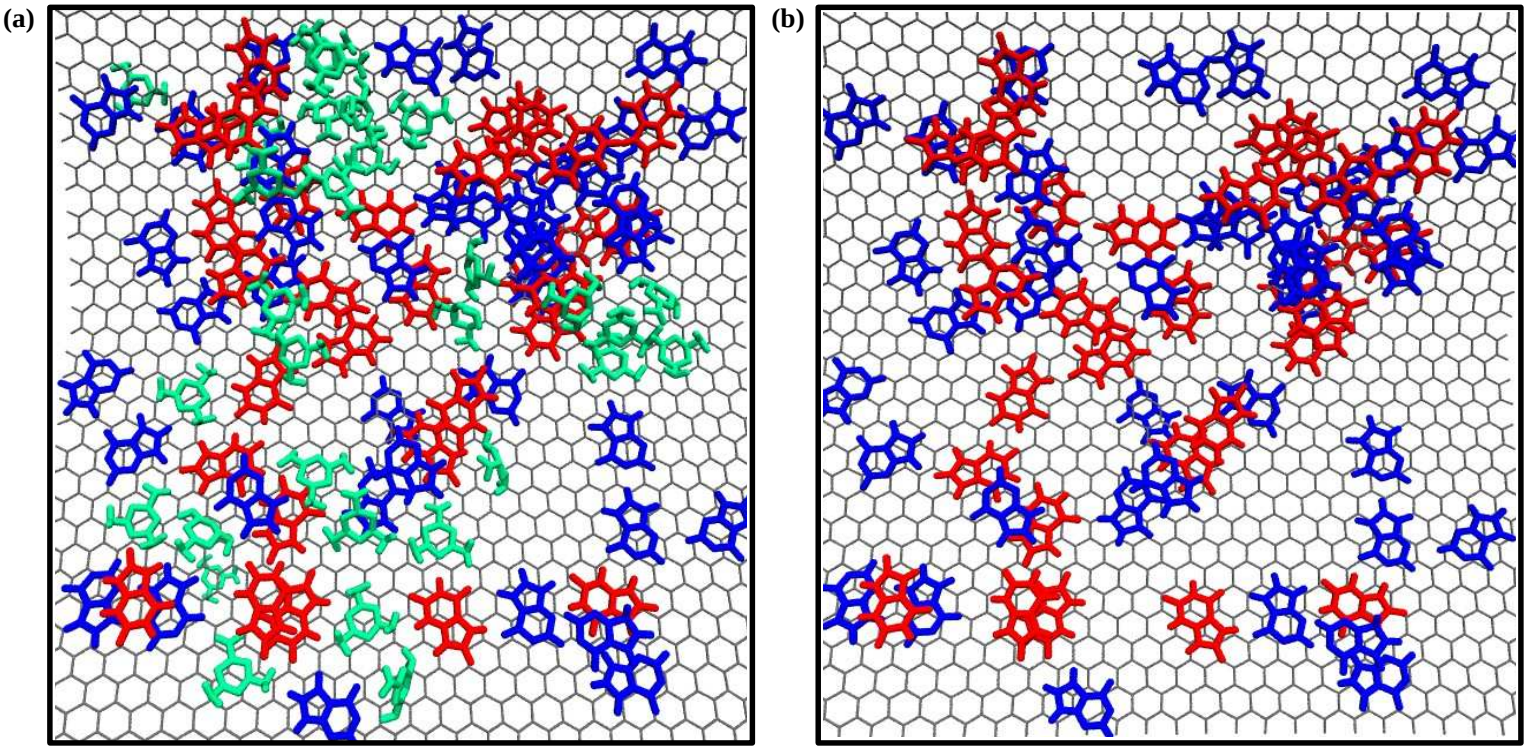

Figure 6b-26. *(a) AP (blue) molecules disseminate themselves between UA (red) and MM (green) molecules and bind them to repress UA-MM aggregation, (b) orientaion of AP and UA molecules in system A40.*

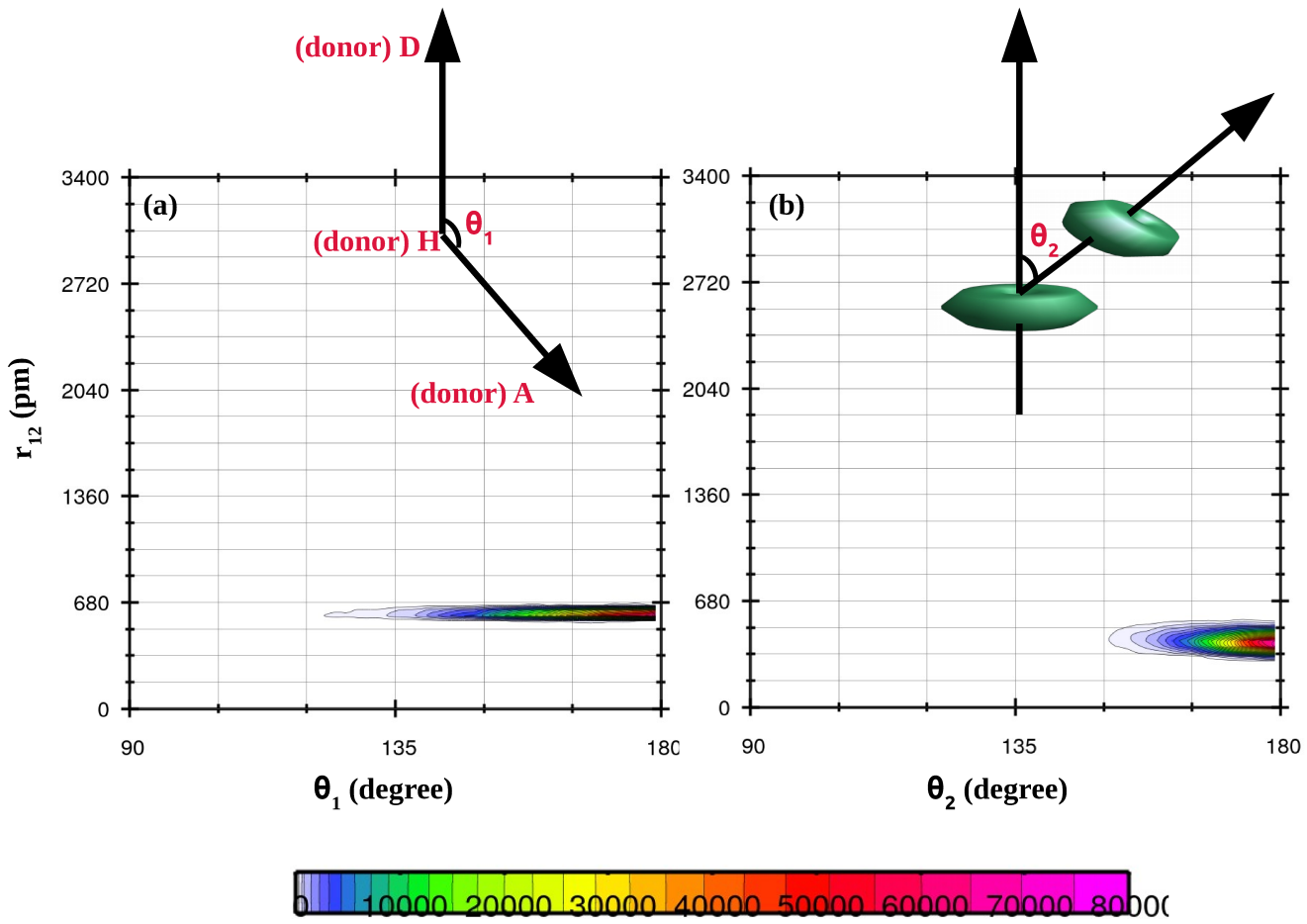

Figure 6b-27. *In system A40, the distribution of orientational angle (θ_1) between UA and AP molecules considering two-point vectors (i.e. the vector connected by donor (D), hydrogen (H), and acceptor (A) atomes of these two molecules) to describe the hydrogen bonding phenomenon, (e) The angle between two vector normals (θ_2) between two aromatic ring is shown to present the π-stacking. Here, r_{12} refers to the center of mass (COM)- center of mass (COM) distance between the respective molecules.*

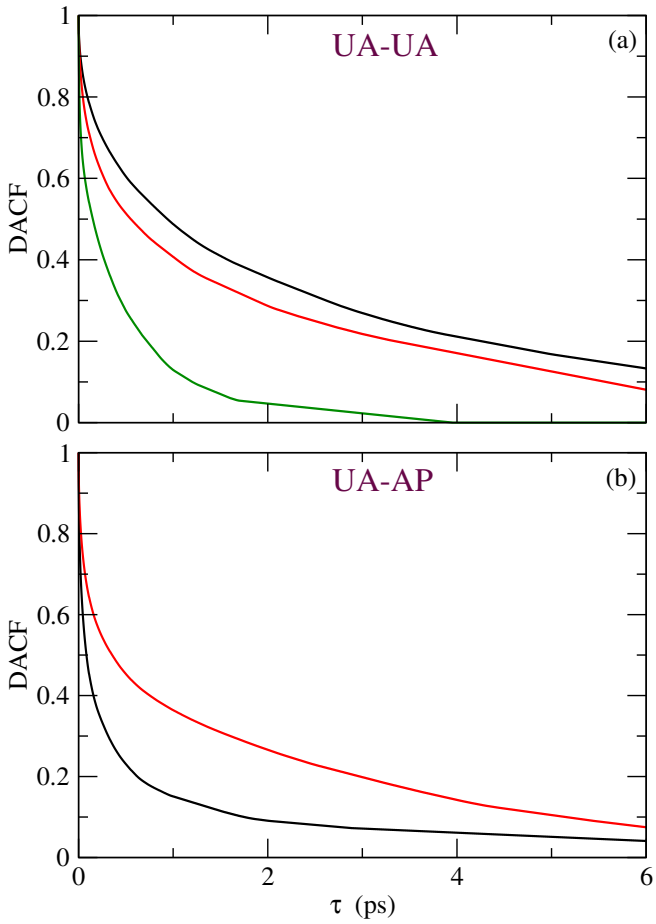

Figure 6b-28. *DACF for (a) UA-UA (upper pannel) pair for systems T0 (black), A15 (red), and A40 (green) and (b) DACF for UA-AP (lower pannel) pair for systems A15 (black) and A40 (red).*

In this section, another inhibitor molecule (i.e., AP) is contemplated to inhibit the UA self-assembly and UA-MM interaction over a monolayer graphene surface. Therefore, two more systems (i.e., systems A15 and A40) are prepared. Firstly, the conjugate UA-MM cluster size is determined in presence of AP and then we compare our observations with the system T0 in which no inhibitor molecules are present. It is comprehended that in the presence of a small AP in system A15, UA-MM conjugate cluster size is reduced compared to system T0. In system A15, 19 to 20 UA molecules are conjoined with 20 to 21 MM molecules (Figure 6b-25 (a)). Similarly, in system A40, 11 UA molecules are appended with 9 MM molecules (Figure 6b-25 (b)). Thus, AP can significantly interfere

with UA-MM interaction. If we assess the overall cluster formation involving UA, MM, and AP molecules in each system (Figure 6b-25 (c)-(d)), it can be noticed that almost all AP molecules are attached to all UA and MM molecules in both systems. Therefore, AP molecules disseminate themselves between UA and MM molecules and bind them to repress their aggregation (Figure 6b-26 (a)-(b)). Moreover, AP interacts stronger with UA molecules over MM molecules. This information can be derived by determining average hydrogen bond numbers and interaction energies between AP-UA and AP-MM pairs (Table 6b-5 and 6b-6). It is seen that in system A40, the average hydrogen bond number of AP-UA pair is 47.10, where the same is for AP-MM pair is 33.19 (Table 6b-5). Again, the decomposition of total energy into its two components, i.e., electrostatic and van der Waals energy, is performed. It determines that AP-UA interaction is more promising over AP-MM (as the electrostatic and vdW energies for AP-UA pair are -538.76 kcal/mol and -162.15 kcal/mol, respectively, and the same for MM-AP pair are -306.70 kcal/mol and -50.40 kcal/mol, respectively (Table 6b-6)). Momentarily, in system A40, the number of UA and MM molecules are the same. Thus, it is apparent that UA-AP interaction is more affirmative than that of the AP-MM pair. For this reason, as stated above, it is asserted that AP substantially breaks the UA cluster. Therefore, a reduced UA cluster then attracts a more diminutive number of MM molecules towards themselves. Notwithstanding, AP-MM interaction can also play a little bit of a role. Experimental studies wholly foretell the UA-AP interaction, and AP-MM interaction is not verified yet.[51] Therefore, we amply analyze the AP-UA interaction over the AP-MM interaction. As AP molecules distribute in between UA and MM molecules on a graphene surface (which can be seen by the distribution of z-axis number density prediction (Figure 6b-25 (e)), it substantially breaks the UA-UA, UA-MM, and MM-MM hydrogen bonds. The total number of hydrogen bonds for UA-UA, UA-MM, and MM-MM pairs in system A40 is 17.13, 55.68, and 39.79, respectively (Table 6b-5). These hydrogen bond numbers are much smaller compared to that of system T0, where the total number of hydrogen bonds for UA-UA, UA-MM, and MM-MM pair are 43.48, 75.93, and 43.21, respectively (Table 6b-5). Thus, AP significantly associates with UA molecules. Consequently, UA clusters are broken into a more inadequate cluster, which can then drags the lower number of MM molecules towards themselves. The AP molecules surround UA and MM molecules in system A40 as the total number of hydrogen bonds for UA-AP and AP-MM pairs are 47.10 and 33.19, respectively. It is fascinating to note that AP molecules do not aggregate, as the total number of hydrogen bonds for the AP-AP pair

is 19.43 in system A40 (Table S4, Supporting Information). Thus, AP-UA interaction is substantial over a monolayer graphene surface. During their interaction, AP interacts with UA through hydrogen bonding as well as π-stacking interaction (Figure 6b-27 (a)-(b)).

Table 6b-5. The total number of hydrogen bonds between various pairs in the respective systems.

system	UA-UA	UA-MM	UA-AP	AP-MM	AP-AP	MM-MM
T0	43.48	75.93	—	—	—	43.21
A40	17.13	55.68	47.10	33.19	19.43	39.79

Table 6b-6. The decompostion of total energy into its two components (i.e., electrostatic and vdW energies) for numerous pais. The energy is expreseed in kcal/mol unit.

Energy	UA-AP	AP-MM
electrostatic	-538.76	-306.70
vdW	-162.15	-50.40

The preferential interaction parameter for UA-UA interaction over UA-AP (τ^u_{ua}) interaction is determined. It is perceived that UA-UA interaction gets reduced from system A15 to system A40 (Figure 6b-25 (f)). Furthermore, the preferential interaction parameter for AP-AP over AP-UA (τ^a_{au}) shows that AP-UA interaction is more preffered in system A40 as compared to system A15 (Figure 6b-25 (f)). Thus, it can be concluded from the preferential interaction parameter calculations that AP considerably interacts with UA over self-aggregation. Consequently, UA-UA interaction gets pestered in the presence of a sufficient number of inhibitors, i.e., AP.

The dimer lifetimes are estimated for UA-UA and UA-AP pairs by the calculation of DACF. It is seen that the dimer lifetime of the UA-UA pair is decreased considerably as one moves from system A15 to system A40 in the presence of AP as compared to system T0, where inhibitor is absent (Figure 6b-28 (a)). Thus, UA aggregation ability is disengaged with the increase of AP molecules. Moreover, the dimer lifetime of UA-AP pair is increased

from system A15 to system A40 (Figure 6b-28 (b)). Consequently, a lower-order UA cluster is conceived, combining with less number of MM molecules present in that system, thus forming a lower-order UA-MM conjugate cluster in the presence of AP.

■ Comparison between GAFF and OPLS-AA force field parameters regarding the effects of AP on MM-UA interaction

Here, the graphene surface force field parameter has been amended to explore the variance in their adsorption properties. A similar situation can be noted in OPLS-AA parameter in A15-a system, which attributes 19 to 20 UA molecules with 20 to 21 MM molecules (Figure 6b-25 (g)). In the contiguity of a small number of AP, the cluster size can then be abbreviated. Furthermore, UA and MM molecules' clusters are significantly diminished if AP is further increased in system A40-a. 10 UA molecules in system A40-a are bound to 7-10 MM molecules, leading to a lower order of MM and UA combination (Figure 6b-25 (h)). A precise result can also be obtained in the case of total cluster size among the MM-UA-AP combination (Figure 6b-25 (i)-(j)). In both instances, the effects of OPLS-AA and GAFF parameters are quite close. Therefore, it is found that the impact of these two force field parameters (i.e., OPLS-AA and GAFF) harmonizes with each other.

■ Quantum Calculation for the adsorption of UA and AP on coronene

The non-bonded communications that furnish the firm complexes of UA-AP-graphene are estimated. Figure 6b-29 (a)-(f) designate the weak non-bonded interaction isosurface and 2D plots for the UA-AP-coronene systems. It can be easily discerned that UA and AP molecules are strongly hydrogen-bonded, and these molecules are adsorbed on a surface by strong vdW interaction (Figure 6b-29 (a)-(c)). The van der Waals interaction is the driving force in the stabilization of the π-stacking interaction between UA and AP molecules (Figure 6b-29 (d)-(f)). Hence, owing to striking vdW interaction, π-π stacking, and hydrogen bonding between UA and AP molecules over a graphene surface can be probable.

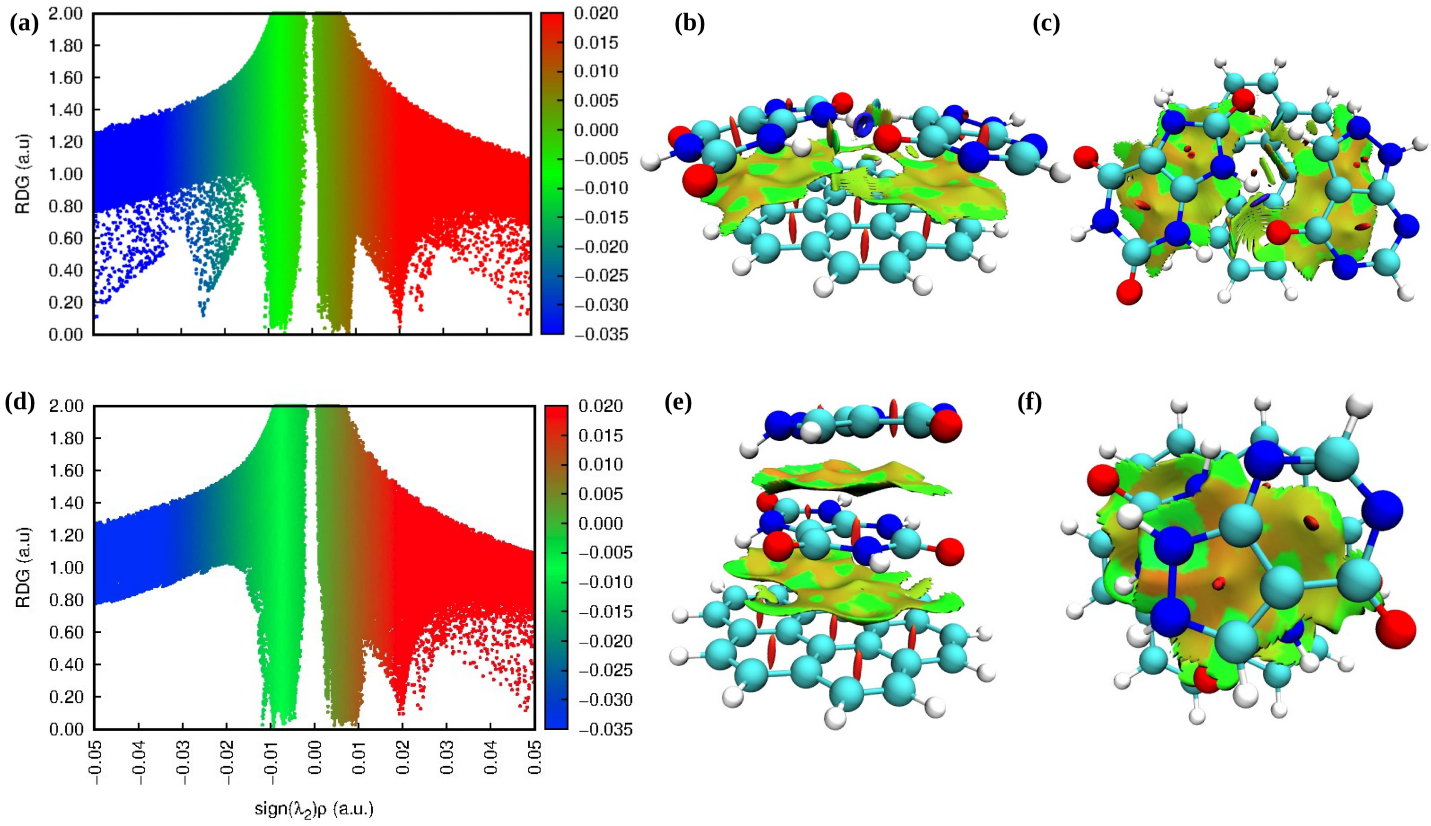

Figure 6b-29. *Color-filled RDG isosurface reciprocates noncovalent interaction (NCI) regions for various interactions among UA, AP, and coronene system. (a)-(c) two hydrogen bonded UA and AP molecules are adsorbed over a coronene surface, and (d)-(f) two π-stacked UA and AP molecules are adsorbed over a coronene surface. The vertical axis of this plot is the reduced density gradient (RDG), and the horizontal axis is the sign of the second largest eigenvalue of the electron density Hessian matrix at position r (sign(λ2(ρ)). Here, the strong repulsive non-bonded steric interaction is observed in the red, and attractive interactions like the hydrogen bonding and van der Waals are blue and green.*

■ Umbrella sampling for UA and AP interaction on a graphene surface

The potentials of mean forces (PMFs) for UA and AP interaction on a monolayer graphene surface are determined for two systems U2A1G1 and U2A1G1-a (Table 6b-1). Here, two molecules are taken with one AP molecule on a graphene surface for system

U2A1G1 (Figure 6b-30 (a)). the AP molecule is then pulled from the UA molecules to verify whether the interaction between the UA and AP is favorable (Figure 6b-30 (b)). It is seen that the interaction between UA and AP on a graphene surface is favorable (Figure 6b-30 (c)). The same protocol is followed for system U2T1G1-a (Figure 6b-30 (d)-(e)) and, it is observed that the interaction is favorable irrespective of the usage of any force field parameter, i.e., GAFF and OPLS-AA (Figure 6b-30 (c)). Therefore, AP can interact with UA on a monolayer graphene surface to inhibit UA aggregation to prevent kidney stones.

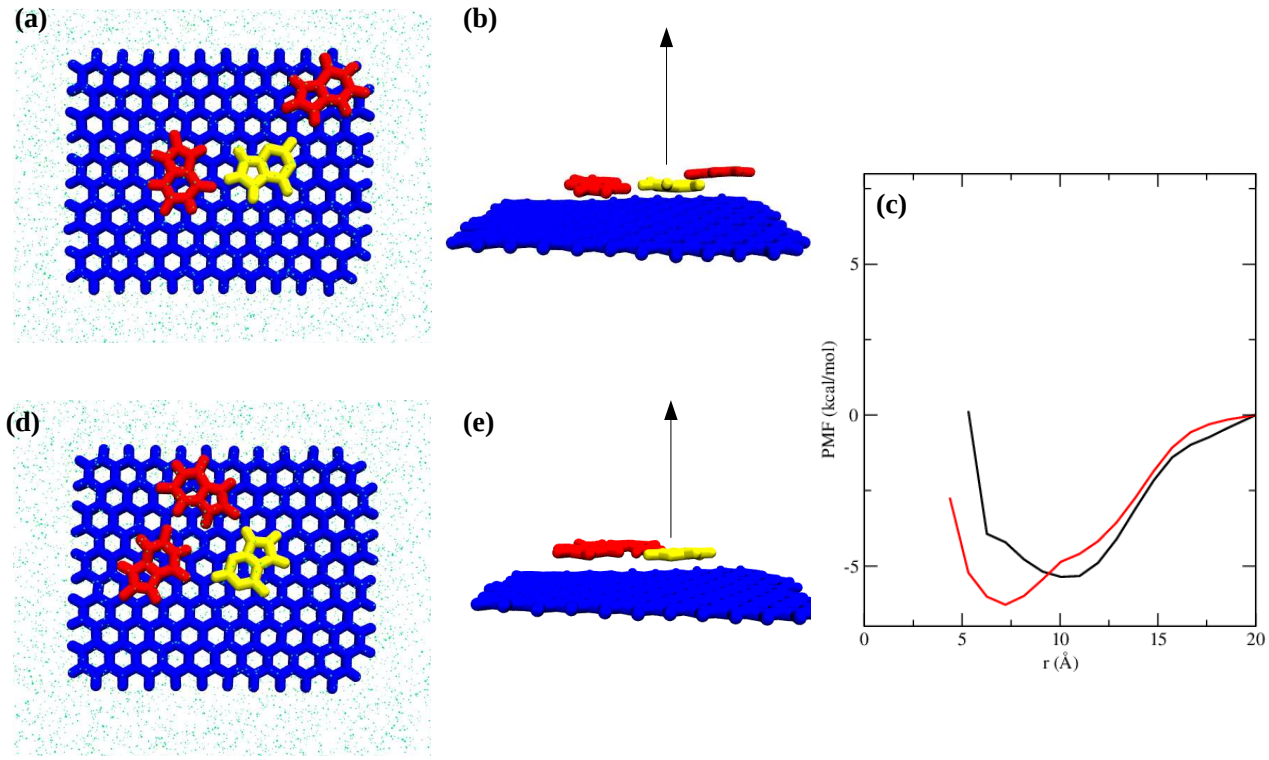

Figure 6b-30. *(a) UA (red) and AP (yellow) molecules are adsorbed on a graphene surface in system U2A1G1, (b) AP molecule is pulled up from UA molecules in system U2A1G1, (c) PMFs for UA and AP interaction in systems U2A1G1 (black) and U2A1G1-a (red), (d) UA (red) and AP (yellow) molecules are adsorbed on a graphene surface in system U2A1G1-a, and (e) AP molecule is pulled up from UA molecules in system U2A1G1-a.*

■ Orientation of AP and UA molecules relative to the surface during their

aggregation on a monolayer graphene surface

To perceive the conformation of UA and AP molecules over the graphene sheets, we studied the probability (P(θ)) of orientational distributions over the graphene sheet in system A15 for these two molecules. The results are shown in Figure 6b-31 (a), where the angle of orientation (θ) denotes the angle between these molecules' vector normals and the normal vector of the graphene surface. There is a sharp orientation peak in the distribution of UA and AP molecules over the graphene sheet, indicating that the adsorbed UA and AP molecules on the graphene sheet exhibit parallel orientation (Figure 6b-31 (b)-(d)) relative to the graphene surface.

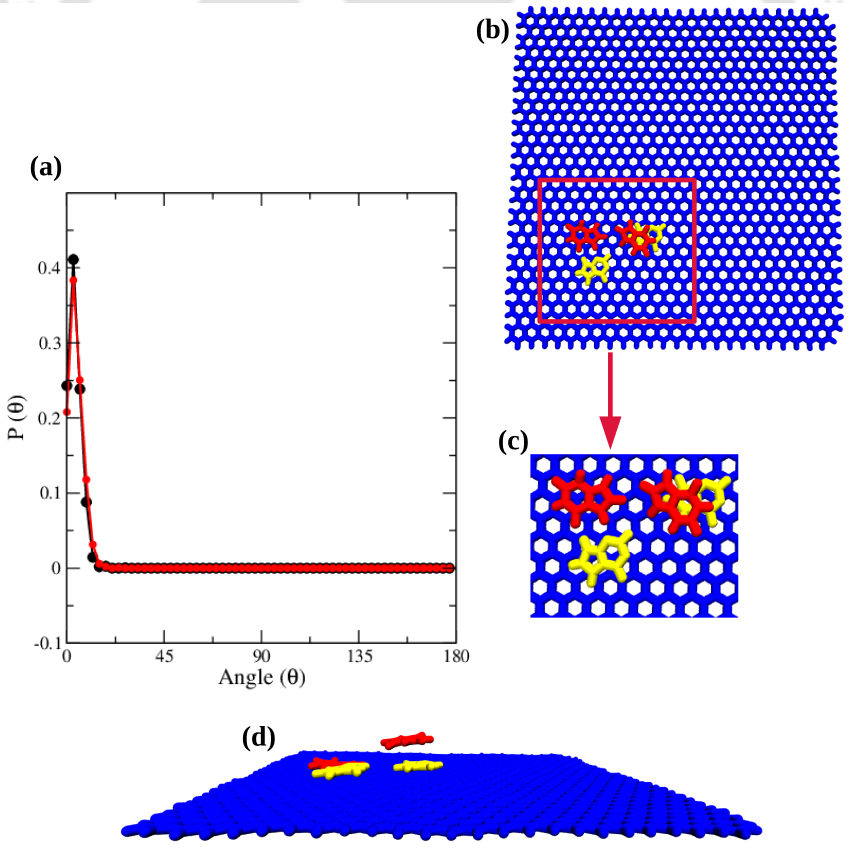

Figure 6b-31. *(a) The probability of orientational angle (θ) between the vector normals of UA (black) and AP (red) molecules with the normal vector of graphene surface in system A15, (b)-(d) the adsorbed UA (red) and AP (yellow) molecules on the graphene sheet (blue) exhibit parallel orientation.*

■ SUMMARY AND CONCLUSIONS

In essence, this study advances qualitative and fundamental insights into the dominant interactions that decide the self-assembly of MM and UA on a monolayer graphene surface. In the presence and absence of inhibitors (TB and AP), a thorough understanding of MM and UA self-assembly may be crucial in unraveling the mechanisms that impersonate the crystal precipitation of human kidney stones. The present study illustrates a pragmatic approach to understanding molecular recognition, aggregation dynamics, and growth of these molecules on graphene and related 2D functional nanomaterials. It is observed that MM and UA aggregation on a 2D surface is spontaneous. Moreover, there is no difference in these molecules adsorption with a change in graphene surface size. The greater the surface area of the graphene surface, the more molecules are absorbed. These solute molecules interact with the surface of graphene via vdW interaction energy. Besides, hydrogen bonding and π-stacking interactions among themselves over the graphene surface necessitate binding all these molecules. The determination of the radius of gyration (R_g) and root mean square deviation (RMSD) of adsorbed molecules (adsorbed in the first layer) demonstrates that they are efficiently organized over the graphene surface. Umbrella sampling is also performed to estimate the potentials of mean forces (PMFs) between the solute and graphene surface. It is noted that the interaction between the solutes and graphene surface is quite promising and energetically favorable. However, once solute molecules are adsorbed over the graphene surface, these aggregated solute molecules strongly attract more solute molecules towards themselves to be adsorbed on the graphene surface. It is seen that a large size cluster is formed between UA and MM in the absence of inhibitors. Over time, the clusters are very stable, indicating that the aggregation is significant. In the presence of a small number of inhibitors (such as TB or AP), the UA-MM interaction is significantly reduced. Interestingly, OPLS-AA and GAFF force field parameters produce similar outcomes. Felix Grases et al.*et al.* concluded that TB could prevent UA crystallization.[203] Thus, one can use TB to treat UA nephrolithiasis. A theoretical analysis where TB prevents UA aggregation and hinders MM-UA cluster formation recommends a similar outcome.[282] AP also acts as a potent inhibitor against UA nephrolithiasis. Therefore, the present study elaborately explains the molecular nature of MM-UA interaction (which causes kidney stones) on a surface in the presence and absence of inhibitors, thus, mimicking the exact nature of kidney stone precipitation. Not only that, the efficacy of an inhibitor against kidney infection can be estimated from this study. Via

hydrogen bonding and π-stacking interaction, TB and AP molecules significantly interact with UA molecules. As a consequence, a smaller order cluster is produced for UA-UA interaction. The smaller UA clusters then attract fewer MM molecules toward themselves. Consequently, it decreases the size of the overall UA-MM conjugate cluster. Therefore, the probability of developing kidney stones is considerably depreciated. Furthermore, liquid-phase exfoliation (LPE) is a promising approach towards producing and dispersing a wide variety of layered materials.[386, 387, 388, 389, 390, 391, 392, 393, 394, 395] Therefore, a detailed analysis of the molecular origin of graphene exfoliation in the presence of MM is also presented. Recent experimental studies showed that MM adsorption on a graphene surface might be capable of graphene sheet exfoliation.[347, 348] The parallel and perpendicular peeling of the graphene sheet in the presence of MM is shown to be possible. This study thus provides valuable insights into the fundamental molecular properties (of molecules linked to kidney stone) on a 2D material along with the graphene exfoliation and dispersion by MM. We expect that our work will lead to recommendations for a priori choice and the design of kidney stone inhibitors in the future.

Chapter 7

Summary and Our View on the Aggregation of Melamine and Uric Acid in Kidney Stone Formation and its Inhibition by Small-Molecule Inhibitors in Solution and at the Solid-Liquid Interface

"Imagination is more important than knowledge. Knowledge is limited. Imagination circles the world."

– Albert Einstein

In the absence and presence of many small molecular inhibitors, this thesis reveals the aggregating properties of the MM, UA, and MM-UA interactions in the solution and solid-liquid interface in interpreting the fundamental mechanisms using classical MD simulation methodologies. Firstly, we have begun with MM molecules' interaction tendency in water. The aggregation propensity of MM is shown to decrease with reduced MM concentration. Besides, the association thermodynamics of MM indicates that the association process is essentially driven by enthalpy. Moreover, MM can produce larger size clusters due to self-aggregation. Consequently, MM can also produce large assembly when consumed excessively, and therefore, can also induce the development of kidney stones. The conclusions of this analysis will help identify and use potential MM aggregates and clusters as theoretical references. The findings from this analysis again prove beneficial in developing new and innovative medicines to prevent the accumulation of MM to eliminate harmful diseases. Next, classical MD simulations are carried out with eight MM molecules in water over a temperature range of between 300K and 380K. The precise analysis implies that MM aggregation is reduced in water with the increase of temperature. Moreover, we have validated our results by comparing between two force field parameters of MM, i.e., CHARMM General Force Field parameters (CGenFF) and General AMBER Force Field(GAFF) parameters.

A series of classic MD simulations are then used to extensively explore the underlying structural properties of MM and UA complexes with compositional heterogeneity under ambient conditions. A strong, insoluble complex is detected either by the presence of MM or UA or by the presence of the two molecules at higher concentrations in the system. Hence, the larger the concentration, the bigger the cluster of MM and UA molecules in water. Besides, as the lifetimes of dimer formation are high for MM-UA and UA-UA interactions, the percentage of higher-order clusters is more eminent for all systems contemplated in this study. These findings designate that the more potent interaction in UA-UA drives the development of steady UA clusters. Consequently, the larger clusters composed of only UA molecules in water "drag" the neighboring MM molecules around themselves to make large MM-UA clusters. Next, the effects of TB on the UA aggregation have been thoroughly examined, along with the possible changes in the size of the MM-UA cluster. As TB obstructs the development of UA clusters rather than UA-MM dimer by providing π-stacking interaction between TB and UA, it can be asserted that the

appearance of TB will lessen the size of overall MM-UA clusters. A comparable mechanism can also be perceived with the use of AP as an inhibitor for UA-MM interaction. Therefore, a straightforward but pragmatic methodology might necessitate either severance of the aggregation of UA or impediment of the hydrogen-bonded cluster of MM and UA. Next, potassium citrate (K_3Cit) is found to be an effective inhibitor for a notable decrease of large UA-MM clusters. The underlying mechanisms of simultaneous interactions between K_3Cit and the MM-UA pair are considered by the classical molecular dynamics simulation coupled with the enhanced sampling method. K_3Cit binds to the MM-UA pair profoundly to provide an MM-UA-K_3Cit conjugate complex with favorable complexation energy. The comprehensive, strategically outlined "direct approach" and "indirect approach" cluster structure analysis explicates that K_3Cit lessens the direct approach MM-UA cluster size significantly by allowing strong hydrogen bonding irrespective of ensemble variation (i.e., NPT and NVT).

We explore Vit-C's impact on the interference and destabilization of UA aggregations. We perceive that Vit-C inundates itself with the aggregated UA molecules; hence, it encapsulates UA clusters. The more Vit-C is present in a system, the more extensive interaction between the aggregated UA cluster and the Vit-C molecules. Also, through the advancement of significant hydrogen bonding, hydrophobic, and π-stacking interactions, Vit-C unites itself admirably with the UA molecules to develop an overall extended conjugate UA-Vit-C cluster. It is also noted that Vit-C associates mainly with the aggregated UA molecules, preferably over self-aggregation among themselves. Thus, randomly dispersed Vit-C molecules are promptly brought by the large UA clusters in a system. The most prevalent type of kidney stone is acquired on the renal papillary. The stone's growth is accomplished on the matrix-coated surface by aggregating pre-formed crystals or secondary crystal nucleation. Substances reduce supersaturation initiation, nucleation, expansion of crystals, accumulation rate, or stone-forming processes. By conflicting with crystals, inhibitors can undeviatingly affect the urinary circumstances or act obliquely. There is, hence, a requisite mechanism for the production and protection of kidney stone deposition and adsorption of antibodies to the crystal surface. In the present work, a graphene sheet is pondered to achieve a surface-mediated UA adsorption. Afterward, the influx of Vit-C into adsorbed UA molecules interprets the variation in the self-aggregation of UA, thus, furnishing Vit-Cs inhibitory mechanism in UA. Likewise, our succeeding study advances qualitative and primary insights into the prevailing interactions that decide the

self-assembly of MM and UA on a monolayer graphene surface. In the presence and absence of inhibitors (TB and AP), a precise understanding of MM and UA self-assembly may be crucial in interpreting the mechanisms of the crystal precipitation of human kidney stones. The study illustrates a pragmatic strategy to surmising molecular recognition, aggregation dynamics, and growth of these molecules on graphene and related 2D functional nanomaterials. Therefore, the present study elaborately defines the occurrence of kidney stones in the presence and absence of inhibitors in presence of graphene, portraying the exact nature of precipitation of the kidney stone. Not only that, the potency of an inhibitor against kidney infection can be ascertained from this study. Via hydrogen bonding and π-stacking interaction, TB and AP molecules significantly interact with UA molecules. In conclusion, UA clusters and UA-MM conjugate clusters are readily diminished in the proximity of AP and TB on a monolayer graphene surface.

In short, this thesis illuminates relevant insight into the inhibition of the interaction between MM and UA in the solution and the solid-liquid interface. Moreover, our studies also contribute helpful information for identifying and exploring new drugs to prevent kidney stones.

Bibliography

1. Dalal, R. P.; Goldfarb, D. S. *Nat. Rev. Nephrol.* **2013**, *7*, 267-274.
2. Hau, A. K.; Kwan, T. H.; Li, P. K. *J. Am. Soc. Nephrol.* **2009**, *20*, 245-250.
3. Lipschitz, W. L.; Stokey, E. *J. Pharmacol. Exp. Ther.* **1945**, *83*, 235-249.
4. http://www.inchem.org/documents/sids/sids/108781.pdf **2005**.
5. http://www.inchem.org/documents/ehc/ehc/ehc192.htm **1997**.
6. Neerman, M. F.; Zhang, W.; Parrish, A. R.; Simanek, E. E. *Int. J. Pharm.* **2004**, *281*, 129-132.
7. Colby, R. W.; Mesler, R. J. Jr. *US Patent 2,819,968* **1958**.
8. Newton, G. L.; Utley, P. R. *J. Anim. Sci.* **1978**, *47*, 1338-1344.
9. Xin, H.; Stone, R. *Science 322* **2008**, 1310-1311.
10. Jeong, W. I. et al. *J. Vet. Sci.* **2006**, *7*, 299-301.
11. Burns, K. *J. Am. Vet. Med. Assoc.* **2007**, *230*, 1600-1620.
12. Osborne, C. A. et al. *Vet. Clin. North Am. Small Anim. Pract.* **2009**, *39*, 1-14.
13. http://www.fda.gov/downloads/NewsEvents/Newsroom/MediaTranscripts/UCM123617.pdf **2007**.
14. http://news.xinhuanet.com/english/2008-09/17/content-10046949.html **2008**.
15. [No authors listed] *Program Tech. Rep. Ser.* **1983**, *245*, 1-171.
16. Melnick, R. L.; Boorman, G. A.; Haseman, J. K.; Montali, R. J.; Huff, J. *Toxicol. Appl. Pharmacol.* **1984**, *72*, 292-303.
17. Ogasawara, H. et al. *Carcinogenesis* **1995**, *16*, 2773-2777.
18. Heck, H. D.; Tyl, R. W. Regul. *Toxicol. Pharmacol.* **1958**, *5*, 294-313.
19. Dixon, R. L. et al. *Toxicol. Sci.* **2008**, *106*, 251-262.

20. Yang, F.; Mao, Y.; Zhang, X.; Ma, Z.; Zhang, X. *J. Sep. Sci.* **2009**, *32*, 2974-2978.

21. Clark, R. *J. S. Afr. Vet. Med. Assoc.* **1966**, **37**, 349-351.

22. Hard, G. C.; Flake, G. P.; Sills, R. C. *Vet. Pathol.* **2009** *46*, 1248-1257.

23. Sun, N. et al. **2008**, *46*, 810-815.

24. Sun, Q. et al. *Eur. J. Pediatr.* **2009**, *169*, 483-489.

25. Jia, L. Q. et al. *Chin. Med. J. (Engl.)* **2009**, *122*, 252-256.

26. Anderson, K. M. et al. *Angew. Chem. Int. Ed. Engl.* **2008**, *47*, 1074-1078.

27. Zhu, S. L. et al. *Pediatrics* **2009**, *123*, e1099-e1102.

28. He, Y. et al. *World J. Pediatr.* **2009**, *5*, 118-121.

29. Lam, C. W. et al. *Clin. Chim. Acta* **2009**, *402*, 150-155.

30. Lam, H. S. et al. *BMJ* **2008**, *337*, a2991.

31. Wu, C. F. et al. *Clin. Chim. Acta* **2010**, *411*, 184-189.

32. Langman, C. B. et al. Pediatr. Nephrol. 2009, 24, 1263-1266.

33. Lau, H. Y.; Wong, C. S.; Ma, J. K.; Kan, E.; Siu, K. L. *Pediatr. Radiol.* **2009**, *39*, 1188-1193.

34. Gao, J. et al. *Chin. Med. J. (Engl.)* **2010**, *123*, 1112-1116.

35. Ministry of Health of the People's Republic of China. Proposed therapy for infants affected by melamine-contaminated milk powder [online], http://www.moh.gov.cn/publicfiles/business/h **2009**.

36. Grases, F. et al. *Urology* **2009**, *73*, 1262-1263.

37. Li, P.; Arman, D. H.; Wang, H.; Weng, L.; Alfooty, K.; Angawi, R. F.; Chen, B. *Cryst. Growth Des.* **2015**, *15*, 1871-1875.

38. Zhang, X. L.; Chen, X. M. *Cryst. Growth Des.* **2005**, *5*, 617-622.

39. Mihai, N. E.; Oltean, M.; Chis, V.; Leopold, N. *Vib. Spectrosc.* **2012**, *62*, 165-171.

40. Li, Z.; Chen, G.; Xu, Y.; Wang, X.; Wang, Z. *J. Phys. Chem. A* **2013**, *117*, 12511-12518.

41. Chen, J.; Lei, X.; Peng, B. *J. Opt.* **2017**, *46*, 183-186.

42. Makowski, S. J.; Lacher, M.; Schnick, W.; Lermer, C. *J. Mol. Struct.* bf 2012, *1013*, 19-25.

43. Yang, C.; Liu, Y.; Li, L.; Zhang, F. *Spectrochim. Acta, Part A* **2010**, *75*, 1329-1332.

44. Dong, W. et al. *J. Mater. Chem. B* **2019**, *7*, 4133-4140.

45. Asami, H et al. *J. Phys. Chem. B* **2014**, *118*, 4851-4857.

46. D. Chen et al. *Spectrochim Acta A Mol Biomol Spectrosc.* **2015**, *135*.

47. Sun, N. et al. *Chin. Med. J. (Engl.)* **2009**, *122*, 245-251.

48. Sun, D. Q.; Zhang, D. Q. et al. *World J. Urol.* **2009**, *28*, 603-607.

49. Zhang, L. et al. *World J. Pediatr.* **2009**, *5*, 31-35.

50. Shen, Y.; Liu, X. R. et al. *Chin. Med. J. (Engl.)* **2009**, *122*, 257-261.

51. Ngo, T. C.; Assimos, D. G. *Rev Urol.* **2007**, *9*, 17-27.

52. Frassetto, L.; Kohlstadt, I. *Am Fam Physician.* **2011**, *57*, 1234-42.

53. Yasui, T.; Sato, M.; Fujita, K.; Ito, Y.; Nomura, S.; Kohri, K. *Nephron* **2001**, *87*, 170-6.

54. Ptolemy, A. S. et al. *J. Chromatogr. B Anal. Technol. Biomed. Life Sci.* **2010**, *878*, 409-416.

55. Rodriguez, A.; Costa-Bauzá, A.; Saez-Torres, C.; Rodrigo, D.; Grases, F. *Clin. Biochem.* **2015**, *48*, 1138-1143.

56. Costa-Bauzá, A.; Grases, F.; Calvó, P.; Rodriguez, A.; Prieto, R. M. *Nutrients* **2018**, *10*, 1516.

57. Pittman, J. R. et al. *Am Fam Physician.* **1999**, *59*, 1799.

58. Li, J. V. M. et al. *Crystal Growth & Design* **2019**, *19*, 7363.

59. Wiederkehr, M .R. et al. *Clin Rev Bone Miner Metab.* **2011**, *9*, 207.

60. Choi, H. K. et al. *Arch Intern Med* **2009**, *169*, 502.

61. Naranjo, C. A. et al. *Clin Pharma col Ther* **1981**, *30*, 239.

62. Stein, H. B. et al. *Ann Intern Med.* **1976**, *84*, 385.

63. Mitch, W. E. et al. *Clinical Pharmacology and Therapeutics* **1981**, *29*, 318.

64. Berger, L. et al. *The American Journal of Medicine* **1977**, **62**, 71.

65. Sutton, J. L. et al. *Hum Nutr Appl Nutr* **1983**, *37*, 136.

66. Azzeh, F. S. et al. *PharmaNutrition* **2017**, *5*, 47.

67. Ratkalkar, V. N.; Kleinman, J. G. *Clin Rev Bone Miner Metab.* **2011**, *9*, 187-197.

68. Aggarwal, K. P.; Narula, S.; Kakkar, M.; Tandon, C. *Biomed Res Int 2013*, 292953.

69. Deshmukh, S.; Kambadakone, A.; Sahani, D. V.; Eisner, B. H. *J Urol.* **2015**, *193*, 1560-1563.

70. Robertson, W. G. *Urolithiasis.* **2017**, *45*, 43-56.

71. Ponder, J. W.; Case, D. A. *Adv. Prot. Chem.* **2003**, *27*, 27-85.

72. Lennard-Jones, J. E. *Proc. R. Soc. London, Ser. A* **1924**, *106*, 463-477.

73. van der Waals, J. D. *Verhandelingen der Koninklijke Akademie der Wetenschappen* **1893**, *1*, 1.

74. Coulomb, C. A. *Collection de ḿemoires relatifs à la physique* **1884**, Gauthier-Villars, 569-638.

75. Verlet, L. *Phys. Rev.* **1967**, *159*, 98-103.

76. Hockney, R. W. *Meth. Comp. Phys.* **1970**, *9*, 136-211.

77. Chan, E.; Griffiths, S.; Chan, C. *Lancet* **2008**, *372*, 1444.

78. Xu, Z.; Liu, Y.; Lu, L. *J. Am. Chem. Soc.* **2009**, *131*, 9496-9497.

79. Jawaid, S.; Talpur, F, N.; Sherazi, S.; Nizamani, S. M.; Khaskheli, A. A. *Food Chem.* **2013**, *141*, 3066-3071.

80. Hughes, E. W. *J. Am. Chem. Soc.* **1941**, *63*, 1737-1752.

81. Larson, A. c.; Cromer, D. T. *J. Chem. Phys.* **1974**, *60*, 185.

82. Wang, Y.; Mebel, A. M.; Wu, C.; Chen, Y.; Lin, C.; Jiang, J. *J. Chem. Soc., Faraday Trans.* **1997**, *93*, 3445-3451.

83. Petelski, A. N.; Duarte, D. J. R.; Pamies, S. C.; Peruchena, N. M. *Theo. Chem. Acc.* **2016**, *135*, 65.

84. Seto, C. T.; Whitesides, G. M. *J. Am. Chem. Soc.* **1993**, *115*, 905-914.

85. Vella-Zarb, L.; Baisch, U. *Cryst. Eng. Comm.* **2014**, *16*, 8147-8159.

86. Shen, Z.; Wang, T.; Liu, M. *Chem. Comm.* **2014**, *50*, 2096-2099.

87. Ma, M.; Bong, D. *Langmuir* **2011**, *27*, 8841-8853.

88. Zhang, X. L.; Chen, X. M. *Crystal Growth & Design* **2005**, *5*, 617-622.

89. Whitesides, G. M.; Simanek, E. E.; Mathias, J. P.; Seto, C. T.; Chin, D. N.; Mammen, M.; Gordon, D. M. *Acc. Chem. Res* **1995**, *28*, 37-44.

90. Ranganathan, A.; Pedireddi, V. R.; Rao, C. N. R. *J. Am. Chem. Soc.* **1999**, *121*, 1752-1753.

91. Ciesielski, A.; Haar, S.; Paragi, G.; Kupihr, Z.; Kele, Z.; Masiero, S.; Guerra, C. F.; Bickelhaupt, F. M.; Spada, G. P.; Kovcs, L.; Samor, P. *Phys. Chem. Chem. Phys.* **2013**, *15*, 12442-12446.

92. Mathias, J. P.; Simanek, E. E.; Zerkowski, J. A.; Seto, Ch. T.; Whitesides, G. M. *J. Am. Chem. Soc.* **1994**, *116*, 4316-4325.

93. Zerkowski, J. A.; Whitesides, G. M. *J. Am. Chem. Soc.* **1994**, *116*, 4298-4304.

94. Zerkowski, J. A.; Seto, C. T.; Wierda, D. A.; Whitesides, G. M. *J. Am. Chem. Soc.* **1990**, *112*, 9025-9026.

95. Zerkowski, J. A.; MacDonald, J. C.; Seto, C. T.; Wierda, D. A.; Whitesides, G. M. *J. Am. Chem. Soc.* **1994**, *116*, 2382-2392.

96. Tukada, H.; Mazaki, Y. *Chem. Lett.* **1997**, *26*, 441.

97. Lange, R. F. M.; Beijer, F. H.; Sijbesma, R. P.; Hooft, R. W. W.; Kooijman, H.; Spek, A. L.; Kroon, J.; Meijer, E. W. *Angew. Chem. Int. Ed. Engl.* **1997**, *36*, 969-971.

98. Zhang, Y. G.; Li, J. M.; Nishiura, M.; Imamoto, T. *Chem. Lett.* **1999**, 543.

99. Staniec, P. A.; Perdigo, L. M. A.; Rogers, B. L.; Champness, N. R.; Beton, P. H. *J. Phys. Chem. C* **2007**, *111*, 886-893.

100. Zhang, H, Pei, Z. K,Xie, Z; Long, L.; Mao, B. W.; Xu, X.; Zheng, L. *J. Phys. Chem. C* **2009**, *113* , 13940-13946.

101. Shi, H.; Wang, W.; Li, Z.; Wang, L.; Shao, X. *Chinese Journal of Chemical Physics* **2017**, *30*, 443.

102. Silly, F.; Shaw, A. Q.; Castell, M. R.; Briggs, G. A. D.; Mura, M.; Martsinovich, N.; Kantorovich, L. *J. Phys. Chem. C* **2008**, *112*, 11476-11480.

103. Wang, L.; Li, P.; Shi, H.; Li, Z.; Wu, K.; Shao, X. *J. Phys. Chem. C* **2017**, *121*, 7977-7984.

104. Schmitz, H. C.; Ikonomov, J.; Sokolowski, M. *Surface Science* **2011**, *605*, 1-6.

105. Lin, Y.; Ourdjini, O.; Giovanelli, L.; Clair, S.; Faury, T.; Ksari, Y.; Themlin, JM.; Porte, L.; Abel, M. *J. Phys. Chem. C* **2013**, *117*, 3895-9902.

106. Zhang, X.; Chen, T.; Chen, Q.; Wang, L.; Wan, L. J. *Phys. Chem. Chem. Phys.* **2009**, *11*, 7708-7712.

107. Wen, J.; Ma, J. *J. Phys. Chem. C* **2012**, *116*, 8523-8534.

108. Saigusa, H.; Nakamura, D.; Urashima, S. *Phys. Chem. Chem. Phys.* **2015**, *17*, 23026.

109. Fenoglio, R. L. M. *OXICOLOGICAL SCIENCES* **2008**, *106*, 251-262.

110. Peng, J.; Li, D.; Chan, K. Y.; Chen, Y.; Lamb, J. R.; Tam, P. K. H.; El-Nezami, H. *Nephrol Dial Transplant* **2012** , *27*, 2225-2231.

111. Ingelfinger, *N. Engl. J. Med.* **2008**, *359*, 2745-2748.

112. Sharma, K.; Paradakar, M. *Food Secur.* **2010**, *2*, 97-107.

113. Skinner, C. G.; Thomas, J. D. Osterloh, J. D. *J. Med. Toxicol.* **2010**, *6*, 50-55.

114. Reimschuessel, R.; Puschner, B. *J. Med. Toxicol.* **2010**, *6*, 468-469.

115. Balabin, R. M.; Smirnov, S. V. *Talanta* **2006**, *85*, 562.

116. Wong, S.; Chiu, M. *HK J Paediatr (New Series)* **2008**, *13*, 230-234.

117. Mauer, L. J.; Chernyshova, A. A.; Hiatt, A.;, Deering, A.; Davis, R. *J. Agric. Food Chem.* **2009**, *57*, 3974.

118. Ma, P.; Liang, F.; Sun, Y.; Jin, Y.;, Chen, Y.; Wang, X.; Zhang, H.; Gao, D.; Song, D. *Microchim. Acta* **2013**, *180*, 1173.

119. Ying, Y. *J. Food Eng.* **2014**, *124*, 97.

120. Guan, H. *Food Control* **2013**, *32*, 35-41.

121. Cook, H. A. *Electrophoresis* **2005**, *26*, 1576-1583.

122. Mura, M.; Martsinovich, N.; Kantorovich, L. *Nanotechnology* **2008**, *19*, 46.

123. Wang, J. *New J. Chem.* **2017**, *41*, 10899-10907.

124. Chapman, R. P.; Averell, P. R.; Harris, R. R. *Ind. Eng. Chem.* **1943**, *35*, 137-138.

125. Li, P.; Arman, D. H.; Wang, H.; Weng, L.; Alfooty, K.; Angawi, R. F.; Chen. B. *Crystal Growth & Design* **2015**, *15*, 1871-1875.

126. Ahromi, A. J.; Moosheimer, U.; *Macromolecules* **2000**, *33*, 7582-7587.

127. Zhang, X. L.; Chen, X. M.; *Crystal Growth & Design* **2005**, *5*, 617-622.

128. Barzi, D.; Mohnani, S.; Llanes-Pallas, A. *Chem. Eur. J.* **2009**, *15*, 7004-7025.

129. Mircescu, N. E.; Oltean, M.; Chis, Vasile.; Leopold, N. *Vib. Spectrosc.* **2012**, *62*, 165-171.

130. Li, Z.; Chen, G.; Xu, Y.; Wang, X.; Wang, Z. *J. Phys. Chem. A* **2013**, *117*, 12511-12518.

131. Mammen, M.; Shakhnovich, E. I.; Deutch, J. M.; Whitesides, G. M. *J. Org. Chem.* **1998**, *63*, 3821-3830.

132. Cox, E. G.; Jeffrey, G. A. Proceedings A, Rsc. **1951**, *207*.

133. Shafaghi, S. *Journal of Applied Polymer Science* **2014**, *131*.

134. Chen, J.; Lei, X.; Peng, B. *J. Opt.* **2017**, *46*, 183-186.

135. Makowski. S. J.; Lacher. M.; Schnick. W. *J. Mol. Struct.* **2012**, *1013*, 19-25.

136. C. Yang.; Liu. Y. *Spectrochim. Acta A* **2010**, *75*, 1329-1332.

137. Li, D.; Cheng, K.; Jia, G. *J. Mol. Liq.* **2017**, *244*, 182-188.

138. Frisch, J. M.; Trucks, G. W. Gaussian 09, Revision A.02.

139. Case, D. A.; Darden, T. A.; Cheatham, T. E., III; Simmerling, C. L.; Wang, J.; Duke, R. E.; Luo, R.; Walker, R. C.; Zhang, W.; Kollman, P. A. *AMBER 12*; University of California: San Francisco, **2012**.

140. Bayly, C. I.; Cieplak, P.; Cornell, W. D.; Kollman, P. A. A. *J. Phys. Chem.* **1993**, *97*, 10269-10280.

141. Wang, J.; Wang, W.; Kollman, P. A.; Case, D. A. *J. Mol. Graphics Modell.* **2006**, *25*, 247-260.

142. Wang, J.; Wolf, R. M.; Caldwell, J. W.; Kollman, P. A.; Case, D. A. *J. Comput. Chem.* **2004**, *25*, 1157-1174.

143. Jorgensen, W. L.; Chandrasekhar, J.; Madura, J. D.; Impey, R. W.; Klein, M. L. *J. Chem. Phys.* **1983**, *79*, 926-935.

144. Martinez, L.; Andrade, R.; Birgin, E. G.; Martinez, J. M. *J Comput Chem.* **2009**, *30*, 2157-2164.

145. Hunenberger, P. H.; *Adv. Polym. Sci.* **2005**, *173*, 105-149.

146. Berendsen, H. J. C.; Postma, J. P. M.; van Gunsteren, W. F.; DiNola, A.; Haak, J. R. *J. Chem. Phys.* **1984**, *81*, 3684-3690.

147. Essmann, U.; Perera, L.; Berkowitz, M. *J. Chem. Phy.* **1995**, *103*, 8577.

148. Ryckaert, J. P.; Ciccotti, G.; Berendsen, H. J. C. *J. Comput. Phys.* **1977**, *23*, 327-341.

149. Humphrey, W.; Dalke, A.; Schulten, K. *J. Mol. Graphics* **1996**, *14*, 33-38.

150. Torrie, G. M.; Valleau, J. P. *J. Comput. Phys.* **1977**, *23*, 187-199.

151. Kumar, S.; Bouzida, D.; Swendsen, R. H.; Kollman, P. A.; Rosenberg, J. M. *J Comput Chem.* **1992**, *13*, 1011-1021.

152. D'Angelo, P.; Serva, A.; Aquilanti, G.; Pascarelli, S.; Migliorati. V. *J. Phys. Chem. B* **2015**, *119*, 14515-14526.

153. Serva. A.; Migliorati, V.; Lapi, A.; Aquilanti, G.; Arcovitod. A.; D'Angelo, P. *Phys. Chem. Chem. Phys.* **2016**, *18*, 16544-16554.

154. Paul, S.; Paul, S. *J. Phys. Chem. B* **2015**, *119*, 1598-1610.

155. Luzer, A.; Chandler, D. *Phys. Rev. Lett.* **1996**, *76*, 928-931

156. Balasubramanian, S.; Pal, S; Bagchi, B. *Phys. Rev. Lett.* **2002**, *89*, 115505.

157. Chandra, A. *J. Phys. Chem. B* **2003**, *107*, 3899-3906.

158. Brehm, M.; Kirchner, B. *J. Chem. Inf. Mod.* **2011**, *51*, 2007-2023.

159. Smith, P. E. *J. Phys. Chem. B* **2006**, *110*, 2862-2868.

160. Pierce, V.; Kang, M.; Aburi, M.; Weerasinghe, W.; Smith, P. E. *Cell Biochem. Biophys.* **2008**, *1*, 1-22.

161. Bandyopadhyay, D.; Bhanja, K.; Mohan, S.; Ghosh, S. K.; Choudhury, N. *J. Phys. Chem. B* **2015**, *119*, 11262-11274.

162. Choudhury, N.; Pettitt, B. M.; *J. Phys. Chem. B* **2006**, *110*, 8459-8463.

163. Mishra, B. K.; Arey, J. S.; Sathyamurthy, N.*J. Phys. Chem. A* **2010**, *114*, 9606-9616.

164. Johnson. E. R.; Mori-Sanchez. P.; Garca. J. C.; Cohen. A. J.; Yang. W. *J. Am. Chem. Soc.* **2010**, *132*, 6498-6506.

165. Lu. T.; Chen. F. *J. Comput. Chem.* **2012**, *33*, 580-592.

166. G. C. Rubena, G. C. et al. *J. Non-Cryst. Solids* **1995**, *186*, 219.

167. Hughes, E. W. *J. Am. Chem. Soc.* **1941**, *63*, 1737.

168. Seto, C. T. et al. *J. Am. Chem. Soc.* **1993**, *115*, 905.

169. Zerkowski, J. A. et al. *J. Am. Chem. Soc.* **1994**, *116*, 2382.

170. Tukada, H. *chem. Lett.* **1997**, *26*, 441.

171. Schmidt, W. F. et al. *Crystals* **2015**, *69*, 398.

172. Zi-Yi Du et al. *J. Mol. Struct* **2013**, *1035*, 183.

173. Shelton, H. et al. *Crystals* **2018**, *8*, 265.

174. Chattaraj, K. G.; Paul, S. *J. Chem. Inf. Model.* **2018**, *58*, 1610.

175. Vanommeslaeghe, K. et al. *J. Comput. Chem.* **2010**, *31*, 671.

176. Kale, L. et al. *J. Comput. Phys.* **1999**, *151* 283.

177. Li, D. et al.*J. Mol. Liq.* **2017**, *244*, 182.

178. Sharma, B. et al. *J. Chem. Phys.* **2013**, *139*, 194504.

179. Sharma, B. et al. *J. Phys. Chem. B.* **2015**, *119*, 6421.

180. Paul, S. *Mol. Phy.* **2016**, *114*, 2098.

181. Paul, S. *RSC Advances* **2014**, *4*, 34267.

182. Patra, M. et al. *J. Comput. Chem.* **2004**, *25*, 678.

183. Perdigao, L. M. A. et al. *Chem. Commun.* **2006**, 538-540.

184. Smith, J. et al. *J. Am. Chem. Soc.* **1998**, *120*, 9401-9409.

185. Jayaram, B. et al. *J. Phys. Chem. B* **1998**, *102*, 9571-9576.

186. Kasimova, A. O. et al. *J. Phys. Chem. B* **2012**, *116*, 4338-4345.

187. Sanner, M. F. et al. *Biopolymers* **1996**, *38*, 305.

188. Das, S et al. *J. Phys. Chem. B* **2017**, *121*, 8774-8785.

189. Das, S et al. *J. Chem. Inf. Model.* **2017**, *57*, 1461.

190. Das, S et al. *PLoS One* **2018**, *13*, e0190209.

191. Das, S et al. *J. Phys. Chem. B* **2016**, *120*, 3540.

192. Das, S et al. *J. Phys. Chem. B* **2016**, *120*, 173.

193. Paul, R et al. *Phys. Chem. Chem. Phys.* **2018**, *20*, 16540.

194. Weerasinghe, S. et al. *J. Phys. Chem. B* **2003**, *107*, 3891-3898.

195. Ganguly, P. et al. *J. Chem. Theory Comput.* **2013**, *9*, 1347-1355.

196. Schnell, S. K. et al. *J. Phys. Chem. B* **2011**, *115*, 10911-10928.

197. Chattaraj, K. G. et al. *J. Chem. Phys.* **2019**, *150*, 064501.

198. Shi, X. et al. *Phys. Chem. Chem. Phys.* **2018**, *20*, 1005.

199. Ma, X. et al. *Chemosphere* **2019**, *214*, 781.

200. Ringertz, H. *Acta Cryst.* **1966**, *20*, 397-403.

201. Toxicological and Health Aspects of Melamine and Cyanuric Acid, WHO, Geneva, (2009).

202. Brikowski, T. H.; Lotan, Y.; Pearle, M. S. *Proc Natl Acad Sci U S A* **2008**, *105* (28), 9841-9846.

203. Grases, F.; Rodriguez, A.; Costa-Bauzá, A. *PLoS One* **2014**, *9* (10), e111184.

204. Grases, F.; Costa-Bauzá, A.; Prieto, R. M. *Nutr J.* **2006**, *5* (23), DOI:10.1186/1475-

205. Grases, F.; Costa-Bauzá, A.; Gomila, I.; Ramis, M.; Garca-Raja, A.; Prieto, R. M. *Urol Res* **2011**, *40* (1), 41-46.

206. Guan, N.; Fan, Q.; Ding, J.; Zhao, Y.; Lu, J.; Ai, Y.; Xu, G.; Zhu, S.; Yao, C.; Jiang, L. *et al. N. Engl. J. Med.* **2009**, *360* (11), 1067-1074.

207. Chattaraj, K. G.; Paul, S. *J. Chem. Phys.* **2019**, *151* (5), 054503.

208. Grases, F.; Villacampa, A. I.; Costa-Bauzá, A.; Sőhnel, O. *Clin. Chim. Acta* **2000**, *302* (1-2), 89-104.

209. Jahromi, S.; Moosheimer, U. *Macromolecules* **2000**, *33* (20), 7582-7587.

210. Concellón, A.; Schenning, A. P. H. J.; Romero, P.; Marcos, M.; Serrano, J. L. *Macromolecules* **2018**, *51* (6), 2349-2358.

211. Blackwell, J.; Lieser, G.; Gutierrez, G. A. *Macromolecules* **1983**, *16* (9), 1418-1422.

212. Liao, Y.; Weber, J.; Faul, C. F. J. *Macromolecules* **2015**, *48* (7), 2064-2073.

213. Moreno, K. X.; Simanek, E. E. *Macromolecules* **2008**, 41 (12), 4108-4114.

214. Song, P.; Xu, Z.; Lu, Y.; Guo, Q. *Macromolecules* **2015**, *48* (12), 3957-3964.

215. Herbst, F.; Schröter Klaus; Gunkel, I.; Gröger Stefan; Thurn-Albrecht, T.; Balbach, J.; Binder, W. H. *Macromolecules* **2010**, *43* (23), 10006-10016.

216. Lalwani, S.; Chouai, A.; Perez, L. M.; Santiago, V.; Shaunak, S.; Simanek, E. E. *Macromolecules* **2009**, *42* (17), 6723-6732.

217. Seto, C. T.; Whitesides, G. M. *J. Am. Chem. Soc.* **1993**, *115* (4), 1330-1340.

218. Seto, C. T.; Mathias, J. P.; Whitesides, G. M. *J. Am. Chem. Soc.* **1993**, *115* (4), 1321-1329.

219. Macdonald, J. C.; Whitesides, G. M. *Chem. Rev.* **1994**, *94* (8), 2383-2420.

220. Whitesides, G.; Mathias, J.; Seto, C. *Science* **1991**, *254* (5036), 1312-1319.

221. Barberá, J.; Puig, L.; Romero, P.; Serrano, J. L.; Sierra, T. *J. Am. Chem. Soc.* **2006**, *128* (13), 4487-4492.

222. Zhang, W.; Gonzalez, S. O.; Simanek, E. E. *macromolecules* **2002**, *35* (24), 9015-9021.

223. Latosińska, J. N.; Latosińska, M.; Olejniczak, G. A.; Seliger, J.; Žagar, V. *J. Chem. Inf. Model.* **2014**, *54* (9), 2570-2584.

224. Craig, W. J.; Nguyen, T. T. *J Food Sci* **1984**, *49* (1), 302-303.

225. Parkin, S.; Hope, H. *Acta Cryst.* **1998**, *B54* (1), 339-344.

226. Case, D.A.; Babin, V.; Berryman, J. T.; Betz, R. M.; Cai, Q.; Cerutti, D. S.; Cheatham III, T. E.; Darden, T. A.; Duke, R. E.; Gohlke, H. *et al.* AMBER 14; University of California: San Francisco, 2014.

227. Miller, B. R.; Mcgee, T. D.; Swails, J. M.; Homeyer, N.; Gohlke, H.; Roitberg, A. E. *J. Chem. Theory Comput.* **2012**, *8* (9), 3314-3321.

228. Kästner, J. *WIREs Comput. Mol. Sci.* 2011, *1* (6), 932-942.

229. Kumar, S.; Rosenberg, J. M.; Bouzida, D.; Swendsen, R. H.; Kollman, P. A. *J. Comput. Chem.* **1992** , *13* (8), 1011-1021.

230. Souaille, M.; Roux Benoit. *Comput. Phys. Commun.* **2001**, *135* (1), 40-57.

231. An, Y.; Singh, S.; Bejagam, K. K.; Deshmukh, S. A. *Macromolecules* **2019**, *52* (13), 4875-4887.

232. Sharma, B.; Paul, S. *J. Chem. Phys.* **2013**, *139* (19), 194504.

233. Paul, S.; Paul, S. *J. Chem. Phys.* **2013**, *139* (4), 044508.

234. Pagnotta, S.; Ricci, M.; Bruni, F.; Mclain, S.; Magaz, S. *Chem. Phys.* **2008**, *345* (2-3), 159-163.

235. Sarma, R.; Paul, S. *J. Chem. Phys.* **2012**, *137* (11), 114503.

236. Sarma, R.; Paul, S. *J. Chem. Phys.* **2012**, *137* (9), 094502

237. Sarma, R.; Paul, S. *J. Chem. Phys.* **2012**, *136* (11), 114510.

238. Sarma, R.; Paul, S. *J. Chem. Phys.* **2011**, *135* (17), 174501.

239. Paul, S. *Mol. Phys.* **2016**, *114* (13), 2098-2107.

240. Gupta, R.; Patey, G. N. *J. Phys. Chem. B* **2011**, *115* (51), 15323-15331.

241. Gupta, R.; Patey, G. N. *J. Chem. Phys.* **2012**, *137* (3), 034509.

242. Gupta, R.; Patey, G. *J. Mol. Liq.* **2013**, *177*, 102109.

243. Bandyopadhyay, D.; Kamble, Y.; Choudhury, N. *J. Phys. Chem. B* **2018**, *122* (34), 8220-8232.

244. Chopra, M.; Choudhury, N. *J. Mol. Liq.* **2016**, *224*, 599-606.

245. Bharadwaj, S.; van der Vegt, N. F. A. *Macromolecules* **2019**, *52* (11), 4131-4138.

246. Vasumathi, V.; Maiti, P. K. *Macromolecules* 2010, *43* (19), 8264-8274.

247. Posocco, P.; Ferrone, M.; Fermeglia, M.; Pricl, S. *Macromolecules* **2007**, *40* (6), 2257-2266.

248. Elder, R. M.; Emrick, T.; Jayaraman, A. *Biomacromolecules* **2011**, *12* (11), 3870-3879.

249. Sevgen, E.; Dolejsi, M.; Nealey, P. F.; Hubbell, J. A.; Pablo, J. J. D. *Macromolecules* **2018**, *51* (23), 9538-9546.

250. Gehrke, S.; Domaros, M. V.; Clark, R.; Hollczki, O.; Brehm, M.; Welton, T.; Luzar, A.; Kirchner, B. *Faraday Discuss.* **2018**, *206*, 219-245.

251. Choudhuri, J. R.; Chandra, A. *J. Chem. Phys.* **2018**, *148* (2), 024702.

252. Choudhuri, J. R.; Chandra, A. *J. Chem. Phys.* **2014**, *141* (13), 134703.

253. Borgohain, G.; Paul, S. *J. Phys. Chem. B* **2016**, *120* (9), 2352-2361.

254. Borgohain, G.; Mandal, B.; Paul, S. *Phys. Chem. Chem. Phys.* **2017**, *19* (20), 13160-13171.

255. Elder, R. M.; Jayaraman, A. *J. Chem. Phys.* **2014**, *140* (15), 155103.

256. Zhong, J.; Tang, N.; Asadzadeh, B.; Yan, W. *J. Chem. Eng. Data* **2017**, *62* (9), 2672-2677.

257. Callahan, M. P.; Gengeliczki, Z.; Svadlenak, N.; Valdes, H.; Hobza, P.; Vries, M. S. D. *Phys. Chem. Chem. Phys.* **2008**, *10* (19), 2819.

258. Mustan, F.; Ivanova, A.; Madjarova, G.; Tcholakova, S.; Denkov, N. *J. Phys. Chem. B* **2015**, *19* (51), 15631-15643.

259. Li, Q.; Song, P.; Wen, J. *J. Curr. Opin. Food Sci.* **2019**, *30*, 79.

260. Guan, X.; Deng, Y. *Int. J. Surg* **2016**, *36*, 613.

261. López, F. J. G; Quereda, C. *Kidney Int.* **2011**, *80*, 694.

262. Zisman, A. L. *CJASN* **2017**, *12*, 1699-1708.

263. Chen, W-C. *et al. J. Agric. Food Chem.* **2012**, *60*, 2753-2757.

264. Tsai, T. H.; Thiagarajan, S.; Chen, S. M. *J. Agric. Food Chem.* **2010**, *58*, 4537-4544.

265. Kim, C. H. *et al. Chem. Res. Toxicol.* **2010**, *23*, 220-227.

266. Sun, N.; Shen, Y.; He, L. *N. Engl. J. Med.* **2010**, *362*, 662-664.

267. V-Santos, A. B.; Neogi, T. *Am J Kidney Dis.* **2017**, *70*, 422.

268. B. H. S. Pai, B. H. S.; Swarnalatha, G.; Ram, R.; Dakshinamurty, K. V. *Indian J Nephrol.* **2013**, *23*, 280.

269. Iqbal, M.; Ezzeldin, E.; Herqash, R. N.; Alam, O. *PLoS ONE* **2019**, *14*, e0213786.

270. Pacher, P.; Nivorozhkin, A.; Szabó, C. *Pharmacol Rev.* **2006**, *58*, 87.

271. Terkeltaub, R. *Nat Rev Rheumatol* **2010**, *6*, 30.

272. Chong, D. P. *Can. J. Chem* **2013**, *6*, 637.

273. Gibson, T.; Rodgers, V.; Potter, C.; Simmonds, H. A. *Ann. Rheum.* **1982**, *41*, 59.

274. Kanbay, M.; Solak, Y.; Gaipov, A.; Takir, M.; Weiner, D. E. *Blood Purif* **2014**, *37*, 172.

275. Vries, A. D.; Frank, M.; Liberman, U. A.; Sperling, O. *Ann. rheum. Dis.* **1966**, *25*,

276. Dew, T. P.; Day, A. J.; Morgan, M. R. A. *J. Agric. Food Chem.* **2005**, *53*, 6510-6515.

277. Li, H.; Zhao, M.; Su, G.; Lin, L.; Yong Wang, Y. *J. Agric. Food Chem.* **2016**, *64*, 4725-4734.

278. Makhdoumi, P.; Karimi, H.; Khazaei, M. *Chem. Res. Toxicol* **2020**, *33*, 2503-2514.

279. Wauchope, O. R.; Beavers, W. N.; Galligan, J. J.; Mitchener, M. M.; Kingsley, P. J.; Marnett, L. J. *Chem. Res. Toxicol* **2015**, *28*, 2334-2342.

280. Zeron, I. M.; Abascal, J. L. F.; Vega, C. *J. Chem. Phys.* **2019**, *151*, 134504.

281. Svishchev, I. M.; Kusalik, P. G. *J. Chem. Phys.* **1993**, *99*, 3049-3058

282. Chattaraj, K. G.; Paul, S. *J. Phys. Chem. B* **2019**, *123*, 10483-10504.

283. Bandara, A.; Panahi, A.; Pantelopulos, G. A.; Straub, J. E. *J. Comput. Chem* **2017**, *38*, 1479-1488.

284. Kulshreshtha, A.; Jayaraman, A. *Macromolecules* **2020**, *53*, 13021313.

285. Ganguly, P.; Boserman, P.; van der Vegt, N. F. A.; Shea, J-E. van der Vegt, N. F. A. *J. Am. Chem. Soc* **2018**, *140*, 483-492.

286. Ganguly, P.; Shea, J-E. *J. Phys. Chem. Lett.* **2019**, *10*, 7406-7413.

287. S. N. Bejagam, M. S. Fonari, B. B. Averkiev, V. N. Khrustalev, J. Lindline, and T. V. Timofeeva, Cryst. Growth Des. **17**, 4237 (2017).

288. Chandra, A. *Phys. Rev. Lett.* **2000**, *85*, 768-771.

289. Chandra, A. *J. Phys. Chem. B* **2003**, *107*, 3899-3906.

290. Indra, S.; Biswas, R. *J. Phys. Chem. B* **2016**, *120*, 11214-11228.

291. Vasumathi, V.; Maiti, P. K. *Macromolecules* **2010**, *43*, 8264-8274.

292. Jain, V.; Maiti, P. K.; Bharatam, P. V. *J. Chem. Phys.* **2016**, *145*, 124902.

293. Chowdhury, R.; Nandi, S.; Halder, R.; Jana, B.; Bhattacharyyaa, K. *J. Chem. Phys.* **2016**, *144*, 065101.

294. Levine, Z. A.; Teranishi, K.; Okada, A. K.; Langen, R.; Shea, J-E. *J. Am. Chem. Soc* **2019**, *141*, 14168-14179.

295. Li, J.; Beuerman, R.; Verma, C. *J. Chem. Phys.* **2018**, *148*, 104902.

296. Espinosa, J. R.; Vega, C.; Valeriani, C.; Sanz, E. *J. Chem. Phys.* **2016**, *144*, 034501.

297. Espinosa, J. R.; Vega, C.; Valeriani, C.; Sanz, E. *J. Chem. Phys.* **2015**, *142*, 194709.

298. Bag, S.; Maingi, V.; Maiti, P. K.; Yelk, J.; Glaser, M. A.; Walba, D. M.; Clark, N. A. *J. Chem. Phys.* **2015**, *143*, 144505.

299. Alelign, T.; Petros , B. *Adv Urol.* **2018**, *2018*, 3068365.

300. Zisman, A. L. *CJASN* **2017**, *12*, 1699-1708.

301. Xu, S. F.; Lu, H. Z. *Biosens. Bioelectron.* **2015**, *73*, 160-166.

302. Cameron, M.; Maalouf, N. M.; Poindexter, J.; Adams-Huet, B.; Sakhaee, K.; Moe, O. W. *Kidney Int.*, **2012**, *81*, 1123-1130.

303. Peng, B.; Li, G.; Li, D.; Dodson, S.; Zhang, Q.; Zhang, J.; Lee, Y. H.; Demir, H. V.; Ling, X. Y.; Xiong, Q. *ACS Nano* **2013**, *7*, 5993-6000.

304. P. M. Ferraro, P. M.; Curhan, G. C. *Am. J. Kidney Dis.* **2017**, *70*, 158-159.

305. Niu, C.; Liu, Q.; Shang, Z.; Zhao, L.; Ouyang, J. *Nanoscale* **2015**, *7*, 8457-8465.

306. Hall, V. M.; Thornton, A.; Miehls, E. K.; Bertke, J. A.; Swift, J. A. *Cryst. Growth Des.* **2019**, *19*, 7363-7371.

307. Joung, I. S.; Cheatham, T. E III *J. Phys. Chem. B* **2008**, *112*, 9020-9041.

308. Y. Xue, H. Zhao, Z. Wu, X. Li, Y. He and Z. Yuan, *Biosens. Bioelectron.*, 2011, **29**, 102.

309. Y. Li, G. Ran, W. J. Yi, H. Q. Luo and N. B. Li, *Microchim. Acta*, 2012, **178**, 115.

310. Z. Wang, J. Xia, L. Zhu, F. Zhang, X. Guo, Y. Li, Y. Xia, *Sens. Actuators B-Chem.*, 2012, **161**, 131.

311. J. Song, J. Qiao, S. Shuang, Y. Guo, and C. Dong, *J. Mater. Chem.*, 2012, **22**, 602.

312. F. Li, J. Chai, H. Yang, D. Han and L. Niu, *Talanta*, 2010, **81**, 1063.

313. Flory, P. J. *J. Chem. Phys.* **1942**, *10*, 51.

314. Huggins, M. L. *J. Chem. Phys.* **1941**, *9*, 440.

315. Huynh, L. *Pharm. Res.* **2008**, *25*, 147.

316. Case, F. H. *Polym. Sci.* **1994**, *2*, 256.

317. Patel, S. et al. *Biomacromolecules* **2008**, *9*, 3014.

318. Held, C. et al. *Ind. Eng. Chem. Res.* **2019**, *58*, 7362.

319. Yang, X. et al. *J. Phys. Chem. C* **2008**, *112*, 17554.

320. SreeHarsha, N. et al. *Int J Nanomedicine.* **2019**, *14*, 7419.

321. Gao, J. ey al. *Chem. Mater.* **2010**, *22*, 2213.

322. Held, C. et al.*Ind. Eng. Chem. Res.* **2019**, *58*, 21761.

323. Randviir, E. P.; Brownson, D. A. C.; Banks, C. E. *Mater. Today* **2014**, *17*, 426-432.

324. Georgakilas, V.; Tiwari, J. N.; Kemp, K. C.; Perman, J. A.; Bourlinos, A. B.; Kim, K. S.; Zboril, R. *Chem. Rev.* **2016**, *116*, 5464-5519.

325. Yin, P. T.; Shah, S.; Chhowalla, M.; Lee, K.-B. *Chem. Rev.* **2015**, *115*, 2483-2531.

326. Dikin, D. A.; Stankovich, S.; Zimney, E. J.; Piner, R. D.; Dommett, G. H. B.; Evmenenko, G.; Nguyen, S. T.; Ruoff, R. S. *Nature* **2007**, *448*, 457-460.

327. Markovic, Z. M.; Harhaji-Trajkovic, L. M.; Todorovic-Markovic, B. M.; Kepic, D. P.; Arsikin, K. M.; Jovanovic, S. P.; Pantovic, A. C.; Dramicanin, M. D.; Trajkovic, V. S. *Biomaterials.* **2011**, *32*, 1121-1129.

328. Bitounis, D.; Ali-Boucetta, H.; Hong, B. H.; Min, D.-H.; Kostarelos, K. *Adv. Mater.* **2013**, *25*, 2258-2268.

329. Feng, L.; Wu, L.; Qu, X. *Adv. Mater.* **2013**, *25*, 168-186.

330. Robinson, J. T.; Tabakman, S. M.; Liang, Y.; Wang, H.; Casalongue, H. S.; Daniel, [illegible] H. *J. Am. Chem. Soc.* **2011**, *133*, 6825-6831.

331. Ying Wang, Y.; Chen, Z.; Wu, Z.; Li, Y.; Yang, W.; Li, Y. *Langmuir* **2018**, *34*, 7797-7804.

332. Ward, S. W.; Abeykoon, P. G.; McDermott, S. T.; Adamson, D. H. *Langmuir* **2020**, *36*, 10421-10428.

333. Zhang, L.; Zhang, Z.; He, C.; Dai, L.; Liu, J.; Wang, L. *ACS Nano* **2014**, *8*, 6663-6670.

334. Alhassan, S. M.; Qutubuddin, S.; Schiraldi, D. A. *Langmuir* **2012**, *28*, 4009-4015.

335. Novoselov, K. S.;Geim, A. K.;Morozov, S. V.;Jiang, D.;Zhang, Y.;Dubonos, S. V.; Grigorieva, I. V.;Firsov, A. A.*Science***2004**,*306*,666-669.

336. Balandin, A. A.;Ghosh, S.;Bao, W.;Calizo, I.;Teweldebrhan, D.;Miao, F.;Lau, C. N. *Nano Lett.***2008**,*8*,902-907.

337. Lee, C.;Wei, X.;Kysar, J. W.;Hone, J.*Science***2008**,*321*,385-388.

338. Cui, X.; Zhang, C. Z.; Hao, R.; Hou, Y. L. *Nanoscale* **2011**, *3*, 2118-2126.

339. Coleman, J. N. *Acc. Chem. Res.* **2013**, *46*, 14-22.

340. Chen, D.; Feng, H.; Li, J. *Chem. Rev.* **2012**, *112*, 6027-6053.

341. Boukhvalov, D. W.; Katsnelson, M. I. *J. Am. Chem. Soc.* **2008**, *130*, 10697-10701.

342. Quintana, M.; Vazquez, E.; Prato, M. *Acc. Chem. Res.* **2013**, *46*, 138-148.

343. Georgakilas, V.; Otyepka, M.; Bourlinos, A. B.; Chandra, V.; Kim, N.; Kemp, K. C.; Hobza, P.; Zboril, R.; Kim, K. S. *Chem. Rev.* **2012**, *112*, 6156-6214.

344. Parviz, D.; Das, S.; Ahmed, H. S. T.; Irin, F.; Bhattacharia, S.; Green, M. J. *ACS Nano* **2012**, *6*, 8857-8867.

345. Kozlov, S. M.; Vines, F.; Goerling, A. *Adv. Mater.* **2011**, *23*, 2638.

346. Saikia, N.; Pandey, R. *J. Phys. Chem. C* **2018**, *122*, 3915-3925.

347. Leon, V.; Rodriguez, A. M.; Prieto, P.; Prato, M.; Vazquez, E. *ACS Nano* **2014**, *8*, 10735-10741.

348. Leo/n, V.; Quintana, M.; Herrero, M. A.; Fierro, J. L. G.; de la Hoz, A.; Prato, M.; Va/zquez, E. *Chem. Commun.* **2011**, *47*, 10936-10938.

349. Uemura, S.; Aono, M.; Komatsu, T.; Kunitake, M. *Langmuir* **2011**, *27*, 1336-1340.

350. Eichhorn, J.; Schløgl, S.; Lotsch, B. V.; Schnick, W.; Heckl, W. M.; Lackinger, M. *CrystEngComm* **2011**, *13*, 5559-5565.

351. Uemura, S.; Aono, M.; Sakata, K.; Komatsu, T.; Kunitake, M. *J. Phys. Chem. C* **2013**, *117*, 24815-24821.

352. Lin, Y. P.; Ourdjini, O.; Giovanelli, L.; Clair, S.; Faury, T.; Ksari, Y.; Themlin, J. M.; Porte, L.; Abel, M. *J. Phys. Chem. C* **2013**, *117*, 9895-9902.

353. Simenas, M.; Tornau, E. E. *J. Chem. Phys.* **2014**, *141*, 054701.

354. Zhu, L.; Xu, X.; Wang, Y. A. N.; Liu, S.; Ling, J. I. E.; Liu, L.; Wei, S.; Cai, F.; Wang, Z.; Liu, X.; Wang, L. I. *Surf. Rev. Lett.* **2014**, *21*, 1450035.

355. Rodriguez, A. M.; Munoz-Garcia, A. B.; Crescenzi, O.; Vazquez, E.; Pavone, M. *Phys. Chem. Chem. Phys.*, **2016**, *18*, 22203-22209.

356. Rosemeyer. H. *Chem. Biodivers.* **2004** *1*, 361.

357. Badenoch-Jones, P.; Buttery, P. J. *Biochem. J.* **1976**, *158*, 549.

358. Yang, J.; Yuan, Y.; Hua, Z. *Molecular Physics*, **114** *14*, 2157-2163.

359. Chen, D.; Wu, Q.; Wang, J.; Wang, Q.; Qiao, H. *Spectrochim. Acta, Part A* **2015**, *135*, 511.

360. Ma, M.; Bong, D. *Langmuir* **2011**, *27*, 8841-8853.

361. Kaur, S.; Sharma, P.; Wetmore, S. D. *Phys. Chem. Chem. Phys.* **2017**, *19*, 30762-30771.

362. Cafferty, B. J.; Fialho, D. M.; Khanam, J.; Krishnamurthy. R.; Hud, N. V. *Nat. Commun.* **2016**, *7*, 11328.

363. Fenton, M. C.; Fogarty, C.E.; Swift, J. A. *Langmuir* **2004**, *20*, 6524-6529.

364. Maiuolo, J.; Oppedisano, F.; Gratteri, S.; Muscoli, C.; Mollace, V. *International Journal of Cardiology* **2016**, *213*, 8-14.

365. Ejuh, G. W.; Ndjaka, J. M. B.; Tchangnwa Nya, F.; Ndukum, P. L.; Fonkem, C.; Tadjouteu Assatse, Y.; Yossa Kamsi, R. A. *Opt. Quantum Electron.* **2020**, *52*, 498.

366. Pacher, P.; Nivorozhkin, A.; Szabó, C. *Pharmacol Rev.* **2006**, *58*, 87-114.

367. Vega, C.; Abascal, J. L. F. *Phys. Chem. Chem. Phys.* **2011**, *13*, 19663-19688.

368. Jorgensen, W. L.; Maxwell, D. S.; Tirado-Rives, J. *J. Am. Chem. Soc.* **1996**, *118*, 11225-11236.

369. Gosika, M.; Velachi, V.; Cordeiro, M. N. D. S.; Maiti, P. K. *ACS Appl. Polym. Mater.* **2020**, *2*, 3587-3600.

370. Kim, H. S.; Brown, N. A.; Zauscher, S.; Yingling, Y. G. *Langmuir* **2020**, *36*, 931-938.

371. Gosika, M.; Mandal, T.; Maiti, P. K. *Langmuir* **2020**, *36*, 5492-5501.

372. Zhaom Y.; Chen, J.; Huang, D.; Su, J. *Langmuir* **2019**, *35*, 13442-13451.

373. Kommu, A.; Velachi, V.; Cordeiro, M. N. D. S.; Singh. J. K. *J. Phys. Chem. A* **2017**, *121*, 9320-9329.

374. Vilhena, J. G.; Rubio-Pereda, P.; Vellosillo, P.; Serena, P. A.; Pérez, R. *Langmuir* **2016**, *32*, 1742-1755.

375. Wu, E.; Coppens, M. O.; Garde, S. *Langmuir* **2015**, *31*, 1683-1692.

376. Roe, D. R.; Cheatham, T. E., III *J. Chem. Theory Comput.* **2013**, *9*, 3084-3095.

377. Lee, Q. S.; Carignano, M. A. *J. Phys. Chem. C* **2015**, *119*, 19415-19422.

378. Kamath, G.; Baker, G. A. *RSC Adv.* **2013**, *3*, 8197-8202.

379. Zabula, A. V.; Petrukhina, M. A. *Advances in Organometallic Chemistry* **2013**, *61*, 375-462.

380. Lee, Q. S.; Carignano, M. A. *J. Phys. Chem. C* **2015**, *119*, 19415-19422.

381. Xu, X.; Cai, L.; Zheng, X.; Xu, Q. *Phys. Chem. Chem. Phys.* **2017**, *19*, 16062-16070.

382. Monteiro, J. P.; Alves, M .G.; Oliveira, P. F.; Silva, B. M. *Molecules* **2016**, *21*, 974.

383. Yu, W.; Sisicd, L.; Haiyana, Y.; Jie, L. *RSC Adv.*, **2020**, *10*, 15328-15345.

384. Pinilla, E. M.; Astibia, A. O.; Franco, R. *Front Pharmacol.* **2015**, *6*, 30.

385. Baltaci, I.; Schulte, M. G. H.; Westphal, C. *J. Phys. Chem. C* **2020**, *124*, 23648-23656.

386. Lopes, J. H.; Ye, S.; Gostick, J. T.; Barralet, J. E.; Merle, G. *Langmuir* **2015**, *31*, 9718-9727.

387. Pattammattel, A.; Pande, P.; Kuttappan, D.; Puglia, M.; Basu, A. K.; Amalaradjou, M. A.; Kumar, C. V. *Langmuir* **2017**, *33*, 14184-14194.

388. Parab, A. D.; Dureja, R.; Rao, R.; Slocik, J. M.; Naik, R. R.; Walsh, T. R.; Knecht, M. R. *Langmuir* **2021**, *37*, 1152-1163.

389. Huang, X.; Li, Y.; Yin, X.; Tian, J.; Wu, W. *Langmuir* **2019**, *35*, 13833-13843.

390. Abedini, A.; Ludwig, T.; Zhang, Z.; Turner, C. H. *Langmuir* **2016**, *32*, 9982-9992.

391. Habib, T.; Devarajan, D. S.; Khabaz, F.; Parviz, D.; Achee, T. C.; Khare, R.; Green, M. J. *Langmuir* **2016**, *32*, 11591-11599.

392. Shinde, D. B.; Brenker, J.; Easton, C. D.; Tabor, R. F.; Neild, A.; Majumder, M. *Langmuir* **2016**, *32*, 3552-3559.

393. Notley. S. M. *Langmuir* **2012**, *28*, 14110-14113.

394. Sham, A. Y. W.; Notley. S. M. *Langmuir* **2014**, *30*, 2410-2418.

395. Zhang, Y.; Chan, C.; Li, Z.; Ma, J.; Meng, Q.; Zhi, C.; Sun, H.; Fan, J. *Langmuir* **2019**, *35*, 6179-6187.

List of Publications

1. Chattaraj, K. G.; Paul, S. Understanding of Structure and Thermodynamics of Melamine Association in Aqueous Solution From a Unified Theoretical and Experimental Approach *J. Chem. Info. and Mod.* **2018**, *58*, 1610-1624.

2. Chattaraj, K. G.; Paul, S. How does Temperature Modulate the Structural Properties of Aggregated Melamine in Aqueous Solution-An Answer from Classical Molecular Dynamics Simulation *J. Chem. Phys.* **2019**, *150*, 064501.

3. Chattaraj, K. G.; Paul, S. Underlying Mechanistic Insights Into the Structural Properties of Melamine and Uric Acid Complexes with Compositional Variation Under Ambient Conditions *J. Chem. Phys.* **2019**, *151*, 054503.

4. Chattaraj, K. G.; Paul, S. Inclusion of Theobromine Modifies Uric Acid Aggregation with Possible Changes in Melamine-Uric Acid Clusters Responsible for Kidney Stones *J. Phys. Chem. B* **2019**, *123*, 10483.

5. Chattaraj, K. G.; Paul, S. An Investigation on the Mechanisms of Synchronous Interaction of K_3Cit with Melamine and Uric Acid Avoids the Introduction of Large Clusters *J. Chem. Inf. Model.* **2020**, *60*, 4827.

6. Chattaraj, K. G.; Paul, R.; Paul, S. Switching of Self-Assembly to Solvent-Assisted Assembly of Molecular Motor: Unveiling the Mechanisms of Dynamic Control on Solvent Exchange *Langmuir* **2020**, *36*, 1773.

7. Paul, R.; Chattaraj, K. G.; Paul, S. The Role of Hydrotropes on Sparingly Soluble Drug Solubilization: An Insight from Molecular Dynamics Simulation and Experimental Perspectives *Langmuir* **2021**, *37*, 4745.

8. Chattaraj, K. G.; Paul, S. Underlying Mechanisms of Allopurinol in Eliminating Renal Toxicity Induced by Melamine-Uric Acid Complex Formation: A Computational Study *Chem. Res. Toxicol.* **2021**, *34*, 2054.

9. Chattaraj, K. G.; Paul, S. The Miscibility and Solubility of Uric Acid and Vitamin C in the Solution Phase and Their Structural Alignment in the Solid-Liquid Interface *Phys. Chem. Chem. Phys.* **2021**, *23*, 15169.

10. Chattaraj, K. G.; Paul, S. Appraising the Potency of Small Molecule Inhibitors and Their Graphene Surface-Mediated Organizational Attributes on Uric Acid-Melamine Clusters *Phys. Chem. Chem. Phys.* **2021**, DOI: 10.1039/D1CP03695E.

11. Chattaraj, K. G.; Paul, R.; Paul, S. Effect of Various Osmolytes on the Configurational Ensembles of Intrinsically Disordered Proteins Addressing Recent Advances in Computational Protocols (Manuscript under preparation).

Conferences Attended

1. Attended a conference "Sorbonne-JNCASR School for Advanced Computational Materials Science (SJSACMS 2018)" held at JNCASR, Bengaluru, India.

2. Presented a poster entitled "Understanding of Structure and Thermodynamics of Melamine Association in Aqueous Solution" in the conference "Frontier in Chemical Sciences (FICS-2018)" held at IIT Guwahati, Assam, India.

2. Presented a poster entitled "How Does Temperature Modulate the Structural Properties of Aggregated Melamine in Aqueous Solution-An Answer From Classical Molecular Dynamics Simulation" in the conference "Theoretical Chemistry Symposium (TCS-2019)" held at BITS Pilani, Pilani, Rajasthan, India.

4. Presented a poster entitled "Unraveling of the mechanisms of different small molecule inhibitors on melamine-uric acid clusters responsible for kidney stones" in the conference "Modern Approaches in Chemistry and Biology-2020 (MACB-2020)" held at JNCASR, Bengaluru, India.